Morten Amundsen

Proximity effects in superconducting hybrid structures with spin-dependent interactions

Doctoral thesis

Morten Amundsen

NTNU
Norwegian University of
Science and Technology

NTNU
Norwegian University of
Science and Technology

NTNU

Morten Amundsen

Proximity effects in superconducting hybrid structures with spin-dependent interactions

Thesis for the Degree of Philosophiae Doctor

Trondheim, September 2020

Norwegian University of Science and Technology
Faculty of Natural Sciences
Department of Physics

NTNU
Norwegian University of
Science and Technology

Abstract

When superconductors are contacted by other, non-superconducting materials, the latter may attain some of the properties of the former, and vice versa. This is the origin of a wealth of interesting phenomena. A striking example is the coexistence of superconductivity and ferromagnetism in superconductor-ferromagnet hybrid structures, which under certain conditions gives rise to dissipationless spin transport.

This work consists of 14 research papers, wherein a variety of superconducting hybrid structures are investigated theoretically using the quasiclassical Green function formalism. Focus is given to two- and three-dimensional geometries, the study of which has been made possible with the use of a numerical framework known as the finite element method.

Among several topics discussed are superconducting vortices nucleated in non-superconducting materials without the application of external magnetic fields. The generation of long ranged triplet superconducting correlations in superconductor-ferromagnet structures is also explored, either as generated by an inhomogeneity of the magnetisation, or by spin-orbit coupling.

Preface

This thesis is submitted in partial fulfilment of the requirements for the degree of philosophiae doctor at the Norwegian University of Science and Technology (NTNU). The research presented herein was conducted as part of a four-year graduate programme in physics. It also included 30 ECTS credits of coursework, and one year of undergraduate teaching assistant duties. My research has been supervised by Professor Jacob Linder, and Professor Asle Sudbø was my co-supervisor.

I have tried to make this thesis as self-contained as possible, and it has been my ambition to give a pedagogical introduction to the theoretical foundation underlying the research conducted. In particular, I have gone to significant lengths in reviewing the quasiclassical Green function formalism, on which the numerical framework relies. This has been a highly challenging undertaking, in which I have attempted to fill in details not discussed in the literature – often requiring a great deal of effort. It is my hope that this will be of use for others wanting to enter this field. In order to increase readability, I have intentionally interspersed technically difficult sections with simple and intuitive derivations and applications of results.

Much of my time has been devoted to software development. I have developed a numerical framework which has been quite successful, and has facilitated the study of a variety of superconducting hybrid structures. The bulk of the work is contained in the research papers, all of which are appended in their entirety at the end of the thesis. I have therefore elected not to review each paper individually, but instead provide summaries of a selection of papers, in a way which fits with the narrative of the thesis.

Acknowledgements

First and foremost I am grateful to my supervisor Jacob Linder. Your insightful guidance, work ethic and passion for physics has been a great source of inspiration for me, and our time working together has been an absolute joy. I would also like to thank my co-supervisor Asle Sudbø for interesting discussions, enjoyable conversations and fruitful collaborations.

I have had the pleasure of sharing an office with several fellow doctoral students, Vetle K. Risinggård, Jabir Ali Ouassou, Eirik H. Fyhn, and Lina G. Johnsen. Our discussions of physics have without doubt contributed to my growth as a researcher. My fondest memories are, however, of when we were just goofing off, which was always a welcome distraction, and a great deal of fun.

I would like to thank everyone at the Centre for Quantum Spintronics for four wonderful years, with special mention to Sol H. Jacobsen, Atousa G. Birgani, Arne Brataas, Karen-Elisabeth Sødahl, Akash Kamra, Alireza Qaiumzadeh, Roberto Troncoso, Arnau Sala, Sverre A. Gulbrandsen, Fredrik Nicolai Krogh, Haakon T. Simensen, Martin F. Jakobsen, Eirik Erlandsen, Håvard H. Haugen, Even Thingstad, Andreas T. G. Janssønn, Jørgen H. Qvist, Jeroen Danon, and Christoph Brüne. I am also grateful to Henning G. Hugdal for our collaborations, and for the weekly support groups when we were navigating the treacherous chasms of functional integral methods in condensed matter physics.

I have also had the privilege of working with several collaborators outside of NTNU, and would like to direct a special thank-you to Kavah Lahabi, Jan Aarts, Hadar Steinberg, Ayelet Zalic, Tom Dvir, Angelo DiBernardo, and Jack Sadleir for discussions through which I have learned a lot.

Finally, I wish to thank my family for unflinching support during my, somewhat unusual, change of career path. In particular, I am eternally grateful to my wife, Helene, for all her patience, understanding and sacrifice. Your gentle encouragement to always follow my dreams is the main reason I have come so far in achieving them. Я тебя люблю.

Contents

viii

Publications

I **M. Amundsen and J. Linder.**
General solution of 2D and 3D superconducting quasiclassical systems: coalescing vortices and nanoisland geometries.
Scientific Reports **6**, 22765 (2016).
DOI: 10/f8dmpk

II **J. Linder, M. Amundsen, and J. A. Ouassou.**
Microwave control of the superconducting proximity effect and minigap in magnetic and normal metals.
Scientific Reports **6**, 38739 (2016).
DOI: 10/gfgr9t

III **M. Amundsen, J. A. Ouassou, and J. Linder.**
Analytically determined topological phase diagram of the proximity-induced gap in diffusive n-terminal Josephson junctions.
Scientific Reports **7**, 40578 (2017).
DOI: 10/f9k69k

IV **M. Amundsen and J. Linder.**
Supercurrent vortex pinball via a triplet Cooper pair inverse Edelstein effect.
Physical Review B **96**, 064508 (2017).
DOI: 10/d2kv

V **J. Linder, M. Amundsen and V. Risinggård.**
Intrinsic superspin Hall current.
Physical Review B **96**, 094512 (2017).
DOI: 10/gc5rrm

VI   **K. Lahabi, M. Amundsen, J. A. Ouassou, E. Beukers, M. Pleijster, J. Linder, P. Alkemade, and J. Aarts.**
Controlling supercurrents and their spatial distribution in ferromagnets.
Nature Communications **8**, 2056 (2017).
DOI: 10/gcrhmz

VII   **M. Amundsen, J. A. Ouassou, and J. Linder.**
Field-Free Nucleation of Antivortices and Giant Vortices in Nonsuperconducting Materials.
Physical Review Letters **120**, 207001 (2018).
DOI: 10/gdg3kd

VIII   **M. Amundsen, H. G. Hugdal, A. Sudbø, and J. Linder.**
Vortex spin valve on a topological insulator.
Physical Review B **98**, 144505 (2018).
DOI: 10/d2k5

IX   **H. G. Hugdal, M. Amundsen, J. Linder, and A. Sudbø.**
Inverse proximity effect in s-wave and d-wave superconductors coupled to topological insulators.
Physical Review B **99**, 094505 (2019).
DOI: 10/gfwst7

X   **M. Amundsen and J. Linder.**
Quasiclassical theory for interfaces with spin-orbit coupling.
Physical Review B **100**, 064502 (2019).
DOI: 10/d2k6

XI   **J. R. Eskilt, M. Amundsen, N. Banerjee, and J. Linder.**
Long-ranged triplet supercurrent in a single in-plane ferromagnet with spin-orbit coupled contacts to superconductors.
Physical Review B **100**, 224519 (2019).
DOI: 10/d2k7

XII   **M. Amundsen and J. Linder.**
Spin accumulation induced by a singlet supercurrent.
arXiv: 2002.08367

XIII   **E. H. Fyhn, M. Amundsen, A. Zalic, T. Dvir, H. Steinberg, and J. Linder.**
Combined Zeeman and orbital effect on the Josephson effect in rippled graphene.
arXiv: 2004.07845

XIV   **A. Zalic, T. Dvir, E. H. Fyhn, M. Amundsen, J. Linder, and H. Steinberg.**
Zeeman and orbital effects in planar graphene-NbSe$_2$ Josephson junctions in a parallel magnetic field.
In preparation

Notation and conventions

This thesis will use SI units, with the convention that the elementary charge is defined as negative, $e = -|e|$. Scalars are typeset in an italic font, A, and vectors in bold italic, $\boldsymbol{A}$. Unit vectors along the Cartesian axes are denoted as $\boldsymbol{e}_x$, $\boldsymbol{e}_y$, and $\boldsymbol{e}_z$.

Many quantities encountered will have a matrix structure. For 2×2 matrices, no additional notation will be introduced, and any ambiguity will be clarified in the text. 4×4 matrices are denoted as $\hat{A}$, and 8×8 matrices as $\check{A}$. The unit matrix is thus denoted as I, $\hat{I}$, or $\check{I}$, depending on matrix size. Matrices can also be vectors, in which case they are given a bold font. An example is the Pauli matrix vector,

$$\boldsymbol{\sigma} = \sigma_x \boldsymbol{e}_x + \sigma_y \boldsymbol{e}_y + \sigma_z \boldsymbol{e}_z,$$

where σ_j, $j \in \{x, y, z\}$ are the conventional, 2×2 Pauli matrices. Block diagonal 4×4 may be expanded in a basis of ρ matrices, defined as

$$
\begin{aligned}
\rho_0 &= \begin{pmatrix} I & 0 \\ 0 & +I \end{pmatrix}, \ \rho_1 = \begin{pmatrix} \sigma_x & 0 \\ 0 & +\sigma_x \end{pmatrix}, \ \rho_2 = \begin{pmatrix} \sigma_y & 0 \\ 0 & +\sigma_y \end{pmatrix}, \ \rho_3 = \begin{pmatrix} \sigma_z & 0 \\ 0 & +\sigma_z \end{pmatrix}, \\
\rho_4 &= \begin{pmatrix} I & 0 \\ 0 & -I \end{pmatrix}, \ \rho_5 = \begin{pmatrix} \sigma_x & 0 \\ 0 & -\sigma_x \end{pmatrix}, \ \rho_6 = \begin{pmatrix} \sigma_y & 0 \\ 0 & -\sigma_y \end{pmatrix}, \ \rho_7 = \begin{pmatrix} \sigma_z & 0 \\ 0 & -\sigma_z \end{pmatrix}.
\end{aligned}
\tag{1}
$$

The Green function, a quantity to be discussed at length, depends on two position variables, $\boldsymbol{r}_1$ and $\boldsymbol{r}_2$, and two time variables, t_1 and t_2. This allows for several variations of the Fourier transform. Considered here are systems of sufficient size for the approximation $\frac{1}{\mathcal{V}} \sum_k \to \int \frac{d\boldsymbol{k}}{(2\pi)^3}$ to be reasonable, with $\mathcal{V}$ the system volume. The spatial Fourier transform is then defined as

$$
\begin{aligned}
G(\boldsymbol{k}_1, \boldsymbol{k}_2) &= \int d\boldsymbol{r}_1 \int d\boldsymbol{r}_2 \, G(\boldsymbol{r}_1, \boldsymbol{r}_2) e^{-i\boldsymbol{k}_1 \cdot \boldsymbol{r}_1 + i\boldsymbol{k}_2 \cdot \boldsymbol{r}_2}, \\
G(\boldsymbol{r}_1, \boldsymbol{r}_2) &= \int \frac{d\boldsymbol{k}_1}{(2\pi)^3} \int \frac{d\boldsymbol{k}_2}{(2\pi)^3} \, G(\boldsymbol{k}_1, \boldsymbol{k}_2) e^{i\boldsymbol{k}_1 \cdot \boldsymbol{r}_1 - i\boldsymbol{k}_2 \cdot \boldsymbol{r}_2}.
\end{aligned}
\tag{2}
$$

A different variation, which will be utilised frequently, is the *mixed representation*, where the Green function is Fourier transformed in the relative coordinate $\boldsymbol{r} = \boldsymbol{r}_1 - \boldsymbol{r}_2$, but not in the centre of mass coordinate, $\boldsymbol{R} = (\boldsymbol{r}_1 + \boldsymbol{r}_2)/2$, thus giving

$$G(\boldsymbol{k}, \boldsymbol{R}) = \int d\boldsymbol{r}\, G\left(\boldsymbol{r} + \frac{1}{2}\boldsymbol{R}, \boldsymbol{r} - \frac{1}{2}\boldsymbol{R}\right) e^{-i\boldsymbol{k}\cdot\boldsymbol{r}}, \qquad (3)$$

or alternatively,

$$G(\boldsymbol{k}, \boldsymbol{R}) = \int \frac{d\delta\boldsymbol{k}}{(2\pi)^3} G\left(\boldsymbol{k} + \frac{1}{2}\delta\boldsymbol{k}, \boldsymbol{k} - \frac{1}{2}\delta\boldsymbol{k}\right) e^{i\delta\boldsymbol{k}\cdot\boldsymbol{R}}, \qquad (4)$$

where $\delta\boldsymbol{k} = \boldsymbol{k}_1 - \boldsymbol{k}_2$, and $\boldsymbol{k} = (\boldsymbol{k}_1 + \boldsymbol{k}_2)/2$.

With one notable exception in Paper II, only stationary systems will be considered, for which the temporal Fourier transform in the relative coordinate $\tau = t_1 - t_2$ is defined as

$$\begin{aligned} G(\varepsilon) &= \int \frac{d\tau}{\hbar}\, G(\tau) e^{i\varepsilon\tau/\hbar}, \\ G(\tau) &= \int \frac{d\varepsilon}{2\pi}\, G(\varepsilon) e^{-i\varepsilon\tau/\hbar}. \end{aligned} \qquad (5)$$

Finally, a convolution G_C, given as

$$G_C(\boldsymbol{r}_1, \boldsymbol{r}_2) = \int d\boldsymbol{r}'\, G_A(\boldsymbol{r}_1, \boldsymbol{r}') G_B(\boldsymbol{r}', \boldsymbol{r}_2),$$

takes the following form in the mixed representation,

$$\begin{aligned} G_C(\boldsymbol{k}, \boldsymbol{R}) &= \exp\left[\frac{i}{2}\left(\nabla_R^A \cdot \nabla_k^B - \nabla_k^A \cdot \nabla_R^B\right)\right] G_A(\boldsymbol{k}, \boldsymbol{R}) G_B(\boldsymbol{k}, \boldsymbol{R}) \\ &\equiv G_A(\boldsymbol{k}, \boldsymbol{R}) \otimes G_B(\boldsymbol{k}, \boldsymbol{R}), \end{aligned} \qquad (6)$$

where $\otimes$ is called the *Moyal product* [1]

Chapter 1

Introduction

1.1   A brief history of modern computing

The 1880 United States national census was largely tabulated using manual methods, and, due to rapid population growth, took eight years to complete. Hence, in 1888 the U.S. Census Bureau – motivated, presumably, by the prospect of never having to go through that again – issued a competition for more efficient means of processing the collected data [2]. The winner of this competition was Herman Hollerith, with his eponymous *Hollerith machine* [3]. It worked by reading punch cards containing the required information, such as age and gender, and was much faster than previous methods, completing the 1890 census in about two years.

The first programmable digital computer was the ENIAC (*Electronic Numerical Integrator And Computer*), which appeared in 1945 [4]. Its ability to perform logical operations was constructed from circuitry containing more than 17 000 electronic switches made from vacuum tubes. These switches were much like the incandescent light bulb in that they were not very durable, and quite power hungry. They were, however, common components in electronic computers until they were replaced by the *transistor* [5]. Invented in 1947, the transistor brought about a new paradigm of electronics, in which semiconductors such as silicon took centre stage. It required much less power than the vacuum tube, had an, in principle, indefinite lifetime, and could be made much more compact. This made possible the creation of the integrated circuit in 1958-1959 [6].

The first microprocessor came in 1971, the Intel 4004 [7]. It consisted of 2300 transistors of the MOSFET type (*metal-oxide-semiconductor field-effect transistor*) [8]. A few years later, in 1974, it was realised that the

power density of a MOSFET does not depend upon its size [9]. Known as the *Dennard scaling law*, this led to a cascade of ever-smaller microprocessors containing increasingly large numbers of transistors, which in turn contributed to making faster processors. In 1975 Gordon Moore made the prediction that the number of transistors used in an integrated circuit would double every two years [10] (a modification of his 1965 prediction of annual doubling [11]). This is known as *Moore's law*, and has proven surprisingly accurate – even today.

Our insatiable need for more powerful electronics is, however, faced with some serious challenges. Cramming more and more components onto integrated circuits, to quote Ref. [11], requires them to be smaller and smaller. This, in turn, makes them more susceptible to damage due to *Joule heating*, i.e., the increase in temperature due to resistance as electric currents are passed through the circuitry. In fact, it is generally agreed that the Dennard scaling law broke down around 2006, due to current leakage and risk of thermal runaway processes [12, 13]. To circumvent this issue, the industry shifted towards multi-core processors, and increased parallelism, rather than increasing the operating speeds of individual processors. Thus far, this has been successful, and Moore's law is still clung to. Nevertheless, with state-of-the-art processors now making use of 7 nm transistors numbering in the billions, and with 3 nm transistors to be released in the immediate future [14], we are nearing the limits of what can physically be achieved. With device improvement by shrinking soon to be an unviable option, the race is on to find the next step in the technological evolution of electronics. One contender for that distinction is *spintronics* [15].

1.2   Spintronics

Electrons possess an intrinsic angular momentum known as *spin*. So named because of its resemblance to the classical picture of a sphere spinning on its own axis, the electron spin is a quantum number which can attain one of two possible values, "up" or "down", along a given quantisation axis. The electron spin is responsible for some materials being ferromagnetic, through a quantum mechanical effect known as the *exchange interaction*, to be discussed in Section 6.1.

While conventional electronics is concerned with the transport of charge, the field of spintronics aims to utilise the electron spin as information carriers. The binary nature of spin makes it a natural choice for use in digital electronics, where the fundamental building blocks of logic consist

of 0s and 1s. In fact, there are devices based on concepts from spintronics in common use today. One such example is the *hard disk drive* (HDD), a data storage device used in most computers. Its design was revolutionised by the effect of *giant magnetoresistance* (GMR) [16, 17], which is the observation that when a non-magnetic (normal) metal is sandwiched between two ferromagnets, and a voltage is applied across the trilayer, the resistance is different whether the two ferromagnets are aligned parallel or antiparallel, as illustrated in Fig. 1.1. Hence, a different current signal can be created by switching the magnetisation in one of the ferromagnets relative to the other, and this can be used to code information. Modern HDDs have transitioned to using *tunnel magnetoresistance* (TMR) [18], which is similar to GMR, except that the conducting normal metal is replaced with an insulator, so that the transfer of electrons occurs through tunnelling. Since the discovery of a significant magnetoresistance ratio of more than 10 % [19, 20] at room temperature, research into such tunnelling junctions has exploded [21–24], reaching a room temperature magnetoresistance ratio of 604 % [25]. This has allowed the industry to increase the storage capacity of HDDs almost fourfold over the past decade [26].
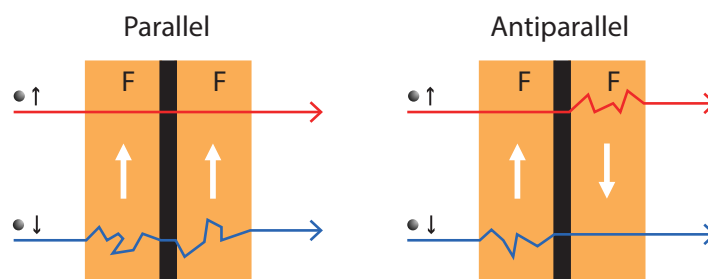
Figure 1.1: Illustration of the giant magnetoresistance (GMR). Stacks of ferromagnets are separated by non-magnetic interlayers. Particles with spins parallel to the magnetisation experience fewer collisions than particles with opposite spins, thereby giving a difference in the net resistance depending on whether the ferromagnetic layers are in a parallel or antiparallel configuration.

Another device in which TMR has found application is the MRAM (*Magnetoresistive Random Access Memory*) [27], where the orientation of the magnetisation is used to form computer memory. While conventional DRAM and SRAM (*Dynamic* and *Static Random Access Memory*, respectively) used in computers today, require continual access to power in order

to store information, MRAM is *non-volatile*, meaning that memory is retained even when the power is turned off. Storing information in an MRAM was initially prohibitively demanding of energy, as switching the relative magnetisation of the TMR was done using magnetic fields, which in turn required large currents. This problem was, however, solved by the use of *spin transfer torque* (STT) [28–30]. The so-called STT-MRAM works by using spin polarised currents to switch the relative magnetisation in the TMR [31, 32], and allowed for much more compact and energy efficient MRAMs, with state-of-the-art commercial STT-MRAM devices reaching 1 Gbit [33].
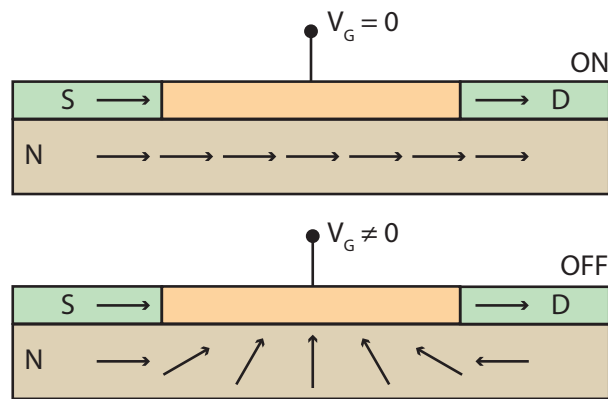
Figure 1.2: The Datta-Das transistor. A ferromagnetic source (S) and drain (D) is attached to a non-magnetic metal (N). A gate voltage V_G is used to manipulate the spin polarisation of the current in the normal metal through spin-orbit coupling. The arrows indicate the spin direction.

There is ongoing research to produce computational logic with spintronics. Utilising spin in a transistor was shown to be conceptually possible with the Datta-Das transistor [34]. It works by using ferromagnetic sources and drains, with a parallel magnetisation, inducing a spin polarisation in the current travelling between them. A gate voltage is used to introduce spin-orbit coupling into the intermediary normal metal layer, which creates a misalignment between the polarisation of the current and the magnetisation in the drain. The gate voltage therefore modifies the conductance of the system, thereby acting as a switch, as shown in Fig. 1.2. Although several experimental realisations of such a spin-based logic devices exist [35–38], more research is required to find a true replacement for the MOSFET.

The examples mentioned so far all have in common that the electron spin is used to add functionality, but they do nothing to mitigate Joule heating. Indeed, the central component in all devices mentioned is a charge current, which means that the same heating issues that occur in conventional electronics appear also in these cases. Several research avenues exists which attempt to solve this problem. For instance, the field of *spin insulatronics* aims to separate spin and charge transport by using magnons in either ferromagnetic or antiferromagnetic insulators as spin carriers, with promising results [39–43]. The focus of this thesis will, however, be on *superconducting spintronics* [44, 45].

1.3 Superconducting spintronics

When some materials, typically metals, are cooled to cryogenic temperatures, their electrical resistance may suddenly vanish completely. This phenomenon is known as *superconductivity*, and was discovered by Kammerlingh Onnes in 1911 [46]. Associated with the superconducting state is also the expulsion of applied magnetic fields, known as the *Meissner effect* [47]. These findings were explained theoretically in 1957 by the *BCS theory*, named after its discoverers Bardeen, Cooper and Schrieffer [48]. Clearly, the access to dissipationless currents would greatly reduce the power consumption of electronics. However, the temperatures required for the onset of superconductivity are prohibitively low – reaching at most 39 K at ambient pressure for conventional (BCS) superconductors [49, 50]. Better off are the so-called *high-temperature superconductors*, which do not conform to the BCS theory, where the record transition temperature of 138 K is held by the cuprates [51]. Creating room temperature superconductivity is therefore still very much an unsolved problem within condensed matter physics. On the other hand, close-to room temperature superconductivity is possible at increased pressure, as was recently shown to be the case for some hydride compounds [52, 53]. Unfortunately, with the required pressure being on the order of hundreds of gigapascals, these materials are hardly an option for everyday electronics.

Setting the challenge of sufficient cooling aside, a marriage of superconductivity and spintronics is an intriguing idea, in which the energy efficiency of the former complements the increased functionality of the latter. This prospect is, however, slightly overshadowed by the fact that ferromagnetic order and superconductivity are antagonistic properties [54, 55]. Superconductivity emerges due to the formation of bound states

between pairs of electrons, called *Cooper pairs* [56], which typically have opposite momentum and opposite spins (the spin singlet state). A magnetic field, on the other hand, will tend to align spins, and hence break up the Cooper pairs. Nevertheless, there exists materials which are both superconducting and ferromagnetic [57], such as the rare-earth compounds $HoMo_6S_8$ [58, 59] and $ErRh_4B_4$ [60, 61], where both types of ordering may be found in a small temperature region surrounding the superconductor-ferromagnet transition. In addition, coexistence of ferromagnetism and superconductivity has been observed in materials labelled as *ferromagnetic superconductors* [62], such as some uranium compounds [63–66]. These materials are likely examples of so-called *unconventional superconductors*, where the Cooper pairs form in an equal spin triplet configuration, which is thus insensitive to the spin splitting generated by the ferromagnetic ordering [67].

Apart from the above examples, which themselves involve rather exotic compounds, materials which intrinsically support both superconductivity and ferromagnetism are rare. Fortunately, there is an alternate approach, which is perhaps more promising with regards to future applications, where conventional metallic superconductors can be combined with common ferromagnetic materials and produce spin-dependent superconducting effects – *the proximity effect* [68–71]. This phenomenon, which will be discussed in Chapters 5 and 6, occurs when a superconductor is contacted by a non-superconducting material. In this case, the superconducting correlations in the former may leak into the latter, and thus influence its properties.

The proximity effect is the origin of interesting phenomena in hybrid structures of ferromagnets and superconductors. In particular, at the interface between two such materials, the spin splitting of the energy bands introduces a finite momentum to the Cooper pairs, giving the superconducting correlations an oscillatory decay into the ferromagnet [72–74]. However, for a homogeneous ferromagnet, the decay is very sharp, due to the aforementioned incompatibility of superconductivity and ferromagnetism. What saves the proximity effect as a viable candidate for superconducting spintronics is what happens when a superconductor is attached to, for instance, an inhomogeneous ferromagnet. As is elaborated in Chapter 6, equal spin triplet superconducting correlations may then be generated in the ferromagnet – even if the sourcing superconductor is of the conventional singlet type [75–77]. Such triplets, when their spins are aligned parallel to the magnetisation in the ferromagnet, do not experience

the pair breaking effect of the spin splitting, and may therefore exhibit much longer decay lengths. This has earned them the name of *long ranged triplet superconducting correlations*. The first experimental verification of this effect came in 2006, when a Josephson effect (see Section 5.2) was measured in CrO_2, which is a half metal, and thus cannot allow a singlet proximity effect, leaving triplets as the only possible explanation [78]. Shortly thereafter, a different breakthrough came with the observation of conductance oscillations in a ferromagnetic Josephson junction, using holmium as the ferromagnetic interlayer [79]. Since the magnetisation in holmium is intrinsically inhomogeneous, having a conical structure, this was another indication of the presence of long ranged triplets. In 2010 a series of other experimental works appeared, providing further evidence of the effect [80–83].

The requirement of inhomogeneous magnetisation for the appearance of long ranged triplets is challenging for device manufacture. Ferromagnets which are intrinsically inhomogeneous (such as holmium) are rare, and artificially generated spatial variations through layers of homogeneous ferromagnets are difficult to control. However, spin-orbit coupling provides an alternative route. Homogeneous ferromagnets in contact with materials with strong spin-orbit coupling, such a platinum or tungsten, results in the necessary spin-mixing to induce long ranged triplets, as was predicted in several works [84–88], and recently verified experimentally [89, 90].

The field of superconducting spintronics is quickly evolving towards a level where it may find use in practical applications [91]. For instance, a memory cell using a ferromagnetic Josephson junction, referred to as a JM-RAM, has been proposed [92], and a very recent experimental work reported an increase in magnetoresistance by three orders of magnitude by the onset of superconductivity in a ferromagnet-superconductor bilayer with interfacial spin-orbit coupling [93]. A three order of magnitude increase with respect to the normal state has also been observed in the inverse spin Hall effect of superconducting NbN [94]. Another observation with great potential is that of giant thermoelectric effects in superconductor-ferromagnet structures, which can exceed that of normal state equivalents [95, 96]. Nevertheless, there is still much to explore in this fascinating topic. This thesis will begin by a thorough derivation of the quasiclassical Green function formalism in Chapter 2, which has been very successful in describing superconducting hybrid structures. In Chapter 3 an introduction to superconductivity is given. After a brief excursion into numerical

solution methods in Chapter 4, the proximity effect in spin-independent systems is studied in some detail in Chapter 5. Finally, superconductor-ferromagnet hybrid structures are tackled in Chapter 6.

Chapter 2

Green Function Formalism

Green functions is the most powerful computational tool for use in condensed matter physics. With it, all observables of interest, such as the current density or density of states, can be calculated. One might expect that such a general mathematical tool is complicated and unwieldy in its use, and indeed, Green functions are very much the artillery in the arsenal of analytical tools. With but a few exceptions, it is not possible to find an exact expression for the Green function of a given process. One must therefore rely on approximations.

In this chapter, an attempt will be made at giving a pedagogical introduction to the Green function formalism. Furthermore, a very successful approximation scheme – particularly for use in superconductivity – will be introduced, namely the quasiclassical approximation.

2.1 Definition of the Green function

Consider the operators $c_v^\dagger$ and c_v, which create and annihilate a particle in the state associated with the set of quantum numbers v, respectively. In the following, only fermions will be discussed, and so these operators satisfy the following relations,

$$\left\{ c_v^\dagger \, , \, c_{v'} \right\} = \delta_{vv'} \quad , \quad \left\{ c_v \, , \, c_{v'} \right\} = \left\{ c_v^\dagger \, , \, c_{v'}^\dagger \right\} = 0. \tag{2.1}$$

To study bosons, one needs only to replace the anticommutators with commutators in Eq. (2.1). From the two operators, a pair of *field operators* may be defined by changing to a position basis,

$$\psi_\sigma^\dagger(\boldsymbol{r}) = \sum_v \langle v | \boldsymbol{r} \rangle \, c_{v\sigma}^\dagger \quad , \quad \psi_\sigma(\boldsymbol{r}) = \sum_v \langle \boldsymbol{r} | v \rangle \, c_{v\sigma}, \tag{2.2}$$

where the spin quantum number σ is displayed explicitly. Note that the field operators have unit $\text{m}^{-3/2}$. The physical interpretation of $\psi_\sigma^\dagger(\boldsymbol{r})$ and $\psi_\sigma(\boldsymbol{r})$ is that they create and annihilate a particle with spin σ at the position $\boldsymbol{r}$. Since the particle is a fermion, they satisfy relations similar to Eq. (2.1),

$$\left\{\psi_\sigma^\dagger(\boldsymbol{r})\,,\,\psi_{\sigma'}(\boldsymbol{r}')\right\} = \delta_{\sigma\sigma'}\delta(\boldsymbol{r}-\boldsymbol{r}'), \tag{2.3}$$

$$\left\{\psi_\sigma(\boldsymbol{r})\,,\,\psi_{\sigma'}^\dagger(\boldsymbol{r}')\right\} = 0, \tag{2.4}$$

$$\left\{\psi_\sigma^\dagger(\boldsymbol{r})\,,\,\psi_{\sigma'}^\dagger(\boldsymbol{r}')\right\} = 0. \tag{2.5}$$

In the Heisenberg picture, these operators are time dependent, and their time evolution is governed by the Heisenberg equation,

$$i\hbar\frac{\partial\psi_\sigma}{\partial t} = \left[H,\psi_\sigma\right], \tag{2.6}$$

$$i\hbar\frac{\partial\psi_\sigma^\dagger}{\partial t} = \left[H,\psi_\sigma^\dagger\right], \tag{2.7}$$

where H is the second-quantised Hamilton operator.

The Green function is defined as a correlation function between two field operators. Several versions exist, and the one with perhaps the easiest interpretation is the *time-ordered Green function*,

$$G_{\sigma\sigma'}(\boldsymbol{r},t;\boldsymbol{r}',t') = -i\left\langle \mathscr{T}\psi_\sigma(\boldsymbol{r},t)\psi_{\sigma'}^\dagger(\boldsymbol{r}',t')\right\rangle. \tag{2.8}$$

The angular brackets symbolise quantum and thermal averaging, which in equilibrium may be performed in the grand canonical ensemble, $\langle A\rangle = Z^{-1}\text{Tr}\left[e^{-\beta(H-\mu N)}A\right]$, where $Z = \text{Tr}\left[e^{-\beta(H-\mu N)}\right]$, μ is the chemical potential and N is the number operator. The parameter $\beta = 1/k_\text{B}T$, where T is the temperature and k_B is the Boltzmann constant. Finally, the time ordering operator $\mathscr{T}$ ensures that the field operators act in chronological order from right to left. In other words, $\mathscr{T}$ does nothing if $t > t'$, otherwise it switches the position of $\psi_\sigma^\dagger$ and $\psi_{\sigma'}$, incurring in the process a minus sign due to the fermion nature of the field operators. Assuming, then, that $t > t'$, the interpretation of $G_{\sigma\sigma'}$ is clear. It is the probability amplitude for finding a particle with spin σ at position $\boldsymbol{r}$ at time t, provided that at time t' a particle with spin σ' is inserted in position $\boldsymbol{r}'$. Colloquially it can be said that the particle propagates from $\boldsymbol{r}'$ to $\boldsymbol{r}$, although this is not entirely correct due to the particles being indistinguishable.

Other useful flavours of Green functions are the *retarded* and *advanced* variations, G^R and G^A, defined as,

$$G^R_{\sigma\sigma'}(\boldsymbol{r}, t; \boldsymbol{r}', t') = -i\theta(t - t')\left\langle \left\{ \psi_\sigma(\boldsymbol{r}, t), \psi^\dagger_{\sigma'}(\boldsymbol{r}', t') \right\} \right\rangle, \tag{2.9}$$

$$G^A_{\sigma\sigma'}(\boldsymbol{r}, t; \boldsymbol{r}', t') = +i\theta(t' - t)\left\langle \left\{ \psi_\sigma(\boldsymbol{r}, t), \psi^\dagger_{\sigma'}(\boldsymbol{r}', t') \right\} \right\rangle, \tag{2.10}$$

which describe processes that are causal and anti-causal, respectively. Notice that they are related through the transformation

$$G^A_{\sigma\sigma'}(\boldsymbol{r}, t; \boldsymbol{r}', t') = \left[G^R_{\sigma'\sigma}(\boldsymbol{r}', t'; \boldsymbol{r}, t) \right]^*, \tag{2.11}$$

and hence it is seldom necessary to discuss G^A explicitly.

As will become clear when considering superconducting systems in Chapter 3, it is advantageous to write the field operators as a vector describing both particles and holes, which is known as Nambu⊗spin space [97],

$$\Psi(\boldsymbol{r}, t) = \begin{pmatrix} \psi_\uparrow(\boldsymbol{r}, t) & \psi_\downarrow(\boldsymbol{r}, t) & \psi^\dagger_\uparrow(\boldsymbol{r}, t) & \psi^\dagger_\downarrow(\boldsymbol{r}, t) \end{pmatrix}^T \tag{2.12}$$

To maintain a familiar form of the anticommutation relation, the anticommutator in Nambu⊗spin space is defined as,

$$\{A, B\} = AB + \left(B^T A^T \right)^T, \tag{2.13}$$

with a similar definition for the commutator. The anticommutation relation for Ψ then becomes

$$\left\{ \Psi(\boldsymbol{r}, t), \Psi^\dagger(\boldsymbol{r}', t) \right\} = \hat{I}\delta(\boldsymbol{r} - \boldsymbol{r}'), \tag{2.14}$$

where $\hat{I}$ is the identity matrix in Nambu⊗spin space. The Green functions now become 4×4 matrices,

$$\hat{G}^R(\boldsymbol{r}, t; \boldsymbol{r}', t') = -i\theta(t - t')\hat{\rho}_4 \left\langle \left\{ \Psi(\boldsymbol{r}, t), \Psi^\dagger(\boldsymbol{r}', t') \right\} \right\rangle, \tag{2.15}$$

$$\hat{G}^A(\boldsymbol{r}, t; \boldsymbol{r}', t') = +i\theta(t' - t)\hat{\rho}_4 \left\langle \left\{ \Psi(\boldsymbol{r}, t), \Psi^\dagger(\boldsymbol{r}', t') \right\} \right\rangle, \tag{2.16}$$

and their matrix structure takes the form,

$$\hat{G}^X(\boldsymbol{r}, t; \boldsymbol{r}', t') = \begin{pmatrix} G^X(\boldsymbol{r}, t; \boldsymbol{r}', t) & F^X(\boldsymbol{r}, t; \boldsymbol{r}', t') \\ \left[F^X(\boldsymbol{r}, t; \boldsymbol{r}', t') \right]^* & \left[G^X(\boldsymbol{r}, t; \boldsymbol{r}', t') \right]^* \end{pmatrix}, \tag{2.17}$$

where G^X and F^X are 2×2 matrices in spin space, and $X \in \{R, A\}$. F^X are known as the *anomalous Green functions*.

2.2   The equation of motion

In order to compute the Green functions, it is necessary to find their equations of motion. For the retarded Green function, this is done by differentiating, e.g., with respect to the time coordinate t, and applying Eq. (2.6). For a given Hamiltonian $\hat{H}$ in Nambu⊗spin space, it is thus found that

$$\left[i\hbar\hat{\rho}_4 \frac{\partial}{\partial t} - \hat{H}(\boldsymbol{r}) \right] \hat{G}^R(\boldsymbol{r}, t; \boldsymbol{r}', t') = \hbar\hat{I}\delta(t - t')\delta(\boldsymbol{r} - \boldsymbol{r}'). \qquad (2.18)$$

If the Hamiltonian is independent of time, as will always be the case for the systems considered here (with the exception of Paper II), Eq. (2.18) may be Fourier transformed in the relative time coordinate $t - t'$, which gives

$$\left[(\varepsilon + i\delta)\hat{\rho}_4 - \hat{H}(\boldsymbol{r}) \right] \hat{G}^R(\boldsymbol{r}, \boldsymbol{r}'; \varepsilon) = \hat{I}\delta(\boldsymbol{r} - \boldsymbol{r}'), \qquad (2.19)$$

Note the convergence factor δ, which is necessary to ensure a well-defined temporal Fourier transform, and is chosen so that $\check{G}^R = 0$ for $t - t' < 0$, as is consistent with the definition of the retarded Green function. A similar equation may be found by differentiation with respect to t',

$$\hat{G}^R(\boldsymbol{r}, \boldsymbol{r}'; \varepsilon) \left[(\varepsilon + i\delta)\hat{\rho}_4 - \hat{H}(\boldsymbol{r}') \right] = \hat{I}\delta(\boldsymbol{r} - \boldsymbol{r}'), \qquad (2.20)$$

where any operators in $\hat{H}$ must act towards the left. The same steps may be repeated to produce equations of motion for the advanced component $\hat{G}^A$, but with $\delta \to -\delta$. From now on, δ will be assumed contained in ε for brevity.

Free electron gas

The simplest example where an analytical expression for the Green function can be found is the free electron gas. In this case the Hamiltonian is given as

$$\hat{H} = -\left[\frac{\hbar^2}{2m}\nabla^2 + \mu \right] \hat{I}, \qquad (2.21)$$

where μ is the chemical potential. The equation of motion for $\hat{G}^R$ therefore takes the form,

$$\left[\varepsilon\hat{\rho}_4 + \left(\frac{\hbar^2}{2m}\nabla^2 + \mu \right)\hat{I} \right] \hat{G}^R(\boldsymbol{r}, \boldsymbol{r}', \varepsilon) = \hat{I}\delta(\boldsymbol{r} - \boldsymbol{r}'). \qquad (2.22)$$

This system has translation invariance, and hence may be Fourier transformed in the relative coordinate $\boldsymbol{r} - \boldsymbol{r}'$, which gives immediately

$$\hat{G}^R(\boldsymbol{k}, \varepsilon) = \left[\varepsilon \hat{\rho}_4 - \left(\frac{\hbar^2 \boldsymbol{k}^2}{2m} - \mu \right) \hat{I} \right]^{-1}. \tag{2.23}$$

2.3 Nonequilibrium Green functions

It is not always straightforward to compute the average in Eq. (2.8). Typically, a perturbation $V(t)$ from a known state H_0 is assumed to be switched on at some time t_0. It is convenient to treat this problem in the interaction picture, where the field operators evolve in time as

$$\psi_I(t) = S(t, t')\psi_I(t'),$$

where $S(t, t')$ is the S matrix [98],

$$S(t, t_0) = \begin{cases} \mathcal{T} \exp\left[-\frac{i}{\hbar} \int_{t_0}^{t} V(t') \, dt' \right] & t > t_0 \\ \tilde{\mathcal{T}} \exp\left[-\frac{i}{\hbar} \int_{t_0}^{t} V(t') \, dt' \right] & t < t_0 \end{cases} \tag{2.24}$$

and $\tilde{\mathcal{T}}$ is the anti-time ordering operator. They are related to the field operators in the Heisenberg picture via

$$\psi(t) = S(t_0, t)\psi_I(t)S(t, t_0). \tag{2.25}$$

Notice that the interaction picture agrees with the Heisenberg picture at $t = t_0$. The time ordered product in Eq. (2.8) may thus be written as

$$\begin{aligned} \mathcal{T}\psi(t_1)\psi^\dagger(t_2) &= \theta(t_1 - t_2)\psi(t_1)\psi^\dagger(t_2) - \theta(t_2 - t_1)\psi^\dagger(t_2)\psi(t_1) \\ &= \theta(t_1 - t_2)S(t_0, t_1)\psi_I(t_1)S(t_1, t_2)\psi_I^\dagger(t_2)S(t_2, t_0) \\ &\quad - \theta(t_2 - t_1)S(t_0, t_2)\psi_I^\dagger(t_2)S(t_2, t_1)\psi_I(t_1)S(t_1, t_0) \\ &= S(t_0, t_{\max})\mathcal{T}\left[S(t_{\max}, t_0)\psi_I(t_1)\psi_I^\dagger(t_2) \right], \end{aligned}$$

where $t_{\max} = \max(t_1, t_2)$. It has been used that V within the second quantisation formalism typically consists of products of an even number of fermion operators, and hence, $S(t_1, t_2)$ commutes with ψ and $\psi^\dagger$ within the time ordering bracket. Notice that, as seen in Eq. (2.24), the fermion operators in $S(t_1, t_2)$ are applied at times $t \in [t_1, t_2]$, which constrains its time ordering properties.

At a temperature $T = 0$, Eq. (2.8) is simply a quantum mechanical average over the ground state, ignoring for the moment the spin and position variables,

$$G(t_1; t_2) = -i \langle \psi_I(t_0)| S(t_0, t_{\max}) \mathcal{T} \left[S(t_{\max}, t_0) \psi_I(t_1) \psi_I^\dagger(t_2) \right] |\psi_I(t_0)\rangle .$$

The ground state $|\psi_I(t_0)\rangle$ is, however, unknown due to the presence of $V(t)$. Since no information about the system prior to t_0 is of interest, it can be assumed that the perturbation is switched on adiabatically, slowly increasing from zero at $t = -\infty$, reaching its full value at $t = t_0$. Similarly, the perturbation may be switched off adiabatically at times $t > t_{\max}$, so that it once again is zero at $t = \infty$. The ground state at $t = -\infty$, $|\psi_I(-\infty)\rangle$, is the ground state of H_0, which is known. Furthermore, since the ground state is non-degenerate, and the Hamiltonian is given by H_0 at $t = \infty$ as well, $|\psi_I(\infty)\rangle$ can only differ from $|\psi_I(-\infty)\rangle$ by a phase factor $e^{i\phi}$. Hence,

$$G(t_1; t_2) = -i \frac{\langle \psi_I(-\infty)| \mathcal{T} \left[S(\infty, -\infty) \psi_I(t_1) \psi_I^\dagger(t_2) \right] |\psi_I(-\infty)\rangle}{\langle \psi_I(-\infty)| S(\infty, -\infty) |\psi_I(-\infty)\rangle}, \qquad (2.26)$$

where it has been used that

$$e^{i\phi} = \langle \psi_I(-\infty)|\psi_I(\infty)\rangle = \langle \psi_I(-\infty)|S(\infty, -\infty)|\psi_I(-\infty)\rangle .$$

This procedure does not work at finite temperatures $T > 0$. In that case, the thermal average of Eq. (2.8) involves all states, not just the ground state, and hence non-degeneracy cannot be guaranteed. That particular issue can be circumvented by using imaginary time (or Matsubara frequencies), in which case the Green function becomes periodic [99]. Such trickery is not possible for nonequilibrium systems, however, where $|\psi_I(\infty)\rangle$ generally cannot be related to $|\psi_I(-\infty)\rangle$. This motivates the introduction of a different formalism. It turns out that it is possible to define real-time Green functions which are valid at both finite temperatures and out of equilibrium. This can be done by allowing the time dependence to evolve – not along the conventional time axis – but along a time contour which eventually doubles back on itself at some time τ^*, as illustrated in Fig. 2.1. In this way, only the ground state at $|\psi_I(-\infty)\rangle$ is required.
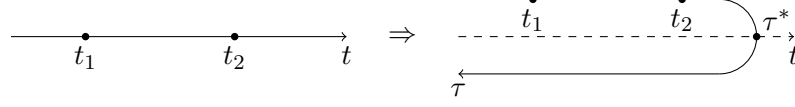
Figure 2.1: Illustration of the time contour along which the contour ordered Green function G_c evolves.

.

A contour ordered Green function may then be defined as

$$G_c(t_1; t_2) = -i \left\langle \mathcal{T}_c \psi(t_1) \psi^\dagger(t_2) \right\rangle, \tag{2.27}$$

where $\mathcal{T}_c$ is an operator which orders the fermion operators along the contour in Fig. 2.1. Note that depending on where t_1 and t_2 are located relative to the contour turning point τ^*, several species of Green functions may be defined,

$$G_c(t_1, t_2) = \begin{cases} G^T(t_1, t_2) & t_1, t_2 < \tau^* \\ G^<(t_1, t_2) & t_1 < \tau^*, \ t_2 > \tau^* \\ G^>(t_1, t_2) & t_1 > \tau^*, \ t_2 < \tau^* \\ G^{\tilde{T}}(t_1, t_2) & t_1, t_2 > \tau^* \end{cases} \tag{2.28}$$

where G^T and $G^{\tilde{T}}$ are the time ordered, and anti-time ordered Green functions, respectively. The former is defined in Eq. (2.8). Furthermore

$$G^<(t_1, t_2) = + i \left\langle \psi^\dagger(t_2) \psi(t_1) \right\rangle \tag{2.29}$$

$$G^>(t_1, t_2) = - i \left\langle \psi(t_1) \psi^\dagger(t_2) \right\rangle \tag{2.30}$$

Note that these Green functions are not linearly independent, but are related through a variety of identities,

$$G^T + G^{\tilde{T}} = G^> + G^<$$
$$G^R = \theta(t_1 - t_2) \left(G^< - G^> \right) = G^T - G^< = G^> - G^{\tilde{T}},$$
$$G^A = \theta(t_2 - t_1) \left(G^> - G^< \right) = G^T - G^> = G^< - G^{\tilde{T}},$$

as is seen by inspecting Eq. (2.9) and Eq. (2.10). Different variations of the time contour are possible. Transient behaviour from an initial time t_0 may be studied via the *Kadanoff-Baym contour* [100], shown in Fig. 2.2a). Only stationary systems are of concern here, however, in which case it is

more convenient to let $t_0 \to -\infty$ and $\tau^* \to \infty$, as shown in Fig. 2.2b). This is known as the *Keldysh contour* [101].
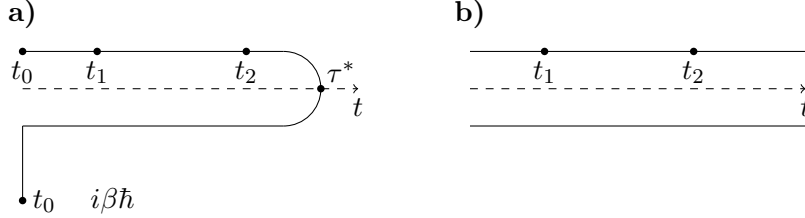

Figure 2.2: Different variations of the time contour. In a) is shown the Kadanoff-Baym contour, and in b) the Keldysh contour.

Special routines are required in order to perform convolutions along the Keldysh contour $\mathscr{C}$. Consider a convolution

$$C^<(t_1, t_2) = \int_{\mathscr{C}} d\tau \, A(t_1, \tau) B(\tau, t_2). \tag{2.31}$$

t_1 should in this case lie on the upper branch of Fig. 2.2, and t_2 on the lower. Integrating over the two branches separately gives

$$
\begin{aligned}
C^<(t_1, t_2) &= \int_{-\infty}^{\infty} d\tau \, A(t_1, \tau) B(\tau, t_2) + \int_{\infty}^{-\infty} d\tau \, A(t_1, \tau) B(\tau, t_2) \\
&= \int_{-\infty}^{\infty} d\tau \left[A^T(t_1, \tau) B^<(\tau, t_2) - A^<(t_1, \tau) B^{\bar{T}}(\tau, t_2) \right],
\end{aligned}
$$

or equivalently,

$$C^<(t_1, t_2) = \int_{-\infty}^{\infty} d\tau \left[A^R(t_1, \tau) B^<(\tau, t_2) + A^<(t_1, \tau) B^A(\tau, t_2) \right]. \tag{2.32}$$

Similarly,

$$C^>(t_1, t_2) = \int_{-\infty}^{\infty} d\tau \left[A^R(t_1, \tau) B^>(\tau, t_2) + A^>(t_1, \tau) B^A(\tau, t_2) \right], \tag{2.33}$$

$$C^R(t_1, t_2) = \int_{-\infty}^{\infty} d\tau \, A^R(t_1, \tau) B^R(\tau, t_2), \tag{2.34}$$

$$C^A(t_1, t_2) = \int_{-\infty}^{\infty} d\tau \, A^A(t_1, \tau) B^A(\tau, t_2). \tag{2.35}$$

Eqs. (2.32) to (2.35) are the *Langreth rules* [102], which convert contour integrals to conventional integrals along the time axis.

Typically, an additional Green function is defined,

$$G^K_{\sigma\sigma'}(\boldsymbol{r}, t; \boldsymbol{r}', t') = -i \left\langle \left[\psi_\sigma(\boldsymbol{r}, t) , \psi^\dagger_{\sigma'}(\boldsymbol{r}', t') \right] \right\rangle, \qquad (2.36)$$

which is known as the *Keldysh Green function*. It satisfies $G^K = G^> + G^<$, and hence its Langreth rule is

$$C^K(t_1, t_2) = \int_{-\infty}^{\infty} d\tau \left[A^R(t_1, \tau) B^K(\tau, t_2) + A^K(t_1, \tau) B^A(\tau, t_2) \right]. \qquad (2.37)$$

Eqs. (2.34), (2.35) and (2.37) can be made more compact by introducing a matrix structure. Including the structure in Nambu⊗spin space, the resulting Green function becomes an 8×8 matrix of the form

$$\check{G} = \begin{pmatrix} \hat{G}^R & \hat{G}^K \\ 0 & \hat{G}^A \end{pmatrix}. \qquad (2.38)$$

In this way, the Langreth rules are automatically incorporated into the matrix product, so that one only needs to worry about conventional time coordinates.

G^K for a stationary system in equilibrium

For a stationary system in equilibrium, the quantum and thermal average of two operators satisfies the identity, with $\bar{H} = H - \mu N$,

$$
\begin{aligned}
\langle A(t)B(0) \rangle &= Z^{-1}\mathrm{Tr}\left[e^{-\beta\bar{H}} A(t)B(0) \right] \\
&= Z^{-1}\mathrm{Tr}\left[e^{-\beta\bar{H}} e^{i\bar{H}t/\hbar} A(0) e^{-i\bar{H}t/\hbar} B(0) \right] \\
&= Z^{-1}\mathrm{Tr}\left[B(0) e^{-\beta\bar{H}} e^{i\bar{H}t/\hbar} A(0) e^{-i\bar{H}t/\hbar} e^{\beta\bar{H}} e^{-\beta\bar{H}} \right] \\
&= \left\langle B(0) A(t + i\beta\hbar) \right\rangle.
\end{aligned}
$$

Applying this to Eq. (2.36), it is clear that G^K can be expressed as

$$G^K(t, 0) = G^>(t, 0) - G^>(t + i\beta\hbar, 0). \qquad (2.39)$$

By Fourier transforming one then gets

$$G^K(\varepsilon) = \left(1 - e^{-\beta\varepsilon} \right) G^>(\varepsilon). \qquad (2.40)$$

Furthermore,

$$G^R(t, 0) - G^A(t, 0) = -i \left\langle \left\{ \psi(t), \psi^\dagger(0) \right\} \right\rangle = G^>(t, 0) + G^>(t + i\beta\hbar, 0), \quad (2.41)$$

which means that an expression for $G^>$ is found to be

$$G^>(\varepsilon) = \left(1 + e^{-\beta\varepsilon}\right)^{-1} \left(G^R(\varepsilon) - G^A(\varepsilon)\right). \qquad (2.42)$$

Combining Eqs. (2.40) and (2.42) thus gives

$$G^K(\varepsilon) = \left(G^R(\varepsilon) - G^A(\varepsilon)\right) \tanh\frac{\beta\varepsilon}{2}. \qquad (2.43)$$

The retarded and advanced Green functions are only concerned with the spectral properties of the system, and the quantity $G^R - G^A$ is a measure of dissipation. The Keldysh Green function, on the other hand, includes the quasiparticle occupation, and thus expresses fluctuations. Hence, Eq. (2.43) is an incarnation of the *fluctuation-dissipation theorem* [103].

2.4   The quasiclassical approximation

The quasiclassical approximation is a technique which can greatly simplify the calculation of Green functions. It requires the existence of a high energy scale in the system, such as the Fermi energy, E_F, compared to which all other energy scales involved are small. This also implies that the spatial variations of any external perturbations included in the theory must be small with respect to the Fermi wavelength λ_F. From Eq. (2.23) it can be seen that the Green function is large if its denominator is small. In other words, if both the quasiparticle energy ε and the term $\hbar^2 \boldsymbol{k}^2/2m - \mu$ is smaller than some arbitrarily chosen small cut-off energy E_c, then $\check{G}$ is at least of the order E_c^{-1}, and is thus a large quantity [104]. With $\mu = E_F = \hbar^2 k_F^2/2m$, it is seen that this occurs for particle momenta close to the Fermi momentum $\hbar k_F$, which is intuitively reasonable; all of the low-energy processes should take place near the Fermi level. Furthermore, at high energies, the kinetic energy dominates all other self-energies (which are small by assumption), and the system approaches a free electron gas. The low-energy regime, therefore, encompasses most of the interesting physics. In order to develop an approximation scheme it is practical to separate the low-energy part of the Green function from the high-energy part [105],

$$\check{G} = \check{G}_l + \check{G}_h \qquad (2.44)$$

where the indices l and h indicate that the corresponding Green function is nonzero only in the low and high-energy regimes, respectively,

$$\check{G} = \begin{cases} \check{G}_l, & |k - k_{\mathrm{F}}| < \delta k \\ \check{G}_h, & \text{otherwise} \end{cases}, \tag{2.45}$$

where $\delta k = \sqrt{2mE_c/\hbar^2}$. Note that $\check{G}_l$ is much larger than $\check{G}_h$, and as a book-keeping device, the size of $\check{G}_l$ can be said to be of order $\alpha^{-1} > (E_c/E_{\mathrm{F}})^{-1}$, whereas $\check{G}_h$ is of order $\alpha^0 = 1$.

Consider next the introduction of a potential $\check{V}(\boldsymbol{r})$ with an arbitrary matrix structure, which has a characteristic size of $V/E_{\mathrm{F}} \sim \alpha$, and is slowly varying in space with a characteristic wave number q. The equation of motion now takes the form

$$\left[\varepsilon \check{\rho}_4 + \left(\frac{\hbar^2}{2m} \nabla^2 + \mu \right) \check{I} - \check{V}(\boldsymbol{r}) \right] \check{G}(\boldsymbol{r}, \boldsymbol{r}', \varepsilon) = \check{I} \delta(\boldsymbol{r} - \boldsymbol{r}'). \tag{2.46}$$

To proceed, it is convenient to transform to the mixed representation, where one gets

$$\left[\varepsilon \hat{\rho}_4 + \left(\mu - \frac{\hbar^2 \boldsymbol{k}^2}{2m} + \frac{i\hbar^2}{2m} \boldsymbol{k} \cdot \nabla_R + \frac{\hbar^2}{8m} \nabla_R^2 \right) \check{I} \right] \check{G}(\boldsymbol{R}, \boldsymbol{k}) - \check{V}(\boldsymbol{R}) \otimes \check{G}(\boldsymbol{R}, \boldsymbol{k}) = \check{I},$$

where the $\otimes$-product is given in Eq. (6). To see which terms are negligible, an order-of-magnitude analysis may be performed. In the low-energy regime, $\check{G} = \check{G}_l \sim \alpha^{-1}$. The quasiparticle energy $\varepsilon/E_{\mathrm{F}}$ is restricted to be of order α by the energy cut-off E_c. Furthermore, the difference $(\mu - \hbar^2 k^2/2m)/E_{\mathrm{F}} \sim \alpha$ as well. The gradient terms $\nabla_R \check{G}$ can be estimated as being of order $\boldsymbol{q}\check{G}$, since $\check{V}$ is its only source of spatial variations. If it is assumed that $|\boldsymbol{q}|/k_{\mathrm{F}} \sim \alpha^2$, then the fourth term on the left hand side is of order $\hbar^2 |\boldsymbol{q}||\boldsymbol{k}|/2mE_{\mathrm{F}} \simeq |\boldsymbol{q}|/k_{\mathrm{F}} \sim \alpha^2$, whereas the fifth term is of order $\hbar^2 |\boldsymbol{q}|^2/8mE_{\mathrm{F}} \sim \alpha^4$. From a Taylor expansion of the $\otimes$-product, known as the *gradient approximation*, it is found that

$$\check{V}(\boldsymbol{R}) \otimes \check{G}(\boldsymbol{R}, \boldsymbol{k}) = \check{V}(\boldsymbol{R})\check{G}(\boldsymbol{R}, \boldsymbol{k}) + \frac{i}{2} \nabla_R \check{V}(\boldsymbol{R}) \cdot \nabla_k \check{G}(\boldsymbol{R}, \boldsymbol{k})$$

$$- \frac{1}{4} \nabla_R^2 \check{V}(\boldsymbol{R}) \nabla_p^2 \check{G}(\boldsymbol{R}, \boldsymbol{k}) + \dots \tag{2.47}$$

The first term of Eq. (2.47) is of order $\alpha^0 = 1$. The term $k_{\mathrm{F}} \nabla_k \check{G}$ is of order α^{-2}, as can be seen by differentiation of Eq. (2.23), and hence the linear gradient terms $\nabla_R \check{V} \cdot \nabla_k \check{G}/E_{\mathrm{F}} \sim \alpha$. The third term in Eq. (2.47) similarly

is of order α^2, with each consecutive term in the expansion acquiring an additional power of α. To order $\alpha^0 = 1$ in the low-energy regime, the equation of motion for the Green function therefore becomes

$$\left[\varepsilon \breve{\rho}_4 + \left(\mu - \frac{\hbar^2 \boldsymbol{k}^2}{2m} \right) \breve{I} - \breve{V}(\boldsymbol{R}) \right] \breve{G}_l(\boldsymbol{R}, \boldsymbol{k}) = \breve{I},$$

which may be solved immediately, giving

$$\breve{G}_l(\boldsymbol{R}, \boldsymbol{k}) = \left[\varepsilon \breve{\rho}_4 + \left(\mu - \frac{\hbar^2 \boldsymbol{k}^2}{2m} \right) \breve{I} - \breve{V}(\boldsymbol{R}) \right]^{-1}. \qquad (2.48)$$

Eq. (2.48) is known as the *quasiparticle approximation* [106, 107]. Assuming for concreteness that $\alpha = 0.01$, and using a typical value for the Fermi wave vector of $k_{\mathrm{F}} \sim 10^{-8}\,\mathrm{cm}^{-1}$ [108], the approximation would be valid for perturbing potentials with characteristic wavelengths of $\sim 1\,\mu\mathrm{m}$. This will turn out to be too restrictive for systems to be studied here.

   If the restraint on the spatial variations of the perturbing potential is relaxed to $|\boldsymbol{q}|/k_{\mathrm{F}} \sim \alpha$, the equation of motion to order $\alpha^0 = 1$ becomes

$$\left[\varepsilon \breve{\rho}_4 + \left(\mu - \frac{\hbar^2 \boldsymbol{k}^2}{2m} + \frac{i\hbar^2}{2m} \boldsymbol{k} \cdot \nabla_R \right) \breve{I} \right] \breve{G}_l(\boldsymbol{R}, \boldsymbol{k}) - \breve{V}(\boldsymbol{R}) \otimes \breve{G}_l(\boldsymbol{R}, \boldsymbol{k}) = \breve{I}, \quad (2.49)$$

The terms in Eq. (2.47) are now all of the same size, so the series cannot be truncated. This problem is, however, solved by the quasiclassical approximation, which is applied by replacing the Green function by a quasiclassical Green function. It is defined as

$$\breve{g}(\boldsymbol{R}, \boldsymbol{k}_{\mathrm{F}}) = \frac{i}{\pi} \int_{-E_c}^{E_c} d\xi_k \, \breve{G}(\boldsymbol{R}, \boldsymbol{k}), \qquad (2.50)$$

where $\xi_k = \hbar^2 \boldsymbol{k}^2 / 2m - \mu$. The effect of integrating $\breve{G}$ over ξ_k is that the dependence on $\boldsymbol{k}$ is replaced by a resultant momentum, which is equal to the Fermi momentum, $\boldsymbol{k}_{\mathrm{F}}$, due to the strongly peaked nature of $\breve{G}$. Notice that while the magnitude of $\boldsymbol{k}$ is locked to the Fermi level, the momentum direction dependence is retained.

   An expression for the quasiclassical form of $\nabla_k \breve{G}_l$ is also required. By

direct computation it is found that

$$
\frac{i}{\pi} \int_{-E_c}^{E_c} d\xi_k \, \nabla_k \check{G}_l = \frac{i}{\pi} \int_{-E_c}^{E_c} d\xi_k \left(\hat{k} \frac{\partial}{\partial k} \check{G}_l + \nabla_{\Omega_k} \check{G}_l \right)
$$

$$
= \hat{k} \frac{i}{\pi} \sqrt{\frac{2\hbar^2}{m}} \int_{-E_c}^{E_c} d\xi_k \, \sqrt{\xi_k + \mu} \frac{\partial}{\partial \xi_k} \check{G}_l + \nabla_{\Omega_k} \check{g}
$$

$$
= \hat{k} \frac{i}{\pi} \sqrt{\frac{2\hbar^2}{m}} \left[\sqrt{\xi_k + \mu} \check{G}_l \right]_{-E_c}^{E_c} - \hat{k} \frac{i}{\pi} \sqrt{\frac{2\hbar^2}{m}} \int_{-E_c}^{E_c} d\xi_k \frac{1}{2\sqrt{\xi_k + \mu}} \check{G}_l + \nabla_{\Omega_k} \check{g}
$$

$$
\simeq -\frac{\hat{k}_{\mathrm{F}}}{k_{\mathrm{F}}} \check{g} + \nabla_{\Omega_k} \check{g},
$$

where $\hat{k}_{\mathrm{F}}$ is a unit vector in the direction of $\boldsymbol{k}_{\mathrm{F}}$. The boundary term has been neglected, as it falls outside the low-energy regime. Furthermore the approximation $\sqrt{\xi_k + \mu} \simeq \sqrt{\mu}$ has been made, with $\mu = \hbar^2 k_{\mathrm{F}}^2/2m$. The quantity $\nabla_{\Omega_k} \check{g}$ is the angular gradient of $\check{g}$, the size of which depends on the spatial variation of the perturbing fields. It is assumed to be of the same size as $\check{g}/k_{\mathrm{F}}$. The integration over ξ_k introduces a factor α. Hence, the first term of Eq. (2.47) is of order α, the second term is of order $|\boldsymbol{q}|V\check{g}/k_{\mathrm{F}}E_{\mathrm{F}} \sim \alpha^2$, and so on.

It seems reasonable to find an equation of motion for the quasiclassical Green function by integrating Eq. (2.49) over ξ_k. However, this does not work. On the right hand side of Eq. (2.49), the factor $\check{I}$ would result in an explicit dependence on the unphysical cut-off E_c. A term $\xi_k \check{G}_l$ is also present on the left hand side, which hinders the formulation of a closed equation for $\check{g}$. To avoid this problem, a different equation of motion can be formulated for the $\boldsymbol{r}'$ dependence of $\check{G}(\boldsymbol{r}, \boldsymbol{r}', \varepsilon)$, as given by Eq. (2.20). Repeating the above steps then results in

$$
\check{G}(\boldsymbol{R}, \boldsymbol{k}) \left[\varepsilon \check{\rho}_4 + \left(\mu - \frac{\hbar^2 \boldsymbol{k}^2}{2m} - \frac{i\hbar^2}{2m} \boldsymbol{k} \cdot \nabla_R \right) \check{I} \right] - \check{G}(\boldsymbol{R}, \boldsymbol{k}) \otimes \check{V}(\boldsymbol{R}) = \check{I}, \quad (2.51)
$$

where the operator ∇_R is now assumed to act towards the left. Subtracting Eq. (2.51) from Eq. (2.49), a procedure first introduced by Eilenberger, removes the problematic terms, giving,

$$
\frac{i\hbar^2}{m} \boldsymbol{k} \cdot \nabla_R \check{G}_l(\boldsymbol{R}, \boldsymbol{k}) + \left[\varepsilon \check{\rho}_4 - \check{V}(\boldsymbol{R}) \, , \, \check{G}_l(\boldsymbol{R}, \boldsymbol{k}) \right] = 0,
$$

where the $\otimes$ product has been truncated so as to yield an accuracy of order α in the quasiclassical regime. This amounts to neglecting all gradient

terms in Eq. (2.47). Since $\check{G}_l$ is nonzero only for momenta close to k_F, the replacement $\mathbf{k} \to \mathbf{k}_F$ can be made in the first term. Integrating over ξ_k then results in the quasiclassical equation of motion,

$$i\hbar \mathbf{v}_F \cdot \nabla_R \check{g}(\mathbf{R}, \mathbf{k}_F) + \left[\varepsilon \check{\rho}_4 - \check{V}(\mathbf{R}) , \; \check{g}(\mathbf{R}, \mathbf{k}_F) \right] = 0, \qquad (2.52)$$

with $\mathbf{v}_F = \hbar \mathbf{k}_F / m$. Eq. (2.52) is known as the Eilenberger equation [109]. Note that the matrix structure of $\hat{g}^R$ and $\hat{g}^A$ now takes the form

$$\hat{g}^X = \begin{pmatrix} g^X & f^X \\ -\tilde{f}^X & -\tilde{g}^X \end{pmatrix}, \qquad (2.53)$$

where $\tilde{a}(\varepsilon) = a^*(-\varepsilon)$, and $X \in \{R, A\}$.

2.5 Normalisation

There is a problem with Eq. (2.52): it is not unique. In fact, any constant function $\check{g} = \check{C}$ which commutes with $\check{\varepsilon} - \check{V}$ is a solution. To gain insight into this issue, an alternative derivation of Eq. (2.52), first made by Shelankov [110], will be presented. Consider the transformation of the Green function to the mixed representation,

$$\check{G}(\mathbf{r}_1, \mathbf{r}_2) = \int \frac{d\mathbf{k}}{(2\pi)^3} \, \check{G}(\mathbf{R}, \mathbf{k}) e^{i\mathbf{k}\cdot\mathbf{r}}, \qquad (2.54)$$

where $\mathbf{r} = \mathbf{r}_1 - \mathbf{r}_2$ and $\mathbf{R} = (\mathbf{r}_1 + \mathbf{r}_2)/2$. Notice that $\check{G}$ is strongly peaked at momentum $|\mathbf{k}| = k_F$, and nowhere else. Consider, for a moment, the following trivial rewrite,

$$\check{G}(\mathbf{r}_1, \mathbf{r}_2) = e^{i\mathbf{k}_F\cdot\mathbf{r}} \int \frac{d\mathbf{k}}{(2\pi)^3} \, \check{G}(\mathbf{R}, \mathbf{k}) e^{i\delta\mathbf{k}\cdot\mathbf{r}},$$

where $\delta\mathbf{k} = \mathbf{k} - \mathbf{k}_F$. The low-energy regime is defined by kinetic energies close to the Fermi level, $\hbar^2(\mathbf{k}^2 - \mathbf{k}_F^2)/2m < E_c$, or equivalently, $|\delta\mathbf{k}| \lesssim E_c/\hbar v_F$, where v_F is the Fermi velocity. To extract only information from this region in momentum space, note that for large r the rapid oscillations of the factor $e^{i\delta\mathbf{k}\cdot\mathbf{r}}$ causes the integral to cancel out – except when $|\delta\mathbf{k}| \sim 1/|\mathbf{r}|$. In other words, the large wavelength limit provides information about small $\delta\mathbf{k}$. Hence, assuming that $\mathbf{r} \sim (E_c/\hbar v_F)^{-1}$, and returning to Eq. (2.54), it is clear that the combination $\mathbf{k}\cdot\mathbf{r} \simeq \mathbf{k}_F\cdot\mathbf{r}$ is a large quantity. An asymptotic expression may be derived by starting with a plane wave expansion,

$$e^{i\mathbf{k}\cdot\mathbf{r}} = \sum_l (2l+1) i^l j_l(kr) P_l(\hat{k}\cdot\hat{r}), \qquad (2.55)$$

where j_l are the spherical Bessel functions and P_l are the Legendre functions. For $kr \gg 1$, j_l may be approximated as

$$j_l(kr) \simeq \frac{\sin\left(kr - l\frac{\pi}{2}\right)}{kr} = \frac{1}{2ikr}\left[(-i)^l e^{ikr} - i^l e^{-ikr}\right],$$

hence,

$$e^{i\boldsymbol{k}\cdot\boldsymbol{r}} = \frac{1}{2ikr}\sum_l (2l+1)\left[P_l(\hat{k}\cdot\hat{r})e^{ikr} - P_l(-\hat{k}\cdot\hat{r})e^{-ikr}\right],$$

where the property $P_l(-x) = (-1)^l P_l(x)$ has been used. Inserting a factor $P_l(1) = 1$ in both terms in the square brackets, and using the property

$$\sum_l (2l+1)P_l(x)P_l(y) = 2\delta(x-y)$$

gives

$$e^{i\boldsymbol{k}\cdot\boldsymbol{r}} \simeq \frac{1}{ikr}\left[\delta(\hat{k}\cdot\hat{r}-1)e^{ikr} - \delta(\hat{k}\cdot\hat{r}+1)e^{-ikr}\right] \tag{2.56}$$

Inserting Eq. (2.56) into Eq. (2.54) gives [110]

$$\check{G}(\boldsymbol{r}_1,\boldsymbol{r}_2) \simeq -\frac{m}{2\pi\hbar^2}\frac{e^{ik_{\mathrm{F}}r}}{r}\check{g}_+(\boldsymbol{r}_1,\boldsymbol{r}_2) + \frac{m}{2\pi\hbar^2}\frac{e^{-ik_{\mathrm{F}}r}}{r}\check{g}_-(\boldsymbol{r}_1,\boldsymbol{r}_2), \tag{2.57}$$

with

$$\begin{aligned}\check{g}_\pm(\boldsymbol{r}_1,\boldsymbol{r}_2) &= \frac{i}{2\pi}\int_{-\infty}^{\infty} dk\, \frac{\hbar^2 k}{m} e^{\pm i(k-k_{\mathrm{F}})r}\check{G}(\boldsymbol{R},\pm k\hat{r})\\ &\simeq \frac{i}{2\pi}\int_{-\infty}^{\infty} d\xi_k\, e^{\pm i\xi_k r/\hbar v_{\mathrm{F}}}\check{G}(\boldsymbol{R},\pm\xi_k\hat{r}),\end{aligned} \tag{2.58}$$

where it has been used that $\xi_k = \frac{\hbar^2 k^2}{2m} - \mu \simeq \hbar v_{\mathrm{F}}(k-k_{\mathrm{F}})$. The functions $\check{g}_\pm$ may be identified as the slowly varying amplitudes to the rapid oscillations of $\check{G}$. Hence,

$$\begin{aligned}\nabla_1^2\check{G}(\boldsymbol{r}_1,\boldsymbol{r}_2) \simeq &-\frac{m}{2\pi\hbar^2}\frac{e^{ik_{\mathrm{F}}r}}{r}\left(-k_{\mathrm{F}}^2\check{g}_+ + 2ik_{\mathrm{F}}\hat{r}\cdot\nabla_1\check{g}_+\right)\\ &+\frac{m}{2\pi\hbar^2}\frac{e^{-ik_{\mathrm{F}}r}}{r}\left(-k_{\mathrm{F}}^2\check{g}_- - 2ik_{\mathrm{F}}\hat{r}\cdot\nabla_1\check{g}_-\right).\end{aligned} \tag{2.59}$$

The equation of motion for the functions $\check{g}_\pm$ is found by realising that Eq. (2.46) may only be solved if, for $\boldsymbol{r}_1 \neq \boldsymbol{r}_2$

$$\pm i\hbar v_{\mathrm{F}}\hat{r}\cdot\nabla_1\check{g}_\pm + \left[\varepsilon\check{\rho}_4 - \check{V}\right]\check{g}_\pm = 0. \tag{2.60}$$

From Eq. (2.60) it is clear that $\check{g}_{\pm}$ express motion along a straight line connecting $\boldsymbol{r}_1$ and $\boldsymbol{r}_2$. This means that Eq. (2.60) may be solved for a given constant trajectory direction $\hat{n}$, which motivates a parametrisation using trajectory coordinates. Indeed, any point $\boldsymbol{r}_i$ along a straight line with direction $\hat{n}$ may be written as

$$\boldsymbol{r}_i = \boldsymbol{\xi} + \eta_i \hat{n}, \tag{2.61}$$

where $\boldsymbol{\xi}$ is an arbitrary point on the line, and η_i is the location of $\boldsymbol{r}_i$ along the line, as illustrated in Fig. 2.3.
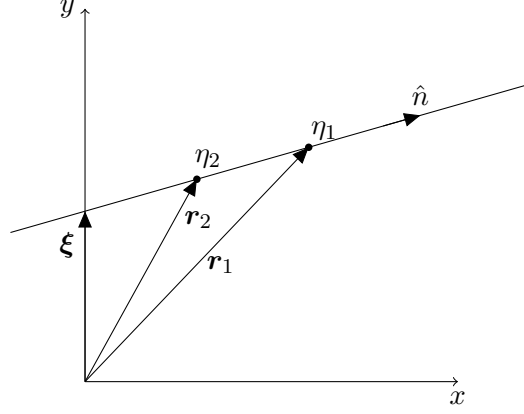

Figure 2.3: Illustration of a trajectory between $\boldsymbol{r}_1$ and $\boldsymbol{r}_2$ in two dimensions. $\hat{n}$ is a unit vector indicating the direction of the trajectory, η_1 and η_2 are parameters indicating the positing of $\boldsymbol{r}_1$ and $\boldsymbol{r}_2$ along the trajectory, and $\boldsymbol{\xi}$ is an arbitrary point on the trajectory, necessary to uniquely define its location in space. For simplicity, it has here been chosen to lie along the y axis.

The trajectory Green function $\check{g}_n$ is then either $\check{g}_+$ or $\check{g}_-$ depending on where the coordinate η_1 is located along the trajectory, relative to η_2,

$$\check{g}_n(\eta_1, \eta_2) = \begin{cases} \check{g}_+ (\boldsymbol{\xi} + \eta_1 \hat{n}, \boldsymbol{\xi} + \eta_2 \hat{n}) & \eta_1 > \eta_2 \\ \check{g}_- (\boldsymbol{\xi} + \eta_1 \hat{n}, \boldsymbol{\xi} + \eta_2 \hat{n}) & \eta_1 < \eta_2 \end{cases} \tag{2.62}$$

Notice that if $\hat{n}$ is chosen such that $\hat{n} \cdot \hat{r} = 1$ when $\eta_1 > \eta_2$, then $\hat{n} \cdot \hat{r} = -1$ when $\eta_1 < \eta_2$. Hence,

$$\check{g}_n(\eta_1, \eta_2) = \frac{i}{2\pi} \int_{-\infty}^{\infty} d\xi_k \, e^{i\xi_k(\eta_1 - \eta_2)/\hbar v_{\mathrm{F}}} \check{G}(\boldsymbol{R}, \xi_k \hat{n}). \tag{2.63}$$

Consider next the quantity

$$\lim_{\varepsilon \to 0} \check{g}_n(\eta + \varepsilon, \eta) - \check{g}_n(\eta - \varepsilon, \eta) = -\frac{1}{\pi} \lim_{\varepsilon \to 0} \int_{-\infty}^{\infty} d\xi_k \, \sin\left(\frac{\xi_k \varepsilon}{\hbar v_{\mathrm{F}}}\right) \check{G}(\boldsymbol{R}, \xi_k \hat{n}).$$

(2.64)

The factor $\sin(\xi_k \varepsilon / \hbar v_{\mathrm{F}})$ in the limit of small ε, has the effect of suppressing the integrand for small values of ξ_k. In other words, the integrand becomes appreciable only for momenta far away from the Fermi surface. Hence, $\check{G}$ may be approximated by a free electron gas. From Eq. (2.23) it is found that $\check{G} \simeq -\frac{1}{\xi_k} \check{I}$, and so

$$\lim_{\varepsilon \to 0} \check{g}_n(\eta + \varepsilon, \eta) - \check{g}_n(\eta - \varepsilon, \eta) = \check{I}.$$

(2.65)

Combining this discontinuity condition with Eq. (2.60), a new equation of motion, valid also for $\boldsymbol{r}_1 = \boldsymbol{r}_2$ may be defined as

$$i\hbar v_{\mathrm{F}} \frac{\partial}{\partial \eta_1} \check{g}_n + \left[\varepsilon \check{\rho}_4 - \check{V}(\eta_1)\right] \check{g}_n = i\hbar v_{\mathrm{F}} \check{I} \delta(\eta_1 - \eta_2),$$

(2.66)

and similarly, if this derivation is repeated for the variable $\boldsymbol{r}_2$,

$$-i\hbar v_{\mathrm{F}} \frac{\partial}{\partial \eta_2} \check{g}_n + \check{g}_n \left[\varepsilon \check{\rho}_4 - \check{V}(\eta_2)\right] = i\hbar v_{\mathrm{F}} \check{I} \delta(\eta_1 - \eta_2).$$

(2.67)

Eqs. (2.66) and (2.67) finally allows the derivation of Shelankov's generalised normalisation condition [110]. To do so, observe that the quantity

$$A(\eta) = \check{g}_n(\eta_1, \eta) \check{g}_n(\eta, \eta_2)$$

(2.68)

is constant for all η except at the points $\eta_1 = \eta_2$. This can be seen by differentiating by η, and inserting Eqs. (2.66) and (2.67). Furthermore, the Green function $\check{g}_n(\eta_1, \eta_2)$ must vanish as $\eta_1 - \eta_2 \to \infty$. This means that for any η in Eq. (2.68) satisfying $\eta < \eta_1$ and simultaneously $\eta < \eta_2$, $A = 0$, since the limit $\eta \to -\infty$ may be chosen without changing its value. By a similar argument, $A = 0$ also for $\eta > \eta_1, \eta_2$. For $\eta_1 < \eta < \eta_2$, η may be chosen as $\eta_2 - \varepsilon$. Taking the limit $\varepsilon \to 0$ and using Eq. (2.65) then gives

$$\begin{aligned}
\lim_{\varepsilon \to 0} A(\eta_2 - \varepsilon) &= \lim_{\varepsilon \to 0} \check{g}_n(\eta_1, \eta_2 - \varepsilon) \check{g}_n(\eta_2 - \varepsilon, \eta_2) \\
&= \lim_{\varepsilon \to 0} \check{g}_n(\eta_1, \eta_2 - \varepsilon) \left(\check{g}_n(\eta_2 + \varepsilon, \eta_2) - \check{I}\right) \\
&= -\check{g}_n(\eta_1, \eta_2).
\end{aligned}$$

Similarly, with $\eta_2 < \eta < \eta_1$ one gets

$$\lim_{\varepsilon \to 0} A(\eta_2 + \varepsilon) = \check{g}_n(\eta_1, \eta_2).$$

Summarised one finds the following generalised normalisation conditions,

$$\check{g}_n(\eta_1, \eta)\check{g}_n(\eta, \eta_2) = \begin{cases} +\check{g}_n(\eta_1, \eta_2) & \eta_2 < \eta < \eta_1 \\ 0 & \text{otherwise} \\ -\check{g}_n(\eta_1, \eta_2) & \eta_1 < \eta < \eta_2 \end{cases} \qquad (2.69)$$

By subtracting Eq. (2.67) from Eq. (2.66), and taking the limit $\eta_1 \to \eta_2$ it is seen that $\check{g}_n(\eta, \eta)$ satisfies the Eilenberger equation, given in Eq. (2.52), where uniqueness is ensured by Eq. (2.69). To see how $\check{g}_n(\eta, \eta)$ is related to Eq. (2.50), consider the quantity

$$\check{g}'(\eta) = \lim_{\varepsilon \to 0} \left[\check{g}_n(\eta + \varepsilon, \eta) + \check{g}_n(\eta - \varepsilon, \eta) \right], \qquad (2.70)$$

which must also solve Eq. (2.52). Eq. (2.63) then gives,

$$\check{g}'(\eta) = \frac{i}{\pi} \lim_{\varepsilon \to 0} \int_{-\infty}^{\infty} d\xi_k \, \cos\left(\frac{\xi_k \varepsilon}{\hbar v_{\mathrm{F}}}\right) \check{G}(\boldsymbol{R}, \xi_k \hat{n}), \qquad (2.71)$$

from which it is clear that $\check{g}'$ is indeed the quasiclassical Green function $\check{g}$ from Eq. (2.50), where the only difference is that the hard cut-off of E_c in the latter is replaced by a soft cut-off in the former. Using Eq. (2.65) and Eq. (2.69), along with the identity

$$\lim_{\varepsilon \to 0} \check{g}(\eta \pm \varepsilon, \eta) = \lim_{\varepsilon \to 0} \check{g}(\eta, \eta \mp \varepsilon)$$

the normalisation for the quasiclassical Green function is found to be

$$\check{g}^2 = \check{I}, \qquad (2.72)$$

where $\check{g}$ may be expressed in terms of the trajectory Green function as

$$\check{g}(\boldsymbol{R}) = \lim_{\varepsilon \to 0} \frac{1}{2} \left(\check{g}_n(\eta \pm \varepsilon, \eta) \mp \check{I} \right). \qquad (2.73)$$

The matrix structure of $\check{g}$ is given in Eq. (2.38), which means that Eq. (2.72) results in the conditions

$$\left(\hat{g}^R \right)^2 = \hat{I}, \qquad (2.74)$$

$$\left(\hat{g}^A \right)^2 = \hat{I}, \qquad (2.75)$$

$$\hat{g}^R \hat{g}^K + \hat{g}^K \hat{g}^A = 0, \qquad (2.76)$$

where Eq. (2.76) may be automatically satisfied by the parametrisation

$$\hat{g}^K = \hat{g}^R \hat{h} - \hat{h} \hat{g}^A. \tag{2.77}$$

The matrix $\hat{h}$ is referred to as the *distribution function.* From Eq. (2.43) it is seen that $\hat{h} = \hat{I} \tanh \frac{\beta \varepsilon}{2}$ in equilibrium.

Eq. (2.69) has an interesting corollary [111, 112]. Consider a system where a boundary is present between two half-spaces, as shown in Fig. 2.4.
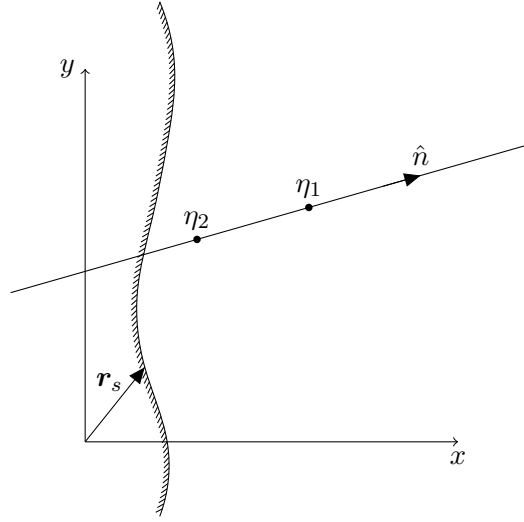

Figure 2.4: The same trajectory as in Fig. 2.3, but now in the presence of a half-space boundary, as determined by $\boldsymbol{r}_s$.

The introduction of such a boundary will, of course, alter the Green function. However, away from the boundary, it must satisfy the same equation of motion as a Green function $\breve{g}^0$ where the boundary is absent – their Hamiltonians are identical. A relationship between $\breve{g}$ and $\breve{g}^0$ may therefore be established by a similar analysis as was used for Eq. (2.69) by defining $B(\eta) = \breve{g}_n^0(\eta_1, \eta) \breve{g}_n(\eta, \eta_1)$. In this case, however, the limit $\eta \to \infty$ can only be reached along a direction which does not cross the boundary. Using Eq. (2.65) and Eq. (2.69), and allowing η_1 to approach η_2 from above, it is seen that

$$\lim_{\varepsilon \to 0} \breve{g}_n^0(\eta + \varepsilon, \eta) \breve{g}_n(\eta, \eta - \varepsilon) = \lim_{\varepsilon \to 0} \left(\breve{g}^0(\eta - \varepsilon, \eta) + \breve{I} \right) \breve{g}_n(\eta, \eta - \varepsilon)$$

$$= \lim_{\varepsilon \to 0} \breve{g}_n(\eta + \varepsilon, \eta),$$

and similarly, with $B(\eta) = \check{g}_n(\eta_1, \eta)\check{g}_n^0(\eta, \eta_2)$,

$$\lim_{\varepsilon \to 0} \check{g}_n(\eta + \varepsilon, \eta)\check{g}_n^0(\eta, \eta - \varepsilon) = \lim_{\varepsilon \to 0} \left(\check{g}_n(\eta - \varepsilon, \eta) + \check{I}\right)\check{g}_n^0(\eta, \eta - \varepsilon)$$
$$= \lim_{\varepsilon \to 0} \check{g}_n^0(\eta + \varepsilon, \eta),$$

By inserting Eq. (2.73), one finds

$$\left(\check{g}^0 - \check{I}\right)\left(\check{g} + \check{I}\right) = 0 \qquad (2.78)$$
$$\left(\check{g} - \check{I}\right)\left(\check{g}^0 + \check{I}\right) = 0 \qquad (2.79)$$

2.6   Impurities

It is also possible to formulate a quasiclassical equation of motion in the presence of impurities. The impurity potential is assumed to be made up of a large number of identical, but randomly located impurities,

$$V_{\text{imp}}(\boldsymbol{r}) = \sum_i U(\boldsymbol{r} - \boldsymbol{r}_i), \qquad (2.80)$$

where $\boldsymbol{r}_i$ is the position of impurity i. Consider first the case where V_{imp} is the only perturbation of a free electron gas. If the unperturbed Green function is denoted as $\check{G}_0$, then the equation of motion in position space can be written as

$$\left[\check{G}_0^{-1} - V_{\text{imp}}(\boldsymbol{r})\check{I}\right]\check{G}(\boldsymbol{r}, \boldsymbol{r}') = \check{\delta}(\boldsymbol{r} - \boldsymbol{r}'), \qquad (2.81)$$

where the operator $\check{G}_0^{-1}$ is short-hand notation for the unperturbed equation of motion. Alternatively, one can write

$$\check{G}(\boldsymbol{r}, \boldsymbol{r}') = \check{G}_0(\boldsymbol{r} - \boldsymbol{r}') + \int d\boldsymbol{r}_1 \, \check{G}_0(\boldsymbol{r} - \boldsymbol{r}_1) V_{\text{imp}}(\boldsymbol{r}_1)\check{G}(\boldsymbol{r}_1, \boldsymbol{r}'), \qquad (2.82)$$

which can be seen by inserting Eq. (2.82) into Eq. (2.81). In momentum space, Eq. (2.82) takes the form

$$\check{G}(\boldsymbol{k}, \boldsymbol{k}') = \check{G}_0(\boldsymbol{k})\delta(\boldsymbol{k} - \boldsymbol{k}') + \check{G}_0(\boldsymbol{k})\int \frac{d\boldsymbol{k}_1}{(2\pi)^3} \, V_{\text{imp}}(\boldsymbol{k} - \boldsymbol{k}_1)\check{G}(\boldsymbol{k}_1, \boldsymbol{k}'), \quad (2.83)$$

where $V_{\text{imp}}(\boldsymbol{q}) = \sum_i U(\boldsymbol{q})e^{-i\boldsymbol{q}\cdot\boldsymbol{r}_i}$. Eq. (2.83) may be solved by iteration;

$$\check{G}(\boldsymbol{k}, \boldsymbol{k}') = \check{G}_0(\boldsymbol{k})\delta(\boldsymbol{k} - \boldsymbol{k}') + \check{G}_0(\boldsymbol{k})V_{\text{imp}}(\boldsymbol{k} - \boldsymbol{k}')\check{G}_0(\boldsymbol{k}')$$
$$+ \check{G}_0(\boldsymbol{k})\int \frac{d\boldsymbol{k}_1}{(2\pi)^3} \, V_{\text{imp}}(\boldsymbol{k} - \boldsymbol{k}_1)\check{G}_0(\boldsymbol{k}_1)V_{\text{imp}}(\boldsymbol{k}_1 - \boldsymbol{k}')\check{G}_0(\boldsymbol{k}') + \dots$$
$$\equiv \check{G}^{(0)} + \check{G}^{(1)} + \check{G}^{(2)} + \dots$$

This process can be repeated *ad infinitum*, which takes higher and higher order corrections into account, and is, of course, impossibly complex. If the density of impurities is large, however, performing an impurity averaging allows for some simplifying approximations [113, 114]. The averaged Green function is defined as

$$\langle \check{G}(\boldsymbol{k}, \boldsymbol{k}') \rangle_{\text{imp}} = \prod_i \left(\frac{1}{V} \int d\boldsymbol{r}_i \right) \check{G}(\boldsymbol{k}, \boldsymbol{k}') \tag{2.84}$$

This process is equivalent to replacing the impurity potentials by their averaged counterparts,

$$\langle V_{\text{imp}}(\boldsymbol{q}) \rangle_{\text{imp}} = \left\langle \sum_i U(\boldsymbol{q}) e^{-i\boldsymbol{q}\cdot\boldsymbol{r}_i} \right\rangle_{\text{imp}} = (2\pi)^3 n U(\boldsymbol{q}) \delta(\boldsymbol{q}), \tag{2.85}$$

where $n = N/V$ is the density of impurities. Products of two impurity potentials become

$$\langle V_{\text{imp}}(\boldsymbol{q}_1) V_{\text{imp}}(\boldsymbol{q}_2) \rangle_{\text{imp}} = \left\langle \sum_i U(\boldsymbol{q}_1) e^{-i\boldsymbol{q}_1\cdot\boldsymbol{r}_i} \sum_j U(\boldsymbol{q}_2) e^{-i\boldsymbol{q}_2\cdot\boldsymbol{r}_j} \right\rangle_{\text{imp}}$$

$$= U(\boldsymbol{q}_1) U(\boldsymbol{q}_2) \left[\left\langle \sum_i e^{-i(\boldsymbol{q}_1+\boldsymbol{q}_2)\cdot\boldsymbol{r}_i} \right\rangle_{\text{imp}} + \left\langle \sum_{i \neq j} e^{-i\boldsymbol{q}_1\cdot\boldsymbol{r}_i} e^{-i\boldsymbol{q}_2\cdot\boldsymbol{r}_j} \right\rangle_{\text{imp}} \right]$$

$$\simeq U(\boldsymbol{q}_1) U(\boldsymbol{q}_2) \left[(2\pi)^3 n \delta(\boldsymbol{q}_1 + \boldsymbol{q}_2) + (2\pi)^6 n^2 \delta(\boldsymbol{q}_1) \delta(\boldsymbol{q}_2) \right],$$

where in the second term it has been used that $N(N-1) \simeq N^2$. Similar expressions may be found for higher powers of impurity potentials. Inserting this into the recurrence relation, it becomes clear that each term ends up with a factor $\delta(\boldsymbol{k} - \boldsymbol{k}')$, which means that $\langle \check{G} \rangle_{\text{imp}}$ is translation invariant – a reasonable result. Furthermore, the notation can be simplified greatly by replacing mathematical expressions with the diagrams given in Table 2.1, along with the instructions that i) momentum is conserved at every vertex, ii) every internal propagator $\check{G}_0$ implies momentum integration, and iii) a factor $(2\pi)^3 \delta(\boldsymbol{k} - \boldsymbol{k}')$ is added to every diagram.

Table 2.1: List of diagrams used in the impurity averaging.

Expression	Diagram
$\check{G}(\boldsymbol{k}, \boldsymbol{k}')$	
$\check{G}_0(\boldsymbol{k})$	
$U(\boldsymbol{q})$	
n	$\times$

We thus get

and so on. The Dyson equation is given diagramatically as

where $\check{\Sigma}$ is the irreducible self energy. To second order, it takes the form,

The first term in $\check{\Sigma}$ is just a constant, which will disappear when the left-right trick discussed in the previous section is applied, and thus may be discarded immediately. The accuracy of the second term may be increased by replacing the internal propagator $\check{G}_0$ with the full propagator $\check{G}$. This amounts to including an infinite number of additional diagrams, giving

Translated back into equations, this results in

$$\check{\Sigma}(\boldsymbol{k}, \boldsymbol{k}') = n \int \frac{d\boldsymbol{q}}{(2\pi)^3} U(\boldsymbol{k} - \boldsymbol{q}) \check{G}\big(\boldsymbol{q}, \boldsymbol{q} - (\boldsymbol{k} - \boldsymbol{k}')\big) U(\boldsymbol{q} - \boldsymbol{k})$$

$$= n \int \frac{d\boldsymbol{q}}{(2\pi)^3} |U(\bar{\boldsymbol{k}} - \boldsymbol{q})|^2 \check{G}\Big(\boldsymbol{q} + \frac{1}{2}\delta\boldsymbol{k}, \boldsymbol{q} - \frac{1}{2}\delta\boldsymbol{k}\Big), \qquad (2.86)$$

where $\bar{\boldsymbol{k}} = (\boldsymbol{k} + \boldsymbol{k}')/2$ and $\delta\boldsymbol{k} = \boldsymbol{k} - \boldsymbol{k}'$. In the mixed representation this becomes

$$\check{\Sigma}(\boldsymbol{R}, \boldsymbol{k}) = n \int \frac{d\boldsymbol{q}}{(2\pi)^3} |U(\boldsymbol{k} - \boldsymbol{q})|^2 \check{G}(\boldsymbol{q}, \boldsymbol{R}), \qquad (2.87)$$

where a change in notation $\bar{\boldsymbol{k}} \to \boldsymbol{k}$ has been made.

To find a quasiclassical expression for $\check{\Sigma}$, the momentum integral in Eq. (2.87) must be restricted to the low-energy regime. This introduces a factor α (e.g. a small quantity) [104]. Next, it is assumed that the impurity potential is of order $n|U|^2/E_{\mathrm{F}}^2 \sim \alpha$. Since in the low-energy regime $\check{G} = \check{G}_l \sim \alpha^{-1}$, this gives $\check{\Sigma} \sim \alpha$, which is appropriate for quasiclassical theory. The integration measure can be written as

$$d\boldsymbol{q} = q^2 d\Omega_q dq \simeq \pi^2 \nu_0 d\Omega_q d\xi_q, \qquad (2.88)$$

where $d\Omega_q$ is the angular integration measure, and $\nu_0 = mk_{\mathrm{F}}/\hbar^2\pi^2$ is the density of states of a free electron gas at the Fermi level. Hence,

$$\check{\Sigma}(\boldsymbol{R}, \boldsymbol{k}) \simeq \frac{n\nu_0}{2} \int \frac{d\Omega_q}{4\pi} \int_{-E_c}^{E_c} d\xi_q \, |U(\boldsymbol{k} - \boldsymbol{q})|^2 \check{G}_l(\boldsymbol{R}, \boldsymbol{q})$$

$$\simeq \frac{n\nu_0}{2} \int \frac{d\Omega_q}{4\pi} \, |U(\boldsymbol{k} - \boldsymbol{q}_{\mathrm{F}})|^2 \int_{-E_c}^{E_c} d\xi_q \, \check{G}_l(\boldsymbol{R}, \boldsymbol{q})$$

$$= -\frac{i\pi n\nu_0}{2} \int \frac{d\Omega_q}{4\pi} \, |U(\boldsymbol{k} - \boldsymbol{q}_{\mathrm{F}})|^2 \check{g}(\boldsymbol{R}, \boldsymbol{q}_{\mathrm{F}}). \qquad (2.89)$$

In other words, only a spherical average of the quasiclassical Green function over the Fermi level remains. The Dyson equation in momentum space now takes the form

$$\check{G}_0^{-1} \check{G}(\boldsymbol{k}, \boldsymbol{k}') - \int \frac{d\boldsymbol{q}}{(2\pi)^3} \check{\Sigma}(\boldsymbol{k}, \boldsymbol{q}) \check{G}(\boldsymbol{q}, \boldsymbol{k}') = \delta(\boldsymbol{k} - \boldsymbol{k}'), \qquad (2.90)$$

which in the mixed representation becomes

$$\left[\varepsilon \check{\rho}_4 + \left(\mu - \frac{\hbar^2 \boldsymbol{k}^2}{2m} + \frac{i\hbar^2}{2m} \boldsymbol{k} \cdot \nabla_R \right) \check{I} - \check{\Sigma}(\boldsymbol{R}, \boldsymbol{k}) \right] \check{G}_l(\boldsymbol{R}, \boldsymbol{k}) = \check{I}, \qquad (2.91)$$

where $\check{\Sigma} \otimes \check{G}_l \simeq \check{\Sigma} \check{G}_l$ to an accuracy of order α. Eq. (2.91) is not closed. It involves both the full Green function $\check{G}$ and the quasiclassical Green function $\check{g}$, a problem which is easily remedied by integration over ξ_k. Repeating the steps made towards obtaining Eq. (2.52) therefore gives,

$$i\hbar \boldsymbol{v}_{\mathrm{F}} \cdot \nabla_R \check{g}(\boldsymbol{R}, \boldsymbol{k}_{\mathrm{F}}) + \left[\varepsilon \check{\rho}_4 - \check{\Sigma}(\boldsymbol{R}, \boldsymbol{k}_{\mathrm{F}}) \, , \, \check{g}(\boldsymbol{R}, \boldsymbol{p}_{\mathrm{F}}) \right] = 0. \qquad (2.92)$$

In the presence of both an external perturbation $\check{V}$, and the impurity potential V_{imp}, a similar perturbation expansion in diagrams may be performed. Tallying up all the diagrams involved, it becomes clear that all diagrams which were used in the impurity averaging, without any external perturbations, still appear. Similarly, diagrams of all orders involving only the external perturbations also contribute. Finally, there are an infinite number of diagrams expressing cross terms between $\check{V}$ and V_{imp}. Since each order η of $\check{V}$ introduces a factor α^η, only first order perturbations ($\eta = 1$) are included. Furthermore, all cross diagrams are at least an order α smaller than the impurity self energy $\check{\Sigma}$ and are neglected. From what remains, the equation of motion may be formulated as,

$$i\hbar \boldsymbol{v}_{\mathrm{F}} \cdot \nabla_R \check{g}(\boldsymbol{R}, \boldsymbol{k}_{\mathrm{F}}) + \left[\varepsilon \check{\rho}_4 - \check{V}(\boldsymbol{R}) - \check{\Sigma}(\boldsymbol{R}, \boldsymbol{k}_{\mathrm{F}}) \, , \, \check{g}(\boldsymbol{R}, \boldsymbol{k}_{\mathrm{F}}) \right] = 0. \qquad (2.93)$$

2.7   Diffusive limit

If there is a high density of impurities, the particles may scatter so frequently that all information about momentum direction is lost - it gets averaged out. In this case, the quasiclassical Green function may be written as a spherically symmetric part, and a much smaller momentum-dependent part,

$$\check{g} = \check{g}_s + \hat{k}_{\mathrm{F}} \cdot \check{\boldsymbol{g}}_k, \qquad (2.94)$$

so that $\check{\boldsymbol{g}}_k^2$ is negligible. Note that from Eq. (2.72), this implies that

$$\left\{ \check{g}_s, \check{\boldsymbol{g}}_k \right\} = 0. \qquad (2.95)$$

Insertion into Eq. (2.89), neglecting $\check{\boldsymbol{g}}_k$ compared with $\check{g}_s$, gives

$$\check{\Sigma}(\boldsymbol{R}) = -\frac{i\hbar}{2\tau_{\mathrm{imp}}} \check{g}_s(\boldsymbol{R}), \qquad (2.96)$$

where $\tau_{\mathrm{imp}} = \frac{\pi n v_0}{\hbar} \int \frac{d\Omega_q}{4\pi} |U(\mathbf{k}_{\mathrm{F}} - \mathbf{q}_{\mathrm{F}})|^2$. Averaging Eq. (2.93) over $\mathbf{k}_{\mathrm{F}}$ the following pair of equations are found,

$$\frac{i\hbar v_{\mathrm{F}}}{3} \nabla \cdot \check{\mathbf{g}}_k + \left[\varepsilon \check{\rho}_4 - \check{V}, \check{g}_s\right] = 0, \tag{2.97}$$

$$i\hbar v_{\mathrm{F}} \nabla \check{g}_s + \left[\varepsilon \check{\rho}_4 - \check{V} - \check{\Sigma}, \check{\mathbf{g}}_p\right] = 0. \tag{2.98}$$

In Eq. (2.97), the impurity self energy vanishes, since $\check{\Sigma} \propto \check{g}_s$. In Eq. (2.98), on the other hand, it is assumed that impurity self energy is dominating, leading to

$$v_{\mathrm{F}} \nabla \check{g}_s + \frac{1}{2\tau_{\mathrm{imp}}} \left[\check{g}_s, \check{\mathbf{g}}_k\right] = 0,$$

which after multiplication with $\check{g}_s$ from the left leads to

$$\check{\mathbf{g}}_k = -\tau_{\mathrm{imp}} v_{\mathrm{F}} \check{g}_s \nabla \check{g}_s. \tag{2.99}$$

The equation of motion in the diffusive limit can therefore be written as

$$\hbar D \nabla \cdot \check{g}_s \nabla \check{g}_s + i \left[\varepsilon \check{\rho}_4 - \check{V}, \check{g}_s\right] = 0, \tag{2.100}$$

where $D = v_{\mathrm{F}}^2 \tau_{\mathrm{imp}}/3$ is the diffusion constant. Eq. (2.100) is known as the Usadel equation [115].

A diffusive normal metal

An infinite diffusive normal metal may be described by removing the gradient term, and setting $\check{V} = 0$ in Eq. (2.100). The solution for the retarded Green function is given as

$$\hat{g}^R = \hat{\rho}_4.$$

The advanced Green function may be found by using the general identity of Eq. (2.11), whose quasiclassical Nambu⊗spin space equivalent is

$$\hat{g}^A = -\hat{\rho}_4 \left(\hat{g}^R\right)^\dagger \hat{\rho}_4, \tag{2.101}$$

leading to

$$\hat{g}^A = -\hat{\rho}_4.$$

Finally, the Keldysh Green function is found from Eq. (2.43) to be

$$\hat{g}^K = 2\hat{\rho}_4 \tanh \frac{\beta\varepsilon}{2}.$$

Chapter 3

Superconductivity

A material may become superconducting at low temperatures if there is an attractive interaction between the constituent electrons. Naïvely one would expect such a phenomenon to be impossible due to the strong Coulomb repulsion between charges of equal sign. To understand why superconductivity nevertheless takes place, and in fact, is quite common, the origin of the attractive interaction will be explored. This discussion will lead up to a description within the Green function formalism.

3.1 Screening in an electron gas

The Coulomb interaction between two charges has an infinite range, and produces a strong repulsion. In a gas of charged particles, this repulsion leads to a greater average distance between the particles, and results in a reduced interaction compared to what would have been the case if they were fixed in place. This can be thought of as each particle being surrounded by an oppositely charged cloud, reducing its net charge. To understand how this effect, known as *screening*, comes about, a simple model will be presented, see e.g. [108] for an extended discussion. Consider a charge density ρ^{ext} introduced somehow to an electron gas, for instance by the insertion of a point charge Q at some position r_0, for which $\rho^{\text{ext}}(r) = Q\delta(r - r_0)$. The Coulomb potential generated by such a charge density is found from the Poisson equation,

$$\nabla^2 V^{\text{ext}}(r) = -\frac{1}{\epsilon_0}\rho^{\text{ext}}(r), \tag{3.1}$$

where ϵ_0 is the vacuum permittivity. The presence of this alien charge density will induce a response in the electron gas, in the form of an addi-

tional charge density, ρ^{ind} which partially screens ρ^{ext}, so that the total charge density becomes $\rho = \rho^{\text{ext}} + \rho^{\text{ind}}$, with the potential given as

$$\nabla^2 V = -\frac{1}{\epsilon_0}\rho(\boldsymbol{r}). \tag{3.2}$$

To proceed, a concept from dielectric materials is borrowed, namely that V^{ext} is related to V via,

$$V^{\text{ext}} = \int d\boldsymbol{r}' \epsilon(\boldsymbol{r} - \boldsymbol{r}')V(\boldsymbol{r}'), \tag{3.3}$$

which gives the relation

$$V(\boldsymbol{q}) = \frac{1}{\epsilon(\boldsymbol{q})}V^{\text{ext}}(\boldsymbol{q}) \tag{3.4}$$

in Fourier space. Similarly, the induced charge density is assumed related to V through

$$\rho^{\text{ind}}(\boldsymbol{q}) = \chi(\boldsymbol{q})V(\boldsymbol{q}). \tag{3.5}$$

Combining Eqs. (3.1), (3.2), (3.4) and (3.5) then gives

$$\epsilon(\boldsymbol{q}) = 1 - \frac{\chi(\boldsymbol{q})}{\epsilon_0 \boldsymbol{q}^2}. \tag{3.6}$$

To determine $\chi(\boldsymbol{q})$, approximations are necessary, and the simplest of which is perhaps the *Thomas-Fermi method* [108]. It is a semiclassical model, where the energy eigenstates of the system are assumed to be of the form

$$\varepsilon(\boldsymbol{k}, \boldsymbol{r}) = \frac{\hbar^2 \boldsymbol{k}^2}{2m} - eV(\boldsymbol{r}). \tag{3.7}$$

In other words, a dependence on both the wave vector $\boldsymbol{k}$ and the position $\boldsymbol{r}$ is retained, which only makes sense if $V(\boldsymbol{r})$ is a slowly varying function. The electron number density may then be found from the Fermi-Dirac distribution,

$$n(\boldsymbol{r}) = 2\int \frac{d\boldsymbol{k}}{(2\pi)^3} \frac{1}{1 + e^{\beta(\varepsilon(\boldsymbol{k}, \boldsymbol{r}) - \mu)}}, \tag{3.8}$$

where the factor 2 stems from the electron spin, and $\beta = 1/k_{\text{B}}T$, with k_{B} the Boltzmann constant and T the temperature. It is assumed that the

screening of ρ^{ext} is efficient enough for the chemical potential μ to be only negligibly perturbed. The induced charge density must then be given by

$$\rho^{\text{ind}}(\boldsymbol{r}) = -e\left(n\left[V(\boldsymbol{r})\right] - n\left[V(\boldsymbol{r}) = 0\right]\right), \tag{3.9}$$

which, if V is small, can be estimated as

$$\rho^{\text{ind}}(\boldsymbol{r}) = -e^2 \frac{\partial n}{\partial \mu} V(\boldsymbol{r}), \tag{3.10}$$

from which $\chi(\boldsymbol{q}) = -e^2 \frac{\partial n}{\partial \mu}$ is found. It is customary to define $q_{\text{TF}}^2 = -\chi(\boldsymbol{q})/\epsilon_0$, so that

$$\epsilon(\boldsymbol{q}) = 1 + \frac{q_{\text{TF}}^2}{\boldsymbol{q}^2}. \tag{3.11}$$

Screening in the electron gas is therefore taken into account by making the replacement $\epsilon_0 \to \epsilon_0\epsilon$ in the Coulomb interaction. For a point charge, where $V^{\text{ext}}(\boldsymbol{q}) = Q/\epsilon_0\boldsymbol{q}^2$, one finds

$$V(\boldsymbol{q}) = \frac{Q}{\epsilon_0\epsilon\boldsymbol{q}^2} = \frac{1}{\epsilon_0}\frac{Q}{\boldsymbol{q}^2 + q_{\text{TF}}^2}. \tag{3.12}$$

In position space, the screened potential has the form of a Yukawa potential,

$$V(\boldsymbol{r}) = \frac{1}{4\pi\epsilon_0}\frac{Q}{|\boldsymbol{r}|}e^{-q_{\text{TF}}|\boldsymbol{r}|}. \tag{3.13}$$

At low temperatures, the Fermi-Dirac distribution may be approximated as a step function $\theta(x)$, and using that

$$\frac{\partial}{\partial\mu}\theta(\varepsilon(\boldsymbol{k},\boldsymbol{r}) - \mu) = -\frac{m}{\hbar^2 k_{\text{F}}}\delta(k - k_{\text{F}}),$$

with $\mu = \hbar^2 k_{\text{F}}^2/2m$, it is found that

$$\frac{\partial n}{\partial\mu} \simeq -\frac{mk_{\text{F}}^2}{\pi^2\hbar^2},$$

which means that

$$q_{\text{TF}} \simeq \sqrt{\frac{e^2 m k_{\text{F}}}{\pi^2\epsilon_0\hbar^2}} = \sqrt{\frac{4k_{\text{F}}}{\pi a_0}}, \tag{3.14}$$

where $a_0 = 4\pi\epsilon_0\hbar^2/me^2$ is the Bohr radius. Typically, $k_{\text{F}} \sim 1/a_0$, which means that q_{TF} is on the order of k_{F}. The conclusion is that an electron gas is excellent at screening charges.

3.2 The jellium model

In a metal, the electrons in the outermost atomic orbitals are quite free to roam about, leaving behind a lattice of charged ions. A typical Hamiltonian for these electrons therefore includes interactions between the electrons, V_{ee}, interactions between the ions V_{ii}, and interactions between the electrons and the ions V_{ei},

$$H = -\frac{\hbar^2}{2m}\nabla^2 + \mu + V_{ee} + V_{ii} + V_{ei}. \tag{3.15}$$

To understand how superconductivity may emerge in a metal, a very simple model will be used, which is called jellium. For concreteness, consider a box of volume $\mathcal{V}$ containing N electrons. Both $\mathcal{V}$ and N are assumed to be large, but with the electron density $n = N/\mathcal{V}$ remaining finite, which is known as the *thermodynamic limit*. The N electrons provide a total charge of $-eN$. In the jellium model, the ion lattice is smeared out, giving a uniform positive background charge density, which in order to maintain charge neutrality, must be $\rho_i = +eN/\mathcal{V}$. For a static lattice, the Coulomb interaction between the ions is then given as

$$V_{ii} = \frac{1}{2}\frac{1}{4\pi\epsilon_0}\int d\boldsymbol{r}\int d\boldsymbol{r}'\frac{\rho_i(\boldsymbol{r})\rho_i(\boldsymbol{r}')}{|\boldsymbol{r}-\boldsymbol{r}'|}e^{-q_{\mathrm{TF}}|\boldsymbol{r}-\boldsymbol{r}'|} = \frac{e^2 N^2}{2\epsilon_0 \mathcal{V} q_{\mathrm{TF}}^2}, \tag{3.16}$$

where the factor $1/2$ is necessary to avoid double counting. The electron-ion interaction is given as

$$V_{ei} = -\frac{e}{4\pi\epsilon_0}\sum_{i=1}^{N}\int d\boldsymbol{r}\frac{\rho_i(\boldsymbol{r}')}{|\boldsymbol{r}-\boldsymbol{r}_i|}e^{-q_{\mathrm{TF}}|\boldsymbol{r}-\boldsymbol{r}_i|} = -\frac{e^2 N^2}{\epsilon_0 \mathcal{V} q_{\mathrm{TF}}^2}. \tag{3.17}$$

Hence, both V_{ii} and V_{ei} give a constant contribution in the jellium model. Furthermore, the second-quantised form of the electron-electron interaction is given as

$$V_{ee} = \frac{1}{2}\frac{e^2}{\epsilon_0 V}\sum_{kk'q}\frac{1}{\boldsymbol{q}^2 + q_{\mathrm{TF}}^2}c_{k+q}^{\dagger}c_{k'-q}^{\dagger}c_{k'}c_k. \tag{3.18}$$

Examining the $\boldsymbol{q} = 0$ term, which expresses an average over the volume $\mathcal{V}$, gives

$$V_{ee}^{\boldsymbol{q}=0} = \frac{e^2}{2\epsilon_0 V q_{\mathrm{TF}}^2}\left(\hat{N}^2 - \hat{N}\right), \tag{3.19}$$

where $\hat{N} = \sum_k c_k^\dagger c_k$ is the number operator. Anticipating that the operator V_{ee} will act on an eigenstate of the number operator, $\hat{N}$ may be replaced by its eigenvalue N for the sake of this discussion. This means that the N^2 term in Eq. (3.19) cancels the contribution from V_{ii} and V_{ei}, which is just a manifestation of charge neutrality. It can also be argued that the N term in Eq. (3.19) gives a negligible contribution in the thermodynamic limit, as the average energy per particle is proportional to $1/V \to 0$, whereas the average kinetic energy per particle remains constant [98]. Nevertheless, the important point is that the static ion lattice does not participate explicitly in the Hamiltonian within the jellium approximation.

3.3 Electron-phonon interaction

As was shown in Section 3.2, the interactions between an electron gas and a static, smeared out ion lattice are trivially absorbed into the electron-electron interactions. However, if the lattice is allowed to vibrate this picture changes, and a new interaction is introduced – the electron-phonon interaction. In the jellium model, these vibrations take the form of density fluctuations $n_i(\boldsymbol{r}, t) = n_{0,i} + \delta n_i(\boldsymbol{r}, t)$, where $n_{0,i} = N_i/\mathcal{V}$ and N_i is the ion number. The charge density is then given by

$$\rho_i(\boldsymbol{r}, t) = Zen_i(\boldsymbol{r}, t) = \rho_{i,0} + \delta\rho_i(\boldsymbol{r}, t). \tag{3.20}$$

Note that the ion number is related to the electron number via $N_i = N/Z$, where Z is the atomic number. This perturbation of the uniform background charge density (which is assumed to be small) generates an electric displacement field,

$$\nabla \cdot \boldsymbol{D}(\boldsymbol{r}, t) = \delta\rho_i(\boldsymbol{r}, t),$$

which is related to the electric field via

$$\boldsymbol{D}(\boldsymbol{r}, t) = \varepsilon_0 \int d\boldsymbol{r}\, \epsilon(\boldsymbol{r} - \boldsymbol{r}') \boldsymbol{E}(\boldsymbol{r}', t).$$

Fourier transforming yields

$$i\boldsymbol{q} \cdot \boldsymbol{E}(\boldsymbol{q}, t) = \frac{1}{\epsilon_0 \epsilon(\boldsymbol{q})} \delta\rho_i(\boldsymbol{q}, t).$$

The force density $\boldsymbol{f}$ induced by this field is given by $\boldsymbol{f} = \boldsymbol{E}\rho_i \simeq \boldsymbol{E}\rho_{i,0}$ to lowest order in the charge density perturbation, thus giving

$$i\boldsymbol{q} \cdot \boldsymbol{f}(\boldsymbol{q}, t) = \frac{1}{\epsilon_0 \epsilon(\boldsymbol{q})} \rho_{i,0} \delta\rho_i(\boldsymbol{q}, t). \tag{3.21}$$

A time variation of the charge density produces a current density $\boldsymbol{J}$, which satisfies the continuity equation

$$\frac{\partial}{\partial t}\delta\rho_i(\boldsymbol{r},t) + \nabla\cdot\boldsymbol{J}(\boldsymbol{r},t) = 0. \tag{3.22}$$

Due to the density fluctuations, the continuum has a velocity $\boldsymbol{v}$, so that the current may be expressed as $\boldsymbol{J} = \rho_i\boldsymbol{v} \simeq \rho_{0,i}\boldsymbol{v}$. Differentiating Eq. (3.22) and using Newton's second law, $\boldsymbol{f} = Mn_i\frac{\partial}{\partial t}\boldsymbol{v} \simeq Mn_{0,i}\frac{\partial}{\partial t}\boldsymbol{v}$ where M is the ion mass, one then gets

$$\frac{\partial^2}{\partial t^2}\delta\rho_i(\boldsymbol{r},t) + \frac{e}{M}\nabla\cdot\boldsymbol{f}(\boldsymbol{r},t) = 0. \tag{3.23}$$

By Fourier transforming in space, and inserting Eq. (3.21) this results in

$$\frac{\partial^2}{\partial t^2}\delta\rho_i(\boldsymbol{q},t) + \frac{Ze\rho_{0,i}}{M\epsilon_0\epsilon(\boldsymbol{q})}\delta\rho_i(\boldsymbol{q},t) = 0, \tag{3.24}$$

which is nothing but a harmonic oscillator, with eigenfrequencies ω_q defined as

$$\omega_q = \sqrt{\frac{Ze\rho_{0,i}}{M\epsilon_0\epsilon(\boldsymbol{q})}}. \tag{3.25}$$

Note that for small q, ω_q approaches a linear dispersion, $\omega_q = cq$, where $c = \frac{1}{3}v_\mathrm{F}\sqrt{Z\frac{m}{M}}$, and the identity $N/V = k_\mathrm{F}^3/3\pi^2$ has been used for the electron density [108]. In other words, the density fluctuations are acoustical in nature. This is known as the *Bohm-Staver relation* [116].

The screening effect of the vibrating lattice may be found by considering Maxwell's equations for the electric field,

$$\nabla\times(\nabla\times\boldsymbol{E}(\boldsymbol{r},t)) = -\mu_0\frac{\partial}{\partial t}\left(\boldsymbol{J}(\boldsymbol{r},t) + \int d\boldsymbol{r}'\,\epsilon(\boldsymbol{r}-\boldsymbol{r}')\frac{\partial}{\partial t}\boldsymbol{E}(\boldsymbol{r}',t)\right).$$

Inserting $\frac{\partial}{\partial t}\boldsymbol{J} \simeq Ze\rho_{0,i}\boldsymbol{E}/M = \omega_q\epsilon_0\epsilon(\boldsymbol{q})$ and Fourier transforming in both space and time gives

$$\boldsymbol{q}^2\boldsymbol{E}(\boldsymbol{q},\omega) + \mu_0\epsilon_0\epsilon(\boldsymbol{q})\left(1 - \frac{\omega_q^2}{\omega^2}\right)\omega^2\boldsymbol{E}(\boldsymbol{q},\omega) = -i\frac{\boldsymbol{q}}{\epsilon_0\epsilon(\boldsymbol{q})}\delta\rho_i(\boldsymbol{q},\omega). \tag{3.26}$$

A new dielectric constant may now be defined,

$$\epsilon_{ep}(\boldsymbol{q},\omega) = \epsilon_0\epsilon(\boldsymbol{q})\left(1 - \frac{\omega_q^2}{\omega^2}\right). \tag{3.27}$$

In this case, the left hand side of Eq. (3.26) takes the form of a (nonlinear) wave equation. The right hand side represents a source term which depends on $\delta\rho_i$. The physical interpretation of this is that a perturbation of the ion lattice propagates as waves throughout the system. An effective Coulomb interaction, which takes into account the effect of both static and dynamic screening effects may therefore be given as

$$V(\omega) = \sum_{kk'q} V^{\text{eff}}(\boldsymbol{q},\omega) c^{\dagger}_{k+q} c^{\dagger}_{k-q} c_{k'} c_k, \tag{3.28}$$

with

$$V^{\text{eff}}(\boldsymbol{q},\omega) = \frac{e^2}{\epsilon_{ep}(\boldsymbol{q},\omega)\boldsymbol{q}^2} = \frac{e^2}{\epsilon_0} \frac{1}{\boldsymbol{q}^2 + q_{\text{TF}}^2} \frac{\omega^2}{\omega^2 - \omega_q^2}, \tag{3.29}$$

which is shown in Fig. 3.1. Note that for $|\omega| < \omega_q$, V^{eff} becomes negative, i.e., it is attractive. Typically, ω_q is approximated as constant and equal to the Debye frequency, ω_D [117].
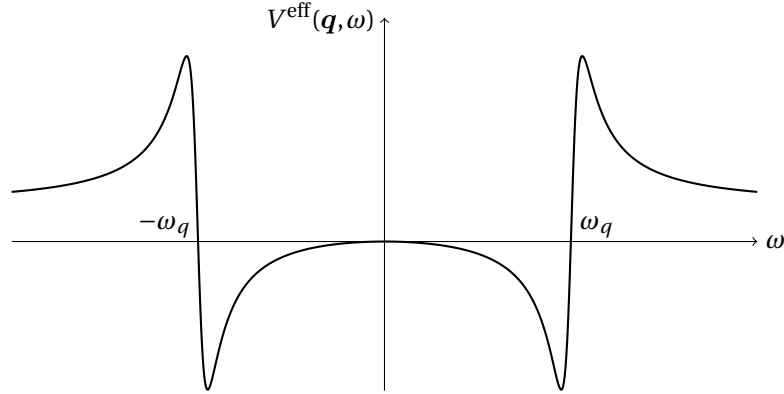
Figure 3.1: The approximate screened Coulomb potential due to both electron-electron and electron-phonon interactions, for an arbitrary $\boldsymbol{q}$.

.

3.4 The Cooper instability

In the previous section it was shown that the electron-phonon interaction in a metal can lead to an attraction between electrons. This has a profound effect on the low temperature behaviour of such systems. To illustrate

this, a brief review of the model problem proposed by Cooper will be presented [56], which will show that attractive interactions lead to an instability of the Fermi surface.

Consider an electron gas at temperature $T = 0$. In this case, all states with energies below the Fermi level, E_F, are occupied, and all states with energies above E_F are empty. To this system, two electrons are added, which then must have energies $\varepsilon_k > E_F$. Coulomb interactions between these superfluous electrons and the occupied states are disregarded, and hence the Pauli exclusion principle prevents any participation of the latter. The picture to have in mind is thus that of two electrons skating on a frozen Fermi sea. The two electrons may however scatter off each other, through an interaction potential V_C. The Shcrödinger equation for the two-particle system may then be written as

$$\left[-\frac{\hbar^2}{2m}\nabla_1^2 - \frac{\hbar^2}{2m}\nabla_2^2 + V_C(\boldsymbol{r}_1 - \boldsymbol{r}_2) \right] \psi(\boldsymbol{r}_1, \sigma_1; \boldsymbol{r}_2, \sigma_2) = \varepsilon \psi(\boldsymbol{r}_1, \sigma_1; \boldsymbol{r}_2, \sigma_2).$$

Due to the translation invariance of this system, it is convenient to Fourier transform, which gives

$$\left(\varepsilon_{k_1} + \varepsilon_{k_2} - \varepsilon\right)\psi(\boldsymbol{k}_1, \boldsymbol{k}_2) + \int \frac{d\boldsymbol{q}}{(2\pi)^3}\, V_C(\boldsymbol{k}_1 - \boldsymbol{q})\psi(\boldsymbol{q}, \boldsymbol{k}_1 + \boldsymbol{k}_2 - \boldsymbol{q}) = 0, \quad (3.30)$$

where $\varepsilon_{k_i} = \hbar^2 \boldsymbol{k}_i^2 / 2m$, and the spin indices are suppressed for brevity. To mimic the effect of the electron-phonon interaction, V_C is assumed to be attractive within an energy shell of thickness $\hbar\omega_D$ surrounding the Fermi level, and zero otherwise,

$$V_C(\boldsymbol{k}) = \begin{cases} -V_0, & E_F < \varepsilon_k < E_F + \hbar\omega_D \\ 0, & \text{otherwise} \end{cases} \qquad (3.31)$$

The centre of mass momentum, $\bar{\boldsymbol{k}} = (\boldsymbol{k}_1 + \boldsymbol{k}_2)/2$ is conserved in the scattering process. Furthermore, introducing $\delta\boldsymbol{k} = \boldsymbol{k}_1 - \boldsymbol{k}_2$, it is clear that the lowest total kinetic energy

$$\varepsilon_{k_1} + \varepsilon_{k_2} = 2\frac{\hbar^2\bar{\boldsymbol{k}}^2}{2m} + \frac{1}{2}\frac{\hbar^2\delta\boldsymbol{k}^2}{2m}$$

is found by assuming that $\boldsymbol{k} = 0$. This eats up the least of the allotted energy interval in which V_C is nonzero, and must therefore maximise the interaction. This further implies that $\boldsymbol{k}_1 = -\boldsymbol{k}_2 \equiv \boldsymbol{k}$. Defining $\psi(\boldsymbol{k}) \equiv \psi(\boldsymbol{k}, -\boldsymbol{k})$, Eq. (3.30) becomes

$$(\varepsilon_k - \varepsilon)\psi(\boldsymbol{k}) - V_0 \int \frac{d\boldsymbol{q}}{(2\pi)^3}\psi(\boldsymbol{q}) = 0, \qquad (3.32)$$

provided that $\varepsilon_k \in [E_{\mathrm{F}}, E_{\mathrm{F}} + \hbar\omega_D]$. A comment needs to be made regarding the symmetry of $\psi(\boldsymbol{q})$. Due to the Pauli exclusion principle, the wave function $\psi(\boldsymbol{r}_1, \sigma_1; \boldsymbol{r}_2, \sigma_2) = \phi(\boldsymbol{r}_1, \boldsymbol{r}_2) \chi(\sigma_1, \sigma_2)$ needs to be antisymmetric. If the spin function $\chi(\sigma_1, \sigma_2)$ is symmetric, which indicates a spin triplet state, then the orbital part $\phi(\boldsymbol{r}_1, \boldsymbol{r}_2)$ must be antisymmetric. This however means that $\psi(\boldsymbol{q})$ is antisymmetric in $\boldsymbol{q}$, so that Eq. (3.32) only admits the trivial solution of $\psi(\boldsymbol{k}) = 0$. On the other hand, for an antisymmetric $\chi(\sigma_1, \sigma_2)$, which is the spin singlet state, $\psi(\boldsymbol{q})$ is symmetric in $\boldsymbol{q}$, and a non-trivial solution is found by integrating over $\boldsymbol{k}$,

$$V_0 \int d\boldsymbol{k} \, \frac{1}{2\varepsilon_k - \varepsilon} = 1. \tag{3.33}$$

Using that $d\boldsymbol{k} = \nu(\varepsilon) d\varepsilon$, where $\nu(\varepsilon)$ is the density of states per volume, the integral becomes

$$V_0 \int_{E_{\mathrm{F}}}^{E_{\mathrm{F}} + \hbar\omega_D} d\varepsilon' \, \frac{\nu(\varepsilon')}{2\varepsilon' - \varepsilon} \simeq \frac{1}{2} V_0 \nu(E_F) \ln\left(\frac{2E_{\mathrm{F}} + 2\hbar\omega_D - \varepsilon}{2E_{\mathrm{F}} - \varepsilon}\right) = 1.$$

The approximation $\nu(\varepsilon') \simeq \nu(E_{\mathrm{F}}) \equiv \nu_0$ is reasonable as long as $\hbar\omega_D \ll E_{\mathrm{F}}$. Solving for the energy ε then finally gives

$$\varepsilon = 2E_{\mathrm{F}} - \frac{2\hbar\omega_D}{e^{2/V_0\nu_0} - 1} \simeq 2E_{\mathrm{F}} - 2\hbar\omega_D e^{-2/V_0\nu_0}, \tag{3.34}$$

in the weak coupling regime $V_0\nu_0 \ll 1$. The conclusion is that the electrons *reduce* their energy by forming a bound pair, known as a *Cooper pair*. This occurs regardless of the strength of V_0.

3.5   Mean field approach to superconductivity

It is an interesting result that the effective Coulomb interaction between electrons moving in a lattice has the potential of forming bound pairs – even more so due to the fact that, under the right circumstances, this state seems to be preferred. To gain more insight into how this behaviour can lead to superconductivity in a many-particle system, a slightly more general model will be described next, namely the BCS Hamiltonian [48]

$$H = \sum_{k\sigma} \left(\varepsilon_k - \mu\right) c_{k\sigma}^\dagger c_{k\sigma} + \sum_{kk'} V_{kk'} c_{k'\uparrow}^\dagger c_{-k'\downarrow}^\dagger c_{-k\downarrow} c_{k\uparrow}, \tag{3.35}$$

where, along the same lines as Eq. (3.31),

$$V_{kk'} = \begin{cases} -V_0, & E_{\mathrm{F}} < \varepsilon_k, \varepsilon_{k'} < E_{\mathrm{F}} + \hbar\omega_D \\ 0, & \text{otherwise} \end{cases} \tag{3.36}$$

To solve Eq. (3.35), the mean field approach will be used. This is done by defining an operator [98]

$$d_k = c_{-k\downarrow} c_{k\uparrow} - \langle c_{-k\downarrow} c_{k\uparrow} \rangle \qquad (3.37)$$

$$d_k^\dagger = c_{k\uparrow}^\dagger c_{-k\downarrow}^\dagger - \langle c_{k\uparrow}^\dagger c_{-k\downarrow}^\dagger \rangle. \qquad (3.38)$$

d_k expresses the deviation from the average of $c_{-k\downarrow} c_{k\uparrow}$. This gives

$$c_{k'\uparrow}^\dagger c_{-k'\downarrow}^\dagger c_{-k\downarrow} c_{k\uparrow} = d_{k'}^\dagger d_k + d_{k'}^\dagger \langle c_{-k\downarrow} c_{k\uparrow} \rangle + d_k \langle c_{k'\uparrow}^\dagger c_{-k'\downarrow}^\dagger \rangle + \langle c_{k'\uparrow}^\dagger c_{-k'\downarrow}^\dagger \rangle \langle c_{-k\downarrow} c_{k\uparrow} \rangle$$

$$\simeq d_{k'}^\dagger \langle c_{-k\downarrow} c_{k\uparrow} \rangle + d_k \langle c_{k'\uparrow}^\dagger c_{-k'\downarrow}^\dagger \rangle + \langle c_{k'\uparrow}^\dagger c_{-k'\downarrow}^\dagger \rangle \langle c_{-k\downarrow} c_{k\uparrow} \rangle.$$

In the last line the term $d_{k'}^\dagger d_k$ has been neglected, under the assumption that the fluctuations around the average, or mean field, result are small. By inserting into Eq. (3.35) one gets

$$H = \sum_{k\sigma} \left(\varepsilon_k - \mu \right) c_{k\sigma}^\dagger c_{k\sigma} - \sum_k \left[\Delta_k d_k^\dagger + \Delta_k^* d_k + \Delta_k^* \langle c_{-k\downarrow} c_{k\uparrow} \rangle \right], \qquad (3.39)$$

where

$$\Delta_k = -\sum_{k'} V_{k'k} \langle c_{-k'\downarrow} c_{k'\uparrow} \rangle. \qquad (3.40)$$

Inserting the expressions for d_k and $d_k^\dagger$ then gives

$$H = \sum_{k\sigma} \left(\varepsilon_k - \mu \right) c_{k\sigma}^\dagger c_{k\sigma} - \sum_k \left[\Delta_k c_{k\uparrow}^\dagger c_{-k\downarrow}^\dagger + \Delta_k^* c_{-k\uparrow} c_{k\uparrow} - \Delta_k \langle c_{k\downarrow}^\dagger c_{-k\uparrow}^\dagger \rangle \right]. \qquad (3.41)$$

Eq. (3.41) can be diagonalised by a Bogoliubov–Valatin transformation [118, 119]

$$\gamma_{k\uparrow} = u_k c_{k\uparrow} - v_k c_{-k\downarrow}^\dagger \qquad (3.42)$$

$$\gamma_{-k\downarrow} = u_k c_{-k\downarrow} + v_k c_{k\uparrow}^\dagger \qquad (3.43)$$

$$\gamma_{k\uparrow}^\dagger = u_k^* c_{k\uparrow}^\dagger - v_k^* c_{-k\downarrow} \qquad (3.44)$$

$$\gamma_{-k\downarrow}^\dagger = u_k^* c_{-k\downarrow}^\dagger + v_k^* c_{k\uparrow}. \qquad (3.45)$$

To ensure that the new operators still describe fermions, they are defined to satisfy

$$\left\{ \gamma_{k\sigma} , \gamma_{k'\sigma'} \right\} = \left\{ \gamma_{k\sigma}^\dagger , \gamma_{k'\sigma'}^\dagger \right\} = 0, \quad \left\{ \gamma_{k\sigma}, \gamma_{k'\sigma'}^\dagger \right\} = \delta_{kk'} \delta_{\sigma\sigma'}, \qquad (3.46)$$

from which the relation

$$|u_k|^2 + |v_k|^2 = 1 \qquad (3.47)$$

emerges. Expressing Eq. (3.41) in terms of the operators $\gamma_{k\sigma}$, it can be shown to take the form

$$H = \sum_k E_k \left(\gamma_{k\uparrow}^\dagger \gamma_{k\uparrow} + \gamma_{-k\downarrow}^\dagger \gamma_{-k\downarrow} \right) \qquad (3.48)$$

$$+ \sum_k \left[2(\varepsilon_k - \mu)|v_k|^2 - 2\Re(\Delta_k u_k v_k) + \Delta_k \langle c_{k\uparrow}^\dagger c_{-k\downarrow}^\dagger \rangle \right], \qquad (3.49)$$

if the parameters u_k and v_k are chosen so that they define

$$2(\varepsilon_k - \mu) u_k v_k + \Delta_k^* v_k^2 - \Delta_k u_k^2 = 0 \qquad (3.50)$$

$$2(\varepsilon_k - \mu) u_k^* v_k^* + \Delta_k v_k^{*2} - \Delta_k^* u_k^{*2} = 0. \qquad (3.51)$$

The excitation energies, E_k are then given as

$$E_k = \pm \sqrt{\left(\varepsilon_k - \mu\right)^2 + |\Delta_k|^2}, \qquad (3.52)$$

which produces a gap around the Fermi level of width $2\Delta_k$, as illustrated in Fig. 3.2. For simplicity, u_k, v_k and Δ_k are assumed to be real. The constraint in Eq. (3.47) hints at a convenient parametrisation. Defining $u_k = \sin\theta_k$ and $v_k = \cos\theta_k$, the solution of Eq. (3.50) readily presents itself as $\tan 2\theta_k = \Delta_k / E_k$.

In the ground state of this system, there are no excitations, which means that the eigenstate must satisfy

$$\gamma_{k\uparrow} |\psi\rangle = \gamma_{-k\downarrow} |\psi\rangle = 0, \qquad (3.53)$$

for all $\boldsymbol{k}$. Due to the Pauli exclusion principle, one may thus write,

$$|\psi\rangle = \prod_k \gamma_{k\uparrow} \gamma_{-k\downarrow} |0\rangle, \qquad (3.54)$$

where $|0\rangle$ is the vacuum state of the $c_{k\sigma}$ operators. By inserting the expression for the γ operators, $|\psi\rangle$ becomes, after normalisation,

$$|\psi\rangle = \prod_k \left(u_k + v_k c_{k\uparrow}^\dagger c_{-k\downarrow}^\dagger \right) |0\rangle. \qquad (3.55)$$

From Eq. (3.55) it is clear that the parameter v_k^2 is the probability of the pair state $|\boldsymbol{k}\uparrow, -\boldsymbol{k}\downarrow\rangle$ being occupied, and u_k^2 is the probability of it being empty.

The presence of an energy gap introduces an associated length scale. Setting $\Delta_k = \Delta_0$ for simplicity, this energy gap represents the binding energy of a Cooper pair. The Heisenberg uncertainty principle then dictates that the constituent quasiparticles must interact for at least a duration of $\tau_\xi = \hbar/\Delta_0$. In a clean material, the quasiparticles move with a velocity of v_{F}, from which the average size of a Cooper pair is found to be [120]

$$\xi_0 = \frac{\hbar v_{\mathrm{F}}}{\pi \Delta_0},$$

(3.56)

where the factor π is a matter of convention.
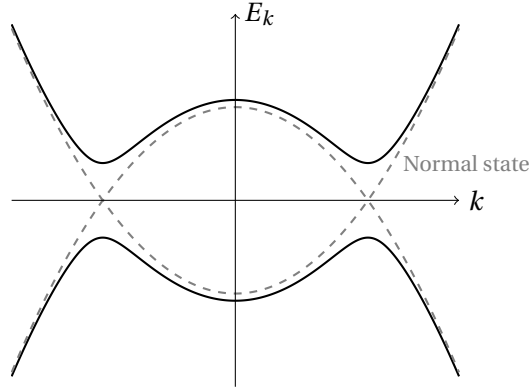
Figure 3.2: The quasiparticle energy band E_k, assuming a constant superconducting gap $\Delta_k = \Delta_0$. For comparison the normal state dispersion is shown in grey.

3.6   Green functions and superconductivity

It is challenging to study complex systems by attempting to diagonalise the corresponding Hamiltonian, and hence it is useful to include a description of superconductivity in the Green function framework developed in Chapter 2.

In a Fermi liquid, it can be shown that the resulting Green function, after a summation of diagrams, takes the form

$$G(\boldsymbol{k}) \sim \frac{1}{\varepsilon - \frac{\hbar^2 \boldsymbol{k}^2}{2m} + \mu - \Sigma(\boldsymbol{k})},$$

for some self energy Σ, which depends on the included interactions. The poles of the Green function determine the energy dispersion $\varepsilon(\boldsymbol{k})$, and

since the excitation energies for a superconductor are given by Eq. (3.52) within the mean field approximation, a naïve guess would be to expect Green functions of the form

$$G(\boldsymbol{k}) \sim \frac{1}{\varepsilon \mp \sqrt{\left(\frac{\hbar^2 \boldsymbol{k}^2}{2m} - \mu\right)^2 + |\Delta_k|^2}}$$

when the attractive potential of the BCS Hamiltonian, given in Eq. (3.35), is treated as a perturbation. This is not correct. In this case, the perturbation expansion turns out to be unstable [121]. A clue as to why that is appeared in the discussion of the Cooper instability in Section 3.4. It was derived in Eq. (3.34) that the formation of a bound state between the introduced electron pair reduced the energy of this system by a quantity proportional to $e^{-2/V_0 v_0}$, which becomes singular in the limit $V_0 \rightarrow 0$. Conventional normal state Green functions are therefore not an appropriate starting point for a perturbation expansion. This is because the appearance of superconducting correlations in a normal metal is an example of a *phase transition*. The behaviour of the material on one side of the phase transition is completely different from the behaviour on the other side. Green functions derived for a normal metal therefore cannot hope to describe the superconducting transition. For that to be possible, a framework in which both sides of the phase transition is properly described is required. This is precisely what the Nambu formalism introduced in Section 2.1 does. Indeed, with the basis defined in Eq. (2.12), it is seen from Eqs. (2.15) to (2.17) that the anomalous Green function,

$$F_{\sigma\sigma'}(\boldsymbol{r}, t; \boldsymbol{r}', t') = -i \left\langle \mathscr{T} \psi_\sigma(\boldsymbol{r}, t) \psi_{\sigma'}(\boldsymbol{r}', t') \right\rangle,$$

describe the superconducting correlations – they take the same form as the order parameter in Eq. (3.40).

The attractive potential in the BCS model is constant if the energies involved are restricted to lie in the interval between E_F and $E_F + \hbar\omega_D$. Typically, $\hbar\omega_D$ is at least an order of magnitude larger than the superconducting gap [122]. Hence, to describe physics taking place at the same energy scales as the latter, it is reasonable to simplify the BCS potential as $V(\boldsymbol{k}_1, \boldsymbol{k}_2) = -V_0$, which in position space becomes a simple contact potential, $V(\boldsymbol{r}_1, \boldsymbol{r}_2) = -V_0 \delta(\boldsymbol{r}_1 - \boldsymbol{r}_2)$. Its second-quantised form is then given as

$$V_{\text{BCS}} = -V_0 \int d\boldsymbol{r} \, \psi_\uparrow^\dagger(\boldsymbol{r}) \psi_\downarrow^\dagger(\boldsymbol{r}) \psi_\downarrow(\boldsymbol{r}) \psi_\uparrow(\boldsymbol{r}) \tag{3.57}$$

As in the previous section, an order parameter may be defined as

$$\Delta(\boldsymbol{r}) = -V_0 \langle \psi_\downarrow(\boldsymbol{r}) \psi_\uparrow(\boldsymbol{r}) \rangle, \tag{3.58}$$

where the minus sign is included by convention. Repeating the mean field analysis then gives,

$$V_{\text{BCS}} = \int d\boldsymbol{r} \left[\Delta(\boldsymbol{r}) \psi_\uparrow^\dagger(\boldsymbol{r}) \psi_\downarrow^\dagger(\boldsymbol{r}) + \Delta^*(\boldsymbol{r}) \psi_\downarrow(\boldsymbol{r}) \psi_\uparrow(\boldsymbol{r}) \right], \tag{3.59}$$

where the constant contribution has been disregarded. The time evolution of the field operators is determined by the Heisenberg equation, which now takes the form

$$i\hbar \frac{\partial}{\partial t} \psi_\sigma(\boldsymbol{r}, t) = -\left(\frac{\hbar^2}{2m} \nabla^2 + \mu \right) \psi_\sigma(\boldsymbol{r}, t) + \delta_{\sigma\uparrow} \Delta(\boldsymbol{r}) \psi_\downarrow^\dagger(\boldsymbol{r}, t) - \delta_{\sigma\downarrow} \Delta(\boldsymbol{r}) \psi_\uparrow^\dagger(\boldsymbol{r}, t),$$

and similarly for the adjoint. By converting to the Nambu basis, and Fourier transforming in time, equations for the retarded, advanced and Keldysh Green functions may be established. The result is

$$\left[\varepsilon \check{\rho}_4 + \left(\frac{\hbar^2}{2m} \nabla^2 + \mu \right) \check{I} + \check{\Delta}(\boldsymbol{r}) \right] \check{G}(\boldsymbol{r}, \boldsymbol{r}') = \check{I} \delta(\boldsymbol{r} - \boldsymbol{r}'), \tag{3.60}$$

where $\check{\Delta} = \mathrm{diag}\left(\hat{\Delta}, \hat{\Delta} \right)$, and $\hat{\Delta}$ is a 4×4 matrix which takes the form

$$\hat{\Delta}(\boldsymbol{r}) = \begin{pmatrix} 0 & 0 & 0 & \Delta(\boldsymbol{r}) \\ 0 & 0 & -\Delta(\boldsymbol{r}) & 0 \\ 0 & \Delta^*(\boldsymbol{r}) & 0 & 0 \\ -\Delta^*(\boldsymbol{r}) & 0 & 0 & 0 \end{pmatrix} \tag{3.61}$$

Note that $\left\{ \hat{\Delta}, \hat{\rho}_4 \right\} = 0$, which has been used in the derivation of Eq. (3.60). Eq. (3.60) has the same form as Eq. (2.46), and hence the quasiclassical equation of motion for a pure superconductor, the Eilenberger equation, may immediately be written down as

$$i\hbar \boldsymbol{v}_{\text{F}} \cdot \nabla \check{g}(\boldsymbol{r}, \boldsymbol{k}_{\text{F}}) + \left[\varepsilon \check{\rho}_4 + \check{\Delta}(\boldsymbol{r}), \, \check{g}(\boldsymbol{r}, \boldsymbol{k}_{\text{F}}) \right] = 0. \tag{3.62}$$

Similarly, the Usadel equation, which is valid in the diffusive limit, is given as

$$\hbar D \nabla \cdot \check{g} \nabla \check{g} + i \left[\varepsilon \check{\rho}_4 + \check{\Delta}, \, \check{g} \right] = 0. \tag{3.63}$$

Physics involving the superconducting correlations take place on the energy scale of the superconducting gap size. By scaling all energies in

Eq. (3.63) by a characteristic gap size Δ_0, it is seen that the corresponding length scale becomes

$$\xi = \sqrt{\frac{\hbar D}{\Delta_0}}, \tag{3.64}$$

which is known as the *diffusive coherence length.* It describes the size of the Cooper pairs in a diffusive material, and is related to the coherence length in a clean material, given in Eq. (3.56), via

$$\xi = \sqrt{\frac{\hbar v_{\mathrm{F}} l_{\mathrm{mfp}}}{3\Delta_0}} \simeq \sqrt{\xi_0 l_{\mathrm{mfp}}}.$$

A uniform superconductor

Consider an infinite, completely isotropic superconductor with a constant gap $\Delta_k = \Delta$. In this case, $\nabla \check{g} = 0$, and Eq. (3.63) may be solved immediately, giving for the retarded component

$$\hat{g}^R = \frac{|\varepsilon|}{\sqrt{\varepsilon^2 - \Delta^2}} \hat{\rho}_4 + \frac{\mathrm{sgn}(\varepsilon)}{\sqrt{\varepsilon^2 - \Delta^2}} \hat{\Delta}, \tag{3.65}$$

and similarly for the advanced component. From Eq. (3.65), the density of states may be computed as

$$\nu_\sigma(\varepsilon) = -\frac{1}{\pi} \Im G^R_{\sigma\sigma}(\boldsymbol{r}, \boldsymbol{r}; \varepsilon). \tag{3.66}$$

Its quasiclassical counterpart becomes, with $\nu = (\nu_\uparrow + \nu_\downarrow)/2$,

$$\nu(\boldsymbol{r}, \varepsilon) = \frac{\nu_0}{4} \Re \mathrm{Tr}\left[\hat{\rho}_4 \hat{g}^R(\boldsymbol{r}, \varepsilon)\right], \tag{3.67}$$

where ν_0 is the density of states at the Fermi level. The result is shown in Fig. 3.3, where the absence of quasiparticle states for $|\varepsilon| < \Delta$ is clearly seen.
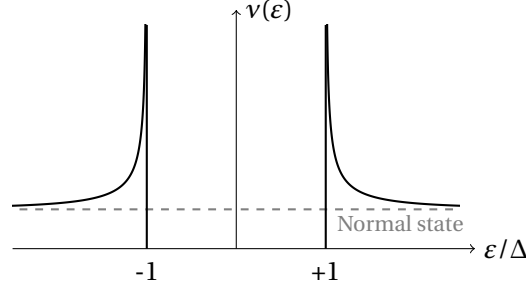
Figure 3.3: Spin-independent density of states for a uniform supercon-
ductor with gap Δ. For comparison, the density of states for a normal
metal is shown in grey.

The current density

At this point it is appropriate to discuss the current density. It is defined
from the continuity equation,

$$\frac{\partial}{\partial t}\rho + \nabla \cdot \boldsymbol{J} = 0, \tag{3.68}$$

where $\rho(\boldsymbol{r}) = e\left\langle \psi_\sigma^\dagger(\boldsymbol{r})\psi_\sigma(\boldsymbol{r})\right\rangle = en_{e,\sigma}$. The time derivative of the charge
density may be found by applying Eqs. (2.6) and (2.7) to $n_{e,\sigma}$, which gives

$$\begin{aligned}
\frac{\partial}{\partial t}n_{e,\sigma} &= \left\langle \left(\frac{\partial}{\partial t}\psi_\sigma^\dagger\right)\psi_\sigma + \psi_\sigma^\dagger\frac{\partial}{\partial t}\psi_\sigma \right\rangle \\
&= -\frac{i\hbar}{2m}\left\langle \left(\nabla^2\psi_\sigma^\dagger\right)\psi_\sigma - \psi_\sigma^\dagger\nabla^2\psi_\sigma \right\rangle, \\
&= -\frac{i\hbar}{2m}\nabla\cdot\left\langle \left(\nabla\psi_\sigma^\dagger\right)\psi_\sigma - \psi_\sigma^\dagger\nabla\psi_\sigma \right\rangle.
\end{aligned}$$

To express $\frac{\partial}{\partial t}\rho$ in terms of G^K requires some sleight of hand. Rather than
evaluating the products of field operators at the same coordinate $\boldsymbol{r}$, two
slightly displaced coordinates $\boldsymbol{r}_1$ and $\boldsymbol{r}_2$ are used instead. This gives the
identity

$$\left\langle \left(\nabla\psi_\sigma^\dagger\right)\psi_\sigma - \psi_\sigma^\dagger\nabla\psi_\sigma \right\rangle = \lim_{\boldsymbol{r}_1\to\boldsymbol{r}_2} -(\nabla_1 - \nabla_2)\left\langle \psi_\sigma^\dagger(\boldsymbol{r}_2)\psi_\sigma(\boldsymbol{r}_1)\right\rangle. \tag{3.69}$$

By applying the anticommutator relations to Eq. (2.36) it is seen that

$$\left\langle \psi_\sigma^\dagger(\boldsymbol{r}_2)\psi_\sigma(\boldsymbol{r}_1)\right\rangle = -\frac{i}{2}G^K_{\sigma\sigma}(\boldsymbol{r}_1,\boldsymbol{r}_2) + \frac{1}{2}\langle\delta(\boldsymbol{r}_1 - \boldsymbol{r}_2)\rangle. \tag{3.70}$$

The second term does not contribute to the current, and is discarded. Hence one finds the following expression for the current density,

$$\boldsymbol{J} = \lim_{\boldsymbol{r}_1 \to \boldsymbol{r}_2} -\frac{\hbar e}{8m} (\nabla_1 - \nabla_2) \operatorname{Tr}\left[\hat{\rho}_4 \hat{G}^K (\boldsymbol{r}_1, \boldsymbol{r}_2)\right], \qquad (3.71)$$

where a generalisation to Nambu⊗spin space has been made, incurring in the process another factor of 1/2, and a $\hat{\rho}_4$. In terms of the mixed representation Green function, this becomes

$$\boldsymbol{J} = -\frac{\hbar e}{8m} \int \frac{d\boldsymbol{k}}{(2\pi)^3} \int \frac{d\varepsilon}{2\pi} 2i\boldsymbol{k}\operatorname{Tr}\left[\hat{\rho}_4 \hat{G}^K (\boldsymbol{k}, \varepsilon)\right], \qquad (3.72)$$

where the integral over ε appears due to the fact that the field operators are evaluated at equal times. Within the quasiclassical approximation, this becomes

$$\boldsymbol{J} = -\frac{ev_0}{16m} \int d\varepsilon \int \frac{d\Omega_k}{4\pi} \boldsymbol{k}_{\mathrm{F}} \operatorname{Tr}\left[\hat{\rho}_4 \hat{g}^K\right]. \qquad (3.73)$$

In the diffusive limit, Eq. (2.99) may be inserted, which results in

$$\boldsymbol{J} = \frac{ev_0 D}{16} \int d\varepsilon \operatorname{Tr}\left[\hat{\rho}_4 \left(\check{g}\nabla\check{g}\right)^K\right]. \qquad (3.74)$$

Equilibrium currents

The defining characteristic of a superconductor is that it allows for equilibrium currents, or *supercurrents*, which appear whenever there is a phase gradient in the superconducting gap. To confirm this, consider a gap function with a constant phase gradient a in the x direction, $\Delta(x) = |\Delta|e^{iax}$, with a, for now, undetermined constant magnitude $|\Delta|$. An infinite diffusive superconductor is assumed, which is described by Eq. (3.63). An appropriate normalisation for the retarded Green function is [123]

$$\hat{g}^R = \begin{pmatrix} I\cosh\theta & i\sigma_y \sinh\theta e^{i\chi} \\ i\sigma_y \sinh\theta e^{-i\chi} & -I\cosh\theta \end{pmatrix}, \qquad (3.75)$$

which automatically satisfies the normalisation condition given in Eq. (2.74). The open boundary conditions dictate that the superconductor be uniform, which implies that the parameter θ must be constant. A solution to Eq. (3.63) is then found by setting $\chi(x) = ax$, with θ satisfying

$$\theta = \operatorname{atanh}\left[\frac{|\Delta|}{\varepsilon} - i\frac{\hbar D a^2}{2\varepsilon} \sinh\theta\right], \qquad (3.76)$$

which is easily solved by fixed point iterations, setting, e.g., $|\Delta| = \Delta_0$, the gap of a bulk superconductor with no phase gradient. The charge current may be found from Eq. (3.74), which turns out to be

$$J = -\frac{1}{2} e v_0 D a \int d\varepsilon \, \Im \left(\sinh^2 \theta \right) \tanh \frac{\beta \varepsilon}{2}, \qquad (3.77)$$

using Eqs. (2.11) and (2.43). Note that there is an implicit dependence on a also in $|\Delta|$, to be discussed shortly.

3.7 The gap equation

As is typical in all but the simplest mean field theories, the order parameter $\Delta(\boldsymbol{r})$ must be determined by self consistency iterations. To do so, Eq. (3.58) at the centre of mass coordinate $\boldsymbol{r}$ must be expressed in terms of Green functions. This can be done using the relation given in Eq. (3.70). One finds that the *pair correlation* becomes

$$\Phi(\boldsymbol{r}) = \langle \psi_\downarrow(\boldsymbol{r}, t) \psi_\uparrow(\boldsymbol{r}, t) \rangle = \lim_{\rho, \tau \to 0} \frac{i}{2} \hat{G}_{23}^K(\rho, \tau), \qquad (3.78)$$

where $\hat{G}_{ij}^K$ refers to the matrix element in row i and column j of $\hat{G}^K$, $\tau = t - t'$, and $\rho = \boldsymbol{r} - \boldsymbol{r}'$. Fourier transforming in relative coordinates gives

$$\Phi(\boldsymbol{r}) = \frac{i}{2} \int \frac{d\boldsymbol{k}}{(2\pi)^3} \int \frac{d\varepsilon}{2\pi} \, \hat{G}_{23}^K(\boldsymbol{r}, \boldsymbol{k}, \varepsilon). \qquad (3.79)$$

Hence, within the quasiclassical approximation, one gets

$$\Phi(\boldsymbol{r}) = \frac{\nu_0}{8} \int d\varepsilon \, \hat{g}_{23}^K(\boldsymbol{r}, \varepsilon), \qquad (3.80)$$

where $\hat{g}^K$ is the diffusive quasiclassical Green function (i.e., an angular averaging has been performed). The order parameter thus becomes

$$\Delta(\boldsymbol{r}) = -V_0 \Phi(\boldsymbol{r}) = -\frac{\lambda}{8} \int d\varepsilon \, \hat{g}_{23}^K(\boldsymbol{r}, \varepsilon), \qquad (3.81)$$

with $\lambda = V_0 \nu_0$ a dimensionless coupling strength. In order to determine $\Delta(\boldsymbol{r})$, one needs to guess at an initial value, solve the Usadel equation a sufficient number of times, at varying ε, for the integral in Eq. (3.81) to be reasonably estimated. This gives a new value for $\Delta(\boldsymbol{r})$, and the process may be repeated until self consistency is achieved. This is in general a highly nontrivial numerical problem to be discussed further in Section 4.4.

The gap of a bulk superconductor

The retarded Green function for a bulk superconductor is given in Eq. (3.65), from which the Keldysh Green function may be found from Eqs. (2.16) and (2.36). When inserted into Eq. (3.81), this leads to the following gap equation,

$$\frac{1}{\lambda} = \int_{\Delta}^{\hbar\omega_D} d\varepsilon \, \frac{\tanh\frac{\beta\varepsilon}{2}}{\sqrt{\varepsilon^2 - \Delta^2}}, \tag{3.82}$$

where the Debye energy $\hbar\omega_D$ has been used as a cut-off. In the low-temperature limit, $\tanh\frac{\beta\varepsilon}{2} \simeq 1$, in which case one gets, after some algebra [87],

$$\omega_D = \frac{\Delta}{\hbar} \cosh\frac{1}{\lambda}. \tag{3.83}$$

On the other hand, $\Delta \simeq 0$ in the limit of $T \to T_c$, the critical temperature of the superconductor, which gives [117, 124]

$$\begin{aligned}
\frac{1}{\lambda} &= \int_0^{\hbar\omega_D} d\varepsilon \, \frac{\tanh\frac{\beta_c\varepsilon}{2}}{\varepsilon} \\
&= \tanh\frac{\beta_c\hbar\omega_D}{2} \ln\left(\frac{\beta_c\hbar\omega_d}{2}\right) - \int_0^{\beta_c\hbar\omega_D/2} dz \, \frac{\ln z}{\cosh^2 z},
\end{aligned}$$

with $\beta_c = 1/k_B T_c$. In the weak coupling limit, with $\hbar\omega_D \gg \beta_c^{-1}$, one gets

$$\frac{1}{\lambda} \simeq \ln\left(\frac{\beta_c\hbar\omega_D}{2}\right) - \ln\left(\frac{\pi}{4e^\gamma}\right) = \ln\left(\frac{2e^\gamma\beta_c\hbar\omega_D}{\pi}\right),$$

where γ is the *Euler-Mascheroni constant*. Hence, in this limit,

$$\omega_D = \frac{\pi k_B T_c}{2\hbar e^\gamma} e^{1/\lambda}. \tag{3.84}$$

Combining Eqs. (3.83) and (3.84) results in the relation, with $\lambda \ll 1$ in the weak coupling limit,

$$\Delta = \frac{\pi}{e^\gamma} k_B T_c \simeq 1.76 k_B T_c. \tag{3.85}$$

Equilibrium currents – revisited

Returning to the problem of finding the supercurrent in a uniform super-
conductor, the task at hand is to find the correct energy gap. Using the θ
parametrisation in Eq. (3.75), along with Eq. (3.83), the gap equation takes
the form

$$\Delta = \frac{1}{\text{acosh}\frac{\hbar\omega_D}{\Delta_0}} \int_0^{\hbar\omega_D} d\varepsilon \, \Re \sinh\theta \tanh\frac{\beta\varepsilon}{2}, \qquad (3.86)$$

where Δ_0 is gap with no currents present. Starting with $\Delta = \Delta_0$, Eq. (3.76)
may be solved to find θ, which is inserted into Eq. (3.86) to produce an
updated value. This procedure is repeated until convergence is achieved,
resulting in Fig. 3.4
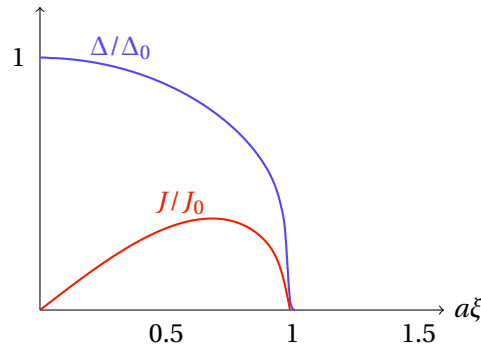
Figure 3.4: Size of the energy gap and the supercurrent as a function of the
phase gradient a, given in units of the superconducting coherence length
ξ. The supercurrent is scaled by $J_0 = ev_0D\Delta_0/\xi$.

For low values of the phase gradient, $|\nabla\phi| = a$, the supercurrent is approx-
imately proportional to a, but as the gradient becomes larger, the increase
in kinetic energy eventually results in a suppression of superconductivity.

3.8   The influence of a magnetic field

When a superconductor is exposed to a magnetic field, interesting things
happen. A superconductor can exhibit perfect diamagnetism, which
means that any entering magnetic flux is screened by circulating supercur-
rents – a phenomenon known as the *Meissner effect* [47]. For an increasing

magnetic field, this complete screening can persist until the superconductivity is quenched, which is the case for type I superconductors. Another possibility is that flux lines eventually begin to penetrate, creating topological excitations known as vortices. This is known as type II superconductivity. To study such effects, it is necessary to include a magnetic field $\boldsymbol{B}$ in the Green function formalism. This is done by altering the $\frac{\hbar}{i}\nabla$ operators to properly represent the canonical momentum,

$$\frac{\hbar}{i}\nabla \rightarrow \frac{\hbar}{i}\tilde{\nabla} = \frac{\hbar}{i}\nabla - e\boldsymbol{A}(\boldsymbol{r}), \tag{3.87}$$

where e is the elementary charge, and $\boldsymbol{A}$ is the vector potential, which satisfies $\boldsymbol{B} = \nabla \times \boldsymbol{A}$. There is a certain freedom in the choice of $\boldsymbol{A}$, in that any transformation $\boldsymbol{A} = \boldsymbol{A}' + \nabla\chi$ leaves the magnetic field $\boldsymbol{B}$ unchanged. This *gauge transformation* modifies the wave function by a phase, $\psi' = \psi e^{ie\chi/\hbar}$, and hence the Green function by

$$\check{G}'(\boldsymbol{r}_1, \boldsymbol{r}_2) = e^{ie\check{\chi}(\boldsymbol{r}_1)/\hbar}\check{G}(\boldsymbol{r}_1, \boldsymbol{r}_2)e^{-ie\check{\chi}(\boldsymbol{r}_2)/\hbar}, \tag{3.88}$$

where $\check{\chi}(\boldsymbol{r}) = \chi(\boldsymbol{r})\check{\rho}_4$. Multiplying Eq. (3.60) with $e^{ie\check{\chi}(\boldsymbol{r})/\hbar}$ from the left, and $e^{-ie\check{\chi}(\boldsymbol{r}')/\hbar}$ from the right one finds that the equation of motion remains invariant if

$$\check{\Delta}'(\boldsymbol{r}) = e^{ie\check{\chi}(\boldsymbol{r})/\hbar}\check{\Delta}(\boldsymbol{r})e^{-ie\check{\chi}(\boldsymbol{r})/\hbar}, \tag{3.89}$$

and hence

$$\Delta'(\boldsymbol{r}) = \Delta(\boldsymbol{r})e^{2ie\chi(\boldsymbol{r})/\hbar}. \tag{3.90}$$

The conclusion is that a gauge transformation results in a modification of the order parameter phase. From this it is clear that a gauge invariant phase, ϕ_{GI}, may be defined as

$$\nabla\phi_{\mathrm{GI}} = \nabla\phi - \frac{2e}{\hbar}\boldsymbol{A}. \tag{3.91}$$

To introduce a magnetic field to the quasiclassical equations of motion is conceptually simple, but there are a few intricacies that warrant discussion. Consider the gauge invariant quantity

$$\begin{aligned}\check{Q}(\boldsymbol{r}_1, \boldsymbol{r}_2) &= \tilde{\nabla}_1^2\check{G}(\boldsymbol{r}_1, \boldsymbol{r}_2) - \check{G}(\boldsymbol{r}_1, \boldsymbol{r}_2)\tilde{\nabla}_2^2 \\ &= \left(\nabla_1 - \frac{ie}{\hbar}\check{\boldsymbol{A}}(\boldsymbol{r}_1)\right)^2\check{G}(\boldsymbol{r}_1, \boldsymbol{r}_2) - \check{G}(\boldsymbol{r}_1, \boldsymbol{r}_2)\left(\nabla_2 - \frac{ie}{\hbar}\check{\boldsymbol{A}}(\boldsymbol{r}_2)\right)^2,\end{aligned}$$

which appears in the equations of motion when performing the left-right subtraction trick necessary to obtain Eq. (2.52). The vector potential takes the form $\hat{A} = \mathrm{diag}\,(+AI\,,\,-AI)$ in Nambu⊗spin space, and $\check{A} = \mathrm{diag}\,\big(\hat{A}\,,\,\hat{A}\big)$ in Keldysh space. In the Coulomb gauge, $\nabla \cdot A = 0$, the mixed representation of $\check{Q}$ becomes

$$\check{Q}(\boldsymbol{R},\boldsymbol{k}) = 2i\boldsymbol{k}\cdot\tilde{\nabla}_R\check{G} - \left\{\frac{ie}{\hbar}\check{A},\,\nabla\check{G}\right\}, \qquad (3.92)$$

where the gauge covariant derivative now takes the form

$$\tilde{\nabla}_R = \nabla_R - \frac{ie}{\hbar}\left[\check{A},\bullet\right]. \qquad (3.93)$$

This redefinition emerges as $\check{\chi}(\boldsymbol{r}_i) \rightarrow \check{\chi}(\boldsymbol{R})$ in the mixed representation equivalent of Eq. (3.88). Note, however, that Eq. (3.92) is no longer gauge invariant. This property has been destroyed in going to the mixed representation. To remedy this, a gauge covariant Wigner transformation may be used [125–127]. Alternatively, assuming that the size of the vector potential is on the order of $e|A|/p_\mathrm{F} \simeq \alpha \ll 1$, the anticommutator in Eq. (3.92) may be neglected. Hence, gauge invariance is retained to this level of accuracy. It is the latter approach which will be used here. This has consequences for the treatment of spin-orbit coupling, encountered in Section 6.7, in that magnetoelectric effects cannot be described. Repeating the steps leading up to Eqs. (2.52) and (2.100) produces identical equations, with all gradients replaced by Eq. (3.93).

3.9   The Meissner effect

The Meissner effect is the expulsion of magnetic fields from superconducting materials. This occurs since the presence of a vector potential induces a phase gradient, as indicated by Eq. (3.91), thereby producing a supercurrent. The supercurrent, in turn, generates its own magnetic field, cancelling the applied field. In other words, superconductors exhibit *perfect diamagnetism*. To describe this effect it is necessary to determine how the supercurrent influences the vector potential. From one of the Maxwell equations one gets

$$\nabla^2 A = -\mu_0 \boldsymbol{J}, \qquad (3.94)$$

where μ_0 is the vacuum permeability and, as before, the Coulomb gauge, $\nabla \cdot \boldsymbol{A} = 0$, has been assumed. Inserting Eq. (3.74) leads to

$$\nabla^2 \boldsymbol{A} = \frac{|e|\mu_0 \nu_0 D}{16} \int d\varepsilon \operatorname{Tr}\left[\hat{\rho}_4 \left(\check{g}\tilde{\nabla}\check{g}\right)^K\right], \tag{3.95}$$

which generally must be solved by iteration, similar to what was the case for the gap equation in Eq. (3.81).

The magnetic field in a superconducting half-space

To get a sense of the screening effect of a superconductor, consider a superconducting half-space, taking up the region $x > 0$. For $x < 0$, there is vacuum. A uniform magnetic field is applied, for which a reasonable choice of gauge is $\boldsymbol{A} = Bx\boldsymbol{e}_y$, where $\boldsymbol{e}_y$ is a unit vector pointing in the y direction, parallel to the interface. The current is thus given from Eqs. (3.74) and (3.93) as

$$
\begin{aligned}
J_y &= \frac{e\nu_0 D}{16} \int d\varepsilon \operatorname{Tr}\left[\hat{\rho}_4 \left(\check{g}\frac{\tilde{\partial}}{\partial y}\check{g}\right)^K\right], \\
&= \frac{e\nu_0 D}{8} \int d\varepsilon \left(\Re\operatorname{Tr}\left[\hat{\rho}_4 \hat{g}^R \frac{\partial}{\partial y} \hat{g}^R\right] + \frac{e}{\hbar}A_y \Im\operatorname{Tr}\left[\left(\hat{\rho}_4 \hat{g}^R\right)^2\right]\right)\tanh\frac{\beta\varepsilon}{2}. \quad (3.96)
\end{aligned}
$$

The Green function $\check{g}$ may be found by inserting the parametrisation in Eq. (3.75) into Eq. (3.63), replacing all gradients with their covariant derivatives, $\nabla \to \tilde{\nabla}$, in which case one finds that θ must satisfy

$$\theta = \operatorname{atanh}\left[\frac{|\Delta|}{\varepsilon} - i\frac{4e^2 D A_y^2}{2\hbar\varepsilon}\sinh\theta\right], \tag{3.97}$$

analogous to Eq. (3.76). Assume next that the applied magnetic field is sufficiently small to neglect all terms of order A_y^2 and higher. In that case it is seen that $\theta \simeq \operatorname{atanh}\frac{|\Delta|}{\varepsilon}$, which means that the first term in the integrand of Eq. (3.96) does not contribute to the current. Hence, one gets

$$J_y = \frac{e^2 \nu_0 D}{\hbar} A_y \int d\varepsilon \, \Im\sinh^2\theta \tanh\frac{\beta\varepsilon}{2}. \tag{3.98}$$

To proceed, note that

$$\Im\sinh^2\theta = |\Delta|^2 \Im\left[\frac{1}{\varepsilon^2 - |\Delta|^2 + i\operatorname{sgn}(\varepsilon)\eta}\right] = -\operatorname{sgn}(\varepsilon)\pi|\Delta|^2\delta\left(\varepsilon^2 - |\Delta|^2\right),$$

where η is an infinitesimal quantity. This results in

$$J_y = -\frac{\pi e^2 \nu_0 D \Delta}{\hbar} A_y \tanh \frac{\beta \Delta}{2}.$$

For low temperatures, $\tanh \frac{\beta \Delta}{2} \simeq 1$, and the superfluid density, n_s, is approximately equal to the electron density. The latter gives the identity $\pi \nu_0 D \Delta / \hbar = n_s l_{\mathrm{mfp}} / m \xi_0$, where l_{mfp} is the mean free path, m is the electron mass, and ξ_0 is the ballistic superconducting diffusion length, given in Eq. (3.56). One thus gets

$$J_y = \frac{n_s e^2}{m} \frac{l_{\mathrm{mfp}}}{\xi_0} A_y, \tag{3.99}$$

which is a diffusive version of the *London equation* [128, 129], differing from the ballistic version by the appearance of the factor l_{mfp}/ξ_0. Inserting Eq. (3.99) into Eq. (3.94) gives

$$\frac{\partial^2}{\partial x^2} A_y = \frac{1}{\lambda^2} A_y, \tag{3.100}$$

where λ is the diffusive penetration depth, and may be expressed in terms of the *London penetration depth*, $\lambda_{\mathrm{L}} = \sqrt{m/\mu_0 n_s e^2}$, as

$$\lambda = \lambda_{\mathrm{L}} \sqrt{\frac{\xi_0}{l_{\mathrm{mfp}}}}. \tag{3.101}$$

The magnetic field profile $B_z(x)$ is found by solving Eq. (3.100) and using that $\boldsymbol{B} = \nabla \times \boldsymbol{A}$. By setting $B_z(0) = B$, the applied field, one gets

$$B_z(x) = B e^{-x/\lambda}. \tag{3.102}$$

Hence, λ dictates the distance over which an applied field vanishes in a superconductor.

Chapter 4

Numerical solution methods

The equation of motion for the Green function, even after performing the quasiclassical approximation, and taking the diffusive limit, is still a challenge to solve. In fact, the Usadel equation, given in Eq. (2.100), is a system of eight nonlinear partial differential equation. Obviously, there is little hope of solving such a system analytically in any but the most trivial of cases, and so this chapter is concerned with numerical solution methods. The *finite element method* will be introduced, which is a numerical framework capable of solving the Usadel equation very efficiently, and for arbitrary model geometries. In addition, other technical details, such as self consistency acceleration, will be discussed.

4.1 Parametrisation

The Usadel equation, given in Eq. (2.100), is the equation of motion for the 8×8 quasiclassical Green function $\check{g}$. In equilibrium, it is sufficient to find the 4×4 retarded component $\hat{g}^R$, since $\hat{g}^A$ is given by Eq. (2.101), and $\hat{g}^K$ from the quasiclassical version of Eq. (2.43). Nonequilibrium systems require in addition the distribution function $\hat{h}$, which is a separate issue to be discussed in Section 4.3. To ease the numerical solution of the Usadel eqaution, the retarded Green function is parametrised as

$$\hat{g}^R = \begin{pmatrix} N & 0 \\ 0 & \tilde{N} \end{pmatrix} \begin{pmatrix} I + \gamma\tilde{\gamma} & 2\gamma \\ -2\tilde{\gamma} & -(I + \tilde{\gamma}\gamma) \end{pmatrix}, \tag{4.1}$$

where $N = (I - \gamma\tilde{\gamma})^{-1}$, $\tilde{N} = (I - \tilde{\gamma}\gamma)^{-1}$, and $\tilde{\gamma}(\varepsilon) = \gamma^*(-\varepsilon)$. This is known as the Riccati parametrisation [130–132]. The Usadel equation may thus be

expressed in terms of the 2×2 matrices γ and $\tilde{\gamma}$ as

$$D\nabla^2\gamma + 2D\nabla\gamma \cdot \tilde{N}\tilde{\gamma}\nabla\gamma + 2i\varepsilon\gamma - \Delta\sigma_y + \Delta^*\gamma\sigma_y\gamma - iV_{11}\gamma + i\gamma V_{22} = 0, \quad (4.2)$$

$$D\nabla^2\tilde{\gamma} + 2D\nabla\tilde{\gamma} \cdot N\gamma\nabla\tilde{\gamma} + 2i\varepsilon\tilde{\gamma} + \Delta^*\sigma_y - \tilde{\Delta}\tilde{\gamma}\sigma_y\tilde{\gamma} + iV_{22}^*\tilde{\gamma} - i\tilde{\gamma}V_{22}^* = 0, \quad (4.3)$$

where an arbitrary self energy $\hat{V} = \text{diag}(V_{11}\ V_{22})$ has been included.

4.2   The finite element method

The most common method of numerically solving a partial differential equation is by using the so-called *finite difference method*, in which derivatives are discretised on a predefined grid $\frac{\partial f}{\partial x_k} = (f_{i+k,j} - f_{i-k,j})/2kh$, with vertices at i and j, and lattice spacing h. This is a simple, and often sufficient method of obtaining approximate solutions, but it has a significant disadvantage. Since the differential operators within the finite difference method are non-local on the grid, i.e., the derivative at a given point depends on function evaluations at its neighbours, the grid must be regular in some sense. In practice, this means that working with non-rectangular geometries is generally very difficult. Furthermore, the application of boundary conditions is challenging as well, with each new system to be considered often requiring individual treatment in order to formulate a proper numerical scheme. These issues are handled much more elegantly by the *finite element method*, which will be discussed in the following. For brevity, a change in notation will be made, so that both γ and $\tilde{\gamma}$ is described by a single vector

$$\Gamma = \begin{pmatrix} \gamma_{11} & \gamma_{12} & \gamma_{21} & \gamma_{22} & \tilde{\gamma}_{11} & \tilde{\gamma}_{12} & \tilde{\gamma}_{21} & \tilde{\gamma}_{22} \end{pmatrix}^T, \quad (4.4)$$

where γ_{ij} and $\tilde{\gamma}_{ij}$ refer to row i and column j of γ and $\tilde{\gamma}$, respectively. Eqs. (4.2) and (4.3) may then be written as

$$\nabla^2\Gamma^{(\alpha)} = Q^{(\alpha)}(\gamma, \tilde{\gamma}, \nabla\gamma, \nabla\tilde{\gamma}). \quad (4.5)$$

In other words, Eq. (4.5) represents eight coupled equations, where $Q^{(\alpha)}$ is to be understood as a function which performs all the necessary matrix multiplications of Eqs. (4.2) and (4.3), and then extracts the appropriate element α, in accordance with the labelling in Eq. (4.4). While doing this by hand is a Herculean task, it is trivial on a computer.

A differential equation requires boundary conditions in order to be properly posed. The quasiclassical boundary conditions to be used with

the Usadel equation will be discussed at length in Sections 5.1 and 6.4. Here, it will be sufficient to assume boundary conditions which are either of the form

$$\hat{n} \cdot \nabla \Gamma^{(\alpha)} = B^{(\alpha)}(\gamma, \tilde{\gamma}), \qquad (4.6)$$

where $\hat{n}$ is an outwards-pointing surface normal, or of the form

$$\Gamma^{(\alpha)} = C^{(\alpha)}(\gamma, \tilde{\gamma}). \qquad (4.7)$$

Eq. (4.6) and Eq. (4.7) are called *Neumann*, and *Dirichlet boundary conditions*, respectively.

The finite element method requires the *weak formulation* of the differential equation. This entails transforming Eq. (4.5) into an integral equation by first multiplying with a, for now unspecified, scalar test function $v(\boldsymbol{r})$ and integrating over the volume to be studied, Ω. This gives

$$-\int_{\Omega} d\boldsymbol{r} \, \nabla \Gamma^{(\alpha)} \cdot \nabla v + \int_{\partial \Omega} dS \, \hat{n} \cdot \nabla \Gamma^{(\alpha)} v - \int_{\Omega} Q^{(\alpha)} v = 0, \qquad (4.8)$$

where $\partial \Omega$ is the boundary (surface) of Ω. Notice that for the Neumann boundary conditions, Eq. (4.6) may be inserted directly into the second term of Eq. (4.8). Dirichlet boundary conditions may be imposed approximately by introducing a Neumann boundary condition (or more correctly a *Robin boundary condition*) of the form

$$\hat{n} \cdot \nabla \Gamma^{(\alpha)} = \lambda \left(\Gamma^{(\alpha)} - C^{(\alpha)} \right), \qquad (4.9)$$

where λ is a parameter chosen large enough, e.g., of order 10^{10}, for the left hand side to be completely negligible compared to the right hand side, and may thus vary freely. This is known as the *penalty method* – a deviation from the boundary condition is heavily penalised.
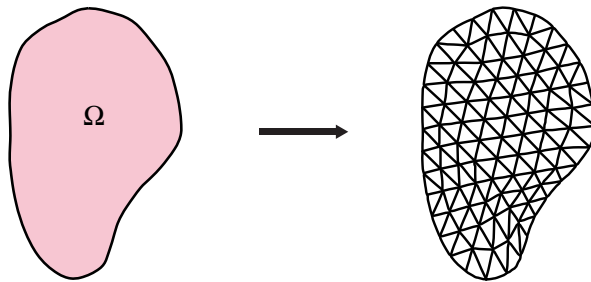
Figure 4.1: Example of the division of a geometry Ω into elements, forming a mesh.

The analysis so far, with the exception of the treatment of the Dirichlet boundary condition, has been exact. In order to reduce Eq. (4.8) to a linear algebra problem fit for the computer, an appropriate basis needs to be introduced. This is where the discretisation comes in. The finite element method consists of dividing the model volume into small pieces, called *elements*, as shown in Fig. 4.1 for an arbitrary geometry Ω. Within each element, the solution Γ is expanded in a finite basis of known functions ϕ_i,

$$\Gamma^{(\alpha)}(\boldsymbol{r}) \simeq \sum_{i=1}^{N} \Gamma_i^{(\alpha)} \phi_i(\boldsymbol{r}), \qquad\qquad (4.10)$$

where the expansion coefficients $\Gamma_i^{(\alpha)}$ are independent of position. This is known as the *Galerkin approximation* [133]. The basis functions ϕ_i are typically polynomials, which means that the accuracy of Eq. (4.10) is increased either by considering smaller elements, or higher polynomial order – in accordance with the *Stone-Wierstrass theorem* [134]. The order of the polynomial is denoted as the order of the element. Similarly, the test function v is chosen as

$$v(\boldsymbol{r}) = \sum_{i=1}^{N} \phi_i(\boldsymbol{r}). \qquad\qquad (4.11)$$

Consider now an element with volume Ω_e. The most common choice for basis functions are the *Lagrange polynomials*, which in one dimension are given as

$$\phi_i = \prod_{\substack{m=1 \\ m \neq i}}^{N} \frac{x - x_m}{x_i - x_m}. \qquad\qquad (4.12)$$

This is a basis which interpolates between N preselected points within the element, with coordinates x_i. These points are known as the *nodes* of the element, and must be placed such that all the symmetries of the element are equally represented, in order to avoid a geometrical bias. The basis functions for the so-called TRI6 element, which is a triangular second order element, are given in Fig. 4.2.
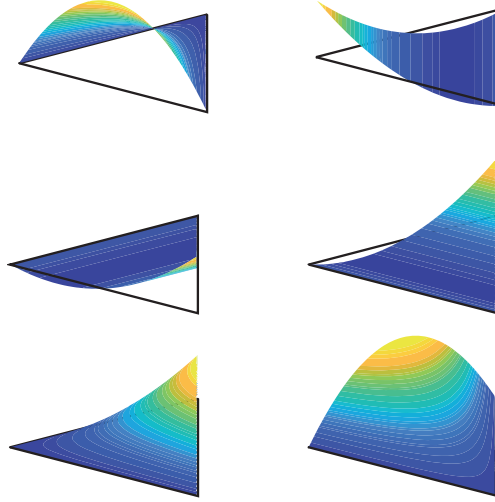
Figure 4.2: The six basis functions used in the description of the TRI6 element, which has six nodes. It is a second order element, meaning that the basis functions are quadratic polynomials.

The contribution to Eq. (4.8) from one element is now given as

$$-\sum_{ij}\int_{\Omega_e} d\boldsymbol{r}\, \nabla\phi_i \cdot \nabla\phi_j \Gamma_i^{(\alpha)} + \sum_{ij}\int_{\partial\Omega_e} dS\, D_i^{(\alpha)}\phi_j - \sum_{ij}\int_{\Omega_e} Q_i^{(\alpha)}\phi_j = 0, \quad (4.13)$$

where $D^{(\alpha)}$ is either given by the right hand side of Eq. (4.6), or the right hand side of Eq. (4.9) depending on the choice of boundary conditions. The surface integral over $\partial\Omega_e$ is nonzero only if the element domain Ω_e intersects with the boundary. Furthermore, while it was possible to factor out the expansion coefficient $\Gamma_i^{(\alpha)}$ in the first term of Eq. (4.13), this is in general not possible for the second and third terms.

Where the finite element method really shines is in its representation of geometry. This is done by allowing the elements to deform. This deformation can be described by the same basis function as Γ,

$$x = \sum_{i=1}^{N}\phi_i(\xi), \quad y = \sum_{i=1}^{N}\phi_i(\eta), \quad z = \sum_{i=1}^{N}\phi_i(\zeta).$$

Such elements are referred to as *isoparametric*. The point is that for a geometrical model made up of a *mesh* of elements with various distortion,

it is sufficient to store information about a single undistorted reference element, along with a Jacobi matrix J which describes the distortion of each individual element, as illustrated in Fig. 4.3. Note that the latter needs to be computed only once, at the moment of mesh generation.
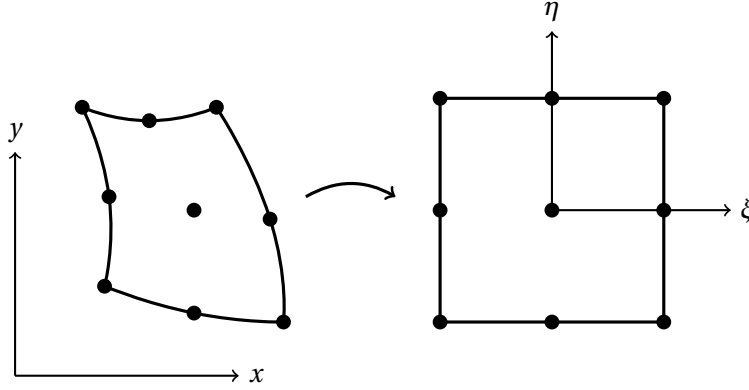
Figure 4.3: Illustration of a coordinate transformation of a QUAD9 element (quadrilateral element with nine nodes), which converts a distorted element into an undistorted reference element.

Hence, expressed with the coordinates of the reference element, $\boldsymbol{\rho} = (\xi, \eta, \zeta)$, the integration measure in Eq. (4.13) becomes $d\boldsymbol{r} = d\boldsymbol{\rho}\,|J|$, and the gradients $\nabla = J^{-1}\nabla_\rho$. Finally, the integrals are found by numerical quadrature, i.e., the integrals are replaced by sums of function evaluations at specific points $\boldsymbol{\rho}_n$, known as *quadrature points*, multiplied by a weight factor w_n. Eq. (4.13) thus becomes

$$\boldsymbol{L}_e^{(\alpha)}\left(\boldsymbol{\Gamma}\right) = \boldsymbol{F}_e, \tag{4.14}$$

with

$$\boldsymbol{L}_{e,ij}^{(\alpha)}\left(\boldsymbol{\Gamma}\right) = \sum_n w_n \left[|J|\left(J^{-1}\nabla\phi_i \cdot J^{-1}\nabla\phi_j\Gamma_i^{(\alpha)} + Q_i^{(\alpha)}\phi_j\right) - |J_s|D_{a,i}^{(\alpha)}\phi_j\right]_{\boldsymbol{\rho}=\boldsymbol{\rho}_n},$$

$$\boldsymbol{F}_{e,j} = \sum_n w_n |J_s| D_b^{(\alpha)}\phi_j\Big|_{\boldsymbol{\rho}=\boldsymbol{\rho}_n},$$

where $D^{(\alpha)}$ has been split into two contributions, $D_a^{(\alpha)}$ and $D_b^{(\alpha)}$, the former of which depends on γ and $\tilde{\gamma}$, whereas the latter does not. Note that $D^{(\alpha)}$ only gives a contribution on the surface of the mesh, where the coordinate transformations are described by the Jacobi matrix J_s. The notation $\boldsymbol{\Gamma}$ represents a matrix with elements $\Gamma_i^{(\alpha)}$. Both w_n and $\boldsymbol{\rho}_n$ are predefined, and

depend on the integration method selected. The number of quadrature points are typically chosen to be the same as the number of nodes in the element, which is known as *full integration.*

The discussion so far has been concerned with the contribution from a single element, and hence for each element in the mesh, Eq. (4.14) applies, which is a dense matrix equation in the nodal indices of that particular element. Assembly of a global matrix equation, which takes into account the entire mesh requires little more than a simple relabelling. Indeed, rather than using a nodal numbering scheme which is local to each element, a global numbering scheme may be used instead. Note that some nodes are shared between several elements, but most are not. Hence, the dense elemental matrices L_e and F_e may be replaced by sparse global matrices L and F. Furthermore, Γ is thus to be understood as the solution for all the eight components in γ and $\tilde{\gamma}$, at every node in the mesh.

The nonlinearity of the Usadel equation is apparent in the fact that Eq. (4.14) is a nonlinear matrix equation, and must be solved by iteration. To proceed, assume that from iteration k to iteration $k+1$, Γ_k changes by a small increment l_k. In that case Eq. (4.14) may be linearised to give,

$$L^{(\alpha)}\left(\Gamma_{k+1}\right) = L^{(\alpha)}\left(\Gamma_k + l_k\right) \simeq L^{(\alpha)}\left(\Gamma_k\right) + K^{(\alpha\beta)} l_k^{(\beta)}.$$

After a slight rearrangement, one gets

$$K^{(\alpha\beta)} l_k^{(\beta)} = R^{(\alpha)}, \tag{4.15}$$

from which one finds $\Gamma_{k+1}^{(\alpha)} = \Gamma_k^{(\alpha)} + l_k^{(\alpha)}$. The matrix K is called the *tangent stiffness matrix* due to the resemblance of Eq. (4.15) to Hooke's law. It is given as

$$
\begin{aligned}
K^{(\alpha\beta)} &= \frac{\partial L^{(\alpha)}\left(\Gamma_k\right)}{\partial \Gamma_k^{(\beta)}} \\
&= \sum_n w_n \left[|J| \left(\delta_{\alpha\beta} \left[J^{-1}\nabla\phi \right]^T \cdot J^{-1}\nabla\phi + \frac{\partial Q^{(\alpha)}}{\partial \Gamma_k^{(\beta)}}\phi \right) - |J_s| \frac{\partial D_a^{(\alpha)}}{\partial \Gamma_k^{(\beta)}}\phi \right]_{\rho=\rho_n}.
\end{aligned}
$$

Moreover, the *residual* is given as

$$R^{(\alpha)} = F - L^{(\alpha)}\left(\Gamma_k\right).$$

Solving the linear system Eq. (4.15) therefore provides Γ_{k+1}, given knowledge about Γ_k. Starting with an initial guess Γ_0, this process is repeated

until the residual vanishes within a chosen accuracy – a procedure known as *Newton-Raphson iterations*. Throughout this work, extensive use has been made of the finite element library libMesh [135] as well as the computational toolkit PETSc [136–138]. The ability of the finite element method to model superconducting hybrid structures is explored in several test cases in Paper I.

4.3 Auxiliary solvers

More complicated systems requires the solution of supplementary equation systems, in addition to solving Eqs. (4.2) and (4.3). These systems will be briefly reviewed in the following.

Nonequilibrium systems

In a nonequilibrium system, $\hat{g}^K$ is no longer trivially found from Eq. (2.43). Rather, it depends on the distribution function $\hat{h}$ via Eq. (2.77). The distribution function is block diagonal in Nambu⊗spin space, which means that it can be expressed in a basis of the eight ρ-matrices, given in Eq. (1) [139],

$$\hat{h} = \sum_{n=0}^{7} \hat{\rho}_n h_n, \tag{4.16}$$

where h_n are scalars. To find an equation for $\hat{h}$, the Keldysh component of Eq. (2.100) must be considered, which after inserting Eq. (4.16) becomes [140]

$$a_{mn}\nabla^2 h_n + \boldsymbol{b}_{mn}\cdot\nabla h_n + c_{mn}h_n = 0, \tag{4.17}$$

with

$$a_{mn} = \frac{1}{4}D\mathrm{Tr}\left(\hat{\rho}_n\hat{\rho}_m - \hat{\rho}_m\hat{g}^R\hat{\rho}_n\hat{g}^A\right), \tag{4.18}$$

$$\boldsymbol{b}_{mn} = \nabla a_{mn} + \frac{1}{4}D\mathrm{Tr}\left(\hat{\rho}_n\hat{\rho}_m\hat{g}^R\nabla\hat{g}^R - \hat{\rho}_m\hat{\rho}_n\hat{g}^A\nabla\hat{g}^A\right), \tag{4.19}$$

$$c_{mn} = -\frac{i}{4}\mathrm{Tr}\left(\left[\hat{\Sigma},\,\hat{\rho}_n\hat{\rho}_m\hat{g}^R.\hat{\rho}_m\hat{\rho}_n\hat{g}^A\right] + \left[\hat{\Sigma},\,\hat{\rho}_m\right]\left(\hat{g}^R\hat{\rho}_n - \hat{\rho}_n\hat{g}^A\right)\right), \tag{4.20}$$

where $\hat{\Sigma} = \varepsilon\hat{\rho}_4 - \hat{V}$. The thing to notice about Eq. (4.17) is that it is linear in $\hat{h}$. Furthermore, Eqs. (4.2) and (4.3), which determine $\hat{g}^R$ and $\hat{g}^A$ are independent of $\hat{h}$ an can be computed separately. By introducing the same

formalism as described in Section 4.2, the resulting numerical problem to be solved takes the form

$$\boldsymbol{K}_h \boldsymbol{h} = \boldsymbol{F}, \tag{4.21}$$

where $\boldsymbol{h} = \begin{pmatrix} h_0 & h_1 & \ldots & h_7 \end{pmatrix}^T$, $\boldsymbol{K}_h$ is the stiffness matrix found from the equation of motion, given in Eq. (4.17), and $\boldsymbol{F}$ is a force vector which in practice will include contributions from the boundary conditions, to be discussed in Chapters 5 and 6. At a given quasiparticle energy ε, a nonequilibrium system may thus be studied by first finding the retarded and advanced Green functions from Eq. (4.15), and then solving Eq. (4.21), using the same mesh in both cases. The major difference between these two equation systems is that while the former is a nonlinear problem, and thus requires tens of Newton-Raphson iterations to converge, the latter is linear, and is solved in a single step. The distribution function is therefore much faster to obtain.

The vector potential

When studying the Meissner effect, an additional solution step is required in order to obtain the vector potential $\boldsymbol{A}$ from Eq. (3.95). This proceeds in the same way as for the nonequilibrium distribution function $\hat{h}$ – it is a three-component linear partial differential equation for which a stiffness matrix $\boldsymbol{K}_A$ may be established. There are, however, a few differences. First of all, it must be solved iteratively until self-consistency is achieved, since the vector potential influences the superconducting gap, which in turn modifies the current density. Fortunately, an update of the vector potential happens rather infrequently during the solution process. It is required at most once every gap iteration, which means that this solution step can be significantly more resource intensive than the Usadel equation without resulting in a noticeable increase in computation time. This observation is beneficial, as finding the proper vector potential requires modelling the vacuum surrounding the materials of interest.

The numerical solution of Eq. (3.95) is done by creating an additional rectangular model Ω_A in which the system model Ω is embedded, as shown in Fig. 4.4. While the Usadel equation is solved solely in Ω, the Maxwell equation is solved in both Ω and Ω_A, enforcing continuity at Γ_1, the boundary between the two regions. Typically, the influence of a uniform magnetic field, B_{ext}, is sought, which gives no explicit contribution to Eq. (3.95). Hence, it is convenient to define $\boldsymbol{a} = \boldsymbol{A} - \boldsymbol{A}_{\text{ext}}$. The vacuum region Ω_A

should be chosen large enough for the magnetic field to be equal to the external field at the outer boundary, which implies the boundary condition $\nabla \times \boldsymbol{a} = 0$ at Γ_2.

In practice, boundary conditions involving tangential derivatives have proven troublesome. However, because Ω_A is rectangular, they can be avoided by imposing the boundary conditions

$$
\begin{aligned}
\hat{n} \cdot \nabla(\hat{n} \cdot \boldsymbol{a}) &= 0, \\
\boldsymbol{a} - \hat{n}(\hat{n} \cdot \boldsymbol{a}) &= 0
\end{aligned}
\tag{4.22}
$$

for surfaces where $\boldsymbol{B}_{\text{ext}} \cdot \hat{n} = 0$, with $\hat{n}$ the surface normal, and

$$
\boldsymbol{a} = 0
\tag{4.23}
$$

for surfaces where $\boldsymbol{B}_{\text{ext}} || \hat{n}$. Notice that these boundary conditions implicitly satisfy $\nabla \times \boldsymbol{a} = 0$. Furthermore, they decouple when the surface normals are aligned with the Cartesian coordinate axes of the system, thereby giving a well-posed boundary value problem.
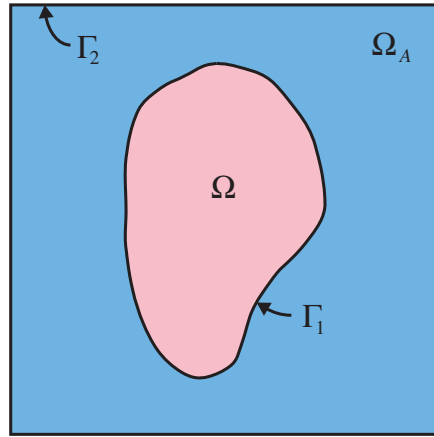
Figure 4.4: When studying the Meissner effect, it is necessary to embed the model geometry Ω into a rectangular vacuum region Ω_A. The Usadel equation is solved only in Ω, whereas the Maxwell equation is solved in both Ω and Ω_A. Continuity is enforced at the boundary Γ_1, whereas Eqs. (4.22) and (4.23) are imposed on Γ_2.

4.4 Fixed point acceleration

The most challenging part of studying superconducting systems numerically with the Usadel equation is finding the correct superconducting gap $\Delta(\boldsymbol{r})$, which is determined from Eq. (3.81). Notice that its determination requires computing an integral over ε, which means that the Usadel equation must be solved several hundreds, if not thousands, of times for varying ε in order to obtain an accurate approximation of the integral. Furthermore, the Keldysh Green function $\hat{g}^K$, which appears in the integrand on the right hand side of Eq. (3.81), depends on $\Delta(\boldsymbol{r})$. Hence, the problem at hand is one of the form

$$\Delta = F(\Delta). \tag{4.24}$$

Lumped into the function F are all the efforts which go into computing $\hat{g}^K$ and performing the ε-integral. Its exact dependence on Δ is therefore unknown. In addition, its evaluation is extremely resource intensive, which motivates using a method that solves Eq. (4.24) with as few function evaluations as possible. The simplest way of solving it is by *fixed point iterations*, where an initial guess for the gap, Δ_0, is made, and the next iteration found from Eq. (4.24), so that one gets

$$\Delta_{n+1} = F(\Delta_n). \tag{4.25}$$

The convergence criterion is then that the change in the gap from one iteration to the next, $\delta_{n+1} = |\Delta_{n+1} - \Delta_n|$, should be less than some given tolerance. This iterative procedure works, and it is straightforward to implement, but it has the significant drawback that its convergence is slow. Hence, unless one is able to come up with an accurate initial guess, a large number of iterations are required. For this reason, two methods of accelerating Eq. (4.25) will be explored in the following.

Steffensen acceleration

The most famous method of finding a root of a function $f(x)$ is perhaps *Newton's method*, where the solution of $f(x) = 0$ is found iteratively via the formula

$$x_{n+1} = x_n - \frac{f(x_n)}{f'(x_n)}.$$

Eq. (4.24) can be transformed into a root finding problem by defining $f(\Delta) = F(\Delta) - \Delta$. A challenge in the application of Newton's method then

becomes finding the derivative $f'(\Delta)$. Note that after discretisation, Δ is a vector containing N values, where N is the number of nodes in the mesh, and so finding the correct slope of $f(\Delta)$ requires determining the $N \times N$ Jacobian matrix – an impossible task in practice. Instead, the multidimensionality of the problem will be ignored, and each element of Δ is assumed independent of the rest, thus reducing the problem to N separate root finding problems. In that case, $f'(\Delta_n)$ for a particular iteration n may be approximated as

$$f'(\Delta_n) \simeq \frac{f(\Delta_{n+1}) - f(\Delta_n)}{\Delta_{n+1} - \Delta_n} = \frac{\Delta_{n+2} - 2\Delta_{n+1} + \Delta_n}{\Delta_{n+1} - \Delta_n}, \qquad (4.26)$$

where Eq. (4.25) has been used in the second equality. With a slight relabelling of indices one then finds

$$\Delta_{n+1} = \Delta_{n-2} - \frac{(\Delta_{n-1} - \Delta_{n-2})^2}{\Delta_n - 2\Delta_{n-1} + \Delta_{n-2}}. \qquad (4.27)$$

This is known as *Steffensen acceleration*. Eq. (4.27) requires as input the three previous iterations. This means that it must be initialised by three fixed point iterations, after which Eq. (4.27) may be used exclusively to produce the next iterations. However, experimentation has shown that it is beneficial to the stability and convergence rate of the numerical iteration procedure to use Eq. (4.27) more sparingly. Improved performance has been observed if $k > 3$ fixed point iterations are made between every application of Eq. (4.27). Hence, the recommended iterative scheme is

$$\Delta_{n+1} = \begin{cases} \Delta_{n-2} - \frac{(\Delta_{n-1} - \Delta_{n-2})^2}{\Delta_n - 2\Delta_{n-1} + \Delta_{n-2}} & n = zk, \\ F(\Delta_n) & \text{otherwise,} \end{cases} \qquad (4.28)$$

where $z \in \{1, 2, 3, \ldots\}$. The integer k is likely to vary from problem to problem, and must be chosen by the analyst.

   Steffensen acceleration is efficient when the spatial variation of the gap is low. In particular, its performance is significantly poorer if there are phase gradients in the system. This is presumably because the coherence between the gap value at different nodes is ignored.

Anderson acceleration

An acceleration method which, in contrast to the Steffensen method, takes into account that Δ is a vector in $\mathbb{R}^N$ is *Anderson acceleration* [141, 142]. Consider again the quantity $f(\Delta_n) = F(\Delta_n) - \Delta_n$. Its norm is a measure

of the residual of a given iteration n, i.e., the deviation from a converged solution. In the Anderson acceleration method, the next iteration of the gap, Δ_{n+1} is constructed from the M_n previous iterations in such a way that the residual is minimised,

$$\Delta_{n+1} = \sum_{j=0}^{M_n} w_j \Delta_{n-M_n+j}, \tag{4.29}$$

where the weight factors w_j satisfy

$$\sum_{j=0}^{M_n} w_j = 0. \tag{4.30}$$

To determine appropriate weight factors, the previous M_n residuals are collected into a matrix R_n,

$$R_n = \begin{pmatrix} f(\Delta_{n-M_n}) & f(\Delta_{n-M_n+1}) & \dots & f(\Delta_n) \end{pmatrix}, \tag{4.31}$$

which then becomes an $N \times M_n$ matrix. The weight factors are chosen by minimising the norm

$$L = |R_n \boldsymbol{w}|^2, \tag{4.32}$$

with $\boldsymbol{w} = \begin{pmatrix} w_0 & w_1 & \dots & w_{M_n} \end{pmatrix}^T$. In other words, this is a constrained least squares problem, and the resulting weight factors w_j will be small if their corresponding residual $f(\Delta_{n-M_n+j})$ is large. This means that the next gap iteration, as given in Eq. (4.29), may be interpreted as a linear combination of previous iterations, where those Δ_j which produced a small residual are favoured.

Eq. (4.32) can be made more convenient by reformulating it as an unconstrained least squares problem. This is done by the coordinate transformations [143]

$$w_j = \begin{cases} \theta_0, & j = 0 \\ \theta_j - \theta_{j-1}, & 1 \le j < M_n \\ 1 - \theta_{M_n-1}, & j = M_n \end{cases} \tag{4.33}$$

With these new weight factors, which automatically satisfy Eq. (4.30), Eq. (4.32) is given as

$$L = |f(\Delta_n) - \tilde{R}_n \boldsymbol{\theta}|^2, \tag{4.34}$$

where $\boldsymbol{\theta} = \begin{pmatrix} \theta_0 & \theta_1 & \dots & \theta_{M_n} \end{pmatrix}^T$, and

$$\tilde{R}_n = \begin{pmatrix} \delta f(\Delta_{n-M_n}) & \delta f(\Delta_{n-M_n+2}) & \dots & \delta f(\Delta_{n-1}) \end{pmatrix}, \qquad (4.35)$$

with $\delta f(\Delta_j) = f(\Delta_{j+1}) - f(\Delta_j)$. The vector $\boldsymbol{\theta}$ which minimises L in Eq. (4.34) may thus be found as

$$\boldsymbol{\theta} = \tilde{R}_n^+ f(\Delta_n), \qquad (4.36)$$

where, $\tilde{R}_n^+$ is the Moore-Penrose pseudoinverse of $\tilde{R}_n$. Finally, Δ_{n+1} is given as

$$\Delta_{n+1} = F(\Delta_n) + \sum_{j=n-M_n}^{n-1} \left(F(\Delta_{j+1}) - F(\Delta_j) \right) \theta_{j-n+M_n}. \qquad (4.37)$$

The integer M_n is typically chosen as $M_n = \min(n, m)$, where m is a memory factor. This means that the number of columns in $\tilde{R}_n$ increases by one every iteration until all m previous iterations are included. m should not be chosen too large, as early gap iterations are usually poor. A suitable value for m is problem dependent, but $m < 10$ is often sufficient.

Chapter 5

Superconducting hybrid structures

In the BCS model for conventional superconductivity, the attractive potential between the quasiparticles is, if only energies lower than $\hbar\omega_D$ are considered, approximated by a contact potential, $V(\boldsymbol{r} - \boldsymbol{r}') = -V_0\delta(\boldsymbol{r} - \boldsymbol{r}')$. This potential is local in space, and so a hybrid structure, i.e., a superconductor attached to non-superconducting materials, may be modelled by allowing V_0 to be nonzero only in the former. At interfaces the potential therefore takes the form of a step function. However, the superconducting correlations do not respond immediately to such a change in potential, but may persists for a distance into an adjacent non-superconducting material on the order of the thermal diffusion length $\xi_T = \sqrt{\hbar D/2\pi k_B T}$. This is known as the *proximity effect*. Such hybrid structures allow for the combination of superconductivity with other quantum phenomena with which it normally would not coexist – for instance ferromagnetism, which will be discussed in Chapter 6. As warm-up, this chapter is concerned with the proximity effect in materials with spin-independent interactions.

5.1 Quasiclassical boundary conditions

The quasiclassical approximation is valid for self energies which are slowly varying in space. This is not the case for interfaces, and so at first sight, one may conclude that the formalism developed in Section 2.4 is inapplicable to superconducting hybrid structures. This problem may, however, be circumvented by treating the interface barrier as a perturbation of the full Green function. The ensuing scattering problem may thus be solved for

the purpose of creating a relationship between the *bulk* Green functions (where the quasiclassical approximation is applicable) on opposite sides of the interface [45, 144–147].

Point impurity

The first step towards formulating a proper set of boundary conditions is to realise that the quasiclassical theory is valid for point impurities [148]. This counter-intuitive fact will now be proven. Consider therefore an impurity represented by the potential $\check{V}_i$ which is strongly localised at some position $\boldsymbol{R}_0$. Its Fourier transform is thus given as

$$\check{V}_i(\boldsymbol{q}) = \check{V}_{0,i}(\boldsymbol{q})e^{-i\boldsymbol{q}\cdot\boldsymbol{R}_0}, \tag{5.1}$$

where $\check{V}_{0,i}(\boldsymbol{q})$ is a slowly varying function. $\check{V}_i$ will be treated as a perturbation of a system with all self energies present, except the point impurity. The equation of motion in Fourier space then takes the form,

$$\int \frac{d\boldsymbol{q}}{(2\pi)^3} \left[\check{G}_0^{-1}(\boldsymbol{k}_0, \boldsymbol{q}) - \check{V}_i(\boldsymbol{k}_0 - \boldsymbol{q}) \right] \check{G}(\boldsymbol{q}, \boldsymbol{k}_n) = \check{I}\delta(\boldsymbol{k}_0 - \boldsymbol{k}_n), \tag{5.2}$$

where $\check{G}_0$ is the unperturbed Green function, corresponding to the operator $\check{G}_0^{-1}$. Written as an integral equation, this becomes

$$\begin{aligned} \check{G}(\boldsymbol{k}_0, \boldsymbol{k}_n) = &\check{G}_0(\boldsymbol{k}_0, \boldsymbol{k}_n) \\ &+ \int \frac{d\boldsymbol{q}_1}{(2\pi)^3} \int \frac{d\boldsymbol{q}_2}{(2\pi)^3} \, \check{G}_0(\boldsymbol{k}_0, \boldsymbol{q}_1) \check{V}_i(\boldsymbol{q}_1 - \boldsymbol{q}_2) \check{G}(\boldsymbol{q}_2, \boldsymbol{k}_0). \end{aligned} \tag{5.3}$$

By repeated iteration Eq. (5.3), it may be recast into a different form,

$$\begin{aligned} \check{G}(\boldsymbol{k}_0, \boldsymbol{k}_n) = &\check{G}_0(\boldsymbol{k}_0, \boldsymbol{k}_n) \\ &+ \int \frac{d\boldsymbol{q}_1}{(2\pi)^3} \int \frac{d\boldsymbol{q}_2}{(2\pi)^3} \, \check{G}_0(\boldsymbol{k}_0, \boldsymbol{q}_1) \check{T}(\boldsymbol{q}_1, \boldsymbol{q}_2) \check{G}_0(\boldsymbol{q}_2, \boldsymbol{k}_0), \end{aligned} \tag{5.4}$$

which defines the T matrix as

$$\check{T}(\boldsymbol{k}_0, \boldsymbol{k}_n) = \check{V}_i(\boldsymbol{k}_0 - \boldsymbol{k}_n) + \int \frac{d\boldsymbol{q}_1}{(2\pi)^3} \int \frac{d\boldsymbol{q}_2}{(2\pi)^3} \, \check{V}_i(\boldsymbol{k}_0 - \boldsymbol{q}_1) \check{G}_0(\boldsymbol{q}_1, \boldsymbol{q}_2) \check{T}(\boldsymbol{q}_2, \boldsymbol{k}_n).$$
$$\tag{5.5}$$

Notice that the T matrix only couples to the unperturbed Green function $\check{G}_0$. This will turn out to be an advantage. Inserting Eq. (5.1) it is seen that it satisfies

$$\check{T}(\boldsymbol{k}_0, \boldsymbol{k}_n) = \check{T}_0(\boldsymbol{k}_0, \boldsymbol{k}_n)e^{-i(\boldsymbol{k}_0 - \boldsymbol{k}_n)\cdot\boldsymbol{R}_0}, \tag{5.6}$$

with

$$\check{T}_0(\boldsymbol{k}_0, \boldsymbol{k}_n) = \check{V}_{0,i}(\boldsymbol{k}_0 - \boldsymbol{k}_n)$$
$$+ \int \frac{d\boldsymbol{q}_1}{(2\pi)^3} \int \frac{d\boldsymbol{q}_2}{(2\pi)^3} \check{V}_{0,i}(\boldsymbol{k}_0 - \boldsymbol{q}_1) \check{G}_0(\boldsymbol{q}_1, \boldsymbol{q}_2) \check{T}(\boldsymbol{q}_2, \boldsymbol{k}_n) e^{i(\boldsymbol{q}_1 - \boldsymbol{q}_2) \cdot \boldsymbol{R}_0}.$$

At low energies, $\check{G}_0$ describes scattering processes between particles that have momenta close to the Fermi level. This means that both $\boldsymbol{q}_1$ and $\boldsymbol{q}_2$ are close to $\boldsymbol{q}_{\mathrm{F}}$. Furthermore, $\check{G}$ is strongly peaked at centre of mass momentum $\boldsymbol{Q} = \boldsymbol{q}_{\mathrm{F}}$. The important contribution to $\check{T}_0$ therefore comes from a region in momentum space where the difference in momenta, $\boldsymbol{q} = \boldsymbol{q}_1 - \boldsymbol{q}_2$, remains small. Since both $\check{V}_{0,i}$ and $\check{T}_0$ are slowly varying functions, this allows the approximation

$$\check{T}_0(\boldsymbol{k}_0, \boldsymbol{k}_n) = \check{V}_{0,i}(\boldsymbol{k}_0 - \boldsymbol{k}_n)$$
$$+ \int \frac{d\boldsymbol{Q}}{(2\pi)^3} \int \frac{d\boldsymbol{q}}{(2\pi)^3} \check{V}_{0,i}(\boldsymbol{k}_0 - \boldsymbol{Q} - \tfrac{1}{2}\boldsymbol{q}) \check{G}_0(\boldsymbol{Q}, \boldsymbol{q}) \check{T}_0(\boldsymbol{Q} - \tfrac{1}{2}\boldsymbol{q}, \boldsymbol{k}_n) e^{i\boldsymbol{q} \cdot \boldsymbol{R}_0}$$
$$\simeq \check{V}_{0,i}(\boldsymbol{k}_0 - \boldsymbol{k}_n) + \int \frac{d\boldsymbol{Q}}{(2\pi)^3} \check{V}_{0,i}(\boldsymbol{k}_0 - \boldsymbol{Q}) \int \frac{d\boldsymbol{q}}{(2\pi)^3} \check{G}_0(\boldsymbol{Q}, \boldsymbol{q}) e^{i\boldsymbol{q} \cdot \boldsymbol{R}_0} \check{T}_0(\boldsymbol{Q}, \boldsymbol{k}_n)$$
$$= \check{V}_{0,i}(\boldsymbol{k}_0 - \boldsymbol{k}_n) + \int \frac{d\boldsymbol{Q}}{(2\pi)^3} \check{V}_{0,i}(\boldsymbol{k}_0 - \boldsymbol{Q}) \check{G}_0(\boldsymbol{Q}, \boldsymbol{R}_0) \check{T}_0(\boldsymbol{Q}, \boldsymbol{k}_n).$$

The equation of motion, rewritten in the form of Eq. (5.2), becomes

$$\int \frac{d\boldsymbol{q}}{(2\pi)^3} \left[\check{G}_0^{-1}(\boldsymbol{k}_0, \boldsymbol{q}) \check{G}(\boldsymbol{q}, \boldsymbol{k}_0) - \check{T}(\boldsymbol{k}_0, \boldsymbol{q}) \check{G}_0(\boldsymbol{q}, \boldsymbol{k}_n) \right] = \check{I} \delta(\boldsymbol{k}_0 - \boldsymbol{k}_n). \quad (5.7)$$

The same arguments which were applied to the dummy variables $\boldsymbol{q}_1$ and $\boldsymbol{q}_2$ above are also applicable to the momenta $\boldsymbol{k}_0$ and $\boldsymbol{k}_n$, since even with the point impurity, the full Green function $\check{G}(\boldsymbol{k}_0, \boldsymbol{k}_n)$ describes only processes that occur close to the Fermi level. Hence, the approximation

$$\check{T}_0(\boldsymbol{k}_0, \boldsymbol{k}_n) \simeq \check{T}_0(\boldsymbol{k}, \boldsymbol{k}),$$

with $\boldsymbol{k} = (\boldsymbol{k}_0 + \boldsymbol{k}_n)/2$ is made. The T matrix in the mixed representation is thus approximately given as

$$\check{T}(\boldsymbol{k}, \boldsymbol{R}) \simeq \check{T}_0(\boldsymbol{k}, \boldsymbol{k}) \delta(\boldsymbol{R} - \boldsymbol{R}_0), \quad (5.8)$$

so that the equation of motion may be written as

$$\check{G}_0^{-1} \otimes \check{G}(\boldsymbol{k}, \boldsymbol{R}) - \check{T}_0(\boldsymbol{k}, \boldsymbol{k}) \check{G}_0(\boldsymbol{k}, \boldsymbol{R}) \otimes \delta(\boldsymbol{R} - \boldsymbol{R}_0) = 1. \quad (5.9)$$

When performing the gradient approximation, the derivatives of the δ function must be interpreted in the sense of a distribution [149]. This means that such gradient terms should be thought of as acting on $\check{G}_0$, which is unaffected by the point impurity by definition. Equivalently, in the weak formulation discussed in Chapter 4, the gradient terms may be neglected, provided that $\check{G}_0$ and the test function $\nu(\boldsymbol{r})$ are sufficiently slowly varying. To lowest order, the Moyal products in Eq. (5.9) may therefore be replaced by matrix products.

The quasiclassical version of the T-matrix, $\check{t}_0 \equiv -i\pi \check{T}_0$, is found by inserting the quasiclassical expression for $\check{G}_0$ [148, 150], which is denoted $\check{g}_0$. Note also the definition $\check{v}_i(\boldsymbol{q}) \equiv -i\pi \check{V}_{0,i}(\boldsymbol{q})$. One gets

$$\check{t}_0(\boldsymbol{k}_\mathrm{F}, \boldsymbol{k}_\mathrm{F}) = \check{v}_i(0) + \frac{\nu_0}{2} \int \frac{d\Omega_q}{4\pi} \, \check{v}_i(\boldsymbol{k}_\mathrm{F} - \boldsymbol{q}_\mathrm{F}) \check{g}_0(\boldsymbol{q}_\mathrm{F}, \boldsymbol{R}_0) \check{t}(\boldsymbol{q}_\mathrm{F}, \boldsymbol{k}_\mathrm{F}). \qquad (5.10)$$

The replacement $\check{t}_0(\boldsymbol{k}, \boldsymbol{k}) \rightarrow \check{t}_0(\boldsymbol{k}_\mathrm{F}, \boldsymbol{k}_\mathrm{F})$ may be made due to the fact that the T matrix appears in a product with $\check{G}_0(\boldsymbol{k}, \boldsymbol{R})$, which is strongly peaked at $\boldsymbol{k} = \boldsymbol{k}_F$. Repeating the steps which led to Eq. (2.52) results in a modified Eilenberger equation, in which the point impurity is accounted for,

$$i\hbar \boldsymbol{v}_\mathrm{F} \cdot \nabla \check{g} + \left[\varepsilon \check{\rho}_4 - \check{V} \, , \, \check{g} \right] = \left[\check{t} \, , \, \check{g}_0 \right] \delta(\boldsymbol{r} - \boldsymbol{r}_0), \qquad (5.11)$$

with a change in notation of $\check{t}_0 \rightarrow \check{t}$, and $\boldsymbol{R} \rightarrow \boldsymbol{r}$. The conclusion is that the quasiclassical approximation is applicable for a point impurity, provided that its localisation is strong enough for its representing potential to be approximated by a δ function.

Planar impurity

An interface is a boundary region of some width ℓ between two materials, wherein a boundary potential $\check{V}_b$ reigns supreme. On quasiclassical length scales, on the other hand, the transition between two materials is sharp. Since it is possible to treat perturbations by a point impurity within quasiclassical theory, it seems reasonable to attempt the same procedure for a potential taking the form of a plane,

$$\check{V}(\boldsymbol{r}) = \check{V}_0 \delta \left[\hat{n} \cdot (\boldsymbol{r} - \boldsymbol{R}_n) \right], \qquad (5.12)$$

with $\check{V}_0 = \check{V}_b \ell$. The unit vector $\hat{n}$ is the interface normal, and $\boldsymbol{R}_n$ is a point on the surface of the interface. $\check{V}_0$ is in this case assumed to be a constant (with units J m), indicating the strength of the interface potential. It is

now clear that the system behaves differently in a direction parallel to $\hat{n}$ than it does in the plane orthogonal to it. It is therefore convenient to introduce the notation $r_\perp = \hat{n} \cdot \boldsymbol{r}$, and define $R_0 = \hat{n} \cdot \boldsymbol{R}$. The T matrix may then straightforwardly be identified as

$$\check{T}(\boldsymbol{k}_0, \boldsymbol{k}_n) = \check{T}_s(\boldsymbol{k}_{0,||}, \boldsymbol{k}_{n,||}) e^{-i(k_{0,\perp} - k_{n,\perp})r_\perp}, \tag{5.13}$$

with

$$\check{T}_s(\boldsymbol{k}_{0,||}, \boldsymbol{k}_{n,||}) = (2\pi)^2 \check{V}_0 \delta(\boldsymbol{k}_{0,||} - \boldsymbol{k}_{n,||})$$
$$+ \check{V}_0 \int \frac{d\boldsymbol{q}_{||}}{(2\pi)^2} \int \frac{dq_\perp}{2\pi} \check{G}_0(\boldsymbol{k}_{0,||}, \boldsymbol{q}_{||}; q_\perp, R_0) \check{T}_s(\boldsymbol{q}_{||}, \boldsymbol{k}_{n,||}). \tag{5.14}$$

In the mixed representation one gets

$$\check{T}(\boldsymbol{k}, \boldsymbol{R}) = \check{T}_s(\boldsymbol{k}_{||}, \boldsymbol{R}_{||}) \delta(R_\perp - R_0), \tag{5.15}$$

where

$$\check{T}_s(\boldsymbol{k}_{||}, \boldsymbol{R}_{||}) \simeq \check{V}_0 + \check{V}_0 \int \frac{dq_\perp}{2\pi} \check{G}_0(q_\perp \hat{n} + \boldsymbol{k}_{||}, R_0 \hat{n} + \boldsymbol{R}_{||}) \check{T}_s(\boldsymbol{k}_{||}, \boldsymbol{R}_{||}), \tag{5.16}$$

to the same level of accuracy as in the previous section (with Moyal products replaced with matrix products). The next step is to find the quasiclassical T matrix, but here there is a subtlety: the integral in Eq. (5.16) is one-dimensional. $\check{G}_0$ in the low-energy regime is expressed in terms of the quasiclassical Green function as

$$\check{G}_0(\boldsymbol{k}, \boldsymbol{R}) \simeq -i\pi \check{g}_0(\boldsymbol{k}_{\rm F}, \boldsymbol{R}) \delta\left(\frac{\hbar^2}{2m}(k^2 - k_{\rm F}^2)\right), \tag{5.17}$$

which contributes to the integral in Eq. (5.16) for $q_\perp = \pm\sqrt{k_{\rm F}^2 - \boldsymbol{k}_{||}^2}$. The result is

$$\check{t}_s(\boldsymbol{k}_{||}, \boldsymbol{R}_{||}) = \check{V}_0 - \frac{i}{|\hbar v_n|} \check{V}_0 \check{g}_0(\boldsymbol{k}_{\rm F}, \boldsymbol{R}) \check{t}_s(\boldsymbol{k}_{||}, \boldsymbol{R}_{||}), \tag{5.18}$$

where $|\hbar v_n| = |\boldsymbol{k}_{\rm F} \cdot \hat{n}|/m$, and a change in notation $\check{T}_s \equiv \check{t}_s$ has been made, indicating that this is an expression valid in the quasiclassical regime. Notice also that $|\boldsymbol{k}_{\rm F} \cdot \hat{n}| = \sqrt{k_{\rm F}^2 - \boldsymbol{k}_{||}^2}$. The Green function $\check{g}_0$ is defined as

$$\check{g}_0(\boldsymbol{k}_{\rm F}, \boldsymbol{R}) = \frac{1}{2} \left[\check{g}_0(\boldsymbol{k}_+, \boldsymbol{R}_{||} + R_0 \hat{n}) + \check{g}_0(\boldsymbol{k}_-, \boldsymbol{R}_{||} + R_0 \hat{n}) \right], \tag{5.19}$$

with

$$\boldsymbol{k}_{\pm} = \pm\sqrt{k_{\mathrm{F}}^2 - \boldsymbol{k}_{||}^2}\,\hat{n} + \boldsymbol{k}_{||}.$$

The wave vectors $\boldsymbol{k}_+$ and $\boldsymbol{k}_-$ represent trajectories directed away from and towards the interface, respectively. $\check{g}_0$ may therefore be interpreted as an average of Green functions describing incoming and outgoing particles. Finally, the Eilenberger equation in the presence of a planar impurity becomes

$$i\hbar\boldsymbol{v}_{\mathrm{F}}\cdot\nabla\check{g} + \left[\varepsilon\check{\rho}_4 - \check{V}\,,\,\check{g}\right] = \left[\check{t}_s\,,\,\check{g}_0\right]\delta(\boldsymbol{r}_{\perp} - \boldsymbol{r}_0), \qquad (5.20)$$

with another change in notation of $R_0 \rightarrow r_0$.

Connection between materials

After having gone through a few initial manoeuvres, it is now time to tackle the boundary conditions themselves. To do so, it is convenient to expand Keldysh space to include indices referring to the opposite sides of the interface. The unperturbed Green function is one where there is no interaction between the two sides of the interface, and may be written as

$$\check{g}_0 = \begin{pmatrix} \check{g}_{0,1} & 0 \\ 0 & \check{g}_{0,2} \end{pmatrix}, \qquad (5.21)$$

where $\check{g}_{0,i}$ indicates the Green function in material i, without the presence of the interface. They are solutions of Eq. (3.62), including any self energies belonging to material i. The interface itself is modelled as a planar impurity, in which a scattering event takes the particle from material 1 to material 2 or vice versa. It must therefore take the form

$$\check{V}_0 = \begin{pmatrix} 0 & \check{V}_0 \\ \check{V}_0 & 0 \end{pmatrix}. \qquad (5.22)$$

The T matrix, on the other hand, is generally dense,

$$\check{t}_s = \begin{pmatrix} \check{t}_{s,11} & \check{t}_{s,12} \\ \check{t}_{s,21} & \check{t}_{s,22} \end{pmatrix}, \qquad (5.23)$$

which means that the full Green function must also take the form

$$\check{g} = \begin{pmatrix} \check{g}_{11} & \check{g}_{12} \\ \check{g}_{21} & \check{g}_{22,} \end{pmatrix}, \qquad (5.24)$$

and satisfy Eq. (5.20). The functions $\breve{g}_{12}$ and $\breve{g}_{21}$ involve field operators on both sides of the interface. They are called *drone amplitudes* [45], and will be eliminated from the theory. Note that both $\breve{g}_0$ and $\breve{g}$ are mathematically valid everywhere in space, but their diagonal elements, $\breve{g}_{0,i}$ and $\breve{g}_{ii}$, are physical only in their respective materials. A relationship between Green functions on opposite sides of the interface may be found by integrating Eq. (5.20) an infinitesimally small distance along a trajectory which crosses the interface. This gives

$$\breve{g}(r_0^+) - \breve{g}(r_0^-) = \frac{1}{i\hbar v_n} \left[\breve{t}_s \, , \, \breve{g}_0(r_0) \right], \tag{5.25}$$

where r_0^+ and r_0^- indicate positions on opposite sides of the interface. They will in the following be assumed to lie in material 2 and material 1, respectively. If boundary conditions for material 1 is desired, then $\breve{g}(r_0^+)$ must be eliminated. To do this, Eqs. (2.78) and (2.79) may be used, which is generalised here to arbitrary trajectory directions,

$$\left(\breve{g} + \mathrm{sgn}(\boldsymbol{k}_\mathrm{F} \cdot \hat{n}) \right) \left(\breve{g}_0 - \mathrm{sgn}(\boldsymbol{k}_\mathrm{F} \cdot \hat{n}) \right) = 0 \tag{5.26}$$

$$\left(\breve{g}_0 + \mathrm{sgn}(\boldsymbol{k}_\mathrm{F} \cdot \hat{n}) \right) \left(\breve{g} - \mathrm{sgn}(\boldsymbol{k}_\mathrm{F} \cdot \hat{n}) \right) = 0 \tag{5.27}$$

It is necessary to further subdivide the Green functions in a given material into those that have a momentum pointing towards the interface, and those with a momentum pointing away from it. They will be labelled as $\breve{g}_{jj}^i$ and $\breve{g}_{jj}^o$, respectively, and equivalently, $\breve{g}_{0,j}^i$ and $\breve{g}_{0,j}^o$. By combining Eqs. (5.25) to (5.27) one gets

$$\breve{g}_{11}^i = \breve{g}_{0,1}^i + \frac{1}{2i\hbar|v_n|} \left(\breve{g}_{0,1}^i - \breve{I} \right) \breve{t}_{s,11} \left(\breve{g}_{0,1}^i + \breve{I} \right), \tag{5.28}$$

$$\breve{g}_{11}^o = \breve{g}_{0,1}^o + \frac{1}{2i\hbar|v_n|} \left(\breve{g}_{0,1}^o + \breve{I} \right) \breve{t}_{s,11} \left(\breve{g}_{0,1}^o - \breve{I} \right), \tag{5.29}$$

where it has been assumed that $\hat{n}$ points from material 1 to material 2. The T matrix component for material 1 is determined from Eq. (5.18),

$$\breve{t}_{s,11} = \frac{1}{i|\hbar v_n|} \breve{V}_0 \breve{g}_{0,2} \breve{t}_{s,21},$$

which, due to the matrix structure of $\breve{V}_0$ is not closed in $\breve{t}_{s,11}$. This problem is solved by iterating Eq. (5.18) once, to give

$$\breve{t}_{s,11} = \frac{1}{i|\hbar v_n|} \breve{V}_0 \breve{g}_{0,2} \breve{V}_0 - \frac{1}{\hbar^2 v_n^2} \breve{V}_0 \breve{g}_{0,2} \breve{V}_0 \breve{g}_{0,1} \breve{t}_{s,11}.$$

When solved for $\check{t}_{s,11}$ this gives

$$\check{t}_{s,11} = \frac{1}{i|\hbar v_n|} \left[\check{I} + \frac{1}{\hbar^2 v_n^2} \check{V}_0 \check{g}_{0,2} \check{V}_0 \check{g}_{0,1} \right]^{-1} \check{V}_0 \check{g}_{0,2} \check{V}_0. \tag{5.30}$$

If the interface is spin-inactive, so that $\check{V}_0 = V_0 \check{I}$, Eq. (5.30) simplifies to

$$\check{t}_{s,11} = \frac{V_0^2}{i|\hbar v_n|} \left[\check{I} + \frac{V_0^2}{\hbar^2 v_n^2} \check{g}_{0,2} \check{g}_{0,1} \right]^{-1} \check{g}_{0,2} \tag{5.31}$$

Since tunnelling from one side to the other is treated as a perturbation, the unperturbed situation is one where there is no tunnelling, i.e., the interface is impenetrable. The unperturbed Green functions $\check{g}_{0,i}$, which are unaware of the presence of the interface altogether, are only to be evaluated in material i. Since the interface is modelled as infinitely thin, they can also be used to describe an impenetrable interface, provided that they satisfy the boundary condition

$$\check{g}_{0,j}^i(r_0) = \check{g}_{0,j}^o(r_0). \tag{5.32}$$

In other words, this means that any particle incoming towards the interface is reflected. It also means that it is not necessary to distinguish between incoming and outgoing Green functions at the interface, and $\check{g}_{0,j} = \check{g}_{0,j}$. The T matrix thus becomes

$$\check{t}_{s,11} = \frac{V_0^2}{i|\hbar v_n|} \left[\check{I} + \frac{V_0^2}{\hbar^2 v_n^2} \check{g}_{0,2} \check{g}_{0,1} \right]^{-1} \check{g}_{0,2}. \tag{5.33}$$

The particle flux through the interface is given as the difference between the incoming and the outgoing full Green function for a given trajectory, averaged over all trajectories. From this, the *matrix current* is defined as

$$J_n = \int \frac{d\Omega}{4\pi} \, \hat{n} \cdot \boldsymbol{v}_{\mathrm{F}} \left(\check{g}_{11}^i - \check{g}_{11}^o \right), \tag{5.34}$$

which in the spin-independent case becomes

$$J_n = \frac{1}{i\hbar} \int \frac{d\Omega}{4\pi} \left[\check{g}_{0,1} \, , \, \check{t}_{s,11} \right]. \tag{5.35}$$

Isotropisation

The discussion so far has been concerned with ballistic Green functions. It is desirable to derive boundary conditions also for the diffusive Green functions. It turns out that the formalism derived so far is applicable also in that case. The crucial point is that, regardless of how dirty a material is, a particle having tunnelled through the interface will travel at least some distance, on the scale of the mean free path l_{mfp} before it encounters its first impurity. This means that, surrounding an interface, there will always be a thin boundary layer in which the particles are governed by ballistic Green functions. This is known as the *ballistic zone*. Far away from the interface, many scatterings have occurred, and the motion is diffusive. This is the *diffusive zone*. The task at hand therefore becomes to find a connection between the ballistic and the diffusive zone, through what is known as the *isotropisation zone* [146, 147]. In this region, it is assumed that the impurity potential, given in Eq. (2.96), dominates all other self energies in the system. Furthermore, the size of the isotropisation zone must also be on the scale of the mean free path, perhaps a few times larger than the ballistic zone, in other words much smaller than the length scales over which the diffusive Green functions, $\check{g}_s$, vary. The Eilenberger equation thus reduces to

$$\boldsymbol{v}_{\mathrm{F}} \cdot \nabla \check{g}_{0,1} + \frac{1}{2\tau} \left[\check{g}_{s,1} , \check{g}_{0,1} \right] = 0. \tag{5.36}$$

Consider the incoming Green function, along a trajectory directed along $\hat{s}$, and let r denote the coordinate along this trajectory. Let further r_0 denote the intersection between this trajectory and the interface. The equation of motion then becomes

$$\frac{d}{dr} \check{g}_{0,1}^i + \frac{\eta}{2\tau v_{\mathrm{F}}} \left[\check{g}_{s,1} , \check{g}_{0,1}^i \right] = 0, \tag{5.37}$$

where $\eta = \mathrm{sgn}(\hat{s} \cdot \boldsymbol{v}_{\mathrm{F}})$. A reasonable ansatz which describes the transition from a ballistic to a diffusive Green function as one moves away from the interface is then,

$$\check{g}_{0,1}^i (r) = \left(\check{g}_{0,1}^i (r_0) - \check{g}_{s,1} \right) e^{-|r - r_0| / \tau v_{\mathrm{F}}} + \check{g}_{s,1}. \tag{5.38}$$

For Eq. (5.38) to be a solution of Eq. (5.37), the following must be satisfied,

$$2 \left(\check{g}_{0,1}^i (r_0) - \check{g}_{s,1} \right) = - \left[\check{g}_{s,1} , \check{g}_{0,1}^i (r_0) \right]. \tag{5.39}$$

By squaring both sides Eq. (5.39), and using that $\left(\breve{g}_{0,1}^i(r_0)\right)^2 = \breve{I}$ and $\left(\breve{g}_{s,1}\right)^2 = \breve{I}$, one gets

$$4\left(2\breve{I} - \left\{\breve{g}_{0,1}^i, \breve{g}_{s,1}\right\}\right) = \left(\left\{\breve{g}_{0,1}^i, \breve{g}_{s,1}\right\} + 2\breve{I}\right)\left(\left\{\breve{g}_{0,1}^i, \breve{g}_{s,1}\right\} - 2\breve{I}\right),$$

which is clearly satisfied when

$$\left\{\breve{g}_{0,1}^i, \breve{g}_{s,1}\right\} = 2\breve{I}. \tag{5.40}$$

By combining Eqs. (5.39) and (5.40) one finds that the incoming Green function at the interface must satisfy the conditions

$$\left(\breve{g}_{0,1}^i + \breve{I}\right)\left(\breve{g}_{s,1} - \breve{I}\right) = 0 \tag{5.41}$$

$$\left(\breve{g}_{s,1} + \breve{I}\right)\left(\breve{g}_{0,1}^i - \breve{I}\right) = 0 \tag{5.42}$$

A similar analysis for the outgoing Green functions yields the conditions,

$$\left(\breve{g}_{0,1}^o - \breve{I}\right)\left(\breve{g}_{s,1} + \breve{I}\right) = 0 \tag{5.43}$$

$$\left(\breve{g}_{s,1} - \breve{I}\right)\left(\breve{g}_{0,1}^o + \breve{I}\right) = 0 \tag{5.44}$$

Eqs. (5.41) to (5.44) thus provide a relationship between the diffusive Green functions and their ballistic counterparts at the interface.

Completion of the boundary conditions

For spin-inactive interfaces, where $\breve{g}_{0,1}^i = \breve{g}_{0,1}^o = \breve{g}_{0,1}$, the conditions given in Eqs. (5.41) to (5.44) can only be satisfied if $\breve{g}_{0,1} = \breve{g}_{s,1}$. From Eq. (5.33) it is found that

$$\left[\breve{g}_1, \breve{t}_{s,1}\right] = \frac{V_0^2}{i\hbar|v_n|}M_{21}\breve{g}_1\breve{g}_2 - \frac{V_0^2}{i\hbar|v_n|}M_{12}\breve{g}_2\breve{g}_1,$$

where $M_{ij} = \left[\breve{I} + \frac{V_0^2}{\hbar^2 v_n^2}\breve{g}_i\breve{g}_j\right]^{-1}$, and $\breve{g}_j \equiv \breve{g}_{s,j}$ for brevity. This expression can be written in a slightly more elegant way by inserting $\breve{I} = M_{12}^{-1}M_{12}$ in front of the first term, and $\breve{I} = M_{21}M_{21}^{-1}$ behind the second term [151], which results in

$$\left[\breve{g}_1, \breve{t}_{s,1}\right] = \frac{V_0^2}{i\hbar|v_n|}\frac{\left[\breve{g}_1, \breve{g}_2\right]}{\breve{I} + \left(\frac{V_0}{\hbar v_n}\right)^2\left\{\breve{g}_1, \breve{g}_2\right\} + \left(\frac{V_0}{\hbar v_n}\right)^4}. \tag{5.45}$$

Note that the denominator commutes with $\check{g}_i\check{g}_j$. When Eq. (5.45) is inserted into Eq. (5.35), the matrix current is found to be

$$J_n = -\int \frac{d\Omega}{4\pi}\, v_n \frac{T_n\left[\check{g}_1\,,\,\check{g}_2\right]}{4\check{I} + T_n\left(\{\check{g}_1\,,\,\check{g}_2\} - 2\check{I}\right)}, \qquad (5.46)$$

where T_n is defined as

$$T_n = \frac{4V_n^2}{\left(1 + V_n^2\right)^2}, \qquad (5.47)$$

with $V_n = V_0/\hbar|v_n|$. In the diffusive zone, the matrix current is given by Fick's first law,

$$J_n = -D\hat{n}\cdot\check{g}_1\nabla\check{g}_1. \qquad (5.48)$$

Combining Eqs. (5.46) and (5.48) finally yields the *Nazarov boundary conditions* [146],

$$D\check{g}_1\nabla\check{g}_1 = \int \frac{d\Omega}{4\pi}\, v_n \frac{T_n\left[\check{g}_1\,,\,\check{g}_2\right]}{4\check{I} + T_n\left(\{\check{g}_1\,,\,\check{g}_2\} - 2\check{I}\right)}. \qquad (5.49)$$

Note that since the unperturbed system is one where the interface is impenetrable, the potential $\check{V}_n$ acts as a coupling between the two materials, and hence $T_n \to 0$ as $\check{V}_n \to 0$. If V_0 is small, as mandated by the quasiclassical approximation, this means that T_n is small for all incidence angles, except for a small region close to $\theta = \pi/2$, where T_n approaches unity. In that case, however, the integrand in Eq. (5.49) is suppressed due to the factor $v_n = v_{\mathrm{F}}\cos\theta$. Hence, it is a reasonable approximation to neglect the anticommutator in the denominator of Eq. (5.49) in this limit, giving

$$D\check{g}_1\nabla\check{g}_1 = T\left[\check{g}_1\,,\,\check{g}_2\right], \qquad (5.50)$$

where

$$T = \frac{V^2 v_{\mathrm{F}}}{2}\int_0^{1/V} dx\, \frac{x^3}{\left(1 + x^2\right)^2} = \frac{v_{\mathrm{F}}}{4}\left[V^2\ln\left(\frac{1 + V^2}{V^2}\right) - \frac{V^2}{1 + V^2}\right]$$
$$\equiv \frac{v_{\mathrm{F}}}{4}\Xi(V),$$

with $V = V_0/\hbar v_{\mathrm{F}}$. The diffusion constant is given as $D = v_{\mathrm{F}}^2\tau/3$, where τ is the elastic scattering time. Expressed in terms of the Drude conductivity one gets $D = \sigma/e^2 v_0$, where $v_0 = mk_{\mathrm{F}}/\pi^2\hbar^2$ is the density of states

at the Fermi level (for a free electron gas). Hence, with $\rho_1 = 1/\sigma$ the bulk resistivity of material 1, one finds that

$$\check{g}_1 \nabla \check{g}_1 = \frac{1}{2} \frac{\rho_1}{\rho_c} \left[\check{g}_1 , \check{g}_2 \right].$$ (5.51)

The contact resistivity ρ_c (with units $\Omega\,m^2$) [152] is defined as

$$\rho_c = \frac{G_0 N}{2\Xi(V)},$$ (5.52)

where $G_0 = 2e^2/h$ is the conductance quantum, and $N = k_F^2/4\pi$ is the number of transversal modes per unit area of the interface cross section. Eq. (5.51) is known as the *Kupriyanov-Lukichev boundary conditions* [153]. While Eq. (5.52) is an elegant theoretical result, realistic interfaces are far too complicated for it to give reasonable predictions. This means that the ratio ρ_1/ρ_c in practice becomes a fitting parameter.

5.2   Model problems

As a small respite from the labours of the previous section, this section is concerned with applications of the quasiclassical theory developed so far to simple model problems.

Ohm's law

While not a superconducting hybrid structure, it is a very useful consistency check to verify that Ohm's law is satisfied when a voltage is applied to a normal metal. Consider therefore a diffusive normal metal wire, contacted at opposite ends by electrodes at a fixed voltage of $+V/2$ and $-V/2$, respectively, as shown in Fig. 5.1.
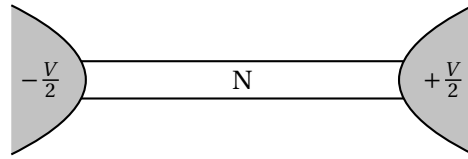
Figure 5.1: A normal metal wire contacted by two electrodes (in grey) at voltage $+V/2$ and $-V/2$, respectively.

With no superconducting correlations in this system, the retarded and advanced Green functions are given simply as $\hat{g}^R = -\hat{g}^A = \hat{\rho}_4$. The Keldysh

Green function, which describes the nonequilibrium properties, thus becomes $\hat{g}^K = 2\hat{\rho}_4 \hat{h}$. The distribution function may be determined from the Keldysh component of Eq. (2.100) (with $\check{V} = 0$), which turns out to be

$$\frac{\partial^2}{\partial x^2} \hat{h} = 0. \tag{5.53}$$

The reservoirs are described as shifted Fermi-Dirac distributions, which corresponds to

$$\hat{h}^{R/L} = \begin{pmatrix} H_\pm & 0 & 0 & 0 \\ 0 & H_\pm & 0 & 0 \\ 0 & 0 & H_\mp & 0 \\ 0 & 0 & 0 & H_\mp \end{pmatrix}$$

for the right and left reservoir, with $H_\pm = \tanh \beta \left(\varepsilon \pm \frac{eV}{2} \right)$. Tunnelling contacts are assumed, and the Keldysh component of Eq. (5.51) gives

$$\frac{\partial}{\partial x} \hat{h} \left(\pm \frac{L}{2} \right) = \pm \frac{1}{2} \frac{\rho_1}{\rho_c} \left[\hat{h}^{R/L} - \hat{h} \left(\pm \frac{L}{2} \right) \right]. \tag{5.54}$$

The charge current density is given as

$$J = \frac{D v_0 e}{16} \int d\varepsilon \, \text{Tr} \left[\hat{\rho}_4 \left(\check{g} \nabla \check{g} \right)^K \right] = \frac{1}{2\rho_1 e} \int d\varepsilon \, \frac{\partial}{\partial x} h_4, \tag{5.55}$$

where the identity $D v_0 = \sigma_1 / e^2$ has been used. From Eq. (5.53) and Eq. (5.54), h_4 is found to be

$$h_4(x) = \frac{\rho_1}{2\rho_c + \rho_1 L} \left[\tanh \beta \left(\varepsilon + \frac{V}{2} \right) - \tanh \beta \left(\varepsilon - \frac{V}{2} \right) \right] x.$$

Insertion into Eq. (5.55) thus gives, after performing the energy integral

$$J = \frac{V}{2\rho_c + \rho_1 L},$$

or, after multiplication with the area of the wire cross section $\mathscr{A}$,

$$I = \frac{V}{2R_c + R_1}, \tag{5.56}$$

where $R_c = \rho_c / \mathscr{A}$ is the contact resistance, and $R_1 = \rho_1 L / \mathscr{A}$ is the bulk resistance of the wire. This shows that the normal metal wire does indeed satisfy Ohm's law, and that the contact resistance from the two interfaces is coupled in series to the bulk resistance, exactly as it should.

Superconductor-normal metal bilayer

A diffusive superconducting bilayer, as shown in Fig. 5.2, may be described by solving the Usadel equation in the superconductor, and in the normal metal, while making sure that Eq. (5.51) is satisfied at the interface.

Figure 5.2: A model for a superconductor-normal metal bilayer, in which each respective material occupies half of space.

In an equilibrium system, only the retarded Green function is needed, for which the equations of motion become

$$\hbar D \nabla \cdot \hat{g}^R \nabla \hat{g}^R + i \left[\varepsilon \hat{\rho}_4 + \hat{\Delta} \, , \, \hat{g}^R \right] = 0, \tag{5.57}$$

$$\hbar D \nabla \cdot \hat{g}^R \nabla \hat{g}^R + i \left[\varepsilon \hat{\rho}_4 \, , \, \hat{g}^R \right] = 0, \tag{5.58}$$

in the superconductor and the normal metal, respectively. The supercon-
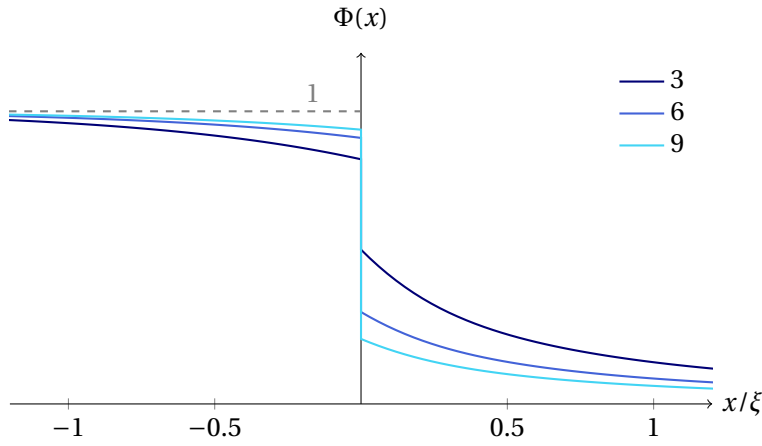
Figure 5.3: The superconducting pair correlation $\Phi(x)$ in a superconductor-normal metal bilayer, shown for various values of the interface resistance $\zeta = \rho_c / \rho_1 \xi$.

ducting pair correlation of this system is shown in Fig. 5.3 for a selection

of interface resistances $\zeta = \rho_c / \rho_1 \xi$, where ξ is the superconducting coherence length, as determined by applying Eq. (2.43) to Eq. (3.80). It is seen that its exponential tail does indeed reach into the normal metal, giving non-zero superconducting correlations. Furthermore, on the superconducting side, the pair correlation is reduced, a phenomenon known as the *inverse proximity effect.*

It is interesting to note that the proximity effect can be controlled by microwave radiation. Indeed, by shining light on a superconductor-normal metal bilayer at suitable frequencies, it was predicted in Paper II that the gap size in the normal metal can be manipulated, and that a rich topography is produced in the density of states.

The Josephson effect

The Josephson effect [154] is perhaps the most famous example of a superconducting proximity effect. It occurs when a normal metal is sandwiched between two superconductors, as shown in Fig. 5.4. This system is called a *Josephson weak link.*
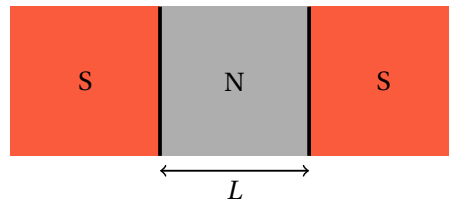
Figure 5.4: A Josephson weak link; two superconductors are separated by a normal metal of length L.

With each of the superconductors, S_i, there is associated a Cooper pair density ρ_i and a constant phase ϕ_i. For an individual superconductor, an overall phase does not influence physical observables, and may be ignored. But a phase difference, on the other hand, is important. It turns out that if the two phases are different, this may manifest as a current passing through the normal metal – even at zero bias voltage. To understand how this comes about, it is instructive to review a particularly simple derivation [155]. Consider a system where the two superconductors are separated by a thin insulator. Each superconductor i is described by a wave function ψ_i, and due to tunnelling through the insulator, they are

assumed coupled in the following way,

$$i\hbar\frac{\partial}{\partial t}\psi_1 = K\psi_2, \tag{5.59}$$

$$i\hbar\frac{\partial}{\partial t}\psi_2 = K\psi_1, \tag{5.60}$$

where K is a coupling constant. The wave function may be written as

$$\psi_i = \sqrt{\rho_i}e^{i\phi_i}. \tag{5.61}$$

When inserting this ansatz into Eqs. (5.59) and (5.60), the real part becomes

$$\frac{\partial}{\partial t}\rho_1 = +\frac{2K}{\hbar}\sqrt{\rho_1\rho_2}\sin\phi,$$

$$\frac{\partial}{\partial t}\rho_2 = -\frac{2K}{\hbar}\sqrt{\rho_1\rho_2}\sin\phi,$$

where $\phi = \phi_2 - \phi_1$. The Cooper pair densities ρ_i only change due to tunnelling through the barrier, and hence the current passing between the superconductors must be $J = 2e\frac{\partial}{\partial t}\rho_1$, leading to

$$J = \frac{4eK}{\hbar}\sqrt{\rho_1\rho_2}\sin\phi = J_c\sin\phi, \tag{5.62}$$

which defines the *critical current density J_c*. The current-phase relation thus has a sinusoidal form, which is typical for Josephson junctions. Within the quasiclassical formalism, a Josephson weak link may be simulated by solving Eq. (5.58) in the normal metal region, with superconducting boundary conditions placed at positions $x = \pm L/2$. If the superconductors are large enough for the overall gap to be only marginally reduced by the presence of the normal metal, the inverse proximity effect may be neglected, and the superconductors considered as reservoirs with a certain, fixed pair correlation and phase. In this case, the retarded Green function in the superconductors is given by Eq. (3.65), and no self-consistency iterations are required – a considerable reduction in numerical complexity. In Fig. 5.5a) is shown the current-phase relation $J(\phi)$ for a normal metal with a length of $L = 2\xi$, corresponding nicely with the prediction of Eq. (5.62). The pair correlation at a point located midway between the superconductors as a function of phase difference ϕ is shown in Fig. 5.5b). Note in particular the absence of superconductivity at $\phi = \pi$, which is due to destructive interference, and results in the gap closing.

a) J/J_0

b) $\Phi(x_m)$
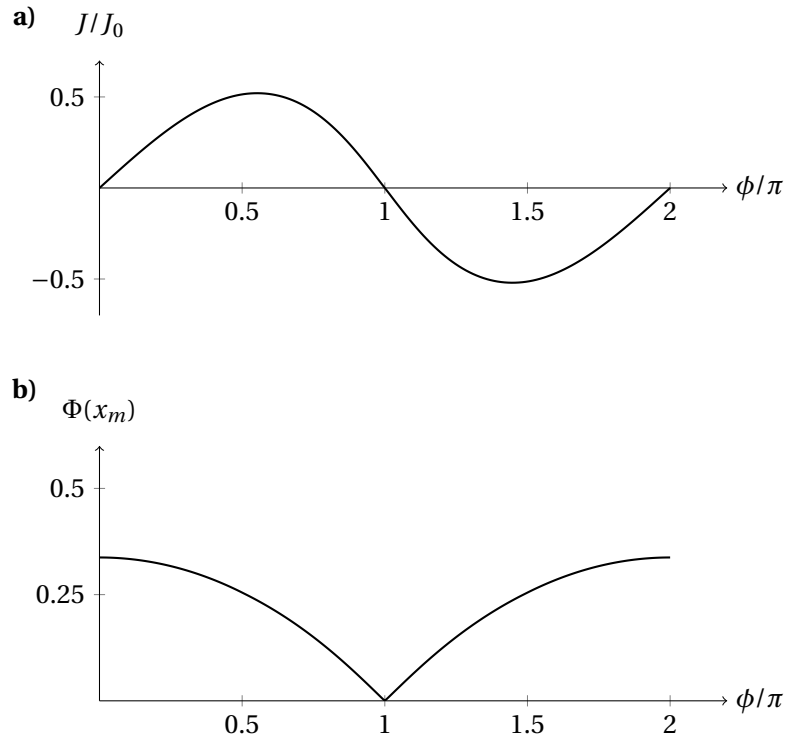
Figure 5.5: The effect of varying the phase difference between the super-conductors in a Josephson weak link. **a)** The supercurrent passing through the normal metal, scaled by $J_0 = eD\nu_0\Delta/16\xi$. **b)** The pair correlation at x_m, midway between the superconductors.

5.3 Multiterminal junctions

In a Josephson junction, it was seen that a supercurrent passes between the superconductors when they have a phase difference of $\pi/2$. Moreover, when the phase difference is π, the superconducting correlations in the non-superconducting material vanish at the centre of the junction due to destructive interference. A natural next step in the study of such systems is to investigate what happens when more than two superconducting terminals are connected via the same non-superconducting material, as illustrated in Fig. 5.6

It turns out that multiterminal junctions are host to several exotic phenomena. In fact, even if all the components of such a junction are topologically
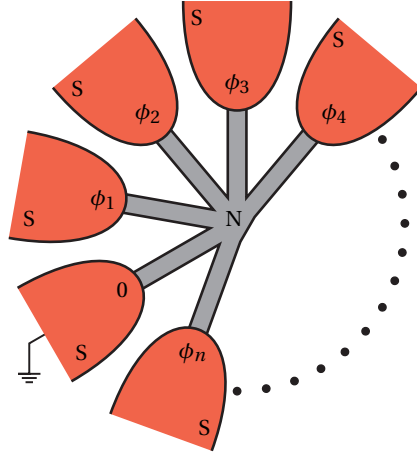
Figure 5.6: A multiterminal Josephson weak link. Due to the gauge invariance, all phases ϕ_i are measured relative to the phase in one of the terminals.

trivial, the junction itself may be topologically non-trivial. It is, however, not the topology of the band structure in momentum space which generates non-trivial physics, but rather the behaviour of the Andreev bound states in the space spanned out by the phase difference between the superconducting terminals. Such a junction therefore constitutes an artificial topological material [156]. A promising system in which to explore these topological properties is the so-called ω-SQUIPT [157], which is a superconducting quantum interference proximity transistor, where a superconductor shaped like an ω is connected to a normal metal at each of its three prongs – thereby forming a three-terminal junction, as shown in Fig. 5.7. The phase difference between the superconducting terminals may in this case be individually tuned by passing magnetic flux through the loops. Depending upon how the phases are tuned, the Andreev bound states may either cross the Fermi level surface, or present with a gap. Consider first the case in which there is no applied flux. The normal metal is then gapped due to its proximity to the superconducting terminals. Hence, if a sufficiently low voltage bias was to be applied to the normal metal, there would be no quasiparticle current due to the absence of current-carrying states. Due to the gauge invariance, it is possible to uniquely manipulate two of the three superconductor phases (since only phase differences matter), which means that the phases $(\phi_1\,,\,\phi_2) = (0\,,\,0)$ may be associated with this
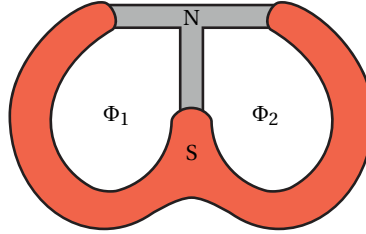
Figure 5.7: A typical geometry, known as the ω-SQUIPT, for the experimental realisation of a three-terminal Josephson weak link. The phase difference between the terminals may be tuned by varying the flux Φ_i through the individual loops.

topologically trivial case. Alternatively, the number of flux quanta through the superconducting loops may be used instead, i.e., $(n_1 , n_2) = (0 , 0)$. By increasing the flux, different gapped regions may be reached, which may all be identified with different integer numbers n_1 and n_2. When passing from one such regions to another, the gap closes, and the normal metal behaves as a conventional gapless contact. It is not possible to change n_1 or n_2 without closing the gap, which therefore play the role of topological invariants. In other words, a three-terminal Josephson weak link behaves as a two-dimensional artificial topological material.

In general it is possible to mimic an $(N-1)$-dimensional topological material by using N superconducting terminals, and the behaviour becomes more complex when the dimension increases. For instance, by setting $N = 4$ it is possible to produce Weyl nodes in the spectrum of the Andreev bound states, which normally would require a three-dimensional topological material [158]. It is clear that multiterminal junctions provide convenient and easily tunable means of experimentally studying exotic topological phenomena.

An easy way of determining whether the normal metal of a given N-terminal junction is gapped is to study the density of states at a quasiparticle energy of $\varepsilon = 0$. To compute the density of states, the Usadel equation must be solved, which generally requires a numerical approach. It does, however, admit an approximate analytical solution for certain selections of phases, which always corresponds to a gapped regime. As is shown in Paper III, this is enough to map out the entire topological phase diagram. The gapless boundaries are identified as the regions in which
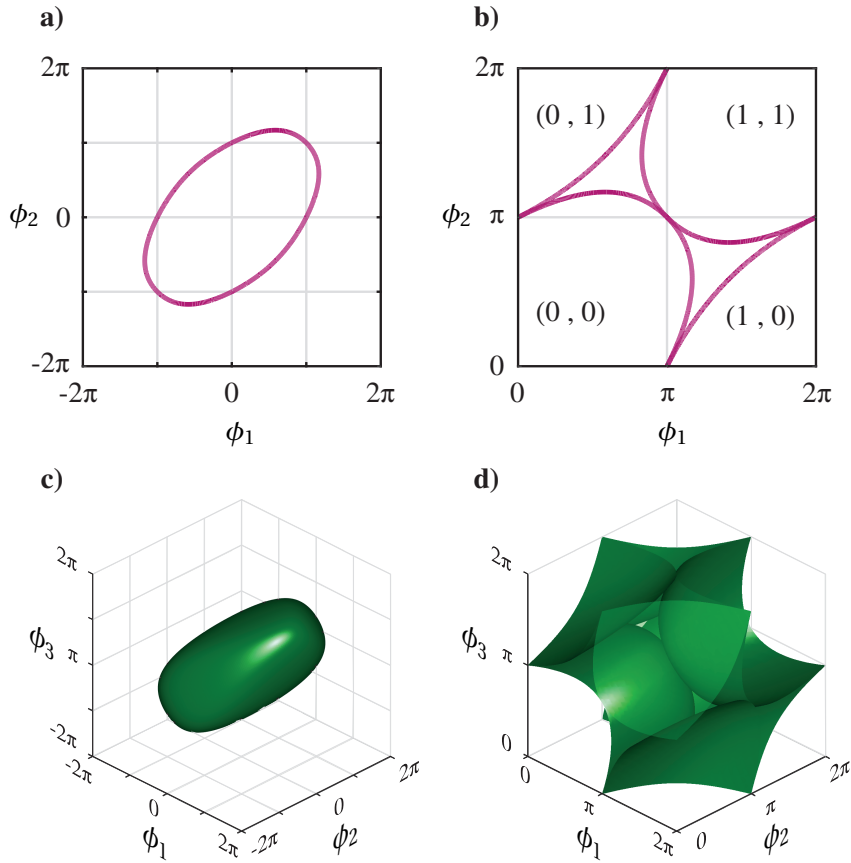
Figure 5.8: Topological phase diagrams for multiterminal Josephson junctions. **a)** Curve along which Eq. (5.63) is satisfied for a three-terminal junction, shown for $(\phi_1, \phi_2) = [-2\pi, 2\pi] \times [-2\pi, 2\pi]$, indicating the boundary between gapped and ungapped regions. **b)** The same curve, folded into the physically relevant $(\phi_1, \phi_2) = [0, 2\pi] \times [0, 2\pi]$. Indicated on the figure are the topological invariants of the different regions. **c)** and **d)** Similar results for a four-terminal junction.

the analytical solution becomes invalid, and are given by the formula,

$$\sum_{j=1}^{N} \frac{\psi_j}{\tan \psi_j} = 0, \tag{5.63}$$

where

$$\psi_j = \phi_j - \langle \phi \rangle = \phi_j - \frac{1}{N} \sum_{i=1}^{N} \phi_i.$$

For a (two-terminal) Josephson junction, one gets that Eq. (5.63) is only satisfied for the discrete points $\phi_1 - \phi_2 = n\pi$, with n an integer – as it should be. In a three-terminal junction, Eq. (5.63) is satisfied along a curve in phase space. As shown in Fig. 5.8a), this curve takes the form of an ellipse in the space $(\phi_1, \phi_2) \in [-2\pi, 2\pi] \times [-2\pi, 2\pi]$. Due to the 2π-periodicity of ϕ_1 and ϕ_2, this curve needs to be folded into the space $[0, 2\pi] \times [0, 2\pi]$ in order to obtain the topological phase diagram, which is shown in Fig. 5.8b). A similar analysis for a four-terminal junction is shown in Fig. 5.8c) and d), where Eq. (5.63) is satisfied along the surface of an ellipsoid-like structure. Additional details, along with a numerical verification of these results may be found in Paper III.

5.4 Current induced Josephson vortices

In Section 3.8 it was discussed how a magnetic field induces a phase gradient in a superconductor. A phase gradient implies the presence of supercurrents, but it also means that a phase difference is established between different regions of a superconducting system. When the magnetic field is large enough to generate a phase difference of π between two points in the system, destructive interference must then lead to a local suppression of the pair correlation midway between them, as was discussed in Section 5.2, potentially leading to the nucleation of vortices. In other words, a magnetic field may produce vortices because it generates circulating supercurrents. A magnetic field is, on the other hand, not a crucial component. Circulating currents induced by any means will have the potential of yielding vortices. In this regard, superconducting hybrid structures have proven useful, where field free nucleation of vortices is possible even in the simplest of systems. Consider, for instance, a Josephson weak link. In section Section 5.2 it was discussed what happens when a phase difference is applied across the junction. If, on the other hand, there are

supercurrents flowing in the superconductors, parallel to the interface, this phase gradient must be transmitted to the superconducting correlations in the normal metal, generating supercurrents also here. Circulating supercurrents in the normal metal may then be simulated by applying oppositely directed tangential supercurrents in the two superconductors, as illustrated in Fig. 5.9, and if these currents are sufficiently strong, vortices may result [159].
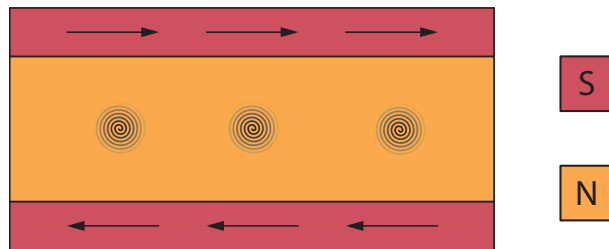
Figure 5.9: A Josephson weak link where supercurrents are flowing, parallel to the interface, in the upper and lower superconductor. When these currents are anti-parallel, vortices may nucleate in the normal metal.

A generalisation of this system would be to surround a normal metal with a continuous superconducting wire which covers all sides, as shown in Fig. 5.10. A phase gradient in the superconductor may then be induced by applying a current bias. By using tunnelling contacts it is reasonable to assume that the only currents in the normal metal are those due to the proximity effect.
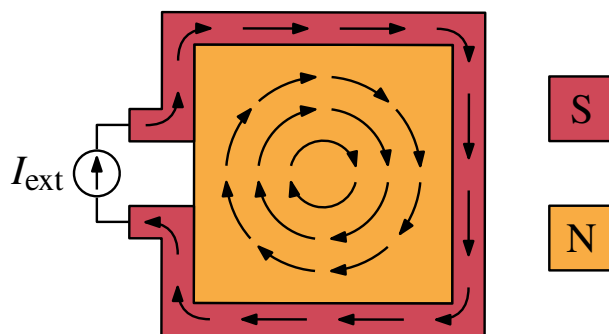
Figure 5.10: The geometry studied in Paper VII. A current bias is applied to a superconductor surrounding a normal metal in order to induce complex vortex patterns in the latter – without application of external flux.

This system is discussed in Paper VII. To model the superconductors, which embodies a uniform supercurrent, or phase gradient $\nabla \phi$, the inverse proximity effect was neglected, which allows for an analytical expression for the superconducting Green function to be found. This simplifies the numerical simulations in that the superconductor may be described by boundary conditions of the normal metal. The Green function in the normal metal may then be found by solving the Usadel equation. The vorticity of the superconducting correlations in the normal metal must be given by

$$N = \frac{1}{2\pi} \oint_{\partial \Omega} (\nabla \phi) \cdot d\boldsymbol{l}, \tag{5.64}$$

where $\partial \Omega$ is the boundary of the normal metal. In other words, the current bias may be used to tune how many times the phase winds around 2π. Each such winding introduces a vortex. It turns out that there is a surprising richness to the manner in which these vortices appear.

Around a vortex, the phase of the superconducting correlations wind by $2\pi n$, where n is the vorticity of the vortex. Vortices with a higher vorticity are more energetically expensive than lower-vorticity vortices. This can be understood by a simple analysis. Consider a circular, closed path surrounding a vortex with vorticity n. Regardless of the radius r of this path, the phase must wind by $2\pi n$. This means that $|\nabla \phi| = |n|/r$. This phase gradient puts the condensate into motion, and its contribution to the kinetic energy density of the system must scale with the square of its velocity, $E_k \sim v^2$. The velocity of the condensate is proportional to the phase gradient, which means that the kinetic energy contributed to the system by a vortex of winding number n is proportional to n^2. Assuming that all vortices are otherwise identical, it is possible to deduce the following algorithm for predicting the vortex patterns: The applied vorticity N will generate a number of vortices N_V, with individual vorticies n_i,

$$N = \sum_{i=1}^{N_V} n_i, \tag{5.65}$$

such that the total energy contributed by a given vortex pattern

$$\frac{E}{E_0} = \sum_{i=1}^{N_V} n_i^2 \tag{5.66}$$

is minimised. However, there is also an additional constraint. The vortex pattern must satisfy the symmetries of the geometry. For a square geometry, this means that individual vortices can only be located at its centre,

otherwise they must appear as quadruplets restricted to the symmetry axes of the system. This means, for instance, that by introducing a vorticity of $N = 2$, a vortex with a phase winding of 4π is generated. Called a giant vortex, such vortices are notoriously difficult to stabilise due to their tendency to split into the energetically favoured conventional 2π-vortices. For $N = 3$, one might expect to produce a 6π-vortex, but this is not what happens. According to Eq. (5.66) it is in fact cheaper for five 2π-vortices to appear. In order for Eq. (5.65) to be satisfied, one of these vortices must have a vorticity of $n = -1$, i.e., it winds in the opposite direction – it is an antivortex. These predictions are perfectly corroborated by the numerical simulations, the results of which are shown in Fig. 5.11
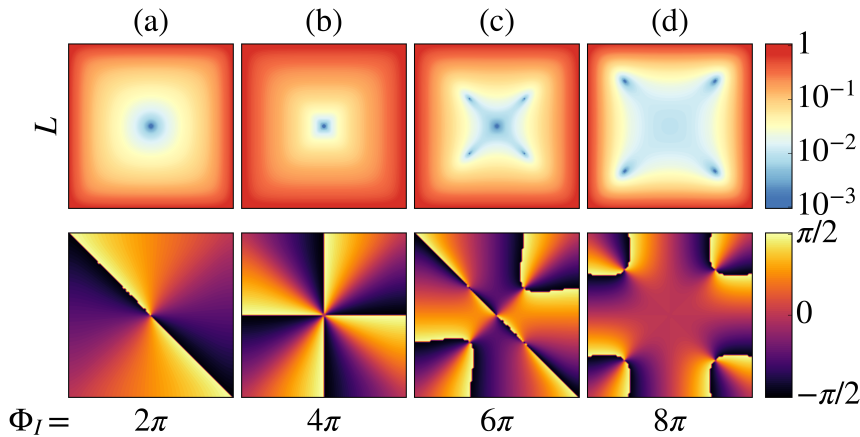
Figure 5.11: The absolute value of the pair correlation (upper row) and its corresponding phase (lower row) for various current windings Φ_I. A conventional vortex with winding number $n = 1$ is shown in column (a), a giant vortex with $n = 2$ is shown in column (b), a central antivortex (n = -1) and four n = 1 vortices is shown in column (c), and four $n = 1$ vortices is shown in column (d).

For a square geometry, the largest vorticity a single vortex can have is $n = 2$. Higher vortex windings are, however, possible in regular polygons with a larger number of sides. Indeed, applying a vorticity of $N = 3$ to a hexagon, the lowest energy vortex pattern is in fact a single 6π-vortex at the centre, as shown in Fig. 5.12, as all other vortex patterns require the appearance of off-centre sextuplets. In general, a polygon with m sides can support a giant vortex with a winding of $n = \lfloor m/2 \rfloor$.
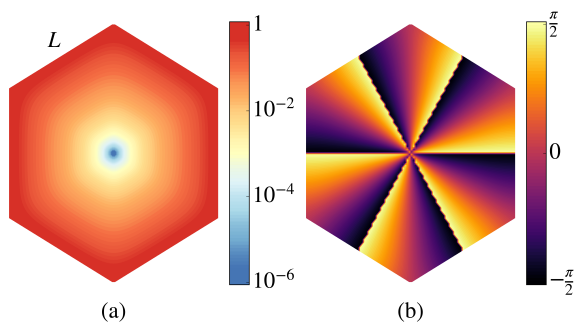
Figure 5.12: An $n = 3$ giant vortex may be created in a hexagonal structure when a current winding of $\Phi_I = 6\pi$ is applied. In (a) is shown the absolute value of the resulting pair correlation, and in (b) its corresponding phase.

The conclusion is that surrounding a non-superconducting material in a superconducting wire, through which flows a suppercurrent, provides convenient means for generating complex vortex patterns – even in the absence of an applied magnetic flux.

Chapter 6

Spin-dependent proximity effects

This chapter will discuss how superconducting correlations may combine with other quantum phenomena. In particular, the focus will be on the spin-dependent proximity effects that emerge when superconductors are attached to ferromagnetic materials. Included in the analysis will also be heavy-metal interlayers, in which spin-orbit coupling plays a prominent role. Such hybrid structures are interesting due to the prospect of creating superconducting correlations that carry spin, an important ingredient in the field of superconducting spintronics.

6.1 Ferromagnetism

As anyone who likes to adorn their refrigerator can attest to, ferromagnetic materials (or magnets) are commonly encountered in every-day life. Nevertheless, ferromagnetism is a quantum phenomenon. It is a consequence of the Coulomb interaction, in conjunction with the Pauli exclusion principle. As a simple illustration of the effects at play, consider the following two-electron system,

$$H(\boldsymbol{r}_1, \boldsymbol{r}_2) \Psi(\boldsymbol{r}_1, \boldsymbol{r}_2) = \left[H_0(\boldsymbol{r}_1) + H_0(\boldsymbol{r}_2) + V(\boldsymbol{r}_1, \boldsymbol{r}_2) \right] \Psi(\boldsymbol{r}_1, \boldsymbol{r}_2)$$
$$= \varepsilon \Psi(\boldsymbol{r}_1, \boldsymbol{r}_2), \tag{6.1}$$

with

$$H_0(\boldsymbol{r}_i) = -\frac{\hbar^2}{2m} \nabla_i^2 - \frac{e^2}{4\pi\epsilon_0} \frac{1}{|\boldsymbol{r}_i - \boldsymbol{R}_1|} - \frac{e^2}{4\pi\epsilon_0} \frac{1}{|\boldsymbol{r}_i - \boldsymbol{R}_2|}, \tag{6.2}$$

and

$$V(\boldsymbol{r}_1, \boldsymbol{r}_2) = \frac{e^2}{4\pi\epsilon_0} \frac{1}{|\boldsymbol{r}_1 - \boldsymbol{r}_2|}. \tag{6.3}$$

Eqs. (6.1) to (6.3) can be thought of as a crude model of an H_2 molecule, ignoring any interactions between nuclei. Ψ must be antisymmetric with respect to an interchange of particles, and by decomposing into an orbital and a spin contribution,

$$\Psi(\boldsymbol{r}_1, \boldsymbol{r}_2) = \Phi(\boldsymbol{r}_1, \boldsymbol{r}_2)\chi(s_1, s_2), \tag{6.4}$$

it becomes clear that Φ must have a well-defined parity. Furthermore, if the centres of the attractive potentials, $\boldsymbol{R}_1$ and $\boldsymbol{R}_2$ are moved far apart, Eqs. (6.1) and (6.2) reduce to individual hydrogen atoms, for which the solution is well-known. To find the ground state of this system it is therefore reasonable to guess at wavefunctions of the form

$$\Phi_s(\boldsymbol{r}_1, \boldsymbol{r}_2) = \frac{1}{\sqrt{2}} \left(\phi_1(\boldsymbol{r}_1)\phi_2(\boldsymbol{r}_2) + \phi_2(\boldsymbol{r}_1)\phi_1(\boldsymbol{r}_2) \right) \tag{6.5}$$

$$\Phi_a(\boldsymbol{r}_1, \boldsymbol{r}_2) = \frac{1}{\sqrt{2}} \left(\phi_1(\boldsymbol{r}_1)\phi_2(\boldsymbol{r}_2) - \phi_2(\boldsymbol{r}_1)\phi_1(\boldsymbol{r}_2) \right), \tag{6.6}$$

where Φ_s and Φ_a indicate orbital wavefunctions with even and odd parity, respectively, and ϕ_i is the ground state eigenfunction of the hydrogen atom, centred at $\boldsymbol{R}_i$. This is known as the *Heitler-London approximation* [108, 160]. The complete wavefunction must then either be of the form $\Psi = \Phi_s\chi_a$, i.e., consist of a symmetric orbital part and an antisymmetric spin part – the spin singlet state, or vice versa, $\Psi = \Phi_a\chi_s$, which is a spin triplet state.

An estimate for the energy of these wavefunctions is given as

$$\varepsilon_x = \frac{\int d\boldsymbol{r}_1 \int d\boldsymbol{r}_2 \, \Phi_x^*(\boldsymbol{r}_1, \boldsymbol{r}_2) H(\boldsymbol{r}_1, \boldsymbol{r}_2) \Phi_x(\boldsymbol{r}_1, \boldsymbol{r}_2)}{\int d\boldsymbol{r}_1 \int d\boldsymbol{r}_2 \, |\Phi_x(\boldsymbol{r}_1, \boldsymbol{r}_2)|^2}, \tag{6.7}$$

which gives

$$\varepsilon_{s/a} = 2\varepsilon_0 + \frac{D \pm J}{1 \pm |\zeta|^2} \simeq 2\varepsilon_0 + D \pm J, \tag{6.8}$$

where ε_0 is approximately equal to the ground state energy of the hydrogen atom (assuming that R_1 and R_2 are sufficiently far apart), and the overlap integral

$$\zeta = \int d\boldsymbol{r} \, \phi_1^*(\boldsymbol{r})\phi_2(\boldsymbol{r})$$

has been assumed small. Furthermore,

$$D = \int d\boldsymbol{r}_1 \int d\boldsymbol{r}_2 \, \phi_1^*(\boldsymbol{r}_1)\phi_2^*(\boldsymbol{r}_2)V(\boldsymbol{r}_1,\boldsymbol{r}_2)\phi_1(\boldsymbol{r}_1)\phi_2(\boldsymbol{r}_2)$$

$$J = \int d\boldsymbol{r}_1 \int d\boldsymbol{r}_2 \, \phi_1^*(\boldsymbol{r}_1)\phi_2^*(\boldsymbol{r}_2)V(\boldsymbol{r}_1,\boldsymbol{r}_2)\phi_2(\boldsymbol{r}_1)\phi_1(\boldsymbol{r}_2).$$

The point is that even though the Hamiltonian is spin-independent, the coupling between the orbital and spin part of the wavefunction, via the Pauli exclusion principle, leads to a splitting of the energy states, depending upon whether the two-particle system is in the singlet or a triplet state. These two energy levels may be parametrised as

$$\varepsilon = \frac{1}{4}\left(\varepsilon_s + 3\varepsilon_a\right) - \frac{2J}{\hbar^2}\boldsymbol{S}_1 \cdot \boldsymbol{S}_2, \tag{6.9}$$

where $\boldsymbol{S}_i$ is the spin of particle i. Note that in the singlet state, where the combined spin quantum number $S = 0$, $\boldsymbol{S}_1 \cdot \boldsymbol{S}_2 = -\frac{3}{4}\hbar^2$, and in a triplet state ($S = 1$), $\boldsymbol{S}_1 \cdot \boldsymbol{S}_2 = \frac{1}{4}\hbar^2$. The parameter J is known as the *exchange coupling*, and can easily be computed. It turns out that J is negative in this case, indicating that the spin singlet state, or an antiferromagnetic coupling, is favoured. This is always the case for the ground state of two-particle systems where the Hamiltonian is spin-independent [108]. In contrast, if excited states are included, or, as is more relevant for the following discussion, in many-particle systems, a ferromagnetic coupling is possible, and as a generalisation of the above discussion, an effective Hamiltonian taking into account the exchange interaction between spins may be written as

$$H = -\sum_{i,j} J_{ij}\boldsymbol{S}_i \cdot \boldsymbol{S}_j, \tag{6.10}$$

which is known as the *Heisenberg model* [161]. Of interest in the following will be how the dislocated conduction electrons in a metal react to a source of spin splitting. The electron spin density operator may be expressed in terms of the field operators defined in Eq. (2.2) as

$$\boldsymbol{s}(\boldsymbol{r}) = \frac{\hbar}{2}\sum_{ss'} \psi_s^\dagger(\boldsymbol{r})\boldsymbol{\sigma}_{ss'}\psi_{s'}(\boldsymbol{r}). \tag{6.11}$$

If the source of the spin splitting stems from the underlying lattice, an appropriate Hamiltonian may thus take the form,

$$H = -\int d\boldsymbol{r}\sum_i J(\boldsymbol{r} - \boldsymbol{R}_i)\boldsymbol{S}(\boldsymbol{R}_i) \cdot \boldsymbol{s}(\boldsymbol{r}),$$

where $\boldsymbol{R}_i$ are the locations of the ions. Of importance in the following however, will not be the origin of the spin splitting field. Therefore, a more general Hamiltonian will be assumed, which takes the form

$$H = -\sum_{ss'} \int d\boldsymbol{r}\, \psi^\dagger(\boldsymbol{r}) \boldsymbol{h} \cdot \boldsymbol{\sigma}_{ss'} \psi(\boldsymbol{r}). \qquad (6.12)$$

The function $\boldsymbol{h}(\boldsymbol{r})$ is called the *exchange field.*

Following the procedure of Chapter 2, the equation of motion for a free electron gas with a spin splitting field becomes

$$\left[\varepsilon \check{\rho}_4 + \left(\frac{\hbar^2}{2m} \nabla^2 + \mu \right) \check{I} + \boldsymbol{h} \cdot \check{\boldsymbol{\sigma}} \right] \check{G}(\boldsymbol{r}, \boldsymbol{r}') = \check{I} \delta(\boldsymbol{r} - \boldsymbol{r}'), \qquad (6.13)$$

where $\check{\boldsymbol{\sigma}} = \mathrm{diag}\,(\hat{\boldsymbol{\sigma}}, \hat{\boldsymbol{\sigma}})$, with $\hat{\boldsymbol{\sigma}} = \mathrm{diag}\,(\boldsymbol{\sigma}, \boldsymbol{\sigma}^*)$. For a constant exchange field pointing in the z direction, this results in

$$\check{G}(\boldsymbol{k}) = \left[\varepsilon \check{\rho}_4 - \left(\frac{\hbar^2 \boldsymbol{k}^2}{2m} - \mu \right) \check{I} + h \cdot \check{\sigma}_z \right]^{-1}, \qquad (6.14)$$

from which the band structure may be read off immediately as

$$\varepsilon_{\uparrow,\downarrow}(\boldsymbol{k}) = \frac{\hbar^2 \boldsymbol{k}^2}{2m} - \mu \mp h,$$

so that the band splitting becomes $\varepsilon_\downarrow - \varepsilon_\uparrow = 2h$, as it should.

If the exchange field $|\boldsymbol{h}|$ is much lower than the Fermi energy, $|\boldsymbol{h}|/E_\mathrm{F} \sim \alpha \ll 1$, and its spatial variation is sufficiently slow, it may be included in the quasiclassical formalism discussed in Section 2.4. The Eilenberger equation then becomes

$$i\hbar v_\mathrm{F} \cdot \nabla \check{g} + \left[\varepsilon \check{\rho}_4 + \boldsymbol{h} \cdot \check{\boldsymbol{\sigma}}, \check{g} \right] = 0, \qquad (6.15)$$

and the Usadel equation,

$$\hbar D \nabla \cdot \check{g} \nabla \check{g} + i \left[\varepsilon \check{\rho}_4 + \boldsymbol{h} \cdot \check{\boldsymbol{\sigma}}, \check{g} \right] = 0. \qquad (6.16)$$

Solution for a diffusive homogeneous ferromagnet

For an infinite, homogeneous ferromagnet, the gradient term in Eq. (6.16) vanishes, and the solution is immediately found to be

$$\check{g} = \check{\rho}_4, \qquad (6.17)$$

which is identical to the solution for a normal metal without any spin splitting.

6.2 Spin-dependent observables

An important observable in systems with a spin splitting is the induced magnetisation, which may be found from Eq. (6.11) via

$$M(r) = -\frac{g\mu_B}{\hbar}\langle s(r)\rangle = -\frac{g\mu_B}{2}\sum_{ss'}\left\langle \psi_s^\dagger(r)\boldsymbol{\sigma}_{ss'}\psi_{s'}(r)\right\rangle, \tag{6.18}$$

where g is the Landé g-factor, and μ_B is the Bohr magneton. Written in terms of Green functions in the mixed representation, this becomes

$$M(r) = \frac{ig\mu_B}{8}\int\frac{d\boldsymbol{k}}{(2\pi)^3}\int\frac{d\varepsilon}{2\pi}\,\mathrm{Tr}\left[\hat{\boldsymbol{\sigma}}\hat{G}^K(r,\boldsymbol{k})\right]. \tag{6.19}$$

For a homogeneous ferromagnet, with the Green function as given in Eq. (6.14), it is found that

$$\mathrm{Tr}\left[\hat{\boldsymbol{\sigma}}\hat{G}^K(r,\boldsymbol{k})\right] = -2\pi i\left[\delta(\varepsilon - h - \xi_k) - \delta(\varepsilon - h - \xi_k)\right.$$

$$\left. -\delta(-\varepsilon + h - \xi_k) + \delta(-\varepsilon + h - \xi_k)\right], \tag{6.20}$$

with $\xi_k = \hbar^2\boldsymbol{k}^2/2m - \mu$. Inserting into Eq. (6.19) and integrating over ε gives

$$M_z = -\frac{g\mu_B}{8}\int d\xi_k\,\nu(\xi_k)\left[\tanh\frac{\beta(\xi_k + h)}{2} - \tanh\frac{\beta(\xi_k - h)}{2}\right], \tag{6.21}$$

with $\nu(\xi_k) = \sqrt{2m^3(\xi_k + \mu)}/\pi^2\hbar^3$ the density of states for a free electron gas. If the exchange field h is small, the integrand in Eq. (6.21) may be Taylor expanded to first order, giving

$$M_z = -\frac{g\mu_B}{8}h\int d\xi_k\,\nu(\xi_k)\beta\frac{1}{\cosh^2\frac{\beta\xi_k}{2}}.$$

For large β (low temperatures), the approximation $\beta/\cosh^2\frac{\beta\xi_k}{2} \simeq 4\delta(\xi_k)$ may be used, and thus it is found that (for an arbitrary exchange field direction)

$$M = -\frac{g\mu_B}{2}h. \tag{6.22}$$

The quasiclassical Green function for a bulk ferromagnet, given in Eq. (6.17), is identical to that of a normal metal, and hence cannot produce a magnetisation. This seems contradictory to the result derived in

Eq. (6.22). The reason for the discrepancy is that the quasiclassical Green function only describes the low-energy behaviour of the system, whereas the integral in Eq. (6.19) involves contributions also from the high-energy regime. Introducing $\hat{G}^K = \hat{G}^K_l + \hat{G}^K_h$ as in Section 2.4, Eq. (6.19) can be written in terms of the quasiclassical Green function as

$$M(r) = M_h(r) + \frac{g\mu_B \nu_0}{32} \int d\varepsilon \, \mathrm{Tr}\left[\hat{\boldsymbol{\sigma}} \hat{g}^K(r,\varepsilon)\right],$$

where M_h is the high-energy contribution, and ν_0 is the density of states at the Fermi level. Recall that, in the formalism of section Section 2.4, $\hat{G}^K_h$ contains all diagrams of order $\alpha^0 = 1$ and lower. A diagram is of order α^0 if it contains no low-energy propagators, or no external perturbations (e.g. h). Each external perturbation adds a power of α, which means that to order α, $\hat{G}^K_h$ is at most linear in h. Furthermore, M_h cannot contain a constant term independent of h, as that would give a contribution even in the normal metal case. The conclusion is that $M_h \propto h$. Using Eq. (6.22), the general expression for the quasiclassical magnetisation becomes

$$M(r) = -\frac{g\mu_B \nu_0}{2} h(r) + \frac{g\mu_B \nu_0}{32} \int d\varepsilon \, \mathrm{Tr}\left[\hat{\boldsymbol{\sigma}} \hat{g}^K(r,\varepsilon)\right]. \qquad (6.23)$$

The spin density $\boldsymbol{\rho}_s = \langle s(r) \rangle$ may also be used to find the spin currents. Provided there are no spin torques acting, and no spin-orbit coupling, the following continuity equation is satisfied,

$$\frac{\partial}{\partial t}\rho_s^\alpha + \nabla \cdot \boldsymbol{J}_s^\alpha = 0, \qquad (6.24)$$

with $\alpha \in \{x, y, z\}$ indicating the spin direction. Following the same procedure in going from Eq. (3.68) to Eq. (3.74) leads to

$$\boldsymbol{J}_s^\alpha = \frac{\hbar \nu_0 D}{32} \int d\varepsilon \, \mathrm{Tr}\left[\hat{\rho}_4 \hat{\sigma}_\alpha \left(\check{g}\nabla\check{g}\right)^K\right]. \qquad (6.25)$$

6.3   Superconductors and ferromagnets

Ferromagnetic ordering occurs when the spins involved find it energetically favourable to point in the same direction. In conventional BCS superconductivity, on the other hand, the electrons form spin singlet Cooper pairs. Ferromagnetism and superconductivity therefore seem to be at odds with each other. Nevertheless there are materials where they coexist, for instance in the so-called ferromagnetic superconductors. A much

more accessible way of inducing both ferromagnetic and superconducting order in a system is, however, via the proximity effect in hybrid structures. This can be done, for instance by attaching a ferromagnetic insulator to a BCS superconductor. If the superconductor is sufficiently thin, an exchange field can be assumed present throughout its entire thickness [162]. Hence, it is straightforward to create a system which displays both types of ordering. But that does not avoid the fact that ferromagnetism and superconductivity are antagonistic phenomena. Clearly, no Cooper pair formation is possible if the spin splitting is larger than the superconducting gap. It turns out that superconductivity is quenched even sooner than that, at the so-called *Chandrasekhar-Clogston limit* [163, 164], which at a temperature $T = 0$ is

$$h_p = \frac{1}{\sqrt{2}}\Delta. \tag{6.26}$$
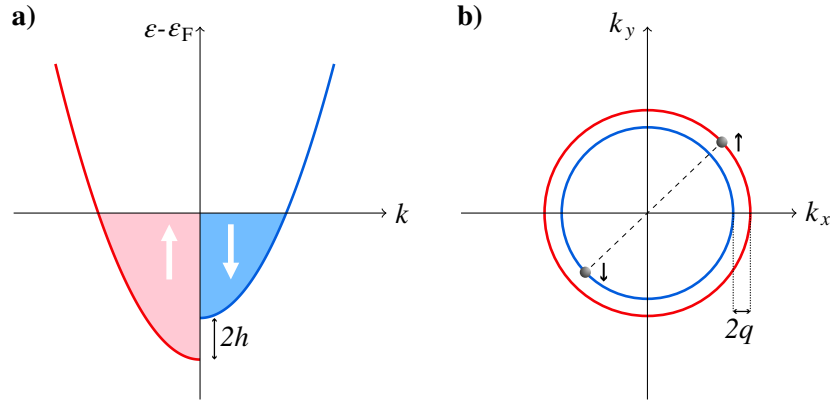
Figure 6.1: Illustration of the FFLO phase. **a)** The energy bands, with a spin splitting due to the exchange field h. **b)** Equipotential surface at ε_F for a two-dimensional system, showing a Cooper pair with a finite momentum $\hbar\boldsymbol{q}$.

In a clean system, the simultaneous presence of both an exchange field and a superconducting gap may lead to an interesting phenomenon in which the superconducting order parameter becomes spatially inhomogeneous. As shown in Fig. 6.1, when a source of spin splitting is introduced, quasiparticles with parallel spin experience a lower potential energy than quasiparticles with antiparallel spin. For two quasiparticles at a given energy level to form a singlet Cooper pair, their kinetic energies must therefore compensate for this difference in potential energy. In other words, a

Cooper pair consisting of quasiparticles e.g. at $(+k_\mathrm{F}, \uparrow)$ and $(-k_\mathrm{F}, \downarrow)$, will experience a momentum shift, q, due to the lowering and raising of the spin up and down energy bands, respectively. The resulting Cooper pair, now consisting of quasiparticles at $(k_\mathrm{F} + q, \uparrow)$ and $(-k_\mathrm{F} + q, \downarrow)$ attain a net momentum of $\hbar q$. This is known as the *Fulde-Ferrell-Larkin-Ovchinnikov* (FFLO or LOFF) *phase* [165, 166]. The net momentum of the Cooper pairs leads to a spatially dependent phase modulation, given as [167]

$$(\uparrow\downarrow - \downarrow\uparrow) \rightarrow \left(\uparrow\downarrow\, e^{i\boldsymbol{q}\cdot\boldsymbol{r}} - \downarrow\uparrow\, e^{-i\boldsymbol{q}\cdot\boldsymbol{r}}\right) = (\uparrow\downarrow - \downarrow\uparrow)\cos\boldsymbol{q}\cdot\boldsymbol{r} + i\,(\uparrow\downarrow + \downarrow\uparrow)\sin\boldsymbol{q}\cdot\boldsymbol{r}.$$
$$(6.27)$$

This means that not only do spatial oscillations of the singlet order parameter appear, but there is also a conversion between the singlet state and the $S_z = 0$ triplet state, which has profound consequences to be discussed shortly.

Superconductor-ferromagnet proximity effects

In a homogeneous diffusive system, the FFLO phase is suppressed, and only the uniform superconducting phase is found. This is because of the frequent elastic impurity scattering processes, which average out the momentum direction. However, in an inhomogeneous system, spatial modulations of the superconducting correlations may still appear. In a diffusive system, the quasiparticles can be thought of as random walkers. Indeed, the Usadel equation, given in Eq. (6.16), is nothing more than a diffusion equation. Hence, the quasiparticles satisfy Fick's first law, which states that there is a particle flow towards regions of lower particle density, as given by $\boldsymbol{J} = -D\check{g}\nabla\check{g}$, in correspondence with Eq. (5.48). This means that the quasiparticles sample the energy band with a bias in the direction of $\boldsymbol{J}$, so that momentum-dependent phenomena do not completely average out. In a superconductor-ferromagnet bilayer, $\boldsymbol{J}$ points in the direction normal to the interface between the two materials, and hence FFLO-like oscillations are to be expected along this direction. To verify this, Eq. (6.16) may be solved in a similar way as was done for a superconductor-normal metal in Section 5.2. The resulting pair correlation is shown in Fig. 6.2 for an exchange field of $\boldsymbol{h} = 5\Delta_0\boldsymbol{e}_z$, where Δ_0 is the gap of a bulk superconductor.

As an interesting aside, oscillations of the pair correlation have also been predicted in the normal metal of superconductor-normal metal-
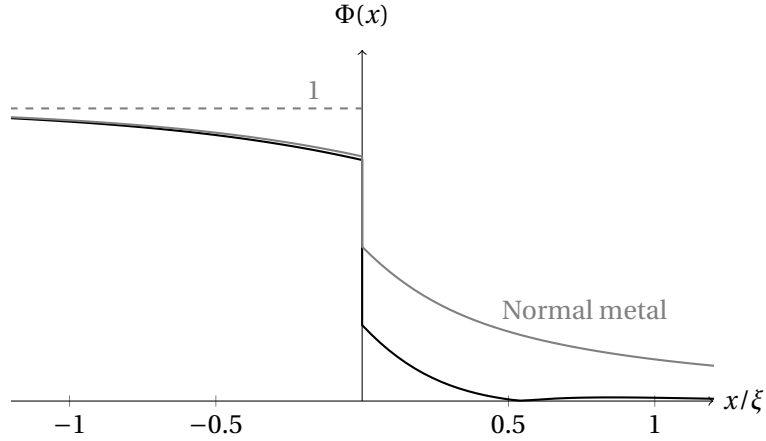
Figure 6.2: The pair correlation for a superconductor-ferromagnet bilayer, where the ferromagnet has an exchange field of $\boldsymbol{h} = 5\Delta_0 \boldsymbol{e}_z$. The interface resistance is $\zeta = \rho_c / \rho_1 \xi = 3$. Shown in grey is the pair correlation for an equivalent superconductor-normal metal bilayer.

ferromagnet trilayers, occurring due to the appearance of quantum-well states, i.e., confinement induced band splittings [168].

An striking demonstration of the oscillations in the singlet supercon-ducting correlations is found in a Josephson weak link with a ferromagnetic interlayer, i.e., a superconductor-ferromagnet-superconductor structure. Depending on the length of the junction or the strength of the exchange field (which dictates the oscillatory wavelength), either constructive or destructive interference between the two superconductors can be induced at a phase difference of $\phi = 0$. The latter is known as a π *junction* [169], due to its resemblance to a conventional Josephson junction with a phase difference of π, as discussed in Section 5.2. The observable consequence of the transition from a conventional 0 junction to a π junction is that the supercurrent flowing between the superconductors at a given phase differ-ence changes sign – and is completely quenched exactly at the transition. This is shown in Fig. 6.3, where the supercurrent has been computed for a variety of exchange fields for a ferromagnetic Josephson weak link at a phase difference of $\frac{\pi}{2}$.

It is possible to mimic a ferromagnetic Josephson weak link by apply-ing a large in-plane magnetic field to a two-dimensional superconductor-normal metal-superconductor structure. In that case the spin splitting is caused by the Zeeman effect. This was done in Paper XIV, where flakes of
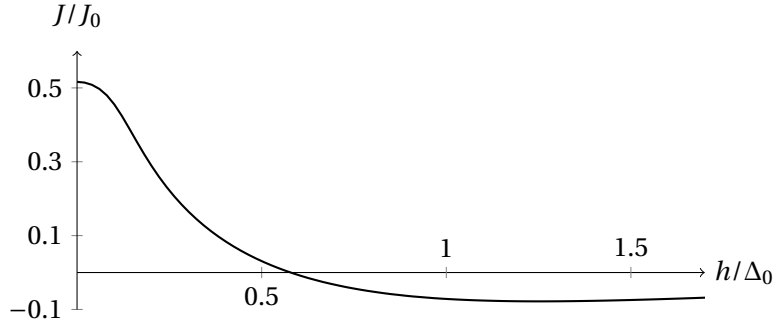
Figure 6.3:   The supercurrent in a superconductor-ferromagnet-superconductor Josephson weak link, for a selection of exchange field strengths, at a phase difference of $\frac{\pi}{2}$. The current is scaled by $J_0 = eDv_0\Delta/16\xi$.

NbSe$_2$ were placed on top of a sheet of graphene. Thin layers of NbSe$_2$ exhibit so-called Ising spin-orbit coupling, which makes them much more resilient against in-plane magnetic fields than conventional superconductors [170]. At a fixed phase difference, this system displays sign reversals of the supercurrent, depending on the size of the magnetic field, which is reminiscent of 0 to π transitions. On the other hand, ripples in the graphene sheet introduces flux through the system, which was shown in Paper XIII to have a similar observable signature, and could not be ruled out as an alternative explanation.

Another interesting observation in superconductor-ferromagnet hybrid structures is that the critical temperature, T_c, can be influenced quite strongly. In a bilayer structure T_c has been found to exhibit a non-monotonic behaviour depending on the thickness of the ferromagnet, even vanishing and reentering in some cases [171]. When two ferromagnets are attached to a superconductor, the behaviour can be even more complex, with T_c reaching a minimum at some non-collinear misalignment angle between the magnetisation of the two ferromagnets [172]. This is due to the appearance of so-called long ranged triplet superconducting correlations, a topic to be discussed next.

Odd frequency superconductivity

The simulations of the SF and SFS structures with the Usadel equation, which are valid in the diffusive limit, revealed a singlet to triplet conver-

sion of the superconducting correlations, as predicted by Eq. (6.27). At first sight, this seems counter-intuitive. The wavefunction of the two-electron system which constitutes a Cooper pair must be antisymmetric with respect to an interchange of particles. A triplet spin configuration is symmetric, which would seem to indicate that the orbital part must be antisymmetric. But an antisymmetric orbital part, given e.g. by *p*-wave superconductivity, should not appear in a diffusive system due to the momentum space averaging effect created by rampant scattering. There is another possibility, however, which allows for both the orbital and the spin part of the wavefunction to be symmetric – the particles can avoid each other in time, giving an antisymmetric time dependence. Known as *odd frequency superconductivity* [173], this effect means that it is possible to induce superconducting correlations carrying spin also in diffusive systems.

As is illustrated in Fig. 6.2, the singlet superconducting correlations survive only a short distance into a ferromagnet. The same is true for the $S_z = 0$ triplet correlations, whose net spin is orthogonal to the exchange field. There are, however, two other triplet states where the spins would be collinear with the exchange field. If generated, they would not be influenced by the spin splitting to the same extent, and could exhibit much longer decay lengths. This prospect warrants a closer look at the two-spin states.

Two spin-1/2 particles combine either into a singlet, which has a total spin quantum number $s = 0$, or one of three triplet states, with $s = 1$. The precise direction of the spins involved is not knowable due to the Heisenberg uncertainty principle, but their magnitude, along with one component can be determined, as they are simultaneous eigenstates. The eigenvalue of the combined spin magnitude S^2, as well as the individual spin magnitudes S_1 and S_2, when acting on some eigenvector χ, is given as

$$S^2 \chi = s(s+1)\hbar^2 \chi,$$
$$S_1^2 \chi = s_1(s_1+1)\hbar^2 \chi,$$
$$S_2^2 \chi = s_2(s_2+1)\hbar^2 \chi.$$

The scalar product between S_1 and S_2 is also an eigenvalue of χ, and is found to be

$$S_1 \cdot S_2 \chi = \frac{1}{2}\left(S^2 - S_1^2 - S_2^2\right)\chi = \frac{1}{2}\left[s(s+1) - s_1(s_1+1) - s_2(s_2+1)\right]\hbar^2 \chi.$$

Using that $s_1 = s_2 = \frac{1}{2}$, the expected angle between the two spins may be computed as

$$\cos\gamma = \frac{\chi^\dagger \boldsymbol{S}_1 \cdot \boldsymbol{S}_2 \chi}{\chi^\dagger |\boldsymbol{S}_1||\boldsymbol{S}_2|\chi} = \frac{1}{3}\left[2s(s+1) - 3\right]. \tag{6.28}$$

The resulting two-spin states are illustrated in Fig. 6.4.
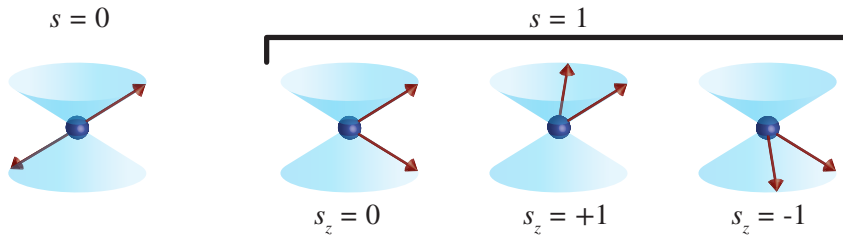
Figure 6.4: The possible spin configurations of a two-spin system. In the singlet state ($s = 0$), the two spins are anti-parallel, whereas in the triplet states ($s = 1$), there is a net magnetisation.

In the presence of a magnetic field it is clear that the $s_z = \pm 1$ triplets behave differently than the singlet and the $s_z = 0$ triplet. In the former case, both spins have a component which is either parallel or antiparallel with the external field. Hence, the spin splitting induces no dephasing of the Cooper pair. Note that this discussion has been with reference to a particular spin quantisation axis, e.g., the z axis. While the singlet state is completely ambivalent to the direction of applied magnetic field, the triplet states are influenced. For instance, when a magnetic field along the x axis is applied to the $s_z = 0$ triplet state it behaves as

$$(\uparrow\downarrow + \downarrow\uparrow)_z = (\uparrow\uparrow)_x + (\downarrow\downarrow)_x,$$

i.e., a linear combination of the $s_x = +1$ and the $s_x = -1$ triplet states. In other words, such "equal spin" Cooper pairs may be induced when the superconductor is attached to a ferromagnet whose exchange field direction is inhomogeneous. This can be done, for instance, by using multidomain ferromagnets, where triplets induced in the domain walls may be long ranged in the adjacent domains [174]. Another possibility is by stacking multiple layers of ferromagnets [175]. Typically, such a structure would prefer a collinear alignment of their magnetisations, but other configurations are also possible. One example is a trilayer in which a uniform ferro-

magnet is sandwiched between two layers of holmium, where the magnet-isation has a conical spatial variation with a certain wavelength [176]. By tuning the holmium thickness to half of this wavelength, the misalignment with the uniform ferromagnet is maximised, and so too is the generation of long ranged triplets [81, 177]. Other examples of systems which display long ranged triplet correlations are discussed in Papers VI and XI, with the former summarised in Section 6.6.

6.4   Spin active boundary conditions

Interfaces to ferromagnetic materials can in principle have spin-dependent tunnelling probabilities. To incorporate such effects, it is necessary to modify the boundary conditions derived in Section 5.1. This can be done by introducing a spin splitting in Eq. (5.12), so that

$$\check{V}_0 = v\check{I} + v_h \hat{m} \cdot \check{\boldsymbol{\sigma}}, \tag{6.29}$$

where the unit vector $\hat{m}$ is the direction of the spin splitting. Note that in Section 5.1, the tunnelling potential is treated as a perturbation of a system with an impenetrable interface. Even for such an interface, an incoming particle may penetrate for some distance before being reflected. To capture the resulting spin dephasing, Eq. (5.32) must be replaced by

$$\check{g}^o_{0,j}(r_0) = \check{S}\check{g}^i_{0,j}(r_0)\check{S}^\dagger, \tag{6.30}$$

where $\check{S}$ is a *scattering matrix*. It may be found by assuming that the interface potential takes up half of space, e.g., $z > 0$ and consider the following first-quantised Hamiltonian

$$H = -\frac{\hbar^2}{2m}\nabla^2 - \mu + \left(\mu + v + v_h\hat{m}\cdot\boldsymbol{\sigma}\right)\theta(z), \tag{6.31}$$

where $\theta(z)$ is the Heaviside step function. Momenta parallel to the interface, $\hbar\boldsymbol{k}_{\parallel}$, are conserved during a scattering process, which motivates considering wavefunctions of the form $\psi(\boldsymbol{r}) = \phi(z)e^{i\boldsymbol{k}_{\parallel}\cdot\boldsymbol{r}_{\parallel}}$. Only energies close to the Fermi level are of interest, and so it is assumed that the excitation energy $\varepsilon \simeq 0$, meaning that $H\psi = 0$. The resulting equations of motion thus become

$$\phi''(z) + \left[\frac{2m}{\hbar^2}\varepsilon_{\mathrm{F}} - \boldsymbol{k}_{\parallel}^2\right]\phi(z) = 0, \quad z < 0, \tag{6.32}$$

$$\phi''(z) - \left[\boldsymbol{k}_{\parallel}^2 + \frac{2m}{\hbar^2}\left(v + v_h\hat{m}\cdot\boldsymbol{\sigma}\right)\right]\phi(z) = 0, \quad z > 0. \tag{6.33}$$

The solution in the two respective regimes are, for $z < 0$,

$$\phi(z) = \begin{pmatrix} A_1 \\ A_2 \end{pmatrix} e^{ik_z z} + \begin{pmatrix} B_1 \\ B_2 \end{pmatrix} e^{-ik_z z}, \tag{6.34}$$

and for $z > 0$, where the wavefunction is evanescent,

$$\phi(z) = C \begin{pmatrix} \cos\frac{\theta}{2} \\ \sin\frac{\theta}{2} e^{i\phi} \end{pmatrix} e^{-q_+ z} + D \begin{pmatrix} -\sin\frac{\theta}{2} \\ \cos\frac{\theta}{2} e^{i\phi} \end{pmatrix} e^{-q_- z}, \tag{6.35}$$

where θ and ϕ denote the polar and azimuthal direction of $\hat{m}$ with respect to the z axis, and

$$q_\pm = \sqrt{\boldsymbol{k}_\parallel^2 + \frac{2m}{\hbar^2}(\nu \pm \nu_h)}.$$

The scattering matrix in spin space is found by matching the wavefunction and its derivative at $z = 0$. In this way, the parameters C and D may be eliminated and the S matrix extracted from the resulting relationship between A and B; $B = SA$. One gets

$$S = \frac{1}{(k_z + iq_+)(k_z + iq_-)} \begin{pmatrix} s_1 + s_2 \cos\theta & s_2 \sin\theta e^{-i\phi} \\ s_2 \sin\theta e^{-i\phi} & s_1 + s_2 \cos\theta \end{pmatrix} \tag{6.36}$$

with $s_1 = k_z^2 + q_+ q_-$ and $s_2 = -ik_z(q_+ - q_-)$. Eq. (6.36) may be parametrised more conveniently as

$$S = e^{i\beta} e^{i\gamma \hat{m}\cdot\boldsymbol{\sigma}}, \tag{6.37}$$

where

$$\tan\gamma = -\frac{k_z(q_+ - q_-)}{k_z^2 + q_+ q_-}. \tag{6.38}$$

The value of the spin-independent phase factor β does not have any physical implications, and will be set to zero in the following. In Nambu⊗spin space, the scattering matrix becomes

$$\hat{S} = \begin{pmatrix} S(\boldsymbol{k}) & 0 \\ 0 & S^*(-\boldsymbol{k}) \end{pmatrix}, \tag{6.39}$$

and in Keldysh space it is given as $\check{S} = \mathrm{diag}\left(\hat{S}, \hat{S}\right)$. The relationship between $\check{g}_{0,j}^i$ and $\check{g}_{0,j}^o$ and the diffusive Green function $\check{g}_{s,j}$ may now be found by combining Eqs. (5.41) to (5.44) and Eq. (6.30), which gives

$$\check{g}_{0,j}^i = \left(\check{S}^\dagger \check{g}_{s,j} \check{S} + \check{g}_{s,j}\right)^{-1} \left(2\check{I} + \check{g}_{s,j} - \check{S}^\dagger \check{g}_{s,j} \check{S}\right), \tag{6.40}$$

$$\check{g}_{0,j}^o = \left(2\check{I} + \check{g}_{s,j} - \check{S}\check{g}_{s,j} \check{S}^\dagger\right) \left(\check{S}\check{g}_{s,j} \check{S}^\dagger + \check{g}_{s,j}\right)^{-1}. \tag{6.41}$$

These expressions are quite unassailable as they stand. To proceed, an approximation is made, namely that

$$
\begin{aligned}
\left(\check{S}^\dagger \check{g}_{s,j} \check{S} + \check{g}_{s,j}\right)^{-1} &= \frac{1}{2}\left[\check{I} + \frac{1}{2}\left(\check{g}_{s,j}\check{S}^\dagger \check{g}_{s,j}\check{S} - \check{I}\right)\right]^{-1}\check{g}_{s,j} \\
&\simeq \frac{1}{2}\left[\check{I} - \frac{1}{2}\left(\check{g}_{s,j}\check{S}^\dagger \check{g}_{s,j}\check{S} - \check{I}\right)\right]\check{g}_{s,j},
\end{aligned}
$$

and similarly for $\left(\check{S}\check{g}_{s,j}\check{S}^\dagger + \check{g}_{s,j}\right)^{-1}$. By inserting into Eqs. (6.40) and (6.41) one gets

$$
\check{g}_{0,j}^i \simeq \frac{1}{2}\check{I} + \frac{3}{2}\check{g}_{s,j} - \frac{1}{2}\check{g}_{s,j}\check{S}^\dagger \check{g}_{s,j}\check{S} - \frac{1}{2}\check{g}_{s,j}\check{S}^\dagger \check{g}_{s,j}\check{S}\check{g}_{s,j}, \tag{6.42}
$$

$$
\check{g}_{0,j}^o \simeq \frac{1}{2}\check{I} + \frac{3}{2}\check{g}_{s,j} - \frac{1}{2}\check{S}\check{g}_{s,j}\check{S}^\dagger \check{g}_{s,j} - \frac{1}{2}\check{g}_{s,j}\check{S}\check{g}_{s,j}\check{S}^\dagger \check{g}_{s,j}. \tag{6.43}
$$

The main motivation for approximating Eqs. (6.40) and (6.41) in this, somewhat peculiar, way is that in the limit of no spin mixing, $\check{S} = \check{I}$, the identity $\check{g}_{0,j}^i = \check{g}_{0,j}^o = \check{g}_{s,j}$ is restored. Following the same steps as in Section 5.1, using Eqs. (5.28) to (5.30), (5.34) and (5.48) one finds to lowest order in the tunnelling limit, after a significant amount of algebra,

$$
\begin{aligned}
\check{g}_1 \nabla \check{g}_1 &= \frac{1}{4}\frac{\rho_1}{\rho_c}\left[\check{g}_1\,,\,\beta_+\check{g}_2 + P\{\hat{m}\cdot\boldsymbol{\sigma},\check{g}_2\} + \beta_-\hat{m}\cdot\boldsymbol{\sigma}\check{g}_2\hat{m}\cdot\boldsymbol{\sigma}\right] \\
&\quad - iG_\phi\left[\check{g}_1,\hat{m}\cdot\boldsymbol{\sigma}\right], \tag{6.44}
\end{aligned}
$$

where, following the notation of Ref. [45] $\nu^2 = \frac{1}{2}T\beta_+$ and $\nu_h^2 = \frac{1}{2}T\beta_-$, with $T = \rho_1/2\rho_c$ and $\beta_\pm = \left(1 \pm \sqrt{1 - P^2}\right)$. Note that $P \in [-1,1]$ plays the role of a polarisation. The parameter G_ϕ appears entirely because of the scattering matrices, and involves no tunnelling. It may thus be used to model a ferromagnetic insulator. In general, G_ϕ depends on both P and T, but can vary independently as the latter two in principle also depend on the thickness of the barrier.

6.5 Singlet spin accumulation

Using the formalism of Eq. (6.44), a very interesting and counter-intuitive phenomenon was predicted in Paper XII, namely that singlet superconducting correlations can produce a nonequilibrium spin accumulation. This was done by considering the system shown in Fig. 6.5.
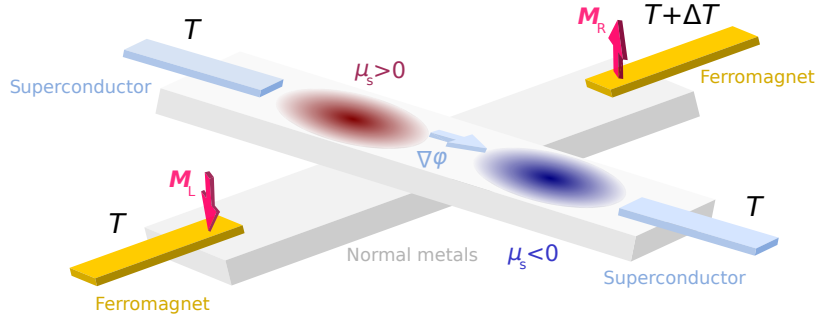
Figure 6.5: Hybrid structure displaying a spin accumulation due to singlet superconducting correlations. Two superconducting electrodes are attached to a four-terminal normal metal to form a Josephson weak link, and two ferromagnetic electrodes are attached to the remaining two arms. When the magnetisation in the two ferromagnets are antiparallel, and a temperature gradient is applied between them, a spin accumulation may be generated by applying a phase difference between the superconductors. Figure courtesy of J. Linder.

Two superconducting electrodes are attached to opposite arms of a four-terminal normal metal device in the form of a cross, thereby forming a Josephson weak link. On the remaining two arms, ferromagnetic electrodes are attached, which thus makes a spin valve, aligned orthogonally to the Josephson weak link. The temperature in one of the ferromagnets is increased relative to the rest of the system, creating a temperature gradient in the normal metal. The total width and height of the normal metal region is assumed to be $L = 3\xi$, where ξ is the superconducting coherence length. For diffusive niobium, a commonly used superconductor, the coherence length is about 10–15 nm. An important point is now that using a normal metal with a very long spin flip scattering length, such as copper, the resulting spin diffusion length, i.e., the length scale over which spin coherence is kept, can be made larger than the system size – even with a high concentration of impurities. Hence, spin relaxation due to elastic scattering processes can be made negligible. Furthermore, at the temperatures relevant for conventional superconductors, spin relaxation due to inelastic electron-electron and electron-phonon scattering are negligible as well. This allows the definition of spin-dependent temperatures T_σ.

To understand how a spin accumulation emerges in this system, consider first a spin valve, with no superconducting correlations, aligned such that a ferromagnetic lead is placed to the left and right of a central normal

metal. A reasonable phenomenological model for the temperature of the two spin species immediately next to the two ferromagnetic reservoirs is

$$T_\uparrow^R = T_0 + \left(1 - \frac{b}{2}\right)\Delta T, \tag{6.45}$$

$$T_\downarrow^R = T_0 + \left(1 - \frac{b}{2}\right)\Delta T, \tag{6.46}$$

$$T_\uparrow^L = T_0 + \frac{b}{2}\Delta T + p(1 - b)\Delta T, \tag{6.47}$$

$$T_\downarrow^L = T_0 + \frac{b}{2}\Delta T, \tag{6.48}$$

where T_0 and $T_0 + \Delta T$ is the temperature of the left and right reservoirs, respectively. The parameter b indicates a spin-independent interface resistance, and p takes into account the interfacial spin polarisation. If the spin-dependent temperatures are assumed to have a linear spatial dependence in the normal metal, the resulting spin temperature $T_s = T_\uparrow - T_\downarrow$ becomes constant,

$$T_s = p(1 - b)\Delta T. \tag{6.49}$$

As discussed in Paper XII, this model can be derived from quasiclassical theory, under the assumption of a sufficiently small temperature gradient. In this case b and p may be expressed in terms of ρ_1/ρ_c and P in Eq. (6.44).
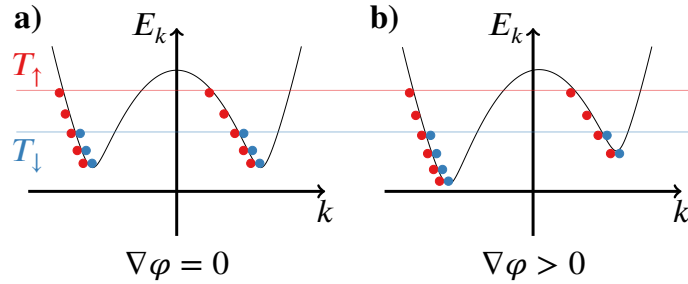
Figure 6.6: Illustration of the mechanism leading to a spin accumulation induced by singlet superconducting correlations. **a)** The quasiparticle band structure with an intra-valley spin imbalance, but no net spin accumulation as there are just as many electron-like quasiparticle excitations as there are hole-like. **b)** A gradient in the superconducting phase $\nabla\phi$ induces a Doppler shift, which breaks the symmetry between the two valleys.
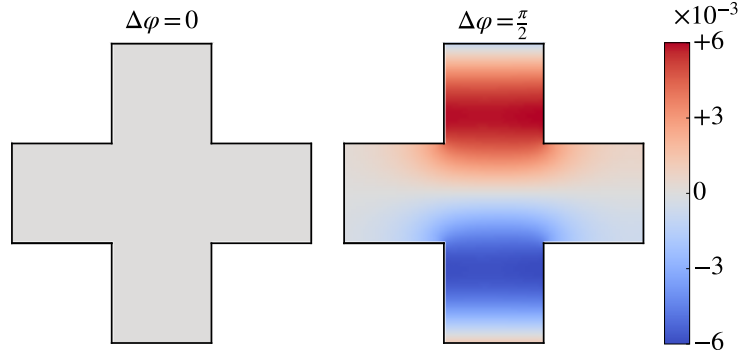
Figure 6.7: The magnetisation generated in the four-terminal device. The superconducting electrodes are placed on the ends of the vertical arms. Whenever a phase difference is applied between them, the magnetisation in the system is non-zero.

Singlet Cooper pairs carry no spin, which means that when the superconducting leads are introduced, the superconducting correlations induced in the normal metal reduce T_s. This reduction is greatest close to the superconducting leads, and less severe at the centre of the system – where the proximity effect is lowest. In other words, a gradient in the spin temperature, ∇T_s, develops in the vertical arms connected to the superconductors. This has interesting consequences. First of all, the superconducting correlations in the normal metal behave in much the same way as a bulk superconductor, forming a gap in the quasiparticle band structure similar to Fig. 3.2. The appearance of a $T_s > 0$ means that spin up quasiparticles experience a higher temperature than spin down quasiparticles. Furthermore, a gradient in T_s means that the distribution of the spin temperature is inhomogeneous in momentum space, being largest in the direction parallel to ∇T_s, and resulting in a spin imbalance within valleys of the band structure. This is illustrated in Fig. 6.6a), where for clarity a situation where there are only quasiparticle excitations with a negative group velocity is shown. Nevertheless, there is still no spin accumulation, as there are just as many electron-like excitations as there are hole-like. However, when a phase difference is applied between the superconductors, the phase gradient in the normal metal, which is collinear with ∇T_s, puts the condensate into motion, thereby inducing a Doppler shift of the band structure [178], as shown in Fig. 6.6b). This breaks the

symmetry between the two valleys, thereby producing a net spin accumulation. Note that these arguments are also applicable in the diffusive limit, due to the inhomogeneity of the system. Indeed, while frequent impurity scattering means that the quasiparticle excitations may be thought of as random walkers, there is a net drift in the direction normal to the superconductor-normal metal interface, in accordance with Fick's first law. Hence, the quasiparticles sample the band structure with a bias, resulting in an incomplete cancellation of effects which depend on the momentum direction parallel to ∇T_s and $\nabla \phi$.

The discussion so far has been largely phenomenological, but it is perfectly corroborated by numerical analyses with the Usadel equation. A quasiclassical discussion of temperature gradients is, however, somewhat complicated by the fact that in such a nonequilibrium situation, temperature is strictly speaking not defined, as the distribution function does not have a Fermi-Dirac form. The closest analogues to a temperature are the energy modes in the quasiclassical distribution function $\hat{h}$, as defined in Eqs. (2.77) and (4.16), where with spins aligned in the z direction, the relevant components are h_0 and h_3. They can be converted to a distribution function for the different spin species via $h_{\uparrow/\downarrow} = h_0 \pm h_3$, which in turn may be used to compute an effective spin temperature T_σ via a Sommerfeld expansion [108].

The numerical simulations of the system were obtained by solving Eq. (2.100), which involves first finding the retarded and advanced Green functions for a given quasiparticle energy, and then the distribution function in a separate solution step, as discussed in Section 4.3. This allowed the magnetisation to be computed from Eq. (6.23). The result is shown in Fig. 6.7, where it is clearly seen that a magnetisation develops whenever there is a phase difference between the superconductors. Even though there are ferromagnetic reservoirs in this system, they are so far removed from the superconductors that any triplet superconducting correlations are completely negligible. Hence, this spin accumulation is solely due to the singlet correlations.

6.6 Controllable supercurrents in ferromagnets

An application of the long ranged triplet superconducting correlations is discussed in Paper VI. It turns out that for a circular disk of cobalt, which is a ferromagnet, micromagnetic simulations reveal that the geometry causes a magnetic vortex structure to be favoured. This means that the

magnetisation points in the circumferential direction of the disk, with the exception of its centre, where it points out of the plane. This motivates the following experimental setup, as shown in Fig. 6.8. The circular cobalt disk is placed at the bottom of a stacked geometry, on top of which is place a copper spacer, followed by a layer of nickel, which is also a ferromagnet. Finally, a layer of niobium is added, which is superconducting at the temperatures considered – around 2–3 K.

By *focused ion beam milling* a trench with a width of about 20 nm is made through the niobium, nickel and copper layers, leaving the cobalt layer intact. Since the superconducting layer is now separated into two halves, the system becomes a Josephson junction. Furthermore, from micromagnetic simulations of the nickel layer it is found that the magnetisation close to the trench tends to align parallel with it. This means that there is a significant degree of misalignment in the magnetisation between the nickel and cobalt layers. An exception, once again, is at the centre of the vortex, where the out-of-plane magnetisation of the cobalt layer forces an out-of-plane alignment of the nickel layer as well. Hence,
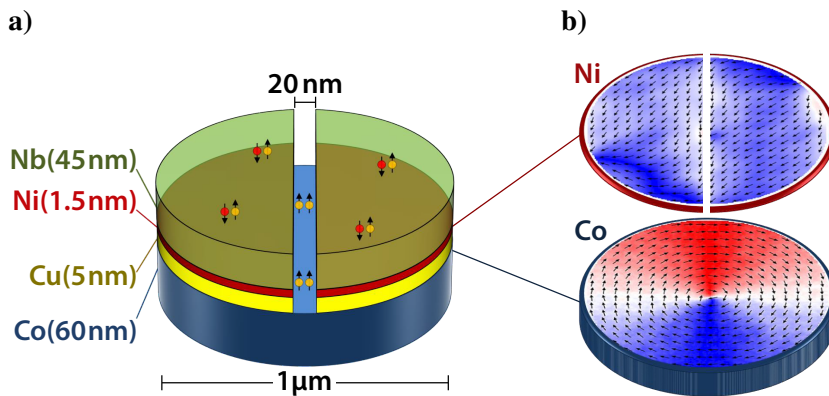
Figure 6.8: Illustration of an experimental setup of a ferromagnetic Josephson junction displaying a strong inhomogeneity of the magnetisation. **a)** Superconducting niobium is placed on top of a stack of ferromagnetic materials, cobalt and nickel, separated by a copper spacer. A trench through the Nb, Ni and Cu layers is created by focused ion beam milling, thereby forming a Josephson junction. **b)** The magnetisation in the Co and Ni layers, as predicted by micromagnetic simulations, indicating that there is significant misalignment between the two layers. Figure courtesy of K. Lahabi.

two regions are formed, separated at the centre of the system, in which long ranged tripled correlations may form. Moreover, typical values for the exchange splitting in cobalt and nickel are in the range of 0.5 eV to 1.0 eV [179–181], which means that it is only the long ranged triplet components that are likely to survive the journey from one superconductor to the other. The presence of any Josephson effect when a phase difference is applied between the superconductors is therefore proof of their existence.

The system was investigated experimentally by applying a magnetic field in the perpendicular direction to the disk plane and measuring the resulting interference pattern of the critical current, an example of which is shown in Fig. 6.9a). From this it was inferred, first of all, that there are indeed long ranged triplets in this system. Furthermore, the interference pattern itself has a peculiar shape, which differs from the Fraunhofer-shape expected from a uniform current density distribution. It is seen that the lobes all have approximately the same width, and the decay of the critical current with increasing magnetic field is slower than expected. These are traits which are more typical of double-slit interference, and are indicative of a two-channel current flow. This is verified by finding the current density corresponding to such an interference pattern, which is shown in Fig. 6.9b), where it is seen that the dominant contribution to the current density does indeed form two channels.
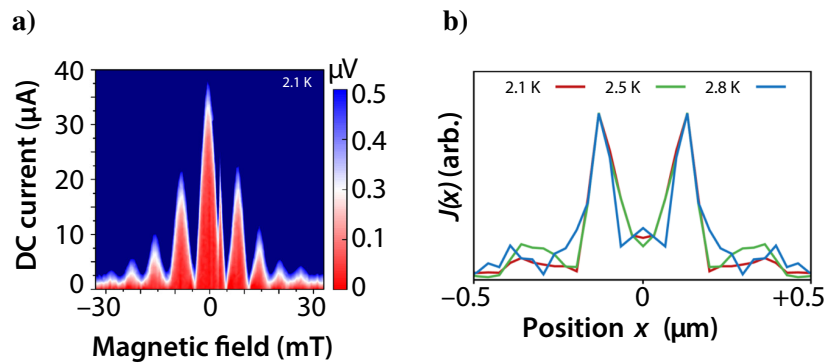
Figure 6.9: An example of the experimental findings. **a)** The interference pattern in the critical current, measured by the application of a magnetic field in the direction perpendicular to the disk plane. **b)** The inferred current density distribution in the direction x transversal to the junction direction (parallel to the trench). A two-channel current flow is seen. Figure courtesy of K. Lahabi and J. A. Ouassou.
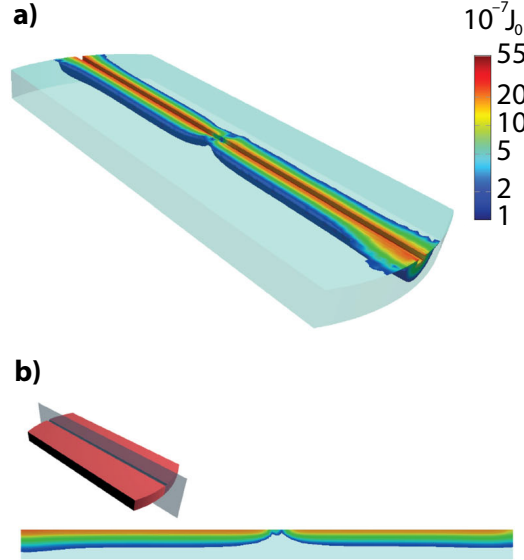
Figure 6.10: Three dimensional numerical simulations of the cylindrical stack. To ease the numerical resource requirement of such an analysis, only the most relevant region surrounding the trench is modelled. **a)** 3D plot of the current density, showing how the current flows from one superconductor to the other (top surfaces) by minimising it distance beneath the trench. **b)** Vertical slice through the centre of the trench, as indicated by the inset. A suppression of the current density is seen exactly at the centre, where there is reduced misalignment of the magnetisation, resulting in a two-channel flow. The current is given in units of $J_0 = ev_0 D\Delta_0/16\xi$.

To provide further support for these interpretations, three-dimensional simulations of the system using the Usadel equation were performed. The ferromagnets were modelled as a single material, which incorporated the exact inhomogeneous magnetisation profile computed from the micromagnetic simulations. The size of the spin splitting in nickel and cobalt are generally too large for quasiclassical theory to be applicable, and so an exchange field with a lower value of $|\boldsymbol{h}| = 30\Delta_0$, where Δ_0 is the superconducting gap, was used instead. This was deemed to be sufficient to suppress any current not carried by the long ranged triplets. The result of this analysis is shown in Fig. 6.10, where currents have been made to flow by imposing a phase difference between the superconductors of $\phi = \pi/2$. Notice in particular that the current density is suppressed at the centre of

the system, forming two separate channels, which is consistent with the experimental findings.

6.7 Spin-orbit coupling

In Section 6.3 it was seen that a ferromagnet with an inhomogeneous magnetisation coupled to a superconductor can generate long ranged triplet superconducting correlations. Spin-orbit coupling provides additional means of doing so. This phenomenon is a relativistic effect that emerges when the electron experiences a change in an electrostatic potential in which it moves, e.g., the crystal lattice. Such a change, of course, leads to an electric field. Electric and magnetic fields intermix in different reference frames, and may thus lead to a coupling with the electron spin. To derive a Hamiltonian which takes this effect explicitly into account, it is convenient to begin with the covariant Dirac equation in the presence of an electrostatic potential V,

$$\begin{pmatrix} mc^2 + V(\boldsymbol{r}) & -i\hbar c\boldsymbol{\sigma}\cdot\nabla \\ -ic\hbar\boldsymbol{\sigma}\cdot\nabla & -mc^2 + V(\boldsymbol{r}) \end{pmatrix}\begin{pmatrix} \psi_e \\ \psi_h \end{pmatrix} = \begin{pmatrix} \varepsilon + mc^2 & 0 \\ 0 & \varepsilon + mc^2 \end{pmatrix}\begin{pmatrix} \psi_e \\ \psi_h \end{pmatrix}, \quad (6.50)$$

where ψ_e and ψ_h are the wavefunctions for electrons and holes, respectively. Eliminating ψ_h gives

$$\left[-\frac{\hbar^2}{2m}\boldsymbol{\sigma}\cdot\nabla\left(1 + \frac{\varepsilon - V(\boldsymbol{r})}{2mc^2}\right)^{-1}\boldsymbol{\sigma}\cdot\nabla + V(\boldsymbol{r}) \right]\psi_e(\boldsymbol{r}) = \varepsilon\psi_e(\boldsymbol{r}).$$

The nonrelativistic limit is found by assuming that all energies involved are much smaller than the electron rest energy mc^2, and hence one finds, to lowest order in a Taylor expansion in $(\varepsilon - V)/2mc^2$

$$\left[\frac{\boldsymbol{p}^2}{2m} + \frac{\boldsymbol{p}^4}{8m^3c^2} + \frac{i\hbar}{4m^2c^2}(\boldsymbol{\sigma}\cdot\nabla V)(\boldsymbol{\sigma}\cdot\boldsymbol{p}) + V \right]\psi_e = \varepsilon\psi_e,$$

where $\boldsymbol{p} = -i\hbar\nabla$, and it has been used that $\varepsilon - V$ approaches $\boldsymbol{p}^2/2m$ as the Dirac equation approaches the Schrödinger equation. This can alternatively be written as

$$\left[\frac{\boldsymbol{p}^2}{2m} + \frac{\boldsymbol{p}^4}{8m^3c^2} + \frac{i\hbar}{4m^2c^2}\nabla V\cdot\boldsymbol{p} - \frac{\hbar}{4m^2c^2}\boldsymbol{\sigma}\cdot(\nabla V\times\boldsymbol{p}) + V \right]\psi_e = \varepsilon\psi_e,$$

from which the spin-orbit term may be identified as

$$H_{\text{soc}} = -\frac{\hbar}{4m^2c^2}\boldsymbol{\sigma}\cdot(\nabla V\times\boldsymbol{p}). \quad (6.51)$$

Quasiclassical formalism

Spin-orbit coupling which is linear in momentum is straightforward to include in the quasiclassical formalism. Consider a general spin-orbit coupling of the form

$$H_{\text{SOC}} = \frac{\hbar^2}{m} \Gamma_{ij} \sigma_i \nabla_j, \tag{6.52}$$

where Γ_{ij} is a spatially constant tensor giving the strength of the spin-orbit coupling. Such a term can be absorbed into the kinetic energy as an effective gauge field,

$$-\frac{\hbar^2}{2m} \left(\nabla^2 - 2\boldsymbol{\Gamma}_i \sigma_i \cdot \nabla \right) = -\frac{\hbar^2}{2m} \left(\nabla - \boldsymbol{\Gamma}_i \sigma_i \right)^2 + \frac{\hbar^2}{2m} \left(\boldsymbol{\Gamma}_i \sigma_i \right)^2.$$

If the last term is discarded, spin-orbit coupling may be included in the quasiclassical Green function formalism simply by making the replacement

$$\frac{\hbar}{i} \nabla \rightarrow \frac{\hbar}{i} \tilde{\nabla} = \frac{\hbar}{i} \nabla - \frac{\hbar}{i} \boldsymbol{\Gamma}_i \sigma_i, \tag{6.53}$$

in the exact same fashion as was done with the vector potential $\boldsymbol{A}$ in Eq. (3.87). Hence, introducing spin-orbit coupling in this way is equivalent to applying an effective vector potential of the form

$$e\boldsymbol{A}_{\text{SOC}} = e\boldsymbol{A} + \boldsymbol{\Gamma}_i \sigma_i. \tag{6.54}$$

In the following, only *Rashba spin-orbit coupling* will be considered, which typically occurs when inversion symmetry is broken along a direction $\hat{n}$, for instance due to an interface. In that case $\Gamma_{ij} = \gamma n_k \varepsilon_{kij}$, and Eq. (6.52) becomes

$$H_{\text{SOC}} = \frac{\hbar^2}{m} \gamma \hat{n} \cdot (\boldsymbol{\sigma} \times \nabla). \tag{6.55}$$

6.8   Spin valve on a topological insulator

As a first exposure to the influence of spin-orbit coupling on superconducting hybrid structures, an application involving the extreme case of topological insulators will be discussed. These are heavy-metal compounds, such as HgTe [182], where the mass of the lattice ions is so great that the spin-orbit coupling and the relativistic corrections to the band structure lead

to a band gap inversion near the centre of the Brillouin zone. This gives the material a topological character, as identified by a non-zero Chern number [183]. By band gap inversion is meant that what would normally be the valence band in the trivial phase gets shifted to above the conduction band in the topologically non-trivial phase. For the case of HgTe, this transition happens at a certian critical sample thickness d_c.

When a topologically non-trivial material is attached to a topologically trivial material, something interesting is bound to happen at their interface. Indeed, for a topological insulator there must be a transition from the inverted band gap to a conventional band structure. This cannot be done without crossing the Fermi level. This implies the existence of topologically protected conducting surface states, even though the bulk of the topological insulator is insulating, which is the hallmark characteristic of these materials.

In a 3D topological insulator, the surface states have a cone-like dispersion. The strong spin-orbit coupling further leads to a fixation of the spin direction relative to the momentum direction, which is known as *spin-momentum locking*. While the exact band structure of typical topological insulators are far too complex to use in calculations, the most important physics may be revealed by using a simplified Hamiltonian, taking into account only the two-dimensional surface states close to the Fermi level,

$$H = -i\hbar v_{\mathrm{F}} \boldsymbol{\sigma} \cdot \nabla, \tag{6.56}$$

which has the form of the Dirac equation. This immediately exposes a curiosity. If an exchange field is introduced in a direction which is in the plane of the surface states, the Hamiltonian takes the form

$$H = -i\hbar v_{\mathrm{F}} \boldsymbol{\sigma} \cdot \left(\nabla - \frac{i}{\hbar v_{\mathrm{F}}} \boldsymbol{h} \right), \tag{6.57}$$

which means that an in-plane exchange field behaves in the exact same way as a vector potential, as seen in Section 3.8. An out-of-plane exchange field can however not be accommodated, as this introduces a gap in the model Hamiltonian. Eq. (6.57) raises the question of what happens when superconducting correlations are introduced to the surface of a topological insulator via the proximity effect. If there is also an exchange field present, can this lead to vortices? This question was answered in the affirmative in Paper VIII, which considers a Josephson junction formed on a topological insulator. Also on top of the topological insulator, between the superconductors, is placed a spin valve – two ferromagnets separated by a
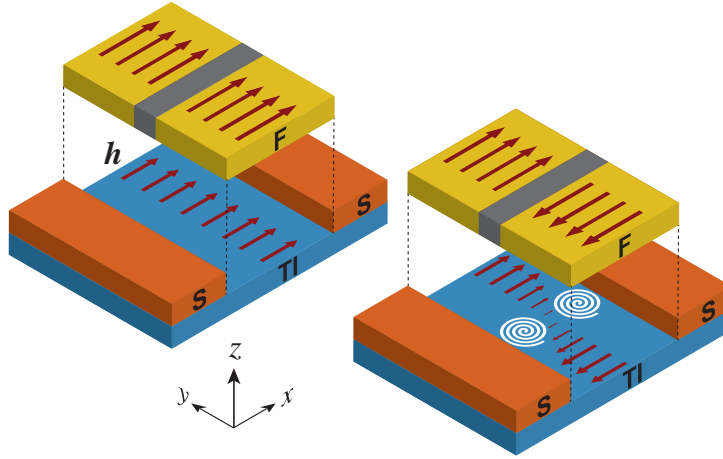
Figure 6.11: Illustration of a spin valve and two superconductors placed on the surface of a topological insulator. The former is displaced for clarity. When the spin valve is in the antiparallel configuration, the resulting inhomogeneous in-plane magnetisation induced on the topological insulator, combined with the superconducting correlations, may produce vortices.

spacer, which can either have a parallel (P) or an antiparallel magnetisation (AP). An illustration of the setup is shown in Fig. 6.11. The Hamiltonian in Eq. (6.57) can be studied using diffusive quasiclassical Green function by following the same procedure as in Section 2.4. The only difference is that the spin-momentum locking needs special care. By a unitary transformation it turns out that the spin dependence of the Green function can be isolated from its momentum dependence. Introducing the quasiclassical approximation and the spherical momentum averaging on the transformed Green function, the resulting equation of motion for the 2D surface states takes the exact same form as the Usadel equation, given in Eq. (6.16) – except that it is formulated for Green function matrices with structure only in particle-hole space. The spin structure is reintroduced via the unitary transformation [184]. The inverse proximity effect is neglected, as is shown to be a reasonable approximation in Paper IX.

The spin valve introduces a non-uniform magnetisation to the region between the superconductors. Since h takes on the role of a vector poten-
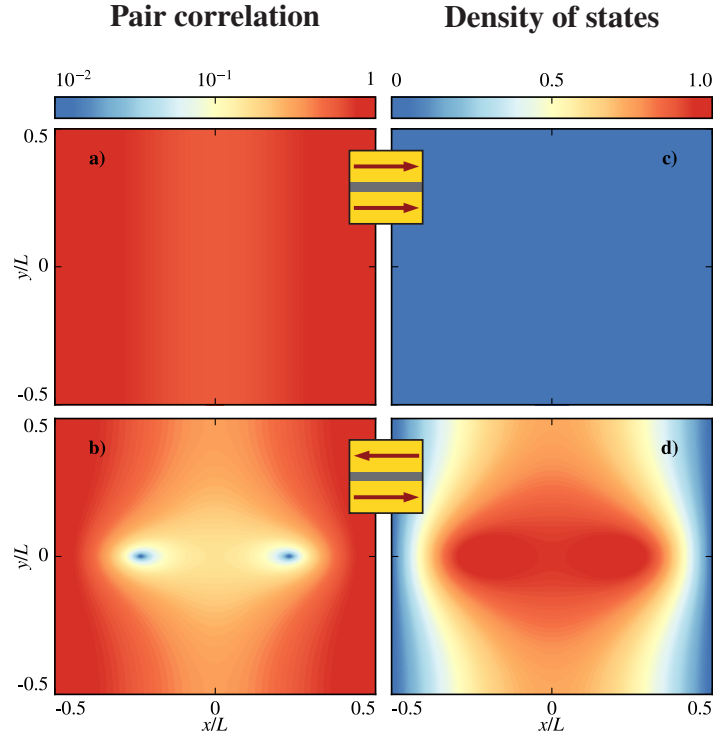
Figure 6.12: Numerical simulations of the system shown in Fig. 6.11. **a)** and **b)** The pair correlation with the spin valve in the parallel and in the antiparallel configuration, respectively. In the latter case, vortices appear. **c)** and **d)** The density of states for the two configurations

tial, the quantity

$$\Phi_h = \int_A \nabla \times \boldsymbol{h} \, d\boldsymbol{r}, \tag{6.58}$$

must describe an effective flux through an area A. The effective flux quantum becomes $\Phi_0 = \pi \hbar v_F$, and hence for sufficiently large effective fields $\boldsymbol{B}_h = \nabla \times \boldsymbol{h}$, vortices are to be expected. Clearly, the AP configuration of the spin valve induces a larger $\boldsymbol{B}_h$ than the P configuration. One may therefore envision toggling between a state in which the system exhibits vortices, and one where it does not, simply by switching the relative magnetisation of the spin valve ferromagnets. Numerical simulations for

reasonable choices of parameter values validates this prediction, as is shown in Fig. 6.12.

6.9   Supercurrent vortex pinball

An explicit application of the formalism derived in Section 6.7 is presented in Paper IV. A two-dimensional system is considered, e.g. a GaAs 2D electron gas (2DEG). Such a system may provide a large *g* factor, so that a Zeeman effect, and thus an exchange field $\boldsymbol{h}$ may be introduced by the application of an external magnetic field in the plane of the 2DEG. Spin-orbit coupling may further be introduced by a gate voltage in the out-of-plane direction. By contacting two superconductors to this system, a superconductor-ferromagnet-superconductor weak link, with an out-of-plane Rashba spin-orbit coupling may be formed. It turns out that this hybrid structure displays highly controllable supercurrent vortex-like patterns, as is illustrated on the system model shown in Fig. 6.13. These are
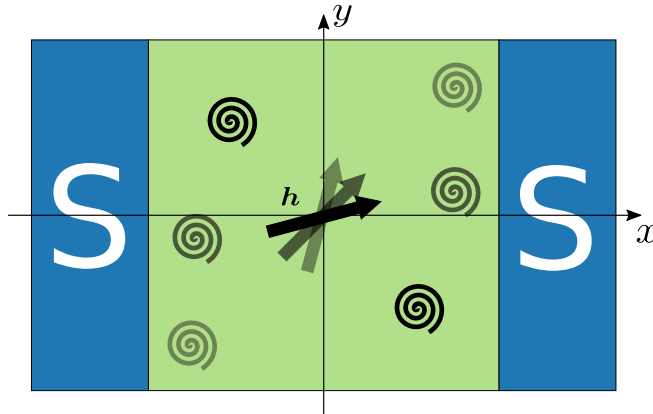
Figure 6.13: Illustration of a two-dimensional ferromagnetic Josephson weak link with an out-of-plane Rashba spin-orbit coupling. Depending on the strength of the exchange field $\boldsymbol{h}$, and its direction, a variety of vortex-like patterns in the current density are formed. These patterns are also influenced by the phase difference between the superconducting leads, and the strength of the spin-orbit coupling.

not vortices in the conventional sense. Rather, they are circulations of the supercurrent around localised points without an associated suppression of the superconducting correlations. There is also no phase winding.

The supercurrent vortices require a phase difference between the superconductors (otherwise there are no currents in the system), and appear close to the 0-π transition (discussed in Section 6.3), as shown in Fig. 6.14, where the exchange field direction points in an angle of $\theta = 45°$ relative to the x axis indicated in Fig. 6.13, and the phase difference was held at $\phi = \pi/2$. The current pattern is seen to vary greatly for different exchange field strengths. An extensive parameter study was made to understand the behaviour of these vortex-like formations. Keeping all other parameters fixed, the exchange field direction, spin-orbit coupling strength and the phase difference were all sequentially varied in a systematic manner, displaying a diverse array of current density patterns, as shown in Fig. 6.15. The richness and complexity of these patterns, along with the many ways in which they can be controlled led to this system receiving the humorous moniker of a supercurrent vortex pinball machine.

To understand the origin of these effects, it is necessary to have a
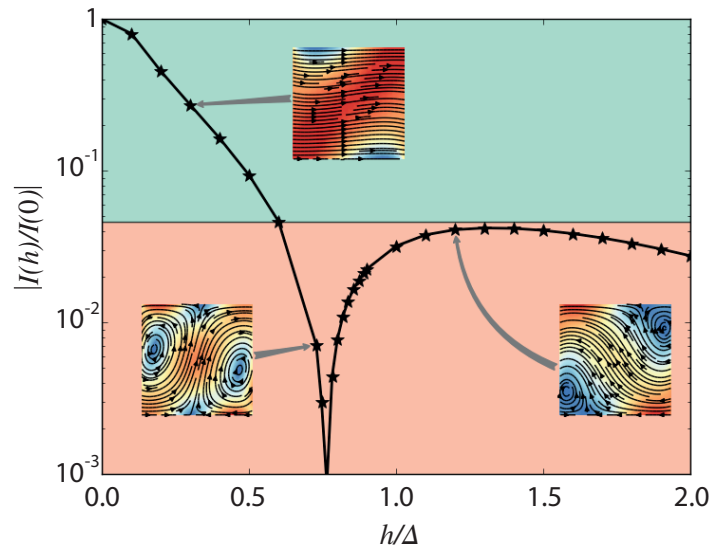
Figure 6.14: The supercurrent I as a function of the exchange field h, which points in a direction $\theta = 45°$ relative to the x axis in Fig. 6.13. Each marker represents a numerical simulation, and the insets show a selection of current density distributions. The lower region of the figure (in red) marks the exchange fields for which vortex-like patterns in the current density appear. Notice also the 0-π transition at $h/\Delta \simeq 0.75$.
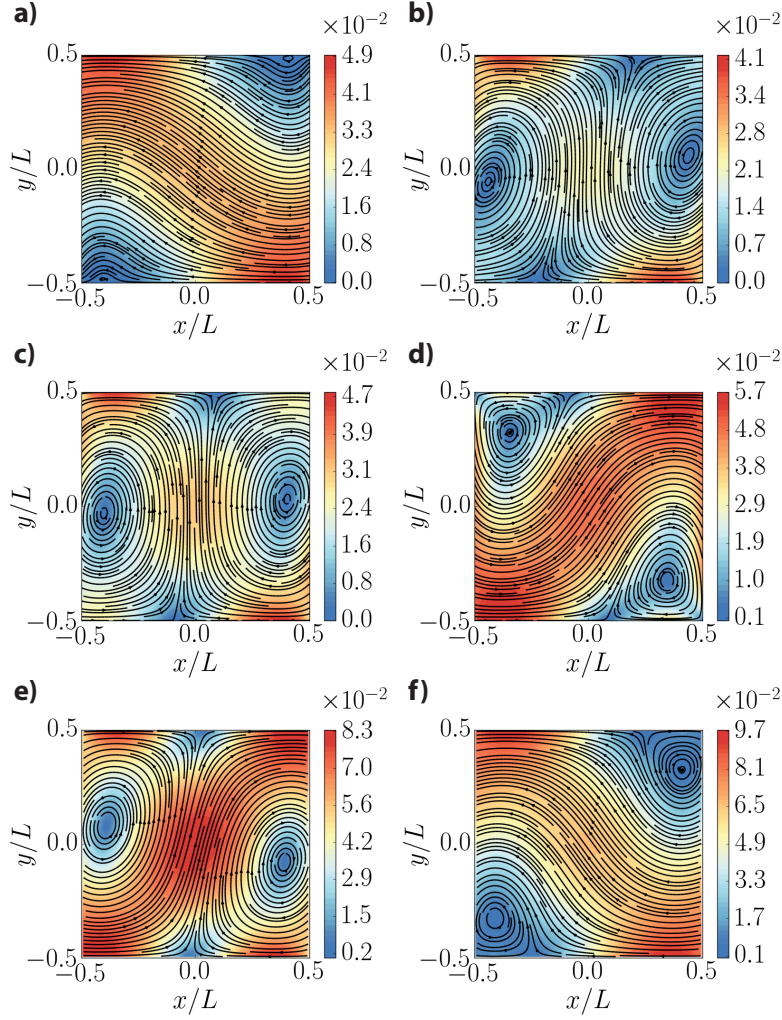
Figure 6.15: A variety of vortex-like current density patterns, produced by varying the system parameters. Unless otherwise stated, the exchange field direction is $\theta = 45°$, the strength of the spin-orbit coupling is $\gamma\xi = 0.5$, the phase difference between the superconducting leads is $\phi = \pi/2$, and the exchange field strength is $h/\Delta = 1.0$. **a)** $\theta = 30°$, **b)** $\theta = 60°$, **c)** $\gamma\xi = 0.6$, **d)** $\gamma\xi = 0.8$, **e)** $\phi = \pi/5$, and **f)** $\phi = 4\pi/5$.

closer look at how the triplet superconducting correlations influence the supercurrent. By inserting Eq. (2.53) into Eq. (3.74), an expression for the

supercurrent density can be found. It will turn out to be elucidating to parametrise the anomalous Green function f (either the retarded or the advanced) in terms of its singlet f_s and triplet $\boldsymbol{f}$ contributions,

$$f = (f_s I + \boldsymbol{f} \cdot \boldsymbol{\sigma}) \, i\sigma_y. \tag{6.59}$$

In that case the supercurrent density may be separated into additive contributions,

$$\boldsymbol{J} = \boldsymbol{J}_I + \boldsymbol{J}_{tt}, \tag{6.60}$$

where $\boldsymbol{J}_I = \boldsymbol{J}_s - \boldsymbol{J}_x - \boldsymbol{J}_y - \boldsymbol{J}_z$, with

$$\boldsymbol{J}_k = \frac{e v_0 D}{4} \int_0^\infty d\varepsilon \, \Re \left(\tilde{f}_k \nabla f_k - f_k \nabla \tilde{f}_k \right) \tanh \frac{\beta \varepsilon}{2}, \tag{6.61}$$

and $\tilde{f}(\varepsilon) = f^*(-\varepsilon)$. This current contribution is identical in form to what one would expect also in the absence of spin-orbit coupling. In the present case, however, an additional term $\boldsymbol{J}_{tt}$ emerges, which describes currents due to interference effects between the triplet correlations,

$$\boldsymbol{J}_{tt} = e\gamma v_0 D \boldsymbol{e}_z \times \int_0^\infty d\varepsilon \, \Re \left(\tilde{\boldsymbol{f}}_t \times \boldsymbol{f}_t \right) \tanh \frac{\beta \varepsilon}{2}, \tag{6.62}$$

where γ is the strength of the spin-orbit coupling. Note that the cross product between the triplet anomalous Green functions in the integrand of Eq. (6.62) expresses the spin polarisation of the triplet Cooper pairs [185, 186]. In other words, $\boldsymbol{J}_{tt}$ is a current induced by the triplet Cooper pair magnetisation – it may therefore be characterised as a triplet induced inverse Edelstein effect. It is precisely this current contribution which is the cause of the current density patterns observed in Figs. 6.14 and 6.15. It turns out that $\boldsymbol{J}_{tt}$ has a significant spatial variation transverse to the junction direction (y axis). This is reasonable as motion near the vacuum interfaces is more restrictive than motion near the centre of the system, which influences the generation of triplet superconducting correlations. This is less important in $\boldsymbol{J}_I$, where these effects cancel out to a greater degree, leading to a weaker spatial variation, as illustrated in Fig. 6.16 for an exchange field $\boldsymbol{h} = \Delta \boldsymbol{e}_x$, where Δ is the superconducting gap.
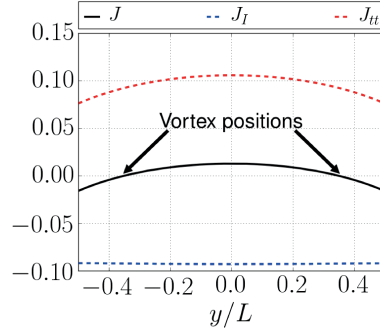
Figure 6.16: The current density distribution along the y axis (centre of the junction), showing the origin of the vortex-like patterns. The current contribution J_{tt} has a greater spatial variation than J_I, and is directed oppositely. This leads to the total current $J = J_I + J_{tt}$ changing direction, and thus quenching the current density in localised regions.

The supercurrent vortices appear when J_I and J_{tt} cancel at particular points. Varying h, its direction θ, the spin-orbit coupling strength γ or the phase difference ϕ has the effect of tuning the the relative size and the spatial variation of the two current contributions, thereby creating the effect. Since it is the triplet spin polarisation that is responsible for the peculiar current patterns, one might expect the inverse process to also take place – the generation of a spin accumulation from a charge current. This cannot be studied at the level of accuracy employed herein, as discussed in Section 3.8. However, such effects are observed when working outside the quasiclassical formalism. This was seen in a ferromagnetic Josephson weak link with interfacial spin-orbit coupling, studied with the tight binding Bogoliubov–de Gennes framework in Paper V. In that case it was found that a transversal spin current is induced by a phase difference between the superconductors.

6.10   Interfaces with spin-orbit coupling

Creating long ranged triplet superconducting correlations in realistic experimental setups can be challenging, requiring either many layers of different materials [80] or scarce rare earth materials [187]. Inducing triplets via spin-orbit coupling is seemingly easier. Any interface breaks inversion symmetry, giving rise to a Rashba spin-orbit coupling. This can, for instance, be done by interfacing a superconductor with a conventional

ferromagnet, via a heavy metal interlayer. Theoretical studies of such systems have revealed that long ranged triplets do indeed appear if the magnetisation is directed such that it has both a component parallel to the interface with significant spin-orbit coupling, and a component orthogonal to it [86, 88]. In other words, the magnetisation must display a certain degree of canting. This, as it turns out, is challenging to achieve experimentally, as the magnetisation in such systems typically favour an alignment parallel to the interface. So far, creating a long ranged Josephson effect in a ferromagnet using heavy metal interlayers has yet to be achieved experimentally [188, 189]. Nevertheless, interfacial spin-orbit coupling as a source of long ranged triplet superconducting correlations is a promising topic, and this raises the question of how to model such systems. Using quasiclassical theory, one way is to model the interface as a thin separate material which connects to a ferromagnetic material on one side and a superconductor on the other side via boundary conditions [88]. While this method works well, it is an approximation of the true interfacial spin-orbit coupling, which takes place over length scales much smaller than quasiclassical theory allows for. It is therefore more appropriate to include spin-orbit coupling in the boundary conditions themselves, as is discussed in Paper X. This can be done by modifying the tunnelling potential of Eq. (5.12) to

$$\check{V}_0 = w\check{I} + w_\alpha \left(\hat{n}_\alpha \times \hat{\boldsymbol{k}}_\mathrm{F} \right) \cdot \check{\boldsymbol{\sigma}}, \tag{6.63}$$

where $\hat{\boldsymbol{k}}_\mathrm{F} = \boldsymbol{k}_\mathrm{F}/|\boldsymbol{k}_\mathrm{F}|$, and $\hat{n}_\alpha$ is a unit vector parallel to the interface normal, indicating the direction in which the symmetry is broken. The scattering matrix, found by considering an insulator with the same spin-dependent field, analogous to Section 6.4, takes the form

$$\check{S} = e^{i\gamma(\hat{n}_\alpha \times \hat{\boldsymbol{k}}) \cdot \hat{\boldsymbol{\sigma}} \hat{\rho}_4}, \tag{6.64}$$

where γ is the spin-mixing angle. For low values of γ, Eq. (6.64) may be approximated as

$$\check{S} \simeq \left(1 - \frac{1}{2}\gamma^2 \right) \check{I} + i\gamma \check{\zeta}_k,$$

with $\check{\zeta}_k = (\hat{n}_\alpha \times \hat{\boldsymbol{k}}_F) \cdot \boldsymbol{\sigma} \hat{\rho}_4$. Following the same steps as in Sections 5.1 and 6.4, leads to a new set of boundary conditions where spin-orbit coupling is

explicitly taken into account,

$$
\begin{aligned}
\hat{n} \cdot \check{g}_1 \nabla \check{g}_1 =\ & T\left[\check{g}_1 \,,\, \check{g}_2\right] + T_\alpha\left[\check{g}_1, \check{\boldsymbol{\sigma}}_{\parallel} \check{g}_2 \check{\boldsymbol{\sigma}}_{\parallel}\right] + T_\alpha'\left[\check{g}_1, \check{\boldsymbol{\sigma}}_{\parallel}\check{g}_1\check{\boldsymbol{\sigma}}_{\parallel}\right] \\
& + i\sqrt{T_\alpha'' T}\left[\check{g}_1, \left\{\check{g}_2\left[\check{\boldsymbol{\sigma}}_{\parallel}, \check{g}_2\right], \check{\boldsymbol{\sigma}}_{\parallel}\right\}\right] \\
& + i\sqrt{T_\alpha'' T}\left[\check{g}_1, \left\{\check{g}_2, \check{\boldsymbol{\sigma}}_{\parallel}\right\}\check{g}_1\check{\boldsymbol{\sigma}}_{\parallel} + \check{\boldsymbol{\sigma}}_{\parallel}\check{g}_1\left\{\check{g}_2, \check{\boldsymbol{\sigma}}_{\parallel}\right\}\right],
\end{aligned}
\tag{6.65}
$$

where $\check{\boldsymbol{\sigma}}_{\parallel} = \mathrm{diag}\left(\hat{\boldsymbol{\sigma}}_{\parallel}, \hat{\boldsymbol{\sigma}}_{\parallel}\right)$, and $\hat{\boldsymbol{\sigma}}_{\parallel} = \mathrm{diag}(+\boldsymbol{\sigma}_{\parallel}, -\boldsymbol{\sigma}_{\parallel}^*)$, where $\boldsymbol{\sigma}_{\parallel}$ are the in-plane Pauli matrix components with respect to the interface. Notice that the lower block of $\hat{\boldsymbol{\sigma}}_{\parallel}$ is defined with a minus sign, in contrast to the conventional definition of Pauli matrices in particle-hole space. The parameter T_α and T_α' describe a spin dephasing upon tunnelling and reflection, respectively, and $T_\alpha'' = T_\alpha T_\alpha'/2$. A special case of Eq. (6.65), which cannot be described by other means within quasiclassical theory, is a boundary condition representing an insulator with spin-orbit coupling. It is found by setting $\check{g}_2 = 0$, which gives

$$
\hat{n} \cdot \check{g}_1 \nabla \check{g}_1 = T_\alpha'\left[\check{g}_1, \check{\boldsymbol{\sigma}}_{\parallel}\check{g}_1\check{\boldsymbol{\sigma}}_{\parallel}\right]
\tag{6.66}
$$

For interfaces to a bulk superconductor (i.e. if the inverse proximity effect is ignored), where the Green function is given by Eq. (3.65), Eq. (6.65) simplifies to

$$
\begin{aligned}
\hat{n} \cdot \check{g}_1 \nabla \check{g}_1 =\ & T\left[\check{g}_1 \,,\, \check{g}_2\right] + T_\alpha'\left[\check{g}_1, \check{\boldsymbol{\sigma}}_{\parallel}\check{g}_1\check{\boldsymbol{\sigma}}_{\parallel}\right] \\
& + i\sqrt{T_\alpha'' T}\left[\check{g}_1, \check{\boldsymbol{\sigma}}_{\parallel}\left\{\check{g}_1, \check{g}_2\right\}\check{\boldsymbol{\sigma}}_{\parallel}\right].
\end{aligned}
\tag{6.67}
$$

In Paper X, Eq. (6.67) is tested on a few applications and compared to previous work. The density of states in a superconductor-ferromagnet bilayer was considered, as shown in Fig. 6.17. The density of states at $\varepsilon = 0$ takes the form,

$$
\nu(\boldsymbol{r}, \varepsilon = 0) = 1 - \frac{1}{2}|f_s|^2 + \frac{1}{2}|\boldsymbol{f}_{\parallel}|^2 + \frac{1}{2}|\boldsymbol{f}_{\perp}|^2,
\tag{6.68}
$$

using the parametrisation in Eq. (6.59). It is seen that the singlet anomalous Green function leads to a suppression of the density of states, as is to be expected. The triplets, on the other hand, increase the zero-energy density of states – they form a zero-energy peak. The triplet anomalous Green functions are in this case decomposed into a component $\boldsymbol{f}_{\parallel}$, which is parallel to the exchange field $\boldsymbol{h}$, and a component $\boldsymbol{f}_{\perp}$, which is orthogonal to it. The latter describes Cooper pairs with spins aligned with the exchange
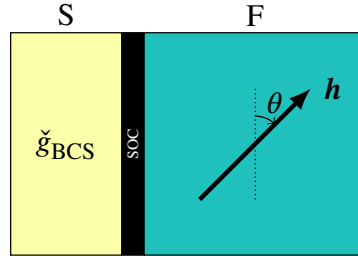
Figure 6.17: The first test case considered. A superconductor is connected to a ferromagnet via a thin intermediary layer with strong spin-orbit coupling. This layer is modelled as an interface, and described by Eq. (6.67). The exchange field h in the ferromagnet is directed at an angle θ relative to the interface.
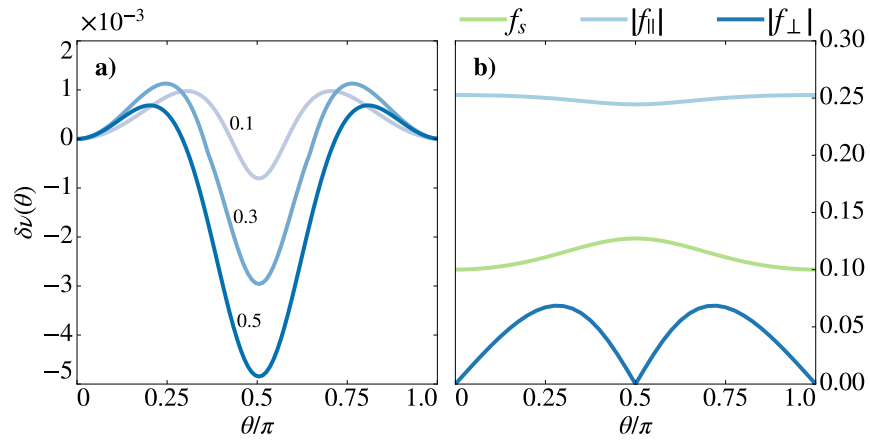
Figure 6.18: Numerical results for the SF bilayer. **a)** The change in the maximum density of states at the energy $\varepsilon = 0$, for a selection of spin-orbit coupling strength $T_\alpha = T'_\alpha$, as indicated on the figure. An increase in δv is seen when the exchange field canting angle θ is directed away from 0 and $\pi/2$. **b)** The anomalous Green functions at $T_\alpha = T'_\alpha = 0.5$. f_s, $f_\parallel$ and $f_\perp$ are the singlet, short ranged triplet and long ranged triplet components, respectively.

field, and are therefore long ranged in the ferromagnet. Fig. 6.18a) shows the change in the maximum density of states as the exchange field canting

angle, θ, is varied for a selection of spin-orbit coupling strengths $T_\alpha = T_\alpha'$,

$$\delta v = v(\boldsymbol{R}_{\max}, \varepsilon = 0, \theta) - v(\boldsymbol{R}_{\max}, \varepsilon = 0, 0),$$

where it is seen that δv is greatest when the exchange field canting angle θ is in the vicinity of $\pi/4$. The size of the different anomalous Green functions are shown in Fig. 6.18b), for $T_\alpha = T_\alpha' = 0.5$. It is seen that the greatest contribution to the modulation of δv stems from the long ranged triplet component, $\boldsymbol{f}_\perp$, which is identical to zero at the points $\theta = 0, \pi/2$, in qualitative agreement with previous theoretical studies [87].
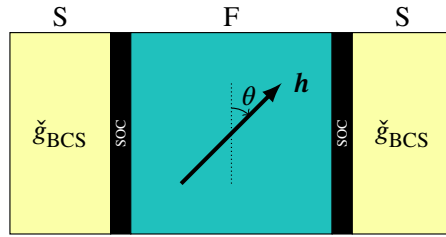
Figure 6.19: The second test case considered. A ferromagnetic Josephson weak link is formed by connecting the superconductors to the ferromagnet via interfaces with strong spin-orbit coupling.

A Josephson weak link was also considered, with the new boundary conditions applied as shown in Fig. 6.19. In this case, the spin currents carried by the long ranged triplets were studied. It was found that the spin current, as determined from Eq. (6.25), is maximal when $\theta \simeq 45°$, and zero when the exchange field is perpendicular or parallel to the interfaces, as shown in Fig. 6.20a). Furthermore, from Fig. 6.20b) it is seen that the current phase relation is approximately sinusoidal, indicating that the effect stems from a spin polarisation of the charge current. Finally, Fig. 6.20c) shows that the size of the spin currents increase with increasing T_α, which is reasonable, but eventually saturates at $T_\alpha = 0.5$. It is not known whether this saturation is because the limits of validity for the size of T_α has been reached.
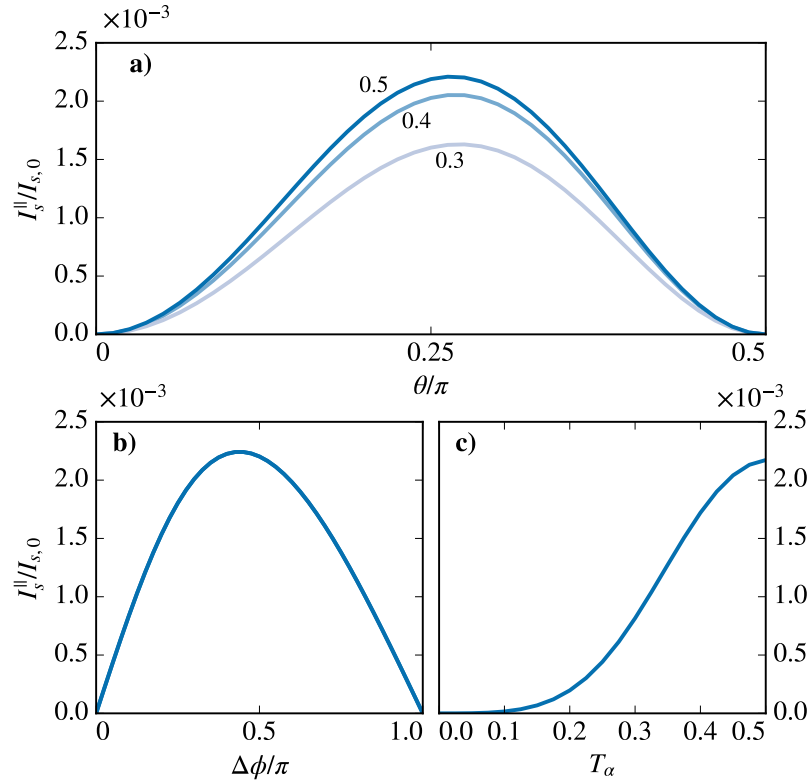
Figure 6.20: Numerical results for the SFS system. **a)** The spin current, carrying spins aligned parallel to the exchange field as a function of canting angle θ. $I_{s,0} = v_0 DW/32$ is the spin current amplitude, where W is the width of the junction. Indicated on the figure is the strength of the spin-orbit coupling $T_\alpha = T'_\alpha$. **b)** The spin current as a function of phase difference between the superconducting leads at $T_\alpha = T'_\alpha = 0.5$, showing a close-to sinusoidal current-phase relation. **c)** The strength of the spin current as a function of the interfacial spin-orbit coupling $T_\alpha = T'_\alpha$.

Chapter 7

Outlook

In this thesis I have reviewed the quasiclassical approximation and its application to nonequilibrium Green functions. I have introduced the phenomenon of superconductivity and incorporated it into the theoretical framework. I have presented the finite element method, which is a powerful numerical method capable of simulating superconducting systems taking virtually any shape. Finally, I have studied superconducting hybrid structures, both with and without spin-dependent fields, and highlighted a selection of my research.

What is not captured in such an exposition is the learning process, which has taken a significant portion of my time. Having arrived at the end of my graduate studies, there still remains much I would like to explore. Hence, I conclude this thesis by discussing future research directions.

Superconducting vortices is a topic I find fascinating, and would have liked to investigate further. It would be interesting to study how vortices interact with spin-dependent fields, for instance generated by proximity to a ferromagnet. In that case, triplet superconducting correlations are induced, which are also influenced by the magnetic field. If the spin of the triplet correlations can be made spatially inhomogeneous, e.g., through spin-orbit coupling, this could possibly give rise to half-quantum vortices. Such vortices have been observed in Sr_2RuO_4 [190] and in superfluid ^3He [191], and could occur by a similar mechanism also in superconducting hybrid structures.

The Meissner effect is another intriguing topic which has not received much attention in this thesis. It is known that triplet superconducting correlations can exhibit a paramagnetic Meissner effect [77, 192, 193]. This competition between the conventional diamagnetic and a paramagnetic

response would be interesting to explore in a variety of superconducting hybrid structures – not in the least in nonequilibrium systems.

Finally, I would like to highlight one additional avenue for future research, namely time-dependent phenomena. The quasiclassical Green function formalism can be used to describe dynamics in superconducting systems, but this is a highly nontrivial numerical problem, which has only been explored to a limited extent [194–197]. Incorporating time dependence into the finite element framework would provide many opportunities. One example is the possibility of studying spin pumping, where interesting effects have been observed in superconductor-ferromagnet structures with spin-orbit coupling [89, 198].

The field of superconducting spintronics is a rich and rapidly evolving landscape of fascinating physics, and superconducting hybrid structures provide accessible means of exploration. One can only wonder what vistas will be discovered in the future.

Bibliography

[1]   J. E. Moyal, Mathematical Proceedings of the Cambridge Philosophical Society **45**, 99 (1949).

[2]   J. J. Parsons and D. Oja, *Computer Concepts 2014 (New Perspectives Series)*, 16th ed. (Cengage Learning, 2014).

[3]   H. Hollerith, Journal of the Royal Statistical Society **57**, 678 (1894).

[4]   S. McCartney, *ENIAC: The Triumphs and Tragedies of the World's First Computer* (Walker & Company, 1999).

[5]   J. Bardeen and W. H. Brattain, Physical Review **74**, 230 (1948).

[6]   A. N. Saxena, *Invention of Integrated Circuits: Untold Important Facts* (World Scientific, 2009).

[7]   J.-L. Baer, *Microprocessor Architecture: From Simple Pipelines to Chip Multiprocessors* (Cambridge University Press, 2010).

[8]   C. T. Sah, Proceedings of the IEEE **76**, 1280 (1988).

[9]   R. H. Dennard, F. H. Gaensslen, H. N. Yu, V. L. Rideout, E. Bassous and A. R. Leblanc, IEEE Journal of Solid-State Circuits **9**, 256 (1974).

[10] G. E. Moore, in Technical digest. international electron devices meeting (Mar. 1975), pp. 11–13.

[11] G. E. Moore, Electronics Magazine **38**, 114 (1965).

[12] W. Haensch, E. J. Nowak, R. H. Dennard, P. M. Solomon, A. Bryant, O. H. Dokumaci, A. Kumar, X. Wang, J. B. Johnson and M. V. Fischetti, IBM Journal of Research and Development **50**, 339 (2006).

[13] M. Bohr, IEEE Solid-State Circuits Newsletter **12**, 11 (2009).

[14] *Future R&D Plans - Taiwan Semiconductor Manufacturing Company Limited*, `www.tsmc.com/english/dedicatedFoundry/technology/future_rd.htm` (visited on 09/06/2020).

[15] I. Žutić, J. Fabian and S. D. Sarma, Reviews of Modern Physics **76**, 323 (2004).

[16] M. N. Baibich, J. M. Broto, A. Fert, F. N. Van Dau, F. Petroff, P. Eitenne, G. Creuzet, A. Friederich and J. Chazelas, Physical Review Letters **61**, 2472 (1988).

[17] G. Binasch, P. Grünberg, F. Saurenbach and W. Zinn, Physical Review B **39**, 4828 (1989).

[18] M. Julliere, Physics Letters A **54**, 225 (1975).

[19] T. Miyazaki and N. Tezuka, Journal of Magnetism and Magnetic Materials **139**, L231 (1995).

[20] J. S. Moodera, L. R. Kinder, T. M. Wong and R. Meservey, Physical Review Letters **74**, 3273 (1995).

[21] D. Wang, C. Nordman, J. M. Daughton, Z. Qian and J. Fink, in Ieee transactions on magnetics, Vol. 40, 4 II (July 2004), pp. 2269–2271.

[22] S. Yuasa, T. Nagahama, A. Fukushima, Y. Suzuki and K. Ando, Nature Materials **3**, 868 (2004).

[23] S. S. Parkin, C. Kaiser, A. Panchula, P. M. Rice, B. Hughes, M. Samant and S. H. Yang, Nature Materials **3**, 862 (2004).

[24] S. Yuasa, A. Fukushima, H. Kubota, Y. Suzuki and K. Ando, Applied Physics Letters **89**, 042505 (2006).

[25] S. Ikeda, J. Hayakawa, Y. Ashizawa, Y. M. Lee, K. Miura, H. Hasegawa, M. Tsunoda, F. Matsukura and H. Ohno, Applied Physics Letters **93**, 082508 (2008).

[26] A. Hirohata, K. Yamada, Y. Nakatani, L. Prejbeanu, B. Diény, P. Pirro and B. Hillebrands, Journal of Magnetism and Magnetic Materials **509**, 166711 (2020).

[27] L. J. Schwee, IEEE Transactions on Magnetics **8**, 405 (1972).

[28] L. Berger, Journal of Applied Physics **49**, 2156 (1978).

[29] L. Berger, Journal of Applied Physics **50**, 2137 (1979).

[30] D. C. Ralph and M. D. Stiles, Journal of Magnetism and Magnetic Materials **320**, 1190 (2008).

[31] J. C. Slonczewski, Journal of Magnetism and Magnetic Materials **159**, L1 (1996).

[32] L. Berger, Physical Review B **54**, 9353 (1996).

[33] *Spin-transfer Torque MRAM Products | Everspin*, `https://www.everspin.com/spin-transfer-torque-mram-products` (visited on 04/06/2020).

[34] S. Datta and B. Das, Applied Physics Letters **56**, 665 (1990).

[35] H. C. Koo, J. H. Kwon, J. Eom, J. Chang, S. H. Han and M. Johnson, Science **325**, 1515 (2009).

[36] P. Chuang, S. C. Ho, L. W. Smith, F. Sfigakis, M. Pepper, C. H. Chen, J. C. Fan, J. P. Griffiths, I. Farrer, H. E. Beere, G. A. Jones, D. A. Ritchie and T. M. Chen, Nature Nanotechnology **10**, 35 (2015).

[37] A. Dankert and S. P. Dash, Nature Communications **8**, 1 (2017).

[38] S. Manipatruni, D. E. Nikonov, C. C. Lin, T. A. Gosavi, H. Liu, B. Prasad, Y. L. Huang, E. Bonturim, R. Ramesh and I. A. Young, Nature **565**, 35 (2019).

[39] Y. Kajiwara, K. Harii, S. Takahashi, J. Ohe, K. Uchida, M. Mizuguchi, H. Umezawa, H. Kawai, K. Ando, K. Takanashi, S. Maekawa and E. Saitoh, Nature **464**, 262 (2010).

[40] P. Wadley, B. Howells, J. Železný, C. Andrews, V. Hills, R. P. Campion, V. Novák, K. Olejník, F. Maccherozzi, S. S. Dhesi, S. Y. Martin, T. Wagner, J. Wunderlich, F. Freimuth, Y. Mokrousov, J. Kuneš, J. S. Chauhan, M. J. Grzybowski, A. W. Rushforth, K. Edmond, B. L. Gallagher and T. Jungwirth, Science **351**, 587 (2016).

[41] R. Lebrun, A. Ross, S. A. Bender, A. Qaiumzadeh, L. Baldrati, J. Cramer, A. Brataas, R. A. Duine and M. Kläui, Nature **561**, 222 (2018).

[42] K. Olejník, T. Seifert, Z. Kašpar, V. Novák, P. Wadley, R. P. Campion, M. Baumgartner, P. Gambardella, P. Nemec, J. Wunderlich, J. Sinova, P. Kužel, M. Müller, T. Kampfrath and T. Jungwirth, Science Advances **4**, eaar3566 (2018).

[43] P. Vaidya, S. A. Morley, J. Van Tol, Y. Liu, R. Cheng, A. Brataas, D. Lederman and E. Del Barco, Science **368**, 160 (2020).

[44] J. Linder and J. W. A. Robinson, Nat Phys **11**, 307 (2015).

[45] M. Eschrig, A. Cottet, W. Belzig and J. Linder, New Journal of Physics **17**, 83037 (2015).

[46] H. Kammerlingh Onnes, Communications from the Physical Laboratory at Leiden **120** (1911).

[47] W. Meissner and R. Ochsenfeld, Naturwissenschaften **21**, 787.

[48] J. Bardeen, L. N. Cooper and J. R. Schrieffer, Physical Review **108**, 1175 (1957).

[49] J. Nagamatsu, N. Nakagawa, T. Muranaka, Y. Zenitani and J. Akimitsu, Nature **410**, 63 (2001).

[50] K. Vinod, N. Varghese and U. Syamaprasad, Superconductor Science and Technology **20**, R31 (2007).

[51] P. Dai, B. C. Chakoumakos, G. F. Sun, K. W. Wong, Y. Xin and D. F. Lu, Physica C: Superconductivity and its applications **243**, 201 (1995).

[52] A. P. Drozdov, M. I. Eremets, I. A. Troyan, V. Ksenofontov and S. I. Shylin, Nature **525**, 73 (2015).

[53] A. P. Drozdov, P. P. Kong, V. S. Minkov, S. P. Besedin, M. A. Kuzovnikov, S. Mozaffari, L. Balicas, F. F. Balakirev, D. E. Graf, V. B. Prakapenka, E. Greenberg, D. A. Knyazev, M. Tkacz and M. I. Eremets, Nature **569**, 528 (2019).

[54] V. L. Ginzburg, Sov. Phys. J. Exp. Theor. Phys. **4** (1957).

[55] B. T. Matthias, H. Suhl and E. Corenzwit, Physical Review Letters **1**, 92 (1958).

[56] L. N. Cooper, Physical Review **104**, 1189 (1956).

[57] A. I. Buzdin, L. N. Bulaevskiĭ, M. L. Kulich and S. V. Panyukov, Soviet Physics - Uspekhi **27**, 927 (1984).

[58] W. A. Fertig, D. C. Johnston, L. E. DeLong, R. W. McCallum, M. B. Maple and B. T. Matthias, Physical Review Letters **38**, 987 (1977).

[59] J. W. Lynn, G. Shirane, W. Thomlinson and R. N. Shelton, Physical Review Letters **46**, 368 (1981).

[60] M. Ishikawa and Fischer, Solid State Communications **24**, 747 (1977).

[61] D. E. Moncton, D. B. McWhan, P. H. Schmidt, G. Shirane, W. Thomlinson, M. B. Maple, H. B. MacKay, L. D. Woolf, Z. Fisk and D. C. Johnston, Physical Review Letters **45**, 2060 (1980).

[62] D. Aoki, F. Hardy, A. Miyake, V. Taufour, T. D. Matsuda and J. Flouquet, Comptes Rendus Physique **12**, 573 (2011).

[63] S. S. Saxena, P. Agarwal, K. Ahilan, F. M. Grosche, R. K. Haselwimmer, M. J. Steiner, E. Pugh, I. R. Walker, S. R. Julian, P. Monthoux, G. G. Lonzarich, A. Huxley, I. Sheikin, D. Braithwaite and J. Flouquet, Nature **406**, 587 (2000).

[64] D. Aoki, A. Huxley, E. Ressouche, D. Braithwaite, J. Flouquet, J. P. Brison, E. Lhotel and C. Paulsen, Nature **413**, 613 (2001).

[65] N. T. Huy, A. Gasparini, D. E. De Nijs, Y. Huang, J. C. Klaasse, T. Gortenmulder, A. De Visser, A. Hamann, T. Görlach and H. V. Löhneysen, Physical Review Letters **99**, 067006 (2007).

[66] V. P. Mineev, Physics-Uspekhi **60**, 121 (2017).

[67] M. Sigrist and K. Ueda, Reviews of Modern Physics **63**, 239 (1991).

[68] P. G. De Gennes and E. Guyon, Physics Letters **3**, 168 (1963).

[69] N. R. Werthamer, Physical Review **132**, 2440 (1963).

[70] J. J. Hauser, H. C. Theuerer and N. R. Werthamer, Physical Review **136**, A637 (1964).

[71] P. G. De Gennes, Reviews of Modern Physics **36**, 225 (1964).

[72] A. I. Buzdin, L. N. Bulaevskiĭ and S. V. Panyukov, JETP Lett. **35**, 178 (1982).

[73] J. S. Jiang, D. Davidović, D. H. Reich and C. L. Chien, Physical Review Letters **74**, 314 (1995).

[74] E. Demler, G. Arnold and M. Beasley, Physical Review B **55**, 15174 (1997).

[75] F. S. Bergeret, A. F. Volkov and K. B. Efetov, Physical Review Letters **86**, 4096 (2001).

[76] A. Kadigrobov, R. I. Shekhter and M. Jonson, Europhysics Letters **54**, 394 (2001).

[77] F. S. Bergeret, A. F. Volkov and K. B. Efetov, Reviews of Modern Physics **77**, 1321 (2005).

[78] R. S. Keizer, S. T. Goennenwein, T. M. Klapwijk, G. Miao, G. Xiao and A. Gupta, Nature **439**, 825 (2006).

[79] I. Sosnin, H. Cho, V. T. Petrashov and A. F. Volkov, Physical Review Letters **96**, 157002 (2006).

[80] T. S. Khaire, M. A. Khasawneh, W. P. Pratt and N. O. Birge, Physical Review Letters **104**, 137002 (2010).

[81] J. W. A. Robinson, J. D. S. Witt and M. G. Blamire, Science **329**, 59 (2010).

[82] D. Sprungmann, K. Westerholt, H. Zabel, M. Weides and H. Kohlstedt, Physical Review B **82**, 060505 (2010).

[83] M. S. Anwar, F. Czeschka, M. Hesselberth, M. Porcu and J. Aarts, Physical Review B **82**, 100501 (2010).

[84] Z. Niu, Applied Physics Letters **101**, 062601 (2012).

[85] F. S. Bergeret and I. V. Tokatly, Physical Review Letters **110**, 117003 (2013).

[86] F. S. Bergeret and I. V. Tokatly, Physical Review B **89**, 134517 (2014).

[87] S. H. Jacobsen, J. A. Ouassou and J. Linder, Physical Review B **92**, 24510 (2015).

[88] S. H. Jacobsen, I. Kulagina and J. Linder, Scientific Reports **6**, 23926 (2016).

[89] K. R. Jeon, C. Ciccarelli, A. J. Ferguson, H. Kurebayashi, L. F. Cohen, X. Montiel, M. Eschrig, J. W. Robinson and M. G. Blamire, Nature Materials **17**, 499 (2018).

[90] N. Banerjee, J. A. Ouassou, Y. Zhu, N. A. Stelmashenko, J. Linder and M. G. Blamire, Physical Review B **97**, 184521 (2018).

[91] K. Ohnishi, S. Komori, G. Yang, K. R. Jeon, L. A. Olde Olthof, X. Montiel, M. G. Blamire and J. W. Robinson, Applied Physics Letters **116**, 130501 (2020).

[92] I. M. Dayton, T. Sage, E. C. Gingrich, M. G. Loving, T. F. Ambrose, N. P. Siwak, S. Keebaugh, C. Kirby, D. L. Miller, A. Y. Herr, Q. P. Herr and O. Naaman, IEEE Magnetics Letters **9**, `10.1109/LMAG.2018.2801820` (2018).

[93] I. Martínez, P. Högl, C. González-Ruano, J. P. Cascales, C. Tiusan, Y. Lu, M. Hehn, A. Matos-Abiague, J. Fabian, I. Žutić and F. G. Aliev, Physical Review Applied **13**, 014030 (2020).

[94] T. Wakamura, H. Akaike, Y. Omori, Y. Niimi, S. Takahashi, A. Fujimaki, S. Maekawa and Y. Otani, Nat Mater **14**, 675 (2015).

[95] A. Ozaeta, P. Virtanen, F. S. Bergeret and T. T. Heikkilä, Physical Review Letters **112**, 057001 (2014).

[96] S. Kolenda, M. J. Wolf and D. Beckmann, Physical Review Letters **116**, 097001 (2016).

[97] Y. Nambu, Physical Review **117**, 648 (1960).

[98] R. A. Jishi, *Feynman Diagram Techniques in Condensed Matter Physics* (Cambridge University Press, Cambridge, 2013).

[99]   A. L. Fetter and J. D. Walecka, *Quantum Theory of Many-Particle Systems* (Dover Publications, 2003).

[100] L. P. Kadanoff and G. Baym, *Quantum statistical mechanics : Green's function methods in equilibrium and nonequilibrium problems*, (1962)

[101] L. V. Keldysh, English, Sov. Phys. J. Exp. Theor. Phys. **20**, 1018 (1965).

[102] D. C. Langreth, in *Linear and nonlinear electron transport in solids* (Springer US, 1976), pp. 3–32.

[103] A. Kamenev, *Field Theory of Non-Equilibrium Systems*, 1st ed. (Cambridge Univeristy Press, 2011).

[104] D. Rainer, Progress in Low Temperature Physics **10**, 371 (1986).

[105] J. W. Serene and D. Rainer, Physics Reports **101**, 221 (1983).

[106] D. Pines and P. Nozieres, *Theory Of Quantum Liquids Volume I: Normal Fermi Liquids*, (1994)

[107] G. Baym and C. Pethick, *Landau Fermi-Liquid Theory: Concepts and Applications* (Wiley Blackwell, Dec. 2007), pp. 1–203.

[108] N. W. Ashcroft and N. D. Mermin, *Solid State Physics*, HRW international editions (Holt, Rinehart and Winston, 1976).

[109] G. Eilenberger, Zeitschrift für Physik **214**, 195.

[110] A. L. Shelankov, Journal of Low Temperature Physics **60**, 29.

[111] D. Rainer, in *Recent progress in many-body theories, vol 1* (Springer US, 1988), pp. 217–223.

[112] L. J. Buchholtz, Journal of Low Temperature Physics **129**, 195 (2002).

[113] A. A. Abrikosov, L. P. Gor'kov and Dzyaloshinski, *Methods of quantum field theory in statistical physics* (Dover Publications, 1975), p. 352.

[114] H. Bruus and K. Flensberg, *Many-Body Quantum Theory in Condensed Matter Physics* (Oxford University Press, 2004).

[115] K. D. Usadel, Physical Review Letters **25**, 507 (1970).

[116] D. Bohm and T. Staver, Physical Review **84**, 836 (1951).

[117] J. F. Annett, *Superconductivity, Superfluids and Condensates* (Oxford University Press, 203).

[118] N. N. Bogoljubov, Il Nuovo Cimento Series 10 **7**, 794 (1958).

[119] J. G. Valatin, Il Nuovo Cimento Series 10 **7**, 843 (1958).

[120]   M. Tinkham, *Introduction to Superconductivity*, 2nd ed. (Dover, 1996).

[121]   R. D. Mattuck, *A Guide to Feynman Diagrams in the Many-Body Problem*, 2nd ed. (Dover Publications, 1992).

[122]   C. Kittel, *Introduction to solid state physics*, 8th ed. (Wiley, 2005), p. 680.

[123]   W. Belzig, F. K. Wilhelm, C. Bruder, G. Schön and A. D. Zaikin, Superlattices and Microstructures **25**, 1251 (1999).

[124]   K. Fossheim and A. Sudbø, *Superconductivity. Physics and applications* (John Wiley & sons, Ltd, 2005).

[125]   C. Gorini, P. Schwab, R. Raimondi and A. L. Shelankov, Physical Review B **82**, 195316 (2010).

[126]   F. Konschelle, The European Physical Journal B 2014 87:5 **87**, 1 (2014).

[127]   I. V. Tokatly, Physical Review B **96**, 060502 (2017).

[128]   F. London and H. London, Proceedings of the Royal Society of London. Series A - Mathematical and Physical Sciences **149**, 71 (1935).

[129]   P. G. De Gennes, *Superconductivity of Metals and Alloys*, 2nd ed. (Perseus Books, Advanced Book Program, 1999), p. 274.

[130]   N. Schopohl, (1998).

[131]   M. Eschrig, Physical Review B **61**, 9061 (2000).

[132]   A. Konstandin, J. Kopu and M. Eschrig, Physical Review B **72**, 140501 (2005).

[133]   R. D. Cook, D. S. Malkus, M. E. Plesha and R. J. Witt, *Concepts and Applications of Finite Element Analysis*, 4th ed. (John Wiley & Sons Inc., 2002).

[134]   M. H. Stone, Mathematics Magazine **21**, 167 (1948).

[135]   B. Kirk, J. Peterson, R. Stogner and G. Carey, English, Engineering with Computers **22**, 237 (2006).

[136]   S. B. Smith, W. D. Gropp, L. C. McInnes and B. F, *Efficient Management of Parallelism in Object Oriented Numerical Software Libraries*, edited by E. A. Langtangen, A. M. Bruaset and H. P (Birkhäuser Press, 1997), pp. 163–202.

[137] S. Balay, S. Abhyankar, M. F. Adams, J. Brown, P. Brune, K. Buschelman, L. Dalcin, V. Eijkhout, W. D. Gropp, D. Kaushik, M. G. Knepley, L. C. McInnes, K. Rupp, B. F. Smith, S. Zampini and H. Zhang, *PETSc Web page*, (2015) `http://www.mcs.anl.gov/petsc`.

[138] S. Balay, S. Abhyankar, M. F. Adams, J. Brown, P. Brune, K. Buschelman, L. Dalcin, V. Eijkhout, W. D. Gropp, D. Kaushik, M. G. Knepley, L. C. McInnes, K. Rupp, B. F. Smith, S. Zampini and H. Zhang, *PETSc Users Manual*, (2015) `https : / / www . mcs . anl . gov / petsc / petsc-current/docs/manual.pdf`.

[139] F. S. Bergeret, M. Silaev, P. Virtanen and T. T. Heikkilä, Reviews of Modern Physics **90**, 041001 (2018).

[140] J. A. Ouassou, T. Doekle Vethaak and J. Linder, Physical Review B **98**, 144509 (2018).

[141] D. G. Anderson, Journal of the ACM (JACM) **12**, 547 (1965).

[142] H. F. Walker and P. Ni, SIAM Journal on Numerical Analysis **49**, 1715 (2011).

[143] H.-r. Fang and Y. Saad, Numerical Linear Algebra with Applications **16**, 197 (2009).

[144] A. V. Zaitsev, Sov. Phys. J. Exp. Theor. Phys. **59** (1984).

[145] A. Millis, D. Rainer and J. A. Sauls, Physical Review B **38**, 4504 (1988).

[146] Y. V. Nazarov, Superlattices and Microstructures **25**, 1221 (1999).

[147] A. Cottet, D. Huertas-Hernando, W. Belzig and Y. V. Nazarov, Physical Review B **80**, 184511 (2009).

[148] E. V. Thuneberg, J. Kurkijärvi and D. Rainer, Physical Review B **29**, 3913 (1984).

[149] R. P. Kanwal, *Generalized Functions* (Birkhäuser Boston, Boston, MA, 2004).

[150] L. J. Buchholtz and D. Rainer, Zeitschrift für Physik B Condensed Matter and Quanta **35**, 151 (1979).

[151] J. Kopu, M. Eschrig, J. C. Cuevas and M. Fogelström, Physical Review B **69**, 094501 (2004).

[152] H. H. Berger, Journal of The Electrochemical Society **119**, 507 (1972).

[153] M. Y. Kupriyanov V. F. and Lukichev, Sov. Phys. J. Exp. Theor. Phys. **67**, 6 (1988).

[154]   B. D. Josephson, Physics Letters **1**, 251 (1962).

[155]   R. P. Feynman, R. B. Leighton and M. L. Sands, *The Feynman lectures on physics, Vol III* (Addison-Wesley Pub. Co., Reading, Mass, 1963).

[156]   R. P. Riwar, M. Houzet, J. S. Meyer and Y. V. Nazarov, Nature Communications **7**, 1 (2016).

[157]   E. Strambini, S. D'ambrosio, F. Vischi, F. S. Bergeret, Y. V. Nazarov and F. Giazotto, Nature Nanotechnology **11**, 1055 (2016).

[158]   N. P. Armitage, E. J. Mele and A. Vishwanath, Reviews of Modern Physics **90**, 015001 (2018).

[159]   D. Roditchev, C. Brun, L. Serrier-Garcia, J. C. Cuevas, V. H. L. Bessa, M. V. Milosevic, F. Debontridder, V. Stolyarov and T. Cren, Nat Phys **11**, 332 (2015).

[160]   W. Heitler and F. London, Zeitschrift für Physik **44**, 455 (1927).

[161]   W. Heisenberg, Zeitschrift für Physik **49**, 619 (1928).

[162]   P. M. Tedrow, J. E. Tkaczyk and A. Kumar, Physical Review Letters **56**, 1746 (1986).

[163]   B. S. Chandrasekhar, Applied Physics Letters **1**, 7 (1962).

[164]   A. M. Clogston, Physical Review Letters **9**, 266 (1962).

[165]   P. Fulde and R. A. Ferrell, Physical Review **135**, A550 (1964).

[166]   A. I. O. Larkin Y. N., Sov. Phys. J. Exp. Theor. Phys. **20** (1965).

[167]   M. Eschrig, Physics Today **64**, 43 (2011).

[168]   G. Csire, A. Deák, B. Nyári, H. Ebert, J. F. Annett and B. Újfalussy, Physical Review B **97**, 024514 (2018).

[169]   A. I. Buzdin, Reviews of Modern Physics **77**, 935 (2005).

[170]   T. Dvir, F. Massee, L. Attias, M. Khodas, M. Aprili, C. H. Quay and H. Steinberg, Nature Communications **9**, 1 (2018).

[171]   Y. V. Fominov, N. M. Chtchelkatchev and A. A. Golubov, Physical Review B **66**, 145071 (2002).

[172]   Y. V. Fominov, A. A. Golubov, T. Y. Karminskaya, M. Y. Kupriyanov, R. G. Deminov and L. R. Tagirov, JETP Letters **91**, 308 (2010).

[173]   J. Linder and A. V. Balatsky, Reviews of Modern Physics **91**, 045005 (2019).

[174]   A. F. Volkov, Y. V. Fominov and K. B. Efetov, Physical Review B **72**, 184504 (2005).

[175] M. Houzet and A. I. Buzdin, Physical Review B **76**, 60504 (2007).

[176] W. C. Koehler, J. W. Cable, M. K. Wilkinson and E. O. Wollan, Physical Review **151**, 414 (1966).

[177] D. Fritsch and J. F. F. Annett, New Journal of Physics **16**, 055005 (2014).

[178] F. Aikebaier, M. A. Silaev and T. T. Heikkilä, Physical Review B **98**, 024516 (2018).

[179] E. Dietz, U. Gerhardt and C. J. Maetz, Physical Review Letters **40**, 892 (1978).

[180] F. J. Himpsel and D. E. F. Astman, Physical Review B **21**, 15 (1980).

[181] R. Miranda, F. Yndurain, D. Chandesris, J. Lecante and Y. Petroff, Physical Review B **25**, `https://doi.org/10.1103/PhysRevB.25.527` (1982).

[182] B. A. Bernevig, T. L. Hughes and S. C. Zhang, Science **314**, 1757 (2006).

[183] M. Z. Hasan and C. L. Kane, Reviews of Modern Physics **82**, 3045 (2010).

[184] H. G. Hugdal, J. Linder and S. H. Jacobsen, Physical Review B **95**, 235403 (2017).

[185] A. J. Leggett, Reviews of Modern Physics **47**, 331 (1975).

[186] A. P. Mackenzie and Y. Maeno, Reviews of Modern Physics **75**, 657 (2003).

[187] N. Banerjee, C. B. Smiet, R. G. J. Smits, A. Ozaeta, F. S. Bergeret, M. G. Blamire and J. W. A. Robinson, Nat Commun **5**, `10.1038/ncomms4048` (2014).

[188] N. Satchell and N. O. Birge, Physical Review B **97**, 214509 (2018).

[189] N. Satchell, R. Loloee and N. O. Birge, Physical Review B **99**, 174519 (2019).

[190] J. Jang, D. G. Ferguson, V. Vakaryuk, R. Budakian, S. B. Chung, P. M. Goldbart and Y. Maeno, Science **331**, 186 (2011).

[191] S. Autti, V. V. Dmitriev, J. T. Mäkinen, A. A. Soldatov, G. E. Volovik, A. N. Yudin, V. V. Zavjalov and V. B. Eltsov, Physical Review Letters **117**, 255301 (2016).

[192] A. F. Volkov, K. B. Efetov and F. S. Bergeret, Physical Review B **64**, 134506 (2001).

[193] A. Di Bernardo, Z. Salman, X. L. Wang, M. Amado, M. Egilmez, M. G. Flokstra, A. Suter, S. L. Lee, J. H. Zhao, T. Prokscha, E. Morenzoni, M. G. Blamire, J. Linder and J. W. Robinson, Physical Review X **5**, 041021 (2015).

[194] J. C. Cuevas, J. Hammer, J. Kopu, J. K. Viljas and M. Eschrig, Physical Review B **73**, 184505 (2006).

[195] M. Houzet, Physical Review Letters **101**, 57009 (2008).

[196] I. V. Bobkova, A. M. Bobkov and M. A. Silaev, Physical Review B **98**, 014521 (2018).

[197] A. Vargunin and M. Silaev, Scientific Reports **9**, 5914 (2019).

[198] K. R. Jeon, C. Ciccarelli, H. Kurebayashi, L. F. Cohen, X. Montiel, M. Eschrig, S. Komori, J. W. Robinson and M. G. Blamire, Physical Review B **99**, 024507 (2019).

Paper I

Reference

M. Amundsen and J. Linder.
General solution of 2D and 3D superconducting quasiclassical systems: coalescing vortices and nanoisland geometries.
Scientific Reports **6**, 22765 (2016).
DOI: 10/f8dmpk

Contributions

MA developed the numerical solution method and performed the analyses with support from JL. MA drafted the manuscript. Both authors contributed to the discussions of the physics and the revision of the final manuscript.

Comment

This publication was not produced as part of my doctoral work, but rather as part of my master thesis. It was, however, greatly influential for the development of the numerical methods used in most of the other publications, and is therefore included here for completeness.

SCIENTIFIC REP⚙RTS

General solution of 2D and 3D superconducting quasiclassical systems: coalescing vortices and nanoisland geometries

Morten Amundsen & Jacob Linder

An extension of quasiclassical Keldysh-Usadel theory to higher spatial dimensions than one is crucial in order to describe physical phenomena like charge/spin Hall effects and topological excitations like vortices and skyrmions, none of which are captured in one-dimensional models. We here present a numerical finite element method which solves the non-linearized 2D and 3D quasiclassical Usadel equation relevant for the diffusive regime. We show the application of this on three model systems with non-trivial geometries: (i) a bottlenecked Josephson junction with external flux, (ii) a nanodisk ferromagnet deposited on top of a superconductor and (iii) superconducting islands in contact with a ferromagnet. In case (i), we demonstrate that one may control externally not only the geometrical array in which superconducting vortices arrange themselves, but also to cause coalescence and tune the number of vortices. In case (iii), we show that the supercurrent path can be tailored by incorporating magnetic elements in planar Josephson junctions which also lead to a strong modulation of the density of states. The finite element method presented herein paves the way for gaining insight in physical phenomena which have remained largely unexplored due to the complexity of solving the full quasiclassical equations in higher dimensions.

Nonlinear differential equations (NLDEs) play a pivotal role in virtually all areas of physics. They are used to describe completely disparate phenomena ranging from the behavior of ocean waves to the elasticity of materials. Thus, techniques to solve such equations are of general interest as they provide a way to obtain insight in a number of different physical systems. NLDEs are known for being notoriously difficult to solve and, more often than not, a set of NLDEs describing a particular physical scenario has to be addressed as a distinct problem since general techniques to solve such equations are scarce.

In quantum condensed matter physics, mesoscopic systems both in and out of equilibrium represent a very important arena where NLDEs are prevalent. A powerful tool used to describe such systems is the quasiclassical Keldysh theory, which has been reviewed in several works[1–7]. The theory is based on a Green function method which thus has a natural way of including disorder and other types of self-energies in the system. The quasiclassical Keldysh theory is capable of treating both ballistic systems and "dirty" systems. In the latter case, quasiparticles are elastically scattered within the mean free path l_{mfp} causing the resulting motion to be diffusive. In essence, the quasiclassical theory is a perturbation expansion valid when all energy scales in the problem are much smaller than the Fermi energy E_F. Conversely, all length scales in the system should be much larger than the Fermi wavelength. This situation is realized in a number of mesoscopic systems, including normal metals, superconductors and weakly polarized ferromagnets. Strongly polarized ferromagnets, where the exchange energy splitting h of the majority and minority spin bands is comparable in size to the Fermi energy E_F, appear to be at odds with the applicability of quasiclassical theory. However, there also exists a way in which such systems can be described in this framework. When the splitting h is sufficiently large, the two spin-bands may be treated separately so that h does not enter the problem at all and one is left with two decoupled spin species[8]. Such an approach is also suitable to address extreme cases such as half-metals using quasiclassical theory, as done recently in refs 9,10.

The equation of motion for the central object in quasiclassical Keldysh theory, the Green function $\check{g}$, is a NLDE (known as the Eilenberger[11] equation for arbitrary impurity scattering and the Usadel[12] equation in the diffusive

Department of Physics, Norwegian University of Science and Technology, N-7491 Trondheim, Norway. Correspondence and requests for materials should be addressed to J.L. (email: jacob.linder@ntnu.no)

limit) and must be supplemented by appropriate boundary conditions. Focusing on the diffusive limit, as it is often the experimentally relevant one, a variety of options are available depending on the physical situation at hand. In the simplest case of perfectly transparent interfaces, the Green function is taken as continuous across the interface. This is clearly an idealized scenario and the more realistic Kupriyanov-Lukichev[13] boundary conditions describe an interface in the tunneling limit where there exists a substantial interface resistance. Boundary conditions for an arbitrary interface transparency were developed in ref. 14. When the interface has magnetic properties, either because of an intrinsically thin magnetic layer inserted between *e.g.* two metals or superconductors or if one of the regions separated by the interface is magnetic on its own, one must use spin-dependent boundary conditions. Pioneered in refs 15,16, these were brought to a more tractable form by Cottet and co-workers in the diffusive limit[17]. However, up until recently there existed a knowledge gap in terms of how to describe strongly polarized magnetic interfaces in quasiclassical theory. Eschrig *et al.* solved this problem in ref. 9.

It is clear that the development of a numerical routine that is able to solve the quasiclassical Keldysh equations in higher dimensions than 1D will be of great value in terms of studying a vast number of physical phenomena, including various types of Hall effects, spin swapping, and topological excitations such as magnetic skyrmions and vortices. None of these phenomena can be captured in an effective 1D model. Furthermore, the ability to handle complex higher dimensional geometries numerically allows for the modeling of systems which are more closely related to experiments. For instance, superconducting nanoisland systems and vortices in mesoscopic structures have received much attention experimentally[18–22]. These systems require not only solution in 2D or 3D, but also the description of non-trivial geometries within the numerical framework. Such solutions have been investigated using the Ginzburg-Landau formalism in the context of flux patterns and vortex states in superconductors[23–25]. The ability to aid experiments with numerical routines that are both geometry and dimension independent would be highly beneficial to their study. Nevertheless, explicit solutions of the full quasiclassical equations in two dimensions have rarely been reported[26,27]. In the linearized regime, corresponding to a weak proximity effect, several works have considered the 2D solution of the Usadel equation[28–32]. Motivated by this, we report as the main result of this paper the description of a finite element method that we have developed which is capable describing mesoscopic systems in 2D and 3D using quasiclassical theory without any linearization. As far as the authors are aware, this is the first work to solve the Usadel equations in 3D. After going through the details of this method, we show its application to three model systems. One of our main findings is that in a 2D Josephson junction exposed to a magnetic flux, it is possible to control not only the geometrical array in which superconducting vortices arrange themselves, but it is also possible to cause coalescence and thus tune the number of vortices. In addition, we show that the supercurrent flow through planar junction geometries can be tailored by the magnetization pattern and strength and also spatially modulates the proximity-induced density of states, which can be probed by STM-measurements. We organize our presentation as follows. First, we introduce the system of coupled NLDEs that define the central equations in quasiclassical theory. The finite element method solving these equations in 2D and 3D is described in detail in the next section. We proceed to show the application of this method to three different hybrid structures where a superconducting material is coupled to a normal metal with external flux, and to a ferromagnet respectively. Finally, we provide a discussion of our results and concluding remarks.

Theory

In this section, we write down the quasiclassical equation of motion for $\check{g}$ in the diffusive limit and its belonging boundary conditions. The task at hand is then to solve this numerically in 2D and 3D, and we demonstrate how this can be accomplished using a finite element method in the next section.

$\check{g}$ is an 8×8 matrix satisfying $\check{g}^2 = \check{1}$ with the following structure:

$$\check{g} = \begin{pmatrix} \hat{g}^R & \hat{g}^K \\ \hat{0} & \hat{g}^A \end{pmatrix},$$

(1)

where $\hat{g}^{R,A,K}$ are the retarded, advanced, and Keldysh 4×4 Green function matrices. The relation $\hat{g}^A = -(\hat{\rho}_3 \hat{g}^R \hat{\rho}_3)^\dagger$ holds both in and out of equilibrium where $\hat{\rho}_3 = \mathrm{diag}(1, 1, -1, -1)$. The relation $\hat{g}^K = (\hat{g}^R - \hat{g}^A) \tanh(\beta\varepsilon/2)$ holds in equilibrium, so that in this scenario one only needs to determine $\hat{g}^R$ in order to completely specify $\hat{g}$. The structure of the retarded Green function looks as follows:

$$\hat{g}^R = \begin{pmatrix} \underline{g} & \underline{f} \\ -\underline{\tilde{f}} & -\underline{\tilde{g}} \end{pmatrix}, \underline{g} = \begin{pmatrix} g_{\uparrow\uparrow} & g_{\uparrow\downarrow} \\ g_{\downarrow\uparrow} & g_{\downarrow\downarrow} \end{pmatrix}, \underline{f} = \begin{pmatrix} f_{\uparrow\uparrow} & f_{\uparrow\downarrow} \\ f_{\downarrow\uparrow} & f_{\downarrow\downarrow} \end{pmatrix}.$$

(2)

where $\underline{g} = \underline{g}(\varepsilon)$ and $\underline{f} = \underline{f}(\varepsilon)$ denote the 2×2 normal and anomalous Green function matrices in spin space, respectively. The $\tilde{\cdot}$ operation means complex conjugation and reversal of the energy argument $\varepsilon \to (-\varepsilon)$.

The Usadel equation reads:

$$D\nabla(\hat{g}\nabla\hat{g}) + \mathrm{i}[\varepsilon\hat{\rho}_3 + \hat{\Sigma}, \hat{g}] = 0$$

(3)

where D is the diffusion coefficient, $\hat{\rho}_3 = \mathrm{diag}(\hat{\rho}_3, \hat{\rho}_3)$, while $\hat{\Sigma}$ is a matrix describing the self-energies of the problem. In general, it can be a functional of the Green function matrix itself, i.e. $\hat{\Sigma} = \hat{\Sigma}(\hat{g})$. In the specific case of a ferromagnetic material, one has

$$\hat{\Sigma} = \text{diag}(\hat{M}, \hat{M}), \quad \hat{M} = \vec{h} \cdot \text{diag}(\underline{\vec{\sigma}}, \underline{\vec{\sigma}}^*) \tag{4}$$

where $\vec{h}$ describes the magnitude and direction of the magnetic exchange field while $\underline{\vec{\sigma}} = (\underline{\sigma}_x, \underline{\sigma}_y, \underline{\sigma}_z)$ is the vector of Pauli matrices. In the presence of gauge fields, such as a U(1) magnetic vector potential $\vec{A}$ describing an external magnetic field one has to replace the gradient operator with its covariant equivalent:

$$\nabla \rightarrow \nabla - iq[\vec{A}\hat{\rho}_3, \hat{g}] \tag{5}$$

where q is the charge of the fermion field. A similar substitution is also made if one wishes to include an SU(2) gauge field $\underline{\vec{A}}$ that describes antisymmetric spin-orbit coupling of Rashba or Dresselhaus type. In this work, we will use the standard Kupriyanov-Lukichev[13] boundary conditions as a realistic description of the interface regions. While originally derived for the tunneling regime, these boundary conditions have been shown to give good results also for moderately to highly transparent interfaces[33], which are considered herein. For an interface separating a material 1 on the left side from a material 2 on the right side, they read:

$$2\zeta_j L_j \check{g}_j \vec{n} \cdot \nabla \check{g}_j = [\check{g}_1, \check{g}_2], j = \{1, 2\}. \tag{6}$$

Here, $\zeta_j = R_B/R_j$ describes the ratio between the interface resistance and the bulk resistance of region j while L_j is the length of region j. Here, $\vec{n}$ is the unit vector normal to the interface pointing from region 1 to 2. At interfaces to air, no current is allowed to flow and the boundary condition is

$$\vec{n} \cdot \nabla \check{g} = 0 \tag{7}$$

where $\vec{n}$ again represents the unit vector normal to the air interface. Equations (3), (6), and (7) define a system of coupled differential equations with belonging boundary conditions and the task is to find the solution $\check{g}$. For concreteness, we restrict our attention to an equilibrium scenario where only the retarded Green function matrix $\hat{g}^R$ must be found. Even with this restriction, the equations are capable of describing a variety of different mesoscopic systems. The equation system for $\hat{g}^R$ is identical to the one for $\check{g}$, as can be verified by direct insertion of Eq. (1) in the place of $\hat{g}$, by replacing all $\cdot\check{\cdot}\cdot$ matrices with their $\cdot\hat{\cdot}\cdot$ equivalents. Before proceeding to a description of the finite element method we have used to solve this equation set in 2D and 3D, it is useful to introduce a Ricatti parametrization[34] of $\hat{g}^R \equiv \hat{g}$. This parametrization, first applied in ref. 35 in the context of the Usadel equation, simplifies the numerical implementation of the equations by exploiting the symmetries and normalization of $\check{g}$. One introduces two matrices in spin-space, $\underline{\gamma}$ and $\underline{\tilde{\gamma}}$, which define $\hat{g}$ as follows:

$$\hat{g} = \begin{pmatrix} \underline{N}(1 + \underline{\gamma}\underline{\tilde{\gamma}}) & 2\underline{N}\underline{\gamma} \\ -2\underline{\tilde{N}}\underline{\tilde{\gamma}} & -\underline{\tilde{N}}(1 + \underline{\tilde{\gamma}}\underline{\gamma}) \end{pmatrix}, \quad \underline{N} = (1 - \underline{\gamma}\underline{\tilde{\gamma}})^{-1}, \quad \underline{\tilde{N}} = (1 - \underline{\tilde{\gamma}}\underline{\gamma})^{-1}. \tag{8}$$

This parametrization satisfies both the proper symmetry relations between the elements of $\hat{g}$ as well as the normalization condition $\hat{g}^2 = \hat{1}$.

Equations (3), (6), and (7) comprise a set of second-order coupled partial nonlinear differential equations which, when solved, determine the Green function $\check{g}$ of the system. Various physical quantities of interest may then be computed, such as the charge current density $\vec{J}_Q$ and the density of states (DOS), given as:

$$\vec{J}_Q = \frac{N_0 e D}{4} \int_{-\infty}^{\infty} d\varepsilon \, \text{Tr}\{\hat{\rho}_3(\check{g}\nabla\check{g})^K\} \tag{9}$$

$$\text{DOS} = \frac{1}{2} \text{Tr}\{\underline{N}(1 + \underline{\gamma}\underline{\tilde{\gamma}})\} \tag{10}$$

Another physical quantity that may be computed is the pair correlation function, Ψ, indicating the degree to which superconducting correlations exist in the system. It is given as:

$$\Psi = \frac{1}{8} \int_{-\infty}^{\infty} d\varepsilon \, [\hat{g}^K(1, 4) - \hat{g}^K(2, 3)] \tag{11}$$

where $\hat{g}^K(i, j)$ refers to the element in column i and row j of the Keldysh Green function matrix.

A general analytical solution of equations (3), (6), and (7) is impossible. Some progress can be made by linearizing the equations, as is often done when considering a superconducting proximity effect. However, this approximation limits the validity of the obtained results and may cause the loss of novel physical phenomena that are only captured when the full equations are used. To do so, one must use a numerical approach. So far, only a handful of works have managed to solve the 2D Usadel equation numerically. This has been done in the full proximity effect regime for a superconductor/normal metal/superconductor junction in refs 26,27. To the best of our knowledge, no work has ever reported a solution of the Usadel equations in 3D.

Implementation of the finite element method. We here present a way to solve the quasiclassical equations in 2D and 3D using a finite element method. Its detailed description follows below. After its presentation, we show its application to 2D and 3D model systems by solving the equations without any approximations.

Inserting 8 into equation 3 results in the following:

$$\nabla^2 \underline{\gamma} + 2\nabla_{\underline{\gamma}} \cdot \underline{\tilde{N}} \underline{\tilde{\gamma}} \nabla_{\underline{\gamma}} - 2i\underline{N}(1 + \underline{\gamma}\underline{\tilde{\gamma}})\vec{A} \cdot \nabla_{\underline{\gamma}} - 2i\vec{A} \cdot \nabla_{\underline{\gamma}}\underline{\tilde{N}}(1 + \underline{\tilde{\gamma}}\underline{\gamma})$$
$$-4\vec{A}^2 \underline{\gamma}\underline{N}(1 + \underline{\tilde{\gamma}}\underline{\gamma}) + i\vec{h} \cdot (\underline{\vec{\sigma}}\underline{\gamma} - \underline{\gamma}\underline{\vec{\sigma}}^*) + 2i(\varepsilon + i\delta)\underline{\gamma} = 0$$
$$\nabla^2 \underline{\tilde{\gamma}} + 2\nabla_{\underline{\tilde{\gamma}}} \cdot \underline{N}\underline{\gamma}\nabla_{\underline{\tilde{\gamma}}} + 2i\underline{\tilde{N}}(1 + \underline{\tilde{\gamma}}\underline{\gamma})\vec{A} \cdot \nabla_{\underline{\tilde{\gamma}}} + 2i\vec{A} \cdot \nabla_{\underline{\tilde{\gamma}}}\underline{N}(1 + \underline{\gamma}\underline{\tilde{\gamma}})$$
$$-4\vec{A}^2 \underline{\tilde{\gamma}}\underline{N}(1 + \underline{\gamma}\underline{\tilde{\gamma}}) - i\vec{h} \cdot (\underline{\vec{\sigma}}^*\underline{\tilde{\gamma}} - \underline{\tilde{\gamma}}\underline{\vec{\sigma}}) + 2i(\varepsilon + i\delta)\underline{\tilde{\gamma}} = 0 \tag{12}$$

where δ models the effect of inelastic quasiparticle scattering (the so-called Dynes parameter[36]). We set $\delta/\Delta = 10^{-3}$ in this paper where Δ is the bulk superconducting gap. In Eq. (12), it is also possible to include self-energies corresponding to spin-flip and spin-orbit scattering on impurities which act pair-breaking on superconducting correlations. This typically amounts to a reduction of the magnitude of the superconducting proximity effect and we omit these terms in the present work. We also note that the effect of Rashba and Dresselhaus spin-orbit interactions were derived in Ricatti-parametrized form very recently[37,38]. As $\underline{\gamma}$ and $\underline{\tilde{\gamma}}$ are 2×2 matrices, thus containing 4 elements each, it is clear that the solution of equation 12 involves solving a system of 8 coupled NLDEs. For brevity, we introduce the notation

$$\chi = (\gamma_{11} \quad \gamma_{12} \quad \gamma_{21} \quad \gamma_{22} \quad \tilde{\gamma}_{11} \quad \tilde{\gamma}_{12} \quad \tilde{\gamma}_{21} \quad \tilde{\gamma}_{22})^T \tag{13}$$

where γ_{ij} and $\tilde{\gamma}_{ij}$ are elements of $\underline{\gamma}$ and $\underline{\tilde{\gamma}}$ respectively. Equation 12 may then be written as

$$\nabla^2 \chi^{(\alpha)} + F^{(\alpha)}(\underline{\gamma}, \underline{\tilde{\gamma}}, \nabla_{\underline{\gamma}}, \nabla_{\underline{\tilde{\gamma}}}) = 0 \tag{14}$$

where α is an element of equation 13 and $F^{(\alpha)}$ is a function that performs the matrix multiplications of equation 12 and extracts the appropriate element. Similarly, the boundary conditions become in the Riccati parametrization:

$$\vec{n} \cdot \nabla_{\underline{\gamma}_i} = \mp \frac{1}{L_i \zeta_i}(1 - \underline{\gamma}_i\underline{\tilde{\gamma}}_j)N_j(\underline{\gamma}_i - \underline{\gamma}_j) + 2i\vec{n} \cdot \vec{A}\underline{\gamma}_i \tag{15}$$

where the negative sign should be used for a boundary where region j is to the right of region i, and the positive sign for a boundary where region j is to the left of region i. A similar expression is found for $\vec{n} \cdot \nabla_{\underline{\tilde{\gamma}}_i}$ by applying the $\tilde{\cdot}$ operation to equation 15. These are Neumann boundary conditions of the type

$$\vec{n} \cdot \nabla\chi^{(\alpha)} = B^{(\alpha)}(\underline{\gamma}, \underline{\tilde{\gamma}}) \tag{16}$$

where $B^{(\alpha)}$ works in a similar manner as $F^{(\alpha)}$.

By multiplying equation 14 by a test function $\eta(\vec{r})$ and integrating over the domain Ω in which the equations are defined, one gets what is called the weak formulation of the NLDEs (not to be confused with the weak proximity effect approximation):

$$-\int_\Omega d\vec{r}\nabla\chi^{(\alpha)} \cdot \nabla\eta + \int_\Omega d\vec{r}F^{(\alpha)}(\underline{\gamma}, \underline{\tilde{\gamma}}, \nabla_{\underline{\gamma}}, \nabla_{\underline{\tilde{\gamma}}})\eta + \int_{\partial\Omega} dS\vec{\nu} \cdot \nabla\chi^{(\alpha)}\eta = 0 \tag{17}$$

where the divergence theorem has been used and $\partial\Omega$ is the boundary of Ω. The unit vector $\vec{\nu}$ is an outward pointing surface normal, and is either parallel or antiparallel with the normal vector $\vec{n}$ as defined in the Kupriyanov-Lukichev boundary conditions. It may thus be expressed as $\vec{\nu} = (\vec{\nu} \cdot \vec{n})\vec{n}$.

It is assumed that the domain Ω can be discretized into a mesh of N_{el} elements, i.e., N_{el} subdomains Ω_n, so that equation 17 becomes

$$\sum_{n=1}^{N_{el}} \int_{\Omega_n} d\vec{r}[-\nabla\chi^{(\alpha)} \cdot \nabla\eta + F^{(\alpha)}(\underline{\gamma}, \underline{\tilde{\gamma}}, \nabla_{\underline{\gamma}}, \nabla_{\underline{\tilde{\gamma}}})\eta] + (\vec{\nu} \cdot \vec{n})\int_{\partial\Omega} dS\vec{n} \cdot \nabla\chi^{(\alpha)}\eta = 0 \tag{18}$$

So far, no approximations have been made, and provided it is continuous in Ω_n, the exact solution of equation 18 exists in the infinite space of polynomials $P(\Omega_n)$. To progress further, we will use the Galerkin method, a common finite element formulation technique treated in most books on the subject, e.g[39]. The method consists of restricting the space in which solutions are sought, from $P(\Omega_n)$ to a finite dimensional space of polynomials $P^N(\Omega_n)$ consisting of all polynomials of degree N or lower. Normally, N is equal to 1 or 2.

On each element there are defined N_n nodes, containing the degrees of freedom of the system - in this case the solution of the Usadel equation at the location of the node - and it is possible to define N_n polynomials, $\phi_j(\vec{r})$, that interpolate between them. These interpolation functions span the space of $P^N(\Omega_n)$ and are used as a basis for the approximate solution of equation 18:

$$\chi^{(\alpha)} \approx X^{(\alpha)} = \sum_{j=1}^{N_n} X_j^{(\alpha)}\phi_j \tag{19}$$

where $X_j^{(\alpha)}$ are the expansion coefficients for the approximate solution of equation α. Furthermore, the test function η is selected as

$$\eta = \sum_{j=1}^{N_n} \phi_j$$

(20)

We now consider the boundary term. Having meshed the domain Ω, it is obvious that some of the element domains Ω_n intersect with the boundary $\partial\Omega$. In fact, the boundary is the union of all these intersections. It follows that the nodes associated with these intersections also lie on the boundary, and so there are defined interpolation functions also here. With the dimensionality of $\partial\Omega$ being one less than Ω, the surface interpolation functions ϕ_j^S, which are zero everywhere but on the boundary, are found by evaluating the element interpolation functions at the surface, i.e., $\phi_j^S = \phi_j(\vec{r}^S)$ where $\vec{r}^S$ is a surface coordinate.

With the approximation given in 19, equation 18 is in general not satisfied, so that for every element the right hand side becomes equal to a residual, $R_j^{(\alpha)}$:

$$R_j^{(\alpha)} = \int_{\Omega_n} d\vec{r}[-\nabla X^{(\alpha)} \cdot \nabla \phi_j + F^{(\alpha)}(\underline{\gamma}, \underline{\tilde{\gamma}}, \nabla\underline{\gamma}, \nabla\underline{\tilde{\gamma}})\phi_j] + (\vec{\nu} \cdot \vec{n}) \int_{\partial\Omega} dS B^{(\alpha)}(\underline{\gamma}, \underline{\tilde{\gamma}})\phi_j^S$$

(21)

Equation 21 is to be solved for $X_j^{(\alpha)}$ so that $R_j^{(\alpha)} = 0$, however due to the nonlinearities introduced by $F^{(\alpha)}$ and $B^{(\alpha)}$ this needs to be done iteratively by Newton-Raphson iterations:

$$(X_i^{(\alpha)})_{k+1} = (X_i^{(\alpha)})_k - [J_{ij}^{(\alpha\beta)}]^{-1}(R_j^{(\beta)})_k$$

(22)

with J_{ij} the Jacobian matrix in the 8 dimensional parameter space, given as

$$J_{ij}^{(\alpha\beta)} = \frac{\partial R_j^{(\beta)}}{\partial X_i^{(\alpha)}} = \int_{\Omega_n} d\vec{r}\left[-\delta_{\alpha\beta}\nabla\phi_i \cdot \nabla\phi_j + \frac{\partial F^{(\beta)}}{\partial X_i^{(\alpha)}}\phi_i\phi_j\right] + (\nu \cdot \vec{n}) \int_{\partial\Omega} dS \frac{\partial B^{(\beta)}}{\partial X_i^{(\alpha)}}\phi_i^S\phi_j^S$$

(23)

Finally, 22 needs to be assembled into a global system of equations by summing over all elements, taking element connectivity into account. This involves restructuring and expanding the element matrices into a global system matrix:

$$\mathbb{X}_{k+1} = \mathbb{X}_k - \mathbb{J}^{-1}\mathbb{R}_k$$

(24)

where $\mathbb{J}$ is an $8M \times 8M$ matrix, and M is the number of nodes in the system. The integrals over the element domains are performed by changing coordinates to a reference element, and integrating numerically by means of a Gauss quadrature. This puts restrictions on how distorted a mesh can be, as the Jacobian for the coordinate transformation has to exist. In general, a structured mesh where the deviation from the geometry of the reference element is small will often give higher accuracy and reduce the computation time as the sparsity of the assembled matrices is increased.

Results

Application: 2D and 3D superconductor/ferromagnet junctions.
The main advantage of the finite element method over the finite difference method, a method commonly used to solve partial differential equations numerically, is that it is formulated entirely without specifying element type, interpolation functions, spatial dimension or the geometry. This gives it the flexibility to solve PDEs on geometries which would be challenging to solve with the finite difference method. Here, we have used second order Lagrange polynomials as interpolation functions with quadrilateral (QUAD9) and hexagonal (HEX27) elements in 2D and 3D respectively. We illustrate this in the following. For the numerical implementation, we use the finite element library libMesh[40] and its integration with the PETSc library of numerical equation solvers[41,42]. In the following, the superconducting regions will be treated as reservoirs such that the bulk expression for the Green function $\check{g} = \check{g}_{BCS}$ will be used. The superconductors thus effectively enter the problem as boundary conditions.

2D Josephson junction with external magnetic flux. It is well known that for a Josephson junction where an external flux is applied to the intermediate region, the supercurrent exhibits a Fraunhofer interference pattern. In refs 26,27 a 2D superconductor/normal/superconductor Josephson junction was studied in the presence of an external magnetic flux. The authors revealed that the Fraunhofer interference pattern would qualitatively change its dependence on the external flux depending on the width of the junction W relative to its length L. When $W \gg L$ a conventional Fraunhofer pattern was found, when $W \ll L$ the supercurrent was monotonically decaying. Moreover, it was shown that the Fraunhofer interference pattern was accompanied by a regular array of proximity-induced vortices in the transversal direction of the normal metal region. The vortices are not present in the narrow width limit. Experimental verification of the appearance of proximity-induced vortices recently reported in ref. 43 which considers Josephson junctions generated by a network of superconducting nanocrystals.

Here, we explore how the vortices disappear from the system as the width is reduced and the system transitions to a vortex-less state. We also determine how a change in the phase difference between the superconducting leads affect the vortices, and will show that this does not always correspond to a shift of the vortex array along the transverse direction. To illustrate the ease with which the finite element method handles non-trivial geometries, we consider a Josephson junction with a bottleneck in the normal metal region, as shown in Fig. 1. We assume that the currents in the system are small, so that the magnetic field remains unaffected. As will be shown, it turns out to be possible to tune the geometry of the array along which the superconducting vortices align, swapping
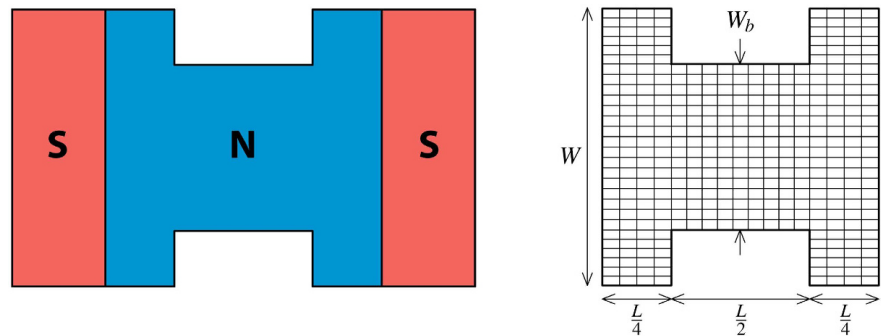
Figure 1. The geometry considered. To the left is shown a general outline of the Josephson junction, and to the right a typical mesh used in the numerical analysis.

from a vertical necklace to a horizontal row of vortices and vice versa. Moreover, we demonstrate that changing superconducting phase difference, tunable *e.g.* via a current-bias, causes vortices to merge. This offers an interesting route to exerting external control over topological excitations in superconducting hybrid structures.

Figure 2 shows the results for varying widths of the normal metal with an applied external flux of $\Phi = 4\Phi_0$, where $\Phi_0 = \frac{2e}{h}$ is the flux quantum. The flux is specified with respect to a rectangular cross section $W \times L$. The resistance ratio in the Kupriyanov-Lukichev boundary conditions is $\zeta = 3$ in both interfaces with the superconductors, and the temperature is $k_B T = 0.001\Delta$. All lengths are in units of the superconducting coherence length ξ.

It is seen that with no bottleneck, and with $W \gg L$, a linear array of vortices along the *y*-axis is found. This is shown in Fig. 2a and is in agreement with refs 26,27. The number of vortices is simply equal to the number of flux quanta in the system. Furthermore, the fact that the vortices align themselves in an array implies that they repel, a feature they share with the Abrikosov vortices found in type II superconductors. Decreasing the width, pushes the vortices closer together which is energetically less favorable. With no phase difference between the superconducting leads, the phase correlation function is symmetric about both the *x*- and *y*-axis. This means that when the system becomes too narrow to sustain four vortices, two vortices must simultaneously translate vertically out of the system in a way which maintains this symmetry, as seen in Fig. 2b. The two remaining vortices are seen to be forced closer together until they eventually meet at the origin, from which it may be inferred that for the given flux and geometry, the presence of two vortices is energetically favorable regardless of their separation. In particular, it is observed that within numerical precision, the vortices are found to completely overlap in Fig. 2c, resulting in a single vortex. The winding of the phase of the pair correlation function along a contour around this vortex is found to be 4π, implying a topological charge of 2, see inset of Fig. 2c. As the bottleneck is introduced, and the width further decreased, the vortices split symmetrically along the *x*-axis, as shown in Fig. 2d,e. This behavior may also be explained by the symmetry of the system, which restrains the positions of the two vortices to be symmetric about the origin, on either the *x*-axis or the *y*-axis. As the vortices evidently feel a stronger repulsion from the edges than from each other, they are pushed together. However once they meet at the origin, they are free to separate along the *x*-axis and thus reduce the energy in the system. By continuing to decrease the bottleneck width, W_b, a point where even two vortices may not be sustained is eventually reached. The boundary conditions that constitute the superconducting leads enforce a constant pair correlation, and so it becomes increasingly difficult to maintain the curvature necessary for the vortices to exist as one approaches the superconductors. In other words, the vortices may not in a continuous fashion exit the system along the *x*-axis. Instead, the vortices are seen to return to the *y*-axis, and be expelled vertically.

While the vortices separate along the *x*-axis for decreasing bottleneck width, the length of the narrowing area is large enough to contain them, and so the system behaves as if the width is uniformly decreased. It has been verified that by reducing the horizontal extent of the bottleneck, it is possible to create a situation where the vortices are pushed to the wide regions of the junction, at which point they become virtually independent of the bottleneck width W_b.

We also show the results for varying phase difference between the superconductors, for a geometry with $W_b = 0.6W$, shown in Fig. 3. We find that not only are the positions of the vortices changed by varying the phase difference ϕ, but also the number of vortices is altered. Figure 3a–c show the absolute value of the pair correlation function. With no phase difference, two vortices are located symmetrically along the *x*-axis. As ϕ increases from 0, the two vortices coalesce at the origin. Further increase translates one of the vortices in the negative *y*-direction, until only a single vortex remains. We have confirmed that the spatial rearrangement of the vortex pattern and the merging of vortices also takes place even without the bottleneck geometry, i.e. for a rectangular N region. The dependence of the vortex positions on the phase difference may be explained by the magnetic field, which in the small current approximation, permeates the normal metal unhindered. The current generated by the phase difference is altered by the field which in turn influences which locations that are energetically favorable for the vortices.
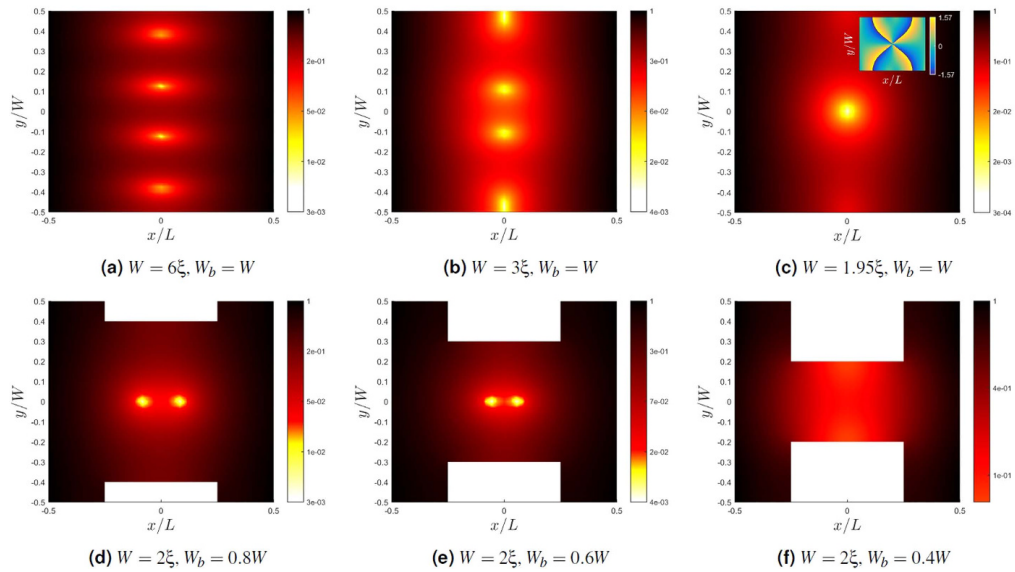
Figure 2. The absolute value of the pair correlation function for different values of the width W and bottleneck width W_b. The length is $L = 2\xi$. The inset of (**c**) shows the phase of the pair correlation function.

The current density for each of the cases considered are shown in Fig. 3d–f. Close to a vortex, where pair correlation is low, currents are induced by the magnetic field and circulate counter-clockwise. Due to the omnipresent magnetic field, screening currents circulating clockwise are generated which dominate when pair correlation is high. As the pair correlation function is weakened upon approaching the vortex core, one observes an abrupt change in the current density pattern at a certain distance from the vortex.

The phase of the pair correlation function is given as $\theta = \arctan(\mathfrak{J}\Psi/\mathfrak{R}\Psi)$. By integrating $\nabla\theta$ along a contour going around a point where the pair correlation function vanishes, a value of 2π is found. This can be seen directly from the phase plots in Fig. 3g–i, as any curve around a zero of the pair correlation function has to traverse two discontinuous jumps of value π. In other words, these points have a topological charge of one, showing that they are indeed vortices. With the approximation of weak currents we do not however find flux quantization, as this requires a self consistent calculation of the magnetic field.

3D ferromagnetic nanoisland. We also demonstrate how the finite element method is capable of dealing with fully three-dimensional structures with non-rectangular geometry by considering a superconductor/ferromagnet bilayer as depicted in Fig. 4. The ferromagnet is cylindrical with a radius of $R = 2\xi$ and a height of $L_z = 0.4R$, and is placed atop an assumed infinite superconductor. Such a geometry is inspired by ref. 44 which experimentally explores the appearance of magnetic field induced superconductivity in a lattice of ferromagnetic islands placed on top of a superconductor. While the experimental setup is far too sophisticated for their results to be recreated by the example considered herein, it does demonstrate the relevance of the model.

We use Kupriyanov-Lukichev boundary conditions with a resistance ratio of $\zeta = 3$. We compute the density of states (DOS) for this structure with an exchange field h equal to 0.3Δ, 0.5Δ and 0.7Δ in the vertical direction, as shown in Fig. 5a. The results are identical with the one-dimensional solution to the S/F bilayer, displaying an enhanced DOS at the Fermi level ($\varepsilon = 0$) and a spin-split minigap structure[45–51]. The spatial distribution of the DOS is nearly constant for this particular parameter set choice in F as illustrated by Fig. 5b, thus proving the correctness of the method.

3D ferromagnet with superconducting islands. To illustrate the 3D capabilities of the method developed on a system which cannot be described by an effective 1D model, we consider two variations of a system where two superconducting islands are placed on a ferromagnet with dimensions $L_x \times L_y \times L_z = 10\xi \times 7\xi \times \xi$, as shown in Fig. 6. To avoid self-consistency iterations, the islands are approximated by bulk BCS superconductors, and are included as Kupriyanov-Lukichev boundary conditions with a resistance ratio of $\zeta = 1.5$. The dimensions of the islands are $2.5\xi \times 2.5\xi$. The motivation for these analyses is to study the current flow between the superconducting islands and the spatial modulation of the density of states due the proximity effect in the presence of a supercurrent. To this end, the islands are given a phase difference of $\phi = \frac{\pi}{2}$. The configurations considered are:
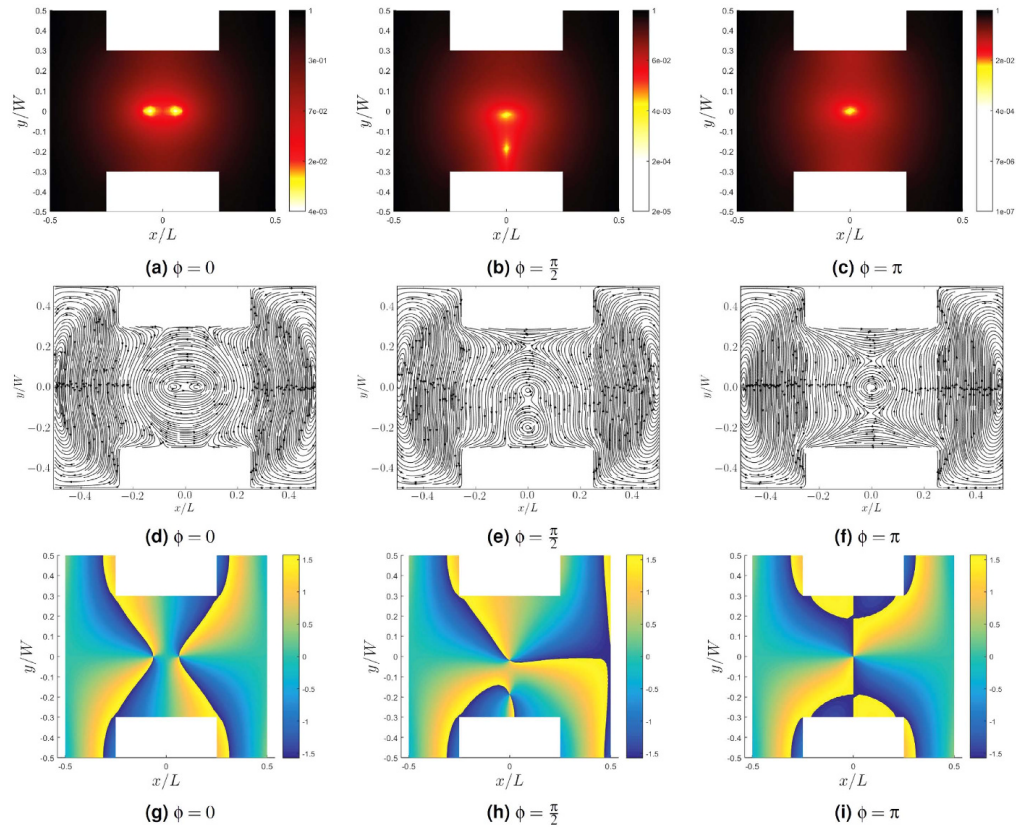
Figure 3. Results based on the solution of the Usadel equation for varying phase difference between the superconductors, with $L = W = 2\xi$, $W_b = 0.6W$ and $\Phi = 4\Phi_0$. (**a–c**) The absolute value of the pair correlation function, (**d–f**) the current density, (**g–i**) the phase of the pair correlation function.
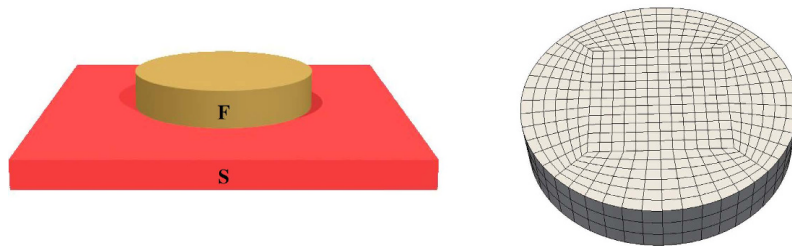
Figure 4. To the left is shown the 3D geometry considered. The superconductor is assumed to have an infinite extent and is included only as a boundary condition. The mesh used when solving the Usadel equation in the ferromagnet is shown to the right. The radius is $R = 2\xi$, and the thickness is $L_z = 0.4R$.

(A) The superconducting islands are placed on the same side of the ferromagnet with a separation of 2.5ξ, as shown if Fig. 6a. The ferromagnet has a constant magnetization of $h = 5\Delta$ in the vertical direction.

(B) One of the superconducting islands is moved to the opposite side of the ferromagnet, shown in Fig. 6b. The magnetization is pointing in the vertical direction, with a spatial distribution shown in Fig. 6c.
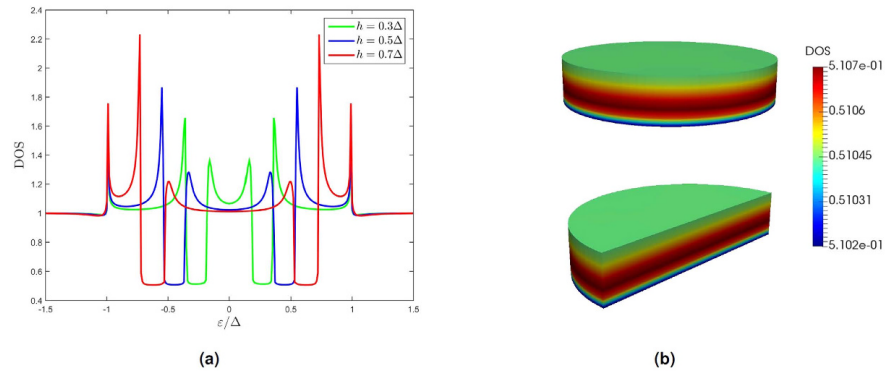
Figure 5. (**a**) Density of states for the 3D ferromagnet structure for various strengths of the vertical exchange field, (**b**) spatial distribution of the density of states for energy $\varepsilon = 0.5\Delta$ and exchange field $h = 0.5\Delta$.
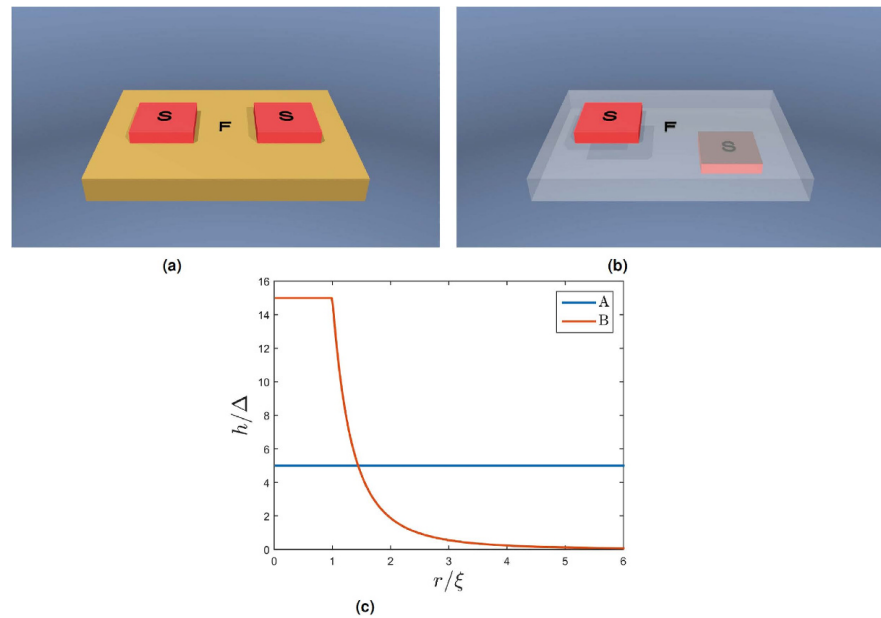
Figure 6. The geometries and magnetization considered. Marked in red are superconducting islands placed on a ferromagnet. The dimensions of the ferromagnet is $L_x \times L_y \times L_z = 10\xi \times 7\xi \times \xi$. In subfigure (**b**) the ferromagnet has been made transparent for visualization purposes. (**a**) Configuration A, (**b**) Configuration B, (**c**) The spatial distribution of the magnetization, where r is a horizontal radius measured from the center of the ferromagnet.

Configuration A may be realized experimentally by growing the ferromagnetic film on a substrate and placing superconducting electrodes on top of it. Configuration B may be created by placing the lower superconducting electrode on the substrate and subsequently grow a normal metal film on top of it (a similar type of geometry was considered in the context of Fraunhofer patterns in ref. 52). The upper superconducting electrode is then placed atop the film. The spatial distribution of the magnetization used in Configuration B can be generated by placing a strong ferromagnet on top of the normal film. This will magnetize the film across the thickness, creating a cross section approximately equal to the ferromagnet within which the magnetization is constant. The ability of the ferromagnet to induce magnetization within the normal film abates quickly as the distance from it increases, thus generating the distribution shown in Fig. 6c.
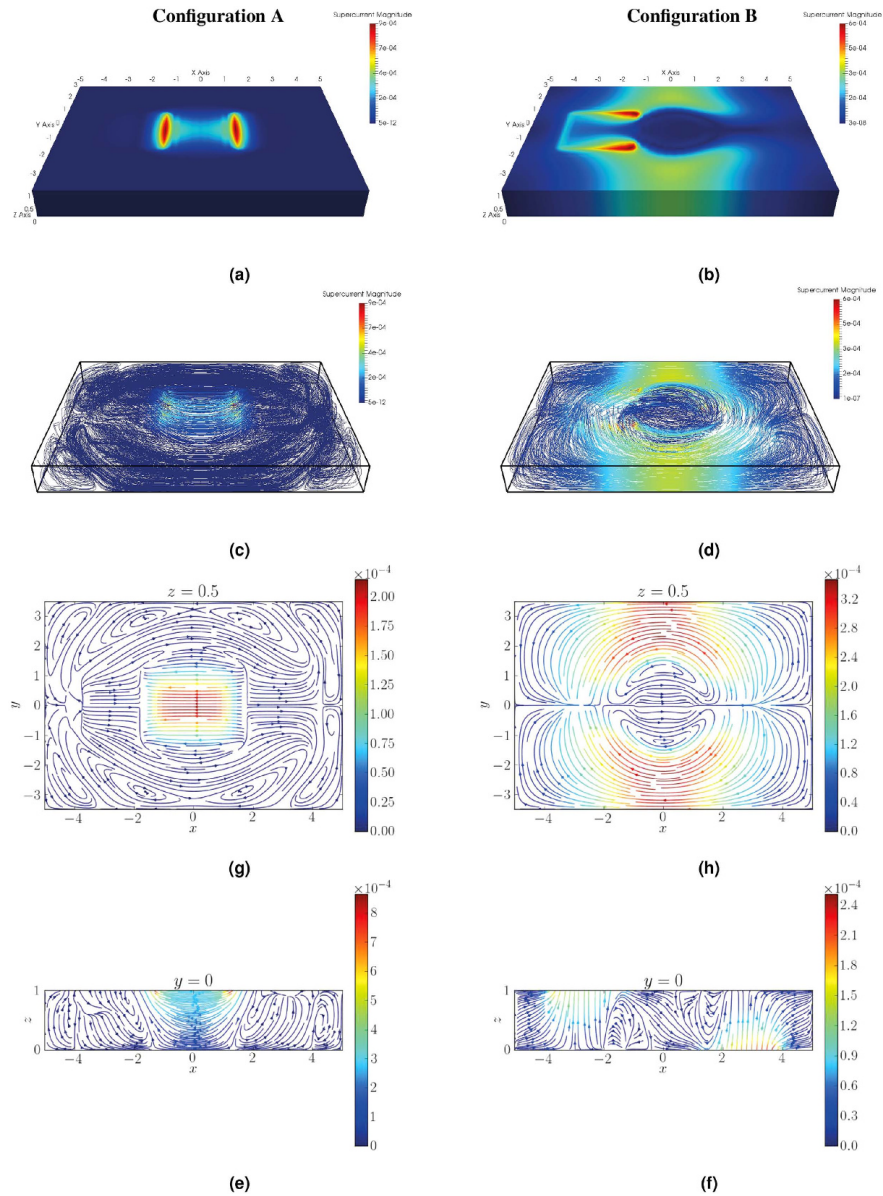
Figure 7. The supercurrent present in both Configuration A and Configuration B. All currents are scaled by $J_0 = \frac{N_0 e D \Delta}{8}$ and all lengths by ξ.

The results from both configurations are given in Fig. 7. For Configuration A it is seen that the current is largely confined to the region between the islands, passing from one to the other, shown in Fig. 7a,g. Due to the magnetization being uniform, the supercurrent travels along a path that minimizes the distance, and thus has no component pointing along the transversal direction (the y-axis of Fig. 7). However, as the current enters and exits the ferromagnet vertically, it is seen to arc into the thickness of the film, as seen in Fig. 7c,e.

Configuration B has a magnetization of $h(\vec{r}) = 15\Delta$ within a horizontal radius $\vec{r}$ of one superconducting coherence length ξ from the center of the ferromagnet. This has a significant effect on the supercurrent. The supercurrent flows vertically into the system from the lower superconductor, as seen in Fig. 7d. However, rather
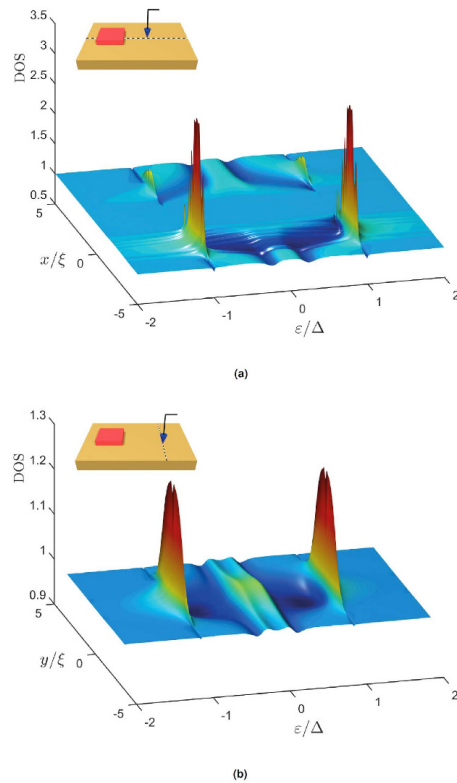
Figure 8. The density of states along two different lines on the surface of the ferromagnet.

than flowing directly to the upper superconductor, as would have been the case for a homogeneous magnetization, the current is seen to avoid the area of highest magnetization by following a semicircular path, shown in Fig. 7b,d,h. The exchange field has a detrimental effect on the superconducting correlations as it breaks up the Cooper pairs. For this reason it is natural that the path selected by the supercurrent eventually transitions from the shortest route, to a path where the central area is avoided as h increases. In this sense, the exchange field is seen to influence the supercurrent in a way which is analogous to the way a resistance influences a normal current. It is interesting that this transition has occurred already for $h = 15\Delta$, which is to be considered a somewhat weak magnetization, and may provide means for customizing the supercurrent path.

In Fig. 8 we show the density of states (DOS) along two different lines on the surface of the ferromagnet in Configuration B, thus simulating the measurement of $\frac{dI}{dV} \propto$ DOS by scanning tunneling microscopy. The DOS is seen to feature a strong spatial modulation. Along the x-axis, as seen in Fig. 8a, the probed line passes directly underneath the upper superconductor. Here the characteristic peaks associated with the superconducting DOS are observed at $\varepsilon = \pm\Delta$. Similar peaks are also created on the surface above the lower superconductor. Furthermore, a slight suppression of the DOS is found in the same regions, at the level of $\varepsilon = \pm h(\vec{r})$, which is typical for superconductor/ferromagnet hybrid structures[49]. The second line is placed opposite the lower superconductor, in the y-direction as shown in Fig. 8b. Also here, the characteristic peaks and split gap is found. The proximity effect is seen to decay as one moves away from the position of the superconductor, so that the DOS approaches that of a normal metal, which is reasonable.

Conclusion

We have demonstrated how the full, spin dependent, Usadel equation may be solved by the finite element method. The method excels in solving differential equations for non-trivial geometries and may find use in solving a wide range of problems which have not been manageable with other methods. A natural development of the finite element method presented herein would be to incorporate the kinetic equations coming from the Keldysh part of the quasiclassical equations in non-equilibrium situations. The methodology may also be generalized to handle time dependent problems such as domain wall motion. Work is currently ongoing on these subjects which may find interesting applications in the field of superconducting spintronics[53,54].

References

1. Schmid, A. Kinetic Equations for Dirty Superconductors in Nonequilibrium Superconductivity, Phonons and Kapitza Boundaries. *Proceedings of NATO Advanced Study Institute* Ch. 14 (Plenum Press, New York, 1981).
2. Serene, J. W. & Rainer, D. The quasiclassical approach to superfluid 3He. *Phys. Rep.* **101,** 221 (1983).
3. Larkin, A. I. & Ovchinnikov, Yu. N. Vortex Motion in Superconductors in Nonequilibrium Superconductivity. *Elsevier Science Publishers*, pp. 493–542 (1986).
4. Rammer, J. & Smith, H. Quantum field-theoretical methods in transport theory of metals. *Rev. Mod. Phys.* **58,** 323–359 (1986).
5. Sauls, J. A. Fermi-Liquid Theory for Unconventional Superconductors. *Strongly Correlated Electronic Materials - The Los Alamos Symposium 1993*, 106–132 (Addison-Wesley Publishing Co., New York, 1994).
6. Belzig, W., Wilhelm, F. K., Bruder, C., Schön, G. & Zaikin, A. D. Quasiclassical Green's function approach to mesoscopic superconductivity. *Superlattices Microstruct.* **25,** 1251 (1999).
7. Kopnin, N. *Theory of Nonequilibrium Superconductivity* (Oxford University Press, 2009).
8. Grein, R., Eschrig, M., Metalidis, G. & Schön, G. Spin-Dependent Cooper Pair Phase and Pure Spin Supercurrents in Strongly Polarized Ferromagnets. *Phys. Rev. Lett.* **102,** 226005 (2009).
9. Eschrig, M., Cottet, A., Belzig, W. & Linder, J. General Boundary Conditions for Quasiclassical Theory of Superconductivity in the Diffusive Limit: Application to Strongly Spin-polarized Systems. *New J. Phys.* **17,** 083037 (2015).
10. Mironov, S. & Buzdin, A. I. Triplet proximity effect in superconducting heterostructures with a half-metallic layer. *arXiv:1507.02429.*
11. Eilenberger, G. Transformation of Gor'kov's equation for type II superconductors into transport-like equations. *Z. Phys.* **214,** 195 (1968).
12. Usadel, K. D. Generalized diffusion equation for superconducting alloys. *Phys. Rev. Lett.* **25,** 507 (1970).
13. Kupriyanov, M. Yu. & Lukichev, K. K. Influence of boundary transparency on the critical current of "dirty" SS'S structures. *Zh. Eksp. Teor. Fiz.* **94,** 139 (1988) [*Sov. Phys. JETP 67,* 1163 (1988)].
14. Nazarov, Yu. V. Novel circuit theory of Andreev reflection. *Superlatt. and Microstruc.* **25,** 1221 (1999).
15. Millis, A., Rainer, D. & Sauls, J. A. Quasiclassical theory of superconductivity near magnetically active interfaces. *Phys. Rev. B* **38,** 4504 (1988).
16. Tokuyasu, T., Sauls, J. A. & Rainer, D. Proximity effect of a ferromagnetic insulator in contact with a superconductor. *Phys. Rev. B* **38,** 8823 (1988),
17. Cottet, A., Huertas-Hernando, D., Belzig, W. & Nazarov, Yu. V. Spin-dependent boundary conditions for isotropic superconducting Green's functions. *Phys. Rev. B* **80,** 184511 (2009). See also their erratum *Phys. Rev. B* **83,** 139901 (2011).
18. Cren, T., Fokin, D., Debontridder, F., Dubost, V. & Roditchev, D. Ultimate Vortex Confinement Studied by Scanning Tunneling Spectroscopy. *Phys. Rev. Lett.* **102,** 127005 (2009).
19. Kim, J. *et al.* Visualization of geometric influences on proximity effects in heterogeneous superconductor thin films. *Nat. Phys.* **8,** 464 (2012).
20. Serrier-Garcia, L. *et al.* Scanning Tunneling Spectroscopy Study of the Proximity Effect in a Disordered Two-Dimensional Metal. *Phys. Rev. Lett.* **110,** 157003 (2013).
21. Cherkez, V. *et al.* Proximity Effect between Two Superconductors Spatially Resolved by Scanning Tunneling Spectroscopy. *Phys. Rev. X* **4,** 011033 (2014).
22. Stepniak, A. *et al.* Temperature dependence of the proximity effect quantified by scanning tunneling spectroscopy. *AIP Advances* **5,** 017125 (2015).
23. Schweigert, V. A. & Peeters, F. M. Phase transitions in thin mesoscopic superconducting disks. *Phys. Rev. B* **57,** 13817 (1998).
24. Schweigert, V. A., Peeters, F. M. & Deo, P. S. Vortex Phase Diagram for Mesoscopic Superconducting Disks. *Phys. Rev. Lett.* **81,** 2783 (1998).
25. Berdiyorov, G. R., Hernandez, A. D. & Peeters, F. M. Confinement Effects on Intermediate-State Flux Patterns in Mesoscopic Type-I Superconductors. *Phys. Rev. Lett.* **103,** 267002 (2009).
26. Cuevas, J. C. & Bergeret, F. S. Magnetic Interference Patterns and Vortices in Diffusive SNS Junctions. *Phys. Rev. Lett.* **99,** 217002 (2007).
27. Bergeret, F. S. & Cuevas, J. C. The Vortex State and Josephson Critical Current of a Diffusive SNS Junction. *J. Low. Temp. Phys.* **153,** 304 (2008).
28. Crouzy, B., Tollis, S. & Ivanov, D. A. Josephson current in a superconductor – ferromagnet – superconductor junction with in-plane ferromagnetic domains. *Phys. Rev. B* **76,** 134502 (2007).
29. Bakurskiy, S. V., Klenov, N. V., Karminskaya, T. Yu., Kupriyanov, M. Yu. & Golubov, A. A. Josephson φ-junctions based on structures with complex normal/ferromagnet bilayer. *Supercond. Sci. Technol.* **26,** 015005 (2013).
30. Mai, S., Kandelaki, E., Volkov, A. & Efetov, K. Stationary Josephson effect in a short multiterminal junction. *Phys. Rev. B* **87,** 024507 (2013).
31. Alidoust, M. & Halterman, K. Proximity Induced Vortices and Long-Range Triplet Supercurrents in Ferromagnetic Josephson Junctions and Spin Valves. *J. Appl. Phys.* **117,** 123906 (2015).
32. Alidoust, M., Sewell, G. & Linder, J. Non-Fraunhofer Interference Pattern in Inhomogeneous Ferromagnetic Josephson Junctions. *Phys. Rev. Lett.* **108,** 037001 (2012).
33. Hammer, J. C., Cuevas, J. C., Bergeret, F. S. & Belzig, W. Density of states and supercurrent in diffusive SNS junctions: Roles of nonideal interfaces and spin-flip scattering. *Phys. Rev. B* **76,** 064514 (2007).
34. Schopohl, N. & Maki, K. Quasiparticle spectrum around a vortex line in a *d*-wave superconductor. *Phys. Rev. B* **52,** 490 (1995).
35. Konstandin, A., Kopu, J. & Eschrig, M. Superconducting proximity effect through a magnetic domain wall. *Phys. Rev. B* **72,** 140501(R) (2005).
36. Dynes, R. C., Garno, J. P., Hertel, G. B. & Orlando, T. P. *Phys. Rev. Lett.* **53,** 2437 2440 (1984).
37. Jacobsen, S. H., Ouassou, J. A. & Linder, J. Critical temperature and tunneling spectroscopy of superconductor-ferromagnet hybrids with intrinsic Rashba-Dresselhaus spin-orbit coupling. *Phys. Rev. B* **92,** 024510 (2015).
38. Jacobsen, S. H. & Linder, J. Giant triplet proximity effect in π-biased Josephson junctions with spin-orbit coupling. *Phys. Rev. B* **92,** 024501 (2015).
39. Cook, R. D., Malkus, D. S., Plesha, M. E. & Witt, R. J. *Concepts and Applications of Finite Element Analysis*, 4th edn (John Wiley & Sons. Inc., 2002).
40. Kirk, B. S., Peterson, J. W., Stogner, R. H. & Carey, G. F. libMesh: A C++ Library for Parallel Adaptive Mesh Refinement/Coarsening Simulations. *Engineering with Computers* **22,** 3–4, pp. 237–254 (2006).
41. Balay, S. *et al.* PETSc Users Manual. ANL-95/11 - Revision 3.5 & 3.6, Argonne National Laboratory (2015).
42. Balay, S., Gropp, W. D., McInnes, L. C. & Smith, B. F. Efficient Management of Parallelism in Object Oriented Numerical Software Libraries. *Modern Software Tools in Scientific Computing*, 163–202 (Birkhäuser Press, 1997).
43. Roditchev, D. *et al.* Direct observation of Josephson vortex cores. *Nat. Phys.* **11,** 332 (2015).
44. Lange, M., Van Bael, M. J., Bruynseraede, Y. & Moshchalkov, V. V. Nanoengineered Magnetic-Field-Induced Superconductivity. *Phys. Rev. Lett.* **90,** 197006 (2003).
45. Buzdin, A. I. Density of states oscillations in a ferromagnetic metal in contact with a superconductor. *Phys. Rev. B* **62,** 11377 (2000).
46. Zareyan, M., Belzig, W. & Nazarov, Yu. V. Superconducting proximity effect in clean ferromagnetic layers. *Phys. Rev. B* **65,** 184505 (2002).

47. Kontos, T., Aprili, M., Lesueur, J. & Grison, X. Inhomogeneous Superconductivity Induced in a Ferromagnet by Proximity Effect. *Phys. Rev. Lett.* **86,** 304 (2001).
48. Yokoyama, T., Tanaka, Y. & Golubov, A. A. Manifestation of the odd-frequency spin-triplet pairing state in diffusive ferromagnet/superconductor junctions. *Phys. Rev. B* **75,** 134510 (2007).
49. Linder, J., Yokoyama, T. & Sudbø, A. Role of interface transparency and spin-dependent scattering in diffusive ferromagnet/superconductor heterostructures. *Phys. Rev. B* **77,** 174514 (2008).
50. SanGiorgio, P., Reymond, S., Beasley, M. R., Kwon, J. H. & Char, K. Anomalous Double Peak Structure in Superconductor/Ferromagnet Tunneling Density of States. *Phys. Rev. Lett.* **100,** 237002 (2008).
51. Linder, J & Robinson, J. W. A. Strong odd-frequency correlations in fully gapped Zeeman-split superconductors. *Sci. Rep.* **5,** 15483 (2015).
52. Alidoust, M. & Linder, J. φ-state and inverted Fraunhofer pattern in nonaligned Josephson junctions. *Phys. Rev. B* **87,** 060503(R) (2013).
53. Eschrig, M. Spin-polarized supercurrents for spintronics: a review of current progress. *Rep. Prog. Phys.* **78,** 104501 (2015).
54. Linder, J. & Robinson, J. W. A. Superconducting Spintronics. *Nat. Phys.* **11,** 307 (2015).

Author Contributions
M.A. developed the numerical code and performed the calculations. Both contributed to the discussion of the results and the writing of the manuscript.

Additional Information
Competing financial interests: The authors declare no competing financial interests.

How to cite this article: Amundsen, M. and Linder, J. General solution of 2D and 3D superconducting quasiclassical systems: coalescing vortices and nanoisland geometries. *Sci. Rep.* **6,** 22765; doi: 10.1038/srep22765 (2016).

Paper II

Reference

J. Linder, M. Amundsen, and J. A. Ouassou.
Microwave control of the superconducting proximity effect and minigap in magnetic and normal metals.
Scientific Reports **6**, 38739 (2016).
DOI: 10/gfgr9t

Contributions

JL did most of the analytical and numerical calculations with support from MA and JAO. All authors contributed to the discussions of the physics and the revision of the final manuscript. More specifically, MA had a minor supporting role in this collaboration, assisting with the analytical calculations, joining the discussions of the results, and contributing to the writing of the final manuscript.

SCIENTIFIC REP⚙RTS

Microwave control of the superconducting proximity effect and minigap in magnetic and normal metals

Jacob Linder, Morten Amundsen & Jabir Ali Ouassou

We demonstrate theoretically that microwave radiation applied to superconducting proximity structures controls the minigap and other spectral features in the density of states of normal and magnetic metals, respectively. Considering both a bilayer and Josephson junction geometry, we show that microwaves with frequency ω qualitatively alters the spectral properties of the system: inducing a series of resonances, controlling the minigap size E_{mg}, and even replacing the minigap with a strong peak of quasiparticle accumulation at zero energy when $\omega = E_{mg}$. The interaction between light and Cooper pairs may thus open a route to active control of quantum coherent phenomena in superconducting proximity structures.

Combining materials with different properties is a certain way to generate exciting physics at their interface. Superconducting hybrid structures are particularly interesting in this regard due to the coherent quantum correlations that give rise to dissipationless transport of both charge and, when combined with magnetic materials, spin. There is currently much interest in discovering ways to exert well-defined control the properties of such proximity structures, including the electronic density of states, the critical temperature at which superconductivity arises, and the appearance of supercurrents[1–3].

The influence of microwave radiation on superconductors has been studied in several works, and includes investigations of its effect on the critical superconducting current[4], the dissipative conductivity[5], the current-phase relation in Josephson junctions[6,7], the non-equilibrium distribution of quasiparticles[8], the photoelectric effect[9], microwave-assisted supercurrents[10], and the temperature for the onset of superconductivity[11,12]. The appearance of coherent excited states and the depairing effect of microwave radiation on dirty superconductors was very recently theoretically considered in ref. 13.

However, what remains virtually unexplored is how microwave radiation alters the superconducting proximity effect, which is the existence of superconducting correlations in an otherwise non-superconducting material when placed in contact with a superconductor, made possible due to electron tunneling between the layers. A concrete manifestation is the strong modification of the density of states, in both normal and magnetic metals proximity-coupled to a superconductor. The reason for why this is of importance is that proximity structures play a key part in creating non-conventional types of coherent electron pairing that are not present in ordinary superconductors. This includes both spin-polarized triplet superconductivity[14] and odd-frequency superconducting order[15], which recently have been experimentally demonstrated to provide diametrically opposite Meissner response[16] and low-energy spectral properties[17,18] compared to Bardeen-Cooper-Schrieffer theory[19]. From another perspective, the opportunity to manipulate low-energy excitations in superconducting proximity structures has clear practical implications for cryogenic technology since it controls the availability of spin- and charge-carriers. In fact, quasiparticles in superconductors can become nearly chargeless spin-1/2 carriers, leading to effects such as[20–24] strongly enhanced spin lifetimes and spin relaxation lengths when compared to injection of spin-polarized currents into normal metals, especially when using Zeeman split superconductors (a thin superconducting film in the presence of an in-plane magnetic field)[25]. This, in turn, allows one to envision various types of devices such as highly sensitive magneto- and thermometers as well as superconducting magnetoresistive elements.

Department of Physics, NTNU, Norwegian University of Science and Technology, N-7491 Trondheim, Norway. Correspondence and requests for materials should be addressed to J.L. (email: jacob.linder@ntnu.no)

In this work, we show that shining light on superconducting hybrid structures offers a way to control the proximity effect in both normal metals and magnetic materials. We discover that an oscillating electric field $\mathcal{E}(t)$ applied transversely to the junction induces a series of resonances in the density of states, and that it can be used to control the size of the minigap E_{mg} in both bilayer superconductor/normal-metal (SN) and Josephson (SNS) junctions. The light interaction even inverts the minigap, generating a peak of quasiparticle accumulation at $E = 0$ when the frequency of the light is tuned to $\omega = E_{mg}$. These findings give interesting prospects for transistor-like functionality via light-superconductor interactions since the density of states controls the availability of charge- and spin-carriers. Providing both analytical and numerical results, including the case of a magnetic exchange-field being present in the metal or in the superconductor, we show how the interaction between light and Cooper pairs controls the low-energy density of states, offering a new way to manipulate superconducting correlations. This may open a new pathway to active control of quantum coherent phenomena in superconducting proximity structures.

Theory

We use the time-dependent quasiclassical Keldysh-Usadel theory[26–29] to describe the superconductivity of these systems in the diffusive limit. We begin with the SN bilayer, in which case superconducting correlations leak into the normal metal via the proximity effect. The electric field $\mathcal{E}(t) = \omega A_0 \sin(\omega t) = -\partial A/\partial t$ is accounted for by the gauge field $A = A_0 \cos(\omega t)$. The Usadel equation in N then reads:

$$D\partial_x(\hat{g}\partial_x\hat{g}) + i\left[E\hat{\rho}_3 + i\alpha\hat{\rho}_3(\hat{g}_+ + \hat{g}_-)\hat{\rho}_3, \hat{g}\right] = 0. \tag{1}$$

Here, D is the diffusion coefficient, $\hat{g} = \hat{g}(x, E)$ is the quasiclassical time-averaged Green function, E is the quasiparticle energy, $\alpha = DA_0^2/4$ is a measure of the strength of the interaction with light, ω is the driving frequency, $\hat{\rho}_3 = \text{diag}(+1, +1, -1, -1)$, while $\hat{g}_\pm \equiv \hat{g}(x, E \pm \omega/2)$. The derivation of this equation is shown in the Methods section and is valid when $\alpha \ll \omega$. We assume that the field is screened in the S region, which is taken to have a size and thickness far exceeding the superconducting coherence length ξ and penetration depth λ, allowing us to use the bulk superconducting Green function $\hat{g}_{BCS}$ there. Practically, our proposed setup could be realized by depositing a thick superconductor to partially cover a thin normal metal layer, such that the microwave field penetrates the normal layer where it is not covered by a superconductor whereas it is shielded in the superconductor (see the inset of e.g. Fig. 1). Such a lateral geometry should be well described by an effective 1D model, as done in ref. 30. The thickness of the N layer should be much smaller than the skin depth and penetration depth λ, which is experimentally feasible (typical values for the skin depth of a normal metal such as Cu is of order μm at microwave frequencies, whereas $\lambda_{Nb} \sim 50$ nm and $\lambda_{Al} \sim 20$ nm). From Eq. (1), we derive the following Ricatti-parametrized[31,32] Usadel equation:

$$D[\partial_x^2\gamma + 2(\partial_x\gamma)\widetilde{\mathcal{N}}\tilde{\gamma}(\partial_x\gamma)] + 2i(E + i\delta)\gamma + i(\boldsymbol{h}\cdot\boldsymbol{\sigma})\gamma - i\gamma(\boldsymbol{h}\cdot\boldsymbol{\sigma}^*) - \alpha G\gamma - \alpha\gamma\widetilde{G} + \alpha(F + \gamma\widetilde{F}\gamma) = 0. \tag{2}$$

The Green function $\hat{g}$ can then be calculated from the 2×2 matrix γ in spin space, the normalization matrix $\mathcal{N} \equiv (1 - \gamma\tilde{\gamma})^{-1}$, and their tilde-conjugates defined by $\tilde{f}(x, E) \equiv f^*(x, -E)$. An equivalent equation for $\tilde{\gamma}$ can be found by tilde-conjugation of Eq. (2). In Eq. (2), we have also incorporated the possibility of a magnetic exchange field $h = |\boldsymbol{h}|$ which allows us to later consider the case of a ferromagnetic metal. The other quantities in the equation are the inelastic scattering rate δ, and the short-hand notations

$$G \equiv \sum_\pm \mathcal{N}_\pm(1 + \gamma_\pm\tilde{\gamma}_\pm), \quad F \equiv -2\sum_\pm \mathcal{N}_\pm\gamma_\pm, \tag{3}$$

where $\gamma_\pm \equiv \gamma(x, E \pm \omega/2)$. From these equations, physical quantities of interest may be computed, such as the proximity-modified density of states

$$N/N_0 = \text{Re}\{\text{Tr}(\mathcal{N})\} - 1. \tag{4}$$

The Usadel equation is supplemented by the Kupriyanov-Lukichev boundary conditions[33], which are valid at low-transparency tunneling interfaces.

We now have at hand a coupled set of non-linear partial differential equations which are non-local in energy space. A numerical solution can be obtained via iteration. After discretizing the energy space, the equations are initially solved for $\alpha = 0$. The procedure is then repeated with $\alpha \neq 0$ until self-consistency is achieved, using the solutions γ and $\tilde{\gamma}$ from the previous iteration to approximate G and F. In this way, we are able to compute the quasiclassical Green function in the presence of microwave radiation, $\hat{g}(\alpha \neq 0)$, and access the density of states N/N_0 in the proximate metal.

Results and Discussion

The light-interaction with the proximity-induced condensate has a strong effect on the spectral properties of the quasiparticles. We show this in what follows, considering an SN bilayer in Fig. 1, an SNS junction in Fig. 2, and an SF bilayer in Fig. 3. In each case, we have provided results for different system parameters in order to demonstrate the robustness of the microwave radiation influence.

Starting with the SN bilayer, it is seen that by tuning the microwave frequency ω, the density of states takes on qualitatively different characteristics. At $\omega/\Delta_0 = 0.4$, there is a strong quasiparticle accumulation at $E = 0$, diametrically opposite to the hallmark minigap that usually is present in SN bilayers. Increasing ω gradually to $\omega/\Delta_0 = 1.0$ causes the density of states to revert to a minigap structure, albeit with a much reduced magnitude. We
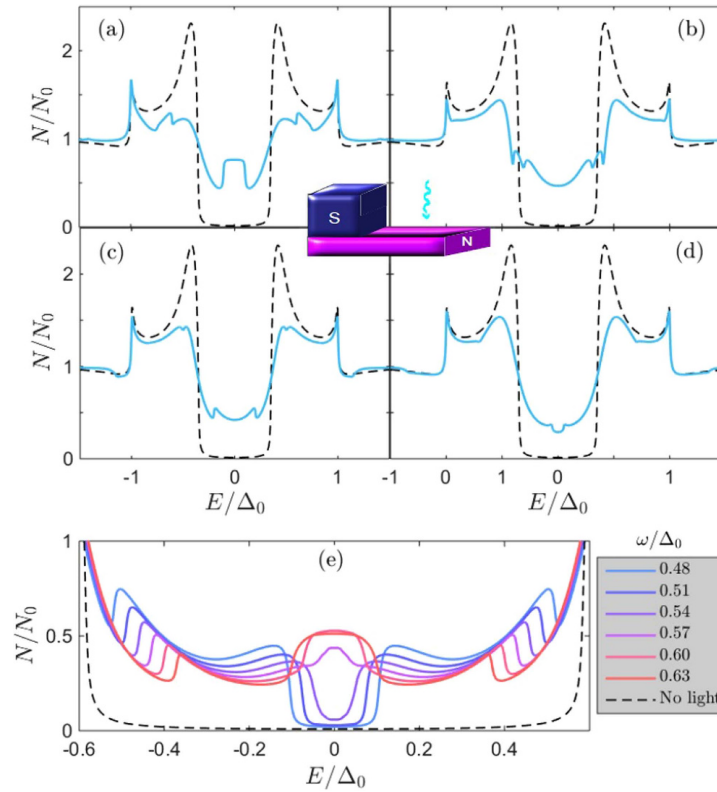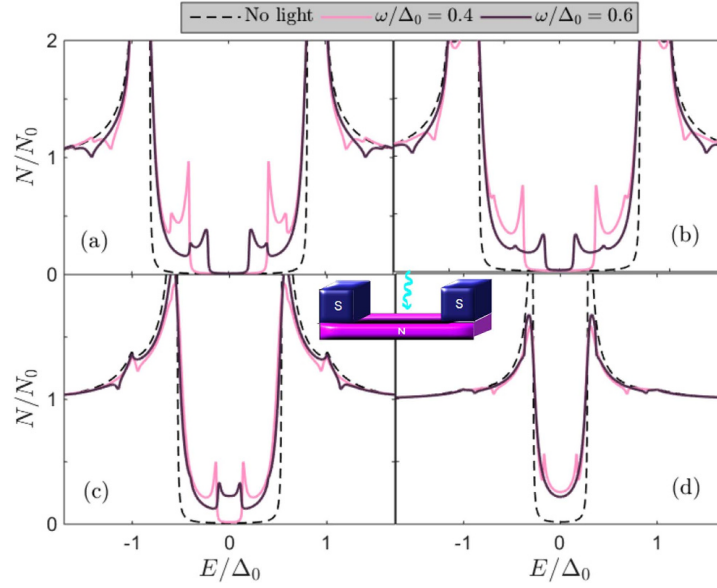
Figure 1. (**a–d**) Proximity-induced density of states at the vacuum edge ($x = L$) of an SN bilayer with length $L/\xi = 0.5$ of the N region, where ξ is the superconducting coherence length. We set the barrier strength $\zeta = 3$ and microwave field amplitude $\alpha/\Delta_0 = 0.1$ and (**a**) $\omega/\Delta_0 = 0.4$, (**b**) $\omega/\Delta_0 = 0.6$, (**c**) $\omega/\Delta_0 = 0.8$, (**d**) $\omega/\Delta_0 = 1.0$. (**e**) Zoom-in near $E = 0$ illustrating the transition from minigap to quasiparticle accumulation peak as ω is tuned to E_{mg}. We set $L/\xi = 0.33$, yielding $E_{\mathrm{mg}} \simeq 0.56\Delta_0$. The black dashed line corresponds to the absence of light, $A = 0$.

will later in this manuscript describe the precise condition leading to the appearance of the quasiparticle accumulation peak and its physical origin, providing also analytical results which supports the underlying explanation. In the plots, we have set $\alpha/\Delta_0 = 0.1$, which gives a maximum ratio of $\alpha/\omega = 0.25$, so that α is always considerably smaller than ω. The criterion $\alpha \ll \omega$ is, however, more strictly satisfied at the higher frequency range considered in the figures.

The minigap itself is monotonically tuned with ω, as shown in Fig. 2 for the SNS case. At zero phase difference ϕ, the minigap is gradually reduced as ω increases, demonstrating that the driving frequency can be used to tailor the minigap size. At a finite phase difference, the light-interaction again inverts the minigap for certain frequencies, and generates a peak of quasiparticle accumulation at $E = 0$, similarly to the bilayer case [see Fig. 1(e)]. This can be seen in Fig. 2(c) for $\phi/\pi = 0.5$. Finally, we show results for when an exchange field is present, i.e. a magnetic metal $h \neq 0$, in Fig. 3, in which case the microwave field also alters the modulation of the density of states. To facilitate comparison with experiments, we note that for a typical diffusion constant of *e.g.* $D = 7 \times 10^{-3}\,\mathrm{m^2/s}$ in Cu[34], the requirement $\omega \gg De^2A_0^2/4\hbar^2$ (having reinstated e and $\hbar$) corresponds to $\omega \gg 0.3\,\mathrm{GHz}$ for a modest electric field magnitude of 0.1 V/m, which is feasible. Moreover, for a superconducting gap $\Delta_0 = 0.5\,\mathrm{meV}$, the parameter choice $\hbar\omega/\Delta_0 = 0.4$ corresponds to a frequency $\omega \simeq 300\,\mathrm{GHz}$.

Besides the control and inversion of the minigap, another particularly noteworthy feature that all the above-mentioned structures have in common is that the low-energy density of states features a series of spectral features resembling weak resonances, which vanish as soon as the microwave field is turned off ($\alpha = 0$). To gain insight into the physical origin of these features seen in the density of states, we provide an analytical solution which is permissible in the ferromagnetic case, but which also seems to account for the nature of the light interaction with the superconducting condensate in the normal case ($h = 0$). In the weak proximity effect regime, the linearized equation governing the behavior of the spinless f_s and spin-polarized f_t Cooper pairs reads

Figure 2. Proximity-induced density of states in the middle ($x = L/2$) of an SNS Josephson junction with $L/\xi = 0.33$, barrier strength $\zeta = 3$, microwave field amplitude $\alpha/\Delta_0 = 0.1$, and (**a**) $\phi/\pi = 0.0$, (**b**) $\phi/\pi = 0.25$, (**c**) $\phi/\pi = 0.5$, (**d**) $\phi/\pi = 0.75$.
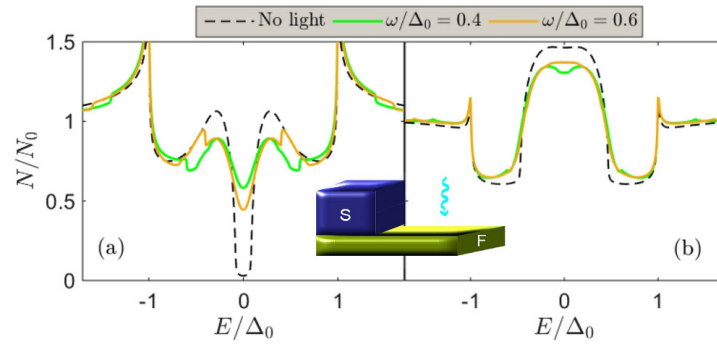
Figure 3. Proximity-induced density of states at the vacuum edge ($x = L$) of an SF bilayer with $L/\xi = 0.23$, barrier strength $\zeta = 3$, microwave field amplitude $\alpha/\Delta_0 = 0.1$, and (**a**) $h/\Delta_0 = 2$ and (**b**) $h/\Delta_0 = 4$.

$$D\partial_x^2 f_\pm(E) + 2i(E + 2i\alpha \pm h)f_\pm(E) - 2\alpha[f_\pm(E + \omega) + f_\pm(E - \omega)] = 0 \qquad (5)$$

with $f_\pm = f_t \pm f_s$. In the regime where $h \gg \{E, \Delta_0\}$, as is usually the case for ferromagnets, one can solve the above equation via Fourier-transformation. Introducing $\mathcal{F}_\pm(t) = \int dE\, e^{iEt} f_\pm(E)$, one obtains

$$D\partial_x^2 \mathcal{F}_\pm(t) + 2i(2i\alpha \pm h)\mathcal{F}_\pm(t) - 4\alpha \cos(\omega t)\mathcal{F}_\pm(t) = 0.$$

The solution is $\mathcal{F}_\pm(t) = A_\pm(t)e^{ik_\pm x} + B_\pm(t)e^{-ik_\pm x}$, where

$$k_\pm = \sqrt{[2i(2i\alpha \pm h) - 4\alpha \cos(\omega t)]D^{-1}}, \qquad (6)$$

while the coefficients $\{A_\pm, B_\pm\}$ are determined via the boundary conditions. For an SF bilayer, the boundary conditions read $\partial_x f_\pm = \pm f_{\mathrm{BCS}}/\zeta L$ at the superconducting interface ($x = 0$), and $\partial_x f_\pm = 0$ at the vacuum border
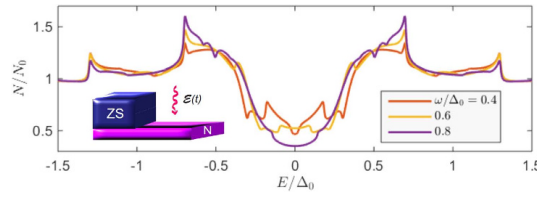
Figure 4. Proximity-induced density of states at the vacuum edge ($x=L$) of a Zeeman-split superconductor/normal-metal bilayer. We set $\zeta=3$, $\alpha/\Delta_0=0.1$, $L/\xi=0.5$, and $h_s/\Delta_0=0.3$, and considered several frequencies of the microwave radiation.

($x=L$), where $\zeta=R_B/R$ is the ratio between the interface barrier resistance and bulk resistance and $f_{\mathrm{BCS}}(E)=\sinh\{\mathrm{atanh}[1/(E+\mathrm{i}\delta)]\}$.

Introducing the auxiliary quantity $D(t)=\int dE\,\mathrm{e}^{\mathrm{i}Et}f_{\mathrm{BCS}}(E)$, a straight-forward calculation leads to

$$A_\pm(t)=\frac{\mp D(t)}{\zeta L\mathrm{i}k_\pm(1-\mathrm{e}^{2\mathrm{i}k_\pm L})},\quad B_\pm(t)=A_\pm(t)\mathrm{e}^{2\mathrm{i}k_\pm L}.\tag{7}$$

Inserting this into our expression for $\mathcal{F}_\pm(t)$ and performing an inverse Fourier-transformation, we end up with the final expression for $f_\pm(E)$:

$$f_\pm(E)=\mp\iint dt\,dE'\,\mathrm{e}^{\mathrm{i}(E'-E)t}f_{\mathrm{BCS}}(E')\,p_\pm(t).\tag{8}$$

where we introduced

$$p_\pm(t)=\cos\,[k_\pm(x-L)]\,[\zeta Lk_\pm\,\sin(k_\pm L)]^{-1}\tag{9}$$

and $k_\pm=k_\pm(t)$. We note that $p_\pm(t)$ is a periodic function in t, while $f_{\mathrm{BCS}}\to 0$ when $E\to\pm\infty$. In the absence of microwave radiation ($\alpha=0$), $k_\pm$ becomes independent of t, and the above simplifies to the usual result $f_\pm(E)=\mp p_\pm\iint dt\,dE'\,\mathrm{e}^{\mathrm{i}(E'-E)t}f_{\mathrm{BCS}}(E')=\mp p_\pm f_{\mathrm{BCS}}(E)$. To solve the integral Eq. (8) in the general case, we make use of the periodicity of $p_\pm(t)$. The period is $T=2\pi/\omega$, so we can write the Fourier series $p_\pm(t)=\sum_n p_{n,\pm}\mathrm{e}^{\mathrm{i}n\omega t}$, where $p_{n,\pm}=\frac{1}{T}\int_{-T/2}^{+T/2}dt\,p_\pm\mathrm{e}^{-\mathrm{i}n\omega t}$. Performing the integral over t in Eq. (8) then leads to a sum over δ-functions, and one obtains:

$$f_\pm(E)=\mp\sum_{n=-\infty}^{n=+\infty}p_{n,\pm}f_{\mathrm{BCS}}(E-n\omega).\tag{10}$$

Numerically, we find that it is usually sufficient with ~15 Fourier-coefficients $p_{n,\pm}$ to obtain a perfect representation of $p_\pm(t)$. Using the same procedure as above, one can also find an expression for the anomalous Green function in a Josephson geometry consisting of a superconductor/ferromagnet/superconductor trilayer. The only difference is the expression for $p_\pm(t)$, which takes the form

$$p_\pm(t)=\{[\cos(k_\pm x)+\mathrm{e}^{\mathrm{i}\phi}\cos[k_\pm(x-L)]\}[\zeta Lk_\pm\,\sin(k_\pm L)]^{-1},\tag{11}$$

where ϕ is the phase difference between the superconductors.

From the analytical expression, it is clear that resonances should be expected whenever $E=\Delta_0\pm n\omega$, $n=0,1,2,\dots$ since $f_{\mathrm{BCS}}(E=\Delta_0)$ formally diverges, although this divergence is in practice diminished due to inelastic scattering. The weight of these resonances, i.e. the magnitude of their spectral peak, is in turn governed by the Fourier series coefficients p_n which depends on the other system parameters. We note that, very recently, similar features were reported for a narrow and thin dirty superconducting strip subject to microwave radiation in ref. 13. In the present proximity-system, there is an additional minigap E_{mg} in the system, and one might expect to have similar resonances at $E=E_{\mathrm{mg}}\pm n\omega$. The density of states plots in Fig. 2 [see for instance (a) for $\omega/\Delta_0=0.4$] are consistent with this statement, demonstrating how additional spectral features, which are not present in the absence of light, occur at such excitation energies. It actually turns out that these resonances are the physical origin behind the transition from the minigap to the quasiparticle accumulation peak at $E=0$. To be exact, the transition from fully gapped DOS to a strong zero-energy peak occurs precisely when $\omega=E_{\mathrm{mg}}$. We show an example of this behavior at the bottom of Fig. 1. It is intriguing that the light-interaction actually induces a second, inner minigap which upon closing generates this feature, whereas the outer minigap E_{mg} remains [see *e.g.* Fig. 2(a) showing a particularly clear example of the inner and outer minigaps].

The fact that the microwave radiation induces a series of weak resonances shifted with $\pm n\omega$ from the conventional spectral peaks ($E=\Delta$ and $E=E_{\mathrm{mg}}$ in the normal metal case) has interesting consequences when a finite magnetic field splits the density of states in the superconductor[35], since the exchange field in the superconductor h_S itself produces a similar shift in the spectral peaks from Δ_0 to $\Delta_0\pm h_S$. We show the corresponding proximity-induced density of states in Fig. 4, where the combined influence of the exchange field and the light

interaction produce a very rich subgap structure in the density of states. Since the superconductor in this particular case, unlike the previous systems considered in this work, has to be sufficiently thin to permit the homogeneous penetration of a magnetic field, the microwave field is not completely shielded by the superconductor and we thus here assumed that $\mathcal{E}(t)$ is applied only to the non-superconducting part.

The most remarkable feature is nevertheless the influence of the microwave field on the minigap in the SN case, controlling its magnitude and even transforming it into a quasiparticle accumulation peak at $E = 0$. These results may represent the first step toward a different way to control the superconducting proximity effect, and thus the available spin- and charge-carriers, in normal and magnetic metals, by using microwave radiation. One advantage of this is the fact that the control is *in situ* and that the length of the system (setting the Thouless energy scale), which normally changes the minigap, does not have to be altered, which would inevitably require fabrication of multiple samples. The zero-energy peak induced by the light-interaction resembles the type of spectral feature that is characteristically seeen in the density of states of conventional SF structures due to odd-frequency superconductivity[36–38], but in this case it occurs without any such pairing at all. It could also be of interest to examine the consequences of the predictions made herein with regard to conductivity experiments[39] and non-equilibrium Josephson contacts[40].

Concluding remarks

Building on these results, an interesting future direction to explore would be the influence of light on supercurrents and the critical temperature in magnetic proximity systems, to see if the microwave radiation may be used to manipulate these quantities as well, which we intend to explore in a future work. The interaction between light and Cooper pairs could in this way open a different route to active control of quantum coherent phenomena in superconducting proximity structures.

Methods

Derivation of the Usadel equation incorporating microwave radiation. The time-dependent Usadel equation may be written as

$$D\overline{\nabla}\circ(\hat{g}\circ\overline{\nabla}\circ\hat{g}) = -i[E\hat{\rho}_3 \overset{\circ}{,} \hat{g}],\tag{12}$$

where we defined the gauge-covariant derivative

$$\overline{\nabla}\circ\hat{g} \equiv \nabla\hat{g} - ie[A\hat{\rho}_3 \overset{\circ}{,} \hat{g}],\tag{13}$$

the commutator $[a \overset{\circ}{,} b] \equiv a\circ b - b\circ a$, and the associated product

$$(a\circ b)(E,\,T) \equiv e^{i\left(\partial_{E_1}\partial_{T_2} - \partial_{E_2}\partial_{T_1}\right)/2} a(E_1,\,T_1) \times b(E_2,\,T_2)\Big|_{E_1=E_2=E,T_1=T_2=T}.\tag{14}$$

Above, e is the electron charge, E is the quasiparticle energy, and A is the time-dependent vector potential which describes, in our case, an ac electric field $E = -\partial A/\partial t$. We note that a useful property of the $\circ$-product is that:

$$a(E,\,T)\circ e^{i\omega T} = e^{i\omega T}a(E - \omega/2,\,T),\quad e^{i\omega T}\circ a(E,\,T) = e^{i\omega T}a(E + \omega/2,\,T).\tag{15}$$

These relations are useful in the present context since we can write the gauge field as

$$A(T) = A_0(e^{i\omega T} + e^{-i\omega T})/2.\tag{16}$$

We set $|e| = 1$ in what follows for brevity of notation and also apply the electric field perpendicularly to the junction direction, so that

$$\nabla \cdot \boldsymbol{A} = \boldsymbol{A} \cdot \nabla = 0.\tag{17}$$

In this case, the left hand side of Eq. (12) becomes

$$D\nabla \cdot (\hat{g}\circ\nabla\hat{g}) - D[A\hat{\rho}_3 \overset{\circ}{,} \hat{g}\circ A\hat{\rho}_3\circ\hat{g} - A\hat{\rho}_3].\tag{18}$$

Since $\boldsymbol{A} = \boldsymbol{A}(T)$ is independent on E we have

$$A\hat{\rho}_3 A\hat{\rho}_3 = A^2\hat{1}.\tag{19}$$

Moreover, the Green function satisfies the normalization condition

$$\hat{g}\circ\hat{g} = \hat{1}.\tag{20}$$

This brings us to

$$D\nabla \cdot (\hat{g}\circ\nabla\hat{g}) - D[A\hat{\rho}_3\circ\hat{g}\circ A\hat{\rho}_3 \overset{\circ}{,} \hat{g}].\tag{21}$$

At this stage, we see that the contribution from the gauge field can be included as a self-energy

$$\hat{\Sigma}_A = iD\boldsymbol{A}\hat{\rho}_3 \circ \hat{g} \circ \boldsymbol{A}\hat{\rho}_3 \qquad (22)$$

in the Usadel equation, which in its complete form reads:

$$D\nabla \cdot (\hat{g}\circ\nabla\hat{g}) + i[E\hat{\rho}_3 + iD\boldsymbol{A}\hat{\rho}_3\circ\hat{g}\circ\boldsymbol{A}\hat{\rho}_3, \hat{g}] = 0. \qquad (23)$$

The next step is the obtain the Fourier-transformed version of the above equation in energy-space. To accomplish this, we make use of similar approximations as in ref. 13. In the presence of a driving field $A(T)$, we take into account A up to second order by deriving an equation for the harmonic Green function at zero frequency (see Appendix of ref. 13) which is essentially the time-averaged Green function. Higher order harmonic time-dependent terms in $\hat{g}$ are induced by A and thus correspond to fourth order in A and higher. This approximation is valid when

$$DA_0^2/4 \ll \omega. \qquad (24)$$

Computing the contribution from the self-energy term $\hat{\Sigma}_A$ in the Usadel equation gives

$$
\begin{aligned}
i[\hat{\Sigma}_A, \hat{g}] &= -\frac{DA_0^2}{4}[(e^{i\omega T} + e^{-i\omega T})\hat{\rho}_3\circ\hat{g}\circ(e^{i\omega T} + e^{-i\omega T})\hat{\rho}_3\circ\hat{g} \\
&\quad - \hat{g}\circ(e^{i\omega T} + e^{-i\omega T})\hat{\rho}_3\circ\hat{g}\circ(e^{i\omega T} + e^{-i\omega T})\hat{\rho}_3].
\end{aligned}
\qquad (25)
$$

We now average Eq. (25) over a period $2\pi/\omega$, which means that all terms that go like $e^{\pm 2i\omega T}$ are removed since $\hat{g}$ is the time-averaged Green function. After laborious calculations, using for instance that

$$
\begin{aligned}
& e^{i\partial_{E_1}\partial_{T_2}/2}\left[1 - \frac{i}{2}\partial_{E_2}\partial_{T_1} + \frac{1}{2}\left(\frac{i}{2}\right)^2(\partial_{E_2}\partial_{T_1})^2 - \dots\right]e^{\pm i\omega T_1}\hat{\rho}_3\hat{g}(E_1 \pm \omega/2)\,e^{\mp i\omega T_2} \\
& \times \hat{\rho}_3\hat{g}(E_2 \mp \omega/2)\big|_{E_1 = E_2 = E, T_1 = T_2 = T}. \\
&= e^{i\partial_{E_1}\partial_{T_2}/2}\left[1 \mp \frac{i}{2}(i\omega)\,\partial_{E_2} + \frac{1}{2}\left(\frac{\omega}{2}\right)^2(\partial_{E_2})^2 - \dots\right]e^{\pm i\omega T_1} \\
& \times \hat{\rho}_3\hat{g}(E_1 \pm \omega/2)\,e^{\mp i\omega T_2}\hat{\rho}_3\hat{g}(E_2 \mp \omega/2)\big|_{E_1 = E_2 = E, T_1 = T_2 = T}. \\
&= e^{i\partial_{E_1}\partial_{T_2}/2}e^{\pm i\omega T_1}e^{\mp i\omega T_2}\hat{\rho}_3\hat{g}(E_1 \pm \omega/2)\,\hat{\rho}_3\hat{g}(E_2)\big|_{E_1 = E_2 = E, T_1 = T_2 = T}. \\
&= \hat{\rho}_3\hat{g}(E \pm \omega)\,\hat{\rho}_3\hat{g}(E)
\end{aligned}
\qquad (26)
$$

via Eq. (15), the remaining terms take the form

$$D\nabla \cdot (\hat{g}\nabla\hat{g}) + i\big[E\hat{\rho}_3 + i\alpha\hat{\rho}_3(\hat{g}_+ + \hat{g}_-)\hat{\rho}_3, \hat{g}\big] = 0, \qquad (27)$$

where the $\circ$-commutators are now replaced with regular matrix commutators, $\alpha \equiv DA_0^2/4$, $\hat{g} = \hat{g}(x, E)$ is the quasiclassical Green function, while

$$\hat{g}_\pm \equiv \hat{g}(x, E \pm \omega/2). \qquad (28)$$

Derivation of the linearized Usadel equation (weak proximity effect). Analytical progress can be made in the so-called weak proximity effect regime, where one assumes that the magnitude of the superconducting proximity effect is small in the sense that the anomalous Green function components f satisfy $|f| \ll 1$. Physically, such a situation is realized either in the case of a low interface transparency between the superconducting and normal part or if the critical temperature is close to the critical temperature of the superconductor. This allows for a linearization of the Usadel equation in the anomalous Green functions in the following manner[3]. The total Green function matrix in Nambu-spin space may be written as the normal-state matrix $\hat{g}_0$ and a small deviation $\hat{f}$:

$$\hat{g} \simeq \hat{g}_0 + \hat{f}, \qquad (29)$$

where $\hat{g}_0 = \hat{\rho}_3$ and the anomalous Green function matrix can be written as

$$\hat{f} = \begin{pmatrix} \underline{0} & \underline{f} \\ -\underline{\tilde{f}} & \underline{0} \end{pmatrix}. \qquad (30)$$

The 2×2 matrix $\underline{f}$ in spin space describes the four types of anomalous Green functions that can be present in the system: one describing spin-singlet Cooper pairs (f_s) and three describing spin-triplet Cooper pairs ($f_{\uparrow\uparrow}, f_{\downarrow\downarrow}, f_t$). The f_t component corresponds to the $S = 1$, $S_z = 0$ component of the triplets with spin-symmetry $\uparrow\downarrow + \downarrow\uparrow$ and the $\sim$ operation is defined in the main text. For the systems considered in our work, with homogene-

ous exchange fields, we find that $f_{\sigma\sigma} = 0$ whereas f_s and f_t can be non-zero. Inserting Eq. (29) into Eq. (2) in the main manuscript produces the linearized equation

$$D\partial_x^2 f_\pm(E) + 2i(E + 2i\alpha \pm h)f_\pm(E) - 2\alpha[f_\pm(E + \omega) + f_\pm(E - \omega)] = 0 \qquad (31)$$

with $f_\pm = f_t \pm f_s$. This governs the behavior of the spinless f_s and spin-polarized f_t Cooper pairs induced in the normal metal.

References

1. J. Linder & J. W. A. Robinson. Superconducting spintronics. *Nat. Phys.* **11**, 307 (2015).
2. J. W. A. Robinson & M. G. Blamire. The interface between superconductivity and magnetism: understanding and device prospects. *J. Phys.: Cond. Mat.* **26**, 453201 (2014).
3. M. Eschrig. Spin-polarized supercurrents for spintronics: a review of current progress. *Rep. Prog. Phys.* **78**, 10 (2015).
4. I. O. Kulik. Nonlinear High-frequency Properties of Thin Superconducting Films. *Sov. Phys. JETP* **30**, 329 (1970).
5. A. Gurevich. Reduction of Dissipative Nonlinear Conductivity of Superconductors by Static and Microwave Magnetic Fields. *Phys. Rev. Lett.* **113**, 087001 (2014).
6. F. S. Bergeret, P. Virtanen, T. T. Heikkilä & J. C. Cuevas. Theory of Microwave-Assisted Supercurrent in Quantum Point Contacts. *Phys. Rev. Lett.* **105**, 117001 (2010).
7. F. Kos, S. E. Nigg & L. I. Glazman. Frequency-dependent admittance of a short superconducting weak link. *Phys. Rev. B* **87**, 174521 (2013).
8. P. Virtanen, T. T. Heikkilä & F. S. Bergeret. Stimulated quasiparticles in spin-split superconductors. *Phys. Rev. B* **93**, 014512 (2016).
9. M. S. Kalenkov & A. D. Zaikin. Diffusive superconductors beyond the Usadel approximation: Electron-hole asymmetry and large photoelectric effect. *Phys. Rev. B* **92**, 014507 (2015).
10. P. Virtanen *et al.* Theory of Microwave-Assisted Supercurrent in Diffusive SNS Junctions. *Phys. Rev. Lett.* **104**, 247003 (2010).
11. J. E. Mooij. In *Nonequilibrium Superconductivity, Phonons and Kapitza Boundaries*, edited by K. E. Gray (Plenum, New York, 1981).
12. V. M. Dmitriev, V. N. Gubankov & F. Y. Nad. In *Nonequilibrium Superconductivity*, edited by D. N. Langenberg & A. I. Larkin (North-Holland, Amsterdam 1986).
13. A. V. Semenov, I. A. Devyatov, P. J. de Visser & T. M. Klapwijk. Coherent Excited States in Superconductors due to a Microwave Field. *Phys. Rev. Lett.* **117**, 047002 (2016).
14. A. P. Mackenzie & Y. Maeno. The superconductivity of Sr_2RuO_4 and the physics of spin-triplet pairing. *Rev. Mod. Phys.* **75**, 657 (2003).
15. V. L. Berizinskii. New model of the anisotropic phase of superfluid He^3. *JETP Lett.* **20**, 287 (1974).
16. A. Di Bernardo *et al.* Intrinsic Paramagnetic Meissner Effect Due to *s*-Wave Odd-Frequency Superconductivity. *Phys. Rev. X* **5**, 041021 (2015).
17. A. Di Bernardo *et al.* Signature of magnetic-dependent gapless odd frequency states at superconductor/ferromagnet interfaces. *Nat. Commun.* **6**, 8053 (2015).
18. Y. Kalcheim, O. Millo, A. Di Bernardo, A. Pal & J. W. A. Robinson. Inverse proximity effect at superconductor-ferromagnet interfaces: Evidence for induced triplet pairing in the superconductor. *Phys. Rev. B* **92**, 060501(R) (2015).
19. J. Bardeen, L. N. Cooper & J. R. Schrieffer. Theory of Superconductivity. *Phys. Rev.* **108**, 1175 (1957).
20. T. Yamashita, S. Takahashi, H. Imamura & S. Maekawa. Spin transport and relaxation in superconductors. *Phys. Rev. B* **65**, 172509 (2002).
21. H. Yang, S.-H. Yang, S. Takahashi, S. Maekawa & S. S. P. Parkin. Extremely long quasiparticle spin lifetimes in superconducting aluminium using MgO tunnel spin injectors. *Nature Mater.* **9**, 586 (2010).
22. C. H. L. Quay, D. Chevallier, C. Bena & M. Aprili. Spin imbalance and spin-charge separation in a mesoscopic superconductor. *Nature Phys.* **9**, 84 (2013).
23. F. Hübler, M. J. Wolf, D. Beckmann & H. v. Löhneysen. Long-range spin-polarized quasiparticle transport in mesoscopic Al superconductors with a Zeeman splitting. *Phys. Rev. Lett.* **109**, 207001 (2012).
24. T. Wakamura, N. Hasegawa, K. Ohnishi, Y. Niimi & Y. Otani. Spin injection into a superconductor with strong spin-orbit coupling. *Phys. Rev. Lett.* **112**, 036602 (2014).
25. D. Beckmann. Spin manipulation in nanoscale superconductors. *J. Phys. Cond. Mat.* **28**, 163001 (2016).
26. J. Rammer & H. Smith. Quantum field-theoretical methods in transport theory of metals. *Rev. Mod. Phys.* **58**, 323 (1986).
27. W. Belzig, F. K. Wilhelm, C. Bruder, G. Schön & A. D. Zaikin. Quasiclassical Green's function approach to mesoscopic superconductivity. *Superlattices Microstruct.* **25**, 1251 (1999).
28. V. Chandrasekhar. *An introduction to the quasiclassical theory of superconductivity for diffusive proximity-coupled systems*, Chapter published in, "The Physics of Superconductors", Vol II, edited by Bennemann & Ketterson, Springer-Verlag (2004).
29. K. Usadel. Generalized Diffusion Equation for Superconducting Alloys. *Phys. Rev. Lett.* **25**, 507 (1970).
30. H. le Sueur *et al.* Phase Controlled Superconducting Proximity Effect Probed by Tunneling Spectroscopy. *Phys. Rev. Lett.* **100**, 197002 (2008).
31. N. Schopohl & K. Maki. Quasiparticle spectrum around a vortex line in a d-wave superconductor. *Phys. Rev. B.* **52**, 490 (1995).
32. N. Schopohl. Transformation of the Eilenberger Equations of Superconductivity to a Scalar Riccati Equation. arXiv:cond-mat/9804064.
33. M. Y. Kupriyanov & V. F. Lukichev. Influence of boundary transparency on the critical current of "dirty" SS'S structures. *Sov. Phys. JETP* **67**, 1163 (1988).
34. S. Gueron *et al.* Superconducting Proximity Effect Probed on a Mesoscopic Length Scale. *Phys. Rev. Lett.* **77**, 3025 (1996).
35. R. Meservey, P. M. Tedrow & P. Fulde. Magnetic Field Splitting of the Quasiparticle States in Superconducting Aluminum Films. *Phys. Rev. Lett.* **25**, 1270 (1970).
36. T. Kontos, M. Aprili, J. Lesueur & X. Grison. Inhomogeneous Superconductivity Induced in a Ferromagnet by Proximity Effect. *Phys. Rev. Lett.* **86**, 304 (2001).
37. T. Yokoyama, Y. Tanaka & A. A. Golubov. Manifestation of the odd-frequency spin-triplet pairing state in diffusive ferromagnet/superconductor junctions. *Phys. Rev. B* **75**, 134510 (2007).
38. J. Linder, A. Sudbø, T. Yokoyama, R. Grein & M. Eschrig. Signature of odd-frequency pairing correlations induced by a magnetic interface. *Phys. Rev. B* **81**, 214504 (2010).
39. M. S. Pambianchi, S. N. Mao & S. M. Anlage. Microwave surface impedance of proximity-coupled Nb/Al bilayer films. *Phys. Rev. B* **52**, 4477 (1995).
40. J. J. A. Baselmans, A. F. Morpurgo, B. J. van Wees & T. M. Klapwijk. Reversing the direction of the supercurrent in a controllable Josephson junction. *Nature* **397**, 43 (1999).

Acknowledgements

Author Contributions

J.L. did the majority of the analytical and numerical calculations with support from M.A. and J.A.O. All authors contributed to the discussion of the results and the writing of the manuscript.

Additional Information

Competing financial interests: The authors declare no competing financial interests.

How to cite this article: Linder, J. *et al.* Microwave control of the superconducting proximity effect and minigap in magnetic and normal metals. *Sci. Rep.* **6**, 38739; doi: 10.1038/srep38739 (2016).

Publisher's note: Springer Nature remains neutral with regard to jurisdictional claims in published maps and institutional affiliations.

Paper III

Reference

Contributions

JL conceived the idea of the project and performed the initial analytical and numerical calculations, with input from JAO and MA. Most of the analytical results were obtained and refined by MA, with support from JL and JAO. All authors contributed to the discussion and writing.

SCIENTIFIC REPRTS

Analytically determined topological phase diagram of the proximity-induced gap in diffusive *n*-terminal Josephson junctions

Morten Amundsen, Jabir Ali Ouassou & Jacob Linder

Multiterminal Josephson junctions have recently been proposed as a route to artificially mimic topological matter with the distinct advantage that its properties can be controlled via the superconducting phase difference, giving rise to Weyl points in 4-terminal geometries. A key goal is to accurately determine when the system makes a transition from a gapped to non-gapped state as a function of the phase differences in the system, the latter effectively playing the role of quasiparticle momenta in conventional topological matter. We here determine the proximity gap phase diagram of diffusive n-terminal Josephson junctions ($n \in \mathbb{N}$), both numerically and analytically, by identifying a class of solutions to the Usadel equation at zero energy in the full proximity effect regime. We present an analytical equation which provides the phase diagram for an arbitrary number of terminals *n*. After briefly demonstrating the validity of the analytical approach in the previously studied 2- and 3-terminal cases, we focus on the 4-terminal case and map out the regimes where the electronic excitations in the system are gapped and non-gapped, respectively, demonstrating also in this case full agreement between the analytical and numerical approach.

The interest in topological quantum phases of matter has grown steadily in recent years, and the fundamental importance of this topic in physics was recently recognized by Thouless, Haldane, and Kosterlitz being awarded the 2016 Nobel prize in physics for their contribution to this field. So far, specific material classes such as telluride-based quantum wells (HgTe, CdTe), bismuth antimony ($Bi_{1-x}Sb_x$) and bismuth selenide (Bi_2Se_3) have received the most attention in the pursuit of symmetry-protected topological phases and excitations[1–4]. However, it was recently proposed[5] that similar physics could be obtained using conventional superconducting materials. More specifically, by using multiterminal Josephson junctions, the authors of ref. 5 showed that it was possible to create an artificial topological material displaying Weyl singularities under appropriate conditions. In multiterminal Josephson junctions hosting well-defined Andreev bound states, the crossing of these states with the Fermi level has been shown to be analogous to Weyl points in 3D solids with the Andreev bound state taking on the role of energy bands and the superconducting phase differences corresponding to quasiparticle momenta. A considerable advantage in utilizing multiterminal Josephson junctions rather than 3D solids to study exotic phenomena such as Weyl singularities and topologically different phases is that the phase differences are much more easily controlled experimentally than the quasiparticle momenta.

In order to probe electronic excitations with topological properties, a key goal is to map out the phase diagram of the system in terms of when it is gapped or not. A gapped system here means that there are no available excitations in a finite interval around the Fermi level. The reason for why this is important is that transitions between topologically protected states can occur via gap closing, and so by identifying under which circumstances the system makes such a transition provides information about when the topological nature of the system's quantum state changes.

The arguably easiest way to probe such a phase transition is via the readily available density of states measurements, which pick up whether or not the system is gapped at a specific energy. The electronic density of states can be probed via conductance measurements, for instance in the form of tunneling between the system and a small metallic tip using so-called scanning tunneling microscopy. Recent previous works have considered the case of

Department of Physics, Norwegian University of Science and Technology, N-7491 Trondheim, Norway. Correspondence and requests for materials should be addressed to M.A. (email: morten.amundsen@ntnu.no)

3-terminal Josephson junctions, both in ballistic[6,7] and diffusive systems[8], and also the 4-terminal case in the case of chaotic cavities being connected to each other and the superconductors[9]. In particular the 4-terminal case is of interest due to the possibility of creating Weyl singularities[5].

In terms of experimental realization, metallic diffusive systems are of high relevance as the conditions for realizing such systems are far less stringent than, for instance, the discrete Andreev bound states of quantum dots. However, the proximity-gap phase diagram has not yet been studied for the 4-terminal case involving diffusive normal metals.

Motivated by this, we here determine the proximity gap phase diagram of diffusive n-terminal Josephson junctions ($n \in \mathbb{N}$), both numerically and analytically, by identifying a class of solutions to the Usadel equation[10] at zero energy in the full proximity effect regime. We present an analytical equation which provides the phase diagram for an arbitrary number of terminals n. After briefly demonstrating the validity of the analytical approach in the previously studied 2- and 3-terminal cases, we focus on the 4-terminal case and map out the regimes where the electronic excitations in the system are gapped and non-gapped, respectively, demonstrating also in this case full agreement between the analytical and numerical approach. Our results may serve as a guideline for exploring the interesting physics of multiterminal devices involving the experimentally prevalent and accessible scenario of diffusive metals connected to superconductors, which has a long history[11].

Theory

We will use the quasiclassical theory of superconductivity which is known to yield good agreement with experimental measurements on mesoscopic superconducting devices. As only non-magnetic structures will be considered here, only singlet Cooper pairs exist and it is possible to work in Nambu-space alone due to the spin degeneracy. Using a field operator basis $\psi = (\psi_\uparrow, \psi_\downarrow^\dagger)$, the 2×2 quasiclassical Green function matrix $\underline{g}$ describing the existence of superconductivity in the system via the anomalous correlation function f reads:

$$\underline{g} = \begin{pmatrix} g & f \\ \widetilde{f} & -\widetilde{g} \end{pmatrix} \tag{1}$$

Here, $\{g, f\}$ are complex scalars that depend on position $\mathbf{r}$ and quasiparticle energy E. In a bulk BCS superconductor with order parameter $\Delta = \Delta_0 e^{i\phi}$, $\underline{g}$ takes the form:

$$\underline{g}_{\text{BCS}} = \begin{pmatrix} c & s e^{i\phi} \\ -s e^{-i\phi} & -c \end{pmatrix} \tag{2}$$

where $c \equiv \cosh(\theta)$, $s \equiv \sinh(\theta)$, and $\theta = \text{atanh}[\Delta_0/(E + i\delta)]$. Here, δ accounts for inelastic scattering processes and causes a smearing of the spectral density. In writing $\underline{g}_{\text{BCS}}$, we have used that $\tilde{c} = c$ and $\tilde{s} = -s$. The above matrix may be Ricatti-parametrized[12] in the same way as one would do in the case of non-degenerate spin (see *e.g.* ref. 13 for a general Ricatti-parametrization in this case) with two differences: (i) we have to let $\tilde{\gamma} \to -\tilde{\gamma}$, and (ii) treat $\{\gamma, \tilde{\gamma}\}$ as scalars rather than matrices. More specifically, we write the Green function in the form

$$\underline{g} = \begin{pmatrix} N(1 - \gamma\tilde{\gamma}) & 2N\gamma \\ 2\widetilde{N}\tilde{\gamma} & -\widetilde{N}(1 - \tilde{\gamma}\gamma) \end{pmatrix} \tag{3}$$

with $N = \widetilde{N} = (1 + \gamma\tilde{\gamma})^{-1}$. The Usadel equation in the normal wires, which governs the behavior of the Green function $\underline{g}$, reads:

$$D\partial_x(\underline{g}\partial_x\underline{g}) + i[E\underline{\tau}_z, \underline{g}] = 0, \tag{4}$$

where D is the diffusion coefficient, $\underline{\tau}_z$ is the third Pauli matrix, and E is the quasiparticle energy. Since we are interested in mapping out the regime where the system is gapped, it suffices to consider the behavior of $\underline{g}$ at the Fermi level ($E = 0$). In this case, we have $\tilde{\gamma} = \gamma^*$, and the Ricatti-parametrized Usadel equation [obtained by inserting Eq. (3) into Eq. (4)] determining γ takes the form

$$\partial_x^2\gamma - \frac{2(\partial_x\gamma)^2\gamma^*}{1 + |\gamma|^2} = 0. \tag{5}$$

This equation has the following general and exact solution if $\gamma \in \mathbb{R}$:

$$\gamma(x) = \tan(c_1 x + c_2). \tag{6}$$

Although a purely real γ might seem like a very particular case, this scenario in fact allows us to gain important information about the proximity-gap phase diagram. To see this, consider the expression for the normalized (against its normal-state value) density of states $\mathcal{N}$ at zero energy:

$$\mathcal{N} = \frac{1 - |\gamma|^2}{1 + |\gamma|^2}. \tag{7}$$

The solution $\gamma = 0$ corresponds to the absence of superconducting correlations, i.e. completely closed gap, in which case the density of states resumes its normal-state value $\mathcal{N} = 1$. The solutions $\gamma = \pm 1$ correspond to the
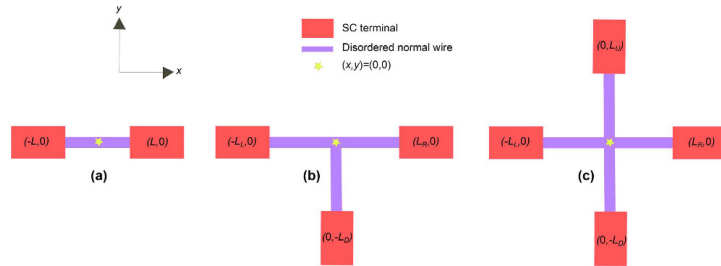
Figure 1. Multiterminal Josephson junctions. The density of states $\mathcal{N}$ at zero energy (Fermi level) is measured at the point indicated by a star, i.e. at the intersection of the diffusive normal wires. **(a)** 2-terminal, **(b)** 3-terminal, and **(c)** 4-terminal setups. Since the wires are assumed to be diffusive, their precise geometrical orientation does not influence the topological properties of the system. For instance, the same 3-terminal topological phase diagram would have been obtained if the leads were connected in a Y-shape rather than a T-shape: only the physical properties of the wires (*e.g.* their Thouless energies) are of consequence.

fully gapped case $\mathcal{N} = 0$ where no available quasiparticle excitations exist at the Fermi level. The existence of such points can now be identified analytically by determining c_1 and c_2 in Eq. (6) via the boundary conditions in the N-terminal system. We later proceed to do so explicitly. It is also worth noting that Eq. (5) also has a general solution when γ is purely imaginary [$\gamma \in \mathbb{C}$, $\mathrm{Re}(\gamma) = 0$]:

$$\gamma(x) = \mathrm{i} \tan(c_1 x + c_2). \tag{8}$$

The solution Eq. (6) is of particular relevance in the case where the phase differences between the terminals is $n\pi$, with $n = 0, 1, 2, \dots$ The reason for this is that in such a scenario, one can choose a gauge where all superconducting order parameters are purely imaginary in the reservoirs (phases $\phi_j = \pi/2$ or $3\pi/2$), which renders the BCS anomalous correlation function $f = se^{\mathrm{i}\phi_j}$ to be purely real at zero energy since $s(E = 0) = -\mathrm{i}$. If one assumes ideal boundary conditions at the superconducting interfaces, meaning that f is continuous, there are no imaginary terms in the boundary conditions or in the equation of motion for γ itself, meaning that the solution γ can be taken as real. From Eq. (7), it is clear that the maximum value of the Fermi-level density of states in the presence of a superconducting proximity effect is $\mathcal{N}_{\mathrm{max}} = 1$. We can thus conclude that the analytical approach presented above is valid whenever the superconducting phase differences between the terminals are $n\pi$.

The above class of exact solutions are useful since they are valid at specific phase differences and provide information about whether or not the DOS is gapped there. However, we have identified an additional class of exact solutions which is useful because it is valid at *any phase-differences where $\mathcal{N} = 0$*, which is precisely the regime of interest. By noting that $\mathcal{N} = 0$ only when $|\gamma| = 1$, a reasonable ansatz is:

$$\gamma = -\mathrm{i}e^{\mathrm{i}S(x)}, \; S(x) \in \mathbb{R}. \tag{9}$$

The prefactor $-\mathrm{i}$ is just a convention that simplifies the boundary conditions for S. Insertion into Eq. (5) gives immediately

$$S(x) = ax + b \tag{10}$$

where a and b are real constants determined by the boundary conditions. Besides allowing us to analytically determine the region in phase-space where the system is gapped, this solution also allows us to analytically compute the topological number associated with the gapped regime defined as[14]:

$$m = \oint \nabla S(\mathbf{r}) \cdot d\mathbf{r} \tag{11}$$

where $S(\mathbf{r})$ is interpreted as the phase of the superconducting correlations at $E = 0$. There are several ways to relate the Riccati parameter γ to the physical properties of the system. First of all, it can be related to the physically observable density of states using Eq. (7). Moreover, when the system is fully gapped so that the zero-energy density of states $\mathcal{N} = 0$, γ is in fact just the anomalous Green function f, which quantifies the superconducting correlations in the system. This can be seen by comparing Eqs (1) and (3): in general, the anomalous Green function is given by $f = 2N\gamma$, but since $\gamma = -\mathrm{i}e^{\mathrm{i}S(\mathbf{r})}$ for a fully gapped system, we find that $N = [1 + e^{+\mathrm{i}S(\mathbf{r})}e^{-\mathrm{i}S(\mathbf{r})}]^{-1} = 1/2$ using the definition given above. It is assumed that the Green functions in the superconductors may be approximated by bulk expressions, and that the interfaces to the normal metals are transparent. This leads to the boundary conditions $S(\mathbf{r}_j) = \phi_j$, where $\mathbf{r}_j$ are the locations of the terminals in Fig. 1, and ϕ_j are the corresponding phases. This can be deduced by comparing with the anomalous Green function in a bulk superconductor, $f_{\mathrm{BCS}} = -\mathrm{i}e^{\mathrm{i}\phi}$.

Although Eq. (9) is exact whenever the system is gapped ($\mathcal{N} = 0$), it cannot be used carelessly because one still has to specify for which choices of the phases ϕ_j it is valid. It is clearly valid when all phases are equal in the system, so that the phase-difference between all terminals is zero. As we will later show, it is also valid in large regimes of phase-space, and one needs a criterion for when Eq. (9) can be used. Such a criterion can be obtained

in a convenient way by noting that as soon as $S(x)$ acquires a non-zero imaginary part, the consequence is that $\mathcal{N} \neq 0$. Identifying the condition for when a complex $S(x)$ becomes a possible solution is thus our strategy for describing analytically the topological phase diagram. By using Eq. (9) with $S(x) \in \mathbb{C}$ and writing $S(x) = S_r(x) + \mathrm{i}S_i(x)$, Eq. (5) becomes

$$\partial_x^2 S + \mathrm{i}(\partial_x S)^2 \left[1 - \frac{2}{1 + e^{2S_i}}\right] = 0 \tag{12}$$

It is observed that the solution of Eq. (12) reduces to Eq. (10) in the limit $S_i(x) \to 0$. This means that by allowing a small $S_i(x)$, it is possible to map out regions where Eq. (10) is not valid and the imaginary component begins to matter. To do so, we Taylor expand the square bracket of Eq. (12), and insert the perturbation expansion

$$S(x) = S_r(x) + \mathrm{i}(\lambda S_{i1}(x) + \lambda^2 S_{i2}(x) + \ldots) \tag{13}$$

where $S_{i1}(x) \ll S_r(x)$ and $S_{ik+1} \ll S_{ik}$. The expansion parameter λ is a helper variable used to collect different orders of the expansion. This gives

$$\lambda^0: \quad \partial_x^2 S_r = 0 \tag{14}$$

$$\lambda^1: \quad \partial_x^2 S_{i1} + (\partial_x S_r)^2 S_{i1} = 0 \tag{15}$$

and similarly for higher orders of λ. It is noticed in particular that Eq. (10) remains a solution for $S_r(x)$. The first order correction $S_{i1}(x)$ is easily solved, giving

$$S_{i1}(x) = C_1 \cos(ax) + C_2 \sin(ax) \tag{16}$$

In an n-terminal Josephson junction with transparent interface between superconductors and the normal metal, it is clear that $|\gamma| = 1$ at the interface regardless of the phase. The proper boundary conditions are therefore that $S_i(x_j) = 0$, with x_j being the position of superconducting interface j. In addition, current conservation at the intersection between the arms of the multiterminal junction requires continuity of the Green function as well as the following relation between derivatives:

$$\sum_j \vec{e}_j \cdot \nabla \gamma_j = 0 \tag{17}$$

where γ_j is the solution of the Usadel equation in arm j, and $\vec{e}_j$ is a unit vector pointing towards the intersection. Using these conditions, it is possible to formulate a criterion for when the purely real solution for $S(x)$ is valid, namely: Any combination of boundary conditions for which the only solution for $S_{i1}(x)$ possible is one where $C_1 = C_2 = 0$. The curves where this is *not* satisfied may be found from the boundary conditions for an n-terminal Josephson junction as

$$\sum_{j=1}^{n} \frac{\psi_j}{\tan \psi_j} = 0 \tag{18}$$

with ψ_j given as

$$\psi_j = \phi_j - \langle \phi \rangle = \phi_j - \frac{1}{n}\sum_{k=1}^{n} \phi_k \tag{19}$$

Equations (18) and (19) represent a key analytical result in this manuscript as they provide the phase diagram for the proximity-induced gap for an arbitrary number of terminals n. It is emphasized that the curves satisfying Eq. (18) only determine when a small imaginary contribution to $S(x)$ is possible and hence for which phases a transition between gapped and ungapped regimes in phase space occur. These curves are therefore referred to as transition curves. Higher order terms in the perturbation expansion are required in order to more accurately describe the ungapped regions. This is however not necessary when only interested in the gapped regions. It will be shown that it is possible to distinguish between the two regimes using only the first order correction.

To complement our analytical considerations, we also perform a fully numerical determination of the proximity-gap phase diagram by solving the Usadel equation numerically for any phase differences ϕ_j and without assuming ideal boundary conditions. In the following sections, we first provide a brief discussion of the already known 2-terminal and 3-terminal cases in order to prove the correctness of our novel analytical approach. Then, we proceed to discuss the less explored 4-terminal case in more detail.

We comment here that multiterminal geometries beyond effective 1D models can also be treated using the recently developed[15] numerical solution of the full Usadel equation in 3D, allowing for the study of non-trivial geometrical effects. Moreover, previous works have considered analytical solutions of the Usadel equation using the so-called θ-parametrization in SN bilayers[16–18] and also approximate solutions in the SNS case[19–21], whereas in our work the analytical solution is *exact* for the key cases of *(i)* $\mathcal{N} = 0$ and *(ii)* for phase differences $n\pi$ between the terminals.
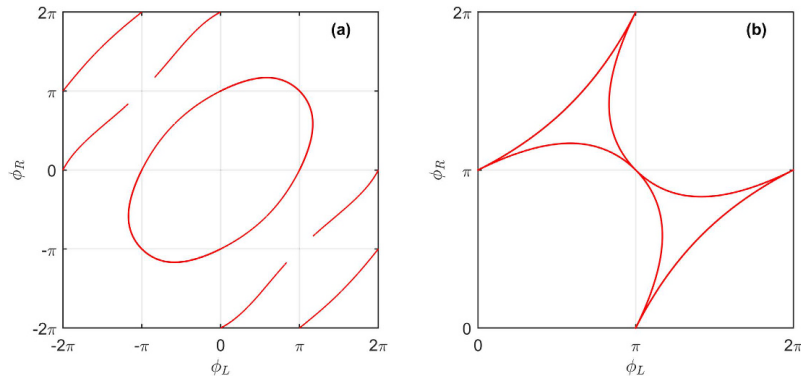
Figure 2. Analytically calculated transition curves between gapped and ungapped regions in the 3-terminal case. Plot of curves where the first order correction $S_{i1}(x)$ can have non-zero solutions. (**a**) Structure of the condition in the extended phase space, showing metastable solutions. (**b**) Translation of physically relevant curves into $[0, 2\pi] \times [0, 2\pi]$.

Results: 2-terminal case

Assuming ideal boundary conditions at the superconducting interfaces $x = -L/2$ and $x = L/2$ see Fig. 1(a), real solutions of γ must satisfy $\gamma = \tan(c_1 x + c_2)$ where:

$$\tan(-c_1 L/2 + c_2) = -\mathrm{i}e^{\mathrm{i}\phi_L} \text{ and } \tan(c_1 L/2 + c_2) = -\mathrm{i}e^{\mathrm{i}\phi_R} \tag{20}$$

This restricts the superconducting phases to be $\phi_j = \{\pi/2, 3\pi/2\}$ in order to ensure $\gamma \in \mathbb{R}$. A number of solutions can be obtained from this. If $\phi_L = \pi/2$ and $\phi_R = 3\pi/2$ or vice versa, the solution is $c_2 = 0$ which gives a DOS in the center of the wire $\mathcal{N}(x = 0) = 1$. This is the expected result for a phase difference of π between the superconducting terminals. If instead the phase difference is zero, meaning $\phi_L = \phi_R = \{\pi/2, 3\pi/2\}$, then the solution is $c_2 = \pm\pi/4$, providing $\mathcal{N}(x = 0) = 0$. This is also consistent with the result that the DOS is allowed to be fully gapped when there is no phase difference. These results are in agreement with the condition given in Eq. (18), which identifies $\phi_L - \phi_R = n\pi$, $n = 1, 2, \ldots$ as the only configurations for which a non-zero density of states is possible. The phase-dependent minigap in an SNS junction was originally considered in ref. 19.

Results: 3-terminal case

In the 3-terminal case, we consider the geometry of Fig. 1(b). The regions in phase space where $\mathcal{N}(x = 0, y = 0) = 0$ is mapped out using Eq. (18). Since only phase differences matter physically, we fix the phase of one superconducting terminal, $\phi_D = 0$, without loss of generality. Transition curves indicating the transition between gapped and ungapped regions are shown in Fig. 2(a) for the extended phase space $[-2\pi, 2\pi] \times [-2\pi, 2\pi]$. It can be seen that one such curve encircles the origin, with a near-elliptical shape, thereby splitting the plane into two regions. It is known that the origin resides in a gapped region, so that the outer region may be identified as ungapped. There also appears several open curves in the second and fourth quadrant. These curves are considered to be metastable solutions, corresponding to a higher phase-winding of the superconducting correlations in the normal wires, and are not investigated further. Due to the 2π-periodicity of the superconducting phases, the physically relevant transition curves must be translated into $[0, 2\pi] \times [0, 2\pi]$, as shown in Fig. 2(b).

The density of states may also be computed analytically in the select points where the boundary conditions are real. Using Eq. (6), the solutions in the left, down, and right arm are written as $\gamma_L = \tan(c_1 x + c_2)$, $\gamma_R = \tan(c_3 x + c_4)$, $\gamma_D = \tan(c_5 x + c_6)$. For this particular calculation, it is necessary to set $\phi_D = \pi/2$ in order to make $\gamma_{\mathrm{BCS},D} = -\mathrm{i}e^{\mathrm{i}\phi_D} = 1$ real. At the intersection point $(x, y) = (0, 0)$ continuity of the Green function and its derivative ensure continuity of the current. We assume here for simplicity equal lengths and normal-state conductances of the three normal wires, although the analytical treatment does not require this in general. In this case, we obtain the boundary conditions

$$\tan(-c_1 L_L + c_2) = -\mathrm{i}e^{\mathrm{i}\phi_L}, \quad \tan(-c_5 L_D + c_2) = 1,$$
$$\tan(c_3 L_R + c_2) = -\mathrm{i}e^{\mathrm{i}\phi_R}, \quad (1 + \tan^2 c_2)(c_1 + c_5 - c_3) = 0. \tag{21}$$

The values of $\{\phi_L, \phi_R\}$ are restricted to $\pi/2$ and $3\pi/2$ in order to ensure the validity of the solution for γ. Since $\tan c_2 \in \mathbb{R}$, the last boundary condition is equivalent to $c_1 + c_5 - c_3 = 0$. The above non-linear system of equations may be solved analytically, keeping the physically acceptable solution which gives $\mathcal{N} > 0$. For instance, for $(\phi_L, \phi_R) = (3\pi/2, 3\pi/2)$ one finds that $\tan(c_2) = -2 \pm \sqrt{3}$. The positive solution is the physically acceptable one since it provides $\mathcal{N} > 0$. The Fermi-level DOS in the center of the system $(x, y) = (0, 0)$ is given by
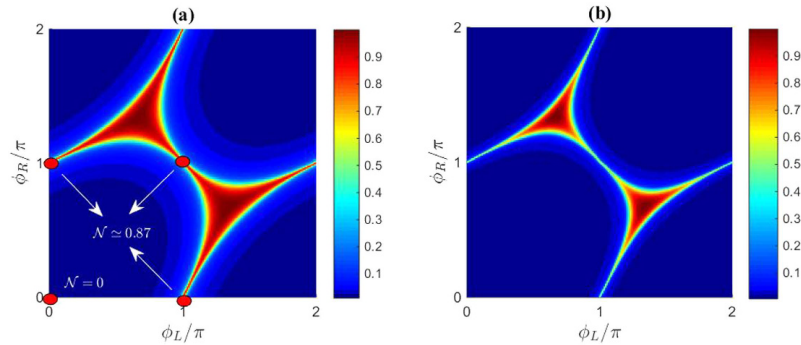
Figure 3. Numerically calculated proximity-gap phase diagram for 3-terminal Josephson junctions. Plot of the Fermi level density of states $\mathcal{N}$ for a 3-terminal setup as a function of the phases ϕ_L and ϕ_R. For both plots, we set $L/\xi = 0.67$ and $\delta/\Delta_0 = 5 \times 10^{-3}$. The phase of the 'down' superconducting terminal has been set to $\phi_D = 0$. (**a**) Ideal boundary conditions. (**b**) Kupriyanov-Lukichev boundary conditions with finite interface resistance. We have set $\zeta_j = 2.5$, $j = \{L, R, D\}$.

$$\mathcal{N}(x = 0, y = 0) = \frac{1 - |\tan(c_2)|^2}{1 + |\tan(c_2)|^2},$$

(22)

and we find from the solution of c_2 that:

$$\mathcal{N}(x = 0, y = 0) = \begin{cases} 0, & \text{if } (\phi_L, \phi_R) = (\pi/2, \pi/2) \\ 0.866, & \text{if } (\phi_L, \phi_R) = (\pi/2, 3\pi/2) \\ 0.866, & \text{if } (\phi_L, \phi_R) = (3\pi/2, \pi/2) \\ 0.866, & \text{if } (\phi_L, \phi_R) = (3\pi/2, 3\pi/2) \end{cases}$$

(23)

These solutions may be compared with the numerical solution of the full proximity-gap phase diagram in Fig. 3(a), where it can be seen that the analytically determined transition curves of Fig. 2(b) trace out exactly the regions where the density of states is non-zero. The excellent correspondance is explained by the rapid transition between the two regimes, as shown by the numerical solution. In addition, the four red circles are gauge-equivalent to the above phase-choices (note that in the figure we have set $\phi_D = 0$). As seen, the analytical expressions match the numerical result. In order to model a more realistic setting with finite interface transparencies, we provide the phase diagram using the Kupriyanov-Lukcihev boundary conditions[22] in Fig. 3(b). The interface transparency is quantified by the parameter $\zeta_j = R_{B,j}/R_{N,j}$ where $R_{B,j}$ is the barrier resistance and $R_{N,j}$ is the normal-state resistance of wire j. As seen, the gapped region extends compared to the fully transparent case, in agreement with ref. 8.

Results: 4-terminal case

We now focus on the 4-terminal case and demonstrate both the robustness of the analytical approach developed above in addition to providing comprehensive numerical results. The transition surface in the, now three dimensional, extended phase space is shown in Fig. 4(a), where ϕ_U has been fixed to zero and metastable solutions have been removed for clarity. It can be seen to have an ellipsoidal shape, which is an expected generalization of the 3-terminal case. Figure 4(b–d) show slices of the surface after translation into the first quadrant for $\phi_D = 0, \frac{\pi}{2}$ and π, respectively. The resulting phase diagram displays a more complicated behavior than in the 3-terminal case. At $\phi_D = 0$, the phase diagram is similar to the 3-terminal case, but as ϕ_D is increased toward $\pi/2$ one of the gapped regions expands greatly at the expense of the other gapped regions which are separated from each other by a "barrier" of finite DOS $\mathcal{N} \neq 0$. As ϕ_D is further increased toward π, the phase-diagram morphs into a qualitatively different shape than at $\phi_D = 0$, and at $\phi_D = \pi$ two of the gapped regions have been almost completely expelled from the phase diagram whereas two gapped "valleys" remain, the latter again separated by a non-gapped region.

With purely real boundary conditions, and $\phi_U = \frac{\pi}{2}$, the solutions in the left, down, right, and up arm are written as $\gamma_L = \tan(c_1 x + c_2)$, $\gamma_D = \tan(c_3 x + c_4)$, $\gamma_R = \tan(c_5 x + c_6)$, $\gamma_U = \tan(c_7 x + c_8)$. As in the previous section, we assume here for simplicity equal lengths and normal-state conductances of the four normal wires. The resulting boundary conditions take the form:

$$\tan(-c_1 L_L + c_2) = -ie^{i\phi_L}, \ \tan(-c_5 L_D + c_2) = -ie^{i\phi_D}, \ \tan(c_3 L_R + c_2) = -ie^{i\phi_R},$$
$$\tan(c_7 L_U + c_2) = 1, \ (c_1 + c_5 - c_3 - c_7) = 0.$$

(24)
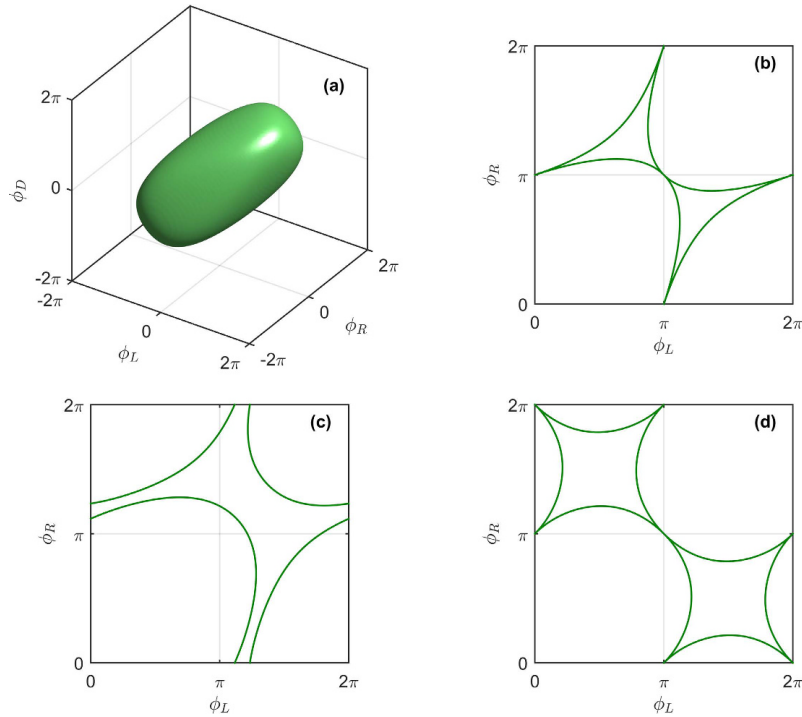
Figure 4. Analytically calculated transition curves between gapped and ungapped regions in the 4-terminal case. The mapping of three-dimensional phase space was performed using Eq. (18), with $\phi_U = 0$. **(a)** Transition surface in extended phase space. **(b–d)** Translation of physically relevant curves into the first quadrant for $\phi_D = 0, \frac{\pi}{2}$ and π, respectively.

	$(\phi_L, \phi_R) = (\pi/2, \pi/2)$	$(\phi_L, \phi_R) = (3\pi/2, \pi/2)$	$(\phi_L, \phi_R) = (\pi/2, 3\pi/2)$	$(\phi_L, \phi_R) = (3\pi/2, 3\pi/2)$
$\phi_D = \pi/2$	$\mathcal{N} = 0.00$	$\mathcal{N} = 0.71$	$\mathcal{N} = 0.71$	$\mathcal{N} = 1.00$
$\phi_D = 3\pi/2$	$\mathcal{N} = 0.71$	$\mathcal{N} = 1.00$	$\mathcal{N} = 1.00$	$\mathcal{N} = 0.71$

Table 1. Analytically obtained values of $\mathcal{N}$ at special points in phase-space. The solution for the zero-energy DOS $\mathcal{N}$ at the intersection point of the wires $(x, y) = (0, 0)$ obtained through analytically solving the non-linear equations for γ_j assuming transparent interfaces to the superconducting terminals (in contrast to Figs 5 and 6 where a finite interface resistance is used). We fixed $\phi_U = \pi/2$. At all points $(\phi_U, \phi_D, \phi_L, \phi_R)$ shown in the table, the analytically obtained value of $\mathcal{N}$ matches the numerically obtained solution.

This non-linear system of equations may be solved analytically. Due to the requirement that $\gamma \in \mathbb{R}$, we restrict our attention to $\{\phi_L, \phi_R, \phi_U\}$ taking the values $\pi/2$ and $3\pi/2$. We provide the solutions in Table 1 which again match the values obtained from a fully numerical solution, thus indicating the correctness of our analytical approach.

We now proceed to present numerical results for the 4-terminal case when there exists a finite interface resistance between the superconducting terminals and the normal wires, which is experimentally more realistic. We fix $\phi_U = 0$ without loss of generality and plot the evolution of the proximity-gap phase diagram, quantified via the zero-energy DOS $\mathcal{N}$ at the intersection point $(x, y) = (0, 0)$, as the remaining superconducting phases $\{\phi_D, \phi_L, \phi_R\}$ are varied in Fig. 5. Once again, the analytical transition curves correspond well with the regions where the numerically computed density of states differs from zero.

In an experimental setting, the phase-differences can be tuned by connecting the superconducting terminals and thus creating loops which a magnetic flux can pass through, the latter controlling ϕ_j. We consider in Fig. 6 the special case where the flux penetrating all loops is the same, meaning that the phase difference between each pair of terminals is equal to ϕ (except between the up and left terminal, see inset of Fig. 6). We set all wire lengths $L_j = L$ and interface resistances to be equal for simplicity, and consider different sizes L. Regardless of L, the super-conducting correlations vanish completely at $\phi = \pi/2$ and $\phi = \pi$, as indicated by $\mathcal{N}$ taking its normal state value
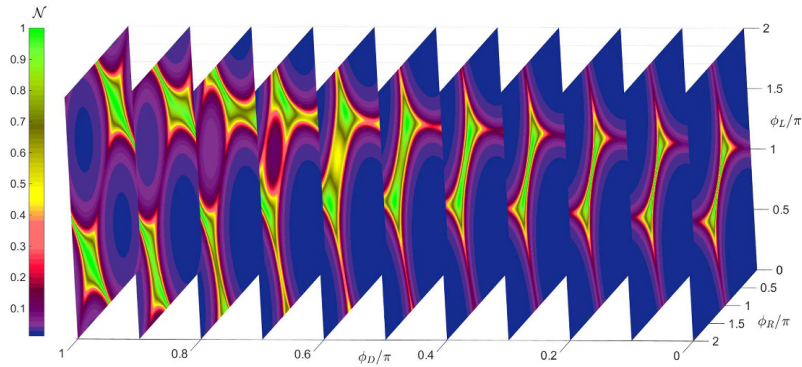
Figure 5. Numerically calculated density of states at $E = 0$ for a 4-terminal Josephson junction for different phase-configurations. Setting the upper superconducting phase to zero without loss of generality, $\phi_U = 0$, we plot the evolution of the proximity-gap phase diagram, quantified via the zero-energy density of states $\mathcal{N}$ at the intersection between the wires, as the phases at the other superconducting terminals are varied. We have set the wire lengths equal to $L/\xi = 0.67$ and the interface contact with the superconductors parametrized by a finite interface resistance ratio to the bulk resistance $\zeta = 2.5$. The blue regions correspond to the gapped regime where $\mathcal{N} = 0$.
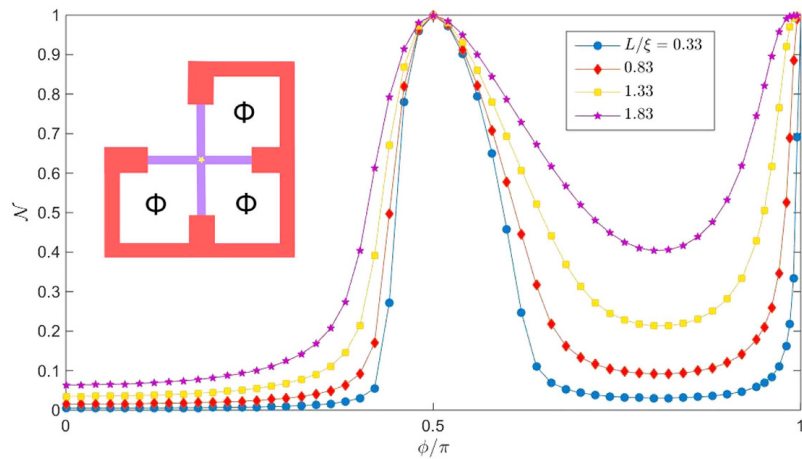
Figure 6. Numerically calculated density of states at $E = 0$ for a 4-terminal Josephson junction for equal flux through the loops. Plot of the Fermi level density of states $\mathcal{N}$ for a 4-terminal setup as a function of ϕ where $\phi_R = \phi$, $\phi_D = 2\phi$, $\phi_L = 3\phi$, which corresponds to a scenario where the same flux Φ penetrates loops that connects the superconducting terminals (see inset). We have set $\phi_U = 0$ without loss of generality, $\delta/\Delta_0 = 3 \times 10^{-3}$, and $\zeta_j = 2.5$, $j = \{L, R, D, U\}$.

($\mathcal{N} = 1$). The gapped region at $0 < \phi < \pi/2$ for small lengths $L/\xi \ll 1$ starts to fill up with available electronic excitations as L increases.

Conclusion

The main new results in this work are the class of analytical solutions of the Ricatti-parametrized Usadel equation at $E = 0$ in the full proximity effect regime, the equations (18) and (19) providing the transition between the gapped and non-gapped regimes for an arbitrary number of terminals n, and the specific results for the 4-terminal case. An interesting expansion of the present work would be to explore how magnetic interfaces[23–25] and spin-orbit coupling would influence the proximity-gap phase diagram and topological properties of multi-terminal Josephson junctions, as recent works have demonstrated that in particular the latter of these can induce several novel effects in both diffusive and ballistic superconducting hybrids[13,26–34].

References

1. C.-K. Chiu, J. C. Y. Teo, A. P. Schnyder & S. Ryu. Classification of topological quantum matter with symmetries. *Rev. Mod. Phys.* **88,** 035005 (2016).
2. M. Z. Hasan & C. L. Kane. Topological insulators. *Rev. Mod. Phys.* **82,** 3045 (2010).
3. J. Alicea. New directions in the pursuit of Majorana fermions in solid state systems. *Rep. Prog. Phys.* **75,** 076501 (2012).
4. X.-L. Qi & S.-C. Zhang. Topological insulators and superconductors. *Rev. Mod. Phys.* **83,** 1057 (2011).
5. R.-P. Riwar, M. Houzet, J. S. Meyer & Y. V. Nazarov. Multi-terminal Josephson junctions as topological materials. *Nat. Commun.* **7,** 11167 (2016).
6. B. van Heck, S. Mi & A. R. Akhmerov. Single fermion manipulation via superconducting phase differences in multiterminal Josephson junctions. *Phys. Rev. B* **90,** 155450 (2014).
7. T. Yokoyama & Y. V. Nazarov. Singularities of Andreev spectrum in multi-terminal Josephson junction. *Phys. Rev. B* **92,** 155437 (2015).
8. C. Padurariu *et al.* Closing the proximity gap in a metallic Josephson junction between three superconductors. *Phys. Rev. B* **92,** 205409 (2015).
9. T. Yokoyama, J. Reutlinger, W. Belzig & Y. V. Nazarov. Order, disorder and tunable gaps in the spectrum of Andreev bound states in a multi-terminal superconducting device. *arXiv:1609.05455.*
10. Usadel, K. D. Generalized diffusion equation for superconducting alloys. *Phys. Rev. Lett.* **25(8),** 507–509 (1970).
11. W. Belzig *et al.* Quasiclassical Green's function approach to mesoscopic superconductivity. *Superlattices and Microstructures* **25,** 1251 (1999).
12. N. Schopohl. Transformation of the Eilenberger equations of superconductivity to a scalar Riccati equation. *arxiv:cond-mat/9804064* (1998).
13. S. H. Jacobsen, J. A. Ouassou & J. Linder. Critical temperature and tunneling spectroscopy of superconductor-ferromagnet hybrids with intrinsic Rashba-Dresselhaus spin-orbit coupling. *Phys. Rev. B* **92,** 024510 (2015).
14. E. Strambini *et al.* The ω-SQUIPT: phase-engineering of Josephson topological materials. arXiv:1603.00338. *Nature Nanotechnology.* **11,** 1055–1059 (2016).
15. M. Amundsen & J. Linder. General solution of 2D and 3D superconducting quasiclassical systems: coalescing vortices and nanoisland geometries. *Sci. Rep.* **6,** 22765 (2016).
16. D. A. Ivanov & Ya. V. Fominov. Minigap in superconductor-ferromagnet junctions with inhomogeneous magnetization. *Phys. Rev. B* **73,** 214524 (2006).
17. B. Crouzy, E. Bascones & D. A. Ivanov. Minigap in a superconductor-normal metal junction with paramagnetic impurities. *Phys. Rev. B* **72,** 092501 (2005).
18. W. Belzig, C. Bruder & G. Schön. Local density of states in a dirty normal metal connected to a superconductor. *Phys. Rev. B* **54,** 9443 (1996).
19. F. Zhou, P. Charlat, B. Spivak & B. Pannetier. Density of States in Superconductor-Normal Metal-Superconductor Junctions. *J. Low Temp. Phys.* **110,** 841 (1998).
20. A. F. Volkov & V. V. Pavlovskii. Long-range thermoelectric effects in mesoscopic superconductor-normal metal structures. *Phys. Rev. B* **72,** 014529 (2005).
21. A. F. Volkov, R. Seviour & V. V. Pavlovskii. Proximity-induced transport in hybrid mesoscopic normal-superconducting metal structures. *Superlattices and Microstructures* **25,** 647 (1999).
22. Kupriyanov, M. Y. & Lukichev, V. F. Influence of boundary transparency on the critical current of dirty SS'S structures. *Soviet Physics JETP,* **67(6),** 1163–1168 (1988).
23. A. Cottet, D. Huertas-Hernando, W. Belzig & Y. V. Nazarov. Spin-dependent boundary conditions for isotropic superconducting Green's functions. Phys. Rev. B 80, 184511 (2009).
24. Eschrig, M., Cottet, A., Belzig, W. & Linder, J. General boundary conditions for quasiclassical theory of superconductivity in the diffusive limit: application to strongly spin-polarized systems. *New J. Phys.* **17,** 83037 (2015).
25. Linder, J. & Robinson, J. W. A. Superconducting spintronics. *Nat. Phys.* **11,** 307 (2015).
26. Bergeret, F. S. & Tokatly, I. V. Spin-orbit coupling as a source of long-range triplet proximity effect in superconductor-ferromagnet hybrid structures. *Phys. Rev. B* **89,** 134517 (2014).
27. M. Houzet & J. S. Meyer. Quasiclassical theory of disordered Rashba superconductors. *Phys. Rev. B* **92,** 014509 (2015).
28. Arjoranta, J. & Heikkilä, T. Intrinsic spin-orbit interaction in diffusive normal wire Josephson weak links: supercurrent and density of states. *Phys. Rev. B* **93,** 024522 (2016).
29. C. Espedal, T. Yokoyama & J. Linder. Anisotropic paramagnetic Meissner effect by spin-orbit coupling. *Phys. Rev. Lett.* **116,** 127002 (2016).
30. P. Högl, A. Matos-Abiague, I. Zutic & J. Fabian. Magnetoanisotropic Andreev Reflection in Ferromagnet-Superconductor Junctions. *Phys. Rev. Lett.* **115,** 116601 (2015).
31. S. H. Jacobsen, I. Kulagina & J. Linder. Controlling superconducting spin flow with spin-flip immunity using a single homogeneous ferromagnet. *Sci. Rep.* **6,** 23926 (2016).
32. F. Konschelle, I. V. Tokatly & F. S. Bergeret. Ballistic Josephson junctions in the presence of generic spin dependent fields. *Phys. Rev. B* **94,** 014515 (2016).
33. J. A. Ouassou, A. Di Bernardo, J. W. A. Robinson & J. Linder. Electric control of superconducting transition through a spin-orbit coupled interface. *Sci. Rep.* **6,** 29312 (2016).
34. K. Sun & N. Shah. General framework for transport in spin-orbit-coupled superconducting heterostructures: Nonuniform spin-orbit coupling and spin-orbit-active interfaces. *Phys. Rev. B* **91,** 144508 (2015).

Acknowledgements

Author Contributions

J.L. conceived the idea of the project and performed the initial analytical and numerical calculations with input from J.A.O. and M.A. The majority of the results for the analytical solution of the Ricatti-equation and belonging phase-diagram were obtained and refined by M.A. with support from J.L. and J.A.O. All authors contributed to the discussion and writing of the manuscript.

Additional Information

Competing financial interests: The authors declare no competing financial interests.

Paper IV

Reference

M. Amundsen and J. Linder.
Supercurrent vortex pinball via a triplet Cooper pair inverse Edelstein effect.
Physical Review B **96**, 064508 (2017).
DOI: 10/d2kv

Contributions

MA performed the numerical simulations, with support from JL, and drafted the manuscript. Both authors contributed to the discussions of the physics and the revision of the final manuscript.

Supercurrent vortex pinball via a triplet Cooper pair inverse Edelstein effect

Morten Amundsen and Jacob Linder

QuSpin Center of Excellence, Department of Physics, Norwegian University of Science and Technology, N-7491 Trondheim, Norway

We consider the Josephson effect through a thin spin-orbit coupled layer in the presence of an exchange field $\boldsymbol{h}$ and discover a set of supercurrent vortices appearing in the system which can be controllably moved around in the system by varying either the direction of $\boldsymbol{h}$, the strength $|\boldsymbol{h}|$, the spin-orbit coupling magnitude α via a gate voltage, or the phase difference. We refer to this phenomenon as a supercurrent vortex pinball effect and show that its origin is the spin polarization of the triplet Cooper pairs induced in the system. The supercurrent vortices are shown to arise from what resembles a Cooper pair-induced inverse Edelstein effect.

I. INTRODUCTION

The proximity effect endows otherwise nonsuperconducting materials with superconducting properties and thus offers an interesting arena to explore how quantum coherence is manifested in unusual physical environments. One of the most actively pursued setups includes so-called Josephson junctions where a material is able to sustain a supercurrent via proximity to two host superconductors. In the presence of a magnetic exchange field $\boldsymbol{h}$, the Cooper pairs that leak from the superconductors oscillate between the conventional singlet spin state and the opposite-spin triplet state [1]. If the exchange field is spatially varying, or the system contains spin-orbit coupling, the triplet Cooper pairs may rotate between different triplet states where the electron spins are parallel, making tunable superconducting spin transport possible [2–4]. In light of this discovery, the effect of spin-orbit coupling on proximitized materials has recently been investigated in several works [5–21].

In this paper, we consider a spin-orbit coupled superconducting hybrid which is found to display novel, inherently two-dimensional, physical phenomena which are hidden in effective one-dimensional models. Specifically, we examine a thin film of a nonsuperconducting material with spin-orbit coupling sandwiched between two superconductors and discover a set of supercurrent vortices appearing in the system which can be controllably moved around by varying either the direction of $\boldsymbol{h}$, the strength $|\boldsymbol{h}|$, the spin-orbit coupling magnitude α via a gate voltage, or the phase difference. We refer to this phenomenon as a supercurrent vortex pinball effect and show that its origin is the spin polarization of the triplet Cooper pairs induced in the system. The supercurrent vortices arise from what is reminiscent of a Cooper pair-induced inverse Edelstein effect.

II. THEORY AND MODEL

A top view sketch of the geometry is given in Fig. 1. The film can for instance be a two-dimensional electron gas (GaAs), which has the advantage of a readily tunable Rashba spin-orbit coupling strength α and a high g factor providing a strong Zeeman effect. The central region is quadratic with lengths $L = 2\xi$ where ξ is the superconducting coherence length and considered to be in the diffusive regime of transport. A magnetic field is applied in the xy plane, in a direction denoted by an angle θ relative to the transverse direction (y axis), creating an exchange field $\boldsymbol{h}$ through the Zeeman effect. We assume that the film is sufficiently thin [$\mathcal{O}$ (nm)] for the orbital effect to be completely negligible. In the diffusive transport regime, the Usadel equation [22] is valid:

$$D\bar{\nabla}\hat{g}\bar{\nabla}\hat{g} + i[\varepsilon\hat{\rho}_3 + \hat{\boldsymbol{\sigma}} \cdot \boldsymbol{h}, \hat{g}] = 0, \tag{1}$$

where D is the diffusion constant, ε is the quasiparticle energy, $\hat{\rho}_3 = \text{diag}(+1, +1, -1, -1)$, and $\hat{\boldsymbol{\sigma}} = \text{diag}(\boldsymbol{\sigma}, \boldsymbol{\sigma}^*)$ where $\boldsymbol{\sigma}$ is a vector of Pauli matrices. Furthermore, $\hat{g} = \hat{g}(x, y, \varepsilon)$ is the retarded, quasiclassical 4×4 Green function matrix, defined as

$$\hat{g} = \begin{pmatrix} g & f \\ -\tilde{f} & -\tilde{g} \end{pmatrix}, \tag{2}$$

where the $\tilde{\ldots}$ operation means complex conjugation and $\varepsilon \to (-\varepsilon)$. The 2×2 matrix g is the conventional Green function, which includes the spin degree of freedom, whereas the anomalous Green function f takes into account the presence of superconducting correlations. Spin-orbit coupling is introduced via the covariant derivative $\bar{\nabla}\hat{g} = \nabla\hat{g} - i[\hat{\boldsymbol{A}}, \hat{g}]$, with $\hat{\boldsymbol{A}} = \text{diag}(\boldsymbol{A}, -\boldsymbol{A}^*)$. Here, we consider Rashba spin-orbit coupling, as generated by a symmetry breaking in the thickness direction (z axis), for which one gets

$$\boldsymbol{A} = -\alpha(\sigma_y \boldsymbol{e_x} - \sigma_x \boldsymbol{e_y}), \tag{3}$$

where α is the strength of the spin-orbit coupling, and $\boldsymbol{e_j}$ is a unit vector in direction j. We consider low-transparency interfaces, which are described by the Kupriyanov-Lukichev boundary conditions [23]

$$\boldsymbol{e}_N \cdot \bar{\nabla}\hat{g} = \frac{1}{\zeta L}[\hat{g}_R, \hat{g}_L]. \tag{4}$$

The phenomenological constant ζ is a measure of the interface resistance (we use $\zeta = 3$ in what follows, corresponding to a realistic low-transparency interface), and the indices $\{L, R\}$ refer to Green functions on the left and right side of the interface, respectively. Inelastic scattering is accounted for by letting $\varepsilon \to \varepsilon + i\delta$ where $\delta/\Delta = 0.01$. The superconductors are assumed to be large enough to be approximated as bulk and therefore appear only in the boundary conditions at $x = \pm L/2$. For the transversal interfaces to vacuum, the boundary conditions reduce to $\bar{\nabla}\hat{g} = 0$.

To demonstrate the inverse Edelstein effect originating from the triplet Cooper pairs, we first consider the charge current
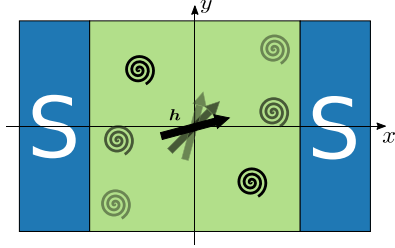
FIG. 1. A top view sketch of the 2D Josephson junction, which is oriented in the xy plane. The green region represents the normal metal, which is quadratic with lengths $L = 2\xi$. The exchange field $\boldsymbol{h}$ is applied in the plane of the junction. The presence of spin-orbit coupling creates vortices in the current density.
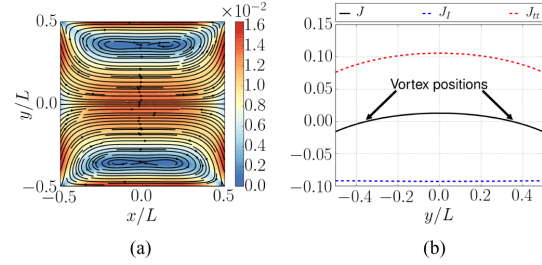

FIG. 2. The current density distribution for an exchange field $h/\Delta = 1.0$ in the x direction. (a) Streamline plot showing vortices. (b) Transversal distribution of the x component of the different currents in the middle of the junction ($x = 0$). All current densities are scaled by $J_0\Delta/L$.

density which in equilibrium is defined as:

$$\boldsymbol{J} = \boldsymbol{J}_0 \int d\varepsilon \ \mathrm{ReTr}\{\hat{\rho}_3 \hat{g} \bar{\nabla} \hat{g}\} \tanh \frac{\beta\varepsilon}{2} \qquad (5)$$

with $J_0 = N_0 e D/2$, where the constant N_0 is the density of states at the Fermi level and $\beta = 1/k_B T$. The temperature T is constant and equal to 1‰ of the critical temperature of the superconductors. By inserting the above expression for $\hat{g}$ into Eq. (5), it is seen that the current density only depends on the anomalous Green function f. Furthermore, f can be split into a contribution from the singlet component f_s and the triplet component $\boldsymbol{f}_t = (f_x, f_y, f_z)$ by inserting the parametrization

$$f = (f_s I + \boldsymbol{f}_t \cdot \boldsymbol{\sigma}) i\sigma_y, \qquad (6)$$

where I is the 2×2 identity matrix. The current density can then be written as

$$\boldsymbol{J} = \boldsymbol{J}_I + \boldsymbol{J}_{tt} \qquad (7)$$

with $\boldsymbol{J}_I = \boldsymbol{J}_s - \boldsymbol{J}_x - \boldsymbol{J}_y - \boldsymbol{J}_z$ being the conventional current contribution from the individual singlet and triplet components, which in turn are given as

$$\boldsymbol{J}_k = 4J_0 \int_0^\infty d\varepsilon \ \mathrm{Re}\{\tilde{f}_k \nabla f_k - f_k \nabla \tilde{f}_k\} \tanh \frac{\beta\varepsilon}{2} \qquad (8)$$

for $k \in \{s,x,y,z\}$. The current $\boldsymbol{J}_I$ is present also in the absence of spin-orbit coupling. With spin-orbit coupling, however, one gets *an additional contribution* from $\boldsymbol{J}_{tt}$, which we find to be:

$$\boldsymbol{J}_{tt} = 16J_0\alpha\boldsymbol{e}_z \times \int_0^\infty d\varepsilon \ \mathrm{Re}\{\tilde{\boldsymbol{f}}_t \times \boldsymbol{f}_t\} \tanh \frac{\beta\varepsilon}{2}. \qquad (9)$$

It is observed that while $\boldsymbol{J}_I$ is a linear combination of currents from each of the four components of f, $\boldsymbol{J}_{tt}$ is generated by interference between the triplet components. Importantly, the cross product in Eq. (9) determines the spin polarization direction of a general triplet Cooper pair state, as is well known from the d-vector formalism used in early works on liquid ^{3}He [24,25]. In other words we find that, due to spin-orbit coupling, the *existence of a finite triplet Cooper pair spin expectation value directly produces a charge current*, which we interpret as a triplet Cooper pair induced inverse Edelstein effect. This is a key result in this paper. We note that another type of Edelstein effect in superconducting hybrid structures has recently been reported in Ref. [10], where a spontaneous

supercurrent induced by magnetization in a Josephson junction with spin-orbit coupling was found. Here, we have presented a different inverse Edelstein effect, in that the spin density responsible for the current is solely generated by the triplet Cooper pairs. This is in contrast to the induced magnetization which requires a nonzero singlet contribution. Recently, the nonequilibrium Edelstein effect and magnetoelectric Andreev transport was discussed in the context of helical metals [18].

III. RESULTS AND DISCUSSION

For the system shown in Fig. 1, we solve the full Usadel equation, given in Eq. (1), by using the finite element method, as thoroughly explained in Ref. [26]. In the results presented herein we apply a phase difference between the superconductors of $\phi = \frac{\pi}{2}$ unless otherwise stated. The first thing to note is that the current density has a nontrivial transversal distribution and even changes sign in certain areas. In the regions where a sign change occurs, supercurrent vortices are generated, i.e., positions around which the current density circulates. Vortices in the current density have been reported in proximitized materials in the presence of an external magnetic flux [26–29], whereas no such flux is required in the present work. These flux-induced vortices are associated with a suppression of superconducting correlations at precisely the location of the vortices in addition to a phase winding of the superconducting phase, analogously to Abrikosov vortices. In the results presented here, we do not find any such suppression, and so the spin-orbit induced supercurrent vortices are therefore of a different nature.

The effect is clearly seen in Fig. 2(a), in which the exchange field is pointing in the x direction. Here, the current density flows in the positive x direction near the center of the junction and in the opposite direction by the edges. This creates a circulation around two oblong vortices at approximately $y = \pm 0.4L$ within which the current density is suppressed. Such a current distribution may be measured experimentally using magneto-optic imaging [30].

Figure 2(b) shows the transverse distribution of the current flowing across the junction. Specifically, it shows the different contributions in Eq. (7) to the total current. It is seen that the transverse distribution of the individual components J_k—the

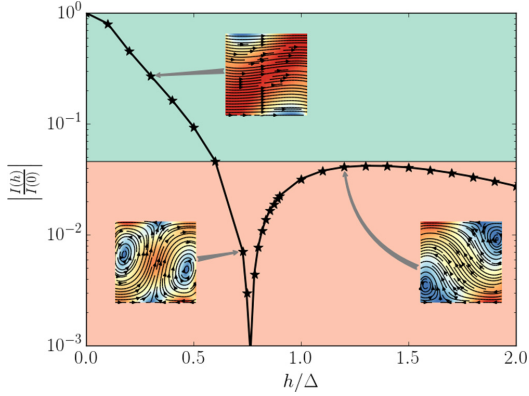FIG. 3. The total current I passing between the superconductors (found by integrating the current density $\boldsymbol{J}$ over the cross section) as a function of the exchange field strength $h = |\boldsymbol{h}|$, applied at an angle $\theta = 45°$ relative to the y axis. The normalized strength of the spin-orbit coupling is $\alpha L = 1$. Pink regions indicate the presence of vortices in the current density. The insets show the current density distribution for selected points.

components not explicitly dependent on α—almost perfectly cancel, rendering their sum J_I constant. It is therefore clear that the main contribution to the transverse distribution stems from J_{tt}, the term responsible for the inverse Edelstein effect induced by the triplet Cooper pair spins.

A key point is that the *existence* of the vortices are found to depend on the strength $h = |\boldsymbol{h}|$ of the exchange field. When examining the current passing between the superconductors for increasing exchange field, a decaying oscillatory pattern is found where, for certain values of h, the current flows in the opposite direction. This is known as a π junction [31], owing to the fact that the ground state of the Josephson junction has a phase difference of π rather than zero [1]. We find that the vortices are harbingers of a 0-π transition, being present only when the total current is significantly reduced. The reason for this is that the transversal distribution of the current density is much less influenced by the strength of the exchange field than the current itself. For increasing h, the curvature of J_{tt} in Fig. 2(b) is more or less retained, while the total current—that is, the average of the current density—is reduced upon approaching a 0-π transition. Close enough to the transition, the minimas of the current density will cross zero and become negative. Evidently, a current density redistribution is less energetically favorable than vortex generation.

It turns out that for an in-plane exchange field, the current is reduced rapidly enough with increasing h for vortices to remain present once they first appear. This can be seen in Fig. 3, which shows the total current I, found by integrating the current density $\boldsymbol{J}$ over the cross section. The exchange field is applied at an angle $\theta = 45°$ with respect to the y axis. In the pink region there are vortices in the current density, and it is observed that the modulation of the curve hinders a reentry into the green region, where vortices are not present. For an out-of-plane exchange field this is not necessarily the case, and

away from the transition points, the current may become large enough for the vortices to disappear.

Interestingly, the *location* of the vortices also changes as the exchange field is increased. The insets of Fig. 3 show the current density distribution for selected points along the current curve. The vortices first appear at the vacuum edges, on opposite sides of the junction, near the superconducting interfaces. As h is increased, they translate vertically and pass the x axis at *precisely* the 0-π transition. At this stage, the current density distribution is symmetric about both the x and the y axis, with no net current passing between the superconductors. Further increase of h causes further translation of the vortices. However, since they must cross the x axis every 0-π transition due to the symmetry requirements, a turning point must be reached, and the motion of the vortices may best be described as resembling a damped harmonic oscillator.

In the study of a 1D Josephson junction with spin-orbit coupling, it was recently discovered that the critical current varies greatly with the direction of an applied exchange field, even creating 0-π transitions [8,13]. It is therefore reasonable to presume that the current density distribution becomes nontrivial. We find that this is indeed the case. With an exchange field of strength $h/\Delta = 1.0$ pointing in the transversal direction ($\theta = 0°$), no vortices are found. Rotating $\boldsymbol{h}$ increases the transversal variation of the current density, and at around $\theta = 30°$ vortices appear, as shown in Fig. 4(a). Further rotation translates the vortices vertically towards the x axis, as seen in Fig. 4(b) for $\theta = 60°$, before translating towards the y axis and ending up like Fig. 2(a) for $\theta = 90°$.

We also determine how the strength of the spin-orbit coupling affects the vortices. Tuning of the Rashba parameter α can be achieved experimentally in a 2DEG by means of a gate voltage [32–34]. For small spin-orbit coupling strength, so too is the contribution from J_{tt}, as can be seen from the explicit dependence on α in Eq. (9). With increasing α, the inverse Cooper pair Edelstein effect predicted here increases both in terms of the curvature and the amplitude of J_{tt}, making the existence of supercurrent vortices possible. Since varying α changes the topography of J_{tt}, it is reasonable that the vortex locations also changes. This can be seen in Figs. 4(c) and 4(d), which show the current density distribution for $\alpha L = 1.2$ and $\alpha L = 1.6$, respectively. It is noted that for large enough Rashba parameter α, no 0-π transition will take place [8], and vortices will only appear for large exchange fields where the conventional contribution to the current, J_I, is sufficiently suppressed relative to J_{tt}.

Finally, we investigate the effect of varying the phase difference ϕ between the superconducting leads. In Figs. 4(e) and 4(f) is shown the current density distribution for select values of ϕ for an exchange field of strength $h/\Delta = 1.0$ applied at an angle of $\theta = 45°$ and a spin-orbit coupling strength of $\alpha L = 1.0$. It can be seen that the phase difference provides yet another means of enacting control over the vortices, with both their presence and location influenced. The two vortices translate vertically in opposite directions as the phase difference is increased. It is noted that the total current has a typical sinusoidal behavior and that the current is zero for $\phi = 0$.

Due to the complexity of the numerical problem, we have here focused on a particular system with a specific set of parameters which we believe to be experimentally relevant.
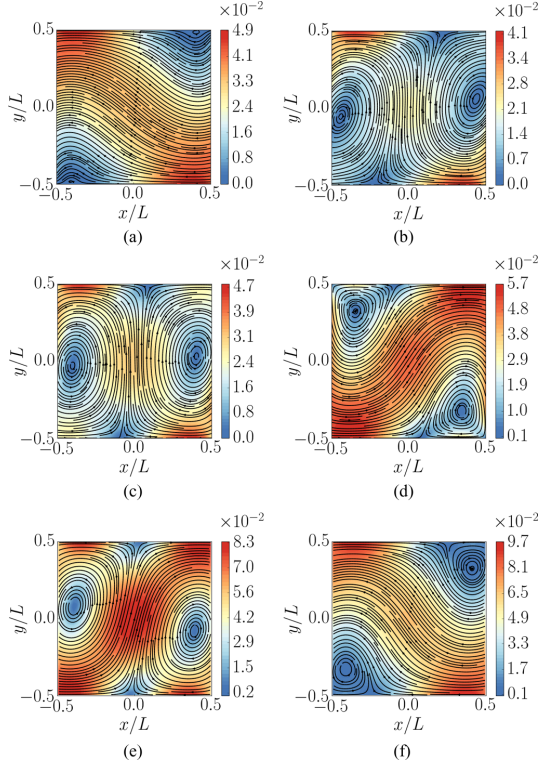
FIG. 4. Streamlines of the current density for (a),(b). Different exchange field directions θ with spin-orbit coupling strength $\alpha L = 1.0$ and phase difference $\phi = \frac{\pi}{2}$. (c),(d) Different αL with $\theta = 45°$ and $\phi = \frac{\pi}{2}$. (e),(f) Different ϕ with $\alpha L = 1.0$ and $\theta = 45°$. The strength of the exchange field is $h/\Delta = 1.0$, which is a realistic magnitude of order $\simeq$ meV accessible via an external magnetic field. All current densities are scaled by $J_0 \Delta / L$.

However, the results can be generalized based on the current findings. For larger exchange fields (but not so large as to destroy the superconducting proximity effect) one can expect that the presence of vortices becomes more common, as the total current is gradually suppressed. Increasing the distance between the superconductors is also known to generate 0-π transitions, around which one may expect vortices. The presence and location of the vortices may also be influenced by the width of the system, as is the case for flux induced vortices [26]. In other words, the results presented herein are not specific to the model considered.

In an experimental setup, a slight misalignment in the orientation of an in-plane field will introduce an out-of-plane component which in turn generates an orbital effect that cannot in general be neglected. To investigate the degree to which this effect influences the current distribution, we have solved the system with an applied external flux $\boldsymbol{A}$. This produces an additional current contribution, given as

$$\boldsymbol{J}_A = 16 \frac{J_0 \boldsymbol{A}}{\hbar^2} \int d\varepsilon \, \mathrm{Im}(f_s \tilde{f}_s - \boldsymbol{f}_t \cdot \tilde{\boldsymbol{f}}_t) \tanh \frac{\beta \varepsilon}{2}. \quad (10)$$
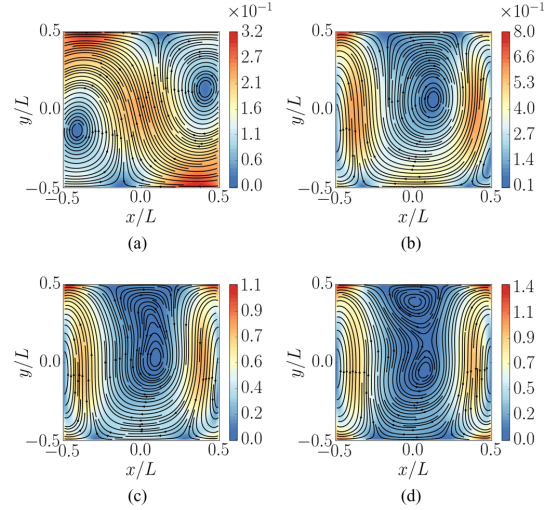
FIG. 5. Streamlines of the charge current density $\boldsymbol{J}$ for increasing external flux Φ passing through the system in the z direction. The exchange field strength is $h/\Delta = 1.0$, applied in an in-plane direction of $\theta = 45°$, and the spin-orbit coupling strength is $\alpha L = 1.0$.

We use the Coulomb gauge, and define the vector potential as $\boldsymbol{A} = -B_\perp y \boldsymbol{e_x}$, where $\boldsymbol{e_x}$ is a unit vector pointing in the x direction and $B_\perp$ is the out-of-plane component of the magnetic field. The flux passing through the system is then given by $\Phi = B_\perp L^2$. In Fig. 5 we show the current density distribution for various flux levels, with $\theta = 45°$ and $h/\Delta = 1.0$. The strength of the spin-orbit coupling is $\alpha L = 1.0$. For $\Phi < \Phi_0$, where $\Phi_0 = \frac{h}{2e}$ is the flux quantum, there are no flux induced vortices, and we see from Figs. 5(a) and 5(b) that the effect of the external flux is to translate the spin-orbit vortices towards the left, with the left-most vortex disappearing from the system. The right-most vortex eventually becomes trapped in the center of the junction for $\Phi \simeq \Phi_0$. For $\Phi > 1.2\Phi_0$, the vortex splits in two and aligns along the y axis, as shown in Figs. 5(c) and 5(d), which is typical for flux-induced vortices [27]. At this point the spin-orbit induced vortices are indistinguishable from flux induced vortices.

To investigate whether spin-orbit vortices will be completely obscured by a small deviation from the in-plane orientation of the magnetic field in an experimental setting, we estimate an effective magnetic field from the exchange field via the Zeeman effect; $\boldsymbol{B}_{\mathrm{eff}} = \frac{2\hbar}{\mu_B g} \boldsymbol{h}$, where μ_B is the Bohr magneton. We assume that the superconductors are niobium, for which the superconducting energy gap is given as $\Delta \simeq 1.5$ meV, and the diffusive coherence length is $\xi \simeq 15$ nm. For a normal metal, where the g factor is given as $g \simeq 2$, an exchange field strength of $|\boldsymbol{h}| = \Delta$ is produced by a magnetic field of $B_{\mathrm{eff}} \simeq 26$ T. This magnitude is not intended as an experimentally feasible field, but is used here to show that even for huge external fields, the supercurrent vortex pattern predicted here remains robust toward an accidental out-of-plane field component. In some doped semiconductors, which are more relevant as candidate

materials for the spin-orbit coupled region in the present study, the g factor can be significantly higher, bringing the required field down to a more tractable level of order $\sim$1–2 T [35]. To estimate the out-of-plane component we use an angle equal to a realistic orientational uncertainty [36] of $\psi = 1°$, so that $B_\perp = B_{\mathrm{eff}} \sin \psi \simeq 0.45$ T. This amounts to a flux of $\Phi \simeq 0.2\Phi_0$, which means that while the out-of-plane component will change the current distribution, it is small enough for the spin-orbit induced vortices to remain visible.

IV. CONCLUSION

We have investigated two-dimensional Josephson junctions with spin-orbit coupling and find that vortices appear in the current density. The presence and location of these vortices may be tuned by varying either the exchange field strength, its direction, the strength of the spin-orbit coupling, or the phase difference. This "supercurrent vortex pinball effect" has its origin in the spin polarization of the triplet Cooper pairs induced in the system and thus arises from what may be interpreted as a Cooper pair-induced inverse Edelstein effect.

[1] A. I. Buzdin, Rev. Mod. Phys. **77**, 935 (2005).

[2] F. S. Bergeret, A. F. Volkov, and K. B. Efetov, Phys. Rev. Lett. **86**, 4096 (2001).

[3] J. Linder and J. W. A. Robinson, Nat. Phys. **11**, 307 (2015).

[4] M. Eschrig, Rep. Prog. Phys. **78**, 104501 (2015).

[5] F. S. Bergeret and I. V. Tokatly, Phys. Rev. Lett. **110**, 117003 (2013).

[6] S. H. Jacobsen and J. Linder, Phys. Rev. B **92**, 024501 (2015).

[7] S. H. Jacobsen, J. A. Ouassou, and J. Linder, Phys. Rev. B **92**, 024510 (2015).

[8] J. Arjoranta and T. T. Heikkilä, Phys. Rev. B **93**, 024522 (2016).

[9] M. Alidoust and K. Halterman, New J. Phys. **17**, 033001 (2015).

[10] F. Konschelle, I. V. Tokatly, and F. S. Bergeret, Phys. Rev. B **92**, 125443 (2015).

[11] S. S. Pershoguba, K. Björnson, A. M. Black-Schaffer, and A. V. Balatsky, Phys. Rev. Lett. **115**, 116602 (2015).

[12] F. Konschelle, I. V. Tokatly, and F. S. Bergeret, Phys. Rev. B **94**, 014515 (2016).

[13] A. Costa, P. Högl, and J. Fabian, Phys. Rev. B **95**, 024514 (2017).

[14] I. V. Bobkova and A. M. Bobkov, Phys. Rev. B **95**, 184518 (2017).

[15] R. Takashima and S. Fujimoto, Phys. Rev. B **94**, 235117 (2016).

[16] S. H. Jacobsen, I. Kulagina, and J. Linder, Sci. Rep. **6**, 23926 (2015).

[17] T. Yu and M. W. Wu, Phys. Rev. B **93**, 195308 (2016).

[18] G. Tkachov, Phys. Rev. Lett. **118**, 016802 (2017).

[19] F. Pientka, A. Keselman, E. Berg, A. Yacoby, A. Stern, and B. I. Halperin, Phys. Rev. X **7**, 021032 (2017).

[20] K. Björnson, S. S. Pershoguba, A. V. Balatsky, and A. M. Black-Schaffer, Phys. Rev. B **92**, 214501 (2015).

[21] A. G. Mal'shukov, Phys. Rev. B **93**, 054511 (2016).

[22] K. Usadel, Phys. Rev. Lett. **25**, 507 (1970).

[23] M. Y. Kupriyanov and V. F. Lukichev, Sov. Phys. JETP **67**, 1163 (1988).

[24] Anthony J. Leggett, Rev. Mod. Phys. **47**, 331 (1975).

[25] A. P. Mackenzie and Y. Maeno, Rev. Mod. Phys. **75**, 657 (2003).

[26] M. Amundsen and J. Linder, Sci. Rep. **6**, 22765 (2016).

[27] J. C. Cuevas and F. S. Bergeret, Phys. Rev. Lett. **99**, 217002 (2007).

[28] F. S. Bergeret and J. C. Cuevas, J. Low Temp. Phys. **153**, 304 (2008).

[29] M. Alidoust, G. Sewell, and J. Linder, Phys. Rev. Lett. **108**, 037001 (2012).

[30] T. H. Johansen, M. Baziljevich, H. Bratsberg, Y. Galperin, P. E. Lindelof, Y. Shen, and P. Vase, Phys. Rev. B **54**, 16264 (1996).

[31] V. V. Ryazanov, V. A. Oboznov, A. Y. Rusanov, A. V. Veretennikov, A. A. Golubov, and J. Aarts, Phys. Rev. Lett. **86**, 2427 (2001).

[32] J. Nitta, T. Akazaki, H. Takayanagi, and T. Enoki, Phys. Rev. Lett. **78**, 1335 (1997).

[33] G. Engels, J. Lange, T. Schapers, and H. Luth, Phys. Rev. B **55**, R1958(R) (1997).

[34] D. Grundler, Phys. Rev. Lett. **84**, 6074 (2000).

[35] R. L. Hota and G. S. Tripathi, J. Phys.: Condens. Matter **3**, 6299 (1991).

[36] G. M. Gusev, A. A. Quivy, J. R. Leite, A. A. Bykov, N. T. Moshegov, V. M. Kudryashev, A. I. Toropov, and Y. V. Nastaushev, Semicond. Sci. Technol. **14**, 1114 (1999).

Paper V

Reference

Contributions

JL initiated the project after discussions with MA. JL did the analytical and numerical work. VR and MA participated in the discussion of the results. JL conceived the physical mechanism responsible for the results after discussions with MA. JL drafted the manuscript. All authors contributed to the discussion of the physics and the revision of the final manuscript.

Intrinsic superspin Hall current

Jacob Linder, Morten Amundsen, and Vetle Risinggård

Department of Physics, NTNU, Norwegian University of Science and Technology, N-7491 Trondheim, Norway and Center for Quantum Spintronics, Department of Physics, Norwegian University of Science and Technology, NO-7491 Trondheim, Norway

We discover an intrinsic superspin Hall current: an injected charge supercurrent in a Josephson junction containing heavy normal metals and a ferromagnet generates a transverse spin supercurrent. There is no accompanying dissipation of energy, in contrast to the conventional spin Hall effect. The physical origin of the effect is an antisymmetric spin density induced among transverse modes k_y near the interface of the superconductor arising due to the coexistence of p-wave and conventional s-wave superconducting correlations with a belonging phase mismatch. Our predictions can be tested in hybrid structures including thin heavy metal layers combined with strong ferromagnets and ordinary s-wave superconductors.

I. INTRODUCTION

By combining materials with different properties at the quantum-mechanical level into hybrid structures, new physics emerges that often cannot be found in pure materials. The field of superconducting spintronics [1] is a prime example of this, where the synthesis of superconducting and magnetic correlations has been shown [2–5] to yield physical effects that are interesting both from a fundamental viewpoint and from the viewpoint of potential cryogenic applications. One actively pursued direction in this field has been the prospect of producing dissipationless currents of spin carried by spin-polarized Cooper pairs [6,7]. The conversion of charge currents to spin currents is known to occur via the spin Hall effect [8–10] in conventional spintronics, but it is accompanied by the dissipation of energy due to the resistive nature of electric currents in nonsuperconducting structures. Here, we show that it is possible to achieve a dissipationless conversion from charge to spin supercurrents, using conventional superconducting materials. We discover that an injected charge supercurrent in a Josephson junction generates a pure transverse spin supercurrent that is thus time-reversal invariant. Due to the analogy with the conventional spin Hall current, we refer to this as a superspin Hall current. The microscopic origin of the superspin Hall current is a spin magnetization induced at the interface that is antisymmetric in transverse momentum k_y. This magnetization is in turn caused by the induction of p-wave superconductivity coexisting with conventional spin-singlet pairing. Our predictions can be verified using hybrid structures with thin heavy-metal layers combined with strong ferromagnets and ordinary s-wave superconductors (see Fig. 1) and open new vistas for making superconductors compatible with spintronics functionality.

II. THEORY

To describe physics occurring at atomic length scales and also incorporating strong spin-orbit coupling, we use the tight-binding Bogoliubov–de Gennes (BdG) framework, which is free from the limitations on length scales and self-energy magnitudes present in, e.g., quasiclassical theory [11]. Our Hamiltonian reads

$$H = -t \sum_{\langle i,j \rangle \sigma} c_{i\sigma}^{\dagger} c_{j\sigma} - \frac{i}{2} \sum_{\langle i,j \rangle \alpha\beta} \lambda_i c_{i\alpha}^{\dagger} \bm{n} \cdot (\bm{\sigma} \times \bm{d}_{ij})_{\alpha\beta} c_{j\beta}$$
$$- \sum_{i\sigma} \mu_i c_{i\sigma}^{\dagger} c_{i\sigma} - \sum_i U_i n_{i\uparrow} n_{i\downarrow} + \sum_{i\alpha\beta} c_{i\alpha}^{\dagger} (\bm{h}_i \cdot \bm{\sigma})_{\alpha\beta} c_{i\beta}. \tag{1}$$

Here, t is the hopping integral, $\{c_{i\sigma}, c_{i\sigma}^{\dagger}\}$ are second-quantized fermion operators for site $\bm{i}$ and spin σ, $\bm{n}$ is a unit vector normal to the interface, λ_i is the site-dependent spin-orbit coupling magnitude, $\bm{d}_{ij} = -\bm{d}_{ji}$ is the nearest-neighbor vector from site $\bm{i}$ to site $\bm{j}$, $n_{i\sigma} = c_{i\sigma}^{\dagger} c_{i\sigma}$, $\bm{\sigma}$ is the Pauli matrix vector, $\bm{h}_i$ is the local magnetic exchange field, μ_i is the local chemical potential, and U_i is the on-site attractive interaction giving rise to superconductivity. For concreteness, we consider a square lattice of size $N_x \times N_y$ with lattice site indices $\bm{i} = (i_x, i_y)$. To demonstrate the superspin Hall current, we consider Fig. 1 which may be experimentally achieved by creating a stack of layers including one magnetic layer (e.g., Fe or Co) and two thin heavy-metal layers (e.g., Pt or Au) sandwiched between two conventional superconductors (e.g., Nb or Al). The various terms in Eq. (1) exist in their respective regions in Fig. 1. For instance, the spin-orbit coupling term λ_i is only finite for lattice points inside the heavy-metal regions. For brevity of notation, the lattice constant is set to $a = 1$ and all length scales are measured relative to a whereas all energies are measured relative to t. Since $\bm{n}$ is the interface normal ($\bm{n} = \hat{\bm{x}}$), the Hamiltonian above is Hermitian without any requirement of symmetrization.

To simplify the calculations, we assume periodic boundary conditions in the $\hat{\bm{y}}$ direction, as is common practice [12–14]. While this represents an approximation to the geometry considered, it will still allow us to determine the presence of transverse currents. Equation (1) may now be diagonalized by Fourier transforming the fermion operators in the $\hat{\bm{y}}$ direction;

$$c_{i\sigma} = 1/\sqrt{N_y} \sum_{k_y} c_{i_x, k_y \sigma} e^{ik_y i_y}. \tag{2}$$

Performing a standard mean-field ansatz $\Delta_i = -U_i \langle c_{i\downarrow} c_{i\uparrow} \rangle$, one arrives at the Hamiltonian

$$H = H_0 + \frac{1}{2} \sum_{ijk} B_{ik}^\dagger H_{ijk} B_{jk}, \qquad (3)$$

where H_0 contains the superconducting condensation energy $N_y \sum_{i \in S} |\Delta_i|^2 / U_i$ (which must be retained when evaluating the free energy of the system). Let $i \equiv i_x$ and $j \equiv j_x$ from now on for brevity of notation. The superconducting regions are comprised of $N_{x,S}$ lattice points each, whereas the heavy metals generating interfacial Rashba spin-orbit coupling and strong ferromagnets have spatial extensions $N_{x,HM}$ and $N_{x,F}$, respectively. The total number of lattice sites is $N_x = N_y$. Setting $k \equiv k_y$, the basis above is

$$B_{ik}^\dagger = [c_{ik\uparrow}^\dagger \ c_{ik\downarrow}^\dagger \ c_{i,-k\uparrow} \ c_{i,-k\downarrow}] \qquad (4)$$

and we defined the 4×4 matrix:

$$H_{ijk} = \epsilon_{ijk} \hat{\sigma}_0 \hat{\tau}_3 + \left[h_i^y \hat{\sigma}_y + (\lambda \sin k/2) \hat{\sigma}_z \right] \hat{\tau}_0$$
$$+ \left(h_i^x \hat{\sigma}_x + h_i^z \hat{\sigma}_z \right) \hat{\tau}_3 + \Delta_i i \hat{\sigma}_y \hat{\tau}^+ - \Delta_i^* i \hat{\sigma}_y \hat{\tau}^-, \qquad (5)$$

where

$$\epsilon_{ijk} \equiv -t \cos(k) \delta_{ij} - t(\delta_{i,j+1} + \delta_{i,j-1})/2 - \mu_i \delta_{ij} \qquad (6)$$

and $2\hat{\tau}^\pm = \hat{\tau}_1 \pm i \hat{\tau}_2$. The matrices $\hat{\tau}_i$ that appear in Eq. (5) are the usual Pauli matrices ($i = 0,1,2,3$, where $\hat{\tau}_0$ is the identity). By diagonalizing the above matrix, we end up with the Hamiltonian

$$H = H_0 + \frac{1}{2} \sum_{nk} E_{nk} \gamma_{nk}^\dagger \gamma_{nk}, \qquad (7)$$

where the new (quasiparticle) fermion operators are related to the original ones via the relations

$$c_{ik\uparrow} = \sum_n u_{ink} \gamma_{nk}, \quad c_{ik\downarrow} = \sum_n v_{ink} \gamma_{nk},$$
$$c_{i,-k,\uparrow}^\dagger = \sum_n w_{ink} \gamma_{nk}, \quad c_{i,-k,\downarrow}^\dagger = \sum_n x_{ink} \gamma_{nk}. \qquad (8)$$

Here, $\{u,v,w,x\}$ are elements of the matrix that diagonalize the Hamiltonian and are numerically obtained. The diagonalized form of the Hamiltonian makes it trivial to evaluate expectation values of the type $\langle \gamma_{nk}^\dagger \gamma_{nk} \rangle = f(E_{nk}/2)$, where f is the Fermi-Dirac distribution function.

With the eigenvectors $\{u,v,w,x\}$ and eigenvalues $\{E_{nk}\}$ at hand, we can compute a number of physical quantities in the system under consideration. For instance, the order parameter takes the form

$$\Delta_i = -\frac{U_i}{L_y} \sum_{nk}' v_{ink} w_{ink}^* [1 - f(E_{nk}/2)], \qquad (9)$$

where the prime superscript on the sum indicates that only energy eigenvalues $|E_{nk}| < \omega_D$ should be included, and ω_D is the BCS Debye cutoff frequency. The free energy reads

$$F = H_0 - \frac{1}{\beta} \sum_{nk} \ln(1 + e^{-\beta E_{nk}/2}), \qquad (10)$$

where $\beta = 1/T$ and T is temperature. The evaluation of charge and spin supercurrent $\boldsymbol{j}_i$ and $\boldsymbol{j}_{i,S}$ operators requires a consid-
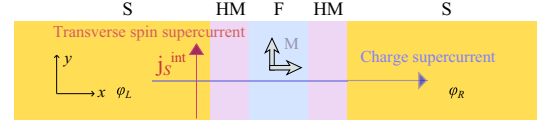

FIG. 1. Suggested experimental setup for demonstration of the superspin Hall current in a Josephson junction. The exchange field in the ferromagnetic region (gray arrows) is directed either along the $\hat{x}$ or $\hat{y}$ axis. In our calculations, we model the system as a 2D square lattice with periodic boundary conditions in the $\hat{y}$ direction.

eration of the combined continuity and Heisenberg equation:

$$-\nabla \cdot \boldsymbol{j}_i = i[H, \rho_i], \quad -\nabla \cdot \boldsymbol{j}_i^S = i[H, \boldsymbol{S}_i]. \qquad (11)$$

Here,

$$\rho_i = \sum_\sigma c_{i\sigma}^\dagger c_{i\sigma} \qquad (12)$$

is the charge-density operator at site $\boldsymbol{i}$, while

$$\boldsymbol{S}_i = \sum_{\alpha\beta} c_{i\alpha}^\dagger \boldsymbol{\sigma}_{\alpha\beta} c_{i\beta} \qquad (13)$$

is the spin-density operator (we omitted constant prefactors such as the electronic charge $|e|$). After a Fourier transformation, the spin-density expectation value at site i reads

$$\boldsymbol{S}_i = \sum_k \boldsymbol{S}_{ik}, \ \boldsymbol{S}_{ik} = \langle c_{ik\alpha}^\dagger \boldsymbol{\sigma}_{\alpha\beta} c_{ik\beta} \rangle. \qquad (14)$$

Here, $\boldsymbol{S}_{ik}$ is the momentum-resolved spin-density expectation value at lattice point i, which will play a prominent role in the discussion later.

A spin supercurrent flowing along the interface has three polarization components and is most conveniently evaluated in the superconducting region:

$$\boldsymbol{j}_{i,S}^{\text{int}} = \langle \boldsymbol{j}_i^S \cdot \hat{\boldsymbol{y}} \rangle = -\frac{8t}{N_y} \sum_{k\alpha\beta} \sin(k) \boldsymbol{\sigma}_{\alpha\beta} \langle c_{ik\alpha}^\dagger c_{ik\beta} \rangle. \qquad (15)$$

For instance, the spin supercurrent polarized in the $\hat{x}$ and $\hat{y}$ directions is

$$j_{i,S}^{\text{int},x} = -\frac{16t}{N_y} \sum_{nk} \sin(k) \text{Re}\{u_{ink} v_{ink}^*\} f(E_{nk}/2),$$
$$j_{i,S}^{\text{int},y} = \frac{16t}{N_y} \sum_{nk} \sin(k) \text{Im}\{u_{ink}^* v_{ink}\} f(E_{nk}/2). \qquad (16)$$

III. RESULTS

A. Superspin Hall current

We first numerically diagonalize the Hamiltonian given by Eqs. (1) and (5) for the Josephson junction shown in Fig. 1 using the parameters $\mu_S = 0.9$, $\mu_N = 0.85$, $\mu_F = 0.8$, $\omega_D = 0.3$, $N_{x,S} = 35$, $N_{x,HM} = 4$, $N_{x,F} = 7$, $U = 2.1$, and $T = 0.01$. The order parameter phase is fixed at the last five lattice points in the S regions in order to model supercurrent injection via a phase difference, as is standard in the BdG lattice treatment. Fixing $\Delta\phi = 0.5\pi$ gives an effective
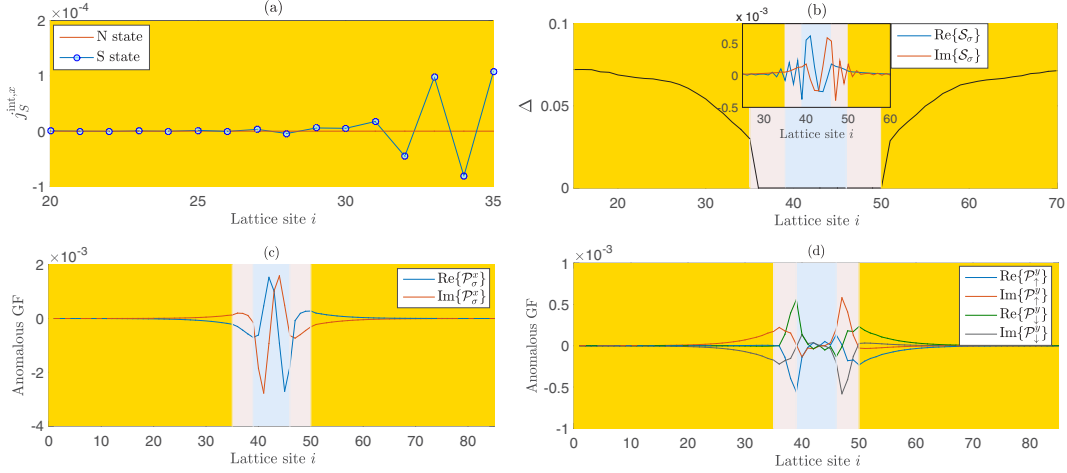
FIG. 2. (a) Superspin Hall current manifested via a transverse spin supercurrent $j_{i,S}^{\text{int},x}$ in the superconducting (S) state. It vanishes in the normal (N) state: $j_{i,S}^{\text{int},x} = 0$. (b) Spatial evolution of the superconducting order parameter. Inset: $\mathcal{S}_{\sigma,i}(\tau)$ with relative time set to $\tau = 5$, (c) $\mathcal{P}_{\sigma,i}^{x}$, and (d) $\mathcal{P}_{\sigma,i}^{y}$. For the inset in panel (b) and in panel (c), the curves are identical for $\sigma = \uparrow$ and $\sigma = \downarrow$. We have used the parameter set specified in the main text, considered the system in Fig. 1, and set $h_y = 0.5$, $\lambda = 0.2$, and $\Delta\phi = 0.5\pi$.

phase difference between the superconducting interfaces of $\Delta\phi \simeq 0.47\pi$ due to the phase drop inside the superconductors. The following results are not qualitatively sensitive to the parameter choice above. For the above parameter set, and all other sets presented in the figures of this paper, we have checked that the superconducting state minimizes the free energy of the system.

When $\Delta\phi \neq 0$, a transverse spin supercurrent appears in the superconducting region as shown in Fig. 2(a). This demonstrates the intrinsic superspin Hall current. The effect occurs even if one removes one of the heavy-metal layers. The spin supercurrent predicted here does not exist in the absence of superconductivity, as also shown in Fig. 2(a). Reversing the phase difference, $\Delta\phi \rightarrow -\Delta\phi$, and thus the charge supercurrent, also reverses the transverse spin supercurrent. Before explaining the microscopic origin of the superspin Hall current, we note that there are both odd- and even-frequency triplet correlations in the system, denoted odd-ω and even-ω from now on. The on-site (s-wave) odd-ω anomalous triplet amplitudes $\mathcal{S}$ are defined as

$$\mathcal{S}_{0,i}(\tau) = \langle c_{i\uparrow}(\tau)c_{i\downarrow}(0)\rangle + \langle c_{i\downarrow}(\tau)c_{i\uparrow}(0)\rangle,$$
$$\mathcal{S}_{\sigma,i}(\tau) = \langle c_{i\sigma}(\tau)c_{i\sigma}(0)\rangle, \tag{17}$$

where τ is the relative time coordinate, and the subscripts 0 and $\sigma = \pm 1 = \uparrow, \downarrow$ denote the spin projection along the quantization axis. All $\mathcal{S}$ vanish at $\tau = 0$. The p-wave even-ω anomalous triplet amplitudes $\mathcal{P}$ have both a p_x- and p_y-wave component. They are defined as

$$\mathcal{P}_{0,i}^{x(y)} = \sum_{\pm} \pm(\langle c_{i\uparrow}c_{i\pm\hat{x}(\hat{y}),\downarrow}\rangle + \langle c_{i\downarrow}c_{i\pm\hat{x}(\hat{y}),\uparrow}\rangle),$$
$$\mathcal{P}_{\sigma,i}^{x(y)} = \sum_{\pm} \pm\langle c_{i\sigma}c_{i\pm\hat{x}(\hat{y}),\sigma}\rangle. \tag{18}$$

The existence of these correlations and their spatial distribution throughout the system are shown in Figs. 2(b)–2(d), proving how they arise precisely near the interfaces between the superconductor and heavy metals where the transverse spin supercurrent flows. The triplet components of the Cooper pairs are generated from the broken spin rotational symmetry in our system, whereas the p-wave orbital symmetry emerges as a result of broken translational symmetry due to the presence of interfaces [16,17] and due to the presence of spin-orbit interactions. Note how the pairing amplitudes $\mathcal{S}$ and $\mathcal{P}$ are by definition k-independent. The k-resolved anomalous Green functions, which are odd under $k \rightarrow (-k)$ for, e.g., p-wave pairing, will be examined in the following subsection as they play an important role in understanding the appearance of a transverse spin supercurrent.

The transverse spin-supercurrent in the present system exists when the exchange field contribution $\boldsymbol{h} \cdot \boldsymbol{\sigma}$ to the Hamiltonian does not commute with the spin-orbit contribution $\lambda \sin(k)\sigma_z$. In effect, the superspin Hall current arises when

$$[\boldsymbol{h} \cdot \boldsymbol{\sigma}, \lambda \sin(k)\sigma_z] \neq 0. \tag{19}$$

This means that the exchange field must be oriented in the xy plane of the system shown in Fig. 1. If the exchange field is oriented along the z axis, no superspin Hall current exists.

The polarization of the transverse spin-supercurrent is also dictated by the orientation of the exchange field $\boldsymbol{h}$. A comparison of Figs. 2(a) and 3(h) shows that the spin-supercurrent polarization is perpendicular to $\boldsymbol{h}$.

B. Microscopic origin

To explain the physical origin of the superspin Hall current in the system, we first note the close relation between the spin magnetization and the spin supercurrent in the system. From Eqs. (14) and (15), the only difference between them is a factor
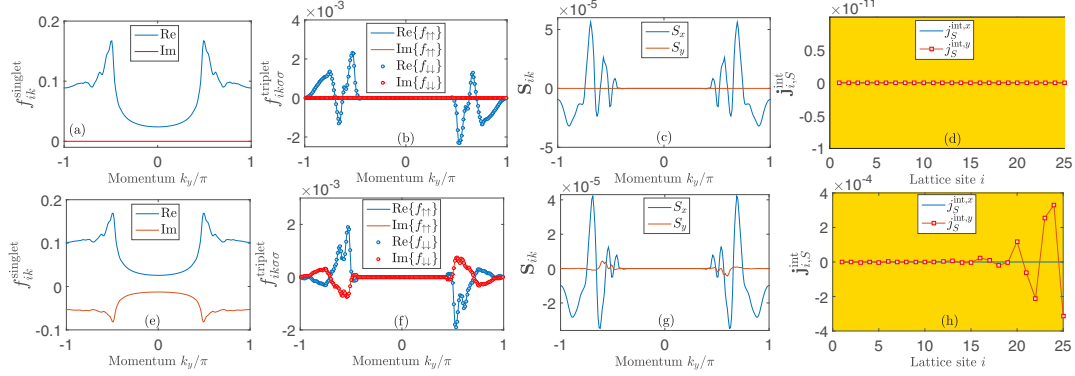
FIG. 3. Upper row: The panels show the induced singlet anomalous Green function f_{ik}^{singlet}, the triplet correlations $f_{ik\sigma\sigma}^{\text{triplet}}$ evaluated at lattice point $i_x = N_S - 1$ (right at the S/N interface), the induced spin-magnetization density $\boldsymbol{S}_{ik}$ evaluated at lattice point $i_x = N_S - 1$ (right at the S/N interface), and the superspin Hall current $\boldsymbol{j}_{i,S}^{\text{int}}$ from left to right. Here, the phase difference has been set to $\Delta\phi = 0$, while $h = 0.3$, $\lambda = 0.3$, $T = 0.005$, $N_S = 25$, $N_{HM} = 4$, $N_F = 5$, $N_y = 200$, and $\boldsymbol{h} = h\hat{\boldsymbol{x}}$. Lower row: Same as the upper row except that $\Delta\phi = \pi/2$. In this case, the coexistence of triplet and singlet correlations that are phase-mismatched produce an antisymmetric spin density $\boldsymbol{S}_{ik}$, which in turn gives rise to a finite superspin Hall current. In the line labels of the second panels from the left, we have abbreviated $f_{ik\sigma\sigma}^{\text{triplet}} \equiv f_{\sigma\sigma}$. In this figure, the exchange field has been rotated to the $\hat{\boldsymbol{x}}$ direction to show that the superspin Hall current exists also in this case. In all other plots in this paper, the exchange field points in the $\hat{\boldsymbol{y}}$ direction.

$\sin(k_y)$ inside the summation. If the momentum-resolved spin magnetization $\boldsymbol{S}_{ik}$ is antisymmetric in momentum k_y, it will vanish when summed over the momentum index. However, due to the extra factor $\sin(k_y)$, an antisymmetric spin magnetization gives a symmetric spin supercurrent, which is thus finite upon summation over k_y. The factor $\sin(k_y)$ and the resulting difference in symmetry are physically reasonable. If a spin density is antisymmetric in momentum k_y, there will exist a net spin flow since the spin current requires an extra multiplication with the group velocity

$$\partial\epsilon_{\boldsymbol{k}}/\partial k_y \propto \sin(k_y a) \qquad (20)$$

for each transverse mode. On the other hand, a spin density that is symmetric in k_y does not induce any spin current.

An antisymmetric spin density in the momentum index k_y may emerge whenever conventional superconducting singlet pairing and triplet pairing (such as a p_y wave) coexist, for instance near interfaces, as we will explain below. A general superconducting order parameter F_{ik} accounting for both singlet and triplet pairing (considering here the even-ω symmetry contribution) can be written as

$$F_{ik} = (f_{i,s} + \boldsymbol{f}_{i,\boldsymbol{k}} \cdot \boldsymbol{\sigma})i\sigma_2, \qquad (21)$$

where $f_{i,s}$ is the singlet component and $\boldsymbol{f}_{i,\boldsymbol{k}} = -\boldsymbol{f}_{i,-\boldsymbol{k}}$ is a vector containing the triplet components according to

$$\boldsymbol{f} = \tfrac{1}{2}[f_{\downarrow\downarrow} - f_{\uparrow\uparrow}, -i(f_{\downarrow\downarrow} + f_{\uparrow\uparrow}), 2f_{\uparrow\downarrow}]. \qquad (22)$$

Above, we suppressed the $(i, \boldsymbol{k})$ indices on the triplet anomalous Green functions $f_{ik\sigma\sigma'}$ for brevity of notation, and we also do so below when the index is not of importance for the argument. A nonunitary superconducting state, where the Cooper pairs have a finite spin expectation value, is defined by $FF^\dagger$ not being proportional to the unit matrix.

A straightforward calculation shows that

$$FF^\dagger = |f_s|^2 + |\boldsymbol{f}_{\boldsymbol{k}}|^2 + \boldsymbol{\sigma} \cdot [(f_s \boldsymbol{f}_{\boldsymbol{k}}^* + f_s^* \boldsymbol{f}_{\boldsymbol{k}}) + i(\boldsymbol{f}_{\boldsymbol{k}} \times \boldsymbol{f}_{\boldsymbol{k}}^*)]. \qquad (23)$$

The term $i(\boldsymbol{f}_{\boldsymbol{k}} \times \boldsymbol{f}_{\boldsymbol{k}}^*)$ determines the spin expectation value of pure triplet Cooper pairs, whereas $(f_s \boldsymbol{f}_{\boldsymbol{k}}^* + f_s^* \boldsymbol{f}_{\boldsymbol{k}})$ determines the spin magnetization of a given mode k_y resulting from the coexistence of singlet and triplet pairing. The spin magnetization arising due to the Cooper pairs in the system thus takes, in general, the following form for a given mode k_y:

$$\boldsymbol{S}_{\boldsymbol{k}}^{\text{Cooper}} \propto (f_s \boldsymbol{f}_{\boldsymbol{k}}^* + f_s^* \boldsymbol{f}_{\boldsymbol{k}}) + i(\boldsymbol{f}_{\boldsymbol{k}} \times \boldsymbol{f}_{\boldsymbol{k}}^*). \qquad (24)$$

Performing a summation over modes k_y, one obtains the total spin density. Therefore, it is clear that if $(f_s \boldsymbol{f}_{\boldsymbol{k}}^* + f_s^* \boldsymbol{f}_{\boldsymbol{k}}) = 2\,\text{Re}\{f_s \boldsymbol{f}_{\boldsymbol{k}}^*\}$ is nonzero, it will be antisymmetric in k_y due to the fundamental property of the triplet vector $\boldsymbol{f}_{\boldsymbol{k}}$. It is crucial to note that the existence of p-wave *triplet pairing alone is not sufficient* to produce an antisymmetric spin density in k_y space. First of all, it has to coexist with singlet pairing. But even such a scenario is not sufficient, as it is only the real part of the product $f_s \boldsymbol{f}_{\boldsymbol{k}}^*$ that contributes. Consider, for instance, the case in which singlet pairing coexists with $S_z = 0$ triplet pairing, such that $\boldsymbol{f}_{\boldsymbol{k}} \parallel \hat{\boldsymbol{z}}$. According to our above argumentation, this should produce a magnetization in the $\hat{\boldsymbol{z}}$ direction. It is not immediately obvious how a magnetization in the $\hat{\boldsymbol{z}}$ direction can arise from singlet pairs (which are spinless) and triplet pairs with zero spin projection along the $\hat{\boldsymbol{z}}$ axis. Therefore, we provide a detailed exposition of the physical mechanism behind this effect in the Appendix.

With this in mind, we can now explain why the superspin Hall current appears. As argued above, this current will exist when an antisymmetric spin density is induced near the interface. The spin density, in turn, is determined by the generation of p-wave superconducting correlations coexisting

with conventional singlet ones when these have an appropriate relative phase such that $\mathrm{Re}\{f_s \boldsymbol{f_k^*}\} \neq 0$ (as explained in the Appendix). The equal spin-pairing triplet anomalous Green functions may be obtained as

$$
\begin{aligned}
f_{ik\sigma\sigma}^{\mathrm{triplet}} &= \langle c_{i,k,\sigma} c_{i,-k,\sigma} \rangle \\
&= \begin{cases} \sum_n u_{ink} w_{ink}^*[1 - f(E_{nk}/2)] & \text{for } \sigma = \uparrow, \\ \sum_n v_{ink} x_{ink}^*[1 - f(E_{nk}/2)] & \text{for } \sigma = \downarrow, \end{cases}
\end{aligned}
\tag{25}
$$

where, as before, we have used the shorthand notation of $k_y \equiv k$. We now illustrate two instructive cases in Fig. 3. In the upper row (a)–(d), the phase difference is $\Delta\phi = 0$ (no current injected) while in the lower row (e)–(h), the phase difference is $\Delta\phi = \pi/2$ (finite current injected). In both cases, we have set $h = 0.3$, $\lambda = 0.3$, and $\boldsymbol{h} = h\hat{\boldsymbol{x}}$. We also chose a different system size, exchange field orientation, and number of transverse modes from those in the previous figures in order to show that the effect does not depend on these details: $N_S = 25$, $N_{HM} = 4$, $N_F = 5$, and $N_y = 200$. As expected, a finite net magnetization S_x exists in the upper row, which comes from the inverse proximity effect caused by the magnetic region. However, there exists no net or k_y-resolved magnetization S_y despite the fact that the anomalous triplet correlations $f_{ik\sigma\sigma}^{\mathrm{triplet}} \equiv f_{\sigma\sigma}$ are nonzero. The reason for this is that they are purely real, as seen in the figure. Consequently, $\mathrm{Re}\{f_s \boldsymbol{f_k^*}\} = 0$ since the singlet ones are purely real in the absence of a phase gradient. Note how the figure shows that $f_{\uparrow\uparrow} = f_{\downarrow\downarrow}$, such that no antisymmetric contribution is made to the $\boldsymbol{x}$ component according to Eq. (22). The finite magnetization induced along the $\boldsymbol{x}$ direction is instead caused by the odd-ω triplet component. In general, the triplet vector $\boldsymbol{f}$ can have both a symmetric term in $\boldsymbol{k}$ (the odd-ω component) and an antisymmetric term in $\boldsymbol{k}$ (the even-ω component). Only the latter contributes to the spin supercurrent in the present context, as explained above.

Consider now instead the lower row, where a finite phase difference exists. The singlet and triplet correlations are now complex because of $\Delta\phi \neq 0$, and as a result the $\boldsymbol{y}$ component of the spin-magnetization (which exists since the term $\mathrm{Re}\{f_s \boldsymbol{f_k^*}\}$ is nonzero) is finite and antisymmetric in k_y. Although no net magnetization exists in the $\boldsymbol{y}$ direction, *a net spin supercurrent now exists* due to the relation between Eqs. (14) and (15) explained above. A phase gradient is thus physically required in order to render the singlet and triplet p_y-wave correlations complex: otherwise, no antisymmetric spin magnetization associated with a nonunitary superconducting state exists, and the spin supercurrent is zero. This explains the origin of the superspin Hall current predicted in this paper.

The above explanation is consistent irrespective of the direction of the in-plane exchange field. For instance, if we instead choose $\boldsymbol{h} = h\hat{\boldsymbol{y}}$, one finds that the triplet anomalous function is purely imaginary at $\Delta\phi = 0$ and that $f_{\uparrow\uparrow} = -f_{\downarrow\downarrow}$. In this case, there is no contribution to the $\hat{\boldsymbol{y}}$ component according to Eq. (22), and although $\boldsymbol{f_k} \cdot \hat{\boldsymbol{x}} \neq \boldsymbol{0}$ there is still no antisymmetric spin density since $\mathrm{Re}\{f_s \boldsymbol{f_k^*}\} = 0$. If $\Delta\phi \neq 0$, on the other hand, $\mathrm{Re}\{f_s \boldsymbol{f_k^*}\}$ is finite in the $\hat{\boldsymbol{x}}$ direction and a spin supercurrent polarized in this direction appears, as seen in the figure.
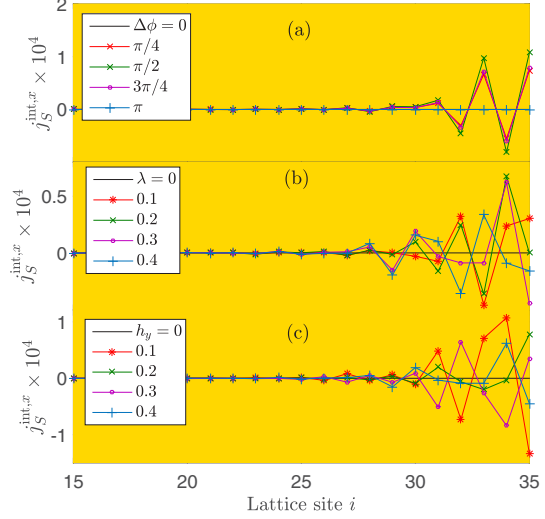

FIG. 4. The dependence of the supenspin Hall current $j_{i,S}^{\mathrm{int},x}$ on physical parameters in the system (Fig. 1). (a) $\lambda = 0.2$ and $h_y = 0.5$ for various values of the phase difference $\Delta\phi$. (b) $\Delta\phi = \pi/2$ and $h_y = 0.4$ for several spin-orbit magnitudes λ. (c) $\lambda = 0.3$ and $\Delta\phi = \pi/2$ for various values of the exchange field h_y. The values of the remaining parameters are the same as in Fig. 2. The background color indicates in which region the current has been evaluated (compare with the left part of Fig. 1).

The spatial dependence of the supenspin Hall current on the phase difference, the Rashba spin-orbit interaction, and exchange field is shown in Fig. 4. The effect vanishes both in the absence of superconductivity ($\Delta\phi = 0$) and in the absence of a charge supercurrent ($\Delta\phi = 0$), as follows from the above explanation of the physical origin of the effect. We also find that the magnitude of the transverse current $j_{i,S}^{\mathrm{int},x}$ evaluated at the superconducting interface ($i = N_S \equiv N_{x,S}$) oscillates with
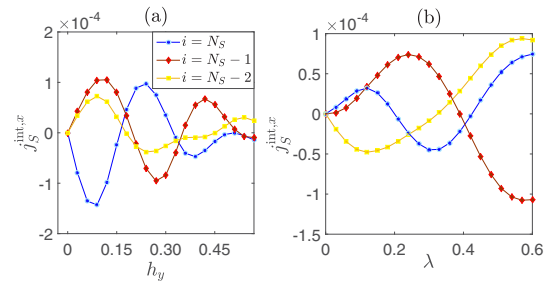

FIG. 5. The dependence of the supenspin Hall current $j_{i,S}^{\mathrm{int},x}$ on physical parameters in the system, evaluated at different lattice sites i. We have set $\Delta\phi = 0.5\pi$ and (a) $\lambda = 0.3$ and (b) $h_y = 0.4$. The values of the remaining parameters are the same as in Fig. 2. A scattering potential $V_{\mathrm{int}} = 0.1$ at each of the interfaces was also added here to show that the effect is resilient toward interfacial scattering. The current oscillates with both h and λ and eventually decays with both as these quantities increase and suppress superconductivity.
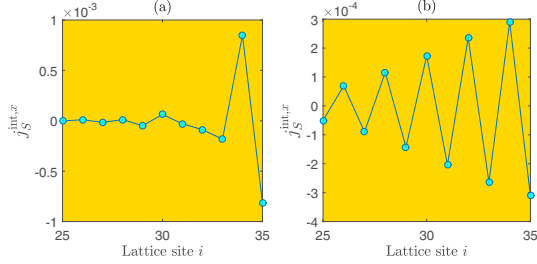
FIG. 6. Change in oscillation length of the superspin Hall current as the magnitude of the Rashba spin-orbit parameter is altered. The plots show the cases (a) $\lambda = 0.1$ and (b) $\lambda = 2.1$. The exchange field is $\boldsymbol{h} = h\hat{\boldsymbol{y}}$ with $h = 0.3$, $T = 0.005$, and the other parameters are the same as in Fig. 2.

both the Rashba strength and the magnitude of the exchange field for the parameter regimes we have investigated, as shown in Fig. 5. The effect is also purely sinusoidal as a function of the superconducting phase difference $\Delta\phi$ (not shown). The oscillations could stem from the change in $\boldsymbol{k}$-space band structure due to the inverse proximity effect near the interface as one varies the magnitude of h and λ, as the detailed $\boldsymbol{k}$ dependence of the spin magnetization (and thus in turn the magnitude of the spin supercurrent after summation over $\boldsymbol{k}$) will be affected by the details of the band structure.

The atomic-scale superimposed oscillations are characteristic for physical quantities in ballistic quantum-mechanical systems and are also present in, e.g., the proximity-induced magnetization in conventional superconductors [15] and helical edge-mode currents in triplet superconductors [14]. It should be noted, however, that the oscillation period of the spin supercurrent depends here on the system parameters. This is shown in Fig. 6, where it is clear that the oscillation period is altered by changing the magnitude of the Rashba parameter. The origin of the oscillations is likely to be similar to that described in Ref. [14], namely due to an interplay between the renormalized spectral weight in the superconductor due to the inverse proximity effect and how the p-wave superconducting correlations decay as a result.

IV. CONCLUDING REMARKS

Previous theoretical work has considered spin accumulation from spin Hall effects in superconducting structures [18–23], and a recent experimental work [24] demonstrated an enhancement of the inverse spin Hall signal [10] in a superconductor by three orders of magnitude. A similar edge spin magnetization might occur from the superspin Hall current predicted in this work. Although the interface between a superconductor and a ferromagnet breaks inversion symmetry on its own, the purpose of the HM layers is to enhance the magnitude of the resulting Rashba interaction. A transverse spin current induced by a charge supercurrent was also considered in Ref. [25], albeit in a different setup where spin-orbit coupling was present in the entirety of one superconducting region and where no magnetism was present. Reference [26] considered spin Hall effects in a Josephson setup both with and without an electric bias voltage applied to the system.

It is worth remarking that in comparison to the typical spin Hall phenomenology, where an injected current in the x direction is deflected in the y direction and polarized in the z direction, the spin supercurrent here is not polarized perpendicularly to the plane defined by its injection and deflection direction. However, similarly to the conventional spin Hall phenomenology, the spin supercurrent arises as a direct consequence of Cooper pairs that are polarized in the z direction. The details regarding how $S_z = \pm 1$ Cooper pairs give rise to a spin supercurrent polarized in the xy plane have been covered in detail in the main body of this paper.

Interesting future directions to explore include the precise circulation pattern of the superspin Hall current predicted herein in a finite-width sample, and the possible accompanying edge spin accumulation due to triplet Cooper pairs.

APPENDIX: MAGNETIZATION ARISING OUT OF A NONUNITARY COEXISTENCE OF SINGLET AND TRIPLET PAIRING

Consider for simplicity a bulk system in which singlet pairing Δ_s coexists with $S_z = 0$ triplet pairing $\Delta_{\boldsymbol{k}} = -\Delta_{-\boldsymbol{k}}$. The Hamiltonian reads

$$H = \sum_{\boldsymbol{k}} \phi_{\boldsymbol{k}}^{\dagger} M_{\boldsymbol{k}} \phi_{\boldsymbol{k}}, \tag{A1}$$

where we used a basis $\phi_{\boldsymbol{k}} = [c_{\boldsymbol{k}\uparrow} \ c_{\boldsymbol{k}\downarrow} \ c_{-\boldsymbol{k}\uparrow}^{\dagger} \ c_{-\boldsymbol{k}\downarrow}^{\dagger}]^{\mathrm{T}}$ and defined

$$M_{\boldsymbol{k}} = \begin{pmatrix} \epsilon_{\boldsymbol{k}} & 0 & 0 & \Delta_{\boldsymbol{k}} + \Delta_s \\ 0 & \epsilon_{\boldsymbol{k}} & \Delta_{\boldsymbol{k}} - \Delta_s & 0 \\ 0 & \Delta_{\boldsymbol{k}}^* - \Delta_s^* & -\epsilon_{\boldsymbol{k}} & 0 \\ \Delta_{\boldsymbol{k}}^* + \Delta_s^* & 0 & 0 & -\epsilon_{\boldsymbol{k}} \end{pmatrix}. \tag{A2}$$

The four eigenvalues are given as $\{E_+, E_-, -E_+, -E_-\}$, where

$$E_{\pm} = \sqrt{\epsilon_{\boldsymbol{k}}^2 + |\Delta_s \pm \Delta_{\boldsymbol{k}}|^2}. \tag{A3}$$

Performing a standard diagonalization of the Hamiltonian by introducing a new quasiparticle basis

$$\gamma_{\boldsymbol{k}} = [\gamma_{1\boldsymbol{k}} \ \gamma_{2\boldsymbol{k}} \ \gamma_{3\boldsymbol{k}} \ \gamma_{4\boldsymbol{k}}]^{\mathrm{T}}, \tag{A4}$$

where $\gamma_{i\boldsymbol{k}}$ are second-quantized fermion operators, one arrives at

$$H = \sum_{\boldsymbol{k}} [E_{\boldsymbol{k}+}(\gamma_{1\boldsymbol{k}}^{\dagger}\gamma_{1\boldsymbol{k}} - \gamma_{2\boldsymbol{k}}^{\dagger}\gamma_{2\boldsymbol{k}}) + E_{\boldsymbol{k}-}(\gamma_{3\boldsymbol{k}}^{\dagger}\gamma_{3\boldsymbol{k}} - \gamma_{4\boldsymbol{k}}^{\dagger}\gamma_{4\boldsymbol{k}})]. \tag{A5}$$

The relation between the original fermion operators c and the new ones γ is

$$\phi_k = P_k \gamma_k, \qquad (A6)$$

where P_k is the diagonalizing matrix containing the eigenvectors of the original Hamiltonian,

$$P_k = \begin{pmatrix} g_+(E_{k+}) & g_+(-E_{k+}) & 0 & 0 \\ 0 & 0 & g_-(E_{k-}) & g_-(-E_{k-}) \\ 0 & 0 & 1 & 1 \\ 1 & 1 & 0 & 0 \end{pmatrix}, \qquad (A7)$$

and we defined the auxiliary quantity

$$g_\pm(E) = \frac{\Delta_k \pm \Delta_s}{E - \epsilon_k}. \qquad (A8)$$

Now, the magnetization of the system in the $\hat{z}$ direction is computed according to Eq. (14):

$$S_z = \sum_{k\sigma} \sigma \langle c_{k\sigma}^\dagger c_{k\sigma} \rangle. \qquad (A9)$$

To see how this magnetization is directly influenced by the coexistence of singlet and triplet pairs in the system, we replace the original fermion operators in Eq. (A9) with the new ones according to Eq. (A6). Considering for simplicity the $T = 0$ limit, one arrives at

$$S_z = \sum_k [|g_+(-E_{k+})|^2 - |g_-(-E_{k-})|^2]. \qquad (A10)$$

At this point, we distinguish between unitary and nonunitary states. In the *unitary case*, we have $\text{Re}\{\Delta_s \Delta_k^*\} = 0$ so that $E_{k+} = E_{k-}$: the magnitudes of both gaps $\Delta_\pm = \Delta_k \pm \Delta_s$ are equal. Moreover, it follows from Eq. (A8) that in the unitary case one has $|g_+(x)| = |g_-(x)|$. Combining these two facts, it follows that the term inside the summation $\sum_k$ in Eq. (A10) is zero for any k value. In effect, there is no magnetization at any k point and obviously no net magnetization either.

Consider now instead a nonunitary state where $\text{Re}\{\Delta_s \Delta_k^*\} \neq 0$. In this case, the magnitudes of the gaps $\Delta_\pm$ are *different*. Now, the term inside the summation of Eq. (A10) is no longer zero for a given k point. In effect, there exists a k-resolved magnetization. The *total magnetization*, obtained after a summation over k, is nevertheless zero even in the nonunitary case. This can be verified by splitting the sum in Eq. (A10) into $k > 0$ and $k < 0$ (the contribution from $k = 0$ vanishes) and using the general relation $E_{k,+} = E_{-k,-}$.

The above derivation establishes mathematically why a k-resolved, antisymmetric spin magnetization exists when singlet and p-wave triplet pairing coexists in a nonunitary state, precisely as in the system considered in the main body of this paper. The *physical picture* can be understood by going back to the fact that there exists two gaps with a different magnitude in the system. It is well known that the superconducting order parameter (gap) determines the condensation energy and binding energy between the electrons comprising the Cooper pairs. In particular, the Cooper pair density is proportional to the square of the magnitude of the gap. The point here is that Cooper pairing between two electron states $|k,\uparrow\rangle$ and $|-k,\downarrow\rangle$ is associated with a gap magnitude $|\Delta_k + \Delta_s| \equiv |\Delta_+|$, whereas pairing between two electron states $|k,\downarrow\rangle$ and $|-k,\uparrow\rangle$ is associated with a different gap magnitude $|\Delta_k - \Delta_s| \equiv |\Delta_-|$. This can be seen directly from the Hamiltonian that contains the terms $c_{k\uparrow}^\dagger c_{-k\downarrow}^\dagger \Delta_+$ and $c_{k\downarrow}^\dagger c_{-k\uparrow}^\dagger \Delta_-$. Now, if $|\Delta_+| > |\Delta_-|$ for a given k value, it is clear that the system will favor Cooper pairs where the $\uparrow$ electron of the pair sits at k whereas the $\downarrow$ electron sits at $-k$, since the Cooper pair state where the $\uparrow$ electron sits at $-k$ and the $\downarrow$ electron sits at k has a smaller binding energy. Therefore, a *net spin magnetization arises at k* since there exists a surplus of $\uparrow$ spins there compared to $\downarrow$ spins due to the difference in Cooper pair density stemming from the different gap magnitudes. Simultaneously, the opposite magnetization arises at $-k$ since at that momentum the situation is reversed: $|\Delta_-|$ is larger than $|\Delta_+|$ at $-k$.

In this way, the different magnitudes of the two gaps in a system where singlet pairing coexists with $S_z = 0$ triplet pairing in a nonunitary state cause the Cooper pairs to provide a k-resolved magnetization in the $\hat{z}$ direction despite the fact that the net Cooper pair spin in the $\hat{z}$ direction is zero.

[1] J. Linder and J. W. A. Robinson, Superconducting spintronics, Nat. Phys. **11**, 307 (2015).

[2] V. V. Ryazanov, V. A. Oboznov, A. Yu. Rusanov, A. V. Veretennikov, A. A. Golubov, and J. Aarts, Coupling of Two Superconductors Through a Ferromagnet: Evidence for a π-Junction, Phys. Rev. Lett. **86**, 2427 (2001).

[3] M. G. Blamire and J. W. A. Robinson, The interface between superconductivity and magnetism: Understanding and device prospects, J. Phys.: Condens. Matter **26**, 453201 (2014).

[4] M. Eschrig, Spin-polarized supercurrents for spintronics: A review of current progress, Rep. Prog. Phys. **78**, 104501 (2015).

[5] D. Beckmann, Spin manipulation in nanoscale superconductors, J. Phys.: Condens. Matter **28**, 163001 (2016).

[6] R. S. Keizer *et al.*, A spin triplet supercurrent through the half-metallic ferromagnet CrO$_2$, Nature (London) **439**, 825 (2006).

[7] M. Eschrig and T. Löfwander, Triplet supercurrents in clean and disordered half-metallic ferromagnets, Nat. Phys. **4**, 138 (2008)

[8] M. I. Dyakonov and V. I. Perel, Possibility of orientating electron spins with current, JETP Lett. **13**, 467 (1971).

[9] M. I. Dyakonov and V. I. Perel, Current-induced spin orientation of electrons in semiconductors, Phys. Lett. A **35**, 459 (1971).

[10] J. E. Hirsch, Spin Hall Effect, Phys. Rev. Lett. **83**, 1834 (1999).

[11] V. Chandrasekhar, *Proximity-Coupled Systems: Quasiclassical Theory of Superconductivity in Superconductivity: Conventional and Unconventional Superconductors*, edited by K. H.

Bennemann and J. B. Ketterson (Springer, Berlin, 2008), Chap. 8, pp. 279–313.

[12] J.-X. Zhu and C. S. Ting, Proximity effect, quasiparticle transport, and local magnetic moment in ferromagnet d-wave-superconductor junctions, Phys. Rev. B **61**, 1456 (2000).

[13] A. M. Black-Schaffer and S. Doniach, Self-consistent solution for proximity effect and Josephson current in ballistic graphene SNS Josephson junctions, Phys. Rev. B **78**, 024504 (2008).

[14] D. Terrade, D. Manske, and M. Cuoco, Control of edge currents at a ferromagnet-triplet superconductor interface by multiple helical modes, Phys. Rev. B **93**, 104523 (2016).

[15] K. Halterman, O. T. Valls, and P. H. Barsic, Induced triplet pairing in clean s-wave superconductor/ferromagnet layered structures, Phys. Rev. B **77**, 174511 (2008).

[16] Y. Tanaka, A. A. Golubov, S. Kashiwaya, and M. Ueda, Anomalous Josephson Effect Between Even- and Odd-Frequency Superconductors, Phys. Rev. Lett. **99**, 037005 (2007).

[17] M. Eschrig, T. Löfwander, T. Champel, J. C. Cuevas, J. Kopu, and G. Schön, Symmetries of pairing correlations in superconductor-ferromagnet nanostructures, J. Low Temp. Phys. **147**, 457 (2007).

[18] S. Pandey, H. Kontani, D. S. Hirashima, R. Arita, and H. Aoki, Spin Hall effect in iron-based superconductors: A Dirac-point effect, Phys. Rev. B **86**, 060507(R) (2012).

[19] H. Kontani, J. Goryo, and D. S. Hirashima, Intrinsic Spin Hall Effect in the s-Wave Superconducting State: Analysis of the Rashba Model, Phys. Rev. Lett. **102**, 086602 (2009).

[20] K. Sengupta, R. Roy, and M. Maiti, Spin Hall effect in triplet chiral superconductors and graphene, Phys. Rev. B **74**, 094505 (2006).

[21] F. S. Bergeret and I. V. Tokatly, Manifestation of extrinsic spin Hall effect in superconducting structures: Nondissipative magnetoelectric effects, Phys. Rev. B **94**, 180502(R) (2016).

[22] A. G. Mal'shukov, S. Sadjina, and A. Brataas, Inverse spin Hall effect in superconductor/normal-metal/superconductor Josephson junctions, Phys. Rev. B **81**, 060502(R) (2010).

[23] A. G. Mal'shukov, Supercurrent generation by spin injection in an s-wave superconductor–Rashba metal bilayer, Phys. Rev. B **95**, 064517 (2017).

[24] T. Wakamura, H. Akaike, Y. Omori, Y. Niimi, S. Takahashi, A. Fujimaki, S. Maekawa, and Y. Otani, Quasiparticle-mediated spin Hall effect in a superconductor, Nat. Mater. **14**, 675 (2015).

[25] Y. Zhi-Hong *et al.*, Interfacial spin Hall current in a Josephson junction with Rashba spin-orbit coupling, Chin. Phys. B **21**, 057402 (2012).

[26] A. G. Mal'shukov and C. S. Chu, Spin Hall effect in a Josephson contact, Phys. Rev. B **78**, 104503 (2008); Spin-Hall current and spin polarization in an electrically biased SNS Josephson junction, *ibid.* **84**, 054520 (2011).

Paper VI

Reference

K. Lahabi, M. Amundsen, J. A. Ouassou, E. Beukers, M. Pleijster, J. Linder, P. Alkemade, and J. Aarts.
Controlling supercurrents and their spatial distribution in ferromagnets.
Nature Communications **8**, 2056 (2017).
DOI: 10/gcrhmz

Contributions

KL and JA conceived of the disk geometry. KL and EB performed the micromagnetic simulations. MA, JAO and JL performed the supercurrent simulations, and assisted in the Fourier analysis of the critical current measurements. KL, MP and PA fabricated the devices. KL and MP performed the measurements. All authors contributed to discussions. More specifically, MA performed the three-dimensional finite element simulations of the considered system.

ARTICLE

OPEN

Controlling supercurrents and their spatial distribution in ferromagnets

Kaveh Lahabi[1], Morten Amundsen[2], Jabir Ali Ouassou [2], Ewout Beukers[1], Menno Pleijster[1], Jacob Linder[2], Paul Alkemade[3] & Jan Aarts [1]

Spin-triplet Cooper pairs induced in ferromagnets form the centrepiece of the emerging field of superconducting spintronics. Usually the focus is on the spin-polarization of the triplets, potentially enabling low-dissipation magnetization switching. However, the magnetic texture which provides the fundamental mechanism for generating triplets also permits control over the spatial distribution of supercurrent. Here we demonstrate the tailoring of distinct supercurrent pathways in the ferromagnetic barrier of a Josephson junction. We combine micromagnetic simulations with three-dimensional supercurrent calculations to design a disk-shaped structure with a ferromagnetic vortex which induces two transport channels across the junction. By using superconducting quantum interferometry, we show the existence of two channels. Moreover, we show how the supercurrent can be controlled by moving the vortex with a magnetic field. This approach paves the way for supercurrent paths to be dynamically reconfigured in order to switch between different functionalities in the same device.

---

[1] Huygens—Kamerlingh Onnes Laboratory, Leiden Institute of Physics, University Leiden, P.O. Box 9504 , 2300 RA Leiden, The Netherlands. [2] Department of Physics, Center of Excellence QuSpin, Norwegian University of Science and Technology, NO-7491 Trondheim, Norway. [3] Kavli Institute of Nanoscience, Delft University of Technology, Lorentzweg 1, 2628 CJ Delft, The Netherlands. Correspondence and requests for materials should be addressed to J.A. (email: aarts@physics.leidenuniv.nl)

The conversion of spin-singlet Cooper pairs to the equal-spin triplets which are needed in superconducting spin-tronics[1,2] requires carefully designed interfaces between a conventional superconductor (S) and a ferromagnet (F). The process entails both spin-mixing and spin-rotation, and can be brought about by magnetic inhomogeneities at the interface[3]. One method to realize this is to place a thin ferromagnet F′ at the S/F interface, and make the magnetization of F and F′ non-collinear[4]. This technique was recently implemented in Josephson junctions described by 1D geometries, where the supercurrent amplitude was controlled by varying degrees of magnetic non-collinearity (MNC)[5–7]. The present letter establishes a different direction. Here, the central goal is to exert dynamic control over the triplet generator and thereby to determine where the super-current spatially flows.

We demonstrate how distinct supercurrent paths in a device can be tailored entirely by spin texture, and altered in a dynamic fashion. Such behavior is intrinsically higher-dimensional and can pave the way for novel hybrid devices in superconducting electronics.

Results

Micromagnetic simulations. The device consists of a disk-shaped planar Josephson junction involving a multilayer of Co/Cu/Ni/Nb, as shown in Fig. 1a. A central trench cuts the top superconducting Cu/Ni/Nb layers in two halves, here connected via a Co weak link. The disk design combines two crucial elements. First, the magnetic moments in Co are arranged in plane and orthogonal to the trench between the superconducting

electrodes, while the moments in Ni lie also in plane but parallel to the trench. Micromagnetic simulations show that this geo-metry results in a well-defined magnetic ground state with a high degree of MNC, a condition optimal for generating triplets (Fig. 1c–e). An equally important element is that the disk shape creates a magnetic vortex state in the Co. This vortex produces a distinct suppression of MNC at the centre of the disk (Fig. 1e), which will be used to distribute the supercurrent in Co over two channels. The MNC suppression is due to the local out-of-plane magnetization at the vortex core, which turns the magnetic moments in the Ni also out-of-plane and, hence, collinear to the Co moments. Incidentally, the in-plane exchange field gradient of a magnetic vortex, without a second ferromagnet, has also been proposed to generate long-ranged triplets[8,9].

Supercurrent calculations. To investigate whether a supercurrent can be expected, we numerically simulate the critical current density passing through the Josephson junction by solving the quasiclassical Usadel equation[10] in 3D using the magnetization texture obtained from the micromagnetic simulations. We do this by means of the finite element method, using the finite element library libMesh[11] in a similar fashion as in ref. [12] (for details, see Supplementary Note 1, Supplementary Fig. 3). The super-conductors are modeled as bulk, with a phase difference of $\Delta\phi = \frac{\pi}{2}$. In Fig. 2a the discretized model is shown. To reduce the calculation time we truncated the otherwise circular geometry to a width of 40% of the disk diameter, as the currents farther away from the trench are negligible. The results are shown in Fig. 2b, c, where it can be seen that the critical current is suppressed at the
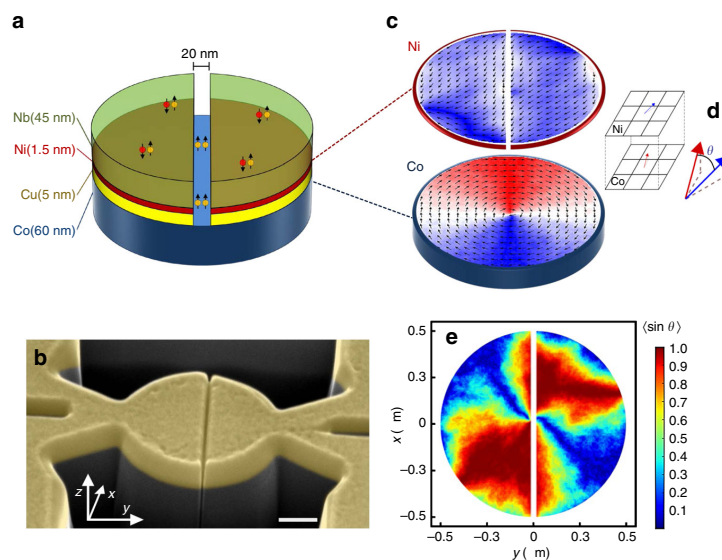
Fig. 1 Micromagnetic simulations and device layout. **a** Schematic of the device layout. **b** False-color scanning electron microscope image of a device. The scale bar corresponds to 250 nm. The disk is structured with Ga$^+$ focused ion beam (FIB) milling. The junction is formed by opening up a gap in the top Nb/Ni/Cu layers, leaving only Co in the weak link (see Methods section for more details). **c** Plane view of the magnetic states of Co and Ni layers in the disk (from 3D OOMMF simulations). The pixel color scheme, red-white-blue, scales with the magnetization along y. Magnetic moments in Ni tend to align with the gap which defines the junction, while the vortex configuration in Co arranges the magnetic moments perpendicular to it. This provides a high degree of magnetic non-collinearity (MNC) for triplet generation. The curled magnetic structure of the vortex is also highly effective in minimizing the stray fields from Co, which otherwise would dominate the Ni magnetization, hence compromising our control of MNC. **d** Representation of our method to obtain the MNC profile. For each cell at the top of the Co layer, we determine the angle θ between its magnetization vector and that of the Ni cell above. **e** Spatially resolved MNC profile calculated from the simulation results shown in **c**. The observed suppression of MNC (the blue region) at the centre of the junction is a result of interlayer dipole coupling at the vortex core
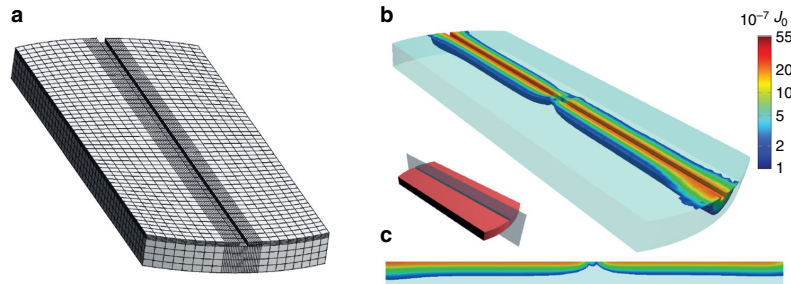
Fig. 2 Numerical simulation of the critical current. **a** The discretized model (or mesh) used in the numerical simulation of the critical current. Since the triplet current is mostly concentrated in the immediate vicinity of the trench, the mesh density (and hence the accuracy) is set to be higher for this region. For the same reason, the regions farthest away from the trench have been removed to reduce the calculation time. **b** The critical current density divided by a factor $J_0 = \frac{N_0 e D \Delta}{2\xi}$, where N_0 is the density of states at the Fermi level, D is the diffusion constant, Δ is the superconducting gap and ξ is the superconducting coherence length. For clarity, currents lower than $10^{-7} J_0$ are not shown. **c** A slice through the centre of the trench, showing how the current passes across the Co barrier in two separate channels, on either side of the vortex core
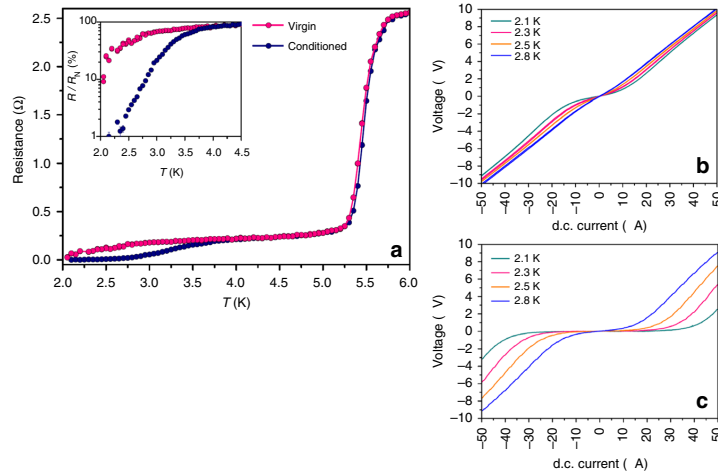
Fig. 3 Junction transport in the virgin and conditioned states. **a** Resistance as a function of temperature, measured using 10 µA, before (pink) and after (navy) conditioning the sample. Each set shows two distinct transitions. At $T = 5.5$ K, the Nb electrodes become superconducting, while the junction is still in the normal state ($R_N \approx 240$ mΩ). Upon cooling further, resistance undergoes a second transition as the barrier begins to proximize by triplet correlations —eventually reaching zero resistance. For clarity, the $R{-}T$ dependence at lower temperatures is plotted on a logarithmic scale in the inset. While the superconducting electrodes are unaffected by conditioning the ferromagnets, we observe substantial enhancement of superconductivity in the barrier. **b**, **c** I −V traces taken at several temperatures before and after conditioning the sample, respectively. The pronounced contrast between the two sets indicates that transport depends strongly on the magnetic configuration of the junction

centre of the disk, thereby effectively creating two separate current channels.

Basic transport properties. As shown in Fig. 3, our junctions show zero resistance and finite critical currents I_c below 3 K. The magnetic state of the sample was conditioned by applying a 2.5 T out-of-plane field at 10 K. This is to reduce the stochastic magnetization introduced by FIB milling when structuring the junction. Figure 3 shows there is a strong difference with data taken before and after conditioning the sample, which is a first indication that MNC and a triplet supercurrent are involved (also see Supplementary Note 2). For instance, conditioning allows the magnetic moments in Ni to rearrange more freely, and align with the gap opened by the FIB. This process increases the MNC in the vicinity of the barrier which, in turn, results in an enhancement of triplet supercurrent at zero field. A consequence of this can be

found in the pronounced contrast between the $I{-}V$ traces measured before and after conditioning the magnetization, as shown in Fig. 3b, c.

Superconducting quantum interferometry. To examine the spatial distribution of current density across our junctions, we apply an out-of-plane magnetic field B_z, and analyze the resulting supercurrent interference pattern. As demonstrated by Dynes and Fulton[13], the shape of such a superconducting quantum interference (SQI) pattern is given by the Fourier transform of the position-dependent critical current density across a junction $J_c(x)$ through

$$I_c(B_z) = \left| \int_{-R}^{R} \mathrm{d}x\, J_c(x)\, e^{2\pi i L B_z x \Phi_0} \right|, \qquad (1)$$
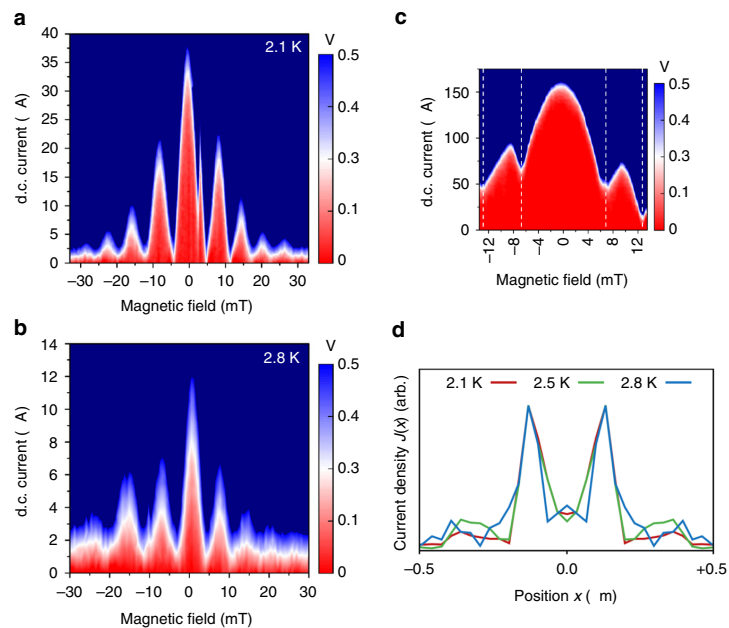
Fig. 4 Interference patterns and the corresponding current density profiles. **a**, **b** the result of superconducting quantum interference (SQI) measurements taken at 2.1 and 2.8 K, respectively. The patterns show clear double-slit interference, with all lobes having the same width. **c** Single-slit interference pattern from a disk junction where transport is dominated by singlet correlations via a non-magnetic barrier. **d** The current density profiles constructed from the Fourier analysis of SQI patterns taken at 2.1, 2.5, and 2.8 K. The presence of two transport channels, responsible for the SQUID-like interference patterns, is evident

where L is the effective length of the junction, $2R$ is its lateral width (here the disk diameter), and $\Phi_0 = h/2e$ is the superconducting flux quantum. In a typical junction, the uniform distribution of supercurrent density ($J_c(x) = $ constant) leads to the well-known Fraunhofer interference pattern with a sinusoidal current-phase relation given by $I_c(B_z)/I_c(0) \sim |\sin(\pi\Phi/\Phi_0)/(\pi\Phi/\Phi_0)|$. Characteristic for the Fraunhofer pattern is a central lobe that is twice as wide as the side lobes (as in Fig. 4c). These oscillations decay with a $1/B$ dependence. Different device configurations may introduce deviations from the standard pattern, but the described relative widths of the lobes persist as a common feature in all Josephson junctions, since it represents a single-slit interference pattern. In contrast, we expect our disk to exhibit a double-slit interference pattern. This is characterized by slowly decaying sinusoidal oscillations with Φ_0-periodicity, where all lobes have the same width. These patterns are typical for superconducting quantum interference devices (SQUIDs) which, contrary to our device, consist of two individual junctions operated in parallel.

As shown in Fig. 4a, b, the period of the oscillations in our disk device is 7.8 mT (i.e., fluxoid quantization over an effective area of $2.65 \times 10^{-13}\,\text{m}^2$), and appears to be temperature-independent. Qualitatively, the SQI patterns in Fig. 4a, b already foretell the presence of two supercurrent channels: the width of the central lobe is comparable to that of the side lobes, and the oscillations decay far more gradually in field than as $1/B$. Two-channel interference patterns were recently observed in junctions with topological weak links[14–16], where the two-slit interference is a result of edge-dominated transport caused by band bending. In our junction however, this is due to the suppression of triplet supercurrent by the (controllable) magnetic vortex core.

To illustrate the contrast with single-slit interference in a similar device configuration, we prepared a disk junction without the Ni layer, and retaining a thin layer of Cu/Nb at the bottom of the trench. This provides a non-magnetic path in the barrier, allowing singlet correlations to contribute to junction transport. Indeed, we observe a typical Fraunhofer-like interference pattern with a two times wider central lobe, shown in Fig. 4c. Provided that singlet current can dominate the transport, similar results can also be produced in presence of the Ni layer (Supplementary Fig. 5).

Figure 4d shows the supercurrent density profiles extracted from Fourier analysis of the measured interference patterns. A description of this method can be found in the Supplementary Note 3, Supplementary Fig. 4 but it should be mentioned that there is some arbitrariness in choosing the position of the sample edge if the effective junction length L is not known. We put the edge at the position where the current density goes to zero, which leads to a value for L of 170 nm. This is a reasonable number. For a homogeneous junction where $L = 2\lambda_L + d$, with d the gap between the electrodes and λ_L the London penetration depth, taking 100 nm for λ_L of the Nb, would yield L to be of the order of 200 nm. There is no reason however to expect very close agreement as discussed in Supplementary Note 3. Important is that for any choice of the edge position, two distinct transport channels are clearly visible in the extracted profiles. Comparing these results with the simulations, the supercurrents appear to follow narrower paths, located near the centre of the disk. We attribute this to current crowding effects, in which the neck-shaped contacts and their sharp corners lead to a forward orientation of the currents.

It is important to note that the origin of the two-channel transport in our junction cannot be explained by singlet

supercurrents in a doubly connected path. Direct evidence for this can be found in the SQI measurements taken before conditioning the sample (the virgin state). If two separate current paths had formed unintentionally during fabrication, and allowed singlet correlations to bypass the Co layer via two symmetric channels, then those channels would have already been present before the magnetic state conditioning, and the device would have behaved as a SQUID from the beginning. In contrast, despite several
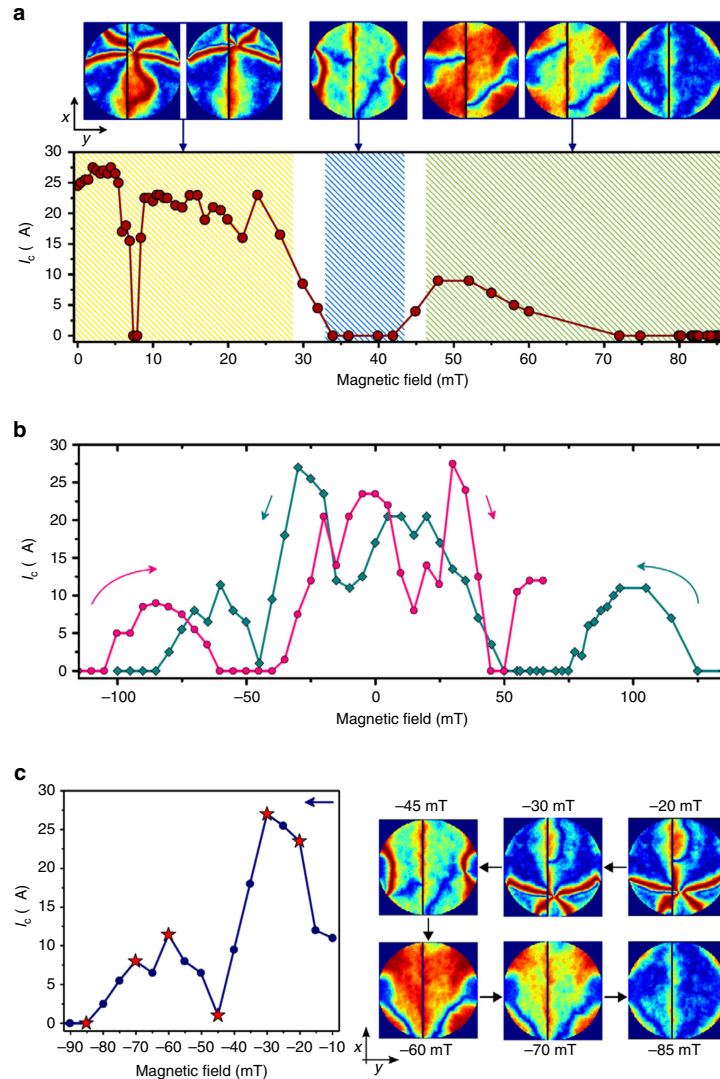
Fig. 5 Critical current variation and MNC simulations with in-plane field. **a** Measured I_c values and the corresponding magnetic non-collinearity (MNC) profiles, as the system is magnetized by sweeping the field in +y direction. For small fields the vortex core moves along the junction (perpendicular to field direction) to the side of the disk. In this range (shaded yellow), highly non-collinear regions are continuously present and appear to follow the position of the vortex core. The vortex state in Co, which has been effective in suppressing the stray fields, is subsequently removed as the field approaches 30 mT. This leads to a negative dipole field from Co which dominates the effective field acting on Ni. As a result, Ni gets magnetized antiparallel to Co (along −y), hence the suppression of MNC and I_c (shaded blue). As the applied field is raised above 45 mT, it begins to compensate for the local stray fields from the Ni layer, ultimately reversing the Ni magnetization along +y. The change in the magnetic orientation associated with this reversal leads to a distinct (re-)emergence of MNC that gradually fades away above 60 mT—as Ni magnetization aligns with Co (shaded green). **b** I_c measured while reversing the field in both directions along y. A clear hysteresis is observed, with individual features are mirrored with respect to field sweep direction. This complex pattern is a result of a changing MNC as the multilayer reverses its magnetization. **c** Positive to negative branch of experimentally measured $I_c(B_y)$ shown together with simulated MNC profiles. Each MNC snapshot is obtained at the specified field, and corresponds to a measurement labeled by the star symbol. Taking steps of 5 mT, simulation shows the vortex enters at −20 mT, moves along −x, and exits the system at −45 mT. The MNC is once again is enhanced at −60 mT, and gradually fades away as the field magnetizes all layers along −y

attempts, no sign of a double-slit interference was found in the virgin state (Supplementary Fig. 1). The SQUID pattern only appeared when the magnetic state was properly conditioned to produce the intended MNC, designed specifically to generate two symmetric triplet channels. More details about the SQI measurements from the virgin state can be found in Supplementary Note 2.

Magnetotransport measurements with an in-plane field. Having established the principal role of MNC in shaping the supercurrent, we also examine the possibility of controlling them by altering the MNC profiles using an in-plane field B_y which moves the vortex along the trench. Figure 5a shows the measured currents $I_c(B_y)$ together with the micromagnetic MNC calculations for various stages during the (zero to positive) field sweep. In the first regime (below 28 mT, shaded yellow), we modify the MNC profile by moving the vortex core along $+x$ toward the side of the disk. As the field is raised beyond 30 mT, we remove the vortex, thereby suppressing the supercurrent. The suppression of I_c in this regime (above 34 mT, shaded blue) is caused by the anti-parallel configuration of the ferromagnets, which occurs through the increase of stray fields from Co (now magnetized along $+y$) when the vortex leaves the disk. In the third regime (above 46 mT, shaded green), Ni magnetization begins to reverse from negative to positive y direction, while Co remains magnetized along $+y$. At first, this process recovers I_c as a MNC re-emerges over the entire disk. As we increase the field however, the MNC begins to fade away as both layers magnetize along $+y$, resulting in a gradual suppression of I_c. Figure 5b shows the variations in $I_c(B_y)$ when sweeping the field from a high positive to negative value, and back. We observe a complex pattern accompanied with a peculiar hysteresis, where individual features are mirrored (and not just shifted) with respect to the direction of field sweep.

The observed field dependence is fundamentally different from the usual hysteresis in SFS junctions, where the self-field of the ferromagnets can distort or introduce a shift in the interference pattern[7,17,18]. This is rather a distinct characteristic of triplet supercurrents produced by a varying degree of MNC, as the multilayer reverses its magnetization. The measured hysteresis is of a similar nature as the ones reported in refs. [6,7] for multilayer vertical stacks. The most notable difference here is arguably the relatively large field range where I_c is zero, and the pronounced reentrant superconductivity that follows. Figure 5c compares one branch (positive to negative) of the measured $I_c(B_y)$ with the simulated MNC snapshots taken at various stages of the vortex reversal. Even though the experiment and the simulation both sweep the field in steps of 5 mT, the simulated fields for vortex entry and exit translate to direct enhancement and suppression of the measured I_c, respectively. For the fields below -45 mT, the behavior is similar to the one described for the third regime (green shade) in Fig. 5a.

As a final point, it should be noted that in the present letter we have assumed the channels have an equal phase. This assumption is reasonable for a symmetric MNC (hence spin-mixing) on each side[4]. Whether both channels are 0 or π, as long as they are symmetric, the SQI results will be indistinguishable. This would not strictly apply to systems with asymmetric spin texture (e.g., caused by vortex displacement), which can result in different phases for the triplet channels[9].

Discussion

Spin-triplet supercurrents in ferromagnets have been bearing the promise of dissipationless use of spin-polarized currents. This study opens up a completely different direction, in which the focus is not the homogeneous amplitude of the supercurrent, but

rather the dynamical control over its spatial distribution. This can lead to novel hybrid devices for superconducting electronics. Moreover, our extensive use of simulations, both of the micromagnetic configurations and of the supercurrents themselves, allow for detailed design and understanding before the actual fabrication of the hybrid device. The next step will be to introduce magnetization dynamics. Magnetic vortices or domain walls can be moved with pulses in the GHz regime, and this can also be simulated. Directing supercurrents then becomes possible on nanosecond timescales, opening the way for high-speed superconducting electronics.

Methods

Device fabrication. Multilayers of Co (60 nm)/Cu (5 nm)/Ni (1.5 nm)/Nb (45 nm) were deposited on unheated SiO$_2$-coated Si substrates by Ar sputtering in an ultra-high vacuum chamber (base pressure below 10^{-8} Pa). The thickness of Co and the diameter of the disk (1 μm) are chosen to ensure stabilization of a magnetic vortex[19,20]. The 5 nm Cu layer is used to avoid exchange coupling between the layers. The thickness of the Ni layer was tuned for optimal triplet generation in similar systems[21,22]. The samples were subsequently coated with Pt (7 nm) to protect them from oxidation and to reduce the damage introduced by Ga$^+$ ions during focused ion beam (FIB) processing.

A combination of electron-beam lithography and FIB milling (50 pA Ga$^+$ beam current) was used to structure the disks. Next, FIB with 1 pA current was applied to open the sub-20 nm gap that forms the junction. The trench depth is controlled by the duration of milling. The 1 pA beam current provided sufficient timespan (several seconds) to vary the depth in a controlled manner. The device used for investigating single-slit transport was subject to the same processing steps, with the following exceptions. First, the multilayer was deposited without Ni to minimize triplet generation. Second, when creating the weak link, the duration of FIB milling was reduced by 20% to retain a layer of Cu/Nb at the bottom of the trench. This provides a non-magnetic path for singlet supercurrent in the weak link (on top of Co).

The trench is presumably deeper near the sides of the disks (where sputtered atoms can escape more easily) than at the centre. Hence, in contrast to triplets, singlet correlations would favor the centre of the disk where a non-magnetic channel may be still present on top of the Co.

Magnetotransport measurements. The magnetic properties of Co and Ni films used in our devices were characterized by ferromagnetic resonance experiments and SQUID magnetometry. Transport measurements were performed in a Quantum Design Physical Properties Measurement System where samples could be cooled down to 2.1 K. For both in-plane and out-of-plane measurements, the field was aligned within 2° of the sample plane. Resistance versus temperature was measured with a current of 10 μA. The current-voltage characteristics were taken in a four-probe configuration using a current-biased circuit and a nanovoltmeter. The critical current was determined using a voltage criterion: $V > 0.3$ μV for SQI and $V > 0.1$ μV for the measurements with an in-plane field.

The virgin state was measured directly after fabrication (Supplementary Note 2). Prior to the $I_c(B_z)$ measurements presented in the letter, the magnetic state of the sample was conditioned by applying a 2.5 T out-of-plane field at 10 K. The sample was stored in a UHV chamber for 106 days and re-wired to a different puck, and the same measurements were repeated using a different magnet. We were able to reproduce the same I_c patterns, and no discernable changes in transport characteristics (e.g., $R(T)$ or I_c) were observed.

Micromagnetic simulations. Micromagnetic modeling of the behavior of magnetic Josephson junctions was reported before[23]. Here, finite element micromagnetic calculations were carried out using the Object Oriented Micromagnetic Framework (OOMMF)[24]. The multilayer is divided into a three-dimensional mesh of 5 nm cubic cells. The exchange coefficient and saturation magnetization of Co were set to 30×10^{-12} Jm^{-1} and 1.40×10^6 Am^{-1}, respectively, while for Ni these values were 9.0×10^{-12} Jm^{-1} and 4.90×10^5 Am^{-1}. The Gilbert damping constant α was set to 0.5 to allow for rapid convergence. The direction of anisotropy was defined by a random vector field to represent the polycrystalline nature of the sputtered films. The Usadel calculations are based on static micromagnetic simulations of a multilayer disk with a diameter of 1 μm. For simulations with an applied in-plane field (shown in Fig. 5), the disk design was extended to include the leads used for transport measurements in the actual device (Supplementary Fig. 2). In the absence of in-plane fields, the overall magnetic configuration remains relatively unaffected by the leads: the vortex core continues to suppress the MNC, resulting in two main channels for long-ranged triplet correlations. However, the influence of the leads on shape anisotropy becomes relevant when sweeping the field along y. This allows for an accurate estimate of the MNC, and the resulting variation in I_c during the magnetization reversal.

Control experiment. In addition to the device used for investigating the triplet currents, a control sample was prepared in parallel, on the same substrate. This was deposited together with the main device, and received the same treatment, with only one exception: the Ga^+ dose used for opening the gap that forms the weak link was lowered by 50%. Reducing the dose stops the milling before it reaches the Co layer in the trench. This leaves a non-magnetic path in the weak link for singlet correlations. The contribution of singlet supercurrent results in a critical current that is around 20 times higher than its neighboring junction (the main device) where the Co weak link can effectively suppress singlet correlations, hence allowing long-ranged triplet supercurrents to dominate the transport. Unlike triplets, the singlet current is not sensitive to the spin texture (i.e., MNC) of the system. This is evident from the single-slit (Fraunhofer-like) interference pattern, shown in Supplementary Fig. 5.

References

1. Eschrig, M. Spin-polarized supercurrents for spintronics: a review of current progress. *Rep. Prog. Phys.* **78**, 104501 (2015).
2. Linder, J. & Robinson, J. W. A. Superconducting spintronics. *Nat. Phys.* **11**, 307–315 (2015).
3. Bergeret, F. S., Volkov, A. F. & Efetov, K. B. Long-range proximity effects in superconductor-ferromagnet structures. *Phys. Rev. Lett.* **86**, 4096–4099 (2001).
4. Houzet, M. & Buzdin, A. I. Long range triplet Josephson effect through a ferromagnetic trilayer. *Phys. Rev. B* **76**, 060504 (2007).
5. Robinson, J. W. A., Blamire, M. G. & Banerjee, N. Reversible control of spin-polarized supercurrents in ferromagnetic Josephson junctions. *Nat. Commun.* **5**, 4771 (2014).
6. Iovan, A., Golod, T. & Krasnov, V. M. Controllable generation of a spin-triplet supercurrent in a Josephson spin valve. *Phys. Rev. B* **90**, 134514 (2014).
7. Silaev, M. A. Possibility of a long-range proximity effect in a ferromagnetic nanoparticle. *Phys. Rev. B* **79**, 184505 (2009).
8. Kalenkov, M. S., Zaikin, A. D. & Petrashov, V. T. Triplet superconductivity in a ferromagnetic vortex. *Phys. Rev. Lett.* **107**, 087003 (2011).
9. Usadel, K. D. Generalized diffusion equation for superconducting alloys. *Phys. Rev. Lett.* **25**, 507–509 (1970).
10. Martinez, W. M., Pratt, W. P. Jr. & Birge, N. O. Amplitude control of the spin-triplet supercurrent in S/F/S Josephson junctions. *Phys. Rev. Lett.* **116**, 077001 (2016).
11. Kirk, B. S., Peterson, J. W., Stogner, R. H. & Carey, G. F. libMesh: a C++ Library for parallel adaptive mesh refinement/coarsening simulations. *Eng. Comput.* **22**, 237–254 (2006).
12. Amundsen, M. & Linder, J. General solution of 2D and 3D superconducting quasiclassical systems: coalescing vortices and nanoisland geometries. *Sci. Rep.* **6**, 22765 (2015).
13. Dynes, R. C. & Fulton, T. A. Supercurrent density distribution in Josephson Junctions. *Phys. Rev.* **B3**, 3015–3023 (1971).
14. Hart, S. et al. Induced superconductivity in the quantum spin Hall edge. *Nat. Phys.* **10**, 638–643 (2014).
15. Pribiag, V. S. et al. Edge-mode superconductivity in a two-dimensional topological insulator. *Nat. Nanotechnol.* **10**, 593–597 (2015).
16. Allen, M. T. et al. Spatially resolved edge currents and guided-wave electronic states in graphene. *Nat. Phys.* **12**, 128–133 (2016).
17. Bol'ginov, V. V., Stolyarov, V. S., Sobanin, D. S., Karpovich, A. L. & Ryazanov, V. V. Magnetic switches based on Nb–PdFe–Nb Josephson junctions with a magnetically soft ferromagnetic interlayer. *JETP Lett.* **95**, 366–371 (2012).
18. Gingrich, E. C. et al. Spin-triplet supercurrent in Co/Ni multilayer Josephson junctions with perpendicular anisotropy. *Phys. Rev. B* **86**, 224506 (2012).
19. d'Albuquerque e Castro, J., Altbir, D., Retamal, J. C. & Vargas, P. Scaling approach to the magnetic phase diagram of nanosized systems. *Phys. Rev. Lett.* **88**, 237202 (2002).
20. Dao, N., Whittenburg, S. L. & Cowburn, R. P. Micromagnetics simulation of deep-submicron supermalloy disks. *J. Appl. Phys.* **90**, 5235–5237 (2001).
21. Khasawneh, M. A., Khaire, T. S., Klose, C., Pratt, W. P. Jr. & Birge, N. O. Spin-triplet supercurrent in Co-based Josephson junctions. *Supercond. Sci. Technol.* **24**, 024005 (2011).
22. Voltan, S., Singh, A. & Aarts, J. Triplet generation and upper critical field in superconducting spin valves based on CrO_2. *Phys. Rev. B* **94**, 054503 (2016).
23. Golovchanskiy, I. A. et al. Micromagnetic modeling of critical current oscillations in magnetic Josephson junctions. *Phys. Rev. B* **94**, 214514 (2016).
24. Donahue, M. J. & Porter, D. G. *OOMMF User's Guide, Version 1.0*, Interagency Report NISTIR 6376, National Institute of Standards and Technology, Gaithersburg, MD, (1999).

Author contributions

K.L. and J.A. conceived the disk geometry, K.L. and E.B. performed the micromagnetic simulations, M.A., J.A.O. and J.L. performed the supercurrent simulations and assisted in the Fourier analysis, K.L., M.P. and P.A. fabricated the devices, K.L. and M.P. performed the measurements. All authors contributed to discussions.

Additional information

Supplementary Information accompanies this paper at https://doi.org/10.1038/s41467-017-02236-2.

Supplementary Figures

a

π 0 π

b

c
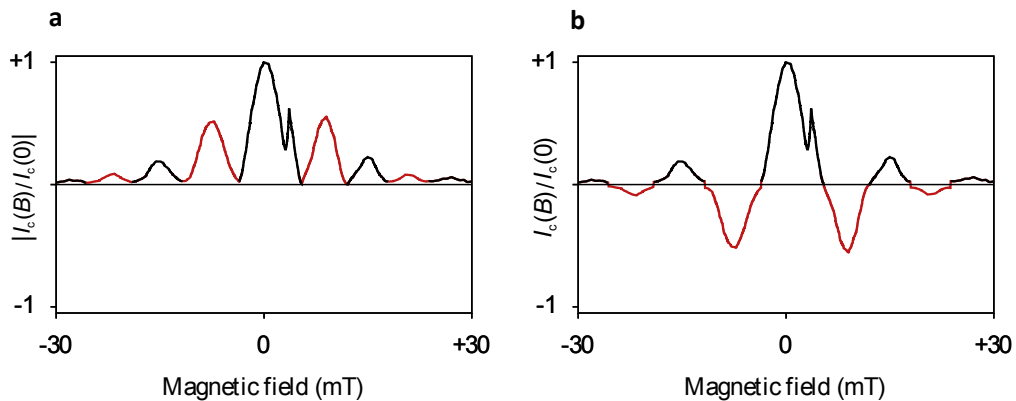

Supplementary Figure 1 | Interference patterns from the virgin magnetic state.
(**a**) Disordered magnetic state of Ni before conditioning (schematic). The stochastic magnetic orientation of Ni on each side of the trench can lead to the formation of multiple 0 and π segments across the junction. (**b**) Supercurrent interference pattern of the virgin magnetic state, measured while sweeping th e out-of-plane field from negative to positive 30 mT in steps of 0.3 mT. On average, the supercurrent is suppressed for small fields (below 5 mT) in both field directions. The interference pattern is characterized by random discontinuities. These irregularities are shown more clearly in (**c**) which shows individual $I - V$ curves taken while scanning the field from 28 mT back to zero . The curves are given an offset to represent the field they were measured at. All measurements are taken at $T = 2.1$ K.
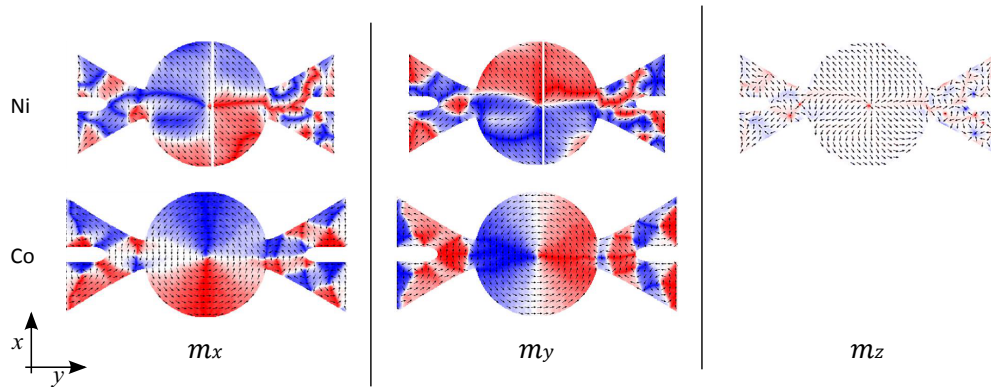
Supplementary Figure 2 | Micromagnetic simulations with an in-plane field. Top views of the magnetic states of Co and Ni layers obtained from OOMMF simulations. The leads are included in the design to produce a more realistic shape anisotropy, needed to accurately describe the system under an in-plane field. Individual components of the magnetization vector $\mathbf{m}$ are plotted separately for clarity. The pixel colour scheme, red-white-blue, scales with the magnitude of each component. The red and blue pixels represent positive and negative values respectively. Out of plane magnetization (m_z) is generally suppressed, except at the vortex core where both layers have a highly localized out of plane component. In the actual device, the trench that forms the junction is slightly off-centred. This feature is accounted for in the simulations by placing the gap in Ni 40 nm away from the centre of the disk.
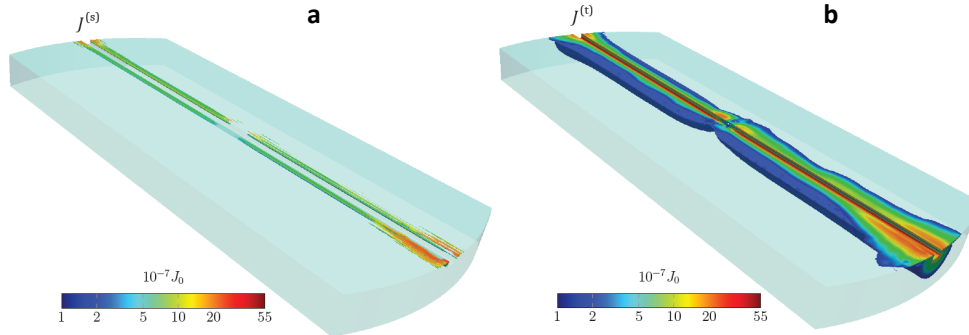
Supplementary Figure 3 | Simulated contributions of singlet and triplet supercurrents (**a**) Magnitude of the current density generated by singlet Cooper pairs, $J^{(s)} = \mathbf{J}^{(s)}$, which is greatly suppressed except for in the immediate vicinity of the superconductors. (**b**) Magnitude of the current density generated by triplet Cooper pairs, $J^{(t)} = \mathbf{J}^{(t)}$. For clarity, currents lower than $10^{-7}J_0$ have been removed, which explains why no singlet current is observed in the trench. It is noted that while the total current $\mathbf{J} = \mathbf{J}^{(s)} + \mathbf{J}^{(t)}$ is conserved, $\mathbf{J}^{(s)}$ and $\mathbf{J}^{(t)}$ are generally not. This is due to the magnetization, which causes oscillations between the singlet and triplet states.

Supplementary Figure 4 | Recovering the complex critical current. (**a**) The (unsigned) $|I(B)|$ pattern extracted from $I - V$ measurements. (**b**) The signed $I_c(B)$ interference pattern reconstructed by flipping the signs of alternate lobes as in ref. 1. The data were taken at 2.1 K.
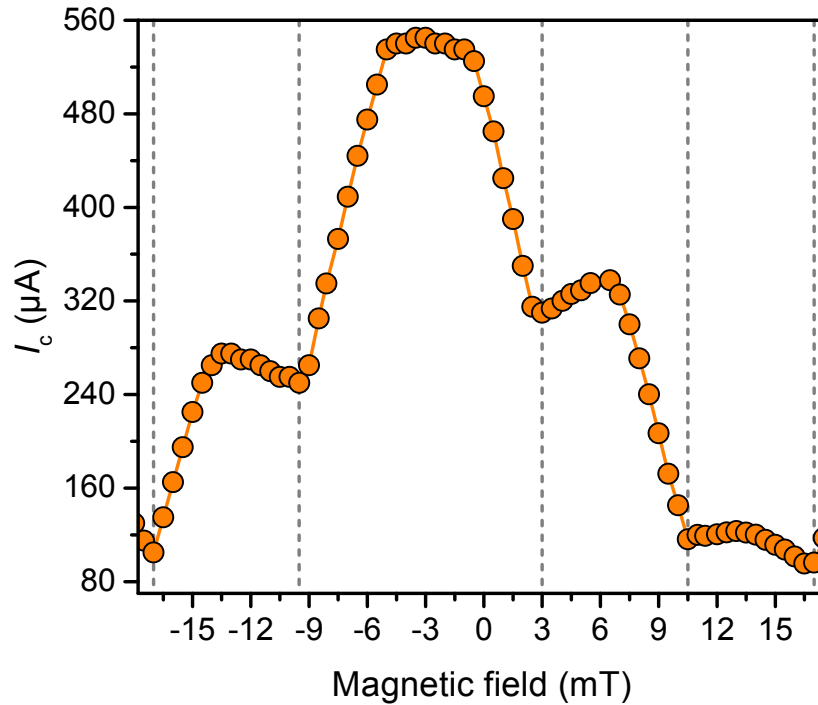
Supplementary Figure 5 | Control experiment. Supercurrent interference pattern measured at $T = 2.1$ K from a control device that was processed in parallel with the one presented in the main text. Deposited together on one substrate, the same multilayer of Pt(7 nm)/Nb(45 nm)/Ni(1.5 nm)/Cu(5 nm)/Co(60 nm) was used in both devices. The Ga$^+$ dose applied in milling the weak link for the control device was reduced by 50%. This provides a nonmagnetic pathway in the weak link, where singlet current is not suppressed, and can therefore dominate the transport. The result is a junction with a substantially higher critical current, showing single-slit interference pattern.

Supplementary Notes

Supplementary Note 1 | Numerical simulations of the critical current.

To calculate the critical current we use the quasiclassical approximation in the diffusive limit, which yields the Usadel equation[5]

$$D \, \nabla \, \widehat{g} \, \nabla \, \widehat{g} + i[\varepsilon \, \widehat{\rho}_3 + \widehat{\sigma} \cdot \boldsymbol{h} \,, \widehat{g}] = 0 \qquad (1)$$

where D is the diffusion constant and ε is the quasiparticle energy. The magnetization texture from the micromagnetic simulations are represented as an exchange field $\mathbf{h} = \mathbf{h}(\mathbf{r})$. Furthermore we have defined $\widehat{\boldsymbol{\sigma}} = \mathrm{diag}(\boldsymbol{\sigma} \,, \boldsymbol{\sigma}^*)$, where $\boldsymbol{\sigma}$ is a vector of Pauli matrices, and $\widehat{\boldsymbol{\rho}}_3 = \mathrm{diag}(1, 1, -1, -1)$. From $\widehat{\mathbf{g}} = \widehat{\mathbf{g}}\,(\mathbf{r}, \varepsilon)$, the 4×4 retarded Green function matrix in Nambu $\otimes$ spin space, the equilibrium current density may be computed as

$$\mathbf{J} = \frac{N_0 eD}{2} \int d\varepsilon \, \mathrm{Re} \, \mathrm{Tr}\{\widehat{\boldsymbol{\rho}}_3 \, \widehat{\mathbf{g}} \, \nabla \, \widehat{\mathbf{g}}\} \tanh\left[\frac{\beta \varepsilon}{2}\right] \qquad (2)$$

where N_0 is the density of states at the Fermi level, and $\beta = 1/k_B T$. We neglect the inverse proximity effect, and assume that the superconductors on each side of the trench are large enough to be approximated as bulk. In the calculations, we have used that the critical current is approximately found for a phase difference between the superconductors of $\Delta \phi = \frac{\pi}{2}$. For simplicity, we use transparent boundary conditions between the Ni and the Co layer, whereas we use the low-transparency Kupriyanov-Lukichev boundary conditions[6] at the Ni-Nb interface.

In the modeling of the geometry, we have assumed an effective superconducting coherence length of $\xi = 10 \, \mathrm{nm}$, so that the radius of the circular disk becomes $R = 50\xi$. In the direction crossing the trench, the model has been truncated to a width of $W = 40\xi$ to reduce the model size. This has been done under the assumption that

any contribution to the current from the removed regions is negligible due to the vast distance to the opposite superconductor. The thickness of the Ni and the Co layers have been set to ξ and 6ξ, respectively, and the width of the trench is 2ξ. The Ni thickness is set larger than in the actual experiment to avoid unnecessarily small elements in the Ni-region, which would substantially increase the calculation time. Although this yields lower values for the triplet current, the purpose of our calculation here is to identify the origin of this current; and not its absolute magnitude.

The spatial distribution of the magnetization in both the Ni and the Co layer are accurately mapped onto the 3D mesh via the exchange field $\mathbf{h}$, where an amplitude of $|\mathbf{h}| = 30\,\Delta \simeq 46\,\text{meV}$ was used. While this is significantly lower than typical exchange fields in Co, it is still sufficient to quench the contribution of singlet Cooper pairs to the current density. To verify this, we make use of the fact that the supercurrent density generated by the singlet $\mathbf{J}^{(s)}$ and triplet $\mathbf{J}^{(t)}$ Cooper pairs contribute additively $\mathbf{J} = \mathbf{J}^{(s)} + \mathbf{J}^{(t)}$. The two components are presented in Supplementary Figure 3. It is clear that the current density of singlet pairs rapidly vanishes away from the superconductors. In contrast, the triplet current density maintains an appreciable value over a substantially larger region, indicating that triplet Cooper pairs are the primary means of transport. The results will therefore be qualitatively the same for a more realistic strength of the exchange field. The advantage of using the reduced value is that the current densities become larger, which in turn make the numerical calculations less resource intensive.

The finite element analysis was carried out using 27-node hexagonal volume elements, and the Green function is interpolated within each element by means of

second order Lagrange polynomials. This means that the current density within each element is interpolated by linear polynomials. To ensure that the spatial distribution of the current density is accurately resolved, we use a refined mesh in a region surrounding the trench, as is shown in Fig. 2a in the main text. For more details regarding the finite element analysis of three-dimensional superconducting heterostructures, please consult ref. 7.

Supplementary Note 2 | Interference patterns from the virgin magnetic state. Prior to conditioning the magnetization, supercurrent interference patterns were measured using small out-of-plane fields. These are presented in Supplementary Figure 1. In contrast to the conditioned sample, $I_c(B_z)$ is generally suppressed around zero field. We observe two maxima, which always occur at fields higher than $5\,\mathrm{mT}$. Note that this offset cannot be attributed to remnant fields from the ferromagnet. The applied field for the interferometry measurements is not sufficient to have an appreciable influence on the magnetization of either layer. This is verified by SQUID magnetometry and ferromagnetic resonance experiments.

It has been proposed that the phase of triplet correlations in a S/F'/F/F'/S junction such as ours, is determined by the relative magnetic orientation of the F and F' layers on each side[2]. On the other hand, this unusual interference pattern, with two maxima and suppressed I_c at zero field, is the characteristic of a junction with multiple parallel 0 and π channels[3,4]. This condition could be fulfilled in the virgin state, where the arbitrary orientation of Ni and Co magnetization can lead to random formation of multiple 0 and π segments across the junction. These interference patterns are also characterized by irregular discontinuities, which could be attributed to the arbitrary arrangement of the 0 and π segments.

Remarkably, we find these features to disappear altogether after conditioning the sample: $I_c(B_z)$ turns into a highly regular and reproducible SQUID pattern, with maximum I_c consistently appearing at $B_z = 0$. This pronounced dependence on magnetic conditioning was absent for junctions where singlet correlations dominated the transport: no significant changes in the interference pattern or the maximum value of I_c were observed.

Supplementary Note 3 | Fourier analysis of supercurrent density profiles.

As shown by Dynes and Fulton[1], the supercurrent density profile $J(x)$ can be determined from the superconducting interference pattern $I_c(B)$ using a Fourier transform:

$$J(x) \sim \int_{-\infty}^{+\infty} dB\, I_c(B)\, e^{\frac{2\pi i L B x}{\Phi_0}} \qquad (3)$$

Here, the coordinate system is defined such that the magnetic field B is applied along the z-axis, the critical current I_c is measured along the y-axis, and the current distribution $J(x)$ can then be determined along the x-axis. The equation also depends on the effective length L of the junction and the flux quantum $\Phi_0 = h/2e$. Note that $I_c(B)$ is the signed critical current, where the sign is determined from the experimentally measured $|I_c(B)|$ by assuming that it consists of alternating positive and negative lobes, as described in more detail in ref. 1. This procedure is justified when the interference pattern consists of well-defined maxima separated by deep minima, as is the case for our measurements.

The original method by Dynes and Fulton was derived for a rectangular junction where the dimensions of each superconductor are much larger than the London penetration depth λ. In that case, the effective junction length $L = 2\lambda + d$, where d is

the thickness of the barrier between the superconducting leads. In our case, however, the junction is cylindrical and the current distribution not uniform, so the length (which determines the amount of flux to be screened) is not well defined. We therefore performed the Fourier analysis without making any assumptions regarding the value of L, but instead assumed that the position along the x-axis where we obtained $J(x) \to 0$ likely corresponded to the junction ends $x \approx \pm R$, where R is the cylinder radius. From this, we obtained an estimate $L \approx 180$ nm for the effective junction length. This value is somewhat lower than expected for a uniform rectangular junction: in that case the effective area is $2RL$ while the first minimum in $I_c(B_z)$ is at 7.8 mT, yielding $L \approx 270$ nm. Both numbers are of correct order of magnitude: the value of λ for a 50 nm Nb film is about 110 nm[8] so $2\lambda + d$ is 240 nm. If we were to take the sharp drop in the current density profile as the sample edge, L would become less than 100 nm, which appears to be too low in view of the value of λ.

The SQI experiments are carried out by measuring the voltage as a function of current for a given applied magnetic field, i.e. $V(I, B)$. The critical current $|I_c(B)|$, used for the Fourier analysis, is obtained by extracting a contour for a small but finite voltage threshold $V(I_c, B) > 0.3 \,\mu\text{V}$. Experimentally we find this criterion to be optimal for reducing noise effects that distort the shape of $I_c(B)$. The result is then adjusted to the y-axis so that $|I_c(B)| = 0$ at the nodes between the lobes of the interference pattern. This is to account for the artificial offset introduced by the $0.3 \,\mu\text{V}$ threshold voltage. We then recover the complex critical current $I_c(B)$, by switching the sign of every other lobe of the measured $|I_c(B)|$. The original $|I_c(B)|$ and the signed $I_c(B)$ curves are shown side-by-side in Supplementary Figure 4.

Note that the measured $I_c(B)$ may slightly deviate from a perfectly symmetric pattern, and yield a complex supercurrent distribution $J(x)$ after Fourier transformation. This apparent asymmetry however is predominantly caused by experimental noise. We therefore discard the complex phase $J(x)$ to approximate the supercurrent distribution profile by $|J(x)|$, shown in Fig. 3f of the main text.

Supplementary References

1. Dynes, R. C. & Fulton, T. A. Supercurrent density distribution in Josephson junctions. *Phys. Rev. B* **3,** 3015-3023 (1971).

2. Houzet, M. & Buzdin, A. I. Long range triplet Josephson effect through a ferromagnetic trilayer. *Phys. Rev. B* **76,** 060504 (2007).

3. Smilde, H. J. H., Ariando, D. H. A., Blank, G. J., Gerritsma, H., Hilgenkamp, H. & Rogalla, H. *d*-Wave–Induced Josephson current counterflow in $YBa_2Cu_3O_7$/Nb zigzag junctions. *Phys. Rev. Lett.* **88,** 057004 (2002).

4. Gürlich, C. *et al.* Visualizing supercurrents in ferromagnetic Josephson junctions with various arrangements of 0 and π segments. *Phys. Rev. B* **81,** 094502 (2010).

5. Usadel, K. D. Generalized diffusion equation for superconducting alloys. *Phys. Rev. Lett.* **25,** 507–509 (1970).

6. Kuprianov, M. Y. & Lukichev, V. F. Influence of boundary transparency on the critical current of 'dirty' SS'S structures. *Sov. Phys. JETP* **67,** 1163 (1988).

7. Amundsen, M. & Linder, J. General solution of 2D and 3D superconducting quasiclassical systems: coalescing vortices and nanoisland geometries. *Sci. Rep* **6,** 22765; doi: 10.1038/srep22765 (2016).

8. Gubin, A. I., Il'in, K. S., Vitusevich, S. A., Siegel, M. & Klein, N. Dependence of magnetic penetration depth on the thickness of superconducting Nb thin films. *Phys. Rev. B* **72,** 064503 (2005).

Paper VII

Reference

M. Amundsen, J. A. Ouassou, and J. Linder.
Field-Free Nucleation of Antivortices and Giant Vortices in Nonsuperconducting Materials.
Physical Review Letters **120**, 207001 (2018).
DOI: 10/gdg3kd

Contributions

MA performed the 2D numerical simulations of vortex patterns, and came up with the explanation of the results in terms of symmetries, energies and winding numbers. JAO contributed to the idea behind the project, analytically derived the radial profile and energy of a giant vortex, and derived the boundary conditions used for the numerical simulations. JL supervised the process and provided support. All authors contributed to the discussion and writing of the manuscript.

Field-Free Nucleation of Antivortices and Giant Vortices
in Nonsuperconducting Materials

Morten Amundsen,[*] Jabir Ali Ouassou, and Jacob Linder

Center for Quantum Spintronics, Department of Physics, Norwegian University of Science and Technology,
NO-7491 Trondheim, Norway

Giant vortices with higher phase winding than 2π are usually energetically unfavorable, but geometric symmetry constraints on a superconductor in a magnetic field are known to stabilize such objects. Here, we show via microscopic calculations that giant vortices can appear in intrinsically nonsuperconducting materials, even without any applied magnetic field. The enabling mechanism is the proximity effect to a host superconductor where a current flows, and we also demonstrate that antivortices can appear in this setup. Our results open the possibility to study electrically controllable topological defects in unusual environments, which do not have to be exposed to magnetic fields or intrinsically superconducting, but instead display other types of order.

Introduction.—It is well known that applying a magnetic field to a type-II superconductor can lead to the formation of Abrikosov vortices [1]. A gradient in the phase φ of the superconducting order parameter $\Delta = |\Delta| e^{i\varphi}$ causes a circulating supercurrent around such vortices, whereas $|\Delta| \to 0$ at their centers. Vortex excitations in superconductors [2,3] remains a vibrant research topic, not least because it lies at the intersection of two major research fields: superconductivity and topology in physics.

It was recently pointed out in Ref. [4] that it is also possible to generate Josephson vortices without applying magnetic fields. Such vortices are also characterized by a quantized phase winding and a suppressed order parameter at their core [5]. Motivated by this, we have performed microscopic calculations using the quasiclassical theory of superconductivity [6] on a normal metal enveloped by a current-biased superconducting wire (Fig. 1). The idea behind the device is simple: an external current source forces a supercurrent through the wire, and this circulation whirls the condensate in a proximitized normal metal as well. Our objective has been to determine what type of electrically controllable vortex physics then emerges. We demonstrate here that both giant vortices and antivortices appear in the nonsuperconducting region even in the absence of any applied magnetic field. This provides an alternative method of creating complex vortex patterns by applying electric currents. Since these patterns are generated in a proximitized nonsuperconductor, this opens up the intriguing prospect of studying unusual topological vortex excitations in materials with other types of quantum order, which do not have to be compatible with bulk superconductivity. One example is a magnetic metal, where the generation of odd-frequency triplet superconducting order could reverse the chirality of some vortices, similarly

to the paramagnetic Meissner effect [7,8]. More fundamentally, it raises the intriguing question: what characterizes a vortex in an odd-frequency order parameter?

Geometric effect and winding number.—Since a circulating supercurrent requires a finite phase-gradient $\nabla \varphi$, and the analyticity of the superconducting wave function implies integral winding numbers $n = \Delta \varphi / 2\pi$ around any point, the system is topologically coerced into nucleating vortices in the normal metal region of Fig. 1. Assuming a thin-film structure, the total charge current associated with this circulation is small, and the magnetic field generated by the circulation can safely be neglected. Note that in contrast to the setup proposed in Ref. [4], our normal metal is surrounded by a continuous superconducting wire on all sides, instead of having two separate wires on the top and bottom, which we will show fundamentally alters the vortex physics in the system. Another important difference is that we model the superconducting wire using an exact solution
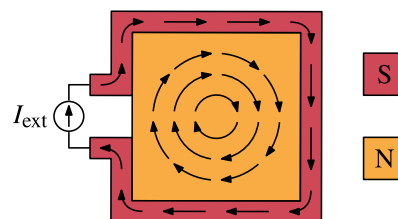

FIG. 1. Conceptual sketch of the physical system. An external current source is used to inject a current into a superconductor (red). The circulating current also affects a proximitized normal metal (yellow), causing an electrically controlled vortex to emerge there.

of the Usadel equation in the current-biased superconductor and tunneling boundary conditions. As we will demonstrate, this is necessary to correctly describe qualitative changes that the phase winding induces in, e.g., the density of states (DOS).

When the current in the superconducting wire makes a total winding number $N > 1$, there are multiple ways to satisfy the boundary conditions. Among other possibilities, we can get (i) N vortices with a winding 1 each, (ii) $N + M$ vortices with a winding $+1$ and M antivortices with winding -1, or (iii) just one giant vortex with a winding N. The kinetic energy of an n-winding vortex scales with n^2, so the most energetically favorable is configuration (i). Hence, giant vortices and antivortices are seldom seen. However, since the superconducting order parameter respects the symmetries of the underlying geometry, vortices only nucleate along the symmetry axes of the system. For highly symmetric geometries, these additional constraints may force the appearance of giant vortices or antivortices. The resulting interplay between topological defects, geometric symmetries, and energy minimization was previously studied in Refs. [9–12] using the phenomenological Ginzburg-Landau formalism for type-II superconductors in a magnetic field. Here, we show that this effect also arises in proximitized normal metals without magnetic fields. This generalization is particularly important as it opens the possibility to study novel vortex physics in materials featuring completely different order than superconductors, e.g., ferromagnets or topological insulators.

2D diffusive metal with phase-winding.—As shown in Fig. 1, we consider a normal metal with a superconducting loop grown on top. We describe the properties of the metal in terms of quasiclassical propagators $\hat{g}$ in Nambu and spin space,

$$\hat{g}(\boldsymbol{r}, \epsilon) = \begin{pmatrix} g(\boldsymbol{r}, +\epsilon)\sigma_0 & f(\boldsymbol{r}, +\epsilon)i\sigma_2 \\ -f^*(\boldsymbol{r}, -\epsilon)i\sigma_2 & -g^*(\boldsymbol{r}, -\epsilon)\sigma_0 \end{pmatrix}, \quad (1)$$

where the normal part g and anomalous part f are complex scalar functions, subject to the normalization constraint $\hat{g}^2 = 1$. Here, σ_0 is the 2×2 identity matrix, and σ_2 is the second Pauli matrix. We assume that all length scales in the problem are large compared to the Fermi wavelength and mean free path; i.e., we take the quasiclassical diffusive limit. The propagators $\hat{g}$ are then governed by the Usadel equation [6,13,14],

$$D\nabla(\hat{g}\nabla\hat{g}) + i[\epsilon\hat{\tau}_3, \hat{g}] = 0, \quad (2)$$

where D is the diffusion constant, ϵ the quasiparticle energy, and $\hat{\tau}_3 = \mathrm{diag}(+\sigma_0, -\sigma_0)$. Furthermore, we assume that the normal region is connected to the superconducting wire by a low-transparency interface. We may then use the Kupriyanov-Lukichev boundary condition $\zeta\boldsymbol{e}_\perp \cdot \nabla\hat{g}_n = [\hat{g}_n, \hat{g}_s]/\xi$ [15], where ζ parametrizes interface resistance,

$\boldsymbol{e}_\perp$ is the outwards-pointing interface normal vector, $\hat{g}_n$ and $\hat{g}_s$ are propagators on the normal and superconducting sides, and ξ the superconducting coherence length. The propagators $\hat{g}_s$ in the current-biased superconductors were evaluated analytically. The applied current also creates a magnetic field which penetrates the proximitized material. Its strength depends on the total applied current, which in turn depends on the pair density and dimensions of the superconductor. However, since the field is perpendicular to and roughly constant within the current loop, its only effect is to slightly perturb the applied current for which a given vortex pattern appears. We have neglected the quantitative correction from the magnetic field herein.

In practice, the differential equations above are Riccati-parametrized for stability [16], and then solved numerically using a finite-element method on a two-dimensional mesh. This lets us handle arbitrary sample geometries, such as the regular polygons considered herein. For more information about the numerical solution procedure itself, see Ref. [17].

Superconducting wire with a uniform current.—As shown in Sec. II of the Supplemental Material [18], the propagator $\hat{g}$ in a current-biased bulk superconductor can be written [23,24]

$$\hat{g} = \frac{1}{\sqrt{\epsilon^2 - \Theta^2}} \begin{pmatrix} +\epsilon\sigma_0 & \Theta e^{+i\varphi}i\sigma_2 \\ \Theta e^{-i\varphi}i\sigma_2 & -\epsilon\sigma_0 \end{pmatrix}, \quad (3)$$

where $\Theta(\epsilon)$ parametrizes the strength of the superconductivity, and φ is the superconducting phase. The phase varies linearly with the distance ℓ along the wire. Defining $\varphi(0) \equiv 0$, and parametrizing the variation using a winding rate $u \equiv \xi|\nabla\varphi|$, we therefore get $\varphi(\ell) = u\ell/\xi$. The function $\Theta(\epsilon)$ is determined by

$$\Theta = \frac{|\Delta|}{1 + u^2/2\sqrt{\Theta^2 - \epsilon^2}}, \quad (4)$$

$$|\Delta| = \frac{1}{\mathrm{acosh}\,\omega_c} \int_0^{\omega_c} d\epsilon\,\mathrm{Re}\left(\frac{\Theta}{\sqrt{\epsilon^2 - \Theta^2}}\right) \tanh\left(\frac{\pi}{2e^\gamma}\frac{\epsilon}{T}\right). \quad (5)$$

These equations have been written in a form where Θ, Δ, ϵ, ω_c are all normalized to the zero-current gap Δ_0, while the temperature T is normalized to the critical temperature T_c. Here, ω_c refers to the Debye cutoff, and γ is the Euler-Mascheroni constant. The first of these equations is a fixpoint iteration equation. This is easily solved by guessing $\Theta(\epsilon) = 1$ and $|\Delta| = 1$, and applying Newton's method to the equation for a discretized set of energies from the Debye cutoff $\epsilon = \omega_c$ to zero energy $\epsilon = 0$. The second is a self-consistency equation for the gap Δ, which is evaluated by numerical integration of the results for $\Theta(\epsilon)$. We then alternate between solving the fixpoint equation and self-consistency equation until satisfactory convergence. The solutions to the equations above are visualized in Fig. 2.
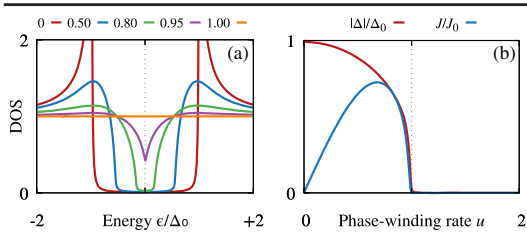
FIG. 2.   Visualization of a bulk superconductor with a uniform current at zero temperature. (a) DOS for varying winding rates u, as shown in the legends above. Note how the coherence peaks are smoothed out for $u > 0$ and the gap closes as $u \to 1$, illustrating a qualitatively different behavior for $u > 0$. (b) Gap Δ and current density J as functions of u, where the unit $J_0 = eDN_0\Delta_0/4\xi$. As long as $u < 1/2$, we see that $\Delta \approx \Delta_0$ and $J \sim u$, and a non-self-consistent solution is reasonably accurate. However, the current becomes nonmonotonic for $u > 2/3$, so this regime is inaccessible in our proposed setup.

When approaching the setup in Fig. 1 numerically, we assumed that the superconducting wire suffers a negligible inverse proximity effect from the normal metal. In this case, we can use the analytical equation above for the superconducting wire, and reduce the superconductor to effective boundary conditions for the normal metal. Furthermore, we numerically only considered phase-winding rates $u \leq 0.5$, in which case Eq. (5) can be replaced by the approximation $|\Delta| \approx 1$. Note that since the phase-winding rate u cannot be arbitrarily large, we need a system much larger than the coherence length to obtain high winding numbers using a current bias.

Quantifying vortices.—We can study the proximity-induced superconductivity in a normal metal via the pair correlation

$$\Psi(\mathbf{r}) \sim \int_0^{\omega_c} d\epsilon\, [f(\mathbf{r}, +\epsilon) - f(\mathbf{r}, -\epsilon)] \tanh(\epsilon/2T), \quad (6)$$

which behaves like a complex order parameter. This pair correlation can be decomposed as $\Psi \equiv |\Psi| \exp(i\varphi)$, and the phase φ can then be extracted using $\varphi = \arctan(\mathrm{Im}\Psi/\mathrm{Re}\Psi)$.

As discussed in the introduction, the circulating current in the enclosing superconductor creates a phase-winding $\nabla\varphi$ along the interface. However, the phase φ is uniquely defined modulo 2π, which means that it is only possible for the phase to vary continuously around the edges of the normal metal if it increases by $\Phi_I = 2\pi N$ after having traversed the entire circumference. In other words, we must have a total vorticity

$$N = \frac{\Phi_I}{2\pi} \equiv \frac{1}{2\pi} \oint_{\partial\Omega} (\nabla\varphi) \cdot d\ell, \quad (7)$$

where $\partial\Omega$ is the boundary of the normal metal. When we have a finite vorticity N, the currents inside the normal
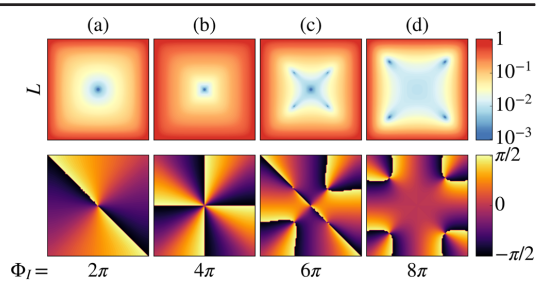

FIG. 3.   Vortex nucleation patterns for various applied current windings Φ_I, for a quadratic normal metal with side lengths $L = 12\xi$. The top row shows the magnitude $|\Psi|$ of the pair correlation, where the minima indicate the vortices. The bottom row shows the phase φ of the pair correlation, from which the winding of individual vortices can be determined. The total windings Φ_I are listed below.

metal will form closed loops, leading to the appearance of vortices. More precisely, the total vorticity N will be equal to the sum of the winding numbers n of all the induced vortices. The vortices manifest as nodes in the pair correlation Ψ.

Numerical results.—In the upper row of Fig. 3, the vortex pattern for increasing applied current winding Φ_I is shown. The winding of the individual vortices may be determined graphically from the phase of the pair correlation function φ, which is plotted in the bottom row of Fig. 3. By using Eq. (7) with the replacements $N \to n$ and $\partial\Omega \to \mathcal{C}$, where $\mathcal{C}$ is any contour encircling a single vortex, one sees that $n \neq 0$ only if the integration path crosses discontinuities. Furthermore, each discontinuity contributes a value to the integral equal to the size of the jump. For $\Phi_I = 2\pi$, shown in Fig. 3(a), there is a single vortex in the center of the normal metal, and any closed contour around this point must traverse two jumps $\Delta\varphi = \pi$, thus showing that the vortex has a winding $n = +1$. We note that the precise locations of these discontinuities depend on the reference point for the phase of the superconductors, and are hence not physically significant. The number of times a closed loop crosses a discontinuity, however, is. In Fig. 3(b), where $\Phi_I = 4\pi$, there is still only a single vortex in the system, but now the plot of φ shows four discontinuities, from which it is inferred that this is a giant vortex with $n = +2$.

For $\Phi_I = 6\pi$, shown in Fig. 3(c), five vortices are found. As the sum of the individual topological numbers should add up to $N = +3$, in accordance with Eq. (7), one of these vortices must be an antivortex. The phase plot shows that this is indeed the case: the central vortex winds in the opposite direction of other vortices. Hence, this configuration consists of one central $n = -1$ antivortex with four surrounding $n = +1$ vortices. For $\Phi_I = 8\pi$, there are four regular $n = +1$ vortices along the diagonals, as shown in Fig. 3(d). Since these vortex patterns arise from symmetry constraints, they are naturally sensitive to asymmetries in
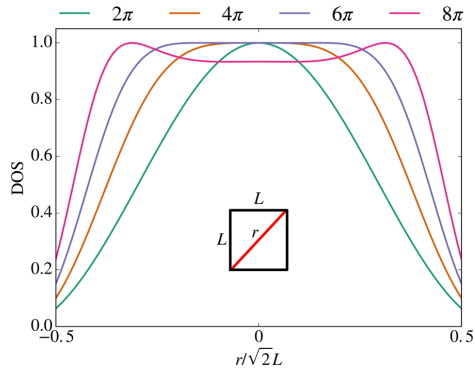
FIG. 4. DOS along the diagonal of the normal metal for various applied current windings Φ_I. Superconductivity is suppressed in the vortex cores, and the normal-state DOS = 1 is recovered.

the geometry. The giant vortex in Fig. 3(b) splits into two $n = +1$ vortices as the geometry becomes rectangular. However, the vortices continue to overlap strongly for sufficiently small deviations, as shown in Sec. III of the Supplemental Material [18]. This means that the giant vortex could in practice be stabilized against deviations from perfect symmetry by creating a pinning potential at this location [25]. Since the vortex positions are also influenced by the applied currents, another option is to fine-tune the currents to experimentally realize the giant vortex. The pattern in Fig. 3(c) is, on the other hand, stable against small deviations in aspect ratio. The reason is that when the geometry becomes increasingly rectangular, it eventually becomes energetically favorable to satisfy $N = +3$ as three $n = +1$ vortices along the longest axis. The transition to such a pattern can only occur in a way which respects the symmetries of the rectangle, and hence the central antivortex turns into a vortex, and additional antivortices must appear so that the off-center vortices can annihilate symmetrically [26].

The vortices also create a spatial modulation of the DOS: at the vortex cores, superconductivity vanishes, and the minigap disappears. This means that the vortices we predict can be directly inferred via local STM measurements. In Fig. 4, the DOS for $\epsilon = 0$ is plotted along the diagonal of the normal metal (i.e., between two opposite corners). This confirms that the normal-state result DOS = 1 is recovered at the vortex cores. For the $n = +2$ vortex produced by $\Phi_I = 4\pi$, the minigap is suppressed in a larger region around the vortex than for $\Phi_I = 2\pi$. For $\Phi_I = 6\pi$, the normal region is larger still, but this is likely due to the close proximity of three vortices. For $\Phi_I = 8\pi$, the vortices are sufficiently far apart for a dip in the DOS to appear in between, providing an observable signature.

The above can be understood by analyzing the pair correlation. In Sec. I of the Supplemental Material [18], it is shown that for small distances r from the vortex center,

$\Psi \sim (r/2\xi_0)^n / n!$, where ξ_0 is the Ginzburg-Landau coherence length. For $r < 2\xi_0 (n!)^{1/n} \approx 2[1 + (n - 1)/e]\xi_0$, these correlations recover more slowly with increasing winding n, and hence the minigap is increasingly suppressed. The fact that the vortex size increases linearly with n also in the diffusive limit can be motivated from Fig. 2. There, we see that superconductivity vanishes entirely as the phase-winding rate $u \equiv \xi|\nabla\varphi| \to 1$. Assuming that this remains approximately valid in nonbulk materials, and using that $|\nabla\varphi| = |n|/r$ around an n-winding vortex, we find that superconductivity vanishes for $r < n\xi$. In other words, we find that the core size of a giant vortex scales linearly with its winding number n, providing an observational signature of giant vortices that can be seen via STM measurements.

The vortex patterns of Fig. 3 may be deduced from energy considerations. In general, the kinetic energy of a vortex with a winding number n scales as n^2. This is because kinetic energy $E_k \sim v^2$, where $v \sim \nabla\varphi \sim n$ is the velocity of the superconducting condensate. In Sec. I of the Supplemental Material [18], we solve the linearized Ginzburg-Landau equation near a vortex with winding number n, and use this to confirm that the kinetic energy is indeed proportional to n^2. Similar n^2 dependencies have previously been noted for magnetic vortices in type-II superconductors [27], and these properties are shared by vortices in proximitized nonsuperconductors [5,28].

The above provides a simple prescription for predicting the vortex nucleation pattern. When a total vorticity N is introduced to the system, it splits into vortices with individual windings n_i in a way that satisfies $N = \sum_i n_i$. Among all patterns permitted by the symmetries of the geometry, the energetically favored is the one that minimizes $E = \sum_i n_i^2$. Note that n_i can be either positive or negative, allowing for antivortex nucleation.

In the geometry considered so far, off-center vortices can only appear in a square formation without breaking the symmetry of the system, as is seen in Fig. 3. This symmetry constraint explains why it is possible to produce a vortex with winding $n = +2$. A higher winding is, however, not possible because it will always be energetically favorable to introduce four new vortices away from the center, and, potentially, an antivortex in the center. Similar results were found for a mesoscopic superconductor in an applied magnetic field [10–12]. The present analysis differs in that the vortex patterns are generated in an intrinsically non-superconducting material solely by an applying an electric current. A regular polygon with a higher symmetry (larger number of sides), will by the same reasoning as above allow for a higher winding at the center, as any alternative will require a larger number of of $n = +1$ vortices to be distributed in a symmetrical fashion. Figure 5 shows the pair correlation function for a hexagonal normal metal surrounded by a superconductor with an applied current equivalent to $\Phi_I = 6\pi$. Here, we find a single vortex of
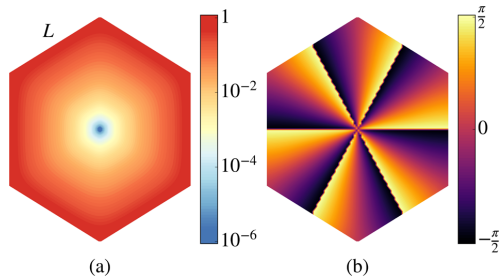
FIG. 5. Hexagonal geometry with side lengths $L = 6\xi$, and an applied current winding $\Phi_I = 6\pi$. (a) The pair correlation Ψ, showing a single vortex at the center. (b) The phase φ of the pair correlation, demonstrating that it is a giant vortex with winding number $n = +3$.

winding $n = +3$. Generally, a regular polygon with m sides allows for a giant vortex with winding up to $n = \lfloor m/2 \rfloor$.

Conclusion.—We have used microscopic calculations to show that one can induce giant vortices and antivortices in nonsuperconducting materials in the absence of magnetic fields. We also analyzed the vortex nucleation pattern using arguments of symmetry and energy minimization. Our results open the possibility to study novel topological defects in unusual environments, which do not have to be intrinsically superconducting or exposed to magnetic fields.

[*] morten.amundsen@ntnu.no

[1] A. A. Abrikosov, J. Phys. Chem. Solids **2**, 199 (1957).
[2] G. Blatter, M. V. Feigel'man, V. B. Geshkenbein, A. I. Larkin, and V. M. Vinokur, Rev. Mod. Phys. **66**, 1125 (1994).
[3] H. Suderow, I. Guillamon, J. G. Rodrigo, and S. Vieira, Supercond. Sci. Technol. **27**, 063001 (2014).
[4] D. Roditchev, C. Brun, L. Serrier-Garcia, J. C. Cuevas, V. H. L. Bessa, M. V. Milošević, F. Debontridder, V. Stolyarov, and T. Cren, Nat. Phys. **11**, 332 (2015).

[5] J. C. Cuevas and F. S. Bergeret, Phys. Rev. Lett. **99**, 217002 (2007).
[6] K. Usadel, Phys. Rev. Lett. **25**, 507 (1970).
[7] A. Di Bernardo *et al.*, Phys. Rev. X **5**, 041021 (2015).
[8] S. Mironov, A. Mel'nikov, and A. Buzdin, Phys. Rev. Lett. **109**, 237002 (2012).
[9] H. J. Fink and A. G. Presson, Phys. Rev. **151**, 219 (1966).
[10] L. F. Chibotaru, A. Ceulemans, V. Bruyndoncx, and V. V. Moshchalkov, Nature (London) **408**, 833 (2000).
[11] L. F. Chibotaru, A. Ceulemans, V. Bruyndoncx, and V. V. Moshchalkov, Phys. Rev. Lett. **86**, 1323 (2001).
[12] L. F. Chibotaru, A. Ceulemans, G. Teniers, and V. V. Moshchalkov, Physica (Amsterdam) **369C**, 149 (2002).
[13] J. Rammer and H. Smith, Rev. Mod. Phys. **58**, 323 (1986).
[14] W. Belzig, F. K. Wilhelm, C. Bruder, G. Schön, and A. D. Zaikin, Superlattices Microstruct. **25**, 1251 (1999).
[15] M. Y. Kupriyanov and V. F. Lukichev, Zh. Eksp. Teor. Fiz. **94**, 139 (1988) [Sov. Phys. JETP **67**, 1163 (1988)].
[16] N. Schopohl, arXiv:cond-mat/9804064.
[17] M. Amundsen and J. Linder, Sci. Rep. **6**, 22765 (2016).
[18] See the Supplemental Material at http://link.aps.org/supplemental/10.1103/PhysRevLett.120.207001 for a calculation of the giant vortex energies, an analytical solution of the Usadel equation in a current-carrying superconductor, and numerical results for asymmetric geometries. The Supplemental Material includes Refs. [19–22].
[19] K. Fossheim and A. Sudbø, *Superconductivity: Physics and Applications* (John Wiley & Sons, Chichester, 2004), Sec. 4.7.
[20] J. P. Morten, Master's thesis, Norwegian University of Science and Technology, Trondheim, Norway, 2003.
[21] S. H. Jacobsen, J. A. Ouassou, and J. Linder, Phys. Rev. B **92**, 024510 (2015).
[22] W. Hu, K. Sarveswaran, M. Lieberman, and G. H. Bernstein, J. Vac. Sci. Technol. B **22**, 1711 (2004).
[23] S. V. Bakurskiy, N. V. Klenov, I. I. Soloviev, M. Y. Kupriyanov, and A. A. Golubov, Phys. Rev. B **88**, 144519 (2013).
[24] J. Romijn, T. M. Klapwijk, M. J. Renne, and J. E. Mooij, Phys. Rev. B **26**, 3648 (1982).
[25] I. V. Grigorieva, W. Escoffier, V. R. Misko, B. J. Baelus, F. M. Peeters, L. Y. Vinnikov, and S. V. Dubonos, Phys. Rev. Lett. **99**, 147003 (2007).
[26] G. Teniers, L. F. Chibotaru, A. Ceulemans, and V. V. Moshchalkov, Europhys. Lett. **63**, 296 (2003).
[27] P. G. de Gennes, *Superconductivity of Metals and Alloys* (W.A. Benjamin, New York, 1966).
[28] F. S. Bergeret and J. C. Cuevas, J. Low Temp. Phys. **153**, 304 (2008).

Supplemental information

Morten Amundsen,[1] Jabir Ali Ouassou,[1] and Jacob Linder[1]

[1]*Center for Quantum Spintronics, Department of Physics, Norwegian University of Science and Technology, NO-7491 Trondheim, Norway*

(Dated: February 24, 2018)

In this supplemental, we derive two sets of equations that are applied in the main manuscript. In Section I, we find an exact solution to the linearized Ginzburg-Landau equation near a vortex with an arbitrary winding number n, and show that the kinetic energy is proportional to n^2. This is used to explain the vortex configurations in the main manuscript. In Section II, we find a selfconsistent solution to the Usadel equation in a bulk superconductor with a uniform charge current. This is used as a boundary condition in the main manuscript.

I. ANALYTICAL SOLUTION AROUND A VORTEX CORE

Let us consider a superconducting vortex with a winding number n. This means that as we move one counter-clockwise turn around the vortex core, the phase of the superconducting condensate changes by $\Delta\varphi = 2\pi n$. We will here calculate the energy of such a vortex, which in the main manuscript is used to understand what nucleation patterns are energetically favored. To keep the calculations simple and intuitive, we approach the problem using the Ginzburg-Landau formalism. Furthermore, we will assume that the energy of a vortex is dominated by the region close to the vortex core, and that this region exhibits a cylindrical symmetry. Since the energy of a vortex ($n > 0$) and antivortex ($n < 0$) are exactly the same, we focus on $n > 0$.

A. Linearized Ginzburg-Landau theory

The starting point of the Ginzburg-Landau framework is the free energy density in a superconducting material,[1]

$$E = \alpha|\Psi|^2 + \frac{\beta}{2}|\Psi|^4 + \frac{1}{2m}|(-i\hbar\nabla - 2e\mathbf{A})\Psi|^2 + \frac{\mathbf{B}^2}{2\mu_0}, \quad (1)$$

where Ψ is the superconducting wavefunction, $\mathbf{A}$ is the magnetic potential, $\mathbf{B} = \nabla \times \mathbf{A}$ is the magnetic field, and we choose $E \equiv 0$ in the normal state. Minimizing the free energy of the system, one arrives at the Ginzburg-Landau equation,[1]

$$\alpha\Psi + \beta|\Psi|^2\Psi + \frac{1}{2m}(-i\hbar\nabla - 2e\mathbf{A})^2\Psi = 0. \quad (2)$$

We now introduce some approximations. Firstly, as in the main manuscript, we are interested in current-induced vortices in thin-films, for which there is a negligible magnetic potential $\mathbf{A} \approx 0$ in the system. Secondly, we are interested in the behaviour near a vortex core, where the superconducting wavefunction is suppressed $|\Psi| \ll 1$, so that we can linearize the equation. We then obtain an effective Helmholtz equation,

$$\nabla^2\Psi \approx \Psi/\xi_0^2, \quad (3)$$

where $\xi_0 \equiv \sqrt{\hbar^2/2m|\alpha|}$ is the Ginzburg-Landau coherence length. We can parametrize the wavefunction as $\Psi \equiv \psi e^{i\varphi}$, where the amplitude ψ and phase φ are real. Substituting this parametrization into the Helmholtz equation, we obtain

$$\nabla^2\psi + 2i(\nabla\psi)(\nabla\varphi) + i\psi(\nabla^2\varphi) - \psi(\nabla\varphi)^2 = \psi/\xi_0^2. \quad (4)$$

This equation can be significantly simplified using the law of charge conservation. The charge current density in a system governed by the Ginzburg-Landau equation is in general:[1]

$$\mathbf{J} = \frac{e}{m}[\Psi^*(-i\hbar\nabla - 2e\mathbf{A})\Psi + \Psi(+i\hbar\nabla - 2e\mathbf{A})\Psi^*]. \quad (5)$$

If we again set $\mathbf{A} \approx 0$ and substitute in $\Psi = \psi e^{i\varphi}$,

$$\mathbf{J} = \frac{2\hbar e}{m}\psi^2\nabla\varphi. \quad (6)$$

From this equation for the charge current, combined with the fact that charge current is conserved $\nabla \cdot \mathbf{J} = 0$, we conclude:

$$2\psi(\nabla\psi)(\nabla\varphi) + \psi^2\nabla^2\varphi = 0. \quad (7)$$

At any point with a finite wavefunction $\psi \neq 0$, this means that two of the terms on the left-hand side of Eq. (4) have to cancel. This lets us write Eq. (4) as simply:

$$\nabla^2\psi - \psi(\nabla\varphi)^2 = \psi/\xi_0^2. \quad (8)$$

B. Exact vortex profile

We now focus on the specific case of a vortex with winding n, meaning that the total phase-difference around the core is $\Delta\varphi = 2\pi n$. At a distance r from the core, this phase-difference occurs over a length $2\pi r$, yielding an average phase-gradient $|\nabla\varphi| = \Delta\varphi/2\pi r = n/r$. Assuming cylindrical symmetry, we expect the amplitude ψ to only depend on the radius r from the vortex core, so that $\nabla^2\psi \to r^{-1}\partial_r(r\partial_r\psi)$. Together, these observations let us reduce Eq. (8) to an ordinary differential equation for the radial profile $\psi(r)$, which can be written as:

$$r^2\frac{d^2\psi}{dr^2} + r\frac{d\psi}{dr} - \left(n^2 + \frac{r^2}{\xi_0^2}\right)\psi = 0. \quad (9)$$

This is the defining equation for the *modified* or *hyperbolic* Bessel functions $I_n(r/\xi_0)$ and $K_n(r/\xi_0)$. However, whereas the first kind $I_n(r/\xi_0)$ always converges to a finite value as $r \to 0$, the second kind diverges there, and is therefore an unphysical solution. The radial profile of a vortex is therefore:

$$\psi(r) = \psi_0 I_n(r/\xi_0). \quad (10)$$

C. Asymptotic kinetic energy

In the previous subsection, we found exact solutions of the linearized Ginzburg-Landau equation in the vicinity of a vortex. These are however not straight-forward to use for analytically comparing vortex energies. Physically, we expect the dominant contributions to the kinetic energy to come from the region close to the vortex. This means that we can do a Taylor expansion around the vortex core $r = 0$,

$$I_n(r/\xi_0) = \sum_{m=0}^{\infty} \frac{1}{m!(m+n)!} \left(\frac{r}{2\xi_0}\right)^{2m+n} \quad (11)$$

and focus on the region near the vortex core $r \ll \xi_0$ where the $m = 0$ term becomes the dominant contribution. This gives us the following asymptotic profile for a vortex with winding n:

$$\psi(r) \approx \frac{\psi_0}{n!} \left(\frac{r}{2\xi_0}\right)^n. \quad (12)$$

We can now go back to the free energy, and use these solutions to determine the energy associated with each vortex. Let us consider the kinetic energy density E_k. In the absence of magnetism, this is just the gradient term in Eq. (1):

$$E_k = \frac{\hbar^2}{2m} |\nabla \Psi|^2. \quad (13)$$

We then switch to polar coordinates $\nabla = \partial_r e_r + r^{-1}\partial_\theta e_\theta$:

$$E_k = \frac{\hbar^2}{2m} \left(|\partial_r \Psi|^2 + r^{-2}|\partial_\theta \Psi|^2\right). \quad (14)$$

Substituting in the asymptotic solutions $\Psi \sim r^n e^{in\theta}$:

$$E_k = \frac{\hbar^2 |\Psi|^2}{mr^2} n^2. \quad (15)$$

Thus, the kinetic energy of a giant vortex is proportional to n^2.

II. SUPERCONDUCTOR WITH A UNIFORM CURRENT

In the main manuscript, we considered a system consisting of a superconducting wire encircling a normal metal. Although the superconductor was assumed to be thick enough to act as a bulk material, the fact that it also carries a supercurrent means that the propagators are no longer given by the standard BCS solution. In order to use as realistic boundary conditions as possible for that setup, we here solve the Usadel equation analytically for a current-carrying superconductor.

A. Background theory

In a superconductor, the Usadel equation can be written[2-4]

$$iD\nabla(\hat{g}\nabla\hat{g}) = [\epsilon\hat{\tau}_3 + \hat{\Delta}, \hat{g}], \quad (16)$$

where $\hat{\tau}_3 = \text{diag}(+1, +1, -1, -1)$, and the gap matrix is defined as $\hat{\Delta} = \text{antidiag}(+\Delta, -\Delta, +\Delta^*, -\Delta^*)$. The superconducting gap can in turn be parametrized as $\Delta = |\Delta|e^{i\varphi}$ where $\varphi \in \mathbb{R}$. The matrices on the left-hand side of the commutator are then:

$$\epsilon\hat{\tau}_3 = \epsilon \begin{pmatrix} +\sigma_0 & 0 \\ 0 & -\sigma_0 \end{pmatrix}, \quad \hat{\Delta} = |\Delta| \begin{pmatrix} 0 & e^{+i\varphi}i\sigma_2 \\ e^{-i\varphi}i\sigma_2 & 0 \end{pmatrix}. \quad (17)$$

The propagator $\hat{g}$ can be written using the θ-parametrization:[4,5]

$$\hat{g} = \begin{pmatrix} +\cosh\theta\,\sigma_0 & e^{+i\chi}\sinh\theta\,i\sigma_2 \\ e^{-i\chi}\sinh\theta\,i\sigma_2 & -\cosh\theta\,\sigma_0 \end{pmatrix}. \quad (18)$$

The parameters θ and χ satisfy the particle-hole symmetries $\theta^*(+\epsilon) = -\theta(-\epsilon)$ and $\chi^*(+\epsilon) = \chi(-\epsilon)$.[5] For brevity, we also use the abbreviations $s \equiv \sinh\theta$ and $c \equiv \cosh\theta$. Finally, the self-consistency equation for the gap is:[8]

$$\Delta = N_0\lambda e^{i\chi} \int_0^{\omega_c} d\epsilon\, \text{Re}[\sinh\theta]\tanh(\epsilon/2T). \quad (19)$$

Comparing this to the parametrization of the gap $\Delta = |\Delta|e^{i\varphi}$, we immediately note that the phases $\varphi = \chi$ must be equal.

B. Zero current

In the absence of charge currents, we must have a homogeneous solution $\nabla\hat{g} = 0$. Thus, the Usadel equation has to reduce to:

$$[\epsilon\hat{\tau}_3 + \hat{\Delta}, \hat{g}] = 0. \quad (20)$$

Writing the terms in the commutator explicitly, we get:

$$[\epsilon\hat{\tau}_3, \hat{g}] = +2\epsilon \begin{pmatrix} 0 & +se^{+i\varphi}i\sigma_2 \\ -se^{-i\varphi}i\sigma_2 & 0 \end{pmatrix}, \quad (21)$$

$$[\hat{\Delta}, \hat{g}] = -2|\Delta| \begin{pmatrix} 0 & +ce^{+i\varphi}i\sigma_2 \\ -ce^{-i\varphi}i\sigma_2 & 0 \end{pmatrix}. \quad (22)$$

From this, we can extract the scalar equation $\epsilon s - |\Delta|c = 0$, which yields the standard BCS solution $\theta = \text{atanh}(|\Delta|/\epsilon)$.

C. Uniform current

Before we attempt to solve the Usadel equation in a current-carrying superconductor with $\partial_z\hat{g} \neq 0$, let us try to constrain the allowed position-dependence of our parameters θ and φ. One such condition can be found from the density of states,

$$N = \frac{1}{2}N_0 \text{Re Tr}[g] = N_0 \text{Re}[\cosh\theta]. \quad (23)$$

For a bulk superconductor carrying a uniform current, we insist that the density of states is uniform as well, i.e. that $\partial_z N = 0$. Using the chain rule, we can rewrite this condition as follows:

$$(\partial_z\theta)(\partial_\theta\text{Re}[\cosh\theta]) = 0. \quad (24)$$

Thus, we may either have $\partial_z\theta = 0$ or $\partial_\theta\text{Re}[\cosh\theta] = 0$. Since θ is a direct function of energy, the latter is equivalent to the

density of states being energy-independent, which we know is false for a superconductor. Thus, we conclude that $\partial_z\theta = 0$.

Now that we know $\partial_z\theta = 0$, differentiating $\hat{g}$ is quite easy:

$$\partial_z\hat{g} = i\partial_z\varphi \begin{pmatrix} 0 & +e^{+i\varphi}si\sigma_2 \\ -e^{-i\varphi}si\sigma_2 & 0 \end{pmatrix}. \quad (25)$$

Multiplying by $\hat{g}$ from the left, we then obtain:

$$\hat{g}\partial_z\hat{g} = i\partial_z\varphi \begin{pmatrix} s^2\sigma_0 & e^{+i\varphi}cs\,i\sigma_2 \\ e^{-i\varphi}cs\,i\sigma_2 & -s^2\sigma_0 \end{pmatrix}. \quad (26)$$

Another constraint can then be found from the spectral current,

$$j_z = \frac{1}{4}j_0\,\mathrm{Tr}[\hat{\tau}_3\hat{g}\partial_z\hat{g}]. \quad (27)$$

Substituting in the expression for $\hat{g}\partial_z\hat{g}$ above, we find that $j_z/j_0 = is^2\partial_z\varphi$. But insisting that the divergence $\partial_z j_z = 0$, and keeping in mind that $\partial_z s = 0$ because we determined that $\partial_z\theta = 0$ above, this gives us the constraint $\partial_z^2\varphi = 0$. One might however argue that perhaps the spectral current does not have to be conserved, since charge conservation only requires that the *integral* of the spectral current above is position-independent. However, for a *uniform current-carrying superconductor*, we can safely insist that the spectral current be constant as well.

Now that we have the additional constraint $\partial_z^2\varphi = 0$, it is straight-forward to differentiate $\hat{g}\partial_z\hat{g}$:

$$\partial_z(\hat{g}\partial_z\hat{g}) = (i\partial_z\varphi)^2 \begin{pmatrix} 0 & +e^{+i\varphi}cs\,i\sigma_2 \\ -e^{-i\varphi}cs\,i\sigma_2 & 0 \end{pmatrix}. \quad (28)$$

This defines the left-hand side of the Usadel equation. Combining the above with the rest of the Usadel equation, we find the following equation from the off-diagonal parts:

$$iD(i\partial_z\varphi)^2cs = 2\epsilon s - 2|\Delta|c. \quad (29)$$

We will now normalize everything with respect to the zero-current gap Δ_0, so that $|\Delta| \equiv \delta\Delta_0$ and $\epsilon \equiv E\Delta_0$. Furthermore, we define a phase-winding rate $u^2 \equiv D(\partial_z\varphi)^2/\Delta_0$. Thus:

$$Es - \delta c + i(u^2/2)cs = 0. \quad (30)$$

Note that since the diffusion constant can be written $D = \Delta_0\xi^2$, we could also write $u = \xi\partial_z\varphi$, which means that this parameter basically measures the phase-winding per coherence length. By substituting the hyperbolic identity $c = \sqrt{1+s^2}$ into Eq. (30), the resulting 4th-order algebraic equation in s can easily be solved to provide the analytical solution. However, for practical reasons we here pursue a numerical approach.

D. Non-selfconsistent solution

In order to solve Eq. (30), it is convenient to reparametrize the equation using the following mapping, where $\Theta(E)$ is an unknown function of energy:[6,7]

$$c = \frac{E}{\sqrt{E^2 - \Theta^2}}, \qquad s = \frac{\Theta}{\sqrt{E^2 - \Theta^2}}. \quad (31)$$

Note that this parametrization manifestly satisfies the identity $c^2 - s^2 = 1$. Substituting the above into Eq. (30) and rearranging, we find that the Usadel equation can be rewritten as:

$$\Theta = \frac{\delta}{1 + u^2/2\sqrt{\Theta^2 - E^2}}. \quad (32)$$

In the absence of currents $u = 0$, we get a trivial solution $\Theta = \delta$. For a finite phase-winding rate u, it takes the form of a fixpoint iteration equation, and can be solved using Newton's method.

In addition to the above equation for Θ, we need to determine the superconducting phase φ. However, in the previous subsection, we discovered that $\partial_z^2\varphi = 0$. This means that the phase φ has to be a linear function of position. Furthermore, since the reference-point for the superconducting phase is arbitrary, we can define $\varphi(0) \equiv 0$. Thus, the phase φ can be expressed as:

$$\varphi(z) = uz/\xi. \quad (33)$$

For small currents, one can safely assume that the gap is nearly the same as for zero current, meaning that $\delta \approx 1$. However, in general, this fixpoint equation has to be accompanied by a selfconsistency equation for the current-dependent gap factor δ.

E. Selfconsistent solution

Let us now revisit the selfconsistency equation for the gap, using the Θ-parametrization from the previous subsection. We normalize the energy $E \equiv \epsilon/\Delta_0$, gap $\delta \equiv |\Delta|/\Delta_0$, Debye cutoff $\Omega_c \equiv \omega_c/\Delta_0$, and temperature $\tau \equiv T/T_c$. Furthermore, the cutoff is in general related to the BCS coupling strength by $\Omega_c \equiv \cosh(1/N_0\lambda)$, while the gap and critical temperature are related by the BCS ratio $\Delta_0/T_c = \pi/e^\gamma$, where γ is the Euler-Mascheroni constant.[8] Combining all of these remarks, Eq. (19) for the current-dependent gap may be written as:

$$\delta = \frac{1}{\mathrm{acosh}\,\Omega_c}\int_0^{\Omega_c} dE\,\mathrm{Re}\left(\frac{\Theta}{\sqrt{E^2 - \Theta^2}}\right)\tanh\left(\frac{\pi}{2e^\gamma}\frac{E}{\tau}\right). \quad (34)$$

In general, the selfconsistent problem is solved in two steps. First, we guess that the solution is $\Theta(E) = 1$ and $\delta = 1$. For each energy in a discretized range from $E = \Omega_c$ to $E = 0$, one solves Eq. (32) for $\Theta(E)$ using Newton's method. The solutions are substituted into Eq. (34), which is integrated to find a new estimate for δ. This procedure is repeated until convergence.

III. GIANT VORTICES IN ASYMMETRIC GEOMETRIES

Giant vortices are inherently unstable and will seek to split into single vortices unless hindered from doing so. For the systems under consideration, the giant vortices are maintained due to symmetry constraints. It is therefore interesting to investigate how, for instance, Fig. 3(b) in the manuscript reacts to a small deviation from perfect symmetry. We do so by introducing a small perturbation ε of the aspect ratio α by defining $\alpha = 1 + \varepsilon$, thereby making the system rectangular. The results are shown in Fig. 1, from which it is seen that vortices

do indeed split as ε is increased, but this splitting occurs in a continuous way, and the resulting vortex pair remains within close proximity to the location of the original giant vortex for a deviation of up to $\varepsilon = 1\%$. This means that the giant vortex can be stabilized against small deviations in the geometry by placing a pinning potential at this position,[9] or by forcing the split vortices together by fine tuning the applied currents. To reduce the influence of unintended asymmetry, it is recommended to use a superconductor with as large a coherence length as possible. Choosing for instance aluminium, one gets an estimated diffusive coherence length of $\xi \simeq 100\,\text{nm}$. For a square geometry with side lengths $L = 12\xi$, a deviation of $\varepsilon = 1\%$ then corresponds to $\Delta L \simeq 12\,\text{nm}$, which is an experimentally achievable level of accuracy.[10]

(a) $\varepsilon = 0.01\%$ (b) $\varepsilon = 0.1\%$ (c) $\varepsilon = 1\%$

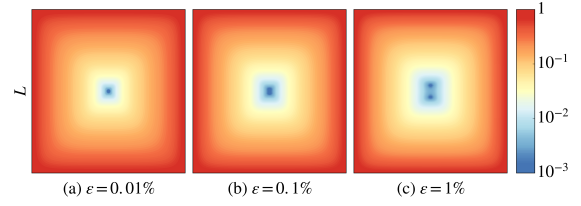FIG. 1: Vortex patterns for an applied current winding of $\Phi_I = 4\pi$, with increasing aspect ratio deviation ε.

[1] K. Fossheim and A. Sudbø, *Superconductivity: Physics and Applications* (John Wiley & Sons, Chichester, 2004), Sec. 4.7.

[2] K. Usadel. *Phys. Rev. Lett.* **25**, 507 (1970).

[3] J. Rammer and H. Smith. *Rev. Mod. Phys.* **58**, 323 (1986).

[4] W. Belzig, F. K. Wilhelm, C. Bruder, G. Schön, and A. D. Zaikin. *Superlattices and Microstructures* **25**, 1251 (1999).

[5] J.P. Morten, Master thesis, NTNU, 2003.

[6] S.V. Bakurskiy, N.V. Klenov, I.I. Soloviev, M.Yu. Kupriyanov, and A.A. Golubov. *Phys. Rev. B* **88**, 144519 (2013).

[7] J. Romijn, T.M. Klapwijk, M.J. Renne, and J.E. Mooij. *Phys. Rev. B* **26**, 3648 (1982).

[8] S.H. Jacobsen, J.A. Ouassou, and J. Linder. *Phys. Rev. B* **92**, 024510 (2015).

[9] I. V. Grigorieva, W. Escoffier, V. R. Misko, B. J. Baelus, F. M. Peeters, L. Y. Vinnikov, and S. V. Dubonos. *Phys. Rev. Lett.* **99**, 147003 (2007).

[10] W. Hu, K. Sarveswaran, M. Lieberman, and G. H. Bernstein. *J. Vac. Sci. Technol. B* **22**, 1711 (2004).

Paper VIII

Reference

Contributions

MA performed the 2D numerical simulations, based on a formalism developed by HGH, with support from HGH, AS and JL. All authors contributed to the discussions of the physics and the revision of the final manuscript.

Vortex spin valve on a topological insulator

Morten Amundsen,[*] Henning G. Hugdal, Asle Sudbø, and Jacob Linder
Center for Quantum Spintronics, Department of Physics, Norwegian University of Science and Technology, NO-7491 Trondheim, Norway

Spin-valve structures are usually associated with the ability to modify the resistance of electrical currents. We here demonstrate a profoundly different effect of a spin-valve. In combination with a topological insulator and superconducting materials, we show that a spin-valve can be used to toggle quantum vortices in and out of existence. In the antiparallel configuration, the spin valve causes superconducting vortex nucleation. In the parallel configuration, however, no vortices appear. This switching effect suggests a new way to control quantum vortices.

I. INTRODUCTION

Topological insulators (TI) are fascinating materials which are insulating in their bulk, but have topologically protected conducting surface states [1]. When a conventional s-wave superconductor is placed in contact with a topological insulator, the superconducting correlations induced on the TI surface gain a topological character [2]. This may give rise to a range of exotic phenomena, such as the appearance of Majorana bound states at vortices [3], which provides an exciting avenue toward non-Abelian statistics and topological quantum computation [4].

A particularly interesting property of the surface states of a TI is the presence of spin–momentum locking. By proximity coupling both superconducting and ferromagnetic elements to the topological insulator, this may be used to create complex supercurrent density distributions [5]. A key observation is that the exchange field enters the Hamiltonian for the surface states of a TI in the same way as the magnetic vector potential does, due to the spin-momentum locking. Because of this, one might expect that quantum vortices with a phase-winding could be induced by an exchange field alone on the surface of a TI in contact with a superconductor, without the need of any external magnetic flux. The study of superconducting vortices induced in nonsuperconducting materials via proximity has recently attracted attention both theoretically [5–9] and experimentally [10].

In this paper, we show that a spin-valve structure combined with a topological insulator and superconducting materials can be used to toggle quantum vortices in and out of existence. These vortices behave in the exact same way as conventional proximity-induced vortices in superconducting heterostructures, except for the crucial difference of being generated by an inhomogeneous in-plane exchange field, rather than the orbital effect of an applied magnetic flux. Indeed, we will show that vortex nucleation may be understood in terms of the presence of an effective flux created by the exchange field, completely analogously to the flux produced by a magnetic vector potential. An advantage of using an exchange field to generate vortices is that it provides greater freedom in studying inhomogeneous effective flux densities than is possible with an applied perpendicular magnetic field, and hence may give rise to more complex vortex patterns. The spin valve consists of two ferromagnetic layers which can be either in a parallel (P) or antiparallel (AP) configuration. In the P configuration, the spin valve does not cause superconducting vortex nucleation. In contrast, vortices can exist in the AP configuration. This switching effect suggests a new way to control quantum vortices in heterostructures. The precise conditions under which this can occur will be detailed below.

II. THEORY AND MODEL

To demonstrate the spin-valve effect, we consider the system shown in Fig. 1. Two superconductors are placed on top of a topological insulator, maintaining a good electrical contact to induce a measurable proximity effect. This can, for instance, be a Nb-Bi$_2$Te$_3$-Nb heterostructure, in which the presence of a Josephson effect has been experimentally verified [11]. Between the superconductors is placed a pair of ferromagnets. This creates an effective SFS Josephson weak link on the two-dimensional surface of the TI via the proximity effect. The distance between the superconductors is $L = 2\xi$, where ξ is the superconducting coherence length, which is assumed to also be the width of the system. The exchange field in the ferromagnet is directed along the x axis (between the superconductors). The magnitude of the exchange field is constant in the x direction, but can be toggled between either a P or AP configuration. Such a system can be experimentally designed by separating the two ferromagnets by a thin nonmagnetic spacer layer. If the ferromagnets have different coercive fields, one may toggle between configurations, for instance, by heating the system to above the critical temperature of the superconductors, T_c, apply a magnetic field in the x direction large enough to switch the magnetization in one of the layers, and then cool the system to below T_c. To ensure different coercive fields, the ferromagnets may either be different materials or have different sizes.

The surface of the three-dimensional diffusive topological insulator here considered may be described by using quasiclassical theory [12,13]. In the following, we use units

---

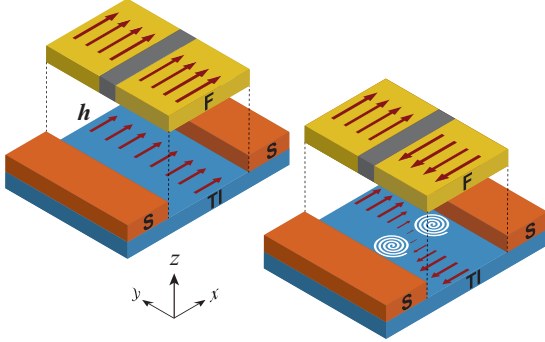*Corresponding author: morten.amundsen@ntnu.no

FIG. 1. The geometry considered. Two superconductors and a spin valve are placed on top of a topological insulator. The spatial variation of the exchange field induced by the antiparallel configuration of the ferromagnets creates vortices in the TI. The spin valve is shown lifted for clarity.

where $\hbar = 1$. In equilibrium, all physical observables may be computed from the 2×2 retarded Green's function

$$G = \begin{pmatrix} g & f \\ \tilde{f} & -g \end{pmatrix}, \qquad (1)$$

where g and f are the normal and anomalous Green's functions, respectively, and $\tilde{f}(\varepsilon) = f^*(-\varepsilon)$. G has structure only in particle–hole space, and the spin structure has been factored out by a unitary transformation to take the spin–momentum locking into account. A detailed description of this procedure is given in Ref. [14]. In the diffusive limit, the Green's function is governed by the Usadel equation [15]

$$2Di\hat{\nabla} \cdot (G\hat{\nabla}G) = [\varepsilon\sigma_3, G], \qquad (2)$$

where $\hat{\nabla}G = \nabla G - \frac{i}{v_F}[\boldsymbol{h}\sigma_3, G]$, $\boldsymbol{h}$ is the in-plane exchange field, D is the diffusion constant, ε is the quasiparticle energy, v_F is the Fermi velocity, and σ_3 is the third Pauli matrix. We solve Eq. (2) in the region of the TI located between the superconductors, which we consider as large enough to be described by their bulk expressions, G_{BCS}, as given in Ref. [14]. The numerical method we employ is described in detail in Ref. [16], and only slight modifications are necessary to adapt it to topological insulators. We neglect the inverse proximity effect, which is a good approximation as long as the Fermi level μ_{TI} in the TI is substantially different from $\pm\sqrt{2mv_F^2\mu_{\text{S}}}$, where m and μ_{S} are the electron mass and Fermi level in the superconductor, respectively [17]. We further assume transparent boundary conditions to the superconductors, while the vacuum interfaces are described by the Neumann boundary condition $\hat{\nabla}G = 0$. We note in particular that the in-plane exchange field enters Eq. (2) in precisely the same way as does the vector potential in a normal metal. A consequence of this is that the system will react to a spatial variation in $\boldsymbol{h}$ in the same way as if an effective flux $\Phi_h = \int_A \nabla \times \boldsymbol{h} \, d\boldsymbol{r}$ is applied, where A is the area of the TI surface. This means that for a sufficiently large inhomogeneous exchange field, vortices may appear. Note that for a curl-free inhomogeneous $\boldsymbol{h}$, vortices do not appear. An analogy to an SNS junction with a uniform applied magnetic flux is found by considering an

exchange field $\boldsymbol{h} = -h_0 y\hat{x}$. In the Fraunhofer limit, where the width of the junction (in the y direction) is much larger than its length, the number of vortices in the system is equal to the number of flux quanta that is applied. The relevant flux quantum for the exchange-field-induced vortices in the present paper is then $\Phi_0 = \pi v_F$. The square geometry of the system studied herein influences the number and position of the vortices. However, the number of flux quanta produced by the effective flux Φ_h still remains a good estimate for the number of vortices.

From the retarded Green's function, G, the density of states, normalized by its value at the Fermi level, may be computed as $N(\boldsymbol{r}, \varepsilon) = \text{Re}\, g(\boldsymbol{r}, \varepsilon)$, with $g(\boldsymbol{r}, \varepsilon)$ defined in Eq. (1). Furthermore, the pair correlation in the TI, which is a measure of the strength of the superconducting correlations induced by the proximity effect, may be computed from

$$\Psi(\boldsymbol{r}) = N_0 \int d\varepsilon \, [f(\boldsymbol{r}, \varepsilon) - f(\boldsymbol{r}, -\varepsilon)] \tanh\frac{\beta\varepsilon}{2}, \qquad (3)$$

where $\beta = 1/k_B T$, T is the temperature and N_0 is the density of states at the Fermi level. Finally, the current density is given as

$$\boldsymbol{J}(\boldsymbol{r}) = J_0 \int d\varepsilon \, \text{Re}\left[f\nabla\tilde{f} - \tilde{f}\nabla f - \frac{4i}{v_F}\boldsymbol{h}f\tilde{f} \right] \tanh\frac{\beta\varepsilon}{2}, \qquad (4)$$

with $J_0 = N_0 eD$.

III. RESULTS AND DISCUSSION

We consider an in-plane exchange field and set $\boldsymbol{h} = h_x(y)\hat{x}$. The necessary (but not sufficient) requirement for inducing vortices is then that $\partial_y h_x \neq 0$. To be specific, we assume that the AP configuration of the ferromagnets induces an antisymmetric exchange field with a spatial variation given by $\boldsymbol{h} = h_0 \tanh(\alpha y/L)\hat{x}$, where α is a shape factor which determines the size of the transition region. We note that the size of the effective flux Φ_h, and thus the net number of vortices introduced, does not depend on the specific shape of the exchange field since, by the fundamental theorem of calculus, $\Phi_h = L[h(L/2) - h(-L/2)]$. To model the P configuration, a constant exchange field $\boldsymbol{h} = h_0\hat{x}$ is assumed.

The two configurations show markedly different behaviors, as is shown in Fig. 2 where we set $\alpha = 20$ (the results are qualitatively the same for all $\alpha \gg 1$, which corresponds to the magnetization saturating before it reaches the outer edges of the magnetic regions). The uniform exchange field in the P configuration introduces a phase shift between the superconductors, so that a net supercurrent flows between them. Otherwise, the system is unaffected. The pair correlation decays towards the center of the TI, but remains nonzero everywhere, as seen in Fig. 2(a). In the AP configuration, there is no net current due to the antisymmetry of the exchange field, which induces an antisymmetric current-density distribution. Furthermore, the exchange field produces a net effective flux $\Phi_h \simeq 2h_0 L$, which may cause vortex nucleation. This is shown in Fig. 2(b) for $h_0 = 2v_F/\xi$. In this case, two vortices appear along the x axis—the region of largest effective flux density. Figures 2(c) and 2(d) show the spatial distribution of the density of states at zero energy for the two configurations. In the P configuration, $N(\boldsymbol{r}, 0)$ is clearly uniformly
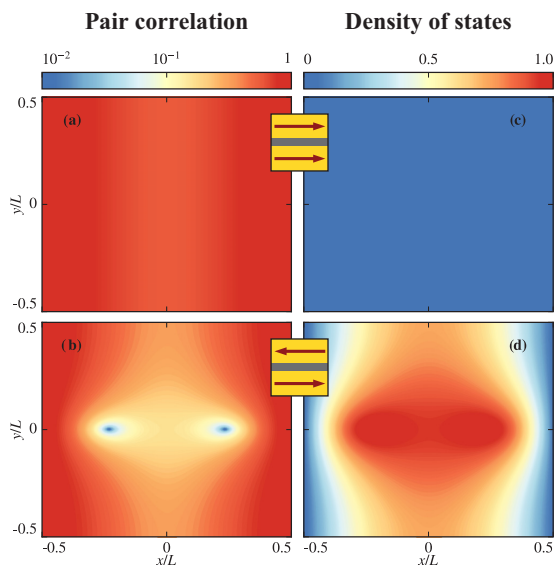
Pair correlation   **Density of states**

FIG. 2. A comparison of the results for the parallel (upper row) and antiparallel (lower row) configuration of the spin valve. (a) and (b) show the absolute value of the pair correlation for the two configurations, as given by Eq. (3). The localized zeros in the antiparallel case indicate vortices. (c) and (d) show the density of states N at zero energy, which is gapped in the parallel configuration and admits a normal state solution at the location of the vortices in the antiparallel configuration.

suppressed throughout the entire system, as is expected due to the presence of a proximity-induced energy gap. In the AP configuration, on the other hand, the presence of the vortices, which have normal cores, leads to a more complicated topography of the density of states, wherein a normal state value of $N = 1$ is found in localized regions surrounding the vortices. The topological nature of these vortices is illustrated by the phase of the pair correlation, which is shown in Fig. 3(a). It is seen that for any closed contour around a vortex, it is necessary to traverse two discontinuous jumps of value π, giving a total winding of 2π. This is the hallmark of a vortex. Another signature of vortices is circulating supercurrents, as is shown in Fig. 3(b), in which streamlines of the current density, as given by Eq. (4), are plotted. Since the eddies produce an out-of-plane magnetic field, which should be detectable using, for instance, a scanning nanoSQUID device [18], this provides means for experimentally verifying the presence of vortices. It is interesting to note that there are currents circulating around the origin of the system, as seen in Fig. 3(b). A conventional vortex has a phase gradient that goes like $\nabla\phi \sim \frac{2\pi n}{r}$, where n is the winding number of the vortex, and r is the radius from its center. This means that the phase gradient diverges at the vortex core, leading to a suppression of the pair correlation. The observed flow pattern in the present case is not accompanied by such a suppression, and is hence not a vortex in the topological sense. Rather, it is caused by an accidental cancellation of the phase gradient at the origin due to the applied exchange field. This can be seen from the current density
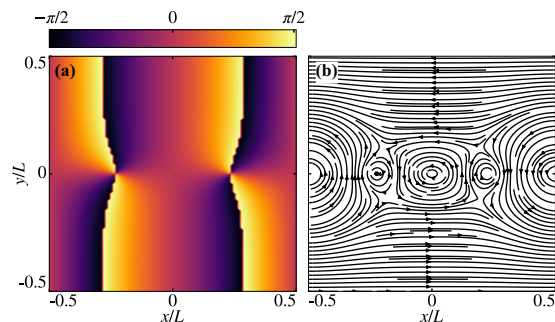

FIG. 3. Evidence of vortex nucleation. (a) The phase of the pair correlation, showing a winding of 2π around each of the vortices. (b) Streamlines of the current density, as given by Eq. (4), which gives its direction at every point, showing that supercurrents circulate around the vortices.

$\mathbf{J} \sim \nabla\phi$. The x component, J_x, is antisymmetric about the x axis due to the antisymmetric exchange field. It therefore vanishes along the x axis. The y component on the other hand, must change direction as one moves along the x axis from one vortex to the other. J_y is therefore zero in the origin as well. This means that the magnitude of the current is zero at this point, thereby producing the observed current pattern. We emphasize that this eddy is not topologically protected, and may be removed by minor perturbations of the exchange field.

The behavior of the vortices is greatly influenced by the symmetries of the system. The model considered herein is symmetric about the y axis, and either symmetric or antisymmetric about the x axis, depending on the applied exchange field. This means that a single vortex pair can only be located on symmetrically opposite sides of the origin, along either the x or the y axis without breaking the symmetries of the system. For an increasing exchange field amplitude, h_0, the AP configuration will lead to the appearance of an increasing number of vortices. The vortices enter the system from the vacuum edges, and must do so in pairs from opposite sides. Due to the low flux density near the vacuum edges, even the slightest additional increase in h_0 will cause the vortices to translate along the y axis, meet at the origin, and stabilize at a location along the x axis, as shown in Fig. 2. As h_0 is increased further, vortices accumulate along the x axis. This will, in turn, result in a complete suppression of the density of states in their vicinity, whereas superconductivity will still be present closer to the vacuum edges. We point out that while the present discussion relies on the symmetry, the symmetry is not crucial to observe the spin-valve effect. The only requirement is the ability to switch between a rotational and an irrotational exchange field. Another interesting feature of the inhomogeneous effective flux density is that it leads to significant vortex pinning. Indeed, if the superconducting leads are given a phase difference, for instance by applying a current bias, so that a net supercurrent flows between them, the vortex positions are only slightly perturbed. This is in contrast to the behavior of conventional SNS Josephson weak links with an applied magnetic flux, where a phase difference leads to a transversal shift of the vortex positions [6,7].
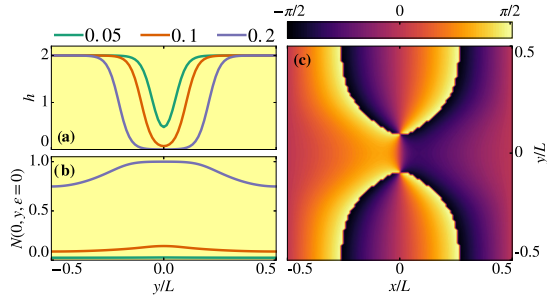
FIG. 4. An analysis of the effect of the spacer layer. (a) The transversal distribution of the exchange field $\boldsymbol{h}$ for increasing size δ of the central region of suppressed magnetization. (b) The zero-energy density of states along the y axis for the exchange fields in (a). (c) The phase of the pair correlation for the case where $\delta = 0.2$, showing the appearance of a vortex–antivortex pair.

The exchange field induced on the topological insulator is assumed generated by two separate ferromagnets with an intermediate spacer layer. In the P configuration, this will likely create a suppression of the induced exchange field beneath the spacer. The resulting $\partial_y h_x \neq 0$ could in itself induce vortices in the system, in addition to the switching-effect we have described above. To investigate this, we consider a P exchange field $\boldsymbol{h}(y) = h_0\{1 + 0.5(\tanh[\alpha(y/L - \delta)] - \tanh[\alpha(y/L + \delta)])\}\hat{x}$, where δ is another shape factor indicating the width of the central dip in $\boldsymbol{h}(y)$. The exchange field is plotted along the transversal direction y for increasing δ in Fig. 4(a). Since the exchange field is symmetric, the effective flux $\Phi_h = 0$. Nonetheless, topological excitations in the form of vortex–antivortex pairs may be induced. It is clear that this can happen if an effective flux greater than Φ_0 passes through any subdomain of the system within which vortex nucleation is allowed by symmetry. The central dip in the exchange field will cause vortices to nucleate where $\nabla \times \boldsymbol{h}$ is largest and positive, at $y = \delta L$, whereas antivortices will nucleate at $y = -\delta L$, where the largest negative effective flux

density is found. To conserve the symmetry of the system, a single vortex–antivortex pair must appear along the y axis. The first appearance of such a pair may therefore be gauged from the zero-energy density of states along this line, as is shown in Fig. 4(b). It is seen that N remains gapped for a sufficiently small dip, as exemplified by $\delta = 0.05$ and $\delta = 0.1$. This shows that the vortex spin-valve effect is robust against small deviations from a constant exchange field due to the presence of the spacer layer. For $\delta = 0.2$, however, a vortex–antivortex pair appears, and the gap in the density of states closes. This is verified from the phase of the pair correlation, shown in Fig. 4(c), where the two vortices along the y axis are seen to have opposite windings.

IV. CONCLUSION

We have considered a Josephson weak link made on the surface of a topological insulator, onto which is proximity coupled two ferromagnets separated by a spacer. By using microscopic calculations, we have shown that it is possible to switch vortices on and off in this system solely by toggling between an AP and P configuration of the ferromagnets, respectively. We further show that this vortex spin-valve effect is robust against small deviations in the induced exchange field caused by the spacer layer.

An interesting direction for future work would be to study the effect of an electrically induced phase gradient in the superconducting leads, which has recently been shown to generate vortices in proximitized normal metals [9].

ACKNOWLEDGMENTS

[1] M. Z. Hasan and C. L. Kane, Rev. Mod. Phys. **82**, 3045 (2010).

[2] X.-L. Qi and S.-C. Zhang, Rev. Mod. Phys. **83**, 1057 (2011).

[3] L. Fu and C. L. Kane, Phys. Rev. Lett. **100**, 096407 (2008).

[4] C. Nayak, S. H. Simon, A. Stern, M. Freedman, and S. Das Sarma, Rev. Mod. Phys. **80**, 1083 (2008).

[5] A. Zyuzin, M. Alidoust, and D. Loss, Phys. Rev. B **93**, 214502 (2016).

[6] J. C. Cuevas and F. S. Bergeret, Phys. Rev. Lett. **99**, 217002 (2007).

[7] F. S. Bergeret and J. C. Cuevas, J. Low Temp. Phys. **153**, 304 (2008).

[8] V. P. Ostroukh, B. Baxevanis, A. R. Akhmerov, and C. W. J. Beenakker, Phys. Rev. B **94**, 094514 (2016)

[9] M. Amundsen, J. A. Ouassou, and J. Linder, Phys. Rev. Lett. **120**, 207001 (2018)

[10] D. Roditchev, C. Brun, L. Serrier-Garcia, J. C. Cuevas, V. H. L. Bessa, M. V. Milošević, F. Debontridder, V. Stolyarov, and T. Cren, Nat. Phys. **11**, 332 (2015).

[11] M. Veldhorst, M. Snelder, M. Hoek, T. Gang, V. K. Guduru, X. L. Wang, U. Zeitler, W. G. van der Wiel, A. A. Golubov, H. Hilgenkamp, and A. Brinkman, Nat. Mater. **11**, 417 (2012).

[12] J. Rammer and H. Smith, Rev. Mod. Phys. **58**, 323 (1986).

[13] W. Belzig, F. K. Wilhelm, C. Bruder, G. Schön, and A. D. Zaikin, Superlattices Microst. **25**, 1251 (1999).

[14] H. G. Hugdal, J. Linder, and S. H. Jacobsen, Phys. Rev. B **95**, 235403 (2017).

[15] K. D. Usadel, Phys. Rev. Lett. **25**, 507 (1970).

[16] M. Amundsen and J. Linder, Sci. Rep. **6**, 22765 (2016).

[17] H. G. Hugdal, M. Amundsen, J. Linder, and A. Sudbø, arXiv:1808.03650.

[18] D. Vasyukov, Y. Anahory, L. Embon, D. Halbertal, J. Cuppens, L. Neeman, A. Finkler, Y. Segev, Y. Myasoedov, M. L. Rappaport, M. E. Huber, and E. Zeldov, Nat. Nanotechn. **8**, 639 (2013).

Paper IX

Reference

Contributions

HGH performed the analytical calculations with support from MA, AS and JL. HGH drafted the manuscript. All authors contributed to the discussions of the physics and the revision of the final manuscript. More specifically, MA had a minor supporting role in this collaboration, assisting with the analytical calculations, joining the discussions of the results, and contributing to the writing of the final manuscript.

Inverse proximity effect in *s*-wave and *d*-wave superconductors coupled to topological insulators

Henning G. Hugdal, Morten Amundsen, Jacob Linder, and Asle Sudbø[*]
Center for Quantum Spintronics, Department of Physics, NTNU,
Norwegian University of Science and Technology, NO-7491 Trondheim, Norway

We study the inverse proximity effect in a bilayer consisting of a thin *s*- or *d*-wave superconductor (S) and a topological insulator (TI). Integrating out the topological fermions of the TI, we find that spin-orbit coupling is induced in the S, which leads to spin-triplet *p*-wave (*f*-wave) correlations in the anomalous Green's function for an *s*-wave (*d*-wave) superconductor. Solving the self-consistency equation for the superconducting order parameter, we find that the inverse proximity effect can be strong for parameters for which the Fermi momenta of the S and TI coincide. The suppression of the gap is approximately proportional to $e^{-1/\lambda}$, where λ is the dimensionless superconducting coupling constant. This is consistent with the fact that a higher λ gives a more robust superconducting state. For an *s*-wave S, the interval of TI chemical potentials for which the suppression of the gap is strong is centered at $\mu_{TI} = \pm\sqrt{2m v_F^2 \mu}$, and increases quadratically with the hopping parameter t. Since the S chemical potential μ typically is high for conventional superconductors, the inverse proximity effect is negligible except for t above a critical value. For sufficiently low t, however, the inverse proximity effect is negligible, in agreement with what has thus far been assumed in most works studying the proximity effect in S-TI structures. In superconductors with low Fermi energies, such as high-T_c cuprates with *d*-wave symmetry, we again find a suppression of the order parameter. However, since μ is much smaller in this case, a strong inverse proximity effect can occur at $\mu_{TI} = 0$ for much lower values of t. Moreover, the onset of a strong inverse proximity effect is preceded by an increase in the order parameter, allowing the gap to be tuned by several orders of magnitude by small variations in μ_{TI}.

I. INTRODUCTION

Topological insulators (TIs) are insulating in the bulk, but host metallic surface states protected by the topology of the material [1–3]. For three-dimensional topological insulators, the two-dimensional (2D) surface states can be described by a massless analog of the relativistic Dirac equation, having linear dispersions and spin-momentum locking. Many interesting phenomena are predicted to occur by coupling the TI to a superconductor, thus inducing a superconducting gap in the TI [4]. For instance, such systems have been predicted to host Majorana bound states [5], which could be used for topological quantum computing. Moreover, the Dirac-like Hamiltonian $\boldsymbol{\sigma} \cdot \mathbf{k}$ has consequences for the response to exchange fields, allowing the phase difference in a Josephson junction to be tuned by an in-plane magnetization to values other than 0 and π [6], and inducing vortices by an in-plane magnetic field [7,8].

Numerous papers have studied the interesting phenomena that have been discovered in topological insulators with proximity-induced superconductivity [9–22]. To our knowledge, however, much less attention has been paid to the inverse superconducting, or topological [23], proximity effect, i.e., the effect that the topological insulator has on the superconductor order parameter. There have been indications that superconductivity might be suppressed [17], while other

studies have found no suppression [20], One recent study demonstrated that the proximity to the TI induces spin-orbit coupling in the superconductor (S), possibly making a Fulde-Ferrel [24] superconducting state energetically more favorable near the interface of a magnetically doped TI [25]. Another study showed that the TI surface states can leak into the superconductor, resulting in a Dirac cone in the density of states [26]. In this paper, we focus on the superconducting gap itself and study under what circumstances the inverse proximity effect is negligible, as is often assumed in theoretical works.

Using a field-theoretical approach, we study an atomically thin Bardeen-Cooper-Schrieffer (BCS) *s*-wave superconductor and *d*-wave superconductor coupled to a TI. While this is an approximation for most conventional and high-T_c superconductors such as, e.g., Nb, Al, and YBa$_2$Cu$_3$O$_7$, superconductivity has been observed in, e.g., single-layer NbSe$_2$ [27] and FeSe [28–30]. Integrating out the TI fermions, we obtain an effective action for the S electrons. Due to the induced spin-orbit coupling, spin-triplet *p*-wave (*f*-wave) correlations are induced in the *s*-wave (*d*-wave) superconductor.

Solving the mean-field equations, using parameters valid for both conventional *s*-wave superconductors and high-T_c *d*-wave superconductors, we find that in both cases a strong suppression of the superconducting gap is possible. For conventional superconductors, where the Fermi energy μ is high compared to the cut-off frequency, the coupling between the S and the TI has to be quite large in order for the inverse proximity effect to be strong for relevant TI chemical potentials μ_{TI}. This can explain the lack of any inverse proximity effect in

----
[*]Corresponding author: asle.sudbo@ntnu.no

experiments [20]. In high-T_c d-wave superconductors, on the other hand, where the Fermi energy is much smaller, we find a strong gap suppression at much lower coupling strengths, which might therefore be experimentally observable. For these systems, we also find an increase in the gap for μ_{TI} just outside the region of strong inverse proximity effect.

The remainder of the paper is organized as follows: The model system is presented in Sec. II, and the effective action for the S fermions and order parameter is derived in Sec. III. In Sec. IV we derive the mean-field gap equations for the order parameter. Numerical results for the superconducting gap are presented and discussed in Sec. V, and summarized in Sec. VI. Further details on the calculation of the criteria for strong proximity effect, the Nambu space field integral, the zero-temperature, noninteracting gap solutions, and the numerical methods used, are presented in the Appendices.

II. MODEL

We model the bilayer consisting of a thin superconductor (S) coupled to a TI by the action

$$S = S_{\mathrm{S}} + S_{\mathrm{TI}} + S_t. \tag{1}$$

In Matsubara and reciprocal space, the superconductor is described by

$$S_{\mathrm{S}} = \frac{1}{\beta V} \sum_k c^\dagger(k) \left(-i\omega_n + \frac{\mathbf{k}^2}{2m} - \mu \right) c(k)$$
$$- \sum_{k,k',q} \frac{V_{\mathbf{k}',\mathbf{k}}}{(\beta V)^3} c^\dagger_\uparrow(k') c^\dagger_\downarrow(-k'+q) c_\downarrow(-k+q) c_\uparrow(k), \tag{2}$$

where $c(k) = [c_\uparrow(k)\, c_\downarrow(k)]^T$ with $c_{\uparrow(\downarrow)}(k)$ denoting the annihilation operator for spin-up (spin-down) electrons, m is the electron mass, and μ is the chemical potential in the S. $\beta = 1/k_B T$ and $V = L_x L_y$ are the inverse temperature and system area, respectively. We have used the notation $k = (\omega_n, \mathbf{k})$ [$q = (\Omega_n, \mathbf{q})$], where ω_n (Ω_n) is a fermionic (bosonic) Matsubara frequency, and $\mathbf{k}$ ($\mathbf{q}$) the fermionic (bosonic) in-plane wave vector. $V_{\mathbf{k},\mathbf{k}'}$ is the pairing potential, which can be written [31]

$$V_{\mathbf{k},\mathbf{k}'} = g v(\mathbf{k}) v(\mathbf{k}'), \tag{3}$$

where $v(\mathbf{k}) = 1$ for s-wave pairing, and $v(\mathbf{k}) = \sqrt{2}\cos(2\phi_{\mathbf{k}})$ for $d_{x^2-y^2}$-wave pairing, where $\phi_{\mathbf{k}}$ is the angle of $\mathbf{k}$ relative to the k_x axis. The coupling constant g is assumed to be nonzero only when $-\omega_- < \mathbf{k}^2/2m - \mu < \omega_+$, where $\pm\omega_\pm$ is the upper (lower) cut-off frequency. For conventional s-wave superconductors this is typically taken to be the characteristic frequency ω_D of the phonons, while the cut-off frequencies in high-T_c superconductors are of the order of the characteristic energy of the antiferromagnetic fluctuations present in these materials [32–35]. We will set $\hbar = 1$ throughout the paper. For the TI we use the Dirac action

$$S_{\mathrm{TI}} = \frac{1}{\beta V} \sum_k \Psi^\dagger(k)(-i\omega_n + v_{\mathrm{F}} \mathbf{k} \cdot \boldsymbol{\sigma} - \mu_{\mathrm{TI}}) \Psi(k), \tag{4}$$

where $\Psi(\mathbf{r}) = [\psi_\uparrow(\mathbf{r})\, \psi_\downarrow(\mathbf{r})]^T$ describes the TI fermions, v_{F} is the Fermi velocity, and μ_{TI} is the TI chemical potential. The

S and TI layers are coupled by a hopping term [25,26,36,37]

$$S_t = -\frac{1}{\beta V} \sum_k t[c^\dagger(k)\Psi(k) + \Psi^\dagger(k)c(k)]. \tag{5}$$

Similar models were recently used in Refs. [25,26] when studying similar systems with an s-wave S. The full partition function of the system is therefore

$$Z = \int \mathcal{D}[c^\dagger, c] e^{-S_{\mathrm{S}}} \left(\int \mathcal{D}[\Psi^\dagger, \Psi] e^{-S_{\mathrm{TI}} - S_t} \right). \tag{6}$$

III. EFFECTIVE ACTION

As we are interested in the inverse proximity effect in the S and its consequences for the superconducting gap, we integrate out the TI fermions by performing the functional integral $Z_{\mathrm{TI},t} = \int \mathcal{D}[\Psi^\dagger, \Psi] e^{-S_{\mathrm{TI},t}}$, where

$$S_{\mathrm{TI},t} = \frac{1}{\beta V} \sum_k \left\{ \Psi^\dagger(k)\big(-G_{\mathrm{TI}}^{-1} \big)\Psi(k) - t[c^\dagger(k)\Psi(k)\right.$$
$$\left. + \Psi^\dagger(k)c(k)] \right\}. \tag{7}$$

Here, we have defined the matrix $G_{\mathrm{TI}}^{-1} = i\omega_n - v_{\mathrm{F}} \mathbf{k} \cdot \boldsymbol{\sigma} + \mu_{\mathrm{TI}}$. Performing the functional integration leads to an additional term in the S action,

$$\delta S_{\mathrm{S}} = \frac{t^2}{\beta V} \sum_k c^\dagger(k) G_{\mathrm{TI}} c(k), \tag{8}$$

with the TI Green's function

$$G_{\mathrm{TI}} = \frac{i\omega_n + \mu_{\mathrm{TI}} + v_{\mathrm{F}} \mathbf{k} \cdot \boldsymbol{\sigma}}{(i\omega_n + \mu_{\mathrm{TI}})^2 - v_{\mathrm{F}}^2 \mathbf{k}^2}. \tag{9}$$

The effective S action thus reads

$$S_{\mathrm{S}}^{\mathrm{eff}} = -\frac{1}{\beta V} \sum_k c^\dagger(k) G_0^{-1} c(k) - \sum_{k,k',q} \frac{V_{\mathbf{k}',\mathbf{k}}}{(\beta V)^3} c^\dagger_\uparrow(k')$$
$$\times c^\dagger_\downarrow(-k'+q) c_\downarrow(-k+q) c_\uparrow(k), \tag{10}$$

where we have defined the inverse noninteracting Green's function

$$G_0^{-1} = i\omega_n - \frac{\mathbf{k}^2}{2m} + \mu - t^2 G_{\mathrm{TI}}. \tag{11}$$

From this we see that the coupling to G_{TI} in Eq. (9) leads to an induced spin-orbit coupling $\sim \mathbf{k} \cdot \boldsymbol{\sigma}$ in the S, in agreement with Ref. [25].

Performing a Hubbard-Stratonovich decoupling [38], the four-fermion term in the S action can be rewritten in terms of bosonic fields $\varphi(q)$ and $\varphi^\dagger(q)$,

$$-\sum_{k,k',q} \frac{V_{\mathbf{k}',\mathbf{k}}}{(\beta V)^3} c^\dagger_\uparrow(k') c^\dagger_\downarrow(-k'+q) c_\downarrow(-k+q) c_\uparrow(k) \to -\frac{1}{\beta V}$$
$$\times \sum_{k,q} [\varphi(q) v(\mathbf{k}) c^\dagger_\uparrow(k) c^\dagger_\downarrow(-k+q) + \mathrm{H.c.}]. \tag{12}$$

This also leads to an additional term in the total system action

$$S_\varphi^0 = \frac{\beta V}{g} \sum_q \varphi^\dagger(q) \varphi(q), \tag{13}$$

and a functional integration of the bosonic fields in the partition function. Note that the decoupling is performed such that the bosonic fields have units of energy.

By defining the Nambu spinor

$$\mathcal{C}(k) = [c_\uparrow(k)\, c_\downarrow(k)\, c_\uparrow^\dagger(-k)\, c_\downarrow^\dagger(-k)]^T, \tag{14}$$

the effective S action can be written

$$S_S^{\text{eff}} = -\frac{1}{2\beta V}\sum_{k,k'}\mathcal{C}^\dagger(k)\mathcal{G}^{-1}(k,k')\mathcal{C}(k'), \tag{15}$$

where

$$\mathcal{G}^{-1}(k,k') = \begin{pmatrix} G_0^{-1}(k)\delta_{k,k'} & \varphi(k-k')v(\mathbf{k})i\sigma_y \\ -\varphi^\dagger(-k+k')v(\mathbf{k})i\sigma_y & -\left[G_0^{-1}(-k)\right]^T\delta_{k,k'} \end{pmatrix}. \tag{16}$$

Performing the functional integration over the fermionic fields, we arrive at the effective action for the bosonic fields

$$S_\varphi = \frac{\beta V}{g}\sum_q \varphi^\dagger(q)\varphi(q) - \frac{1}{2}\,\text{Tr}\ln(-\mathcal{G}^{-1}). \tag{17}$$

The additional factor $1/2$ in front of the trace is due to the change in integration measure when changing to the Nambu

spinor notation (see Appendix B and, e.g., Ref. [39] for details).

IV. MEAN-FIELD THEORY

Since $G_0^{-1}(i\omega_n, \mathbf{k})$ is still inversion symmetric in the diagonal basis (see below), we assume that the bosonic field $\varphi(q)$ is temporally and spatially homogeneous as in the regular BCS case. However, a recent study has shown that introducing in-plane magnetic fields in the TI breaks this symmetry and can make a Fulde-Ferrel [24] order parameter energetically more favorable in an s-wave S [25]. Calculating the matrix $\mathcal{G}(k)$ assuming a spatially homogeneous bosonic field $\phi(q) = \delta_{q,0}\Delta$, and defining the superconducting order parameter $\Delta(\mathbf{k}) = \Delta \cdot v(\mathbf{k})$, we get

$$\mathcal{G}(k) = \begin{pmatrix} G(k) & F(k) \\ F^\dagger(k) & -G^T(-k) \end{pmatrix}, \tag{18}$$

where to leading order in t

$$G(k) = -\frac{\epsilon_\mathbf{k}+i\omega_n}{\xi_\mathbf{k}^2+\omega_n^2} - t^2\frac{(\epsilon_\mathbf{k}+i\omega_n)^2[(i\omega_n+\mu_{\text{TI}})+v_\text{F}\mathbf{k}\cdot\boldsymbol{\sigma}]}{\left(\xi_\mathbf{k}^2+\omega_n^2\right)^2\left[v_\text{F}^2\mathbf{k}^2-(i\omega_n+\mu_{\text{TI}})^2\right]} - t^2\frac{|\Delta(\mathbf{k})|^2[(i\omega_n-\mu_{\text{TI}})-v_\text{F}\mathbf{k}\cdot\boldsymbol{\sigma}]}{\left(\xi_\mathbf{k}^2+\omega_n^2\right)^2\left[v_\text{F}^2\mathbf{k}^2-(i\omega_n-\mu_{\text{TI}})^2\right]}, \tag{19}$$

$$F(k) = \frac{\Delta(\mathbf{k})}{\xi_\mathbf{k}^2+\omega_n^2}\left\{1 + 2t^2\frac{\left(v_\text{F}^2\mathbf{k}^2-\mu_{\text{TI}}^2-\omega_n^2\right)\epsilon_\mathbf{k}\mu_{\text{TI}}-\omega_n^2\left(v_\text{F}^2\mathbf{k}^2+\mu_{\text{TI}}^2+\omega_n^2\right)}{\left(\xi_\mathbf{k}^2+\omega_n^2\right)\left[(v_\text{F}|\mathbf{k}|-\mu_{\text{TI}})^2+\omega_n^2\right]\left[(v_\text{F}|\mathbf{k}|+\mu_{\text{TI}})^2+\omega_n^2\right]}\right.$$

$$\left. + 2t^2\frac{\left(v_\text{F}^2\mathbf{k}^2-\mu_{\text{TI}}^2+\omega_n^2\right)\epsilon_\mathbf{k}-2\omega_n^2\mu_{\text{TI}}}{\left(\xi_\mathbf{k}^2+\omega_n^2\right)\left[(v_\text{F}|\mathbf{k}|-\mu_{\text{TI}})^2+\omega_n^2\right]\left[(v_\text{F}|\mathbf{k}|+\mu_{\text{TI}})^2+\omega_n^2\right]}v_\text{F}\mathbf{k}\cdot\boldsymbol{\sigma}\right\}i\sigma_y, \tag{20}$$

with $\epsilon_\mathbf{k} = \mathbf{k}^2/2m - \mu$ and $\xi_\mathbf{k} = \sqrt{\epsilon_\mathbf{k}^2+|\Delta(\mathbf{k})|^2}$. As mentioned above, the proximity-induced spin-orbit coupling leads to nondiagonal terms in $G(k)$. Moreover, $F(k)$ now has diagonal terms $\propto \mathbf{k}\cdot\boldsymbol{\sigma}i\sigma_y$, signaling that p-wave (f-wave) triplet superconducting correlations are induced in the s-wave (d-wave) superconductor. This has been shown to be the case in s-wave superconductors when the spin degeneracy is lifted by spin-orbit coupling [40]. A similar expression was found for the anomalous Green's function on the TI side of an S-TI bilayer in Ref. [41]. The results in Ref. [41] also suggest that odd-frequency triplet pairing could be induced in the S by including a magnetic exchange term $\mathbf{m}\cdot\boldsymbol{\sigma}$ in the TI Lagrangian.

Gap equation

While the above Green's functions contain information about the correlations in the superconductor, the superconducting gap must be determined self-consistently. We first change to the basis which diagonalizes the nonsuperconducting normal inverse Green's function G_0^{-1}. We find $G_{d,0}^{-1}(k) = P(k)G_0^{-1}(k)P^\dagger(k)$, where $G_{d,0}^{-1}(k) = \text{diag}[G_{+,0}^{-1}(k), G_{-,0}^{-1}(k)]$,

with

$$G_{\pm,0}^{-1}(k) = i\omega_n - \epsilon_\mathbf{k} - \frac{t^2}{i\omega_n+\mu_{\text{TI}}\mp v_\text{F}|\mathbf{k}|} \tag{21}$$

and

$$P(k) = \frac{1}{\sqrt{2}}\begin{pmatrix} 1 & e^{-i\phi_\mathbf{k}} \\ 1 & -e^{-i\phi_\mathbf{k}} \end{pmatrix}t. \tag{22}$$

Here $\phi_\mathbf{k}$ is the angle of $\mathbf{k}$ relative to the k_x axis. $+$ $(-)$ here denotes the Green's function for positive (negative) chirality states. Inverting $G_{d,0}^{-1}$ we find the Green's functions

$$G_{\pm,0}(k) = \frac{i\omega_n \mp v_\text{F}|\mathbf{k}| + \mu_{\text{TI}}}{[i\omega_n - \epsilon_\pm^+(\mathbf{k})][i\omega_n - \epsilon_\pm^-(\mathbf{k})]}, \tag{23}$$

where

$$\epsilon_\alpha^\gamma(\mathbf{k}) = \frac{1}{2}[\epsilon_\mathbf{k} + \alpha v_\text{F}|\mathbf{k}| - \mu_{\text{TI}}$$
$$+ \gamma\sqrt{(\epsilon_\mathbf{k} - \alpha v_\text{F}|\mathbf{k}| + \mu_{\text{TI}})^2 + 4t^2}], \tag{24}$$

with $\alpha, \gamma = \pm 1$. The Green's function has residues

$$w_\alpha^\gamma(\mathbf{k}) = \frac{1}{2} + \frac{\epsilon_\mathbf{k} - \alpha v_\mathrm{F}|\mathbf{k}| + \mu_\mathrm{TI}}{2\gamma\sqrt{(\epsilon_\mathbf{k} - \alpha v_\mathrm{F}|\mathbf{k}| + \mu_\mathrm{TI})^2 + 4t^2}}. \quad (25)$$

We next transform the entire inverse Green's function $\mathcal{G}$ using $\mathcal{G}_d^{-1}(k) = \mathcal{P}(k)\mathcal{G}^{-1}(k)\mathcal{P}^\dagger(k)$, where

$$\mathcal{P}(k) = \begin{pmatrix} P(k) & 0 \\ 0 & P^*(-k) \end{pmatrix}, \quad (26)$$

which yields

$$\mathcal{G}_d^{-1}(k) = \begin{pmatrix} G_{d,0}^{-1}(k) & -\Delta(\mathbf{k})e^{-i\phi_\mathbf{k}}\sigma_z \\ -\Delta^\dagger(\mathbf{k})e^{i\phi_\mathbf{k}}\sigma_z & -G_{d,0}^{-1}(-k) \end{pmatrix}. \quad (27)$$

Hence the full Green's function matrix for the superconductor is

$$\mathcal{G}_d(k) = \begin{pmatrix} G_d(k) & F_d(k) \\ F_d^\dagger(k) & -G_d(-k) \end{pmatrix}, \quad (28)$$

where we have defined the 2×2 matrices $G_d(k) = \mathrm{diag}[G_+(k), G_-(k)]$ and $F_d(k) = \mathrm{diag}[F_+(k), F_-(k)]$, and Green's functions

$$G_\pm(k) = \frac{[i\omega_n + \epsilon_\pm^+(\mathbf{k})][i\omega_n + \epsilon_\pm^-(\mathbf{k})][i\omega_n \mp v_\mathrm{F}|\mathbf{k}| + \mu_\mathrm{TI}]}{[i\omega_n - \xi_\pm^+(\mathbf{k})][i\omega_n + \xi_\pm^+(\mathbf{k})][i\omega_n - \xi_\pm^-(\mathbf{k})][i\omega_n + \xi_\pm^-(\mathbf{k})]}, \quad (29a)$$

$$F_\pm(k) = \pm\frac{\Delta(\mathbf{k})e^{-i\phi_\mathbf{k}}[(i\omega_n)^2 - (\pm v_\mathrm{F}|\mathbf{k}| - \mu_\mathrm{TI})^2]}{[i\omega_n - \xi_\pm^+(\mathbf{k})][i\omega_n + \xi_\pm^+(\mathbf{k})][i\omega_n - \xi_\pm^-(\mathbf{k})][i\omega_n + \xi_\pm^-(\mathbf{k})]}. \quad (29b)$$

The eigenenergies of the system are now given by the poles in the above equation, where

$$\xi_\alpha^\gamma(\mathbf{k}) = \frac{1}{\sqrt{2}}\left\{\xi_\mathbf{k}^2 + (\alpha v_\mathrm{F}|\mathbf{k}| - \mu_\mathrm{TI})^2 + 2t^2 + \gamma\sqrt{\left[\xi_\mathbf{k}^2 - (\alpha v_\mathrm{F}|\mathbf{k}| - \mu_\mathrm{TI})^2\right]^2 + 4t^2[(\epsilon_\mathbf{k} + \alpha v_\mathrm{F}|\mathbf{k}| - \mu_\mathrm{TI})^2 + |\Delta(\mathbf{k})|^2]}\right\}^{1/2}. \quad (30)$$

The gap equation for the amplitude Δ is found by requiring $\frac{\delta S_\varphi}{\delta\Delta} = 0$ [38], which yields

$$\Delta^\dagger = -\frac{g}{2\beta V}\sum_k \mathrm{tr}\, F_d^\dagger(k)v(\mathbf{k})\sigma_z e^{-i\phi_\mathbf{k}}. \quad (31)$$

Inserting the Hermitian conjugate of Eq. (29b) and performing the sum over Matsubara frequencies, we get the gap equation,

$$1 = \frac{g}{4V}\sum_\mathbf{k} v(\mathbf{k})^2 \left\{ \frac{\xi_+^+(\mathbf{k})^2 - (v_\mathrm{F}|\mathbf{k}| - \mu_\mathrm{TI})^2}{\xi_+^+(\mathbf{k})[\xi_+^+(\mathbf{k})^2 - \xi_+^-(\mathbf{k})^2]}\tanh\frac{\beta\xi_+^+(\mathbf{k})}{2} \right.$$
$$- \frac{\xi_+^-(\mathbf{k})^2 - (v_\mathrm{F}|\mathbf{k}| - \mu_\mathrm{TI})^2}{\xi_+^-(\mathbf{k})[\xi_+^+(\mathbf{k})^2 - \xi_+^-(\mathbf{k})^2]}\tanh\frac{\beta\xi_+^-(\mathbf{k})}{2}$$
$$+ \frac{\xi_-^+(\mathbf{k})^2 - (v_\mathrm{F}|\mathbf{k}| + \mu_\mathrm{TI})^2}{\xi_-^+(\mathbf{k})[\xi_-^+(\mathbf{k})^2 - \xi_-^-(\mathbf{k})^2]}\tanh\frac{\beta\xi_-^+(\mathbf{k})}{2}$$
$$\left. - \frac{\xi_-^-(\mathbf{k})^2 - (v_\mathrm{F}|\mathbf{k}| + \mu_\mathrm{TI})^2}{\xi_-^-(\mathbf{k})[\xi_-^+(\mathbf{k})^2 - \xi_-^-(\mathbf{k})^2]}\tanh\frac{\beta\xi_-^-(\mathbf{k})}{2} \right\}. \quad (32)$$

Setting $t = 0$ simply yields the regular BCS gap equation, which results in a gap $\Delta_0 = 2\omega_D e^{-1/\lambda}$ in the s-wave case [42], where $\lambda = gD_0/V$ is a dimensionless coupling constant, and D_0 is the density of states at the Fermi level. d-wave pairing results in a slightly smaller gap for the same values for λ and the cut-off frequencies (see Appendix C for details). For $t \neq 0$, the above equation can be expressed in terms of an energy integral over $\epsilon_\mathbf{k}$ using $v_\mathrm{F}|\mathbf{k}| = v_\mathrm{F}\sqrt{2m(\epsilon_\mathbf{k} + \mu)}$.

V. RESULTS AND DISCUSSION

From the expressions for the system eigenenergies in the nonsuperconducting case, Eq. (24), we see that the S and TI bands have hybridized, leading to avoided crossings. The effect of this hybridization is largest when the chemical potential of both the S and TI is tuned such that the Fermi momenta coincide, i.e., for $\mu_\mathrm{TI} = \pm\sqrt{2mv_\mathrm{F}^2\mu}$. A possibly strong proximity effect should therefore be expected to occur in a region close to these values of μ_TI, the size of which increases with increased hopping t. In the following we numerically solve the gap equations for both s- and d-wave superconductors for relevant parameter values.

A. s-wave pairing

Using numerical values $\mu \sim 5$ eV, a cutoff corresponding to the Debye frequency, $\hbar\omega_\pm = \hbar\omega_D \sim 25$ meV [43], $\hbar^2/2m \sim 40$ meV nm^2, $\hbar v_\mathrm{F} \sim 300$ meV nm [20,44], and $\lambda = 0.2$, we solve the gap equation in Eq. (32) for different values of t and μ_TI at $T = 0$ for an s-wave superconductor. The results in Fig. 1(a) show that the absolute value of the gap is not changed significantly due to the inverse proximity effect for small t, except for μ_TI close to $\sqrt{2mv_\mathrm{F}^2\mu}$. Both for μ_TI above and below this region, the inverse proximity effect is small, signifying that the disappearing gap in the region where the inverse proximity effect is strong cannot be simply related to the increasing density of states in the TI. For increasing t, the region where superconductivity is suppressed increases quadratically with t, eventually leading to suppressed superconductivity also at $\mu_\mathrm{TI} = 0$.

The strong suppression of the order parameter can be understood from the fact that the pairing potential is attractive only when $|\mathbf{k}^2/2m - \mu| \lesssim \omega_D$, corresponding to wave vectors between $k_\pm \equiv \sqrt{2m(\mu \pm \omega_\pm)}$. This means that the Fermi wave vectors k_F of the bands in Eq. (24), the value of $|\mathbf{k}|$ for which $\epsilon_\alpha^\gamma(\mathbf{k}) = 0$, have to satisfy $k_- < k_\mathrm{F} < k_+$ in order to contribute significantly to the integral in the gap equations and thus give a finite gap. This can be seen by comparing the left panels in Fig. 1(b), where the upper left panel shows
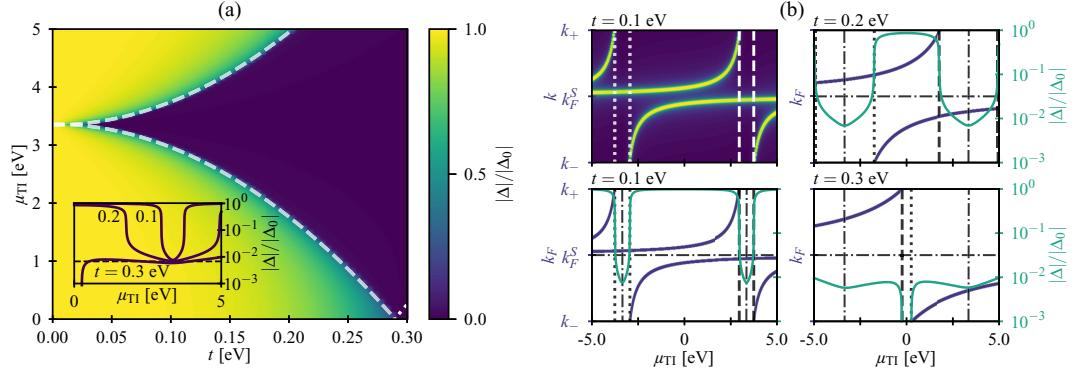
FIG. 1. (a) Plot of the superconducting gap at $T = 0$ for an s-wave superconductor as a function of μ_{TI} and t and with an upper cutoff $\omega_+ = 0.0025$ eV, normalized to the bulk value $|\Delta_0|$ for parameter values relevant for Nb-HgTe bilayers. The k_{F} values for the TI appear vertical on this plot as a function of μ_{TI} due to the small value of the cutoff ω_+. The numerical results show that the zero-temperature gap essentially is unaffected by the proximity to the TI for small values of t, where the suppression is severe only for values of μ_{TI} close to $\sqrt{2mv_{\mathrm{F}}^2\mu}$, a value far too large to be experimentally achievable. However, for increasing t, the region where superconductivity is suppressed increases quadratically with t, eventually leading to a suppression also for $\mu_{\mathrm{TI}} = 0$. The inset shows the normalized gap at $t = 0.1, 0.2$, and 0.3 eV, indicating that the gap is not suppressed entirely in most cases, but rather to a reduced value of $\Delta_0 e^{-1/\lambda}$ (dashed line), consistent with there being only one band contributing to superconductivity in this region. The exception is close to $\mu_{\mathrm{TI}} = 0$ for $t = 0.3$ eV, where there are no bands with Fermi wave vector between k_- and k_+, resulting in $\Delta = 0$. This is the case in the area restricted by the dotted line in the main figure. (b) The upper left panel is a plot of the integrand in the gap equation, Eq. (32), evaluated at Δ_0 for wave vectors $k_- < |\mathbf{k}| < k_+$ and $t = 0.1$ eV, where light colors correspond to high values of the integrand. The three remaining panels show the magnitude of the Fermi wave vectors k_{F} of the bands defined in Eq. (24) (left axis) in the same interval at $t = 0.1, 0.2$ and 0.3 eV, and the normalized gap (right axis). Notice that the plots are close to symmetric around $\mu_{\mathrm{TI}} = 0$ since $\omega_D \ll \mu$. The dash-dotted lines are $k_{\mathrm{F}}^{\mathrm{S}}$ and $k_{\mathrm{F}}^{\mathrm{TI}}(\mu_{\mathrm{TI}})$, the Fermi wave vectors of the S and TI for $t = 0$, respectively. Comparing the two left panels it is clear that the main contribution to the integral in the gap equation comes from wave vectors close to the Fermi wave vectors of the bands in the relevant $|\mathbf{k}|$ interval. $\mu_{\mathrm{TI}}^{\alpha,\pm}(t)$ are plotted as dashed ($\alpha = 1$) and dotted ($\alpha = -1$) lines in all plots, indicating the onset of the region in parameter space where superconductivity is greatly suppressed.

the integrand of the gap equation, Eq. (32), and the lower left panel plots k_{F} for the bands in Eq. (24) as a function of μ_{TI}. The main contribution to the gap equation clearly comes from the values $|\mathbf{k}| = k_{\mathrm{F}}$. From Fig. 1(b) we also see that as μ_{TI} approaches $\pm\sqrt{2mv_{\mathrm{F}}^2\mu}$, the value where the Fermi wave vectors for the bare the S and TI bands, $k_{\mathrm{F}}^{\mathrm{S}}$ and $k_{\mathrm{F}}^{\mathrm{TI}}(\mu_{\mathrm{TI}})$, cross, the wave vector of one of the bands exceeds k_+ and thus does not contribute to the gap equation. Now there is only one nondegenerate band inside the relevant region, meaning that the density of states and thus λ is halved compared to the $t = 0$ case, where the band is doubly degenerate. Hence the resulting gap is suppressed to $\Delta_0 e^{-1/\lambda} = 2\omega_D e^{-2/\lambda}$, in good agreement with the numerical results, as shown by the dashed line in the inset in Fig. 1(a). This also means that the suppression is less severe for higher λ, which we have confirmed by numerical simulations.

For positive μ_{TI}, the Fermi wave vector in one band exits the integration interval $[k_-, k_+]$ at $\mu_{\mathrm{TI}} = \mu_{\mathrm{TI}}^{+,-}$, while a new band enters this region at $\mu_{\mathrm{TI}} = \mu_{\mathrm{TI}}^{+,+}$, where we have defined

$$\mu_{\mathrm{TI}}^{\alpha,\pm}(t) = \alpha\sqrt{2mv_{\mathrm{F}}^2(\mu \mp \omega_D)} \pm \frac{t^2}{\omega_D} \qquad (33)$$

(see Appendix A for details). A similar argument holds for negative μ_{TI}, and hence superconductivity is strongly suppressed for

$$\mu_{\mathrm{TI}}^{\alpha,-} < \mu_{\mathrm{TI}} < \mu_{\mathrm{TI}}^{\alpha,+}, \qquad (34)$$

indicated by the dashed and dotted lines in Fig. 1. If the hopping parameter is large enough, $t^2 > \omega_D\sqrt{2mv_{\mathrm{F}}^2(\mu \mp \omega_D)} \equiv (t_\mp)^2$, $\mu_{\mathrm{TI}}^{-,+}$ and $\mu_{\mathrm{TI}}^{+,-}$ change sign. Hence, for $|t| > |t_+| > |t_-|$ and $\mu_{\mathrm{TI}}^{+,-} < \mu_{\mathrm{TI}} < \mu_{\mathrm{TI}}^{-,+}$, no bands have a Fermi wave vector between k_- and k_+, resulting in $\Delta = 0$, as seen for $t \approx 0.3$ eV and low μ_{TI} in Fig. 1. Since $\mu \gg \omega_D$, all results are close to symmetric about $\mu_{\mathrm{TI}} = 0$, as seen in Fig. 1(b).

In order for strong suppression to occur for some value of μ_{TI}, we must require $\mu_{\mathrm{TI}}^{\alpha,-} < \mu_{\mathrm{TI}}^{\alpha,+}$. For $\alpha = -1$ this always holds, while for $\alpha = +1$ we get a lower limit for t^2,

$$t^2 > \omega_D\left[\sqrt{2mv_{\mathrm{F}}^2(\mu + \omega_D)} - \sqrt{2mv_{\mathrm{F}}^2(\mu - \omega_D)}\right]. \qquad (35)$$

For conventional s-wave superconductors $\mu \gg \omega_D$, meaning strong suppression can occur even at low values of t, though for TI chemical potentials close to $\pm\sqrt{2mv_{\mathrm{F}}^2\mu}$.

While this result is strictly only valid in the limit of an atomically thin superconductor, we expect that this effect in principle could reduce the zero-temperature gap and thus also reduce the critical temperature in superconducting thin films. However, for typical parameter values in TIs and s-wave superconductors, the values of μ_{TI} where superconductivity vanishes is inaccessible, tuning μ_{TI} by several eV would place the Fermi level inside the bulk bands of the TI, where our model is no longer valid. The only exception from this is when $|t| \gtrsim |t_-|$, when superconductivity is suppressed even at $\mu_{\mathrm{TI}} = 0$. The fact that no strong inverse proximity effect
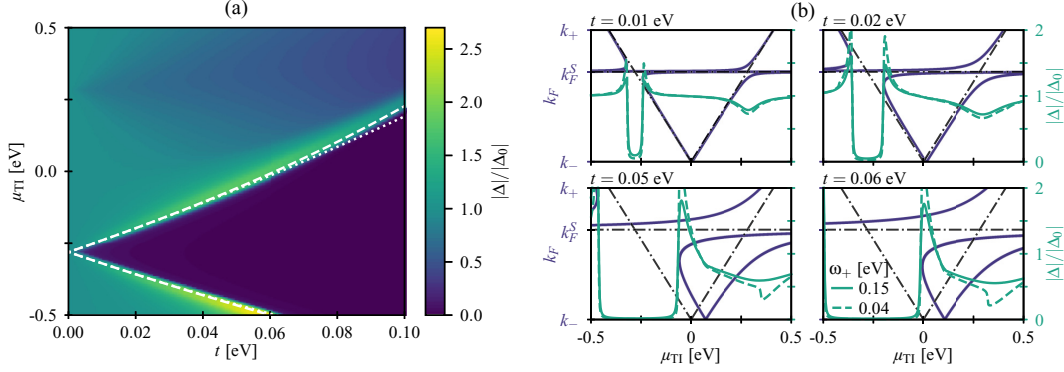
FIG. 2. (a) Plot of the superconducting gap at $T = 0$ for a d-wave superconductor as a function of μ_{TI} and t with upper cutoff $\omega_+ = 0.15$ eV, normalized to the bulk value $|\Delta_0|$ for parameter values relevant for bilayers consisting of HgTe and high-T_c superconductors. The gap is strongly suppressed for $\mu_{\mathrm{TI}}^- < \mu_{\mathrm{TI}} < \mu_{\mathrm{TI}}^+$, where the approximate (exact numerical) functions $\mu_{\mathrm{TI}}^\pm(t)$ in Eq. (36) are plotted as dotted (dashed) lines. The approximate solution is only valid for $k_{\mathrm{F}} \approx k_{\mathrm{F}}^{\mathrm{S}}$, corresponding to small t. For $\mu_{\mathrm{TI}} \approx \mu_{\mathrm{TI}}^\pm(t)$ the gap increases beyond Δ_0. (b) Plot of the magnitude of the Fermi wave vectors of the bands in Eq. (24) in the interval $k_- < k_{\mathrm{F}} < k_+$ (left axis), together with the normalized gap (right axis) for $\omega_+ = 0.15$ and 0.04 eV. The upper limit k_+ in the left axis corresponds to $\omega_+ = 0.04$ eV. The black dash-dotted lines show the S and TI Fermi wave vectors for $t = 0$. As for the s-wave case, the strong suppression of the gap is due to only one band having a Fermi wave vector in the integration interval. Note how the values of $k_{\mathrm{F}}(\mu_{\mathrm{TI}})$ of the hybridized bands (originating with the left $t = 0$ crossing of the k_{F}'s of the TI and the S) bend back in a pronounced way as a function of μ_{TI} (k_{F} is a multivalued function of μ_{TI} since there are four bands). This leads to an enhanced density of states for these values of μ_{TI}. This in turn gives an enhancement of the gap in the immediate vicinity of the region of μ_{TI} where the gap is suppressed by the disappearance of bands crossing the TI Fermi surface. This effect is not seen in the s-wave case, where the pronounced back bending of $k_\pm(\mu_{\mathrm{TI}})$ does not occur inside the integration interval with the much lower values of $\omega_\pm$ [see Fig. 3(a)].

has been observed, e.g., in Ref. [20], might indicate that the coupling constant t is below this limit, meaning that an unphysical high chemical potential is needed in the TI to observe the vanishing of superconductivity. Since conventional s-wave superconductors have high Fermi energies, it might not be possible to reach the parameter regions where superconductivity vanishes, unless the chemical potential in the S can be lowered significantly, the Fermi velocity of the TI is lowered by renormalization, as was proposed in Ref. [26], or the coupling between the layers can be increased beyond t_-. However, as we show below, similar effects are present also for unconventional, high-T_c superconductors, for which the Fermi energy is lower. Examples of such superconductors would be the high-T_c cuprates and the heavy-fermion superconductors.[1]

B. d-wave pairing

Using a much lower chemical potential in the S, $\mu \sim 35$ meV [45], and an upper cut-off frequency comparable to the spin fluctuation energy in the high-T_c cuprates, $\omega_+ \sim 0.04$–0.15 eV [32,33,46], $\omega_- = \mu$, and parameters otherwise as for the s-wave case, we solve the gap equations for a d-wave superconductor. First of all, the effect of the d-wave gap structure, compared to an s-wave gap, is an overall change in scaling, just as is the case for Δ_0 (see Appendix C). Hence, the results for $\Delta^{s-\mathrm{wave}}/\Delta_0^{s-\mathrm{wave}}$ are identical to $\Delta^{d-\mathrm{wave}}/\Delta_0^{d-\mathrm{wave}}$

when using the same parameters, and we have therefore solved the numerically more efficient s-wave gap equations with parameters valid for high-T_c superconductors.

Figure 2(a) shows the numerical results for the normalized gap as a function of μ_{TI} and t. The most prominent difference compared to the results in Fig. 1 is that the results are no longer symmetric about $\mu_{\mathrm{TI}} = 0$, which can be understood from the fact that $\omega_\pm$ is of the same order of magnitude or larger than μ. Due to the anticrossing of the Fermi wave vectors at negative μ_{TI}, there is only one Fermi wave vector between k_- and k_+ for $\mu_{\mathrm{TI}}^- < \mu_{\mathrm{TI}} < \mu_{\mathrm{TI}}^+$ [dashed lines in Fig. 2(a)], leading to strong suppression for negative μ_{TI}. This is illustrated in Fig. 2(b), where we plot the Fermi wave vectors of the bands together with the normalized gap as a function of μ_{TI} for different values of t. The figure also shows how the regions of strong mixing between the bands increases with increasing t. Interestingly, the suppression of the gap is preceded by an increased Δ at $\mu_{\mathrm{TI}}^\pm$, due to the bending of the Fermi wave vectors away from the crossing point of $k_{\mathrm{F}}^{\mathrm{S}}$ and $k_{\mathrm{F}}^{\mathrm{TI}}(\mu_{\mathrm{TI}})$, which leads to an increase in the density of states at the Fermi level. This is illustrated in Fig. 3(b), where for TI chemical potentials $\mu_{\mathrm{TI}}^\pm$ the bands have a minimum (maximum) at the Fermi level, resulting in high densities of states. The difference in the gap enhancement between μ_{TI}^+ and μ_{TI}^- is due to the combined effects of different spectral weights, indicated by the linewidths in Fig. 3(b), and the size of the Fermi surface, leading to a net larger increase in $|\Delta|$ at μ_{TI}^-. In the small t limit, we find the approximate expressions

---

[1]Although heavy-fermion superconductors nominally have a quitelow critical temperature in absolute terms, they are nevertheless high-T_c superconductors. Their critical temperatures are a significant fraction of their Fermi-temperatures.

$$\mu_{\mathrm{TI}}^\pm = -\sqrt{2mv_{\mathrm{F}}^2\mu} \pm 2\left(\frac{mv_{\mathrm{F}}^2}{2\mu}\right)^{1/4} t + \frac{1}{4\mu}t^2. \qquad (36)$$
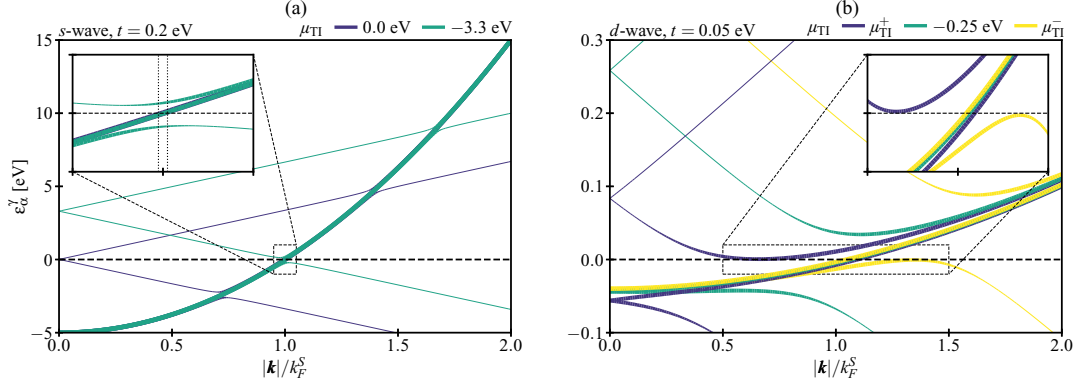
FIG. 3. Plots of the bands $\epsilon_\alpha^\gamma(\mathbf{k})$ in Eq. (24) for (a) *s*-wave and (b) *d*-wave parameter values and different values of μ_{TI}. The linewidths are proportional to the spectral weights $w_\alpha^\gamma(\mathbf{k})$ of the bands [see Eq. (25)]. In (a) the values of μ_{TI} correspond to a barely suppressed ($\mu_{\text{TI}} = 0.0$ eV) and strongly suppressed ($\mu_{\text{TI}} = -3.3$ eV $\approx -\sqrt{2mv_F^2\mu}$) gap for coupling $t = 0.2$ eV. The inset shows that there is no hybridization of bands close to the Fermi level (dashed line) for the lowest μ_{TI}, while the strong hybridization for $\mu_{\text{TI}} = 3.3$ eV leads to only one band crossing the Fermi level in the interval $[k_-, k_+]$ (dotted lines). In (b) we see that only one band crosses the Fermi level for $\mu_{\text{TI}} = -0.25$ eV, explaining the strong suppression in this case. At $\mu_{\text{TI}} = \mu_{\text{TI}}^\pm$ we have an increase in $|\Delta|$, which can be explained by the bands having minima/maxima at the Fermi level in these cases, leading to high densities of states.

These lines are plotted in Fig. 2(a) (dotted lines) together with the exact numerical solutions (dashed lines) (see Appendix A for details). This increase in $|\Delta|$ is not due to the the *d*-wave symmetry, and should therefore be present for $\mu_{\text{TI}} = \mu_{\text{TI}}^\pm$ whenever the interval $[k_-, k_+]$ includes either of the points $k_F^S \pm |\delta k_F|$, where δk_F is defined in Eq. (A7).

For positive μ_{TI} there is a small reduction in Δ close to $\mu_{\text{TI}} = \sqrt{2mv_F^2\mu}$, even though there are three bands with $k_F \in [k_-, k_+]$. However, since the numerator of each term in the gap equation, Eq. (32), can be written $\xi_\alpha^\pm(\mathbf{k})^2 - (\alpha v_F|\mathbf{k}| - \mu_{\text{TI}})^2$, regions where $\xi_\alpha^\pm(\mathbf{k})$ are similar to the bare TI bands contribute little to the gap equations, resulting in a small decrease of Δ.

The effect of using a lower upper cutoff in the solution of the gap equations is also shown in Fig. 2. Comparing the $\omega_+ = 0.15$ and 0.04 eV lines, we see that for high t, the mixing of the S and TI bands is still significant at $k_F = k_+$, leading to abrupt changes in Δ. For the negative μ_{TI} the main effect of lowering the upper cutoff ω_+ is a further increase of Δ at $\mu_{\text{TI}}^\pm$.

From the above results, it is clear that a strong suppression of the gap is more probable in S-TI bilayers consisting of a high-T_c S, where both the chemical potential $-\sqrt{2mv_F^2\mu}$ corresponding to $k_F^S = k_F^{\text{TI}}(\mu_{\text{TI}})$ and the hopping strength needed for strong suppression at $\mu_{\text{TI}} = 0$ is much lower. Hence, we may expect a strong inverse proximity effect in such systems, with a strength determined by λ, as illustrated in Fig. 4 for both the *s*- and the *d*-wave case. Increasing λ leads to a reduced suppression of the gap, consistent with the fact that the superconducting state is more robust for higher λ. For the *s*-wave case, the suppression is proportional to $e^{-1/\lambda}$. This holds only approximately for the *d*-wave case due to other factors than Fermi level crossings affecting the suppression, such as changes in the spectral densities at the Fermi level and changes in the size of the Fermi surface (see Fig. 3), effects which are small in the *s*-wave case. From the results in Fig. 2 we also see that it should be possible to change Δ by several

orders of magnitude by small changes in μ_{TI}, again depending on the value of λ as illustrated in Fig. 4.

VI. SUMMARY

We have theoretically studied the inverse superconducting proximity effect between a thin *s*-wave or *d*-wave superconductor and a topological insulator. Using a field-theoretical approach, we have found that in both cases there are regions in parameter space where the inverse proximity effect is strong, leading to a strong suppression of the gap approximately proportional to $e^{-1/\lambda}$. The suppression can be related to the

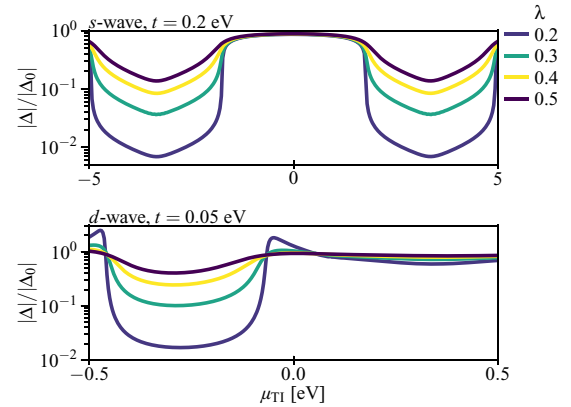FIG. 4. The figure shows how the dimensionless coupling constant λ affects the suppression of the superconducting gap for *s*-wave S with $t = 0.2$ eV (top) and *d*-wave S with $t = 0.05$ eV and $\omega_+ = 0.15$ eV (bottom). Increasing λ makes the superconducting state more robust, reducing both the suppression of Δ, and also the increase in Δ at $\mu_{\text{TI}}^\pm$ in the *d*-wave case.

hybridization of the TI and S bands, and the large degree of mixing which occurs when the Fermi wave vectors of the S and TI coincide for chemical potential $\mu_{\mathrm{TI}} = \pm\sqrt{2mv_{\mathrm{F}}^2\mu}$. A larger value of λ results in a more robust superconducting state, and hence less suppression.

For parameter values relevant for s-wave superconductors, the interval of suppression grows quadratically with the hopping t, and eventually leads to strong suppression even at $\mu_{\mathrm{TI}} = 0$. However, since there have been no experimental indications of a strong inverse proximity effect, we must conclude that the hopping is too weak to lead to suppression for experimentally accessible values of μ_{TI}. Neglecting the inverse proximity effect regarding the stability of the superconducting order therefore seems to be a good approximation for conventional s-wave superconductors.

A similar effect of suppressed superconductivity is also present for d-wave superconductors with parameter values relevant for the high-T_c superconductors. In this case the strong suppression is found for TI chemical potentials close to $-\sqrt{2mv_{\mathrm{F}}^2\mu}$, where the interval of strong suppression of the gap grows approximately linearly with t. Since the Fermi energy μ is much lower for high-T_c superconductors, both the magnitude of the chemical potential $-\sqrt{2mv_{\mathrm{F}}^2\mu}$, and the hopping strength needed for strong suppression at $\mu_{\mathrm{TI}} = 0$ is much lower, making a strong inverse proximity effect more probable in such systems. In contrast to the s-wave case, the region of strong suppression was preceded by an increase in Δ above Δ_0. This is, however, not a consequence of the pairing symmetry, but rather the difference in system parameters. For large enough cut-off frequencies, the integration region will include a band minimum/maximum just touching the Fermi level, leading to a large increase in the density of states, and thus increased gap.

We also find that the spin-triplet p-wave (f-wave) superconducting correlations are induced in the s-wave (d-wave) S due to the proximity-induced spin-orbit coupling. Possible further work could include breaking the translation symmetry in the x or y direction and probing the density of states normal to the z axis, possibly revealing signatures of p-wave or f-wave pairing. Moreover, it could be interesting to study the spatial variation of the order parameter in a superconductor with finite thickness.

ACKNOWLEDGMENTS

APPENDIX A: CRITERIA FOR STRONG PROXIMITY EFFECT

For superconductivity to occur, the Fermi wave vector of at least one of the bands has to lie within the interval

of attractive pairing, which for s-wave superconductors is $\sqrt{2m(\mu - \omega_D)} < |\mathbf{k}| < \sqrt{2m(\mu + \omega_D)}$. We find the Fermi wave vector of the energy bands by setting $\epsilon_\alpha^\gamma(\mathbf{k}) = 0$, which yields the equation

$$[\alpha v_{\mathrm{F}}|\mathbf{k}| - \mu_{\mathrm{TI}}]\epsilon_{\mathbf{k}} - t^2 = 0. \tag{A1}$$

Inserting $|\mathbf{k}| = k_\pm$ we get the value of μ_{TI} for which the Fermi wave vector of a band enters or leaves the interval of attractive pairing,

$$\mu_{\mathrm{TI}}^{\alpha,\pm}(t) = \alpha\sqrt{2mv_{\mathrm{F}}^2(\mu \mp \omega_D)} \pm \frac{t^2}{\omega_D}. \tag{A2}$$

The Fermi wave vectors of the bands $\epsilon_\alpha^-(\mathbf{k})$ exceed k_+ at $\mu_{\mathrm{TI}}^{\alpha,-}$, while the Fermi wave vectors of $\epsilon_\alpha^+(\mathbf{k})$ enter the interval $[k_-, k_+]$ at $\mu_{\mathrm{TI}}^{\alpha,+}$. $\mu_{\mathrm{TI}}^{+,+}$ ($\mu_{\mathrm{TI}}^{-,-}$) is always positive (negative), while $\mu_{\mathrm{TI}}^{+,-}$ and $\mu_{\mathrm{TI}}^{-,+}$ change sign when $t^2 > \omega_D\sqrt{2mv_{\mathrm{F}}^2(\mu + \omega_D)} \equiv (t_0^+)^2$ and $t^2 > \omega_D\sqrt{2mv_{\mathrm{F}}^2(\mu - \omega_D)} \equiv (t_0^-)^2$, respectively, where $|t_0^+| > |t_0^-|$.

Hence we have strong suppression when

$$\mu_{\mathrm{TI}}^{\alpha,-} < \mu_{\mathrm{TI}} < \mu_{\mathrm{TI}}^{\alpha,+}, \tag{A3}$$

which for $\alpha = +1$ requires

$$t^2 > \omega\left[\sqrt{2mv_{\mathrm{F}}^2(\mu + \omega_D)} - \sqrt{2mv_{\mathrm{F}}^2(\mu - \omega)}\right].$$

Moreover, for $|t| > |t_+|$ and $\mu_{\mathrm{TI}}^{+,-} < \mu_{\mathrm{TI}} < \mu_{\mathrm{TI}}^{-,+}$ no bands have a Fermi wave vector inside the relevant interval, and the gap is zero.

For the d-wave S we find an increase in the gap function for certain values of μ_{TI}. An increase in the gap would occur in regions where the Fermi wave vectors of two bands approach each other and finally coincide as a function of μ_{TI}, resulting in a region of closely spaced Fermi wave vectors. This can be seen to happen in Fig. 2(b). To find the value of μ_{TI} corresponding to the increase in Δ we find the local minima of

$$\mu_{\mathrm{TI}}(k_{\mathrm{F}}) = \alpha v_{\mathrm{F}} k_{\mathrm{F}} - \frac{t^2}{\epsilon_{k_{\mathrm{F}}}} \tag{A4}$$

by requiring $\partial_{k_{\mathrm{F}}}\mu_{\mathrm{TI}}(k_{\mathrm{F}}) = 0$, from which we get the equation for k_{F},

$$\alpha v_{\mathrm{F}} + \frac{t^2 k_{\mathrm{F}}}{m\epsilon_{k_{\mathrm{F}}}^2} = 0. \tag{A5}$$

Solving this equation numerically with $\alpha = -1$ and inserting the results into Eq. (A4) yields the dashed lines in Fig. 2, in good agreement with the numerical results of the gap equation. To get an approximate analytical expression, we assume that $k_{\mathrm{F}} = k_{\mathrm{F}}^{\mathrm{S}} + \delta k_{\mathrm{F}}$, where $\delta k_{\mathrm{F}} \ll k_{\mathrm{F}}^{\mathrm{S}}$, which is valid for sufficiently small t. Neglecting terms of $O(\delta k_{\mathrm{F}}^3)$ and higher, we get

$$\delta k_{\mathrm{F}}^2 + \frac{t^2 m}{\alpha v_{\mathrm{F}} k_{\mathrm{F}}^{\mathrm{S}}} + \frac{t^2 m}{\alpha v_{\mathrm{F}}\left(k_{\mathrm{F}}^{\mathrm{S}}\right)^2}\delta k_{\mathrm{F}} = 0. \tag{A6}$$

Neglecting the last term yields, effectively keeping terms up to $O(t^2)$, results in

$$\delta k_{\mathrm{F}} = \pm\sqrt{-\frac{1}{\alpha}}\left(\frac{m}{2v_{\mathrm{F}}^2\mu}\right)^{1/4} t, \tag{A7}$$

from which it is clear that we only have solutions for $\alpha = -1$. Inserting this expression into Eq. (A4), we get to $O(t^2)$

$$\mu_{\mathrm{TI}}^{\pm} \approx -\sqrt{2mv_{\mathrm{F}}^2\mu} \pm 2\left(\frac{mv_{\mathrm{F}}^2}{2\mu}\right)^{1/4} t + \frac{1}{4\mu}t^2. \qquad \text{(A8)}$$

This result is plotted as dotted lines in Fig. 2(a), and is in good agreement with the exact numerical results for small t. For $\mu_{\mathrm{TI}}^- < \mu_{\mathrm{TI}} < \mu_{\mathrm{TI}}^+$, there is only one Fermi wave vector in the integration region, leading to a suppressed gap.

APPENDIX B: FUNCTIONAL INTEGRAL IN NAMBU SPINOR NOTATION

We begin by considering the Gaussian integral over Grassmann variables [47],

$$I = \left(\prod_i \int da_i\right) e^{-1/2\sum_{i,j} a_i M_{ij}a_j} = \left(\prod_i \int da_i\right) \prod_{i,j}\left(1 - \frac{1}{2}a_i M_{ij}a_j\right) = \mathrm{Pf}\left(\frac{M - M^T}{2}\right), \qquad \text{(B1)}$$

where $\mathrm{Pf}[(M - M^T)/2]$ is the Pfaffian of the antisymmetric part of M, where $\mathrm{Pf}(A)^2 = \det(A)$. As an example we consider only two variables, a_1 and a_2. In this case, terms containing M_{ii} disappear, since $a_i^2 = 0$, as do second-order terms in M. For the above integral we therefore get

$$I = \int da_1 da_2 \frac{1}{2}(-a_1 M_{12}a_2 - a_2 M_{21}a_1) = \frac{M_{12} - M_{21}}{2} = \sqrt{\det\frac{M - M^T}{2}} = \sqrt{\det M^A} = \mathrm{Pf}(M^A). \qquad \text{(B2)}$$

Here, M^A is the antisymmetric part of M.

Applying this to the problem of integrating $\exp(-S_{\mathrm{S}}^{\mathrm{eff}})$, we first write the action in terms of the Nambu spinor $\mathcal{C}$:

$$S_{\mathrm{S}}^{\mathrm{eff}} = -\frac{1}{\beta V}\sum_{k,k'} \mathcal{C}^T(-k)\begin{pmatrix}\varphi^\dagger(k'-k)\frac{\sigma_x - i\sigma_y}{2} & 0 \\ \mathcal{G}_0^{-1}(k)\delta_{k,k'} & \varphi(k-k')\frac{\sigma_x + i\sigma_y}{2}\end{pmatrix}\mathcal{C}(k') \equiv -\frac{1}{2\beta V}\sum_{k,k'}\mathcal{C}^T(-k)A(k,k')\mathcal{C}(k')$$

$$= -\frac{1}{\beta V}\sum_{k,k'}\mathcal{C}^T(k)\begin{pmatrix}-\varphi^\dagger(k-k')\frac{\sigma_x + i\sigma_y}{2} & -[\mathcal{G}_0^{-1}(k)]^T\delta_{k,k'} \\ 0 & -\varphi(k'-k)\frac{\sigma_x - i\sigma_y}{2}\end{pmatrix}\mathcal{C}(-k') \equiv -\frac{1}{2\beta V}\sum_{k,k'}\mathcal{C}^T(k)[-A(k',k)]^T\mathcal{C}(-k').$$

Combining these two expressions, we get

$$S_{\mathrm{S}}^{\mathrm{eff}} = -\frac{1}{2\beta V}\sum_{k,k'}\mathcal{C}^T(-k)\begin{pmatrix}-\varphi^\dagger(k'-k)i\sigma_y & -[\mathcal{G}_0^{-1}(-k)]^T\delta_{k,k'} \\ \mathcal{G}_0^{-1}(k)\delta_{k,k'} & \varphi(k-k')i\sigma_y\end{pmatrix}\mathcal{C}(k')$$

$$= -\frac{1}{2\beta V}\sum_{k,k'}\mathcal{C}^T(-k)\frac{A(k,k') - A^T(-k',-k)}{2}\mathcal{C}(k') = -\frac{1}{2\beta V}\sum_{k,k'}\mathcal{C}^T(-k)A^A(k,k')\mathcal{C}(k'), \qquad \text{(B3)}$$

where $A^A(k,k')$ denotes the antisymmetric part of A. This is exactly equal to Eq. (15), as can be seen by the following manipulations. For notational simplicity we use the two-vector notation

$$\mathcal{C}(k) = \begin{pmatrix} c(k) \\ c^*(-k) \end{pmatrix}, \qquad \text{(B4)}$$

i.e., $[\mathcal{C}(k)]_1 = c(k)$, $[\mathcal{C}(k)]_2 = c^*(-k)$. Hence the matrix multiplication in Eq. (B3) can be written

$$\sum_{ij}[\mathcal{C}^T(-k)]_i[A^A(k,k')]_{ij}[\mathcal{C}(k')]_j = -[\mathcal{C}^T(-k)]_1\varphi^\dagger(k'-k)i\sigma_y[\mathcal{C}(k')]_1 - [\mathcal{C}^T(-k)]_1[\mathcal{G}_0^{-1}(-k)\delta_{k,k'}]^T[\mathcal{C}(k')]_2$$

$$+ [\mathcal{C}^T(-k)]_2\mathcal{G}_0^{-1}(-k)\delta_{k,k'}[\mathcal{C}(k')]_1 + [\mathcal{C}^T(-k)]_2\varphi(k-k')i\sigma_y[\mathcal{C}(k')]_2. \qquad \text{(B5)}$$

We use the fact that $[\mathcal{C}^\dagger(k)]_1 = [\mathcal{C}^T(-k)]_2$ and $[\mathcal{C}^\dagger(k)]_2 = [\mathcal{C}^T(-k)]_1$, and relate the remaining factors to the elements of $\mathcal{G}^{-1}(k,k')$ in Eq. (16),

$$C^T(-k)A^A(k,k')C(k') = [\mathcal{C}^\dagger(k)]_2[\mathcal{G}^{-1}(k,k')]_{21}[\mathcal{C}(k')]_1 + [\mathcal{C}^\dagger(k)]_2[\mathcal{G}^{-1}(k,k')]_{22}[\mathcal{C}(k')]_2 + [\mathcal{C}^\dagger(k)]_1[\mathcal{G}^{-1}(k,k')]_{11}[\mathcal{C}(k')]_1$$

$$+ [\mathcal{C}^\dagger(k)]_1[\mathcal{G}^{-1}(k,k')]_{12}[\mathcal{C}(k')]_2$$

$$= \mathcal{C}^\dagger(k)\mathcal{G}^{-1}(k,k')\mathcal{C}(k'), \qquad \text{(B6)}$$

which shows that Eqs. (B3) and (15) are equivalent. Using Eq. (B1), the functional integral of the action in Eq. (B3) results in

$$Z = \int \mathcal{D}c^\dagger \mathcal{D}c\, e^{-S_{\mathrm{S}}^{\mathrm{eff}}} = \sqrt{\det[-A^A]}, \qquad \text{(B7)}$$

where we have neglected various numerical constants. By interchanging an even number of rows, it can be shown that $A^A(k, k') \to \mathcal{G}^{-1}(k, k')$, and since the determinant is invariant under an even number of interchanges, we find [39]

$$Z = e^{1/2 \operatorname{Tr} \ln(-\mathcal{G}^{-1})}. \tag{B8}$$

APPENDIX C: ZERO-TEMPERATURE GAP FOR $t = 0$

When $t = 0$, the gap equation, Eq. (32), reduces to

$$1 = \frac{g}{2V} \sum_{\mathbf{k}} \frac{v^2(\mathbf{k})}{\sqrt{\epsilon_{\mathbf{k}} + |\Delta_0(\mathbf{k})|^2}} \tag{C1}$$

in the zero-temperature limit. Transforming this to an integration over $\phi_{\mathbf{k}}$ and energy, we get

$$1 = \frac{\lambda}{2} \int_{-\omega_-}^{\omega_+} d\epsilon \int_0^{2\pi} \frac{d\phi_{\mathbf{k}}}{2\pi} \frac{v^2(\phi_{\mathbf{k}})}{\sqrt{\epsilon + |\Delta_0(\phi_{\mathbf{k}})|^2}}, \tag{C2}$$

where $\omega_\pm$ are positive. Performing the energy integral we get

$$
\begin{aligned}
1 &= \frac{\lambda}{2} \int_0^{2\pi} \frac{d\phi_{\mathbf{k}}}{2\pi} v^2(\phi_{\mathbf{k}}) \ln \frac{\sqrt{|\Delta_0(\phi_{\mathbf{k}})|^2 + \omega_+^2} + \omega_+}{\sqrt{|\Delta_0(\phi_{\mathbf{k}})|^2 + \omega_-^2} - \omega_-^2} \\
&\approx \frac{\lambda}{2} \int_0^{2\pi} \frac{d\phi_{\mathbf{k}}}{2\pi} v^2(\phi_{\mathbf{k}}) \left[\ln \frac{4\omega_-\omega_+}{\Delta_0^2} - 2 \ln |v(\phi_{\mathbf{k}})| \right],
\end{aligned} \tag{C3}
$$

where we in the last line have assumed that the gap is small compared to the cut-off energy. For an s-wave superconductor $v(\phi_{\mathbf{k}}) = 1$, and we get simply $\Delta_0 = 2\sqrt{\omega_-\omega_+} e^{-1/\lambda}$. For d-wave pairing we can instead write the gap as

$$\Delta_0 = 2\sqrt{\omega_-\omega_+} e^{-(1/\lambda) - I}, \tag{C4}$$

where we have defined the integral

$$I = \int_0^{2\pi} \frac{d\phi_{\mathbf{k}}}{2\pi} v^2(\phi_{\mathbf{k}}) \ln |v(\phi_{\mathbf{k}})| = \frac{1 - \ln 2}{2} \approx 0.153\,426. \tag{C5}$$

Hence, the maximum d-wave gap amplitude is marginally smaller than the s-wave gap for the same values of λ and $\omega_\pm$.

APPENDIX D: NUMERICAL INTEGRATION PROCEDURES

When solving the gap equation numerically, the $\mathbf{k}$ sum is rewritten in terms of an energy integral over $\epsilon_{\mathbf{k}}$ and an integral over $\phi_{\mathbf{k}}$, which in the s-wave case is simply equal to 2π. In the s-wave case we therefore only have to perform the energy integral for energies in the interval $[-\omega_-, \omega_+]$, in our case using Python and the implementation TRAPZ of the trapezoidal method in the SCIPY library. In the d-wave case, we use QUADPY library's implementation of the numerical integration method in Ref. [48] when calculating the 2D integral in the $\epsilon_{\mathbf{k}}$-$\phi_{\mathbf{k}}$ plane.

[1] M. Z. Hasan and C. L. Kane, Rev. Mod. Phys. **82**, 3045 (2010).

[2] X. L. Qi and S. C. Zhang, Rev. Mod. Phys. **83**, 1057 (2011).

[3] T. O. Wehling, A. M. Black-Schaffer, and A. V. Balatsky, Adv. Phys. **63**, 1 (2014).

[4] J. Alicea, Rep. Prog. Phys. **75**, 076501 (2012).

[5] L. Fu and C. L. Kane, Phys. Rev. Lett. **100**, 096407 (2008).

[6] Y. Tanaka, T. Yokoyama, and N. Nagaosa, Phys. Rev. Lett. **103**, 107002 (2009).

[7] A. Zyuzin, M. Alidoust, and D. Loss, Phys. Rev. B **93**, 214502 (2016).

[8] M. Amundsen, H. G. Hugdal, A. Sudbø, and J. Linder, Phys. Rev. B **98**, 144505 (2018).

[9] L. Fu and C. L. Kane, Phys. Rev. Lett. **102**, 216403 (2009).

[10] A. R. Akhmerov, J. Nilsson, and C. W. J. Beenakker, Phys. Rev. Lett. **102**, 216404 (2009).

[11] J. Linder, Y. Tanaka, T. Yokoyama, A. Sudbø, and N. Nagaosa, Phys. Rev. Lett. **104**, 067001 (2010).

[12] J. Linder, Y. Tanaka, T. Yokoyama, A. Sudbø, and N. Nagaosa, Phys. Rev. B **81**, 184525 (2010).

[13] D. Zhang, J. Wang, A. M. DaSilva, J. S. Lee, H. R. Gutierrez, M. H. W. Chan, J. Jain, and N. Samarth, Phys. Rev. B **84**, 165120 (2011).

[14] A. Cook and M. Franz, Phys. Rev. B **84**, 201105 (2011).

[15] F. Qu, F. Yang, J. Shen, Y. Ding, J. Chen, Z. Ji, G. Liu, J. Fan, X. Jing, C. Yang, and L. Lu, Sci. Rep. **2**, 339 (2012).

[16] A. M. Cook, M. M. Vazifeh, and M. Franz, Phys. Rev. B **86**, 155431 (2012).

[17] I. Sochnikov, A. J. Bestwick, J. R. Williams, T. M. Lippman, I. R. Fisher, D. Goldhaber-Gordon, J. R. Kirtley, and K. A. Moler, Nano Lett. **13**, 3086 (2013).

[18] G. Koren, T. Kirzhner, Y. Kalcheim, and O. Millo, Europhys. Lett. **103**, 67010 (2013).

[19] L. Galletti, S. Charpentier, M. Iavarone, P. Lucignano, D. Massarotti, R. Arpaia, Y. Suzuki, K. Kadowaki, T. Bauch, A. Tagliacozzo, F. Tafuri, and F. Lombardi, Phys. Rev. B **89**, 134512 (2014).

[20] I. Sochnikov, L. Maier, C. A. Watson, J. R. Kirtley, C. Gould, G. Tkachov, E. M. Hankiewicz, C. Brüne, H. Buhmann, L. W. Molenkamp, and K. A. Moler, Phys. Rev. Lett. **114**, 066801 (2015).

[21] Z.-Z. Li, F.-C. Zhang, and Q.-H. Wang, Sci. Rep. **4**, 6363 (2015).

[22] Y. Kim, T. M. Philip, M. J. Park, and M. J. Gilbert, Phys. Rev. B **94**, 235434 (2016).

[23] T. Shoman, A. Takayama, T. Sato, S. Souma, T. Takahashi, T. Oguchi, K. Segawa, and Y. Ando, Nat. Commun. **6**, 6547 (2015).

[24] P. Fulde and R. A. Ferrell, Phys. Rev. **135**, A550 (1964).

[25] M. J. Park, J. Yang, Y. Kim, and M. J. Gilbert, Phys. Rev. B **96**, 064518 (2017).

[26] N. Sedlmayr, E. W. Goodwin, M. Gottschalk, I. M. Dayton, C. Zhang, E. Huemiller, R. Loloee, T. C. Chasapis, M. Salehi, N. Koirala, M. G. Kanatzidis, S. Oh, D. J. Van Harlingen, A. Levchenko, and S. H. Tessmer, arXiv:1805.12330.

[27] M. M. Ugeda, A. J. Bradley, Y. Zhang, S. Onishi, Y. Chen, W. Ruan, C. Ojeda-Aristizabal, H. Ryu, M. T. Edmonds, H.-Z. Tsai, A. Riss, S.-K. Mo, D. Lee, A. Zettl, Z. Hussain, Z.-X. Shen, and M. F. Crommie, Nat. Phys. **12**, 92 (2016).

[28] Q.-Y. Wang, Z. Li, W.-H. Zhang, Z.-C. Zhang, J.-S. Zhang, W. Li, H. Ding, Y.-B. Ou, P. Deng, K. Chang, J. Wen, C.-L. Song, K. He, J.-F. Jia, S.-H. Ji, Y.-Y. Wang, L.-L. Wang, X. Chen, X.-C. Ma, and Q.-K. Xue, Chin. Phys. Lett. **29**, 037402 (2012).

[29] D. Liu, W. Zhang, D. Mou, J. He, Y.-B. Ou, Q.-Y. Wang, Z. Li, L. Wang, L. Zhao, S. He, Y. Peng, X. Liu, C. Chen, L. Yu, G. Liu, X. Dong, J. Zhang, C. Chen, Z. Xu, J. Hu, X. Chen, X. Ma, Q. Xue, and X. J. Zhou, Nat. Commun. **3**, 931 (2012).

[30] S. He, J. He, W. Zhang, L. Zhao, D. Liu, X. Liu, D. Mou, Y.-B. Ou, Q.-Y. Wang, Z. Li, L. Wang, Y. Peng, Y. Liu, C. Chen, L. Yu, G. Liu, X. Dong, J. Zhang, C. Chen, Z. Xu, X. Chen, X. Ma, Q. Xue, and X. J. Zhou, Nat. Mater. **12**, 605 (2013).

[31] K. Fossheim and A. Sudbø, *Superconductivity: Physics and Applications* (Wiley, Chichester, 2004).

[32] T. Moryia, Y. Takahashi, and K. Ueda, J. Phys. Soc. Jpn. **59**, 2905 (1990).

[33] P. Monthoux, A. V. Balatsky, and D. Pines, Phys. Rev. B **46**, 14803 (1992).

[34] D. Pines, J. Phys. Chem. Solids **54**, 1447 (1993).

[35] T. Moriya and K. Ueda, J. Phys. Soc. Jpn. **63**, 1871 (1994).

[36] A. M. Black-Schaffer and A. V. Balatsky, Phys. Rev. B **87**, 220506(R) (2013).

[37] Y. Takane and R. Ando, J. Phys. Soc. Jpn. **83**, 014706 (2014).

[38] A. Altland and B. Simons, *Condensed Matter Field Theory*, 2nd ed. (Cambridge University Press, Cambridge, 2010).

[39] F. N. Krohg and A. Sudbø, Phys. Rev. B **98**, 014510 (2018).

[40] L. P. Gor'kov and E. I. Rashba, Phys. Rev. Lett. **87**, 037004 (2001).

[41] T. Yokoyama, Phys. Rev. B **86**, 075410 (2012).

[42] J. Bardeen, L. N. Cooper, and J. R. Schrieffer, Phys. Rev. **108**, 1175 (1957).

[43] N. W. Ashcroft and N. D. Mermin, *Solid State Physics* (Holt, Rinehart and Winston, New York, 1976).

[44] C. Brüne, C. X. Liu, E. G. Novik, E. M. Hankiewicz, H. Buhmann, Y. L. Chen, X. L. Qi, Z. X. Shen, S. C. Zhang, and L. W. Molenkamp, Phys. Rev. Lett. **106**, 126803 (2011)

[45] Y. M. Gerbstein, N. E. Timoschenko, and F. A. Chudnovskii, Phys. C **162–164**, 961 (1989).

[46] N. Nagaosa, Science **275**, 1078 (1997).

[47] F. Wegner, *Supermathematics and its Applications in Statistical Physics: Grassmann Variables and the Method of Supersymmetry* (Springer, Berlin/Heidelberg, 2016), Chap. 5.

[48] H. Xiao and Z. Gimbutas, Comput. Math. Appl. **59**, 663 (2010).

Paper X

Reference

Contributions

MA derived the boundary conditions, with support from JL. MA performed the numerical simulations of the test cases and drafted the manuscript. Both authors contributed to the discussions of the physics, and the revision of the final manuscript.

Quasiclassical theory for interfaces with spin-orbit coupling

Morten Amundsen and Jacob Linder

Center for Quantum Spintronics, Department of Physics, Norwegian University of Science and Technology, NO-7491 Trondheim, Norway

In recent years, substantial progress has been made regarding the application of quasiclassical theory on superconducting hybrid structures. This theoretical framework is reliant on a proper set of boundary conditions in order to describe multilayered systems. With the advent of the field of superconducting spintronics, systems that combine heavy metal layers, in which there is large spin-orbit coupling, with ferromagnets have received a great deal of attention, due to their potential for generating long-range triplet superconductivity. In contrast to interfaces of strongly spin-polarized materials, which are well understood, a quasiclassical theory for interfaces in systems in which there is significant spin-orbit coupling does not yet exist. After reviewing the quasiclassical theory for interfaces, we solve this problem here by deriving a set of boundary conditions that take spin-orbit coupling explicitly into account. We then go on to apply these boundary conditions to a superconductor-ferromagnet bilayer and a superconductor-ferromagnet-superconductor Josephson weak link, demonstrating the emergence of long-range triplet superconductivity in these systems.

I. INTRODUCTION

The quasiclassical approximation [1–3] is a versatile tool with which complex quantum mechanical problems can be simplified to such an extent that they become numerically solvable. The main assumption of this approximation is that the relevant quantities under study vary on length scales that are much larger than the Fermi wavelength so that the computationally challenging shorter length scale oscillations may be integrated out. This makes the quasiclassical approximation particularly well suited for superconductors, in which the superconducting condensate may remain correlated over mesoscopic distances. Indeed, the most general theoretical framework used to describe superconductors, the Green function technique, requires the solution of the Gor'kov equation [4], which is too cumbersome in all but a few select problems. Instead, progress can be achieved with its quasiclassical equivalents, the Eilenberger [5] and the Usadel equation [6], which govern quasiclassical Green functions describing only the envelopes of the original propagators, and remain the only viable solution method for many problems of practical interest.

When nonsuperconducting materials are attached to a superconductor to form superconducting hybrid structures, an interesting phenomenon occurs. In such systems, superconducting correlations may leak into the adjoining nonsuperconducting materials, so that they too attain superconducting properties. This is known as the proximity effect. The study of such systems necessarily involves the proper treatment of interfaces between materials. However, while the bulk properties of superconductors are easily described within quasiclassical theory, interfaces between materials is another matter entirely. In the vicinity of an interface, the governing Hamiltonian changes abruptly, which invalidates the use of the quasiclassical approximation. The consequence of this is that the quasiclassical Green functions feature a discontinuous jump at interfaces, the size of which is impossible to determine within

quasiclassical theory—additional information is needed. This jump was first computed for ballistic superconductor-normal metal structures using a full microscopic description of the interface [7], thereby giving a set of boundary conditions linking the two materials. These boundary conditions were generalized with the use of a projection operator method [8–10]. Alternative derivations, where the interface is treated perturbatively via a T-matrix approach [11–13], have also been proposed. In the diffusive limit, boundary conditions may be arrived at by connecting the momentum-independent diffusive Green functions far away from the interface to ballistic Green functions present in a region immediately surrounding the interface [14,15].

For hybrid structures involving strongly polarized magnetic materials, the interfacial boundary conditions generally become spin-active. Such boundary conditions have been formulated heuristically using a tunneling Hamiltonian [16]. Another, more fundamental, approach is to connect the two sides of the interface by means of scattering or transfer matrices, in which the spin dependence of the scattering processes is taken into account [17–19]. Both the projection operator and the T-matrix method have also been successfully generalized to handle spin-active interfaces in ballistic systems [20–24]. The latter method was also applied to diffusive systems in Ref. [25], in which a completely general theory for boundary conditions in spin-polarized hybrid structures was derived.

When hybrid structures are made from superconducting and ferromagnetic materials, the proximity effect allows for the coexistence of both magnetic and superconducting correlations. This produces a number of interesting effects. One of the more fascinating effects is perhaps the appearance of triplet superconductivity, due to the Zeeman splitting endowing the Cooper pairs with a net momentum [26]. In homogeneous ferromagnets, the triplet Cooper pairs remain in the spinless state, and hence the magnetization has a strong depairing effect. In ferromagnets where the magnetization is

inhomogeneous, on the other hand, the triplet Cooper pairs may be converted to an equal spin state [27,28], giving them a net spin. In such a state, the Cooper pairs are insensitive to a parallel magnetization, and may therefore persist for long distances into proximitized ferromagnets, a phenomenon known as long-range triplet superconductivity. In addition, since these correlations are spin-polarized, they may carry spin currents, a realization that has strongly contributed to the field of superconducting spintronics [29,30].

Another avenue toward triplet superconductivity is by introducing layers with spin-orbit coupling [31–33]. In such systems, spin-polarized supercurrents may be generated even in homogeneous ferromagnets, which is advantageous from an experimental point of view. However, while the boundary conditions for spin-polarized systems are well understood, a theory for interfaces in which spin-orbit coupling is prominent does not yet exist. In this paper, we seek to remedy this by deriving a set of boundary conditions that take spin-orbit coupling into account, using the general framework of Ref. [25]. This result consequently allows for a proper treatment of spin-orbit coupled interfaces in quasiclassical theory, which is in principle relevant for any heterostructure, since interfaces break inversion symmetry, but particularly so for heterostructures with heavy metal interlayers.

We state here our main analytical result and comment briefly on the qualitative physical meaning of each term in the boundary condition. Below, we shall derive this result rigorously and provide a clear description of how the various terms arise, and the meaning of each of the symbols:

$$
\begin{aligned}
\hat{n} \cdot \check{g}_1 \nabla \check{g}_1 = {}& T[\check{g}_1 , \ \check{g}_2] + T_\alpha[\check{g}_1 , \ \check{\boldsymbol{\sigma}}_{\|}\check{g}_2\check{\boldsymbol{\sigma}}_{\|}] \\
& + T_\alpha'[\check{g}_1 , \ \check{\boldsymbol{\sigma}}_{\|}\check{g}_1\check{\boldsymbol{\sigma}}_{\|}] \\
& + i\sqrt{T_\alpha''T}[\check{g}_1, \{\check{g}_2[\check{\boldsymbol{\sigma}}_{\|}, \check{g}_2], \check{\boldsymbol{\sigma}}_{\|}\}] \\
& + i\sqrt{T_\alpha''T}[\check{g}_1 , \ \{\check{g}_2, \check{\boldsymbol{\sigma}}_{\|}\}\check{g}_1\check{\boldsymbol{\sigma}}_{\|} + \check{\boldsymbol{\sigma}}_{\|}\check{g}_1\{\check{g}_2, \check{\boldsymbol{\sigma}}_{\|}\}].
\end{aligned}
\tag{1}
$$

The usual Kupriyanov-Lukichev term [14] is the one proportional to T. The term proportional to T_α represents a correction to the usual tunneling boundary condition from the spin-orbit coupling part of the tunneling matrix. The term T_α' represents spin-dependent phase-shifts occurring due to spin-orbit coupling at the interface and thus exists even in the absence of any tunneling. The terms $\sqrt{T_\alpha''T}$ are higher-order corrections that exist only in the presence of spin-independent tunneling, spin-orbit coupled tunneling, and spin-orbit coupled reflection.

The quasiclassical theory for boundary conditions is quite intricate, involving many details, so to ensure complete clarity of the ensuing derivation, we include in Sec. II a review of the treatment of interfaces within quasiclassical theory. In Sec. III we formulate the boundary conditions in the presence of spin-orbit coupling, and in Sec. IV we apply the boundary conditions to example problems in order to demonstrate their use.

II. REVIEW OF THE QUASICLASSICAL THEORY FOR INTERFACES

In this section, a review of quasiclassical boundary conditions will be given, starting with a brief excursion into general quasiclassical theory.

A. Quasiclassical equations of motion

All physical observables of interest may be expressed in terms of Green functions, and we use the Keldysh formalism, in which the Green functions take the form of 8×8 matrices in spin $\otimes$ Nambu $\otimes$ Keldysh space, defined as

$$
\check{G} = \begin{pmatrix} \hat{G}^R & \hat{G}^K \\ 0 & \hat{G}^A \end{pmatrix} \quad , \quad \hat{G}^R = \begin{pmatrix} G^R & F^R \\ (F^R)^* & (G^R)^* \end{pmatrix}, \tag{2}
$$

where $\hat{G}^A = -\hat{\rho}_3(\hat{G}^R)^\dagger \hat{\rho}_3$, with $\hat{\rho}_3 = \mathrm{diag}(+1, +1, -1, -1)$, and $\hat{G}^K = \hat{G}^R\hat{h} - \hat{h}\hat{G}^A$ for a given distribution function $\hat{h}$ [2]. Furthermore, G^X and F^X, with $X \in \{R, A, K\}$, are 2×2 matrices in spin space. We assume time translation invariance and Fourier transform in the relative time coordinate, so that we may write $\check{G} = \check{G}(\boldsymbol{r}_0, \boldsymbol{r}_n; \varepsilon) \equiv \check{G}(\boldsymbol{r}_0, \boldsymbol{r}_n)$, where ε is the quasiparticle energy. The equation of motion may then be written as

$$
\begin{aligned}
\Big[\varepsilon\hat{\rho}_3 &- \frac{1}{2m}(-i\nabla_0\check{I} - \check{\boldsymbol{A}}(\boldsymbol{r}_0))^2 + \mu\check{I} - \check{\Sigma}(\boldsymbol{r}_0) \\
&- V_{\mathrm{imp}}(\boldsymbol{r}_0)\check{I} \Big] \check{G}(\boldsymbol{r}_0, \boldsymbol{r}_n; \varepsilon) = \delta(\boldsymbol{r}_0 - \boldsymbol{r}_n)\check{I},
\end{aligned}
\tag{3}
$$

where $\check{I}$ is the 8×8 identity matrix, $\check{\boldsymbol{A}}(\boldsymbol{r}_0)$ is the vector potential, $V_{\mathrm{imp}}(\boldsymbol{r}_0)$ is the impurity potential, and $\check{\Sigma}(\boldsymbol{r}_0)$ encompasses any other local self-energies, such as the superconducting gap, or an exchange field. The impurity potential is defined in the conventional way—as a perturbation in momentum space. Toward that end, Eq. (3) is reformulated as

$$
\begin{aligned}
\check{G}(\boldsymbol{k}_0, \boldsymbol{k}_n) = {}& \check{G}_0(\boldsymbol{k}_0, \boldsymbol{k}_n) + \int \frac{d\boldsymbol{k}_1}{(2\pi)^3} \int \frac{d\boldsymbol{k}_2}{(2\pi)^3} \ \check{G}_0(\boldsymbol{k}_0, \boldsymbol{k}_1) \\
& \times V_{\mathrm{imp}}(\boldsymbol{k}_1 - \boldsymbol{k}_2)\check{G}(\boldsymbol{k}_2, \boldsymbol{k}_n),
\end{aligned}
\tag{4}
$$

where the Fourier transform of the Green function is defined as

$$
\check{G}(\boldsymbol{k}_0, \boldsymbol{k}_n) = \int d\boldsymbol{r}_0 \int d\boldsymbol{r}_n \ \check{G}(\boldsymbol{r}_0, \boldsymbol{r}_n)e^{-i\boldsymbol{k}_0\cdot\boldsymbol{r}_0 + i\boldsymbol{k}_n\cdot\boldsymbol{r}_n}. \tag{5}
$$

Note that by changing variables to $\boldsymbol{R} = (\boldsymbol{r}_0 + \boldsymbol{r}_n)/2$ and $\boldsymbol{r} = \boldsymbol{r}_0 - \boldsymbol{r}_n$, the Fourier transform may also be written as

$$
\check{G}(\boldsymbol{k}_0, \boldsymbol{k}_n) = \int d\boldsymbol{R} \ \check{G}(\boldsymbol{k}, \boldsymbol{R})e^{-i\Delta\boldsymbol{k}\cdot\boldsymbol{R}}, \tag{6}
$$

with $\boldsymbol{k} = (\boldsymbol{k}_0 + \boldsymbol{k}_n)/2$ and $\Delta\boldsymbol{k} = \boldsymbol{k}_0 - \boldsymbol{k}_n$, and

$$
\check{G}(\boldsymbol{k}, \boldsymbol{R}) = \int d\boldsymbol{r} \ \check{G}(\boldsymbol{r}, \boldsymbol{R})e^{-i\boldsymbol{k}\cdot\boldsymbol{R}}. \tag{7}
$$

Equation (7) is known as the *mixed representation* of $\check{G}$, as it involves both the center-of-mass position $\boldsymbol{R}$ and the center-of-mass momentum $\boldsymbol{k}$. The unperturbed Green function $\check{G}_0(\boldsymbol{k}_0, \boldsymbol{k}_n)$ satisfies

$$
\begin{aligned}
\int \frac{d\boldsymbol{k}_1}{(2\pi)^3} & \Big[\Big(\varepsilon\rho_3 - \frac{k_0^2}{2m} + \mu\check{I} \Big)\delta(\boldsymbol{k}_0 - \boldsymbol{k}_1) + \frac{1}{m}\boldsymbol{k}_0 \cdot \check{\boldsymbol{A}}(\boldsymbol{k}_0 - \boldsymbol{k}_1) \\
& - \frac{1}{2m}[\check{\boldsymbol{A}}(\boldsymbol{k}_0 - \boldsymbol{k}_1)]^2 - \check{\Sigma}(\boldsymbol{k}_0 - \boldsymbol{k}_1) \Big] \check{G}_0(\boldsymbol{k}_1, \boldsymbol{k}_n) \\
& = \check{I}\delta(\boldsymbol{k}_0 - \boldsymbol{k}_n).
\end{aligned}
$$

By making use of standard techniques for diagram summation [4], taking into consideration that $\check{G}_0(\boldsymbol{k}_0, \boldsymbol{k}_n)$ depends on two

momentum indices, Eq. (4) can be written as

$$\check{G}(\boldsymbol{k}_0, \boldsymbol{k}_n) = \check{G}_0(\boldsymbol{k}_0, \boldsymbol{k}_n)$$
$$+ \int \frac{d\boldsymbol{k}_1}{(2\pi)^3} \int \frac{d\boldsymbol{k}_2}{(2\pi)^3} \check{G}_0(\boldsymbol{k}_0, \boldsymbol{k}_1) \check{\Sigma}_{\mathrm{imp}}(\boldsymbol{k}_1, \boldsymbol{k}_2) \check{G}(\boldsymbol{k}_2, \boldsymbol{k}_n),$$
$$(8)$$

with the impurity self-energy $\check{\Sigma}(\boldsymbol{k}_0, \boldsymbol{k}_n)$ defined as

$$\check{\Sigma}_{\mathrm{imp}}(\boldsymbol{k}_0, \boldsymbol{k}_n) = V_{\mathrm{imp}}(\boldsymbol{k}_0 - \boldsymbol{k}_n) + \int \frac{d\boldsymbol{k}_1}{(2\pi)^3} \int \frac{d\boldsymbol{k}_2}{(2\pi)^3}$$
$$\times V_{\mathrm{imp}}(\boldsymbol{k}_0 - \boldsymbol{k}_1) \check{G}_0(\boldsymbol{k}_1, \boldsymbol{k}_2) \check{\Sigma}_{\mathrm{imp}}(\boldsymbol{k}_2, \boldsymbol{k}_n). \quad (9)$$

It is customary to employ the self-consistent Born approximation, in which Eq. (9) is truncated at second order in V_{imp}, and the replacement $\check{G}_0 \to \check{G}$ is made on the right-hand side. The latter is equivalent to including a much greater number of diagrams in the self-energy. The impurity potential is assumed to consist of a large number of randomly distributed identical impurities, so that $V_{\mathrm{imp}}(\boldsymbol{r}) = \sum_j U(\boldsymbol{r} - \boldsymbol{r}_j)$. After impurity averaging, ignoring terms that only depend on $U(0)$ since these simply renormalize the chemical potential, the self-energy becomes

$$\check{\Sigma}_{\mathrm{imp}}(\boldsymbol{k}_0, \boldsymbol{k}_n) = \int \frac{d\boldsymbol{q}}{(2\pi)^3} |U(\boldsymbol{k}_0 - \boldsymbol{q})|^2 \check{G}(\boldsymbol{q}, \boldsymbol{q} - \Delta\boldsymbol{k}). \quad (10)$$

In the mixed representation, arrived at by Fourier transforming in the relative momentum $\Delta\boldsymbol{k}$, this expression becomes particularly simple,

$$\check{\Sigma}_{\mathrm{imp}}(\boldsymbol{k}, \boldsymbol{R}) = \int \frac{d\boldsymbol{q}}{(2\pi)^3} |U(\boldsymbol{k} - \boldsymbol{q})|^2 \check{G}(\boldsymbol{q}, \boldsymbol{R}). \quad (11)$$

By comparing with the full Fourier transform, given in Eq. (5), we may identify $\boldsymbol{R}$ as the center-of-mass position. Equation (3) takes the following form in the mixed representation:

$$\left[\varepsilon \hat{\rho}_3 - \frac{1}{2m} \left[-i \left(i\boldsymbol{k} + \frac{1}{2}\nabla_R \right) \check{I} - \check{A}(\boldsymbol{R}) \right]^2 + \mu \check{I} - \check{\Sigma}(\boldsymbol{R}) \right.$$
$$\left. - \check{\Sigma}_{\mathrm{imp}}(\boldsymbol{k}, \boldsymbol{R}) \right] \otimes \check{G}(\boldsymbol{k}, \boldsymbol{R}) = \check{I}, \quad (12)$$

where the operator $\otimes$ indicates the Moyal product, which is defined as $A(\boldsymbol{k}, \boldsymbol{R}) \otimes B(\boldsymbol{k}, \boldsymbol{R}) = e^{i(\nabla_R^{(A)} \cdot \nabla_k^{(B)} - \nabla_k^{(A)} \cdot \nabla_R^{(B)})/2} A(\boldsymbol{k}, \boldsymbol{R}) B(\boldsymbol{k}, \boldsymbol{R})$. If the spatial variation of $A(\boldsymbol{k}, \boldsymbol{R})$ and $B(\boldsymbol{k}, \boldsymbol{R})$ is slow, one may approximate $A(\boldsymbol{k}, \boldsymbol{R}) \otimes B(\boldsymbol{k}, \boldsymbol{R}) \simeq A(\boldsymbol{k}, \boldsymbol{R}) B(\boldsymbol{k}, \boldsymbol{R})$.

Equation (12) may be further simplified by introducing the quasiclassical approximation, wherein the rapid oscillations of the Green function are integrated out [3],

$$\check{g}(\boldsymbol{k}_F, \boldsymbol{R}) = \frac{i}{\pi} \int d\xi_k \, \check{G}(\boldsymbol{k}, \boldsymbol{R}), \quad (13)$$

where $\xi_k = \frac{1}{2m}(\boldsymbol{k}^2 - k_F^2)$. In Eq. (13) there is an implicit assumption that the Green function $\check{G}(\boldsymbol{k}, \boldsymbol{R})$ is strongly peaked at the Fermi level k_F, so that only the angular dependence of the momentum $\boldsymbol{k}$ appears in the quasiclassical Green function $\check{g}(\boldsymbol{k}_F, \boldsymbol{R})$. This is satisfied as long as the spatial variation of the self-energies appearing in $\check{G}$ is sufficiently slow. The quasiclassical approximation may not be applied to Eq. (12)

directly, as it contains both constant terms and terms proportional to ξ_k. These terms can be removed by employing the so-called "left-right" trick [1,5,34], where one instead considers the difference between Eq. (12) and its adjoint, thereby canceling out the problematic terms. Doing so leads to the Eilenberger equation [5],

$$i\boldsymbol{v}_F \cdot \check{\nabla}\check{g}(\boldsymbol{k}_F, \boldsymbol{r}) + [\varepsilon \hat{\rho}_3 + \check{\Sigma}(\boldsymbol{k}_F, \boldsymbol{r})$$
$$- \check{\Sigma}_{\mathrm{imp}}(\boldsymbol{k}_F, \boldsymbol{r}) \,, \; \check{g}(\boldsymbol{k}_F, \boldsymbol{r})] = 0. \quad (14)$$

Equation (14) is accompanied by a normalization condition on the quasiclassical Green function, $\check{g}^2 = \check{I}$.

In the limit of large concentrations of impurities, the effect of frequent scatterings may be included by averaging over the momentum direction. This defines a diffusive Green function $\check{g}_d = \langle \check{g} \rangle$, and its governing equation of motion, the Usadel equation [2,3,6],

$$D\nabla \cdot \check{g}_d \nabla \check{g}_d + i[\varepsilon \rho_3 - \check{\Sigma} \,, \; \check{g}_d] = 0, \quad (15)$$

where D is the diffusion constant.

B. Distinguished impurities

We next consider a case in which there is an additional impurity $\check{V}(\boldsymbol{r}_0)$ present, which may in some way be distinguished from the averaged impurities described by $\check{\Sigma}_{\mathrm{imp}}$. We further assume that this impurity is strongly localized at some position. This means that impurity averaging is not possible. Even so, the quasiclassical formulation of the equation of motion for such a system may be arrived at by perturbation theory [35]. Indeed, if any interference between the averaged and the localized impurity is neglected, the integral equation for the Green function once again takes the form of Eq. (4), where $\check{V}$ replaces V_{imp} as the perturbing potential, and $\check{G}_0$ is the Green function for a system in which $\check{\Sigma}_{\mathrm{imp}}$ is included, but where $\check{V} = 0$. By repeated iteration of this equation, it is seen that it may be written in the form

$$\check{G}(\boldsymbol{k}_0, \boldsymbol{k}_n) = \check{G}_0(\boldsymbol{k}_0, \boldsymbol{k}_n)$$
$$+ \int \frac{d\boldsymbol{k}_1}{(2\pi)^3} \int \frac{d\boldsymbol{k}_2}{(2\pi)^3} \check{G}_0(\boldsymbol{k}_0, \boldsymbol{k}_1) \check{T}(\boldsymbol{k}_1, \boldsymbol{k}_2) \check{G}_0(\boldsymbol{k}_2, \boldsymbol{k}_n),$$
$$(16)$$

with the T matrix defined as

$$\check{T}(\boldsymbol{k}_0, \boldsymbol{k}_n) = \check{V}(\boldsymbol{k}_0 - \boldsymbol{k}_n)$$
$$+ \int \frac{d\boldsymbol{k}_1}{(2\pi)^3} \int \frac{d\boldsymbol{k}_2}{(2\pi)^3} \check{V}(\boldsymbol{k}_0 - \boldsymbol{k}_1) \check{G}_0(\boldsymbol{k}_1, \boldsymbol{k}_2) \check{T}(\boldsymbol{k}_2, \boldsymbol{k}_n).$$
$$(17)$$

If the distinguished impurity is localized at a position $\boldsymbol{R}_0$, the Fourier transform of the impurity potential is given as $\check{V}(\boldsymbol{q}) = \check{V}_0(\boldsymbol{q})e^{-i\boldsymbol{q} \cdot \boldsymbol{R}_0}$, where $\check{V}_0(\boldsymbol{q})$ is a slowly varying function of $\boldsymbol{q}$. By inserting this into Eq. (17), it is seen that the T matrix can be written as

$$\check{T}(\boldsymbol{k}_0, \boldsymbol{k}_n) = \check{T}_0(\boldsymbol{k}_0, \boldsymbol{k}_n)e^{-i(\boldsymbol{k}_0 - \boldsymbol{k}_n) \cdot \boldsymbol{R}_0}, \quad (18)$$

where $\check{T}_0(\boldsymbol{k}_0, \boldsymbol{k}_n)$ has the exact same form as Eq. (17), with the replacements $\check{V} \to \check{V}_0$ and $\check{T} \to \check{T}_0$. It is thus a slowly varying function of $\boldsymbol{k}_0$ and $\boldsymbol{k}_n$, so that we may approximate

$\check{T}_0(\boldsymbol{k}_0, \boldsymbol{k}_n) \simeq \check{T}_0(\boldsymbol{k}, \boldsymbol{k})$, where $\boldsymbol{k}$ is the center-of-mass momentum. In the mixed representation, the T matrix then becomes

$$\check{T}(\boldsymbol{k}, \boldsymbol{R}) = \check{T}_0(\boldsymbol{k}, \boldsymbol{k})\delta(\boldsymbol{R} - \boldsymbol{R}_0). \tag{19}$$

The equation of motion in the mixed representation becomes identical to Eq. (12), but with the addition of a term $\check{T}(\boldsymbol{k}, \boldsymbol{R}) \otimes \check{G}_0(\boldsymbol{k}, \boldsymbol{R})$, which is once again approximated by a product. Following the same steps used in deriving Eq. (14) then gives

$$i\boldsymbol{v}_F \cdot \check{\nabla}\check{g}(\boldsymbol{k}_F, \boldsymbol{R}) + [\varepsilon\check{\rho}_3 + \check{\Sigma}(\boldsymbol{k}_F, \boldsymbol{R})$$
$$- \check{\Sigma}_{\text{imp}}(\boldsymbol{k}_F, \boldsymbol{R}) \, , \, \check{g}(\boldsymbol{k}_F, \boldsymbol{R})]$$
$$= [\check{t}_0(\boldsymbol{k}_F, \boldsymbol{R}) \, , \, \check{g}(\boldsymbol{k}_F, \boldsymbol{R})]\delta(\boldsymbol{R} - \boldsymbol{R}_0), \tag{20}$$

where $\check{t}_0(\boldsymbol{k}_F, \boldsymbol{R})$ is the quasiclassical version of the T matrix, given as

$$\check{t}_0(\boldsymbol{k}_F, \boldsymbol{R}) = \check{V}_0(0)$$
$$+ N_0 \int \frac{d\Omega_q}{4\pi} \, \check{V}_0(\boldsymbol{k}_F - \boldsymbol{q}_F) \, \check{g}(\boldsymbol{q}_F, r)\check{t}_0(\boldsymbol{q}_F, \boldsymbol{R}). \tag{21}$$

C. Interface

An interface, which is a plane in three dimensions, may be treated as an impurity that is localized along a specific direction, having translation invariance along the two orthogonal directions. This implies that a similar perturbation expansion as was discussed in the previous section may be applied also in this case. However, the interface may not be constructed from an ensemble of point impurities satisfying Eq. (20) [35]. This is because (i) the pointlike nature of the impurity was explicitly made use of in Eq. (18), and (ii) interference between different impurities is neglected. Instead, we follow Ref. [36] and consider a model surface of the form $\check{V}(\boldsymbol{r}_0) = \check{V}_0\delta[\hat{n} \cdot (\boldsymbol{r}_0 - \boldsymbol{R}_n)]$, where $\hat{n}$ is the normal vector of the surface, and $\boldsymbol{R}_n$ is a point on the surface. To simplify the notation, we define $\hat{n} \cdot \boldsymbol{r}_0 = r_\perp$ and $\hat{n} \cdot \boldsymbol{R}_n = R_0$. Furthermore, we have that $\boldsymbol{r}_0 = r_\perp\hat{n} + \boldsymbol{r}_{||}$. Insertion into Eq. (17) allows us to define

$$\check{T}(\boldsymbol{k}_0, \boldsymbol{k}_n) = \check{T}_s(\boldsymbol{k}_{0,||}, \boldsymbol{k}_{n,||})e^{-i(k_{0,\perp} - k_{n,\perp})R_0}, \tag{22}$$

with $k_{j,\perp}$ and $\boldsymbol{k}_{j,||}$, respectively, the orthogonal and parallel components of momentum j, with respect to the surface. Moreover,

$$\check{T}_s(\boldsymbol{k}_{0,||}, \boldsymbol{k}_{n,||}) = \check{V}_0 (2\pi)^2 \delta(\boldsymbol{k}_{0,||} - \boldsymbol{k}_{n,||})$$
$$+ \check{V}_0 \int \frac{d\boldsymbol{q}_{||}}{(2\pi)^2} \check{Q}(\boldsymbol{k}_{0,||}, \boldsymbol{q}_{||})\check{T}_s(\boldsymbol{q}_{||}, \boldsymbol{k}_{n,||}), \tag{23}$$

where

$$\check{Q}(\boldsymbol{k}_{0,||}, \boldsymbol{q}_{||})$$
$$= \int \frac{dk_{1,\perp}}{2\pi} \int \frac{dk_{2,\perp}}{2\pi} \check{G}_0(\boldsymbol{k}_{0,||} + k_{1,\perp}\hat{n}, \boldsymbol{q}_{||} + k_{2,\perp}\hat{n})$$
$$\times e^{i(k_{1,\perp} - k_{2,\perp})R_0}$$
$$= \int \frac{dq_\perp}{2\pi} \check{G}_0(\boldsymbol{k}_{0,||}, \boldsymbol{q}_{||}; q_\perp, R_0). \tag{24}$$

In the mixed representation, Eq. (22) simply becomes

$$\check{T}(\boldsymbol{k}, \boldsymbol{R}) = \check{T}_s(\boldsymbol{k}_{||}, \boldsymbol{R}_{||})\,\delta(R_\perp - R_0), \tag{25}$$

with

$$\check{T}_s(\boldsymbol{k}_{||}, \boldsymbol{R}_{||}) = \check{V}_0 + \check{V}_0 \, \check{Q}(\boldsymbol{k}_{||}, \boldsymbol{R}_{||}) \otimes \check{T}_s(\boldsymbol{k}_{||}, \boldsymbol{R}_{||})$$
$$\simeq \check{V}_0 + \check{V}_0 \, \check{Q}(\boldsymbol{k}_{||}, \boldsymbol{R}_{||}) \, \check{T}_s(\boldsymbol{k}_{||}, \boldsymbol{R}_{||}) \tag{26}$$

and

$$\check{Q}(\boldsymbol{k}_{||}, \boldsymbol{R}_{||}) = \int \frac{dq_\perp}{2\pi} \, \check{G}_0(q_\perp\hat{n} + \boldsymbol{k}_{||}, R_0\hat{n} + \boldsymbol{R}_{||}). \tag{27}$$

To find the quasiclassical version of Eq. (27), we insert the inverse of Eq. (13), namely $\check{G}(\boldsymbol{k}, \boldsymbol{R}) = -i\pi \check{g}(\boldsymbol{k}_F, \boldsymbol{R}) \, \delta(\frac{1}{2m}(\boldsymbol{k}^2 - k_F^2))$. Performing the integral over $q_\perp$ gives

$$\check{Q}(\boldsymbol{k}_{||}, \boldsymbol{R}_{||}) = -\frac{i}{|v_n|}\check{\bar{g}}(\boldsymbol{k}_{||}, \boldsymbol{R}_{||}), \tag{28}$$

with $v_n = \frac{\boldsymbol{k}_F \cdot \hat{n}}{m}$,

$$\check{\bar{g}}(\boldsymbol{k}_{||}, \boldsymbol{R}_{||}) = \tfrac{1}{2}[\check{g}(\boldsymbol{k}_+, \boldsymbol{R}_{||} + R_0\hat{n}) + \check{g}(\boldsymbol{k}_-, \boldsymbol{R}_{||} + R_0\hat{n})], \tag{29}$$

and $\boldsymbol{k}_\pm = \pm\sqrt{k_F^2 - \boldsymbol{k}_{||}^2}\hat{n} + \boldsymbol{k}_{||}$. This means that the quasiclassical T matrix for an interface,

$$\check{t}_s(\boldsymbol{k}_{||}, \boldsymbol{R}_{||}) = \check{V}_0 - \frac{i}{|v_n|}\check{V}_0 \check{\bar{g}}(\boldsymbol{k}_{||}, \boldsymbol{R}_{||}) \check{t}_s(\boldsymbol{k}_{||}, \boldsymbol{R}_{||}), \tag{30}$$

only depends on the *average* of Green functions whose normal components of the momentum direction point, respectively, toward and away from the interface. The equation of motion takes the same form as Eq. (20), with the replacements $\check{t}_0 \to \check{t}_s$ and $\delta(\boldsymbol{R} - \boldsymbol{R}_0) \to \delta(R_\perp - R_0)$.

D. Formulation of boundary conditions

We next want to consider an interface between two different materials. This is done by expanding Hilbert space into two domains, which represent the two sides of the interface. The Green function in this space can be written as

$$\check{g} = \begin{pmatrix} \check{g}_{11} & \check{g}_{12} \\ \check{g}_{21} & \check{g}_{22} \end{pmatrix}, \tag{31}$$

where the subscripts "1" and "2" indicate the two materials. The matrices $\check{g}_{12}$ and $\check{g}_{21}$ contain creation and annihilation operators on both sides of the interface. These quantities are drone amplitudes that do not have physical meaning, and since they will be eliminated from the theory, we do not specify them further. The interface itself is described as an infinite surface located at some position, and which mediates tunneling between its two sides. Such a potential may be described as

$$\check{V}_0 = \begin{pmatrix} 0 & \check{V}_0 \\ \check{V}_0 & 0 \end{pmatrix}. \tag{32}$$

The surface is treated as a perturbation, and the T matrix is given by Eq. (30).

Without the presence of the interface potential, there is no coupling between the two sides. The unperturbed Green function, $\check{g}_0$, therefore takes the form

$$\check{g}_0 = \begin{pmatrix} \check{g}_{0,1} & 0 \\ 0 & \check{g}_{0,2} \end{pmatrix}. \tag{33}$$

Note that Eq. (33) satisfies a generalized version of Eq. (14), given as

$$i\boldsymbol{k}_F \cdot \bar{\boldsymbol{\nabla}}\check{g}_0 + \left[\check{\Xi} \,,\, \check{g}_0\right] = 0, \tag{34}$$

where

$$\check{\Xi} = \begin{pmatrix} \varepsilon\check{\rho}_3 + \check{\Sigma}_1 - \check{\Sigma}_{\mathrm{imp}} & 0 \\ 0 & \varepsilon\check{\rho}_3 + \check{\Sigma}_2 - \check{\Sigma}_{\mathrm{imp}} \end{pmatrix}. \tag{35}$$

Similarly, we can define an equation of motion for $\check{g}$ as

$$i\boldsymbol{k}_F \cdot \bar{\boldsymbol{\nabla}}\check{g} + \left[\check{\Xi} \,,\, \check{g}x\right] = [\check{t}_s \,,\, \check{g}_0]\delta(R_\perp - R_0), \tag{36}$$

which is clearly satisfied by $\check{g}_{11}$ and $\check{g}_{22}$. To find a relationship between $\check{g}$ and $\check{g}_0$, Eq. (36) may be integrated along a small interval surrounding R_0. For a trajectory (as determined by $\boldsymbol{k}_F$) crossing the interface, this leads to

$$\check{g}(R_0^+) - \check{g}(R_0^-) = \frac{1}{i\boldsymbol{k}_F \cdot \hat{n}}[\check{t}_s \,,\, \check{g}_0(R_0)], \tag{37}$$

where we henceforth define $\hat{n}$ to be an outward-pointing surface normal. While Eq. (31) is defined everywhere in space, its diagonal elements, $\check{g}_{11}$ and $\check{g}_{22}$, only make sense physically in, respectively, material 1 and 2, i.e., on opposite sides of the interface. Without loss of generality, we choose material 1 to be the active material, that is, the material for which we formulate the boundary conditions. This means that $\hat{n}$ points from material 1 to material 2. If $\check{g}(R_0^-)$ is located in material 1, we thus need to eliminate $\check{g}(R_0^+)$, which is located in material 2. This can be done by making use of a generalized normalization condition, given by [37–39]

$$[\check{g} + \mathrm{sgn}(\boldsymbol{k}_F \cdot \hat{n})][\check{g}_0 - \mathrm{sgn}(\boldsymbol{k}_F \cdot \hat{n})] = 0, \tag{38}$$

$$[\check{g}_0 + \mathrm{sgn}(\boldsymbol{k}_F \cdot \hat{n})][\check{g} - \mathrm{sgn}(\boldsymbol{k}_F \cdot \hat{n})] = 0. \tag{39}$$

These conditions are clearly satisfied in the special case of $\check{g} = \check{g}_0$. That they are valid also in the more general case is shown in Appendix A. In material 1, the Green function that describes a particle on a trajectory toward the interface satisfies $\mathrm{sgn}(\boldsymbol{k}_F \cdot \hat{n}) = +1$. We label these Green functions as $\check{g}_{11}^i$ and $\check{g}_{0,1}^i$, indicating that they are incoming with respect to the interface. Similarly, Green functions where $\mathrm{sgn}(\boldsymbol{k}_F \cdot \hat{n}) = -1$ are labeled as outgoing; $\check{g}_{11}^o$ and $\check{g}_{0,1}^o$. By evaluating Eqs. (38) and (39) immediately adjacent to, and on opposite sides of, the interface, and inserting Eq. (37), the following boundary conditions may be derived at the interface:

$$\check{g}_{11}^i = \check{g}_{0,1}^i + \frac{1}{2i|v_n|}\big(\check{g}_{0,1}^i - \check{I}\big)\check{t}_{s,11}\big(\check{g}_{0,1}^i + \check{I}\big), \tag{40}$$

$$\check{g}_{11}^o = \check{g}_{0,1}^o + \frac{1}{2i|v_n|}\big(\check{g}_{0,1}^o + \check{I}\big)\check{t}_{s,11}\big(\check{g}_{0,1}^o - \check{I}\big). \tag{41}$$

Due to the form of the interface potential $\check{V}_0$, $\check{t}_s$ is in general dense in 1-2 space. However, a closed solution for the $\check{t}_{s,11}$ element may be found by iterating Eq. (30) once [24],

$$\check{t}_{s,11} = -\frac{i}{|v_n|}\check{V}_0\,\check{g}_{0,2}\check{V}_0 - \frac{1}{v_n^2}\check{V}_0\,\check{g}_{0,2}\check{V}_0\,\check{g}_{0,1}\check{t}_{s,11}. \tag{42}$$

Note that $\check{g}_{0,j} = \frac{1}{2}(\check{g}_{0,j}^i + \check{g}_{0,j}^o)$ for a given side of the interface j. Equation (42) may easily be solved for $\check{t}_{s,11}$, giving

$$\check{t}_{s,11} = \frac{1}{i|v_n|}\left[\check{I} + \frac{1}{v_n^2}\check{V}_0\,\check{g}_{0,2}\check{V}_0\,\check{g}_{0,1}\right]^{-1}\check{V}_0\,\check{g}_{0,2}\check{V}_0. \tag{43}$$

To summarize the progress so far, we have found boundary conditions for the quantities $\check{g}_{11}^i$ and $\check{g}_{11}^o$, given in Eqs. (40) and (41), expressed entirely in terms of $\check{g}_{0,j}^{i/o}$. While these unperturbed Green functions exist everywhere in space, they are only physically valid solutions on their respective sides of the interface. Furthermore, as discussed in Ref. [25] and in Appendix B, they can be easily modified to describe a system with an impenetrable interface by having them satisfy the condition

$$\check{g}_{0,j}^o = \check{S}\check{g}_{0,j}^i\check{S}^\dagger \tag{44}$$

at the location of the interface, where $\check{S}$ is a scattering matrix. For Nambu $\otimes$ spin space, the scattering matrix has the structure

$$\hat{S} = \begin{pmatrix} S(\boldsymbol{k}) & 0 \\ 0 & S^*(-\boldsymbol{k}) \end{pmatrix}. \tag{45}$$

For spin-independent scattering, $\check{S} = \check{I}$. The point is that rather than considering the interface as a perturbation to omnipresent Green functions, we may exploit the fact that we only evaluate $\check{g}_{0,j}$ in one region of space to redefine them to represent a system with an impenetrable interface, simply by imposing Eq. (44). This provides significant benefits. Ultimately, the goal is to derive boundary conditions for diffusive systems, which are governed by diffusive Green functions $\check{g}_{d,j}$. Even for such a system, there will always be a ballistic zone immediately surrounding an interface, since a particle traveling away from the interface will traverse a distance on the order of the mean free path before encountering its first impurity. Diffusive systems with an interface are therefore governed by ballistic Green functions $\check{g}_{0,j}^{i/o}$, with $\check{\Sigma}_{\mathrm{imp}} = 0$, close to the interface, and by $\check{g}_{d,j}$ far away from the interface. In between is an asymptotic matching region known as the *isotropization zone*, within which the momentum dependences of the ballistic Green functions are averaged out by repeated impurity scatterings. Matching the Green functions of the two regimes is only possible if the following conditions are satisfied [15,17,18]:

$$\big(\check{g}_{0,j}^i + \check{I}\big)\big(\check{g}_{d,j} - \check{I}\big) = 0, \tag{46}$$

$$\big(\check{g}_{d,j} + \check{I}\big)\big(\check{g}_{0,j}^i - \check{I}\big) = 0, \tag{47}$$

$$\big(\check{g}_{0,j}^o - \check{I}\big)\big(\check{g}_{d,j} + \check{I}\big) = 0, \tag{48}$$

$$\big(\check{g}_{d,j} - \check{I}\big)\big(\check{g}_{0,j}^o + \check{I}\big) = 0. \tag{49}$$

Using Eqs. (46)–(49) and Eq. (44), the ballistic Green functions at the interface may be expressed in terms of their diffusive counterparts as

$$\check{g}_{0,j}^i = (\check{S}^\dagger\check{g}_{d,j}\check{S} + \check{g})^{-1}(2\check{I} + \check{g} - \check{S}^\dagger\check{g}_{d,j}\check{S}), \tag{50}$$

$$\check{g}_{0,j}^o = (2\check{I} + \check{g} - \check{S}\check{g}_{d,j}\check{S}^\dagger)(\check{S}\check{g}_{d,j}\check{S}^\dagger + \check{g})^{-1}. \tag{51}$$

The quasiclassical boundary conditions are completed by computing the *matrix current* directed at the interface. In the ballistic zone, it is defined as

$$\check{J}_n = \int \frac{d\Omega}{2\pi}\hat{n} \cdot \boldsymbol{v}_F\big(\check{g}_{jj}^i - \check{g}_{jj}^o\big), \tag{52}$$
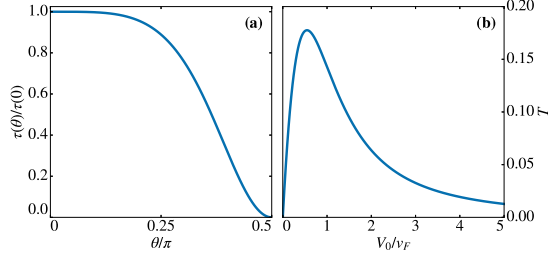
FIG. 1. (a) The angular distribution of the coupling constant $\tau(\theta)$, as determined from Eq. (55). (b) The strength of the angularly averaged coupling constant T in the tunneling limit, as given in Eq. (57).

where the integration measure is an angular average over a hemisphere. In the diffusive zone, the matrix current is given as [15]

$$\check{J}_n = \sigma_j \hat{n} \cdot \check{g}_{d,j} \mathbf{\nabla} \check{g}_{d,j}, \tag{53}$$

where σ_j is the normal state conductivity of material j. The matrix current is conserved across the isotropization zone [18], and hence Eq. (53) may be equated with Eq. (52), which in turn is determined from Eqs. (40) and (41) and Eqs. (50) and (51), thus giving the complete boundary conditions solely in terms of the diffusive Green functions.

For spin-independent scattering we have $\check{S} = \check{I}$, which gives $\check{g}_{0,j}^i = \check{g}_{0,j}^o = \check{g}_{d,j}$. This means that the difference between Eqs. (40) and (41) reduces to $\check{g}_{11}^i - \check{g}_{11}^o = \frac{1}{i|v_n|}[\check{t}_{11}, \check{g}_{d,1}]$. By using Eqs. (43), (52), and (53), one may, with some algebra [23], produce Nazarov's boundary conditions [15],

$$\sigma_1 \hat{n} \cdot \check{g}_{d,1} \mathbf{\nabla} \check{g}_{d,1} = \int_0^{\frac{\pi}{2}} d\theta \, \frac{\sin\theta \, \tau(\theta)[\check{g}_{d,1} \, , \, \check{g}_{d,2}]}{4\check{I} + \tau(\theta)(\{\check{g}_{d,1} \, , \, \check{g}_{d,2}\} - 2\check{I})}, \tag{54}$$

where the coupling constant $\tau(\theta)$ is given as

$$\tau(\theta) = \frac{4\upsilon^2 \cos^2\theta}{(\cos^2\theta + \upsilon^2)^2}, \tag{55}$$

with $\upsilon = V_0/v_F$, and θ is the angle of incidence with respect to the interface. $\tau(\theta)$ is shown in Fig. 1(a), where it is seen that it attains its maximum value for normal incidence ($\theta = 0$), and goes to zero for trajectories parallel to the interface ($\theta = \frac{\pi}{2}$), which is intuitively reasonable.

When $\tau(\theta)$ is small, e.g., in the tunneling limit, we may neglect its contribution to the denominator of Eq. (54). This gives the Kupriyanov-Lukichev boundary conditions [14],

$$\hat{n} \cdot \check{g}_{d,1} \mathbf{\nabla} \check{g}_{d,1} = T[\check{g}_{d,1}, \check{g}_{d,2}], \tag{56}$$

where T is the angular average of the coupling constant, and it is given as

$$T = \frac{\upsilon^2}{2\sigma_1}\left[\frac{1}{\upsilon}\arctan\left(\frac{1}{\upsilon}\right) - \frac{1}{1 + \upsilon^2}\right]. \tag{57}$$

T is shown for increasing V_0 in Fig. 1(b). For $V_0 = 0$, there is no coupling between the two sides. The system reduces to its unperturbed state in which the interface is impenetrable,

and hence $T = 0$. For large values of V_0, T also goes to zero. The reason for this is that when the barrier potential increases, incoming particles are more likely to be reflected than transmitted, which means that the two sides eventually become decoupled also in this limit.

III. INTERFACES WITH SPIN-ORBIT COUPLING

We will now consider an interface to a material within which spin-orbit coupling plays a prominent role, for instance a heavy metal. This means that the transmission probability will depend on both the spin of the incoming particle and its angle of incidence. We model this with a Rashba-like tunneling coupling,

$$\check{V}_0 = w\check{I} + w_\alpha(\hat{n}_\alpha \times \hat{\boldsymbol{k}}_F) \cdot \check{\boldsymbol{\sigma}}, \tag{58}$$

where $\hat{n}_\alpha$ is a unit vector indicating the direction in which the symmetry is broken, and w is a spin-independent contribution to the tunneling between the two sides separated by the interface, while w_α is the strength of the spin-orbit coupling contribution to the tunneling. As the barrier region increases in width, both w and w_α decrease toward zero.

A. Scattering matrix

As a step toward formulating the boundary conditions, we need to find the scattering matrix for a system in which the interface is impenetrable. However, even though the probability for transmission through the interface is zero, an incoming particle may still penetrate the barrier for some distance before being reflected. While inside the scattering region, the particle will experience spin-orbit coupling and accumulate a spin-dependent phase, the size of which depends on the incoming angle of incidence. To find the scattering matrix for this process, we assume that sufficiently close to the interface, the interface potential is large enough to dominate all other self-energies [17]. This means that we may follow the procedure of Ref. [19] and describe the interface as a step function potential in a free-electron gas. For simplicity, we use a cylindrical coordinate system in which the z axis is aligned with the surface normal. The Hamiltonian for such a system is given as

$$H = -\frac{1}{2m}\nabla^2 - \mu + [\mu + \varepsilon_g + i\alpha(\hat{z} \times \mathbf{\nabla}) \cdot \boldsymbol{\sigma}]\theta(z), \tag{59}$$

where α expresses the strength of the spin-orbit interaction at the interface, $\mu = \varepsilon_F$ is the chemical potential, and $\theta(z)$ is the Heaviside step function. We consider particles with energies close to the Fermi energy, meaning excitation energies $\varepsilon \simeq 0$, which is the relevant energy regime for quasiclassical theory. The wave function, therefore, satisfies $H\psi \simeq 0$. The parameter ε_g expresses an energy gap, and it is included to ensure that the wave function is evanescent in the barrier region. Since the interface is assumed to be perfectly smooth, the momentum parallel to the interface, $\boldsymbol{k}_{||}$, is conserved during the scattering process. Hence, we may use the ansatz $\psi(\boldsymbol{r}) = e^{i\boldsymbol{k}_{||}\cdot\boldsymbol{r}_{||}}\phi(z)$. Equation (59) then takes the form

$$\phi''(z) + [2m\varepsilon_F - \boldsymbol{k}_{||}^2]\phi(z) = 0, \quad z < 0, \tag{60}$$

$$\phi''(z) - [\boldsymbol{k}_{||}^2 + 2m[\varepsilon_g + \alpha(\hat{z} \times \boldsymbol{k}_{||}) \cdot \boldsymbol{\sigma}]]\phi(z) = 0, \quad z > 0. \tag{61}$$

For $z < 0$, the solution of Eq. (60) is given as

$$\phi(z) = \begin{pmatrix} A_1 \\ A_2 \end{pmatrix} e^{ik_\perp z} + \begin{pmatrix} B_1 \\ B_2 \end{pmatrix} e^{-ik_\perp z}, \qquad (62)$$

where $k_\perp = \sqrt{k_F^2 - \mathbf{k}_{||}^2}$. For $z > 0$, we get

$$\phi(z) = C \begin{pmatrix} 1 \\ -ie^{i\varphi} \end{pmatrix} e^{-q_+ z} + D \begin{pmatrix} 1 \\ ie^{i\varphi} \end{pmatrix} e^{-q_- z}, \qquad (63)$$

where φ is the azimuthal incidence angle. The momentum $q_\pm$ is given as

$$q_\pm = \sqrt{\mathbf{k}_{||}^2 + 2m(\varepsilon_g \pm \alpha|\mathbf{k}_{||}|)}. \qquad (64)$$

The scattering matrix is found by relating the coefficients $A_{1,2}$ to $B_{1,2}$ via the matrix equation $B = SA$. This is done by enforcing continuity of ϕ and ϕ' at $z = 0$, and it leads to

$$S = \frac{1}{(k_\perp + iq_+)(k_\perp + iq_-)}$$
$$\times \begin{pmatrix} k_\perp^2 + q_+ q_- & e^{-i\varphi} k_\perp(q_+ - q_-) \\ e^{i\varphi} k_\perp(q_- - q_+) & k_\perp^2 + q_+ q_- \end{pmatrix}. \qquad (65)$$

Since the scattering matrix is unitary, $SS^\dagger = I$, it may be parametrized as

$$S = e^{i\beta} e^{i\gamma(\hat{e} \cdot \boldsymbol{\sigma})} = e^{i\beta}(\cos\gamma + i\hat{e} \cdot \boldsymbol{\sigma} \sin\gamma), \qquad (66)$$

where γ is a spin mixing angle and $\hat{e}$ is a unit vector. By inspection, we see that we may define $\hat{e} \cdot \boldsymbol{\sigma} = -\sigma_x \sin\theta \sin\varphi + \sigma_y \sin\theta \cos\varphi$. To find an expression for γ, we define the constants $a = \sqrt{\frac{\varepsilon_g}{\varepsilon_F}}$ and $b = \frac{2m\alpha}{k_F}$. The former expresses the strength of the barrier potential, and the latter the strength of the spin-orbit coupling. Furthermore, we have $|\mathbf{k}_{||}| = k_F \sin\theta$, where $\theta \in [0, \pi/2]$ is the polar angle of incidence. We assume that the barrier potential is strong, so that an incoming particle only penetrates a short distance into the scattering region before being reflected, and hence $a \gg b$. From Eq. (65) we may then identify the spin mixing angle as

$$\gamma = \arctan\left(\frac{k_\perp(q_+ - q_-)}{\sin\theta\left(k_\perp^2 + q_+ q_-\right)}\right) \simeq K\cos\theta, \qquad (67)$$

with $K = \frac{b}{a^3}$ when we assume that $a \gg 1$, corresponding to a large band gap in the insulator. The parameter β describes an overall phase, which is inconsequential for the boundary conditions, and hence we set $\beta = 0$. In coordinate free form, the scattering matrix therefore takes the form

$$S = e^{i\gamma(\hat{n}_\alpha \times \hat{k}) \cdot \boldsymbol{\sigma}}. \qquad (68)$$

As before, $\hat{n}_\alpha$ is a unit vector that is either parallel or antiparallel to the interface normal, depending on the direction of symmetry breaking. In Nambu space, the scattering matrix becomes

$$\hat{S} = \begin{pmatrix} S(\mathbf{k}) & 0 \\ 0 & S^*(-\mathbf{k}) \end{pmatrix} = e^{i\gamma(\hat{n}_\alpha \times \hat{k}) \cdot \hat{\boldsymbol{\sigma}} \hat{\rho}_3}, \qquad (69)$$

with $\hat{\boldsymbol{\sigma}} = \text{diag}(\boldsymbol{\sigma} , \boldsymbol{\sigma}^*)$. Note that the spin mixing angle is antisymmetric in $\mathbf{k}$, e.g., $\gamma(\mathbf{k}) = -\gamma(-\mathbf{k})$. Finally, the scattering matrix is diagonal in Keldysh space, e.g., $\check{S} = \text{diag}(\hat{S} , \hat{S})$.

B. Boundary conditions

Finding the correct boundary conditions has now become a matter of identifying the terms in Eq. (52). To achieve this, we include only the lowest-order tunneling contributions,

$$\check{t}_{s,11} \simeq \frac{1}{i|v_n|} \check{V}_0 \check{g}_{0,2} \check{V}_0.$$
$$= \frac{1}{i|v_n|} \left[w^2 \check{g}_{0,2} + w_\alpha w \{\check{g}_{0,2}, \check{\zeta}_k\} + w_\alpha^2 \check{\zeta}_k \check{g}_{0,2} \check{\zeta}_k \right], \quad (70)$$

where $\check{\zeta}_k = (\hat{n}_\alpha \times \hat{k}) \cdot \check{\boldsymbol{\sigma}} \check{\rho}_3$. Furthermore, the spin mixing angle γ is assumed to be small, and we therefore keep terms in the scattering matrix only up to second order. This gives

$$\check{S} \simeq \left(1 - \frac{1}{2}\gamma^2\right)\check{I} + i\gamma\check{\zeta}_k. \qquad (71)$$

In addition, we approximate

$$[\check{S}^\dagger \check{g}_{d,j}\check{S} + \check{g}_{d,j}]^{-1} = \frac{1}{2}\left[\check{I} + \frac{1}{2}(\check{g}_{d,j}\check{S}^\dagger \check{g}_{d,j}\check{S} - \check{I})\right]^{-1} \check{g}_{d,j},$$
$$\simeq \frac{1}{2}\left[\check{I} - \frac{1}{2}(\check{g}_{d,j}\check{S}^\dagger \check{g}_{d,j}\check{S} - \check{I})\right]\check{g}_{d,j},$$

and similarly for $[\check{S}\check{g}_{d,j}\check{S}^\dagger + \check{g}_{d,j}]^{-1}$, leading to

$$\check{g}_{0,j}^i \simeq \frac{1}{2}\check{I} + \frac{3}{2}\check{g}_{d,j} - \frac{1}{2}\check{S}^\dagger \check{g}_{d,j}\check{S} - \frac{1}{2}\check{g}_{d,j}\check{S}^\dagger \check{g}_{d,j}\check{S}\check{g}_{d,j}, \quad (72)$$

$$\check{g}_{0,j}^o \simeq \frac{1}{2}\check{I} + \frac{3}{2}\check{g}_{d,j} - \frac{1}{2}\check{S}\check{g}_{d,j}\check{S}^\dagger \check{g} - \frac{1}{2}\check{g}_{d,j}\check{S}\check{g}_{d,j}\check{S}^\dagger \check{g}_{d,j}. \quad (73)$$

By performing the first-order expansion in this way, we ensure that in the limit of spin-independent scattering, $\check{S} = \check{I}$, we get $\check{g}_{0,j}^i = \check{g}_{0,j}^o = \check{g}_{d,j}$. By inserting Eq. (71), we get

$$\check{g}_{0,j}^i \simeq \check{g}_{d,j} - \frac{1}{2}\gamma^2(\check{g} - \check{I}) + \frac{1}{2}i\gamma(\check{g}_{d,j} - \check{I})[\check{\zeta}_k , \check{g}_{d,j}]$$
$$- \frac{1}{2}\gamma^2 \check{g}\check{\zeta}_k\check{g}\check{\zeta}_k(\check{g} + \check{I}), \qquad (74)$$

$$\check{g}_{0,j}^o \simeq \check{g}_{d,j} - \frac{1}{2}\gamma^2(\check{g} - \check{I}) + \frac{1}{2}i\gamma(\check{g}_{d,j} + \check{I})[\check{\zeta}_k , \check{g}_{d,j}]$$
$$- \frac{1}{2}\gamma^2(\check{g} + \check{I})\check{\zeta}_k\check{g}\check{\zeta}_k\check{g}. \qquad (75)$$

Finally, we compute the full Green functions from Eqs. (40) and (41), and we find the boundary conditions from Eqs. (52) and (53). Note that due to the angular averaging, all odd terms in $\check{\zeta}_k = (\hat{n}_\alpha \times \hat{k}) \cdot \check{\boldsymbol{\sigma}} \check{\rho}_3$ cancel, and thus we remove them immediately. Furthermore, the spin-orbit coupling is assumed to stem from the interface, which means that $\hat{n}_\alpha$ is parallel to $\hat{n}$. Since only even orders of the former appear, we may set $\hat{n}_\alpha = \hat{n}$. The matrix current is then given as

$$\sigma_1 \hat{n} \cdot \check{g}_1 \nabla \check{g}_1 = \int \frac{d\Omega}{2\pi} \frac{1}{|v_n|} [\check{g}_1 , \check{\mathcal{I}}], \qquad (76)$$

with $d\Omega = \sin\theta\, d\theta\, d\phi$, $v_n = v_F \cos\theta$, and

$$\check{\mathcal{I}} = w^2 \check{g}_2 + \check{\zeta}_k \left(w_\alpha^2 \check{g}_2 + \frac{1}{2}\gamma^2 \check{g}_1\right)\check{\zeta}_k$$
$$+ \frac{1}{2}i\gamma w_\alpha w \{\check{g}_2[\check{\zeta}_k, \check{g}_2], \check{\zeta}_k\}$$
$$+ \frac{1}{2}i\gamma w_\alpha w(\{\check{g}_2, \check{\zeta}_k\}\check{g}_1\check{\zeta}_k + \check{\zeta}_k\check{g}_1\{\check{g}_2, \check{\zeta}_k\}), \qquad (77)$$

where we have neglected terms of order $w^2\gamma^2$. From the ϕ integration we find that, for an arbitrary matrix $\check{M}$,

$$\int_0^{2\pi} d\phi\, \check{\zeta}_k \check{M} \check{\zeta}_k = \pi \sin^2\theta\, \check{\sigma}_{||} \check{M} \check{\sigma}_{||},$$

where $\check{\sigma}_{||} = [\check{\sigma} - \hat{n}(\hat{n} \cdot \check{\sigma})]\check{\rho}_3$, i.e., only spin directions parallel to the interface contribute to the boundary conditions.

The θ integration of the spin-independent term in Eq. (76) diverges. However, when $\alpha = 0$, we know that including all orders of the T matrix, given in Eq. (43), yields a finite expression—namely Eq. (54). This means that the divergence appears when the T matrix is truncated to give Eq. (70). The interpretation of this is that microscopic analytical expressions for the coupling constants due to w, w_α, and γ cannot be found within the present theory, and they instead become input parameters. After the θ integration, therefore, we get

$$\begin{aligned}
\hat{n} \cdot \check{g}_1 \nabla \check{g}_1 = {} & T[\check{g}_1, \check{g}_2] + T_\alpha[\check{g}_1, \check{\sigma}_{||}\check{g}_2\check{\sigma}_{||}] + T'_\alpha[\check{g}_1, \check{\sigma}_{||}\check{g}_1\check{\sigma}_{||}] \\
& + i\sqrt{T''_\alpha T}[\check{g}_1, \{\check{g}_2[\check{\sigma}_{||}, \check{g}_2], \check{\sigma}_{||}\}] \\
& + i\sqrt{T''_\alpha T}[\check{g}_1, \{\check{g}_2, \check{\sigma}_{||}\}\check{g}_1\check{\sigma}_{||} + \check{\sigma}_{||}\check{g}_1\{\check{g}_2, \check{\sigma}_{||}\}],
\end{aligned}$$

$$(78)$$

where $T''_\alpha = \frac{1}{2}T_\alpha T'_\alpha$. The parameter T may be identified by comparing with Eq. (56), and is hence given by Eq. (57). The parameter T_α arises from the spin-orbit coupling part (w_α) of the tunneling potential in Eq. (58), whereas T'_α arises from the interfacial spin-orbit coupling (α) giving rise to a spin-mixing angle in Eq. (67). Equation (78) is the main result of this paper.

Special case: Spin-orbit coupled insulator

A special case is worth commenting on. In the absence of any tunneling, as is the case for a superconductor interfaced by a spin-orbit coupled insulator, only T'_α is nonzero, whereas all other terms vanish, giving the boundary condition

$$\hat{n} \cdot \check{g}_1 \nabla \check{g}_1 = T'_\alpha[\check{g}_1, \check{\sigma}_{||}\check{g}_1\check{\sigma}_{||}]. \qquad (79)$$

This boundary condition could thus be used to look for possible bound states induced at the interface of a superconductor and a spin-orbit coupled insulator. The fact that the T'_α term exists despite the absence of a material to tunnel into on the other side of the interface is clear from the fact that this term only depends on $\check{g}_1$. In this sense, it may be thought of as the spin-orbit coupled equivalent of the spin-dependent phase-shift term G_ϕ previously discussed in the context of ferromagnetic insulators [18,25].

IV. APPLICATIONS

In the following, we will apply the boundary conditions derived in Eq. (78) to a set of example problems. In particular, we will consider superconducting hybrid structures in which a nonsuperconducting material is proximitized to a superconductor. The boundary conditions are assumed to represent a thin intermediary layer of a material with strong spin-orbit coupling. We neglect the inverse proximity effect, in which case the superconductors are approximately described by the
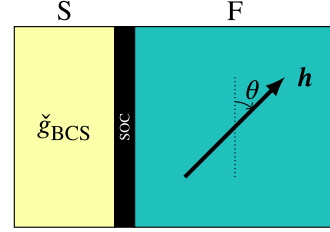

FIG. 2. The investigated bilayer, consisting of a ferromagnet and a superconductor. There is assumed to be significant spin-orbit coupling at the interface between the two materials, as shown in black. The ferromagnet is modeled by an exchange field $|\boldsymbol{h}| = 2\Delta$, pointing in a direction θ relative to the interface.

Bardeen-Cooper-Schrieffer (BCS) bulk Green function,

$$\check{g}_{\text{BCS}} = \begin{pmatrix} \cosh\theta I & e^{i\phi}\sinh\theta i\sigma_y \\ e^{-i\phi}\sinh\theta i\sigma_y & \cosh\theta I \end{pmatrix}, \qquad (80)$$

where $\theta = \arctan\frac{\Delta}{\varepsilon}$ for a given quasiparticle energy ε and gap size Δ, and ϕ is the superconducting phase. In other words, we solve the Usadel equation only in the nonsuperconducting material. We note that $[\check{g}_{\text{BCS}}, \check{\sigma}_{||}] = 0$, and hence the boundary conditions simplify to

$$\begin{aligned}
\hat{n} \cdot \check{g}_1 \nabla \check{g}_1 = {} & (T + T_\alpha)[\check{g}_1, \check{g}_2] + T'_\alpha[\check{g}_1, \check{\sigma}_{||}\check{g}_1\check{\sigma}_{||}] \\
& + i\sqrt{T''_\alpha T}[\check{g}_1, \check{\sigma}_{||}\{\check{g}_1, \check{g}_2\}\check{\sigma}_{||}].
\end{aligned} \qquad (81)$$

For simplicity, in the following we will set $T_\alpha = T'_\alpha$.

A. Superconductor-ferromagnet bilayer

As a first example, we consider a bilayer consisting of a superconductor and a ferromagnet, as shown in Fig. 2. The exchange field in the ferromagnet is directed at an angle θ from the plane of the interface, with a strength of $|\boldsymbol{h}| = 2\Delta$. In this case the Usadel equation takes the following form:

$$D\nabla \cdot \check{g}\nabla\check{g} + i[\varepsilon\rho_3 - \boldsymbol{h} \cdot \check{\boldsymbol{\sigma}}, \check{g}] = \boldsymbol{0}. \qquad (82)$$

When both spin-orbit coupling and magnetization are present in the system, this may lead to long-range spin-triplet superconducting correlations. Such correlations can penetrate a long distance inside the ferromagnet equal to the penetration length of conventional superconducting singlet correlations into a normal metal. This distance can reach large values of 100 nm and more as shown experimentally [40]. Such correlations were found in a previous work that considered a similar system [41]. There, a ferromagnet with Rashba spin-orbit coupling was attached to a superconductor via conventional spin-independent boundary conditions. Long-range spin-triplet correlations were then observed as a zero-energy peak in the density of states, the size of which depended upon the angle of the exchange field, θ. Here, we seek to explore whether similar results emerge when the sole contribution to the spin-orbit coupling stems from the boundary conditions. To quantify the presence of long-range spin-triplet correlations, we compute the density of states, which is given as

$$\nu(\boldsymbol{R}, \varepsilon) = \tfrac{1}{2}N_0\text{Re}[g_{\uparrow\uparrow}(\boldsymbol{R}, \varepsilon) + g_{\downarrow\downarrow}(\boldsymbol{R}, \varepsilon)], \qquad (83)$$
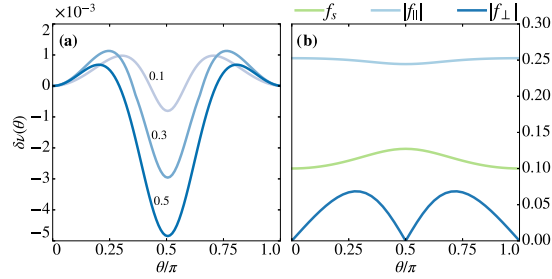
FIG. 3. Evidence of long-range triplet superconducting correlations. (a) The maximum density of states in the ferromagnet at zero energy, $\delta\nu(\theta) \equiv \nu(\varepsilon = 0, \boldsymbol{R}_{\max}, \theta) - \nu(\varepsilon = 0, \boldsymbol{R}_{\max}, 0)$, as a function of the angle of the exchange field θ relative to the interface. The strength of the spin-orbit coupling at the interface, T_α, is indicated in the figure. (b) The anomalous Green function components as a function of θ at $T_\alpha = 0.5$. f_s is the singlet contribution, and $\boldsymbol{f}_{\|}$ and $\boldsymbol{f}_\perp$ are the parallel and orthogonal parts of the triplet contribution, respectively.

where N_0 is the density of states at the Fermi level, and $g_{\sigma\sigma}(\boldsymbol{R}, \varepsilon)$ are spin components of the normal Green function. The presence of long-range spin triplets can be inferred from the density of states at $\varepsilon = 0$, at which point Eq. (83) may be expressed in terms of the contributions from the anomalous Green function $f = (f_s I + \boldsymbol{f}_t \cdot \boldsymbol{\sigma}) i\sigma_y$. With this particular parametrization, where the scalars f_s and $\boldsymbol{f}_t$ give the singlet and triplet parts of f, respectively, Eq. (83) takes the form

$$\nu(\boldsymbol{R}, 0) = 1 - \tfrac{1}{2}|f_s|^2 + \tfrac{1}{2}|\boldsymbol{f}_{\|}|^2 + \tfrac{1}{2}|\boldsymbol{f}_\perp|^2. \qquad (84)$$

For an exchange field direction indicated by the unit vector $\hat{h}$, the triplet correlation is decomposed into a parallel, $\boldsymbol{f}_{\|} = (\boldsymbol{f}_t \cdot \hat{h})\hat{h}$, and an orthogonal, $\boldsymbol{f}_\perp = \boldsymbol{f}_t - \boldsymbol{f}_{\|}$, component. The motivation for this decomposition is that the spin expectation value of the triplet Cooper pairs is given as $\langle \boldsymbol{S} \rangle \propto i\boldsymbol{f}_t(\varepsilon) \times \boldsymbol{f}_t^*(-\varepsilon)$ [30,42]. The triplet Cooper pairs whose spins are aligned with the exchange field will not experience a pair-breaking effect, in contrast to orthogonal spin alignments, and hence $\boldsymbol{f}_{\|}$ and $\boldsymbol{f}_\perp$ express the short- and long-range triplet correlations, respectively. From Eq. (84) it is clear that while the presence of singlet superconducting correlations causes a suppression of the density of states, triplet correlations lead to an increase, and thus a potential for the formation of a zero-energy peak.

Figure 3(a) shows the change in the density of states at zero energy as the exchange field is rotated away from the interface, $\delta\nu(\theta) \equiv \nu(\varepsilon = 0, \boldsymbol{R}_{\max}, \theta) - \nu(\varepsilon = 0, \boldsymbol{R}_{\max}, 0)$, where $\boldsymbol{R}_{\max}$ is the location at which the maximum density of states is found. A modulation of the zero-energy peak is found, similar to the results of Ref. [41]. At $\theta = 0$ and $\theta = \pi$, i.e., for an exchange field parallel to the interface, the T_α'-dependent terms of Eq. (81) do not contribute, and the boundary conditions are reduced to a conventional, spin-independent tunneling barrier. As θ is increased from zero, so too is the zero-energy peak of the density of states, indicating the generation of triplet Cooper pairs. However, as θ approaches $\pi/2$, a dip is found instead. These results
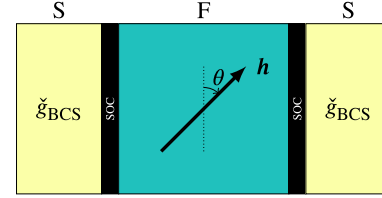

FIG. 4. A Josephson weak link, where a ferromagnet is sandwiched between two superconductors, with spin-orbit coupling present at the interfaces. The exchange field $\boldsymbol{h}$ is directed at an angle θ relative to the transverse direction of the junction, and it has a strength of $|\boldsymbol{h}| = 2\Delta$. The distance between the superconductors is assumed to be $L = 2\xi$, where ξ is the superconducting coherence length.

are further elucidated in Fig. 3(b), which shows the angular dependence of the singlet and triplet correlations. The largest modulation is clearly seen in the long-range triplets, $\boldsymbol{f}_\perp$, which is nonzero only when the exchange field has both an in-plane and an out-of-plane component with respect to the interface. In other words, it vanishes for $\theta \in \{0, \frac{\pi}{2}, \pi\}$, in agreement with Ref. [41]. Interestingly, it is not purely sinusoidal, but has maxima that are slightly tilted toward $\theta = \pi/2$. A small angular dependence in the singlet, f_s, and the short-range triplet, $\boldsymbol{f}_{\|}$, is also observed. At $\theta = \pi/2$, f_s has a slight increase, whereas $|\boldsymbol{f}_{\|}|$ decreases. This explains the reduction in the zero-energy peak of the density of states at $\theta = \frac{\pi}{2}$.

B. Superconductor-ferromagnet-superconductor Josephson weak link

When two superconductors are separated by a nonsuperconducting material, they may form a Josephson weak link. When a phase difference $\Delta\phi$ is induced between the superconductors of such systems, for instance by applying a current bias, dissipationless charge currents will flow between them, mediated by the Cooper pairs present in the nonsuperconducting material due to the proximity effect. It is well known that when the intermediary layer consists of a ferromagnet with an inhomogeneous magnetization, long-range triplet Cooper pairs may be generated, which are spin-polarized, and hence may carry a dissipationless spin current. It was recently predicted that a spin current may also emerge in homogeneous ferromagnets if thin normal-metal layers with strong spin-orbit coupling are added between the ferromagnet and the superconductors [43]. To achieve this, the spin-orbit coupling was introduced in thin separate layers, coupled to the surrounding layers by tunneling barriers, within which the Usadel equation was solved. While experimental verification of these results has proven elusive [44,45], the theoretical predictions provide an excellent benchmark for the new boundary conditions, as similar results should be obtained when the spin-orbit coupling is introduced as an interface effect. To verify this, we consider the system illustrated in Fig. 4. A homogeneous exchange field is defined in the ferromagnet, with a strength of $|\boldsymbol{h}|$, pointing in a direction θ relative to the transversal direction of the weak link. For this system, we
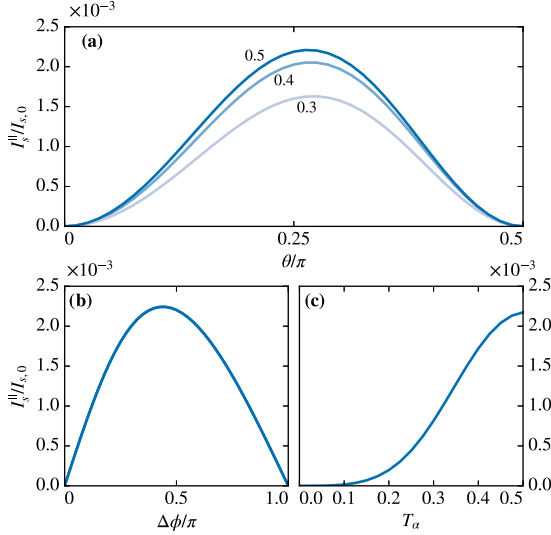
FIG. 5. The spin-current component parallel to the exchange field in the superconductor-ferromagnet-superconductor (SFS) Josephson weak link, scaled by $I_{s,0} = N_0 DW/8$. Part (a) shows its variation with the canting angle θ, where the strength of the interface spin-orbit coupling T_α is indicated in the figure, (b) shows its dependence on the phase difference between the superconductors, $\Delta\phi$, and (c) shows the maximum spin current as a function of the interface spin-orbit coupling.

compute the spin supercurrent, which in equilibrium is found from the Green function as

$$I_s = I_{s,0} \int d\varepsilon \, \mathrm{Re} \, \mathrm{Tr}\big[\hat{\rho}_3 \hat{\boldsymbol{\sigma}} (\hat{g} \partial_x \hat{g})^K\big] \tanh \frac{\beta\varepsilon}{2}, \qquad (85)$$

where it has been assumed that the junction is aligned along the x axis, and $I_{s,0} = \frac{N_0 DW}{8}$, for a given junction width W, and $\beta = 1/k_{\mathrm{B}}T$, with T the temperature.

The results are given in Fig. 5, which shows the spin-current component aligned parallel to the exchange field, in other words the spin current induced by the long-range triplets. In Fig. 5(a), its dependence on the canting angle θ is shown. It is noticed that the spin current goes to zero for $\theta = 0$ and for $\theta = \frac{\pi}{2}$. This means that an exchange field with both an in-plane and an out-of-plane component is required in order to observe an effect, similarly to the superconductor-ferromagnet (SF) bilayer. The physical reason behind this behavior is that the interface causes a greater suppression of the triplet component normal to the interface, f_x, relative to the in-plane components. This means that the short-ranged triplets generated by the exchange field, $\boldsymbol{f}_{\parallel}$, will experience a reorientation due to the presence of the spin-orbit coupling. In other words, for an exchange field that is neither parallel nor perpendicular to the interface, the resulting triplets $\boldsymbol{f}$ generated in the ferromagnet, near the interface, are not parallel to $\boldsymbol{h}$, meaning that they have a long-ranged component. In Fig. 5(b), we show the dependence of the spin current on the phase difference $\Delta\phi$ between the superconductors. It is seen that the current phase relation is approximately sinusoidal,

similar to the conventional Josephson effect, indicating that the charge currents have become spin-polarized. Finally, we show in Fig. 5(c) the maximum spin current as a function of the interface spin-orbit coupling T_α. For low values of the spin-orbit coupling, the spin current has an approximately parabolic form, but reaches a plateau as T_α approaches 0.5, the maximum value investigated in this study. A possible interpretation of this is that we are nearing the edge of the domain of validity for the small-angle approximation used in the derivation of the boundary conditions, which requires T_α to be small.

V. CONCLUSION

We have derived a set of boundary conditions for systems in which there is large spin-orbit coupling. This allows the study of, for instance, superconducting hybrid structures with thin heavy metal layers. We demonstrate the use of these boundary conditions by considering an SF bilayer and an SFS Josephson weak link. In both cases, we find that whenever the exchange field of the ferromagnet has both an in-plane and an out-of-plane component, long-range triplet superconductivity is induced. The findings reported herein are consistent with results found in previous works, where the spin-orbit coupling is approximated by other means.

APPENDIX A: GENERALIZED NORMALIZATION CONDITION

The quasiclassical Green function may be expressed in terms of a trajectory Green function, $\breve{g}_T(\boldsymbol{k}, \boldsymbol{r}_p, y_1, y_2)$, as [37]

$$\breve{g}(\boldsymbol{k}_F, \boldsymbol{R}) = \breve{g}_+(\boldsymbol{k}_F, \boldsymbol{r}_p, y, y) + \breve{g}_-(\boldsymbol{k}_F, \boldsymbol{r}_p, y, y), \qquad (A1)$$

where

$$\breve{g}_\pm(\boldsymbol{k}_F, \boldsymbol{r}_p, y, y) = \lim_{\eta \to 0} \breve{g}_T(\boldsymbol{k}_F, \boldsymbol{r}_p, y \pm \eta, y). \qquad (A2)$$

The parameters y_1 and y_2 indicate two points that are connected by a straight line pointing along $\boldsymbol{k}_F$, and $\boldsymbol{r}_p$ is the location of the trajectory in a plane perpendicular to it. In other words, $\boldsymbol{R} = y\hat{\boldsymbol{k}}_F + \boldsymbol{r}_p$. By comparison with Eq. (36) and Ref. [37], we see that $\breve{g}_T$ satisfies

$$ik_F \frac{\partial}{\partial y_1} \breve{g}_T(y_1, y_2) + \breve{\Xi}(y_1)\breve{g}_T(y_1, y_2) - \breve{t}_s \breve{g}_0 \, \delta(y_1 - y_\star)$$

$$= ik_F \breve{I} \delta(y_1 - y_2), \qquad (A3)$$

$$-ik_F \frac{\partial}{\partial y_2} \breve{g}_T(y_1, y_2) + \breve{g}_T(y_1, y_2)\breve{\Xi}(y_2) - \breve{g}_0 \breve{t}_s \, \delta(y_2 - y_\star)$$

$$= ik_F \breve{I} \delta(y_1 - y_2), \qquad (A4)$$

where $y_\star$ is the point at which the trajectory intersects with the interface. We note that for $y_1, y_2 \neq y_\star$, the third term on the left-hand side of Eqs. (A3) and (A4) is zero, and $\check{g}_T$ reduces to the trajectory Green function for $\check{g}_0$, which we name $\check{g}_T^0$. In this case, we may integrate Eq. (A3) over y_1 in a small interval surrounding y_2 to get the relation

$$\check{g}_+(y, y) - \check{g}_-(y, y) = \check{I}. \tag{A5}$$

Proceeding according to Ref. [37], we define the quantity

$$\check{A}(y) = \check{g}_T(y_1, y)\check{g}_T^0(y, y_2). \tag{A6}$$

By using Eqs. (A3) and (A4) (setting $\check{i}_s = 0$ when applied to $\check{g}_T^0$), it can be shown that $\frac{\partial}{\partial y}\check{A} = 0$, except at the points $y \in \{y_1, y_2, y_\star\}$. Furthermore, for fixed y_1 and y_2, it is a property of the Green function that it approaches zero when y approaches infinity. Next we consider the region $y < y_1 < y_2 < y_\star$, in which $\check{A}(y)$ is constant, and a trajectory directed toward the interface, $\mathrm{sgn}(\boldsymbol{k}_F \cdot \hat{n}) = 1$. Since the region is unbounded on one side, we may take the limit $y \to -\infty$ and conclude that $\check{A}(y) = 0$. This is equally valid if we set $y = y_1 - \eta$, and take the limit $\eta \to 0$. Letting also y_1 approach y_2 gives

$$\check{g}_+(y, y)\check{g}_-^0(y, y) = 0. \tag{A7}$$

From (A1) and (A5) we may express $\check{g}_\pm$ in terms of the conventional quasiclassical Green functions, to get

$$(\check{g} + \check{I})(\check{g}^0 - \check{I}) = 0. \tag{A8}$$

For an outgoing particle, with $\mathrm{sgn}(\boldsymbol{k}_F \cdot \hat{n}) = -1$, we may instead consider $y > y_1 > y_2 > y_\star$, giving

$$(\check{g} - \check{I})(\check{g}^0 + \check{I}) = 0. \tag{A9}$$

The above procedure may be repeated with $\check{A}(y) = \check{g}_T^0(y_1, y)\check{g}_T(y, y_2)$, and the final result may be summarized as

$$[\check{g} + \mathrm{sgn}(\boldsymbol{k}_F \cdot \hat{n})][\check{g}_0 - \mathrm{sgn}(\boldsymbol{k}_F \cdot \hat{n})] = 0, \tag{A10}$$

$$[\check{g}_0 + \mathrm{sgn}(\boldsymbol{k}_F \cdot \hat{n})][\check{g} - \mathrm{sgn}(\boldsymbol{k}_F \cdot \hat{n})] = 0. \tag{A11}$$

APPENDIX B: THE SCATTERING MATRIX

The retarded Green function is defined as

$$\hat{G}^R(\boldsymbol{r}, t; \boldsymbol{r}', t') = -i\theta(t - t')\hat{\rho}_3 \langle \{\Psi(\boldsymbol{r}, t), \, \Psi^\dagger(\boldsymbol{r}', t')\} \rangle, \tag{B1}$$

where the vector operator $\Psi(\boldsymbol{r}, t)$ is given as

$$\Psi(\boldsymbol{r}, t) = \psi_\uparrow(\boldsymbol{r}, t)\psi_\downarrow(\boldsymbol{r}, t) \quad \psi_\uparrow^\dagger(\boldsymbol{r}, t)\psi_\downarrow^\dagger(\boldsymbol{r}, t)^T \tag{B2}$$

in Nambu $\otimes$ spin space, and $\psi_\sigma(\boldsymbol{r}, t)$ are field operators. Note that the anticommutator in Eq. (B1) takes the form $\{A, B\} = AB + (B^T A^T)^T$ in order to obtain the correct matrix structure. $\Psi(\boldsymbol{r}, t)$ satisfies the anticommutation relation $\{\Psi(\boldsymbol{r}, t), \Psi^\dagger(\boldsymbol{r}', t)\} = \hat{I}\delta(\boldsymbol{r} - \boldsymbol{r}')$, and its time evolution is given as

$$i\frac{\partial}{\partial t}\hat{\rho}_3\Psi(\boldsymbol{r}, t) = \hat{H}\Psi(\boldsymbol{r}, t). \tag{B3}$$

The Hamiltonian matrix is given as

$$\hat{H} = \begin{pmatrix} H(\frac{1}{i}\boldsymbol{\nabla}) & 0 \\ 0 & H^*(-\frac{1}{i}\boldsymbol{\nabla}) \end{pmatrix}, \tag{B4}$$

with $H(\frac{1}{i}\boldsymbol{\nabla})$ given in Eq. (59). Inserting Eq. (B3) into Eq. (B1) and Fourier transforming in the relative time coordinate, $t - t' \to \varepsilon$, it can be shown that the Green function satisfies

$$(\varepsilon\hat{\rho}_3 - \hat{H})\hat{G}^R(\boldsymbol{r}, \boldsymbol{r}') = \hat{I}\delta(\boldsymbol{r} - \boldsymbol{r}'), \tag{B5}$$

$$\hat{G}^R(\boldsymbol{r}, \boldsymbol{r}')(\varepsilon\hat{\rho}_3 - \hat{H}')^\dagger = \hat{I}\delta(\boldsymbol{r} - \boldsymbol{r}'), \tag{B6}$$

with $\hat{H}'$ identical to $\hat{H}$, except that it acts on the coordinate $\boldsymbol{r}'$. Following Ref. [17], the Green function may be parametrized as

$$\hat{G}^R(\boldsymbol{r}, \boldsymbol{r}') = \Phi(\boldsymbol{r})\Phi^\dagger(\boldsymbol{r}'), \tag{B7}$$

where $\Phi(\boldsymbol{r}) = (\Phi_e(\boldsymbol{r}) \quad \Phi_h(\boldsymbol{r}))^T$ is a four-component spinor in Nambu $\otimes$ spin space. Neglecting ε in Eqs. (B5) and (B6) compared to the much larger interface potential contained in $\hat{H}$ and $\hat{H}'$, and subtracting Eq. (B6) from Eq. (B5), we get

$$(\hat{H}\Phi(\boldsymbol{r}))\Phi^\dagger(\boldsymbol{r}') - \Phi(\boldsymbol{r})(\hat{H}'\Phi(\boldsymbol{r}'))^\dagger = 0. \tag{B8}$$

It is seen that Eq. (B8) is satisfied if

$$\hat{H}\Phi(\boldsymbol{r}) = \begin{pmatrix} H(\frac{1}{i}\boldsymbol{\nabla}) & 0 \\ 0 & H^*(-\frac{1}{i}\boldsymbol{\nabla}) \end{pmatrix}\begin{pmatrix} \Phi_e(\boldsymbol{r}) \\ \Phi_h(\boldsymbol{r}) \end{pmatrix} = 0. \tag{B9}$$

Notice that the equation for Φ_e is precisely the same as that given in Eqs. (59)–(61), and its solution is given in Eq. (62). This implies that at the location of the interface (at $z = 0$ for this particular case), the solution for an outgoing electron with respect to the interface, Φ_e^o, is related to its incoming counterpart, Φ_e^i via $\Phi_e^o = S(\boldsymbol{k})\Phi_e^i$, for a given momentum $\boldsymbol{k}$ when using a plane-wave ansatz $\Phi_e^i \sim e^{i\boldsymbol{k}\cdot\boldsymbol{r}}$. For holes, we similarly have the relation $\Phi_h^o = S^*(-\boldsymbol{k})\Phi_h^i$, as can be deduced from Eq. (B9). We emphasize that the hole excitations described by Eq. (B9) have group velocity in the same direction as their momentum. Combined, we thus get

$$\Phi^o = \hat{S}\Phi^i, \tag{B10}$$

with

$$\hat{S} = \begin{pmatrix} S(\boldsymbol{k}) & 0 \\ 0 & S^*(-\boldsymbol{k}) \end{pmatrix}. \tag{B11}$$

Inserting Eq. (B10) into Eq. (B7) gives the boundary condition

$$\hat{G}^{R,o} = \hat{S}\hat{G}^{R,i}\hat{S}^\dagger. \tag{B12}$$

Both $\hat{H}$ and $\hat{S}$ are diagonal in Keldysh space, and hence the above procedure may be repeated for $\hat{G}^A$ and $\hat{G}^K$ to yield

$$\check{G}^o = \check{S}\check{G}^i\check{S}^\dagger. \tag{B13}$$

Since the interface is assumed impenetrable, the scattering matrix is diagonal in the extended Hilbert space including both sides of the interface, e.g., $\check{S}_{12} = \check{S}_{21} = 0$. This means that Eq. (B13) may be used to relate outgoing Green functions to incoming for each material individually. By introducing the quasiclassical approximation, we thus arrive at Eq. (44).

[1] J. W. Serene and D. Rainer, Phys. Rep. **101**, 221 (1983).

[2] W. Belzig, F. K. Wilhelm, C. Bruder, G. Schön, and A. D. Zaikin, Superlatt. Microstruct. **25**, 1251 (1999).

[3] J. Rammer and H. Smith, Rev. Mod. Phys. **58**, 323 (1986).

[4] A. A. Abrikosov, L. P. Gorkov, and I. E. Dzyaloshinski, *Methods of Quantum Field Theory in Statistical Physics* (Dover, New York, 1975).

[5] G. Eilenberger, Z. Phys. **214**, 195 (1968).

[6] K. D. Usadel, Phys. Rev. Lett. **25**, 507 (1970).

[7] A. V. Zaitsev, Zh. Eksp. Teor. Fiz. **86**, 1742 (1984) [Sov. Phys. JETP **59**, 1015 (1984)].

[8] K. Yip, J. Low Temp. Phys. **109**, 547 (1997).

[9] M. Eschrig, Phys. Rev. B **61**, 9061 (2000).

[10] A. Shelankov and M. Ozana, Phys. Rev. B **61**, 7077 (2000).

[11] B. Ashauer, G. Kieselmann, and D. Rainer, J. Low Temp. Phys. **63**, 349 (1986).

[12] K. Nagai and J. Hara, J. Low Temp. Phys. **71**, 351 (1988).

[13] S. Graser and T. Dahm, Phys. Rev. B **75**, 014507 (2007).

[14] M. Yu. Kupriyanov and V. F. Lukichev, Zh. Eksp. Teor. Fiz. **94**, 139 (1988) [Sov. Phys. JETP **67**, 1163 (1988)].

[15] Y. V. Nazarov, Superlatt. Microstruct. **25**, 1221 (1999).

[16] F. S. Bergeret, A. Verso, and A. F. Volkov, Phys. Rev. B **86**, 214516 (2012).

[17] A. Millis, D. Rainer, and J. A. Sauls, Phys. Rev. B **38**, 4504 (1988).

[18] A. Cottet, D. Huertas-Hernando, W. Belzig, and Y. V. Nazarov, Phys. Rev. B **80**, 184511 (2009).

[19] T. Tokuyasu, J. A. Sauls, and D. Rainer, Phys. Rev. B **38**, 8823 (1988).

[20] M. Eschrig, J. Kopu, J. C. Cuevas, and G. Schön, Phys. Rev. Lett. **90**, 137003 (2003).

[21] M. Fogelström, Phys. Rev. B **62**, 11812 (2000).

[22] E. Zhao, T. Löfwander, and J. A. Sauls, Phys. Rev. B **70**, 134510 (2004).

[23] J. Kopu, M. Eschrig, J. C. Cuevas, and M. Fogelström, Phys. Rev. B **69**, 094501 (2004).

[24] J. C. Cuevas and M. Fogelström, Phys. Rev. B **64**, 104502 (2001).

[25] M. Eschrig, A. Cottet, and J. Linder, New J. Phys. **17**, 083037 (2015).

[26] A. I. Buzdin, Rev. Mod. Phys. **77**, 935 (2005).

[27] F. S. Bergeret, A. F. Volkov, and K. B. Efetov, Phys. Rev. Lett. **86**, 4096 (2001).

[28] F. S. Bergeret, A. F. Volkov, and K. B. Efetov, Rev. Mod. Phys. **77**, 1321 (2005).

[29] M. Eschrig, Rep. Prog. Phys. **78**, 104501 (2015).

[30] J. Linder and J. W. A. Robinson, Nat. Phys. **11**, 307 (2015).

[31] L. P. Gor'kov and E. I. Rashba, Phys. Rev. Lett. **87**, 037004 (2001).

[32] G. Annunziata, D. Manske, and J. Linder, Phys. Rev. B **86**, 174514 (2012).

[33] F. S. Bergeret and I. V. Tokatly, Phys. Rev. B **89**, 134517 (2014).

[34] A. I. Larkin and Yu. N. Ovchinnikov, Zh. Eksp. Teor. Fiz. **55**, 2262 (1968) [Sov. Phys. JETP **28**, 1200 (1969)].

[35] E. V. Thuneberg, J. Kurkijärvi, and D. Rainer, Phys. Rev. B **29**, 3913 (1984).

[36] L. J. Buchholtz and D. Rainer, Z. Phys. B **35**, 151 (1979).

[37] A. L. Shelankov, J. Low Temp. Phys. **60**, 29 (1985).

[38] L. J. Buchholtz, J. Low Temp. Phys. **129**, 195 (2002).

[39] D. Rainer, *Recent Progress in Many Body Theories* (Plenum, New York, 1988), Vol. 1.

[40] R. Keizer, S. T. B. Goennenwein. T. M. Klapwijk, G. Miao, G. Xiao, and A. Gupta, Nature (London) **439**, 825 (2006).

[41] S. H. Jacobsen, J. A. Ouassou, and J. Linder, Phys. Rev. B **92**, 024510 (2015).

[42] A. J. Leggett, Rev. Mod. Phys. **47**, 331 (1975).

[43] S. H. Jacobsen, I. Kulagina, and J. Linder, Sci. Rep. **6**, 23926 (2016).

[44] N. Satchell and N. O. Birge, Phys. Rev. B **97**, 214509 (2018).

[45] N. Satchell, R. Loloee, and N. O. Birge, Phys. Rev. B **99**, 174519 (2019).

Paper XI

Reference

J. R. Eskilt, M. Amundsen, N. Banerjee, and J. Linder.
Long-ranged triplet supercurrent in a single in-plane ferromagnet with spin-orbit coupled contacts to superconductors.
Physical Review B **100**, 224519 (2019).
DOI: 10/d2k7

Contributions

NB and JL conceived the idea of the project. JRE performed the analytical calculations and the 1D numerical simulations, with support from JL. MA performed the 2D numerical simulations. All authors contributed to the discussions of the physics, and the revision of the final manuscript.

Long-ranged triplet supercurrent in a single in-plane ferromagnet with spin-orbit coupled contacts to superconductors

Johannes R. Eskilt

Center for Quantum Spintronics, Department of Physics, Norwegian University of Science and Technology,
NO-7491 Trondheim, Norway

Morten Amundsen

Center for Quantum Spintronics, Department of Physics, Norwegian University of Science and Technology,
NO-7491 Trondheim, Norway

Niladri Banerjee

Department of Physics, Loughborough University, Loughborough, LE11 3TU, United Kingdom

Jacob Linder ⬤

Center for Quantum Spintronics, Department of Physics, Norwegian University of Science and Technology,
NO-7491 Trondheim, Norway

By converting conventional spin-singlet Cooper pairs to polarized spin-triplet pairs, it is possible to sustain long-ranged spin-polarized supercurrents flowing through strong ferromagnets. Obtaining such a conversion via spin-orbit interactions, rather than magnetic inhomogeneities, has recently been explored in the literature. A challenging aspect with regard to experimental detection has been that in order for Rashba spin-orbit interactions, present, e.g., at interfaces due to inversion symmetry breaking, to generate such long-ranged supercurrents, an out-of-plane component of the magnetization is required. This limits the choice of materials and can induce vortices in the superconducting region complicating the interpretation of measurements. Therefore, it would be desirable to identify a way in which Rashba spin-orbit interactions can induce long-ranged supercurrents for purely in-plane rotations of the magnetization. Here, we show that this is possible in a lateral Josephson junction where two superconducting electrodes are placed in contact with a ferromagnetic film via two thin, heavy normal metals. The magnitude of the supercurrent in such a setup becomes tunable by the in-plane magnetization angle when using only a single magnetic layer. These results could provide a new and simpler way to generate controllable spin-polarized supercurrents than previous experiments which utilized complicated magnetically textured Josephson junctions.

I. INTRODUCTION

When a conventional superconductor is placed in proximity to a normal state metal, the Cooper pairs will start leaking across the interface from the superconductor and into the metal. These singlet superconducting correlations will, in the metal, start decaying over a length scale of $\xi_N = \sqrt{D/T}$ where D is the diffusion constant of the metal and T is the temperature [1]. If the metal is a ferromagnet, then the antiparallel electrons of the singlet Cooper pair will be injected into two different subbands (majority and minority) in the ferromagnet, making their Fermi momenta different. This makes the pair decay even faster, namely on a length scale of order $\xi_F = \sqrt{D/M}$ where M is the amplitude of the exchange field. This pair breaking effect can be avoided if the singlet pair can be converted into a triplet pair with a nonzero spin projection along the exchange field. With these so-called long-ranged triplets (LRTs), the pairs will decay slower and be comparable to correlation lengths of normal metal ξ_N. Physical quantities like supercurrents will be on the same order, and it is thus of great interest to be able to manipulate and create such LRTs. This topic is currently under intense focus [2,3] because of the potential to develop not only cryogenic spintronics devices, but also radically novel theoretical and experimental aspects of how such pairs can be generated and tuned in a controllable manner.

It is well known theoretically and experimentally that LRT components can be created in ferromagnets where the exchange field has an inhomogenous orientation. Such an exchange field can either be intrinsic to the ferromagnet or can be fashioned artificially by stacking several layers of homogeneous ferromagnets with misaligned exchange fields [4–9]. The former severely limits the selection of materials, making the latter more feasible for practical applications. On the other hand, stacks of misaligned ferromagnets present their own challenges, particularly in terms of exerting control over the triplet generation, as manipulating the relative angle between ferromagnetic layers can be difficult. This is what makes the discovery that spin-orbit coupling can act as a source of LRTs [10] so promising. Indeed, the presence of

LRTs in superconductor-ferromagnet structures with only a single homogeneous ferromagnet has been theoretically predicted if heavy metal layers are introduced to the system. This requires, however, that the exchange field in the ferromagnetic layer has both an in-plane and an out-of-plane component [11]. Although such a scenario is possible to obtain experimentally [12–14], it complicates the unambiguous identification of spin-polarized Cooper pairs due to the additional flux injection into the superconductor from the ferromagnet and also severely restricts the choice of materials showing a tailored out-of-plane anisotropy. Recently, further experimental corroboration for the generation of LRTs in superconductor-ferromagnet hybrid structures due to the presence of interfacial spin-orbit coupling has been found in magnetoresistance measurements [15] and in spin pumping experiments [16–18]. However, LRTs remain undetected in Josephson junctions. In fact, Refs. [12,13] found no clear signature of a long-ranged triplet supercurrent in a Josephson weak link with heavy metal layers attached to a ferromagnet with an effective canted magnetization direction, which is in stark contrast to theoretical predictions [19].

It has been proposed [10] that lateral geometries may provide less stringent requirements to generate LRTs compared to a stacked geometry, which has the potential to ease their experimental detection in Josephson junctions. In particular, it would be desirable to identify a setup where the LRTs can be tuned with a solely in-plane variation of the magnetization, in order to minimize the stray field effect on the superconductor itself. This would be a different result than previous works [12,13,19–23] that have considered how to control the supercurrent via magnetization in Josephson contacts with spin-orbit coupling. A long-ranged supercurrent was predicted in Ref. [10] but without any accompanying study of its dependence on the magnetization direction in the ferromagnetic film.

In this paper, we consider a lateral Josephson junction where two superconducting electrodes are placed in contact with a ferromagnetic layer through a heavy metal (see Fig. 1). Due to the inversion symmetry breaking and the large atomic number of such metals, Rashba spin-orbit coupling is assumed to be present at these interfaces. As we will show, such a setup will not only host long-ranged triplet Cooper pairs but also give a long-ranged supercurrent only for certain in-plane rotations of the exchange field. Thus, the supercurrent in the ferromagnet is extremely sensitive to this in-plane rotation as long as there is a nonzero spin-orbit coupling present in the heavy metals. We will also show that for some parameters, the in-plane rotation is able to create 0-π transitions, which means that for a certain in-plane rotation of the exchange field, the supercurrent is zero. Therefore, such a geometry can work as a transistor for supercurrents by simply rotating the in-plane magnetization. We emphasize that the main novelty and benefit of the present result and setup compared to previous works is that the supercurrent is tuned with a single ferromagnetic layer *and* the magnetization only needs to rotate in the plane of the magnet. Experimental observation of this effect would represent a significant advance with regard to simplifying control over long-ranged spin-polarized supercurrents, which has proved challenging before [9].
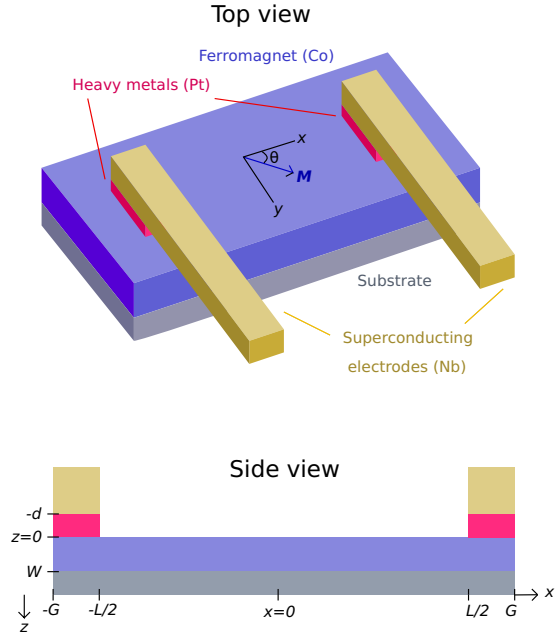

FIG. 1. A lateral SFS Josephson junction with Rashba spin-orbit coupling in the heavy metals. The exchange field lies in the plane of the ferromagnet. A supercurrent is sent through the magnetic layer via the superconducting electrodes and is tuned via the in-plane angle θ of the ferromagnet. Possible choices of materials for the various layers are indicated in the figure. We emphasize that by lateral geometry, we mean a geometry where the superconducting electrodes are attached on top of the sides of the film through which the supercurrent passes, as shown in the figure. This should be viewed in contrast to a *stacked* geometry in which case the structure is built up of successive layers placed on top of each other.

II. THEORY

In this paper we will use the quasiclassical theory of superconductivity [24,25] and consider the dirty limit so that the quasiclassical Green's function $\check{g}$ in the ferromagnet can be described by the Usadel diffusion equation [26]

$$iD\tilde{\nabla} \cdot (\check{g}\tilde{\nabla}\check{g}) = [\epsilon\hat{\rho}_3 + M \cdot \hat{\sigma}, \check{g}]_-, \tag{1}$$

where D is the diffusion constant for the ferromagnet, ϵ is the energy of the quasiparticles, $\hat{\rho}_3 = \text{diag}(1, 1, -1, -1)$, and M is the exchange field. The Pauli matrix vector is $\hat{\sigma} = \text{diag}(\underline{\sigma}, \underline{\sigma}^*)$. The Green's function $\check{g}$ is the 8×8 Green's function in Keldysh space

$$\check{g} = \begin{bmatrix} \hat{g}^R & \hat{g}^K \\ 0 & \hat{g}^A \end{bmatrix}. \tag{2}$$

Due to the triangular structure of $\check{g}$, the Usadel equation becomes the same for the retarded Green's function $\hat{g}^R$.

To incorporate spin-orbit coupling into our theory, we have defined [10] $\tilde{\nabla}(\cdot) = \nabla(\cdot) - i[\hat{A}, (\cdot)]_-$. Here, $\hat{A} =$

diag($\underline{A}$, $-\underline{A}^*$), where $\underline{A}$ is a 2×2 matrix in spin space which couples to the momentum $\boldsymbol{k}$. In effect, the spin-orbit coupling is included as an effective SU(2) gaugelike field, which is possible if it is linear in momentum. We will include both Rashba and Dresselhaus effects in this paper denoted by their respective constants α and β, both being precisely linear in momentum. However, we emphasize that the main merit of the present setup is that *only* Rashba spin-orbit coupling and an in-plane rotation of the magnetization is required to get a tunable long-ranged supercurrent. The Dresselhaus term is thus simply included to make the results more general. Rashba spin-orbit coupling can arise from the lack of inversion symmetry at the interface between two materials. We will later consider two heavy metals where the width in the z direction is small, and thus the Rashba Hamiltonian is of the form

$$H_R = \frac{\alpha}{m}(k_x \underline{\sigma}_y - k_y \underline{\sigma}_x), \tag{3}$$

where $\boldsymbol{k}$ is the momentum of the quasiparticles. The Dresselhaus SOC, on the other hand, can be caused by lack of inversion center in the crystal structure. For two-dimensional structures in the xy plane this Hamiltonian becomes

$$H_D = \frac{\beta}{m}(k_y \underline{\sigma}_y - k_x \underline{\sigma}_x). \tag{4}$$

A term proportional to σ_z can appear if the heavy metal has a noncentrosymmetric crystal structure and additionally is not confined along one axis, i.e., not thin. This is a different scenario than the one considered in this work. The two Hamiltonians above can be incorporated into the Usadel equation by using the 2×2 spin-space vector potential $\underline{A}$. This gives us

$$\underline{A} = (\beta \underline{\sigma}_x - \alpha \underline{\sigma}_y)\boldsymbol{e}_x + (\alpha \underline{\sigma}_x - \beta \underline{\sigma}_y)\boldsymbol{e}_y. \tag{5}$$

We will complement the Usadel diffusion equation with Kupriyanov-Lukichev (KL) boundary conditions [27]

$$2\zeta L \check{g} \tilde{\nabla} \check{g} = [\check{g}_l, \check{g}_r]_-, \tag{6}$$

where l and r denote the left and right side of the interface, respectively. L is the length of the respective materials and ζ is the ratio between the barrier resistance and the bulk resistance. Here, we have also added the gauge covariant derivative $\tilde{\nabla}$ to include spin-orbit coupling. The interface parameter ζ depends on microscopic parameters such as the normal-state conductivity and its magnitude determines the magnitude of the proximity-induced superconducting correlations. Our results do not change qualitatively when varying the strength of ζ and we thus choose to treat it as a phenomenological parameter rather than specifying the exact value of the normal-state conductivities and resistance of the interface regions.

To calculate the supercurrent going through the ferromagnetic bridge, we will use quasiclassical expression for the electric current, following the notation of [28,11]

$$I_Q = \frac{N_0 D A e}{4} \int_{-\infty}^{\infty} d\epsilon \, \mathrm{Tr}(\hat{\rho}_3 (\check{g} \tilde{\nabla} \check{g})^K). \tag{7}$$

Here, A is the cross section, N_0 is the density of states at the Fermi level, and e is the electric charge. The superscript K denotes the Keldysh component of the 8×8 matrix. The system in consideration will be in equilibrium, and thus we can use the relation $\hat{g}^K = \tanh(\beta \epsilon /2)(\hat{g}^R - \hat{g}^A)$ where β in this

context is the inverse temperature $1/k_B T$ and should not be confused with the Dresselhaus constant. The expression for the charge supercurrent then takes the form

$$I_Q = I_0 \int_{-\infty}^{\infty} d\epsilon \, \tanh(\beta \epsilon /2) \mathrm{Tr}(\hat{\rho}_3 (\hat{g}^R \tilde{\nabla} \hat{g}^R - \hat{g}^A \tilde{\nabla} \hat{g}^A)), \tag{8}$$

where $I_0 = \frac{N_0 D A e}{4}$. We can find $\hat{g}^R$ with the Usadel equation, and with the relation $\hat{g}^A = -\hat{\rho}_3 (\hat{g}^R)^\dagger \hat{\rho}_3$, we have everything we need to find the supercurrent. Later, we will compare our result with the supercurrent through a ferromagnetic film when no interfacial spin-orbit coupling is present. In this case, the derivatives become normal derivatives i.e., $\tilde{\nabla} \to \nabla$. It can easily be shown that this current is conserved in regions that are governed by the Usadel equation, both with and without spin-orbit coupling, i.e., $\nabla \cdot I_Q = 0$ [11]. Thus the supercurrent in ferromagnetic region in Fig. 1 will be conserved.

Our problem is inherently two dimensional, but we will make it effectively one dimensional by assuming that the total width of the heavy metals and ferromagnetic film $W + d$ is much smaller than length scale over which the Green's function varies. Thus, we can assume the Green's function stays roughly constant along the z axis, and by averaging the condensate function along the z axis we can apply the KL boundary condition at the superconductor/heavy-metal interfaces. This effectively gives the differential equations a source of singlet Cooper pairs in the two regions $-G < x < -L/2$ and $L/2 < x < G$.

We need to solve three sets of differential equations: The condensate functions in the two superconducting nodes and in the ferromagnetic bridge. In order to get an exact solution we need an appropriate set of boundary conditions. At the two vacuum interfaces, $x = -G$ and $x = G$, we use the KL boundary conditions here. At $x = -L/2$ and $x = L/2$ we require that the condensate functions are continuous and we also use the KL boundary conditions here. Since the two condensate functions must be continuous, the right side of the KL boundary condition in Eq. (6) will be zero. Thus, we effectively get the condition

$$\check{g}_i \tilde{\nabla} \check{g}_i = \check{g}_j \tilde{\nabla} \check{g}_j, \tag{9}$$

where (i, j) are two regions in contact. This also ensures supercurrent conservation.

III. RESULTS AND DISCUSSION

A. Analytical results: General considerations

Before resorting to a numerical analysis, we can draw several conclusions by making use of the weak proximity effect approximation. The assumption is that in any nonsuperconducting materials, the Cooper pair correlations will be weak, and thus the retarded Green's function only slightly deviates from its normal-state value:

$$\hat{g} = \begin{bmatrix} \underline{1} & \underline{f} \\ -\underline{\tilde{f}} & -\underline{1} \end{bmatrix}, \tag{10}$$

where the tilde conjugation $(\tilde{\cdot})$ changes the sign of the energy and complex conjugates. We insert this 4×4 Green's function matrix to the Usadel equation, and by looking exclusively at

the top-right 2×2 element, we will get an equation that is completely independent of $\tilde{\underline{f}}$. Thus, we only need to solve for the four elements in $\underline{f}$ and to get $\tilde{\underline{f}}$ we perform the tilde-conjugation, i.e., change sign of the energy and complex conjugate.

By applying the weak proximity approximation to the Usadel equation, we can linearize it in the anomalous Green's function $\underline{f}$ to obtain

$$\nabla^2 \underline{f} - 2i[\underline{A}, \nabla \underline{f}]_+^* - [\underline{A}, [\underline{A}, \underline{f}]_+^*]_+^*$$
$$+ \frac{2\epsilon i}{D} \underline{f} + \frac{i}{D} \boldsymbol{M} \cdot [\underline{\sigma}, \underline{f}]_-^* = 0, \quad (11)$$

where we have used the notation $[A, B]_+^* = AB + BA^*$. We now proceed to show that the KL boundary condition provides an effective source of singlet pairs in our linearized Usadel equation. We will make the standard simplifying assumption that the inverse proximity effect can be neglected and the Green's function in the superconductor is the BCS bulk solution given as

$$\hat{g} = \begin{bmatrix} \cosh(\theta) & i\sigma^y \sinh(\theta) e^{i\phi} \\ -i\sigma^y \sinh(\theta) e^{-i\phi} & -\cosh(\theta) \end{bmatrix}, \quad (12)$$

where $\theta = \theta(\epsilon) = \mathrm{atanh}(\Delta/\epsilon)$. We then average over the z direction, which causes the KL boundary condition to act as a source of singlet state pairs in the linear Usadel equation. Inserting the weak proximity Green's function for the ferromagnetic region and the BCS bulk Green's function, we get

$$\frac{\partial \underline{f}}{\partial z} - i[\underline{A}_z, \underline{f}]_+^*|_{S/F} = \frac{\cosh(\theta)}{\zeta L} \underline{f} - \frac{\sinh(\theta)}{\zeta L} e^{i\phi} i\underline{\sigma}^y. \quad (13)$$

As we already have seen, $\underline{A}_z = 0$. Since we are assuming that the elements of $\underline{f}$ are much smaller in magnitude than unity, the first term on the right-hand side can be neglected. We will now use this boundary condition by first expanding the Laplace operator $\nabla^2 \underline{f} = \frac{\partial^2 \underline{f}}{\partial x^2} + \frac{\partial^2 \underline{f}}{\partial z^2}$, integrate over the z direction, and use the KL boundary conditions,

$$\int_{-d}^{W} \frac{\partial^2 \underline{f}}{\partial z^2} dz = \frac{\partial \underline{f}}{\partial z}\bigg|_{z=W} - \frac{\partial \underline{f}}{\partial z}\bigg|_{z=-d} = \frac{\sinh(\theta)}{\zeta(W+d)} e^{i\phi} i\underline{\sigma}^y. \quad (14)$$

Here, we used that the length normal to the interface is simply $W + d$. By now averaging over all components in the linear Usadel equation, we get

$$\frac{\partial^2}{\partial x^2} \underline{f} - \frac{2id}{W+d} \left[\underline{A}, \frac{\partial}{\partial x} \underline{f}\right]_+^* - \frac{d}{W+d} [\underline{A}, [\underline{A}, \underline{f}]_+^*]_+^*$$
$$+ \frac{\sinh(\theta)}{\zeta(W+d)^2} e^{i\phi} i\underline{\sigma}^y + \frac{2\epsilon i}{D} \underline{f} + \frac{i}{D} \boldsymbol{M} \cdot [\underline{\sigma}, \underline{f}]_-^* = 0. \quad (15)$$

This equation has to be solved in three regions, the two superconducting nodes, i.e., $L/2 < x < G$ and $-G < x < -L/2$, and in the ferromagnetic bridge, i.e., $-L/2 < x < L/2$. In the ferromagnetic bridge, we have no spin-orbit coupling and we can simply set $\underline{A} = 0$ in this region. In the superconducting nodes, the effective magnetization $\boldsymbol{M}$ will be smaller than in the ferromagnetic film since there is no exchange field present in the heavy metals, so the effective exchange field is thus $\boldsymbol{M} \to \frac{W}{d+W} \boldsymbol{M}$, assuming similar normal-state conductivities of the spin-orbit coupled and ferromagnetic layers. We also allow for different macroscopic phases for the nodes such that the phase difference is $\Delta\phi = \phi_R - \phi_L$. Note that we have performed the standard approximation of neglecting the inverse proximity effect in the superconductors which is formally valid under the assumption that there exists a strong mismatch between the normal-state conductivity of the superconducting material compared to the other layers.

Before solving equations, we have to know our boundary conditions. This two-dimensional problem is solved by making the problem effectively one dimensional, and thus we apply the KL boundary conditions at the vacuum interfaces $x = -G$ and $x = G$ which effectively sets the current moving in the x direction to zero at these edges. At the two interfaces between the three regions, $x = -L/2$ and $x = L/2$, we require that the Green's functions are continuous and the KL boundary condition is satisfied. As mentioned, since the Green's functions are continuous we get Eq. (9). In the weak proximity limit, this gives us

$$\partial_x \underline{f}(-L/2^+) = \partial_x \underline{f}(-L/2^-) - \frac{d}{W+d} i[\underline{A}_x, \underline{f}(-L/2^-)]_+^* \quad (16)$$

$$\partial_x \underline{f}(L/2^-) = \partial_x \underline{f}(L/2^+) - \frac{d}{W+d} i[\underline{A}_x, \underline{f}(L/2^+)]_+^*. \quad (17)$$

For the anomalous Green's function f, we will make use of the so-called d-vector formalism [29] where all triplet correlations are compactly expressed through a vector $\boldsymbol{d}$. The total superconducting anomalous Green's function matrix may then be written as:

$$\underline{f} = (f_s + \boldsymbol{d} \cdot \underline{\sigma}) i\sigma^y = \begin{bmatrix} id_y - d_x & d_z + f_s \\ d_z - f_s & id_y + d_x \end{bmatrix}. \quad (18)$$

The d-vector representation has the advantage of clearly separating the long-ranged and short-ranged triplet component of f [11]. The long-ranged component will be a component that is perpendicular to the exchange field $d_{LRC} = |\boldsymbol{d} \times \boldsymbol{M}|$ while the short-ranged component is parallel to the exchange field $d_{SRC} = \boldsymbol{d} \cdot \boldsymbol{M}$. We can now enter our d vector into Eq. (15). The set of Pauli matrices with the addition of the identity matrices form a basis for a general 2×2 matrix. Therefore, by using the identity $\sigma^a \sigma^b = \delta_{ab} \underline{I} + i\epsilon_{abc}\sigma^c$, we get four equations for each of the four matrices:

$$\frac{\partial^2 f_s}{\partial x^2} + \frac{\sinh(\theta)}{\zeta(W+d)^2} e^{i\phi} + \frac{2\epsilon i}{D} f_s + \frac{2i}{D}(M_x d_x + M_y d_y) = 0, \quad (19)$$

$$\frac{\partial^2 d_x}{\partial x^2} + \frac{d}{W+d}\left(-4\alpha \frac{\partial d_z}{\partial x} - 4(\alpha^2 + \beta^2)d_x - 8\alpha\beta d_y\right) + \frac{2\epsilon i}{D} d_x + \frac{2iM_x}{D} f_s = 0, \quad (20)$$

$$\frac{\partial^2 d_y}{\partial x^2} + \frac{d}{W + d}\left(-4\beta\frac{\partial d_z}{\partial x} - 4(\alpha^2 + \beta^2)d_y - 8\alpha\beta d_x\right) + \frac{2\epsilon i}{D}d_y + \frac{2iM_y}{D}f_s = 0, \tag{21}$$

$$\frac{\partial^2 d_z}{\partial x^2} + \frac{d}{W + d}\left(4\alpha\frac{\partial d_x}{\partial x} + 4\beta\frac{\partial d_y}{\partial x} - 8(\alpha^2 + \beta^2)d_z\right) + \frac{2\epsilon i}{D}d_z = 0. \tag{22}$$

We can immediately draw several conclusions before attempting to solve the differential equations. First of all, the transformation $d_x \leftrightarrow d_y, \alpha \leftrightarrow \beta, M_x \leftrightarrow M_y$ leaves the equations invariant. We will mostly look at the case where we only have Rashba spin-orbit coupling present since this case is experimentally more feasible, but due to this invariance, our conclusions of the supercurrent and triplets will also be invariant to this transformation.

We continue by looking at the case $\beta = M_y = 0$, and $M_x \neq 0$. This decouples the third equation from the rest of the equations, and thus there is no way for the singlet state f_s to be transformed into a triplet d_y state. In a spatially homogeneous system, the long-ranged triplet state $d_{LRC} = |\boldsymbol{d} \times \boldsymbol{M}| \propto d_z$ decouples as well, and hence only the short ranged triplets d_x emerge. If, on the other hand, there is an uneven distribution of the triplet correlations, this may lead to a precession of the triplet Cooper pairs due to the Rashba spin-orbit coupling. In particular, $\frac{\partial d_x}{\partial x} \neq 0$ causes a precession about the y axis, and the generation of d_z triplets. This is precisely the case for the lateral geometry of Fig. 1; the superconducting correlations are largest directly beneath the superconducting electrodes, and reduces in strength as one moves along the x axis, towards $x = 0$, producing the necessary gradient.

While increasing α increases the production of long-ranged triplets, a larger α also has a detrimental effect on all triplet Cooper pairs due to the Dyakonov-Perel-like spin relaxation [10]. The manifestation of this effect is the appearance of an imaginary term in the quasiparticle energy, which for the long-ranged triplets takes the form,

$$\epsilon_{LRT} = \epsilon - i\frac{4dD}{W + d}\alpha^2. \tag{23}$$

Imaginary contributions to the energy are normally associated with pair-breaking processes, and therefore, these LRT components will decay faster if the Rashba coefficient is large. On the other hand, if the Rashba coefficient is zero, then there will be no LRTs at all. We therefore expect to find a maximum value for the triplets and supercurrent for a certain intermediate value of α. We will later show numerically that this reasoning is correct, resulting in a nonmonotonic behavior of the supercurrent as a function of α, and that an in-plane rotation of the exchange field will drastically change the magnitude of the supercurrent.

If we instead set $\beta = M_x = 0$, and $M_y \neq 0$, we decouple the second and fourth differential equations from the other two, and thus $d_x = d_z = 0$. The Rashba coupling has in this case a very small impact on the system and will only impact singlet pairs and the short range triplets (SRTs) with no LRTs present. Thus, in the case of Rashba coupling, an in-plane rotation of the exchange field from $M_x\boldsymbol{e}_x$ to $M_y\boldsymbol{e}_y$ will make all LRTs vanish and only SRTs will remain.

B. Analytical results: In-plane magnetization

We will now show explicitly that we get a long-ranged triplet pair correlation with spin-orbit coupling which in turn gives a long-ranged charge supercurrent. We will only be looking at a pure Rashba spin-orbit coupling and set $\beta = 0$. We will also place the magnetic field in the x direction and thus $M_y = 0$.

We assume now that the distance L between the two superconducting electrodes is so large that the solution for the anomalous Green's function in the ferromagnetic bridge will consequently be the superposition of the Green's function in two systems with only one effective superconducting node. In this way, we only need to solve the anomalous Green's function in a lateral geometry with one effective superconducting node with spin-orbit coupling present. Thus, we start by finding the solution for an effective bilayer in which a superconductor with spin–orbit coupling is located in the region $x \leqslant 0$, and a ferromagnet at $x \geqslant 0$. Far into the semi-infinite regions the solutions will converge to zero, and we only take into account the boundary conditions at $x = 0$ in Eqs. (16) and (17) with the addition of continuity of the anomalous Green's functions. We will also assume that the Rashba coupling is weak, $\alpha^2 \ll |M|/D$, so that we can remove any second order term in α in the differential equation. The general solution of the differential equations then becomes

$$f_s = -\frac{2\alpha k}{K_p^2 - k^2}C_4 e^{kx} + C_5 e^{K_p x} + C_6 e^{K_m x} + \frac{k^2}{K_p^2(2k^2 - K_p^2)}he^{i\phi_1} \tag{24}$$

$$d_x = C_5 e^{K_p x} - C_6 e^{K_m x} - \frac{K_p^2 - k^2}{K_p^2(2k^2 - K_p^2)}he^{i\phi_1} \tag{25}$$

$$d_y = 0 \tag{26}$$

$$d_z = C_4 e^{kx} - \frac{2\alpha K_p}{K_p^2 - k^2}C_5 e^{K_p x} - \frac{2\alpha K_m}{K_p^2 - k^2}C_6 e^{K_m x} \tag{27}$$

when $x < 0$. Here, $k = \sqrt{-2i\epsilon/D}$, $K_{p(m)} = \sqrt{-2i(\epsilon + (-)M_x)/D}$ and $h = \sinh(\theta)/\zeta(W + d)^2$ and in the ferromagnetic bridge when $x > 0$ the solution is

$$f_s = -C_1 e^{-K_m x} + C_2 e^{-K_p x} \tag{28}$$

$$d_x = C_1 e^{-K_m x} + C_2 e^{-K_p x} \tag{29}$$

$$d_z = C_3 e^{-kx}. \tag{30}$$

As expected, only d_z has any long-ranged triplet components in the purely ferromagnetic region, and thus we are mostly interested in finding C_3. Applying the boundary

conditions at $x = 0$, we get to the first order in α,

$$C_3 = -\frac{3K_p^4 - kK_p^3 + (kK_m - 6k^2)K_p^2 + 2k^3K_p + k^4}{\left(4kK_p^6 - 12k^3K_p^4 + 8k^5K_p^2\right)}$$
$$\times \frac{d}{W+d}\alpha h e^{i\phi_L}, \tag{31}$$

which clearly shows that we only get a long-ranged triplet component if we have Rashba spin-orbit coupling present. Letting $|M_x| \gg \epsilon$, we get $|K_{(m/p)}| \gg |k|$ and

$$C_3 = -\frac{3d\alpha h e^{i\phi_L}}{4(W+d)kK_p^2}. \tag{32}$$

We now place a second superconducting electrode at $x = L/2$ and push the first electrode back to $x = -L/2$. We solve the differential equations for the second node and assume that total condensate function $\underline{f}$ is a superposition of the two solutions and that the superconducting nodes are so far apart that the overlap between the two solutions is small. The complete solution for the long-ranged component is thus

$$d_z = C_3^- e^{-k(x+L/2)} + C_3^+ e^{k(x-L/2)}. \tag{33}$$

Here, C_3^- is the coefficient for the left superconducting node and C_3^+ for the other node. C_3^- is given in Eq. (31), while C_3^+ is found by making the replacements $k \rightarrow -k$, $K_{(p/m)} \rightarrow -K_{(p/m)}$, and $\phi_L \rightarrow \phi_R$ Entering this LRT component into the formula for the supercurrent, we get

$$I_Q = 4N_0 De \int_0^\infty d\epsilon \tanh(\beta\epsilon/2) \tag{34}$$
$$\times \Re(k(C_3^+ \tilde{C}_3^- - C_3^- \tilde{C}_3^+)e^{-kL}). \tag{35}$$

Here the tilde conjugation is as mentioned just doing the transformation $\epsilon \rightarrow -\epsilon$ and $i \rightarrow -i$. Using the approximated C_3 in Eq. (32), the long-ranged supercurrent becomes

$$I_Q = 8N_0 De \sin(\Delta\phi) \int_0^\infty d\epsilon \tanh(\beta\epsilon/2)\left(\frac{3d\alpha}{4(W+d)}\right)^2$$
$$\times \Re\left(-i\frac{h\tilde{h}}{kK_m^2K_p^2}e^{-kL}\right), \tag{36}$$

where $\Delta\phi = \phi_R - \phi_L$. Therefore, this long-ranged triplet component also gives a long-ranged supercurrent that is proportional to α^2 for small α. When the interlayer length exceeds considerably the ferromagnetic coherence length, the Josephson current in the middle of the interlayer is only carried by the LRT component. Therefore, it is sufficient to compute this component of the anomalous Green function to $\mathcal{O}(\alpha)$ in order to determine the supercurrent, which is quadratic with respect to the LRT component, to $\mathcal{O}(\alpha^2)$.

In the above expression for the supercurrent, we have used the simplified C_3 solution which amounts to the approximation that the main contribution to the integral for the supercurrent comes from the region $\varepsilon \ll |M_x|$. Numerically, we have confirmed that the main contribution indeed comes from the region near $\varepsilon = \Delta$. Alternatively, and more accurately, we could simply use the whole solution for C_3 in

Eq. (31) which results in a much longer expression for I_Q. The point is nevertheless that we get a long-ranged supercurrent when $\alpha \neq 0$. As previously argued, if we rotate the exchange field from a pure x-direction to lie along the y-axis, the long-ranged component will become zero. An in-plane rotation of the exchange field from $\boldsymbol{M} = M\boldsymbol{e}_x$ to $\boldsymbol{M} = M\boldsymbol{e}_y$ with Rashba coupling should therefore result in a significant drop in the magnitude of the supercurrent.

As mentioned above, the system is invariant under the transformation $d_x \leftrightarrow d_y$, $\alpha \leftrightarrow \beta$, $M_x \leftrightarrow M_y$ and hence we get the same expression for the long-ranged supercurrent with β instead of α if we set $\alpha = M_x = 0$ and keep β and M_y nonzero. This means that pure Dresselhaus spin-orbit coupling would also be sufficient to get a long-ranged supercurrent.

C. Numerical results

The weak proximity approximation is only valid if the magnitude of the elements of $\underline{f}$ are much smaller than unity which limits the choice of parameter values that can be explored. We will solve the full proximity effect Usadel equation numerically in this section, which is free from this restriction.

We will solve the problem by using the Riccati parametrization with spin-orbit coupling derived in Ref. [11],

$$D(\nabla^2\gamma + 2(\nabla\gamma)\tilde{N}\tilde{\gamma}(\nabla\gamma))$$
$$= -2i\epsilon\gamma - i\boldsymbol{M} \cdot (\boldsymbol{\sigma}\gamma - \gamma\boldsymbol{\sigma}^*) + D(\underline{A}^2\gamma - \gamma(\underline{A}^*)^2)$$
$$+ 2(\underline{A}\gamma + \gamma\underline{A}^*)\tilde{N}(\underline{A}^* + \tilde{\gamma}\underline{A}\gamma))$$
$$+ 2iD((\nabla\gamma)\tilde{N}(\underline{A}^* + \tilde{\gamma}\underline{A}\gamma) + (\underline{A} + \gamma\underline{A}^*\tilde{\gamma})N(\nabla\gamma)). \tag{37}$$

The corresponding equation for $\tilde{\gamma}$ can be found by tilde conjugating the equation above. Here, the Green's functions are given as $\underline{g} = N(1 + \gamma\tilde{\gamma})$ and $\underline{f} = 2N\gamma$. And $N = (1 - \gamma\tilde{\gamma})^{-1}$, and thus we need to solve for γ and $\tilde{\gamma}$. We will still be approximating the system to be one dimensional with the KL boundary conditions in the two nodes working as two sources of singlet states. The KL boundary conditions are

$$\frac{\partial}{\partial z}\gamma = \frac{1}{L\zeta}(1 - \gamma\tilde{\gamma}_S)N_S(\gamma - \gamma_S) + i\underline{A}_z\gamma + i\gamma\underline{A}_z^* \tag{38}$$

where ζ is the ratio between the barrier resistance and the bulk resistance of the heavy metal, and L is the width of the normal metal and ferromagnetic layer which is $L = W + d$. γ_S and N_S are the Riccati parameters for the BCS bulk superconductor. Since the width W of the heavy metal and the ferromagnetic film is small, we will neglect the inverse proximity effect and use the bulk BCS Green's functions in the superconductors. We will as in the last section use this boundary condition between the heavy metal and the superconductor as an effective source of singlet state pairs. Since the normal vector of the interface points in the z-direction, we get $\underline{A}_z = 0$. The z-component of $\nabla^2\gamma$ will be nonzero when averaged over the z-direction, and the effective Usadel equation

becomes:

$$D\left[\frac{\partial^2}{\partial x^2}\gamma + \frac{1}{(W+d)\zeta}(1 - \gamma\tilde{\gamma}_S)N_S(\gamma - \gamma_S) + 2\left(\frac{\partial}{\partial x}\gamma\right)\tilde{N}\tilde{\gamma}\left(\frac{\partial}{\partial x}\gamma\right)\right]$$

$$= -2i\epsilon\gamma - i\boldsymbol{M}\cdot(\boldsymbol{\sigma}\gamma - \gamma\boldsymbol{\sigma}^*) + D\frac{d}{W+d}\left[\underline{\boldsymbol{A}}^2\gamma - \gamma(\underline{\boldsymbol{A}}^*)^2 + 2(\underline{\boldsymbol{A}}\gamma + \gamma\underline{\boldsymbol{A}}^*)\tilde{N}(\underline{\boldsymbol{A}}^* + \tilde{\gamma}\underline{\boldsymbol{A}}\gamma)\right]$$

$$+ 2iD\frac{d}{W+d}\left[\left(\frac{\partial}{\partial x}\gamma\right)\tilde{N}_F(\underline{\boldsymbol{A}}^* + \tilde{\gamma}\underline{\boldsymbol{A}}\gamma) + (\underline{\boldsymbol{A}} + \gamma\underline{\boldsymbol{A}}^*\tilde{\gamma})N\left(\frac{\partial}{\partial x}\gamma\right)\right]. \tag{39}$$

The corresponding equation for $\tilde{\gamma}$ can be found by tilde conjugation the equation above. By using the bulk BCS Green's function, we can easily calculate N_S and γ_S.

We consider the system depicted in Fig. 1. The diffusive limit coherence length of the superconductor is $\xi_S = \sqrt{D/\Delta}$, where Δ is the superconducting gap energy. We will use the lengths $W/\xi_S = d/\xi_S = 0.08$ and $L/\xi_S = 1$. We will also let the length of the spin-orbit coupled region be $0.2\xi_S$, which gives us $G/L = 0.7$. The interface transparency will be $\zeta = 5$, and the exchange field is placed in the xy-plane $\boldsymbol{M} = M(\cos(\theta), \sin(\theta), 0)$. We normalize ϵ and M to the gap energy Δ. We choose a strong ferromagnet $M_F = 50\Delta$ and with $W = d$, the effective exchange field will be $M = 25\Delta$ in the two superconducting electrodes and $M = 50\Delta$ in the middle region. The value of the exchange field is reasonable considering an ultra-thin strong ferromagnet like cobalt in contact with a heavy metal like platinum [14]. The macroscopic phase difference has been set to $\Delta\phi = \phi_R - \phi_L = \pi/2$, while the temperature is $T = 0.5T_C$, and in addition, we will now only assume a pure Rashba coupling which we will normalize to the length of the ferromagnetic bridge L such that αL will be a dimensionless quantity. The spin-orbit coupling term is then

$$\underline{\boldsymbol{A}} = -\alpha\underline{\sigma}_y\boldsymbol{e}_x + \alpha\underline{\sigma}_x\boldsymbol{e}_y. \tag{40}$$

The supercurrent is plotted as a function of the exchange field angle θ and Rashba coupling in Figs. 2 and 3.

respectively, where $I_0 = N_0DAe$. With Rashba coupling, we clearly see an enhanced supercurrent when the exchange field points in the x direction ($\theta = 0$). There also seems to be a certain magnitude of the Rashba constant where the supercurrent is peaked when $\theta = 0$, namely at $\alpha L \approx 5$. Interestingly, we also see from Fig. 3 that we are able to create 0-π transitions when the strength of the Rashba coupling is $\alpha L \leqslant 6$. Thus, there exists an angle close to $\theta = \pi/2$ where the current is zero as long as $\alpha L < 6$. It also seems that the supercurrent becomes independent of θ when $\alpha L \to \infty$. This is, as we explained in the weak proximity limit, because the energy of the LRTs get an imaginary part which destroy the coherence of these components.

To more properly understand the behavior of the supercurrent in the system, we compute the triplet pair correlation, which is defined as [30,31]

$$\boldsymbol{\Phi} = \int_0^\infty d\varepsilon \, \boldsymbol{d} \tanh\frac{\beta\varepsilon}{2}. \tag{41}$$

The pair correlation for the long-ranged triplet component, Φ_z, for the exact two-dimensional geometry considered is computed using a Galerkin finite element method [32] and is shown in Fig. 4. We note in passing that this finite element method divides the system into elements defined by nodes. Some of these nodes are corner nodes, but the actual solution of the partial differential equation within each element requires functional evaluations at points which differ from the nodal points. As a result, one does not have to deal
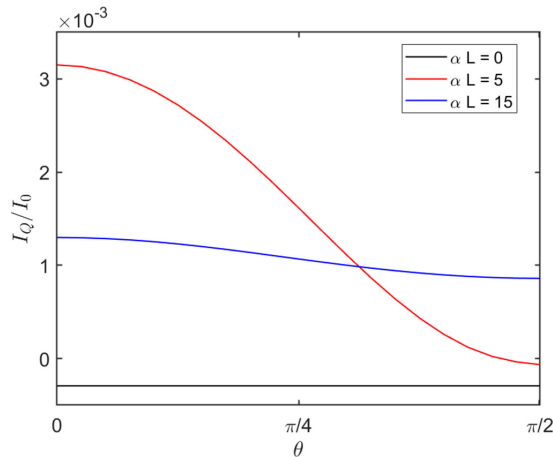

FIG. 2. The supercurrent is plotted as a function of exchange field θ. When $\theta = 0$ the exchange field points along the x-direction, while $\theta = \pi/2$ corresponds to the exchange field pointing in the y direction.
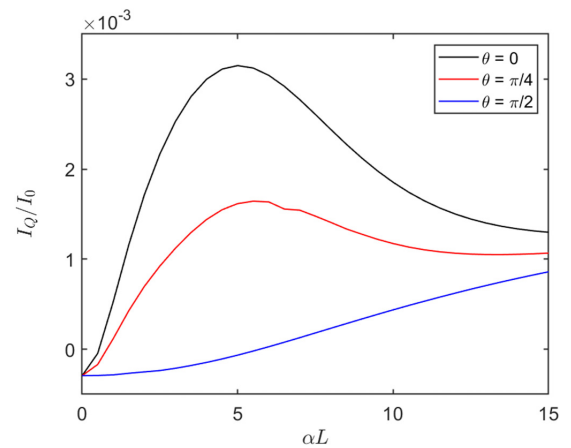

FIG. 3. The supercurrent is plotted as a function of Rashba coupling α in the heavy metals.
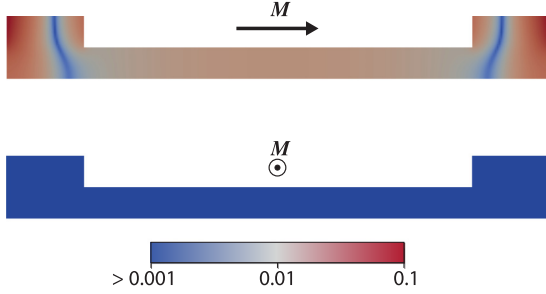
FIG. 4. The long-ranged triplet pair correlation Φ_z plotted for an exchange field pointing in the x direction (top) and the y direction (bottom). Only the former yields a nonzero Φ_z.

with surface discontinuities at corners. Transparent boundary conditions have been assumed between the heavy metal layers and the ferromagnet. It is seen that when the exchange field is pointing in the x direction, d_z triplets accumulate along the vacuum edges of the heavy metal layers. The reason for this is that the vacuum edges constrain the Cooper pair diffusion in the x direction, giving a nonzero gradient $\frac{\partial d_x}{\partial x}$ in the density of these triplet pairs. Due to the spin-orbit coupling, such a gradient acts as a source for d_z triplets due to spin precession. The corresponding pair correlation leaks into the ferromagnet, and being long ranged with respect to the exchange field, it permeates the entire ferromagnetic bridge, thus acting as a mediator for the supercurrent. In contrast, no d_z triplets are found when the exchange field points in the y direction, which is consistent with the reduction in the magnitude of the supercurrent seen in Fig. 2. It is clear that a finite thickness d of the heavy metal layers is essential for the generation of d_z triplets. This means that models which approximate the spin-orbit coupling as solely an interface effect, e.g., as discussed in Refs. [33], will fail to capture the correct θ dependence.

The key observation is that there should be a change in the critical current of the system with an in-plane magnetization rotation, an effect which is absent in systems with spin-singlet supercurrents. The supercurrent is also plotted as a function of the length of the ferromagnetic region in Fig. 5 where we have set $\alpha\xi = 5$. This choice corresponds to the maximum supercurrent in Fig. 3 when $L/\xi = 1$. We see that the supercurrent in the case of a pure x-directed exchange field ($\theta = 0$) decays much slower than in the case where the exchange field points along the y axis ($\theta = \pi/2$). This is precisely due to the fact that the supercurrent is now carried by long-ranged triplet Cooper pairs. Note that the supercurrent rapidly changes sign when $\theta = \pi/2$ due to 0-π oscillations. In contrast, for $\theta = 0$ there are no 0-π transitions in the interval $0.5 < L/\xi < 2$. This allows for an interesting observation, namely that there exists several possible intervals of L/ξ where a 90 degree
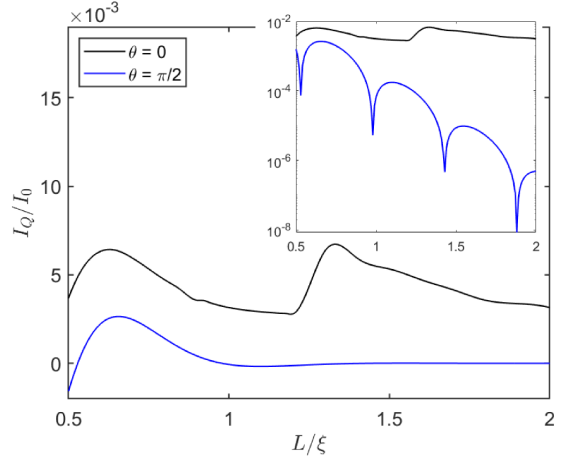

FIG. 5. The supercurrent plotted as a function of the length of the ferromagnetic bridge L. The inset is a log plot of the absolute value of the current and shows how vastly different the exponential decay is for the two in-plane directions of the exchange field. The sharp dips in the log graph shows where the short ranged current switches sign.

in-plane rotation of the magnetization essentially turns the supercurrent on and off.

IV. CONCLUDING REMARKS

We have shown that a lateral Josephson junction with spin-orbit coupled contacts to a ferromagnetic film that is magnetized in-plane is able to carry a long-ranged triplet supercurrent. This supercurrent is highly sensitive to the in-plane rotation of the magnetic field, and our system thus effectively acts as a magnetic transistor for the supercurrent. The main merit of our result is that the long-ranged triplet supercurrent is tuned with a single ferromagnetic layer without any requirement for an out-of-plane magnetization. We believe this could provide a way to realize tunable triplet supercurrents via Rashba spin-orbit coupling in a considerably simpler way than previous proposals.

Note Added. After we submitted this manuscript, a related work appeared as a preprint on arXiv [34].

[1] K. K. Likharev, Sov. Tech. Phys. Lett. **2**, 12 (1976).

[2] J. Linder and J. W. A. Robinson, Superconducting spintronics, Nat. Phys. **11**, 307 (2015).

[3] M. Eschrig, Spin-polarized supercurrents for spintronics: a review of current progress, Rep. Prog. Phys. **78**, 104501 (2015).

[4] J. W. A. Robinson, J. D. S. Witt, and M. G. Blamire, Controlled injection of spin-triplet supercurrents into a strong ferromagnet, Science **329**, 59 (2010).

[5] T. S. Khaire, M. A. Khasawneh, W. P. Pratt, and N. O. Birge, Observation of Spin-Triplet Superconductivity in Co-Based Josephson Junctions, Phys. Rev. Lett. **104**, 137002 (2010).

[6] X. L. Wang, A. D. Bernardo, N. Banerjee, A. Wells, F. S. Bergeret, M. G. Blamire, and J. W. A. Robinson, Giant triplet proximity effect in superconducting pseudo spin valves with engineered anisotropy, Phys. Rev. B **89**, 140508(R) (2014).

[7] P. V. Leksin, N. N. Garifyanov, I. A. Garifullin, Y. V. Fominov, J. Schumann, Y. Krupskaya, V. Kataev, O. G. Schmidt, and B. Buchner, Evidence for Triplet Superconductivity in a Superconductor-Ferromagnet Spin Valve, Phys. Rev. Lett. **109**, 057005 (2012).

[8] F. S. Bergeret, A. F. Volkov, and K. B. Efetov, Odd triplet superconductivity and related phenomena in superconductor-ferromagnet structures, Rev. Mod. Phys. **77**, 1321 (2005).

[9] N. Banerjee, J. W. A. Robinson, and M. G. Blamire, Reversible control of spin-polarized supercurrents in ferromagnetic Josephson junctions, Nat. Commun. **5**, 4771 (2014).

[10] F. S. Bergeret and I. V. Tokatly, Spin-orbit coupling as a source of long-range triplet proximity effect in superconductor-ferromagnet hybrid structures, Phys. Rev. B **89**, 134517 (2014).

[11] S. H. Jacobsen, J. A. Ouassou, and J. Linder, Critical temperature and tunneling spectroscopy of superconductor-ferromagnet hybrids with intrinsic Rashba-Dresselhaus spin-orbit coupling, Phys. Rev. B **92**, 024510 (2015).

[12] N. Satchell and N. O. Birge, Supercurrent in ferromagnetic Josephson junctions with heavy metal interlayers, Phys. Rev. B **97**, 214509 (2018).

[13] N. Satchell, R. Loloee, and N. O. Birge, Supercurrent in ferromagnetic Josephson junctions with heavy metal interlayers. II. Canted magnetization, Phys. Rev. B **99**, 174519 (2019).

[14] N. Banerjee, J. A. Ouassou, Y. Zhu, N. A. Stelmashenko, J. Linder, and M. G. Blamire, Controlling the superconducting transition by spin-orbit coupling, Phys. Rev. B **97**, 184521 (2018).

[15] I. Martínez, P. Högl, C. González-Ruano, J. P. Cascales, C. Tiusan, Y. Lu, M. Hehn, A. Matos-Abiague, J. Fabian, I. Žutić, and F. G. Aliev, Interfacial Spin-Orbit Coupling: New Platform for Superconducting Spintronics, arXiv:1812.08090.

[16] K.-R. Jeon, C. Ciccarelli, A. J. Ferguson, H. Kurebayashi, L. F. Cohen, X. Montiel, M. Eschrig, J. W. A. Robinson, and M. G. Blamire, Enhanced spin pumping into superconductors provides evidence for superconducting pure spin currents, Nat. Mater. **17**, 499 (2018).

[17] K.-R. Jeon, C. Ciccarelli, H. Kurebayashi, L. F. Cohen, S. Komori, J. W. A. Robinson, and M. G. Blamire, Abrikosov vortex nucleation and its detrimental effect on superconducting spin pumping in Pt/Nb/Ni80Fe20/Nb/Pt proximity structures, Phys. Rev. B **99**, 144503 (2019).

[18] K.-R. Jeon, X. Montiel, C. Ciccarelli, H. Kurebayashi, L. F. Cohen, S. Komori, M. G. Blamire, and J. W. A. Robinson, Tunable creation of pure spin supercurrents via Rashba spin-orbit coupling with Pt/Co/Pt spin sinks, arXiv:1908.00873

[19] S. Jacobsen, I. Kulagina, and J. Linder, Controlling superconducting spin flow with spin-flip immunity using a single homogeneous ferromagnet, Sci. Rep. **6**, 23926 (2016)

[20] E. Nakhmedov, O. Alekperov, F. Tatardar, Y. M. Shukrinov, I. Rahmonov, and K. Sengupta, Effect of magnetic field and Rashba spin-orbit interaction on the Josephson tunneling between superconducting nanowires, Phys. Rev. B **96**, 014519 (2017).

[21] A. Costa, P. Högl, and J. Fabian, Magnetoanisotropic Josephson effect due to interfacial spin-orbit fields in superconductor/ferromagnet/superconductor junctions, Phys. Rev. B **95**, 024514 (2017).

[22] A. Buzdin, Direct Coupling Between Magnetism and Superconducting Current in the Josephson φ_0 Junction, Phys. Rev. Lett. **101**, 107005 (2008).

[23] J. Arjoranta and T. T. Heikkilä, Intrinsic spin-orbit interaction in diffusive normal wire Josephson weak links: Supercurrent and density of states, Phys. Rev. B **93**, 024522 (2016).

[24] W. Belzig, F. K. Wilhelm, C. Bruder, G. Schön, and D. Zaikin, Quasiclassical Green's function approach to mesoscopic superconductivity, Superlattices Microstruct. **25**, 1251 (1999).

[25] J. Rammer and H. Smith, Quantum field-theoretical methods in transport theory of metals, Rev. Mod. Phys. **58**, 323 (1986).

[26] K. D. Usadel, Generalized Diffusion Equation for Superconducting Alloys, Phys. Rev. Lett. **25**, 507 (1970).

[27] M. Yu. Kupriyanov and V. F. Lukichev, Influence of boundary transparency on the critical current of "dirty" SS'S structures, Zh. Eksp. Teor. Fiz. **94**, 139 (1988).

[28] I. Gomperud and J. Linder, Spin supercurrent and phase-tunable triplet Cooper pairs via magnetic insulators, Phys. Rev. B **92**, 035416 (2015).

[29] A. J. Leggett, A theoretical description of the new phases of liquid 3He, Rev. Mod. Phys. **47**, 331 (1975).

[30] T. Löfwander, T. Champel, J. Durst, and M. Eschrig, Interplay of Magnetic and Superconducting Proximity Effects in Ferromagnet-Superconductor-Ferromagnet Trilayers, Phys. Rev. Lett. **95**, 187003 (2005).

[31] X. Montiel and M. Eschrig, Generation of pure superconducting spin current in magnetic heterostructures via nonlocally induced magnetism due to Landau Fermi liquid effects, Phys. Rev. B **98**, 104513 (2018).

[32] M. Amundsen and J. Linder, General solution of 2D and 3D superconducting quasiclassical systems: coalescing vortices and nanoisland geometries, Sci. Rep. **6**, 22765 (2016)

[33] M. Amundsen and J. Linder, Quasiclassical theory for interfaces with spin–orbit coupling, Phys. Rev. B **100**, 064502 (2019).

[34] B. Bujnowski, R. Biele, and F. S. Bergeret, Switchable Josephson current in junctions with spin-orbit coupling, Phys. Rev. B **100**, 224518 (2019).

Paper XII

Reference

M. Amundsen and J. Linder.
Spin accumulation induced by a singlet supercurrent.
arXiv: 2002.08367

Contributions

MA performed the numerical simulations, and formulated the simplified physical explanation, with support from JL. MA drafted the manuscript. Both authors contributed to the discussions of the physics, and revision of the final manuscript.

Spin accumulation induced by a singlet supercurrent

Morten Amundsen and Jacob Linder[1]

[1]*Center for Quantum Spintronics, Department of Physics, Norwegian University of Science and Technology, NO-7491 Trondheim, Norway*

We show that a supercurrent carried by spinless singlet Cooper pairs can induce a spin accumulation in the normal metal interlayer of a Josephson junction. This phenomenon occurs when a nonequilibrium spin-energy mode is excited in the normal metal, for instance by an applied temperature gradient between ferromagnetic electrodes. Without supercurrent, the spin accumulation vanishes in the Josephson junction. With supercurrent, a spatially antisymmetric spin accumulation is generated that can be measured by tunneling to a polarized detector electrode. We explain the physical origin of the induced spin accumulation by the combined effect of a Doppler shift induced by a flow of singlet Cooper pairs, and the spin-energy mode excited in the normal metal. This effect shows that spin control is possible even with singlet Cooper pairs in conventional superconductors, a finding which could open new perspectives in superconducting spintronics.

Introduction.—. Using superconductors to achieve interesting spin-dependent quantum effects is the central goal in the growing field of superconducting spintronics [1, 2]. Despite the fact that superconductivity is usually antagonistic to magnetism, a series of experiments have in recent years proven that superconductors can be used to achieve phenomena such as long-ranged and dissipationless spin currents [3, 4], large thermoelectric effects when combined with spin-polarized barriers [5], spin Hall signals exceeding the normal-state value by three orders of magnitude [6], and quantum phase batteries [7].

A key component of superconducting spintronics has traditionally been to find ways to generate polarized triplet Cooper pairs which can transport spin without resistance. In contrast, conventional superconductors described by Bardeen-Cooper-Schrieffer theory [8] are condensates of singlet Cooper pairs. While such condensates support supercurrents of charge, they do not generate supercurrents of spin. It might therefore seem like supercurrents in conventional superconductors do not have much use in spintronics, where the aim is to control and detect spin-polarized signals [9].

Here, we show that supercurrents carried by singlet Cooper pairs can induce a spin accumulation in a normal metal despite the fact that they have no spin. This phenomenon occurs when a nonequilibrium spin-energy mode is excited in the normal metal. We show that the induced spin accumulation can be understood physically from the combined effect of a Doppler shift induced by the supercurrent and the existence of a spin-energy excitation in the normal metal. The fact that the spin accumulation can be controlled by a superflow of spinless Cooper pairs opens up for a different way in which conventional superconductors can merge with spintronics.

Results.—. The proposed setup for measuring this effect is shown in Fig. 1. Two thin normal metals are stacked on top of each other, creating a four-terminal device. Two ferromagnetic leads with antiparallel magnetizations are attached to opposite terminals, and superconducting leads are attached to the remaining two terminals. When a supercurrent is passed through the superconducting electrodes, a spin accumulation is generated in the normal metal separating them. In the absence of supercurrent, the spin accumulation vanishes in the region between the superconductors. The length of each of the normal metals is assumed to be 3ξ, where ξ is the coherence length
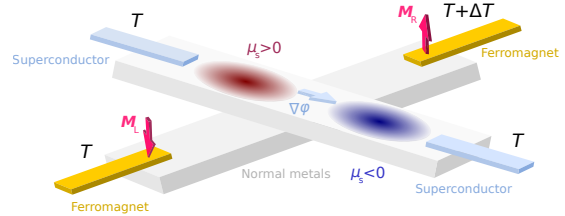

FIG. 1: (Color online) Two superconducting electrodes (S) are deposited on top of a normal metal film (purple region). Far away from the superconducting electrodes, two antiparallel ferromagnets are in contact with the normal metal film. When a temperature gradient is applied between the ferromagnets, a spin-energy mode is excited throughout the normal metal. In the middle of the normal metal, between the superconductors, there exists no spin accumulation in the absence of a supercurrent. This corresponds to zero phase-gradient across the Josephson junction, $\nabla\varphi = 0$. When a supercurrent is applied, $\nabla\varphi \neq 0$, an antisymmetric spin accumulation is induced in the normal metal between the superconductors.

of the superconductors, which then gives the distance between opposite terminals. We assume that the system is in the diffusive limit, with a short mean free path. On the other hand, the spin flip scattering length is assumed to be longer than the size of the system, so that the spin diffusion in the normal metal is negligible. This is achievable, e.g., by using niobium superconductors, which has a coherence length of ξ =10-15 nm in the diffusive limit, and copper normal metals, in which the spin diffusion length at low temperatures can be longer than 100 nm, even with a high concentration of impurities [10, 11].

The physical mechanism behind this result can then be understood by the following simplified picture. Consider a ferromagnet - normal metal - ferromagnet (FNF) spin valve, with an antiparallel orientation of the magnetization in the ferromagnets. We increase the temperature of the right F by a certain amount ΔT relative to the temperature T_0 of the left F. The tunnelling amplitude of particles at the F-N metal interfaces is higher when their spin is parallel to the magnetization than if it is antiparallel. The former is therefore influenced by a temperature increase in the F reservoir to a greater degree than the latter, leading to a temperature difference between particles

of opposite spin. The temperature on the right and left side of the normal metal for spin j, T_R^j and T_L^j, respectively, are then given as

$$T_R^\uparrow = T_0 + \Delta T, \tag{1}$$

$$T_R^\downarrow = T_0 + (1 - P)\Delta T, \tag{2}$$

$$T_L^\uparrow = T_0 + P\Delta T, \tag{3}$$

$$T_L^\downarrow = T_0, \tag{4}$$

where the polarization $P \in [0, 1]$ takes into account the spin dependence of the tunnelling. For $P = 0$, both sides are given the temperature of their respective reservoir, regardless of spin. For $P = 1$, $T_R^\downarrow$ and $T_L^\uparrow$ are completely insulated from the adjacent interface, and thus equilibrate to the temperature of the reservoir at the opposite end. The temperature distribution throughout the normal metal is simply given by

$$T^j(x) = \frac{1}{2}\left(T_R^j + T_L^j\right) + \left(T_R^j - T_L^j\right)\frac{x}{L}, \tag{5}$$

where L is the distance between the ferromagnets and $x \in (-L/2, L/2)$. The temperature difference T_s between spin up and spin down electrons then becomes

$$T_s(x) = T^\uparrow(x) - T^\downarrow(x) = P\Delta T. \tag{6}$$

In other words, a spin valve in the antiparallel configuration gives a spatially constant temperature difference between electrons of opposite spin.

When the superconducting leads are added to the spin valve as shown in Fig. 1, the picture is modified. In a superconductor, any temperature difference between spins of quasiparticles with energies below the superconducting gap will decay with a length scale of the superconducting coherence length, as these particles convert into singlet Cooper pairs. The superconducting correlations induced in the normal metal via the proximity effect therefore have a detrimental effect on T_s. The decay is largest near the superconducting leads, where the superconducting correlations are greatest. In addition, heat transfer between the superconducting leads (where both spin species have the same temperature) and the normal metal reduces T_s as well. T_s is therefore expected to have a transversal variation, with a maximum at the center of the spin valve. However, a nonuniform T_s is not enough to generate a spin accumulation. A phase gradient parallel to ∇T_s is required as well. This is illustrated in Fig. 2, which shows the quasiparticle energy band of a superconductor with an applied spin temperature gradient. For simplicity, we assume that the temperature on its left side is so low that there are no right-moving quasiparticle excitations. On its right side, a higher temperature is applied, along with a $T_s > 0$, both of which reduce towards the left. When the phase gradient $\nabla\varphi$ is zero, in Fig. 2a), there is indeed a higher number of spin up quasiparticles excited than spin down. However, there are just as many hole-like excitations as there are electron-like. There is therefore no net spin accumulated. In contrast, when $\nabla\varphi > 0$, a Doppler shift of the energy band is created, reducing the gap for momentum $k < 0$, and vice versa,
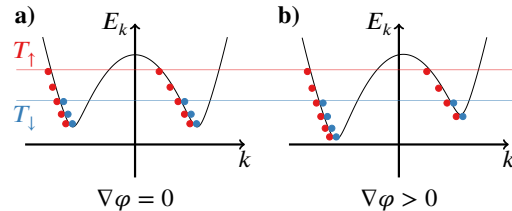

FIG. 2: Illustration of how a phase gradient in a superconductor leads to a spin imbalance when there is a gradient in the temperature difference between spin up and spin down particles, $T_s = T_\uparrow - T_\downarrow$. a) The energy band of the superconductor when there is no phase gradient. b) The same energy band when $\nabla\varphi > 0$. The resulting Doppler shift leads to a net spin imbalance. We show here for simplicity an extreme example of a case where $\nabla T_s < 0$, in which there are only left moving quasiparticle excitations.

as shown in Fig. 2b). This creates an imbalance between spin up and spin down excitations, resulting in a net magnetization.

To summarize, the simplified analysis above implies the generation of a spin accumulation in the system shown in Fig. 1. The role of the singlet superconductors is twofold. Firstly, they introduce a transversal variation to an otherwise constant temperature difference between spin up and down particles. Secondly, when a phase gradient is applied parallel to ∇T_s, a net spin imbalance is produced. To prove this, we have to consider both the superconducting correlations induced in the normal metal due to the proximity effect as well as the non-equilibrium population of quasiparticles caused by the temperature gradient applied across the normal metal. A suitable theoretical framework for this purpose is the Keldysh-Usadel theory for non-equilibrium Green functions [12, 13]. In recent years, this formalism has been used to predict several interesting phenomena in superconducting hybrid structures driven out of equilibrium [19–21]. We consider the diffusive regime of transport, where impurity scattering randomizes the momentum of quasiparticles, in which case the Green function matrix in the normal metal can be obtained by solving the Usadel equation,

$$D\nabla \cdot \check{g}\nabla\check{g} + i\left[\varepsilon\check{\rho}_4 , \check{g}\right] = 0, \tag{7}$$

where D is the diffusion constant and ε is the quasiparticle energy. The Green function matrix has the structure

$$\check{g} = \begin{pmatrix} \hat{g}^R & \hat{g}^K \\ 0 & \hat{g}^A \end{pmatrix}, \tag{8}$$

in Keldysh space, where $\hat{g}^X$ are 4×4 matrices in particle-hole and spin space. Furthermore, we have $\check{\rho}_4 = \text{diag}(\hat{\rho}_4 , \hat{\rho}_4)$, with $\hat{\rho}_4 = \text{diag}(+1, +1, -1, -1)$. The retarded and advanced Green functions, $\hat{g}^R$ and $\hat{g}^A$, determine the band structure of the system, and these components satisfy an equation which is identical in form to Eq. (7). The quasiparticle excitations are determined by the Keldysh Green function, $\hat{g}^K$. Without loss of generality, this matrix can be parametrized has $\hat{g}^K = \hat{g}^R\hat{h} - \hat{h}\hat{g}^A$, where $\hat{h}$ is a distribution function. Its matrix structure in
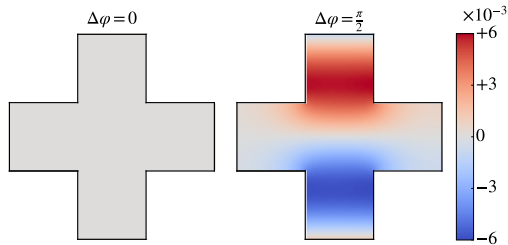
FIG. 3: Numerical simulations of the spin accumulation, scaled by μ_0, in the presence of temperature gradient. The superconducting terminals (top and bottom), and the left ferromagnet have a temperature of $T_l = 0.1T_c$, whereas the right ferromagnet has a temperature of $T_h = 0.5T_c$. No magnetization is induced when $\Delta\varphi = 0$.
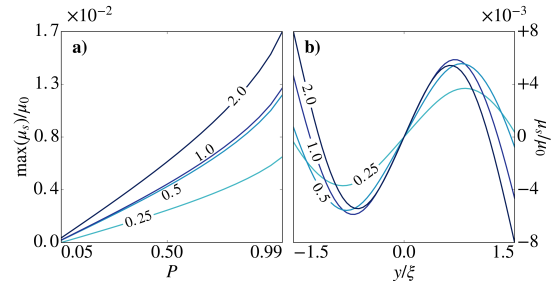

FIG. 4: The effect of varying the temperature in the right ferromagnetic reservoir. a) shows the maximum spin accumulation as a function of the interface polarization P, and b) shows the distribution of the spin accumulation along a coordinate y moving in a straight line between the superconductors. The annotations denote different T_h/T_c, and $\max(\mu_s)$ is the maximum spin accumulation located along y.

particle-hole and spin space can be further parametrized as

$$\hat{h} = \sum_n h_n \hat{\rho}_n, \tag{9}$$

where $\hat{\rho}_0 = \hat{I}$, $\hat{\rho}_j = \hat{\sigma}_j$, and $\hat{\rho}_{4+j} = \hat{\rho}_4 \hat{\rho}_j$ for $j \in \{1, 2, 3\}$. The matrix $\hat{I}$ is the identity, and $\hat{\sigma}_j = \text{diag}\left(\sigma_j, \sigma_j^*\right)$ for Pauli matrix σ_j. In the following, we assume that both ferromagnets are aligned in the z direction, in which case the only relevant distribution functions become h_0, h_3, h_4 and h_7. Insertion into Eq. (7) gives,

$$a_{mn}\nabla^2 h_n + \boldsymbol{b}_{mn} \cdot \nabla h_n = 0, \tag{10}$$

where $a_{mn} = D\text{Tr}\left[\hat{\rho}_m\hat{\rho}_n - \hat{\rho}_m\hat{g}^R\hat{\rho}_n\hat{g}^A\right]/4$, and $\boldsymbol{b}_{mn} = \nabla a_{mn} + D\text{Tr}\left[\hat{\rho}_n\hat{\rho}_m\hat{g}^R\nabla\hat{g}^R - \hat{\rho}_m\hat{\rho}_n\hat{g}^A\nabla\hat{g}^A\right]/4$. The function h_0 is the energy mode, and gives the temperature distribution of the system, with $h_0 = \tanh\frac{\varepsilon}{2k_BT}$, where k_B is the Boltzmann constant, being the only nonzero component of $\hat{h}$ in equilibrium. h_3 is a spin-energy mode, and expresses an effective temperature difference between spin up and down quasiparticles. The charge mode h_4 gives the quasiparticle charge distribution in the system, and the spin mode h_7 gives the spin accumulation, through the relation

$$\mu_s(\boldsymbol{r}) = 4\mu_0 \int d\varepsilon\, h_7(\varepsilon, \boldsymbol{r})\nu(\varepsilon, \boldsymbol{r}). \tag{11}$$

In Eq. (11), we have neglected any triplet superconducting correlations, as is the case in our system, which would otherwise also give a contribution. Furthermore, $\nu(\varepsilon, \boldsymbol{r})$ is the local density of states, and $\mu_0 = g\mu_B\nu_0/8$, where g is the Landé g-factor, μ_B is the Bohr magneton and ν_0 is the density of states of the normal metal, at the Fermi level.

To describe the interfaces to the reservoirs, we use a generalization of the Kupriyanov-Lukichev tunnelling boundary conditions, which take spin polarization into account [14, 15],

$$\zeta\hat{n} \cdot \check{g}\nabla\check{g} = [\check{g}', \check{g}] + \zeta_{mr}\left[\{\check{\sigma}_3, \check{g}'\}, \check{g}\right] + \zeta_1\left[\check{\sigma}_3\check{g}'\check{\sigma}_3, \check{g}\right], \tag{12}$$

where $\hat{n}$ is the interface normal, ζ expresses the interface resistance, and $\check{g}'$ is the reservoir Green function. The parameters $\zeta_{mr} = P/\left(1 + \sqrt{1-P^2}\right)$ and $\zeta_1 = \left(1 - \sqrt{1-P^2}\right)/\left(1 + \sqrt{1-P^2}\right)$ give the spin filtering at the interface, for a given polarization P. For interfaces to the ferromagnets, we set $\zeta = 3$ and $P = 0.6$, whereas for the superconductors, we set $\zeta = 1$ and $P = 0$. To generate a temperature gradient in the normal metal, we set the temperature in the left ferromagnetic reservoir, as well as in the two superconducting leads to be $T_l = 0.1T_c$, and the temperature in the right ferromagnetic reservoir to be $T_h = 0.5T_c$. The retarded and advanced components of Eq. (7), and subsequently, Eq. (10), are solved using the finite element method [16], and the resulting magnetization is computed using Eq. (11). The results are shown in Fig. 3. It is seen that when the phase difference $\Delta\varphi$ is zero, no magnetization is induced in the normal metal. In stark contrast, an antisymmetric magnetization appears when $\Delta\varphi = \pi/2$. Thus, a supercurrent carried by spinless Cooper pairs induces a magnetization.

A magnetization can also be generated due to the presence of the ferromagnets, which in proximity to a superconductor can produce triplet superconducting correlations [17]. Another source of triplet correlations are the spin filtering at the interfaces, which would polarize the supercurrent if it detours via the ferromagnets on its way from one superconducting lead to the other. However, for the present geometry, the ferromagnets are located sufficiently far away from the superconducting leads that these mechanisms can be disregarded. In other words, the triplet superconducting correlations are completely negligible in this system, and the magnetization is induced solely by the interaction between the singlet (spin-0) Cooper pairs and the nonequilibrium temperature distribution.

It is interesting to investigate how the induced magnetization depends on the system parameters. In Fig. 4a) we show the maximum spin accumulation as a function of the interface polarization P, for a variety of different temperature gradients. Polarizations up to 90% can be obtained e.g. by replacing the

ferromagnetic reservoirs in Fig. 1 with normal reservoirs that couple to the central normal metal via a ferromagnetic insulator such as EuS [18]. It is seen that the magnetization increases with P, and that this increase is steeper for higher T_h. This result is reasonable, as both parameters combined generate a spin temperature difference T_s, in correspondence with Eq. (6). Fig. 4b) shows the distribution of the spin accumulation along a straight line between the superconducting leads. For a low temperature difference $T_h - T_l$, the largest spin accumulation takes place about half way between the center of the system and the superconductors. However, as T_h increases these maxima are eventually overtaken by a larger spin accumulation at the superconductor interfaces. This is likely because of the increasing temperature gradient between the right ferromagnet and the superconductors, which leads to an increasing heat exchange between the two. Since the temperature in the latter is spin independent, this serves to mollify the spin temperature difference T_s near the superconductors, and thus increase the gradient in h_3. This, in turn, leads to a higher spin accumulation when a phase gradient is applied. We note, however, that these results are obtained while assuming the superconductors act as temperature reservoirs. A continued increase in T_h will likely invalidate this assumption, and lead to a saturation of the induced spin accumulation. We also note that a spin-heat accumulation, described by a finite h_3 and T_s, should in general also occur close to the interface on the ferromagnetic side [22].

Finally, we remark that it is also possible to generate a spin dependent temperature difference by applying a voltage bias between the ferromagnets, rather than a temperature gradient.

In this case, the largest average T_s in the system would be obtained for a parallel alignment of the ferromagnets. A phase gradient between the superconducting leads will then produce a spin accumulation by the same mechanism as previously described. However, in addition to providing a T_s, the injected quasiparticles lead to a spin imbalance, and thus directly contribute to the spin accumulation. This spin accumulation is independent of the phase gradient, and will likely dominate any measurement.

Conclusion.—. We have shown that a supercurrent carried by spinless Cooper pairs can induce a spin accumulation in a normal metal. This is possible when a spin-energy distribution mode is excited in the normal metal out of equilibrium, which allows a spin accumulation to arise due to the Doppler shift caused by the supercurrent in the quasiparticle energies. Our finding shows that spin control is possible even with singlet Cooper pairs in conventional superconductors, which could open interesting avenues for further research in superconducting spintronics.

[1] J. Linder and J. W. A. Robinson, Nature Physics 11, 307 (2015).
[2] M. Eschrig, Rep. Prog. Phys. 78, 104501 (2015).
[3] J. W. A. Robinson, J. D. S. Witt, and M. G. Blamire, Science 329, 5987 (2010).
[4] T. Khaire, M. A. Khasawneh, W. P. Pratt, and N. O. Birge, Phys. Rev. Lett. 104, 137002 (2010).
[5] S. Kolenda, M. J. Wolf, and D. Beckmann, Phys. Rev. Lett. 116, 097001 (2016).
[6] T. Wakamura, Y. Akaike, Y. Omori, Y. Niimi, S. Takahashi, A. Fujimaki, S. Maekawa, and Y. Otani, Nat. Mater. 14, 675 (2015).
[7] D. B. Szombati et al. , Nat. Phys. 12, 568 (2016).
[8] J. Bardeen, L. N. Cooper, and J. R. Schrieffer, Phys. Rev. 108, 1175 (1957).
[9] I. Zutic, J. Fabian, and S. Das Sarma, Rev. Mod. Phys. 76, 323 (2004).
[10] J. Bass, and W. P. Pratt Jr, J. Phys.: Condens. Matter 19, 183201 (2007).
[11] Q. Fowler, B. Richard, A. Sharma, N. Theodoropoulou, R. Loloee, W. P. Pratt Jr, and J. Bass, J. Magn. Magn. Mater 321, 99 2009.
[12] K. Usadel, Phys. Rev. Lett. 25, 507 (1970).
[13] J. Rammer and H. Smith, Rev. Mod. Phys. 58, 323 (1986).
[14] M. Yu. Kupriyanov, and V. F. Lukichev, Sov. Phys. JETP 67, 1163 (1988).
[15] M. Eschrig, A. Cottet, W. Belzig, and J. Linder, New J. Phys. 17, 083037 (2015).
[16] M. Amundsen and J. Linder, Sci. Rep. 6, 22765 (2016).
[17] A. I. Buzdin, Rev. Mod. Phys. 77, 935 (2005).
[18] N. Müller, W. Eckstein, W. Heiland, and W. Zinn Phys. Rev. Lett. 29, 1651 (1972).
[19] D. Beckmann, J. Phys.: Cond. Mat. 16, 163001 (2016).
[20] F. S. Bergeret, M. Silaev, P. Virtanen, and T. Heikkilä, Rev. Mod. Phys. 90, 041001 (2018).
[21] D. S. Rabinovich, I. V. Bobkova, A. M. Bobkov, and M. A. Silaev, Phys. Rev. Lett. 123, 207001 (2019).
[22] F. K. Dejene, J. Flipse, G. E. W. Bauer, and B. J. van Wees, Nature Physics 9, 636 (2013).

Paper XIII

Reference

E. H. Fyhn, M. Amundsen, A. Zalic, T. Dvir, H. Steinberg, and J. Linder
Combined Zeeman and orbital effect on the Josephson effect in rippled graphene.
arXiv: 2004.07845

Contributions

EHF performed the analytical calculations and the numerical simulations, with support from MA and JL. EHF drafted the manuscript. All authors contributed to the discussions of the physics, and the revision of the final manuscript. More specifically, MA had a minor supporting role in this collaboration, assisting with the discussion of the physics, and contributing to the writing of the final manuscript.

Combined Zeeman and orbital effect on the Josephson effect in rippled graphene

Eirik Holm Fyhn,[1] Morten Amundsen,[1] Ayelet Zalic,[2] Tom Dvir,[2] Hadar Steinberg,[2] and Jacob Linder[1]

[1]*Center for Quantum Spintronics, Department of Physics, Norwegian University of Science and Technology, NO-7491 Trondheim, Norway*
[2]*The Racah Institute of Physics, The Hebrew University of Jerusalem, Jerusalem 91904, Israel*
(Dated: April 20, 2020)

The two-dimensional nature of graphene Josephson junctions offers the possibility of creating effective superconductor-ferromagnet-superconductor junctions with tunable Zeeman splitting caused by an in-plane magnetic field. Such junctions would be able to alternate between a conventional superconducting ground state and a ground state with an intrinsic phase difference, making them controllable 0-π Josephson junctions. However, in addition to the Zeeman splitting, an in-plane magnetic field will in general also produce an orbital effect because of height variations in graphene, colloquially known as ripples. Both the Zeeman and orbital effect will thus affect the critical current, so to be able to identify 0-π transitions it is necessary to understand their combined effect. From both analytical and numerical solutions of the Usadel equation we find that ripples can in fact produce a current response similar to that which is characteristic of a 0-π transition. Hence, additional analysis is required in order to reveal the presence of a 0-π transition caused by spin-splitting in graphene with ripples. We provide a closed form analytical expression for the critical current in the presence of exchange field and ripple effects as well as an expression for the scaling of critical current zeroes with junction parameters.

I. INTRODUCTION

When the spinless superconducting order of a conventional superconductor comes in contact with a ferromagnet, it can adapt by creating spin-triplet Cooper pairs [1]. The synergy between superconductivity and ferromagnetism, two seemingly incompatible orders, is a topic of fundamental interest, but could also be of practical value. One interesting consequence is that it allows for spinfull supercurrents. The promise of low-dissipation spin transport has helped spawn the field of superconducting spintronics [2].

In the last decade, the possibility of creating Josephson junctions with graphene has attracted interest[3–7]. Superconductor-graphene-superconductor (SGS) junctions provide an arena for understanding the interplay between superconductivity and otherwise distinct physical phenomena, such as special relativity [3] and the quantum Hall effect [8, 9]. Here, we are interested in how the two-dimensional nature of monolayer graphene can be utilized to create an effective superconductor-ferromagnet-superconductor (SFS) junction with a tunable exchange field. This is done by introducing a Zeeman splitting between the spin-bands in the graphene by use of a strong in-plane magnetic field. This is possible because the two-dimensional nature of the graphene minimizes the magnetic depairing effect that would otherwise quench the superconducting correlations. By using electrodes with Ising-like superconductivity, like thin NbSe$_2$, one avoids destroying the superconducting state of the electrodes via the Pauli limitation.

The possibility of *in situ* control of the exchange field could open new avenues for manipulations that take advantage of the combined effect of magnetic and superconducting order. In addition to giving rise to the possibility of Cooper pairs with non-zero total spin [2], the presence of a magnetic field gives the Cooper pairs a non-zero total momentum, as first explained by Fulde, Ferrel, Larkin and Ovchinnikov [10, 11]. The total momentum of the Cooper pairs in the so-called FFLO-state is given by the strength of the exchange field, as this determines the displacement of the two Fermi surfaces corresponding to spin-up and spin-down electrons. The non-zero momentum produces spatial variations in the superconducting order parameter [12].

One consequence of the spatial variations, is that the ground state of a superconductor-ferromagnet-superconductor (SFS) Josephson junction can be one in which the phases of the order parameter in the two superconductors differs by π, which is known as a π-junction. Such junctions could have an important role in the design of components for quantum computing [13–15], superconducting computing [16, 17] or as cryogenic memory [18].

Whether an SFS-junction is a π-junction or not depends on its length as well as the strength of the exchange field, which are typically fixed parameters. If, however, the exchange field could be tuned, this would allow for a controllable switching between the 0-junction state and π-junction state. Zeeman-effect-induced 0-π transitions have previously been observed in a Dirac semimetal with a g factor on the order of 10^3 [19]. The large g factor allowed the 0-π transition to occur before the magnetic field extinguished the superconducting correlations. Using a junction with a two-dimensional material, such as monolayer graphene, would allow for Zeeman driven 0-π transitions without the need for large g factors, since such junctions can withstand much larger in-plane magnetic fields.

The prospect of a graphene Josephson junction being used as a tunable SFS-junctions is interesting, but it also demands a thorough investigation into how the supercurrent in an SGS-junction responds to the strong in-plane magnetic field necessary for an appreciable Zeeman splitting. Even though monolayer graphene is two-dimensional, it will in general not be perfectly flat. It will have a curvature that depends on the underlying substrate. If the graphene is placed on SiO$_2$, it will be rippled with peak-to-peak height difference of about 1 nm and typical feature size of 30 nm [20]. Hence, the in-plane magnetic field will have a component orthogonal to the graphene surface, giving rise to an orbital effect. This orthogonal component has been observed to suppress phase-coherent weak localization [21, 22]. Consequently, extra care must be taken when considering phase-coherent transport experiments relying on

in-plane magnetic fields. Here, we show that attention must also be paid to ripples when considering SGS-junction with tunable Zeeman splitting.
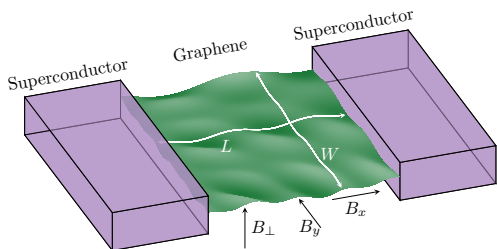

FIG. 1: Sketch of superconductor-graphene-superconductor junction with rippled graphene and external magnetic field. The magnetic field has out-of-plane component $B_\perp$ and in-plane components B_x and B_y.

One property of a 0-π transition is that the current changes sign, giving zero net current exactly at the transition [23]. Characterization of an SGS-junction and the identification of a possible 0-π transition will typically be done by measuring the current response to an applied magnetic field. Therefore, it is important to know whether features in the critical current, such as the decay rate and zeros, can also be produced by an interference effect that arises from ripples in the graphene. Of particular interest is whether interference effects can give a vanishing critical current at magnetic field strengths that are comparable to the magnetic field necessary for a 0-π transition. The Zeeman energy necessary for the transition is typically smaller for diffusive systems [12], so diffusive systems are most promising for tunable π-junctions. However, computing the supercurrent in a model with ripples in graphene is a challenging task due to the non-trivial geometry of the system.

A sketch of the system under consideration is shown in fig. 1. In order to model this geometry, we add a spatially varying magnetic field to the equations governing diffusive SFS-junctions, where the exchange field in the ferromagnet comes from the Zeeman effect. In order to fully model the disorderly ripples, one must be able to solve the equations with arbitrary magnetic field distributions. We are able to do that numerically by using the finite element method. Additionally, we extend the analytical result by Bergeret and Cuevas [24] for superconductor-normal-superconductor (SNS) junctions with uniform magnetic fields to SFS-junctions with arbitrary magnetic field distributions and arbitrary exchange fields.

II. METHODOLOGY

The critical current, as well as other physical quantities such as the local density of states, can be calculated using the quasiclassical Keldysh Green's function formalism [25, 26]. Previous studies of ballistic systems have investigated the interplay of the Zeeman and the orbital effect using an analytical propagator approach [27, 28]. The diffusive limit considered here, however, is more appropriately described by the Usadel equation, which previously has been done to successfully model experimental results for the supercurrent in SGS junctions [29]. We use natural units throughout, meaning that $c = \hbar = 1$.

In thermal equilibrium it is sufficient to solve for the retarded Green's function, $\hat{g}$, which is normalized to $\hat{g}^2 = 1$ and solves the Usadel equation,

$$D\tilde{\nabla} \cdot \left(\hat{g}\tilde{\nabla}\hat{g}\right) + i\left[\hat{\Sigma}, \hat{g}\right] = 0, \tag{1}$$

provided that the Fermi wavelength and the elastic impurity scattering time is much shorter than all other relevant length scales, and the Fermi wavelength is much smaller than the scattering time. Here D is the diffusion coefficient and the covariant derivative is $\tilde{\nabla}\hat{g} \equiv \nabla\hat{g} - ie\mathbf{A}[\hat{\rho}_3, \hat{g}]$, where $\mathbf{A}$ is the vector potential. The self-energy is

$$\hat{\Sigma} = \begin{cases} (\varepsilon + i\delta)\hat{\rho}_3 + \begin{pmatrix} & & & \Delta \\ & & -\Delta & \\ & \Delta^* & & \\ -\Delta^* & & & \end{pmatrix} & \text{in the superconductors,} \\ (\varepsilon + i\delta)\hat{\rho}_3 + \begin{pmatrix} \mathbf{h} \cdot \boldsymbol{\sigma} & \\ & \mathbf{h} \cdot \boldsymbol{\sigma}^* \end{pmatrix} & \text{in the ferromagnet,} \end{cases} \tag{2}$$

where ε is the energy, δ^{-1} is the inelastic scattering time, $\hat{\rho}_3 = \mathrm{diag}(1, 1, -1, -1)$, Δ is the superconducting gap parameter, $\mathbf{h}$ is the exchange field and $\boldsymbol{\sigma}$ is the vector consisting of Pauli matrices. Defining "spin up" and "spin down" parallel to the in-plane magnetic field gives $\mathbf{h} = h\hat{\mathbf{z}}$. We here disregard the effect of the very weak $\mathbf{k}$-dependent spin-orbit induced effective Zeeman-field caused by ripples in graphene, which is opposite in direction at the two inequivalent Dirac points of graphene [30].

Let x and y be an orthogonal coordinate system of the graphene surface such that the superconductors are located at $x = \pm L/2$ and the interfaces with vacuum are at $y = \pm W/2$. The curved geometry of graphene will in general enter into the Usadel equation (1) in two ways. First, the divergence operator is altered by the presence of nonzero Christoffel symbols. However, since the curvature of rippled graphene typically is very small [20], this effect is negligible. Consequently, we use $\nabla \equiv \hat{\mathbf{x}} \, \partial/\partial x + \hat{\mathbf{y}} \, \partial/\partial y$. Second, and crucial for the effect considered here, the in-plane magnetic field has a component orthogonal to the surface. In the external coordinate system, or "lab frame", the magnetic field can be written $\mathbf{B} = (B_x, B_y, B_\perp)^\intercal$, as illustrated in fig. 1, but in the coordinate system of the curved graphene, the magnetic field has a z-component equal to

$$\mathbf{B} \cdot \hat{\mathbf{z}} = -B_x \sin\left[\arctan\left(\frac{\partial \eta}{\partial x'}\right)\right] - B_y \sin\left[\arctan\left(\frac{\partial \eta}{\partial y'}\right)\right]$$
$$+ B_\perp \approx -B_x \frac{\partial \eta}{\partial x} - B_y \frac{\partial \eta}{\partial y} + B_\perp, \tag{3}$$

where η is the height distribution of the graphene, x' and y' are the coordinates in the lab frame and we have used the assumption

that $\partial\eta/\partial x \approx \partial\eta/\partial x' \ll 1$ and $\partial\eta/\partial y \approx \partial\eta/\partial y \ll 1$. We have also neglected the modulation effect that the curvature has on the out-of-plane magnetic field component $B_\perp$, since this only gives a contribution that is negligible compared to that of the much larger in-plane field, given by B_x and B_y.

In order to capture the magnetic field given by eq. (3), we use the vector potential

$$\mathbf{A} = \left(B_y \eta + B_x \int_0^y \frac{\partial\eta}{\partial x} \, d\tilde{y} - B_\perp y \right) \hat{\mathbf{x}}. \qquad (4)$$

Choosing the vector potential parallel to the x-axis allows us to set $\mathbf{A} = \mathbf{0}$ in the superconductors, which means that the ground states in the superconductors have constant phases. In the following we denote the superconducting phase in the left $(x < -L/2)$ and right $(x > L/2)$ superconductors by ϕ_l and ϕ_r, respectively.

The Usadel equation (1) is not valid across boundaries of different materials since the associated length scales are not negligible compared to the Fermi wavelength. Instead, the Green's function in the different materials must be connected through a boundary condition. For low-transparency tunneling interfaces, one may use the Kupriyanov-Lukichev boundary condition [31],

$$\zeta_i L_i \hat{\mathbf{n}} \cdot \left(\hat{g}_i \tilde{\nabla} \hat{g}_i \right) = \frac{1}{2} \left[\hat{g}_i, \hat{g}_j \right], \qquad (5)$$

where the subscripts i and j denote the different sides of the interface, $\hat{\mathbf{n}}$ is a normal unit vector pointing out of region i, L_i is the length of region i in the $\hat{\mathbf{n}}$-direction and ζ_i is the ratio of the normal-state conductance of region i to the interface conductance. Equation (5) is used along the interface between the superconductors and graphene at $x = -L/2$ and $x = L/2$. Along the boundaries with vacuum at $y = \pm W/2$, the boundary condition is $\hat{\mathbf{n}} \cdot \tilde{\nabla} \hat{g} = 0$.

It has been shown that one may use the bulk solution in the superconductors,

$$\hat{g}_{\text{BCS}} = \frac{\hat{\Sigma}}{\sqrt{(\varepsilon + i\delta)^2 - |\Delta|^2}}, \qquad (6)$$

when the interface conductance is much smaller than the normal-state conductance of length ξ of the superconductor [32], where

$$\xi = \sqrt{\frac{D}{\Delta}} \qquad (7)$$

is the coherence length. The square root in eq. (6) must be chosen such that it has a positive imaginary part.

Having found the Green's function, the electrical current density can be calculated from [33]

$$\mathbf{j} = \frac{N_0 e D}{4} \int_{-\infty}^{\infty} \text{Tr} \left(\hat{\rho}_3 \hat{g} \tilde{\nabla} \hat{g} - \hat{g}^\dagger \tilde{\nabla} \hat{g}^\dagger \hat{\rho}_3 \right) \tanh\left(\frac{\beta\varepsilon}{2} \right) d\varepsilon, \qquad (8)$$

where N_0 is the normal density of states and β is inverse temperature. Finally, eq. (8) allows for calculation of the critical current, given by

$$I_c = \max_{\phi_r - \phi_l} \int_{-W/2}^{W/2} \hat{\mathbf{x}} \cdot \mathbf{j}(x, y) \, dy, \qquad (9)$$

where the choice of x is arbitrary.

In order to solve eq. (1) numerically, we use the Ricatti parametrisation,

$$\hat{g} = \begin{pmatrix} N & \\ & -\tilde{N} \end{pmatrix} \begin{pmatrix} 1 + \gamma\tilde{\gamma} & 2\gamma \\ 2\tilde{\gamma} & 1 + \tilde{\gamma}\gamma \end{pmatrix}, \qquad (10)$$

where $N = (1 - \gamma\tilde{\gamma})^{-1}$ and tilde conjugation is defined as $\tilde{\gamma}(\varepsilon) = \gamma^*(-\varepsilon)$. This respects the normalization and underlying symmetries of $\hat{g}$. The resulting equations for the 2×2 matrices γ and $\tilde{\gamma}$ are discretized by the finite element method [34] with quadratic elements, and Gauss-Legendre quadrature rules of fourth order is used to integrate over the elements. The resulting nonlinear set of algebraic equations are solved by the Newton-Raphson method [35], where the Jacobian is determined by forward-mode automatic differentiation [36].

III. RESULTS AND DISCUSSION

In order to linearize the Usadel equation, we write

$$\hat{g} = \hat{g}_0 + \hat{f}, \qquad (11)$$

where $\hat{g}_0$ is the bulk solution. In a ferromagnet, the self-energy $\hat{\Sigma}$, given by eq. (2), is diagonal. Hence, the bulk equation $[\hat{\Sigma}, \hat{g}_0] = 0$ is solved by any diagonal matrix satisfying $\hat{g}_0^2 = 1$. In order to find the correct solution one must solve the full Gor'kov equation. The result is that $\hat{g}_0 = \hat{\rho}_3$. If we assume that the proximity effect is weak, we can keep only linear terms in $\hat{f}$, yielding

$$D\hat{\rho}_3 \tilde{\nabla}^2 \hat{f} + i [\Sigma, \hat{f}] = 0, \qquad (12)$$

In order for the normalization $\hat{g}^2 = 1$ to hold to linear order in $\hat{f}$, we need $\{\hat{f}, \hat{\rho}_3\} = 0$. This implies that

$$\hat{f} = \begin{pmatrix} 0 & f \\ -\tilde{f} & 0 \end{pmatrix} \qquad (13)$$

and

$$\tilde{\nabla}\hat{f} = \nabla\hat{f} - 2ie\mathbf{A}\hat{\rho}_3\hat{f}. \qquad (14)$$

In the weak proximity effect regime, the boundary conditions read

$$\zeta L \hat{\rho}_3 \hat{\mathbf{n}} \cdot \tilde{\nabla}\hat{f} = \frac{1}{2} \left[\hat{\rho}_3 + \hat{f}, \hat{g}_s + \hat{f}_s \right] = \hat{\rho}_3 \hat{f}_s - \hat{g}_s \hat{f}, \qquad (15)$$

where $\hat{g}_s$ is the part of $\hat{g}_{\text{BCS}}$ proportional to $\hat{\rho}_3$ and $\hat{f}_s$ is the remaining part proportional to antidiag$(\Delta, -\Delta, \Delta^*, -\Delta^*)$. Additionally, we must have $[\hat{f}, \hat{f}_s] = 0$, since this term would be block diagonal.

Since $\hat{\Sigma}$ is diagonal in the ferromagnet, the different components of $\hat{f}$ decouple. Only the elements which are nonzero in $\hat{f}_s$ will have a constant term in the boundary conditions. The remaining elements must be zero. Hence, $\hat{f}$ must be antidiagonal, just like $\hat{f}_s$. This in turn implies that $[\hat{\Sigma}, \hat{f}] = 2\hat{\Sigma}\hat{f}$.

In order to solve the Usadel equation for arbitrary magnetic fields, we first define

$$\hat{u} = \exp\left(-2ie\hat{\rho}_3 \int_{-L/2}^{x} A(x', y)\,\mathrm{d}x'\right)\hat{f} \qquad (16)$$

With this, the Usadel equation can be written

$$D\hat{\rho}_3\nabla^2\hat{u} + 2i\hat{\Sigma}\hat{u} - 2Die\hat{\rho}_3\hat{u}\int_{-L/2}^{x}\frac{\partial B}{\partial y}\,\mathrm{d}x'$$
$$- 4De^2\hat{u}\left(\int_{-L/2}^{x} B\,\mathrm{d}x'\right)^2 - 4Die\frac{\partial\hat{u}}{\partial y}\int_{-L/2}^{x} B\,\mathrm{d}x' = 0, \quad (17)$$

where we have used that $B = -\partial A/\partial y$. We can neglect the terms involving B (the magnetic field component orthogonal to the graphene) by assuming that the magnetic field is sufficiently weak. That is, for all $x \in (-L/2, L/2)$,

$$\int_{-L/2}^{x} B\,\mathrm{d}x' \ll \Phi_0\sqrt{\frac{\delta}{D}}, \qquad (18a)$$

and

$$\int_{-L/2}^{x}\frac{\partial B}{\partial y}\,\mathrm{d}x' \ll \frac{\Phi_0\delta}{D}, \qquad (18b)$$

where $\Phi_0 = \pi/e$ is the magnetic flux quantum.

The boundary conditions for $\hat{u}$ at $y = \pm W/2$ is

$$\left.\frac{\partial\hat{u}}{\partial y}\right|_{y=\pm W/2} = -i\hat{u}\int_{-L/2}^{x} B\,\mathrm{d}x'. \qquad (19)$$

Equations (15), (17) and (19) can be solved exactly when $B = 0$ by assuming $\partial^2\hat{u}/\partial y^2 = 0$. For B satisfying eq. (18) we can find an approximate solution by neglecting the term $\partial^2\hat{u}/\partial y^2$ in eq. (17).

With these approximations, the Usadel equation becomes an ordinary differential equation,

$$\frac{\partial^2\hat{u}}{\partial x^2} + \frac{2i\hat{\rho}_3\hat{\Sigma}}{D}\hat{u} = 0, \qquad (20)$$

with solution

$$\hat{u} = \mathrm{e}^{\hat{k}x}\hat{A} + \mathrm{e}^{-\hat{k}x}\hat{B}, \qquad (21)$$

for some coefficients $\hat{A}$ and $\hat{B}$. Here

$$\hat{k} = \sqrt{-\frac{2i\hat{\rho}_3\hat{\Sigma}}{D}}, \qquad (22)$$

which, since $\hat{\rho}_3\hat{\Sigma}$ is diagonal, $\hat{k}$ can be obtained simply by taking the elementwise square root. To determine $\hat{A}$ and $\hat{B}$ one must use eq. (15). The solution is

$$\hat{u} = \left[(\zeta L\hat{k} + \hat{\rho}_3\hat{g}_s)^2\mathrm{e}^{\hat{k}L} - (\zeta L\hat{k} - \hat{\rho}_3\hat{g}_s)^2\mathrm{e}^{-\hat{k}L}\right]^{-1}$$
$$\times \left[\hat{p}(x) + \mathrm{e}^{i\hat{\rho}_3\theta}\hat{p}(-x)\right]\hat{f}_s, \quad (23)$$

where

$$\theta = \phi_r - \phi_l + 2e\int_{-L/2}^{L/2} A(x, y)\,\mathrm{d}x \qquad (24)$$

and

$$\hat{p}(x) = (\zeta L\hat{k} + \hat{\rho}_3\hat{g}_s)\mathrm{e}^{\hat{k}(x-L/2)} + (\zeta L\hat{k} - \hat{\rho}_3\hat{g}_s)\mathrm{e}^{-\hat{k}(x-L/2)}. \quad (25)$$

Note that the boundary condition for the interfaces with vacuum, eq. (19), is only approximately satisfied.

To find the current from eq. (23) we can use that the x-component of the current, as given by eq. (8) can be written

$$\mathbf{j}\cdot\hat{\mathbf{x}} = \frac{N_0eD}{4}\int_{-\infty}^{\infty}\mathrm{Tr}\left(\hat{\rho}_3\hat{u}\frac{\partial\hat{u}}{\partial x} - \hat{u}^{\dagger}\frac{\partial\hat{u}^{\dagger}}{\partial x}\hat{\rho}_3\right)\tanh\left(\frac{\beta\varepsilon}{2}\right)\mathrm{d}\varepsilon \qquad (26)$$

To simplify this expression, note that eq. (23) can be written

$$\hat{u} = \begin{pmatrix} & & & d(h)\mathrm{e}^{i\phi_l} \\ & & -d(-h)\mathrm{e}^{i\phi_l} & \\ & \tilde{d}(h)\mathrm{e}^{-i\phi_l} & & \\ -\tilde{d}(-h)\mathrm{e}^{-i\phi_l} & & & \end{pmatrix} \qquad (27)$$

where

$$d(h) = \frac{[p(x) + \mathrm{e}^{i\theta}p(-x)]|\Delta|/\sqrt{(\varepsilon + i\delta)^2 - |\Delta|^2}}{\left[(\zeta Lk + g_s)^2\mathrm{e}^{kL} - (\zeta Lk - g_s)^2\mathrm{e}^{-kL}\right]} \qquad (28)$$

with $g_s = (\varepsilon + i\delta)/\sqrt{(\varepsilon + i\delta)^2 - |\Delta|^2}$, the square roots are those which have positive imaginary parts, $k = \sqrt{-2i(\varepsilon + h + i\delta)/D}$ and

$$p(x) = (\zeta Lk + g_s)\mathrm{e}^{k(x-L/2)} + (\zeta Lk - g_s)\mathrm{e}^{-k(x-L/2)}. \quad (29)$$

Inserting eq. (28) into eq. (26) gives

$$\mathbf{j}\cdot\hat{\mathbf{x}} = N_0eD\int_{-\infty}^{\infty}\mathrm{Re}\left[d(h)\frac{\partial\tilde{d}(-h)}{\partial x} + d(-h)\frac{\partial\tilde{d}(h)}{\partial x}\right]$$
$$\times\tanh\left(\frac{\beta\varepsilon}{2}\right)\mathrm{d}\varepsilon. \quad (30)$$

By evaluating $\mathbf{j}$ at $x = 0$ we can factorize out the dependence on the vector potential, since

$$\left.\frac{\partial\tilde{d}(h)}{\partial x}\right|_{x=0} = \frac{2i\sin\theta}{1 + \mathrm{e}^{i\theta}}\times\left.\frac{\partial\ln p}{\partial x}d(-h)\right|_{x=0}. \qquad (31)$$

Inserting this into eq. (30) and integrating the current density over y to obtain the total current finally gives

$$I = 2N_0eD\int_{-W/2}^{W/2}\sin\left(\phi_r - \phi_l + 2e\int_{-L/2}^{L/2} A(x, y)\,\mathrm{d}x\right)\mathrm{d}y$$
$$\times\int_{-\infty}^{\infty}\mathrm{Im}\left[\kappa_+ + \kappa_-\right]\tanh\left(\frac{\beta\varepsilon}{2}\right)\mathrm{d}\varepsilon, \quad (32)$$

where

$$\kappa_\pm = \frac{4|\Delta|^2 k_\pm}{(\varepsilon + i\delta)^2 - |\Delta|^2} \times \frac{[\zeta L k_\pm \cosh(k_\pm L/2) - g_s \sinh(k_\pm L/2)] \times [\zeta L k_\pm \sinh(k_\pm L/2) - g_s \cosh(k_\pm L/2)]}{\left[(\zeta L k_\pm + g_s)^2 e^{k_\pm L} - (\zeta L k_\pm - g_s)^2 e^{-k_\pm L}\right]^2}, \qquad (33)$$

with $k_\pm = \sqrt{-2i(\varepsilon \pm h + i\delta)/D}$.

Equation (32) is our main analytical result and allows for evaluation of the current at arbitrary exchange field strengths and magnetic field distributions. Of particular interest is the fact that the contribution from the vector potential and exchange field decouples. One consequence of this is that a constant magnetic field gives rise to a Fraunhofer pattern in the current regardless of the strength of the exchange field, as long as the magnetic field is weak enough. This can be seen from the fact that for a constant magnetic field $eA = -\pi\Phi_\perp y/\Phi_0 WL$, where $\Phi_\perp$ is the magnetic flux from the perpendicular field, so

$$I \propto \int_{-W/2}^{W/2} \sin\left(\phi_r - \phi_l - 2\pi \frac{\Phi_\perp y}{\Phi_0 W}\right) dy$$
$$= -W \sin(\phi_r - \phi_l) \frac{\sin(\pi\Phi_\perp/\Phi_0)}{\pi\Phi_\perp/\Phi_0}. \quad (34)$$

Figure 2 shows the critical current found analytically using eq. (32) for the case of no ripples, compared to the critical current obtained numerically from the full nonlinear Usadel equation. In addition to showing the agreement between the full solution and the analytical approximation, fig. 2 also shows that there is an exchange-driven 0-π transition at $h \approx 2\varepsilon_\mathrm{T}$, where

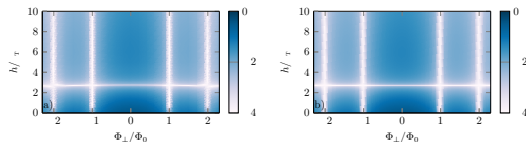$$\varepsilon_\mathrm{T} = \frac{D}{L^2} \qquad (35)$$

is the Thouless energy.

FIG. 2: Color plot of $\log_{10}(I_c/I_0)$, where I_c is the critical current and $I_0 = N_0 e W D^2/L^3$ for various exchange fields h and out-of-plane magnetic fluxes. Figure a) shows the solution found numerically from the full Usadel equation, and b) shows the analytical solution found using eq. (32). Here, $\varepsilon_\mathrm{T} = D/L^2$, $W = 10L$, $L = 6\xi$, $\delta/\Delta = 0.01$ and $B_x = B_y = 0$.

Since the contribution from the exchange field is independent of the vector potential, we can focus on how the magnetic field alters the critical current. With the vector potential given by eq. (4), we get

$$\int_{L/2}^{L/2} A(x, y)\, dx = B_y L \bar{\eta}(y) - \Phi_\perp \frac{y}{W}$$
$$+ B_x \int_0^y [\eta(L/2, \tilde{y}) - \eta(-L/2, \tilde{y})]\, d\tilde{y}, \quad (36)$$

where

$$\bar{\eta}(y) = \frac{1}{L} \int_{-L/2}^{L/2} \eta(x, y)\, dx \qquad (37)$$

is the longitudinally averaged height. From eq. (36) it can be observed that the contribution proportional to B_x is small for variations that are fast in the y-direction, since the integrand will oscillate rapidly, and small for very slow variations, which will contribute little to $\eta(L/2, y) - \eta(-L/2, y)$. Similarly, variations that are fast in the x-direction will contribute little to the term proportional to B_y. Otherwise, the contributions from the terms proportional to B_y and B_x is similar, so we set $B_x = 0$ in the following. We also set $\beta = 1000/\Delta$, corresponding to $T/T_c \approx 1.8 \times 10^{-3}$, where T_c is the critical temperature.

From eqs. (32) and (36) we can find how big the height variations must be in order to possibly cause a vanishing critical current at $\Phi_\perp = 0$. In order for the critical current to vanish, the argument of the sine function in eq. (32) must have variations of at least $\pi/2$. Otherwise, the phase difference, $\phi_r - \phi_l$, can be chosen such that the integrand is of one sign. This means that in order for there to be a root in the critical current at $\Phi_\perp = 0$, the in-plane magnetic field must be at least

$$B_y = \frac{\Phi_0}{4L(\max \bar{\eta} - \min \bar{\eta})}, \qquad (38)$$

assuming $B_x = 0$.

In order to apply eq. (32) to the case of rippled graphene with vector potential given by eq. (4), we need a model of the height distribution η of the ripples. From eq. (36) we find that it is reasonable to categorize ripples into short ripples and long ripples, depending on whether the wavelength is shorter or longer than $2L$. Ripples with wavelength shorter than $2L$ will have a smaller contribution to $\bar{\eta}$ in eq. (36) since the integrand oscillates between positive and negative values. For this reason, short ripples will contribute less to interference effects than long ripples with the same amplitude. On the other hand, faster variations in the y-direction gives a larger magnetic field component perpendicular to the graphene surface, and therefore a larger depairing effect. Short ripples are therefore expected to lead to larger deviations from the analytical approximation given by eq. (32). In particular, they are expected to cause a faster decay, which, as we will see, is also what happens.

In general, the height distribution will be a superposition of long and short ripples. We look first at only long ripples, then at only short ripples and finally at the combination of both short and long ripples. In order to simplify the presentation and analysis, we present solutions for height distributions that can be written as product of cosines. We obtain qualitatively similar result for more realistic, randomized height distributions.
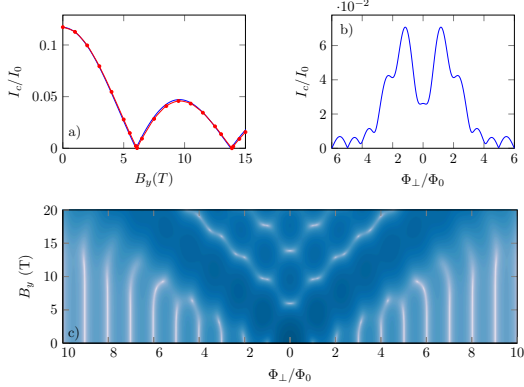
FIG. 3: Critical current I_c for various in-plane magnetic field strengths B_y and out-of-plane magnetic fluxes $\Phi_\perp$ for the height distribution given by eq. (39) with $n = 1$ and $m = 2$. Here, $I_0 = N_0 e W D^2/L^3$, $W = 10L$, $L = 10\xi = 400$ nm, $\eta_0 = 1$ nm, $\delta/\Delta = 0.02$ and $B_x = 0$. Figure a) shows the analytical solution of I_c against B_y for $\Phi_\perp = 0$ (blue line), compared to the numerical solution (red dots). b) shows analytical solution of I_c against $\Phi_\perp$ for $B_y = 5$ T and c) shows a logarithmically scaled color plot of analytical I_c where white means zero current and deep blue corresponds to large current.
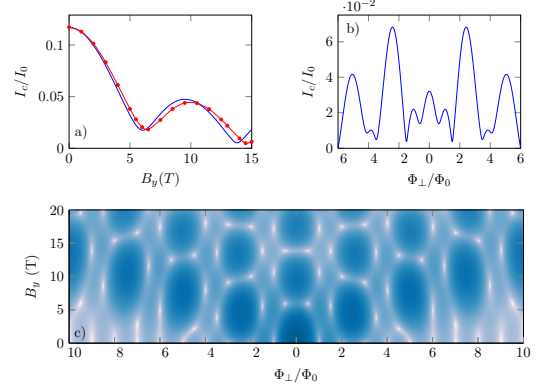

FIG. 4: Critical current I_c for various in-plane magnetic field strengths B_y and out-of-plane magnetic fluxes $\Phi_\perp$ for the height distribution given by eq. (39) with $n = 1$ and $m = 5$. Here, $I_0 = N_0 e W D^2/L^3$, $W = 10L$, $L = 10\xi = 400$ nm, $\eta_0 = 1$ nm, $\delta/\Delta = 0.02$ and $B_x = 0$. Figure a) shows the analytical solution of I_c against B_y for $\Phi_\perp = 0$ (blue line), compared to the numerical solution (red dots). b) shows analytical solution of I_c against $\Phi_\perp$ for $B_y = 5$ T and c) shows a logarithmically scaled color plot of analytical I_c where white means zero current and deep blue corresponds to large current.

To model n uniform ripples in the x-direction and m uniform ripples in the y-direction, we use the height distribution

$$\eta(x, y) = \frac{\eta_0}{2} \cos\left(n\pi \frac{x}{L}\right) \cos\left(m\pi \frac{y}{W}\right), \qquad (39)$$

where η_0 is the peak-to-peak height difference. Figures 3–5 show the critical current, given by eq. (9), for the height distribution in eq. (39) with $n = 1$ and $m = 2$, $m = 5$ and $m = 10$, respectively. The exchange field, h, is set to zero in order to isolate the orbital effect, such that it can be observed whether the orbital effect alone is sufficient to produce roots in the critical current. Physically, the situation with negligible exchange field would be the case if the Thouless energy, ε_T, is much larger than the Zeeman splitting $\mu_B B_y$, where μ_B is the Bohr magneton.

It can be seen from figs. 3–5 that a height variation of only 1 nm is sufficient to produce oscillations in the critical current. In particular, the critical current is zero for $\Phi_\perp = 0$ and finite B_y when $m = 2$ and $m = 10$. Both zeros satisfies eq. (38), which is $B_y = 2$ T in this case. We can conclude from this that a zero in the critical current of an SGS junction is not sufficient to identify an exchange-driven 0-π transition, since zeros can also be produced from the ripples.

Since the junction widths are equal in figs. 3–5, larger m means a larger orthogonal component from the in-plane magnet field. Consequently, the magnetic field strengths for which the weak field assumption, eq. (18), remains valid is reduced when m increases. This is reflected in the correspondence between the numerical simulations and the analytical predictions.

The color plots in figs. 3–5 c) show that the critical current has especially large maxima at $\Phi_\perp/\Phi_0 = km/2$ for integer k.

This is also reflected in figs. 3–5 b), which show that the lobe structure has strong maxima at $\Phi_\perp/\Phi_0 = m/2$. To understand why, note that the orbital part of the current can be written as a Fourier transform. That is,

$$
\begin{aligned}
I &= C(h) \int_{-W/2}^{W/2} \sin\left(\phi_r - \phi_l + 2\pi \frac{B_y L \bar{\eta}}{\Phi_0} - 2\pi \frac{\Phi_\perp y}{\Phi_0 W}\right) \mathrm{d}y \\
&= C(h) \, \mathrm{Im}\left\{ e^{i(\phi_r - \phi_l)} \int_{-W/2}^{W/2} \exp\left[2\pi i \left(\frac{B_y L \bar{\eta}}{\Phi_0} - \frac{\Phi_\perp y}{\Phi_0 W}\right)\right] \mathrm{d}y \right\},
\end{aligned}
\tag{40}
$$

where C is a function of the exchange field. Hence, the critical current can be written as

$$
I_c = C(h) \left| \mathcal{F}\left[\mathrm{rect}(y/W) e^{2\pi i B_y L \bar{\eta}/\Phi_0} \right] \left(\frac{2\pi \Phi_\perp}{W \Phi_0} \right) \right|, \tag{41}
$$

where rect is the rectangular function and $\mathcal{F}$ means Fourier transform. Accordingly, a Fourier analysis of the current response to out-of-plane magnetic fields can uncover properties of the ripple structure. In this case, $\bar{\eta}$ is a cosine with wavenumber $m\pi/W$, so it is reasonable that the Fourier transform peaks at $2\pi \Phi_\perp/W\Phi_0 = km\pi/W$ with strengths that depends on B_y.

Figures 3–5 a) also give clues to how the full solution of the Usadel equation deviates from eq. (32) when the magnetic field is strong. Two things seem to happen when the flux density is strong. First, compared to the analytical solution, the full solution decays more rapidly as B_y increases. That the critical current decays faster than the analytical solution predicts is unsurprising, since we neglected the depairing effect of the magnetic field in our derivation of eq. (32).
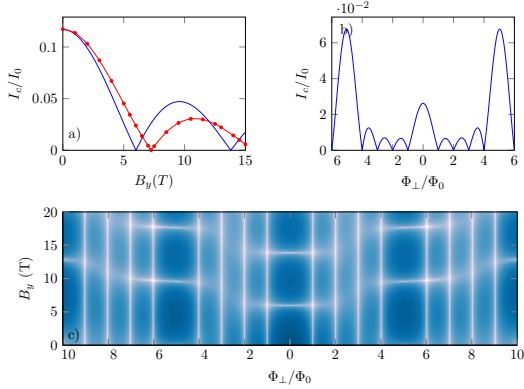
FIG. 5: Critical current I_c for various in-plane magnetic field strengths B_y and out-of-plane magnetic fluxes $\Phi_\perp$ for the height distribution given by eq. (39) with $n = 1$ and $m = 10$. Here, $I_0 = N_0 e W D^2 / L^3$, $W = 10L$, $L = 10\xi = 400$ nm, $\eta_0 = 1$ nm, $\delta/\Delta = 0.02$ and $B_x = 0$. Figure a) shows the analytical solution of I_c against B_y for $\Phi_\perp = 0$ (blue line), compared to the numerical solution (red dots). b) shows analytical solution of I_c against $\Phi_\perp$ for $B_y = 5$ T and c) shows a logarithmically scaled color plot of analytical I_c where white means zero current and deep blue corresponds to large current.

Second, the functional dependence on B_y is slower in the numerical case, in the sense that roots and extremal values in the critical current are skewed towards larger values of B_y. A plausible explanation for this phenomenon is that the full solution varies more slowly in the y-direction compared to the analytical approximation in eq. (23). The analytical solution has $\partial \hat{f}/\partial y \propto B$, but it neglects the boundary condition that demands $\partial \hat{f}/\partial y = 0$ when $y = \pm W/2$. Hence, it is possible that the analytical solution overestimates the variation of f with respect to y, at least close to $y = \pm W/2$. The roots in the critical current occur because the magnetic field creates mutually cancelling oscillations in the current density as a function of y. If the analytical approximation overestimates how fast these oscillations occur, it will underestimate the magnetic field required to give $I_c = 0$. The faster decay, but slower variation is also exactly what happens in the case of uniform magnetic fields, as can be seen from fig. 3 in Ref. [24].

Moving on to short ripples, fig. 6 shows the critical current for the distribution given by eq. (39) with $n = 11$, $m = 10$ and $\eta_0 = 1$ nm. With $L = 400$ nm, this corresponds to a ripple length of 40 nm, which is comparable to the short ripples observed in graphene on SiO$_2$ [20]. The exchange field is again set to 0. What matters for the analytical approximation is the longitudinally averaged height, $\bar{\eta}$, which in this case is small because of the rapid oscillations. Hence, the analytical approximation predicts very little change in the critical current at $\Phi_\perp = 0$. On the other hand, the orbital depairing effect is quite large because of the short ripples, which is reflected in the decay of the critical current observed in the numerical solution of the full Usadel equations.

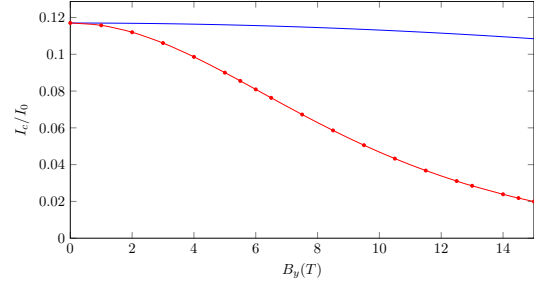Finally, fig. 7 shows the critical current for combinations

FIG. 6: Critical current I_c for $B_\perp = 0$ and various in-plane magnetic field strengths B_y with the height distribution given by eq. (39) with $n = 11$ and $m = 10$. Here, $I_0 = N_0 e W D^2 / L^3$, $W = L = 10\xi = 400$ nm, $\eta_0 = 1$ nm, $\delta/\Delta = 0.02$ and $B_x = 0$. The blue line shows the analytical solution, as found by eq. (32), and the red line with dots shows the numerical solution found by solving the full Usadel equation.

of short and long ripples, both with and without a non-zero exchange field. The height distribution is in this case given by

$$\eta = 1 \text{ nm} \times \cos\left(2\pi \frac{y}{W}\right) + A \cos\left(n\pi \frac{x}{L}\right) \cos\left(n\pi \frac{y}{L}\right), \quad (42)$$

where $n = 4$ for "hBN" and "Large" and $n = 10$ for "SiO$_2$". The amplitude of the short ripples are $A = 0.1$ nm, $A = 0.5$ nm, $A = 2$ nm for "hBN", "SiO$_2$" and "Large", respectively. The values for "SiO$_2$" and "hBN" are chosen such that the short ripple sizes correspond to the observed values for SiO$_2$ and hBN [20]. The values for "Large" are chosen such that amplitudes of the short ripples are twice as large as the long ripples. In this case the orthogonal component of the magnetic field is much too high for the analytical solution to give accurate results.

Since n is even, the analytical solution given by eq. (32) is equal for the three cases. The only difference is the magnitude of the additional magnetic flux density that comes from the short ripples. As mentioned above, we should expect a faster decay for larger and faster ripples. This is indeed also what we observe from the numerical results in fig. 7. Interestingly, the location of the roots is not substantially altered by the short ripples. Even in the lowermost panels, where the short ripples are twice as large as the long ripples, the roots in the numerical solution occurs not far from the values of B_y predicted by the analytical solution, even if the amplitude decays much faster.

Long ripples, as we have seen, can give rise to interference effects that produce oscillations and possibly roots in the critical current. Short ripples, on the other hand, increase the magnetic flux density and can lead to a substantial magnetic depairing effect, which manifest as a rapidly decaying critical current. Hence, the combined effect of short and long ripples can yield a rapidly decaying critical current with zeros, much like what one would expect from a ferromagnet undergoing a 0-π transition.

From fig. 7 it can also be observed that the deviation between the analytical and numerical solutions is smaller when the exchange field is non-zero. This is as expected, since neglecting the contribution from B in eq. (17) is a better approximation
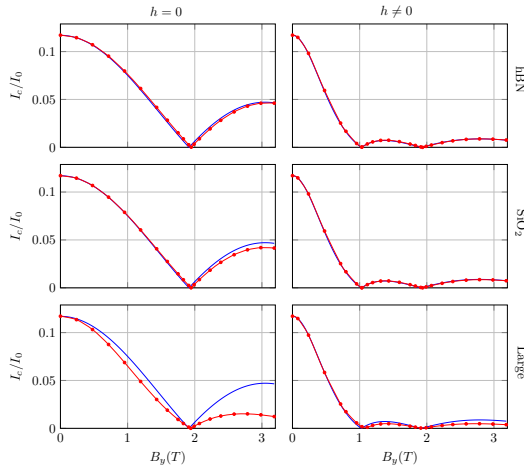
FIG. 7: Critical current I_c for $B_\perp = 0$ and various in-plane magnetic field strengths B_y with the height distribution given by eq. (42) with $(A, N) = (0.1\,\text{nm}, 4)$, $(0.5\,\text{nm}, 10)$ and $(2\,\text{nm}, 4)$, respectively from top to bottom. The exchange field is $h = 0$ in the left panels and $h = \mu_B B_y$ in the right panels, where μ_B is the Bohr magneton. Here, $I_0 = N_0 e W D^2/L^3$, $W = 10L$, $L = 10\xi = 400\,\text{nm}$, $\delta/\Delta = 0.02$, $\Delta = 1.5\,\text{meV}$ and $B_x = 0$. The blue line shows the analytical solution, as found by eq. (32), and the red line with dots shows the numerical solution found by solving the full Usadel equation.

when the self-energy $\hat{\Sigma}$ is larger. Note that in fig. 7, the presence of the exchange field induces a 0-π transition around $B_y = 1$ T, which manifests as a root in the critical current.

Since the ripples and the exchange field both give rise to oscillating and decaying critical currents, it is useful determine whether a 0-π transition is expected to occur before or after a possible zero in the critical current coming from ripples. The exact values of B_y at which these events take place will in general depend on several parameters, but we can give some order of magnitude estimates based on eq. (32) and numerical simulations. The first 0-π transition typically occurs around $h = 2\varepsilon_\text{T}$, but can occur at larger values if the inelastic scattering time, $1/\delta$, is small. Inserting the definition of the Thouless energy, ε_T, and using that $h = \mu_B B_y$, this means that the Zeeman driven 0-π transition occurs at

$$B_y \approx \frac{2D}{\mu_B L^2}. \tag{43}$$

Equation (38) gives a minimal value for B_y at which a zero can be produced from the interference effect that is due to ripples. In the numerical result presented here, we see that the zero occurs for a value of B_y that is about three times larger. An order of magnitude estimate is that, for long ripples with peak-to-peak height of η_0, the first zero in the critical current can occur at around

$$B_y \approx \frac{\Phi_0}{\eta_0 L}. \tag{44}$$

Notice that eqs. (43) and (44) scales differently with junction length L. Therefore, it is more plausible that an observed zero in the critical current correspond to a 0-π transition when the junction is long. Alternatively, one could try to limit the presence of variations in the y-direction that are longer than L by making $W \ll L$.

From figs. 3–5 we also observe that the ripples can substantially alter the Fraunhofer lobe structure found when varying $B_\perp$, while fig. 2 shows that the Fraunhofer pattern is unaltered when the effect of ripples is negligible. Hence, investigating how I_c depend on $B_\perp$ could also be useful when identifying 0-π transitions. As long as the junction width and diffusivity are approximately constant, a 0-π transition will give rise to a vanishing critical current for all values of out-of-plane magnetic flux densities $B_\perp$. If in addition the effect of ripples is small, one should expect that the critical current as a function of $B_\perp$ is a Fraunhofer pattern at any constant value of the in-plane magnetic field $B_\parallel$. Accordingly, determining whether the minima in critical current as a function of $B_\perp$ and $B_\parallel$ are straight lines, as in fig. 2, or curved, as in figs. 3–5, can give clues as to whether ripples are important. If ripples are important, eq. (41) could give insight to their structure.

IV. CONCLUSION

We have solved the Usadel equation analytically in the presence of an exchange field and an arbitrary magnetic field distribution, under the assumption of a weak proximity effect and a weak magnetic field. The solution has been applied to SGS-junctions with the combined Zeeman effect and orbital effect coming from an in-plane magnetic field. Deviations from the analytical solution at large magnetic fields have been studied numerically. We find that the orbital effect that results from a curvature in the graphene can produce a critical current response that is similar to what one would get by increasing the exchange field. Slow variations in the graphene height distributions give rise to interference effects that produce oscillations in the critical current, while rapid variations cause larger orbital depairing effects that lead to a faster critical current decay rate.

Since both the Zeeman splitting and orbital effects in rippled graphene can cause similar behaviour, extra care must be taken when identifying possible 0-π transitions. The interference effect from ripples is reduced if the width of the junction is much smaller than the length. In addition to reducing the relative effect of ripples compared to the Zeeman splitting, which is achieved by increasing the length of the junction and minimizing the height variations, it could also be useful to look at how the critical current varies with a perpendicular magnetic field. The effect of ripples, if present, will then typically alter the Fraunhofer pattern observed at zero in-plane magnetic field. Because slow height variations are difficult to detect using surface probe techniques, we suggest the use of parallel magnetic field as a means to probe the presence of such variations.

Acknowledgments

[1] M. Eschrig, Rep. Prog. Phys. **78**, 104501 (2015).
[2] J. Linder and J. W. A. Robinson, Nat. Phys. **11**, 307 (2015).
[3] G.-H. Lee and H.-J. Lee, Rep. Prog. Phys. **81**, 056502 (2018).
[4] P. Kumaravadivel and X. Du, Sci. Rep. **6**, 24274 (2016).
[5] U. C. Coskun, M. Brenner, T. Hymel, V. Vakaryuk, A. Levchenko, and A. Bezryadin, Phys. Rev. Lett. **108**, 097003 (2012).
[6] K. Komatsu, C. Li, S. Autier-Laurent, H. Bouchiat, and S. Guéron, Phys. Rev. B **86**, 115412 (2012).
[7] H. B. Heersche, P. Jarillo-Herrero, J. B. Oostinga, L. M. K. Vandersypen, and A. F. Morpurgo, Nature **446**, 56 (2007).
[8] F. Amet, C. T. Ke, I. V. Borzenets, J. Wang, K. Watanabe, T. Taniguchi, R. S. Deacon, M. Yamamoto, Y. Bomze, S. Tarucha, and G. Finkelstein, Science **352**, 966 (2016).
[9] J. Liu, H. Liu, J. Song, Q.-F. Sun, and X. C. Xie, Phys. Rev. B **96**, 045401 (2017).
[10] P. Fulde and R. A. Ferrell, Phys. Rev. **135**, A550 (1964).
[11] A. I. Larkin and Y. N. Ovchinnikov, Sov. Phys. JETP **20**, 762 (1965).
[12] A. I. Buzdin, Rev. Mod. Phys. **77**, 935 (2005).
[13] G. Blatter, V. B. Geshkenbein, and L. B. Ioffe, Phys. Rev. B **63**, 174511 (2001).
[14] T. Yamashita, K. Tanikawa, S. Takahashi, and S. Maekawa, Phys. Rev. Lett. **95**, 097001 (2005).
[15] M. I. Khabipov, D. V. Balashov, F. Maibaum, A. B. Zorin, V. A. Oboznov, V. V. Bolginov, A. N. Rossolenko, and V. V. Ryazanov, Supercond. Sci. and Technol. **23**, 045032 (2010).
[16] A. K. Feofanov, V. A. Oboznov, V. V. Bol'ginov, J. Lisenfeld, S. Poletto, V. V. Ryazanov, A. N. Rossolenko, M. Khabipov, D. Balashov, A. B. Zorin, V. P. K. P. N. Dmitriev, and A. V. Ustinov, Nat. Phys. **6**, 593 (2010).
[17] A. V. Ustinov and V. K. Kaplunenko, J. Appl. Phys. **94**, 5405 (2003).
[18] E. C. Gingrich, B. M. Niedzielski, J. A. Glick, Y. Wang, D. L. Miller, R. Loloee, W. P. P. Jr, and N. O. Birge, **12**, 564 (2016).
[19] C. Li, B. de Ronde, J. de Boer, J. Ridderbos, F. Zwanenburg, Y. Huang, A. Golubov, and A. Brinkman, Phys. Rev. Lett. **123**, 026802 (2019).
[20] J. Xue, J. Sanchez-Yamagishi, D. Bulmash, P. Jacquod, A. Deshpande, K. Watanabe, T. Taniguchi, P. Jarillo-Herrero, and B. J. LeRoy, Nat. Mater. **10**, 282 (2011).
[21] M. B. Lundeberg and J. A. Folk, Phys. Rev. Lett. **105**, 146804 (2010).
[22] S. Zihlmann, P. Makk, M. K. Rehmann, L. Wang, M. Kedves, D. Indolese, K. Watanabe, T. Taniguchi, D. M. Zumbühl, and C. Schönenberger, arXiv:2004.02690 [cond-mat.mes-hall] (2020).
[23] V. A. Oboznov, V. V. Bol'ginov, A. K. Feofanov, V. V. Ryazanov, and A. I. Buzdin, Phys. Rev. Lett. **96**, 197003 (2006).
[24] F. Bergeret and J. Cuevas, J. Low. Temp. Phys. **153**, 304 (2008).
[25] K. D. Usadel, Phys. Rev. Lett. **25**, 507 (1970).
[26] J. Rammer and H. Smith, Rev. Mod. Phys. **58**, 323 (1986).
[27] S. Hart, H. Ren, M. Kosowsky, G. Ben-Shach, P. Leubner, C. Brüne, H. Buhmann, L. W. Molenkamp, B. I. Halperin, and A. Yacoby, Nat. Phys. **13**, 87 (2017).
[28] A. Q. Chen, M. J. Park, S. T. Gill, Y. Xiao, D. Reig-i Plessis, G. J. MacDougall, M. J. Gilbert, and N. Mason, Nat. Commun. **9**, 1 (2018).
[29] C. Li, S. Guéron, A. Chepelianskii, and H. Bouchiat, Phys. Rev. B **94**, 115405 (2016).
[30] J.-S. Jeong, J. Shin, and H.-W. Lee, Phys. Rev. B **84**, 195457 (2011).
[31] M. Y. Kuprianov and V. Lukichev, J. Exp. Theor. Phys. **94**, 149 (1988).
[32] E. H. Fyhn and J. Linder, Phys. Rev. B **100**, 214503 (2019).
[33] W. Belzig, F. K. Wilhelm, C. Bruder, G. Schön, and A. D. Zaikin, Superlattices Microstruct. **25**, 1251 (1999).
[34] M. Amundsen and J. Linder, Sci. Rep. **6**, 22765 (2016).
[35] R. Burden and J. Faires, *Numerical Analysis* (Brooks/Cole, Cengage Learning, 2011).
[36] J. Revels, M. Lubin, and T. Papamarkou, arXiv:1607.07892 [cs.MS] (2016).